



HAL
open science

Robust Control for MEMS Gyroscopes

Fabrício Saggin

► **To cite this version:**

Fabrício Saggin. Robust Control for MEMS Gyroscopes. Automatic Control Engineering. Ecole Centrale Lyon, 2021. English. NNT: . tel-03363650v1

HAL Id: tel-03363650

<https://hal.science/tel-03363650v1>

Submitted on 4 Oct 2021 (v1), last revised 1 Feb 2022 (v3)

HAL is a multi-disciplinary open access archive for the deposit and dissemination of scientific research documents, whether they are published or not. The documents may come from teaching and research institutions in France or abroad, or from public or private research centers.

L'archive ouverte pluridisciplinaire **HAL**, est destinée au dépôt et à la diffusion de documents scientifiques de niveau recherche, publiés ou non, émanant des établissements d'enseignement et de recherche français ou étrangers, des laboratoires publics ou privés.



ÉCOLE
CENTRALE LYON

N° d'ordre NNT : xxx

THÈSE DE DOCTORAT DE L'UNIVERSITÉ DE LYON
opérée au sein de
l'École Centrale de Lyon

Spécialité : **Automatique**

préparée dans le laboratoire **Ampère (UMR 5005)**

dans le cadre de l'École Doctorale (**ED160**)
Électronique, Électrotechnique, Automatique (EEA)

Soutenance prévue le 13/09/2021 (sous réserve de l'avis des rapporteurs), par :

Fabrizio SAGGIN

Robust Control for MEMS Gyroscopes

Devant le jury composé de :

M. Alexandre TROFINO NETO, Professeur, UFSC, Florianópolis, Brésil	Rapporteur
M. Jean-Marc BIANNIC, Directeur de Recherche, ONERA	Rapporteur
Mme. Suzanne LESECQ, Directrice de Recherche, CEA	Examinatrice
M. Jérôme JUILLARD, Professeur, CentraleSupélec	Examineur
M. Christophe LE BLANC, Ingénieur R&D Électronique, Asygn	Invité
M. Guillaume PAPIN, <i>System Architect</i> , TDK Tronics	Invité
M. Anton KORNIENKO, Maître de Conférence, École Centrale de Lyon	Encadrant
M. Xavier BOMBOIS, Directeur de Recherche, CNRS	Co-directeur de thèse
M. Gérard SCORLETTI, Professeur, École Centrale de Lyon	Directeur de thèse

Abstract

Fabrício SAGGIN

Robust Control for MEMS Gyroscopes

Micro-electro-mechanical systems (MEMS) gyroscopes are micromachined devices used to measure the angular rate of objects. They are ubiquitous in many applications thanks to their low cost, low power consumption, and ease of integration into electronic devices. However, when compared to traditional gyroscopes, MEMS gyroscopes have degraded performance. To improve their performance, feedback control loops are widely used.

MEMS gyroscopes are composed of two perpendicular vibrating modes: the drive mode and the sense mode. The working principle is based on the transfer of energy between these modes caused by the Coriolis force, which is proportional to the angular rate. Then, by controlling the drive mode oscillations with an excitation frequency and by estimating the Coriolis force, the angular rate can be recovered. Moreover, the better the drive mode oscillations are controlled and the Coriolis force is estimated, the better is the measure.

The control architectures are usually optimized in terms of cost and simple implementation. Most of them are based on the complex envelope (amplitude and phase) of the signals, such that simple PI controllers can be used to independently regulate the amplitude and phase of the oscillations along each axis. To extract the complex envelope of the oscillating signals, nonlinear elements are introduced in the control loops. Moreover, the couplings between the drive and sense modes, as well as the dependence on environmental conditions, are not taken into account. The associated methods do not provide guarantees of stability or performance for the closed-loop system.

An alternative approach is to consider the classical feedback control architecture, referred to as the direct control architecture, based on the signals themselves instead of their complex envelope. For this architecture, advanced control techniques have been developed for vibration control of mechanical systems. The potential interest is to explicitly take into account the different couplings and the dependence on the environmental condition, with formal guarantees of stability and performance. Nevertheless, their applicability to MEMS gyroscopes, including implementability, is still an open question. A possible reason is the inherent complexity of the controllers.

In this thesis, we aim to propose design methods for both control architectures, guaranteeing stability and a certain performance level for the MEMS gyroscope, and to experimentally validate the obtained controllers.

In the first part, we review the literature on MEMS gyroscopes and define the key performance indicators of the sensor, which are not usually connected to the closed-loop performance specifications. Then, by using an input-output approach, we establish the relationships

between the performance indicators and the closed-loop behavior. These relationships are a valuable tool for the control design and constitute the first contribution of this thesis. Based on these relationships, we then propose design methods for the direct control architecture. First, we consider the case where the MEMS gyroscope works with a fixed operating condition and the excitation frequency, which is set to the drive-mode resonance one. In this context, the control objectives include the tracking of a sinusoidal signal and standard \mathcal{H}_∞ synthesis is applied for the controller design. The excitation frequency, however, may vary over time. A control objective is then to track a “time-varying-frequency sinusoidal” signal. We reveal that this particular problem can be formulated as a weighted \mathcal{L}_2 criterion with a new class of weighting functions modeling “time-varying-frequency sinusoidal” signals.

We then revisit the theory of complex envelopes, which allows us to define a formal framework for the analysis of the envelope-based control architectures. If the complex envelope is ideally measured in real time, we establish links between the direct control approach and the envelope-based ones. These links reveal that the performances achieved with both strategies are equivalent. When the signal envelope cannot be ideally measured, the same framework allows us to precisely model the nonidealities and to design controllers with formal guarantees of stability. These results are also an important contribution of this thesis.

The last part is dedicated to the controller design for their digital implementation on two platforms: a flexible one, which can implement complex control architectures; and a platform designed for the so-called electro-mechanical $\Sigma\Delta$, which is a very particular control architecture. For both platforms, the practical results validate the proposed methods.

Résumé

Fabrizio SAGGIN

Robust Control for MEMS Gyroscopes

Les gyromètres MEMS (de l'anglais, *micro-electro-mechanical system*) sont des dispositifs micro-usinés utilisés pour mesurer la vitesse de rotation des objets. Ils sont omniprésents dans de nombreuses applications grâce à leur faible coût, leur faible consommation d'énergie et leur facilité d'intégration dans les dispositifs électroniques. Cependant, par rapport aux gyromètres traditionnels, les gyromètres MEMS ont une performance dégradée. Pour l'améliorer, des boucles de commande sont largement utilisées.

Les gyromètres MEMS sont composés de deux modes de vibration perpendiculaires : le mode *drive* et le mode *sense*. Le principe de fonctionnement est basé sur le transfert d'énergie entre ces modes causé par la force de Coriolis, qui est proportionnelle à la vitesse angulaire. Ainsi, en asservissant les oscillations du mode *drive* avec une fréquence d'excitation et en estimant la force de Coriolis, la vitesse angulaire peut être récupérée. De plus, mieux les oscillations du mode *drive* sont asservies et mieux la force de Coriolis est estimée, meilleure est la mesure.

Les architectures de commande sont généralement optimisées en termes de coût et de simplicité d'implémentation. La plupart d'entre elles sont basées sur l'enveloppe complexe (amplitude et phase) des signaux, de sorte que de simples correcteurs PI peuvent être utilisés pour réguler indépendamment l'amplitude et la phase des oscillations le long de chaque axe. Pour extraire l'enveloppe complexe des signaux oscillants, des éléments non linéaires sont introduits dans les boucles de commande. De plus, les couplages entre les modes *drive* et *sense*, ainsi que la dépendance aux conditions environnementales, ne sont pas pris en compte. Les méthodes associées ne fournissent pas de garanties de stabilité ou de performance pour le système en boucle fermée.

Une autre approche consiste à considérer l'architecture classique de rétroaction, appelée architecture de commande directe, basée sur les signaux eux-mêmes plutôt que sur leur enveloppe complexe. Pour cette architecture, des techniques d'automatique avancée ont été développées pour le contrôle des vibrations des systèmes mécaniques. L'intérêt potentiel est de prendre en compte explicitement les différents couplages et la dépendance aux conditions environnementales, avec des garanties formelles de stabilité et de performance. Néanmoins, leur applicabilité aux gyromètres MEMS, y compris leur implémentation, reste une question ouverte. Une raison possible est la complexité inhérente des correcteurs.

Dans cette thèse, nous avons pour objectif de proposer des méthodes de conception pour les deux architectures de commande, garantissant la stabilité et un certain niveau de performance pour le gyromètre MEMS, et de valider expérimentalement les correcteurs obtenus.

Dans la première partie, nous révisons la littérature sur les gyromètres MEMS et définissons les indicateurs clés de performance du capteur, qui ne sont généralement pas liés aux spécifications de performance en boucle fermée. Ensuite, en utilisant une approche entrée-sortie, nous établissons les relations entre les indicateurs de performance et le comportement en boucle fermée. Ces relations sont un outil précieux pour la conception de la commande et constituent la première contribution de cette thèse. Sur la base de ces relations, nous proposons ensuite des méthodes de conception pour l'architecture de commande directe. Tout d'abord, nous considérons le cas où le gyromètre MEMS fonctionne avec une condition de fonctionnement fixe et une fréquence d'excitation qui est fixée à la fréquence de résonance du mode *drive*. Dans ce contexte, les objectifs de contrôle incluent la poursuite d'un signal sinusoïdal et la synthèse \mathcal{H}_∞ standard est appliquée pour la conception du correcteur. Cependant, la fréquence d'excitation peut varier dans le temps. L'objectif de la commande est alors de suivre un signal "sinusoïdal à fréquence variable". Nous révélons que ce problème particulier peut être formulé comme un critère \mathcal{L}_2 pondéré avec une nouvelle classe de fonctions de pondération modélisant les signaux "sinusoïdaux à fréquence variable".

Nous revisitons ensuite la théorie des enveloppes complexes, ce qui nous permet de définir un cadre formel pour l'analyse des architectures de commande basées sur l'enveloppe. Si l'enveloppe complexe est idéalement mesurée en temps réel, nous établissons des liens entre l'approche de commande directe et celle basée sur l'enveloppe. Ces liens révèlent que les performances obtenues avec les deux stratégies sont équivalentes. Lorsque l'enveloppe du signal ne peut pas être idéalement mesurée, le même cadre nous permet de modéliser précisément les non-idéalités et de concevoir des correcteurs avec des garanties formelles de stabilité. Ces résultats constituent également une contribution importante de cette thèse.

La dernière partie est consacrée à la conception des correcteurs en vue de leur implémentation numérique sur deux plateformes : une plateforme flexible, qui permet d'implémenter des architectures de commande complexes, et une plateforme conçue pour le $\Sigma\Delta$ électromécanique, qui est une architecture de commande particulière. Pour les deux plateformes, les résultats pratiques valident les méthodes proposées.

Resumo

Fabrcio SAGGIN

Robust Control for MEMS Gyroscopes

Os giroscópios MEMS (do inglês, *micro-electro-mechanical system*) são dispositivos micro-maquinados usados para medir a velocidade angular de objetos. Eles são onipresentes em muitas aplicações graças a seu baixo custo, baixo consumo de energia e facilidade de integração em dispositivos eletrônicos. Entretanto, quando comparados aos giroscópios tradicionais, os giroscópios MEMS têm desempenho degradado. Para melhorar seu desempenho, malhas de controle são amplamente utilizados.

Os giroscópios MEMS são compostos de dois modos de vibração perpendiculares: o modo de atuação e o modo de detecção. O princípio de funcionamento é baseado na transferência de energia entre esses modos causada pela força de Coriolis, que é proporcional à velocidade angular. Então, controlando as oscilações do modo de atuação com uma frequência de excitação e estimando a força de Coriolis, a velocidade angular pode ser calculada. Além disso, quanto melhor forem controladas as oscilações do modo de atuação e estimada a força de Coriolis, melhor será a medida.

As arquiteturas de controle são normalmente otimizadas em termos de custo e simples implementação. A maioria delas é baseada no envelope complexo (amplitude e fase) dos sinais, de modo que simples controladores PI podem ser usados para regular independentemente a amplitude e fase das oscilações em cada eixo. Para extrair o envelope complexo dos sinais oscilantes, são introduzidos elementos não lineares nas malhas de controle. Além disso, não são levados em conta os acoplamentos entre os modos de atuação e de detecção, nem a dependência nas condições do ambiente. Os métodos associados não oferecem garantias de estabilidade ou desempenho para o sistema em malha fechada.

Uma abordagem alternativa é considerar a arquitetura clássica de controle, chamada de arquitetura de controle direto, baseada nos próprios sinais em vez de seu envelope complexo. Para esta arquitetura, foram desenvolvidas técnicas avançadas de controle para o controle de vibração de sistemas mecânicos. O interesse potencial é levar em conta explicitamente os diferentes acoplamentos e a dependência nas condições do ambiente, com garantias formais de estabilidade e desempenho. No entanto, sua aplicabilidade aos giroscópios MEMS, incluindo a implementabilidade, ainda é uma questão em aberto. Uma razão possível é a complexidade inerente dos controladores.

Nesta tese, propomos métodos de sintonia de controladores para ambas arquiteturas, garantindo estabilidade e um certo nível de desempenho para o giroscópio MEMS, e validamos experimentalmente os controladores obtidos.

Na primeira parte, revisamos a literatura sobre os giroscópios MEMS e definimos os principais indicadores de desempenho do sensor, que normalmente não estão associados às

especificações de desempenho em malha fechada. Depois, usando uma abordagem entrada-saída, estabelecemos as relações entre os indicadores de desempenho e o comportamento do sistema em malha fechada. Estas relações são uma ferramenta valiosa para o projeto de controle e constituem a primeira contribuição desta tese. Com base nestas relações, propomos métodos de projeto para a arquitetura de controle direto. Primeiro, consideramos o caso em que o giroscópio MEMS trabalha com uma condição de operação fixa e uma frequência de excitação definida pela frequência de ressonância do modo de atuação. Neste contexto, os objetivos de controle incluem o seguimento de um sinal sinusoidal e a síntese \mathcal{H}_∞ é aplicada para o projeto do controlador. A frequência de excitação, entretanto, pode variar ao longo do tempo. Um objetivo de controle é então rastrear um sinal “sinusoidal de frequência variável”. Revelamos que este problema particular pode ser formulado como um critério \mathcal{L}_2 ponderado com uma nova classe de funções de ponderação modelando sinais “sinusoidais de frequência variável”.

Revisitamos então a teoria dos envelopes complexos, o que nos permite definir uma base formal para a análise das arquiteturas de controle baseadas em envelopes. Se o envelope complexo for medido idealmente em tempo real, estabelecemos ligações entre a abordagem de controle direto e a abordagem baseada em envelopes. Estas ligações revelam que os desempenhos alcançados com ambas as estratégias são equivalentes. Quando o envelope de sinal não pode ser medido idealmente, a mesma base nos permite modelar com precisão as não idealidades e projetar controladores com garantias formais de estabilidade. Estes resultados também são uma contribuição importante desta tese.

A última parte é dedicada ao projeto do controlador para sua implementação digital em duas plataformas: uma flexível, que pode implementar arquiteturas de controle complexas; e uma plataforma projetada para o chamado $\Sigma\Delta$ eletromecânico, que é uma arquitetura de controle bastante particular. Para ambas as plataformas, os resultados práticos validam os métodos propostos.

Contents

Contents	ix
List of Abbreviations	xiii
Notation	xv
List of Symbols	xvii
1 General Introduction	1
1.1 Context and Motivations	1
1.2 Scope and Contributions	4
1.3 Project Next4MEMS	6
1.4 List of Publications and Collaborations	7
1.5 Organization of this Document	8
2 MEMS Gyroscopes and the Control Challenges	11
2.1 A Background on MEMS Gyroscopes	11
2.1.1 Working Principle: a Foucault Pendulum in a Chip	12
2.1.2 Ideal MEMS Gyroscope and Closed-Loop Operation	14
2.1.3 Actuation and Instrumentation	18
2.1.4 Ideal Synchronous Demodulation and Angular Rate Estimation	23
2.1.5 Real (Nonideal) MEMS Gyroscopes	27
2.1.6 Global Performance Indicators of MEMS Gyroscopes	36
2.2 Control Architectures in the Literature	39
2.2.1 Drive-Mode Control Architectures	39
2.2.2 Sense-Mode Control Architectures	44
2.2.3 Multivariable Control Architectures	47
2.2.4 Summary of the Control Architectures	48
2.3 Experimental Setups	49
2.3.1 AS3125-SDK: a Flexible Sensor Development Kit	51
2.3.2 Tronics' Platform with Dedicated ASIC	52
2.4 Research Questions	53
3 From Global Performance Specifications to Closed-Loop Specifications	55
3.1 Problem Statement	56
3.1.1 System Description and Control Objectives	56
3.1.2 Analysis Model	59
3.1.3 Analysis Problems	60
3.2 Analysis of the Angular Rate Estimate $\hat{\Omega}_z$	62
3.2.1 Noiseless Analysis	62
3.2.2 Analysis with Respect to the Noise	64

3.3	Closed-loop Specifications for Nominal Performance	64
3.3.1	Closed-Loop Specifications for Conventional Closed-loop Operation	65
3.3.2	Closed-Loop Specifications for SFNL	68
3.3.3	Closed-Loop Specifications for Bandwidth	69
3.3.4	Closed-Loop Specifications Related to Noise	70
3.4	Closed-loop Specifications for Robust Stability	71
3.4.1	Weighted Small Gain Theorem	72
3.4.2	Robust Stability Against Additive Uncertainties	72
3.5	Summary of the Chapter	73
4	Direct Control I: A Robust Approach	75
4.1	\mathcal{H}_∞ Synthesis: Principles	76
4.1.1	Standard \mathcal{H}_∞ Control Problem	76
4.1.2	Defining an \mathcal{H}_∞ Criterion	77
4.1.3	Solving the Standard \mathcal{H}_∞ Control Problem	81
4.1.4	\mathcal{H}_∞ Synthesis: Summary	81
4.2	SISO Control Architectures	82
4.2.1	Drive-Mode Control	82
4.2.2	Sense-Mode Control	91
4.3	MIMO Control Architectures	97
4.3.1	MIMO 2DoF Control Architecture	97
4.3.2	MIMO 2DoF Control Architecture with Joint Estimation	103
4.4	Validation of the Proposed Solutions	110
4.4.1	Assessing the Stability of the Closed-Loop System	110
4.4.2	Validation Through Simulation	111
4.5	Summary of the Chapter	115
5	Direct Control II: Toward a Time-Varying Solution	117
5.1	Problem Statement	119
5.2	Main Result: \mathcal{L}_2 Criterion and LTV Weighting Functions	122
5.2.1	The \mathcal{L}_2 Criterion	122
5.2.2	A New Class of LTV Weighting Functions	124
5.2.3	LPV Control Problem	128
5.3	Solving the LPV Control Problem: a Polytopic Approach	129
5.3.1	Some Definitions in the LPV Framework	130
5.3.2	The Standard LPV Synthesis	131
5.3.3	Solution to Problem 5.1	132
5.4	Numerical Results and Simulation	132
5.5	Summary and Conclusions of the Chapter	139
6	Envelope-Based Control: Bringing the Dynamics to Low Frequency	141
6.1	Problem Statement	143
6.2	System Modeling Through Dynamic Phasors	145
6.2.1	Dynamic Phasor Modeling	145
6.2.2	Properties of the Dynamic Phasor Model	149
6.3	Dynamic Phasor Control	156
6.3.1	Connections Between Direct Control and Dynamic Phasor Control	157
6.4	Implementation of the Operators s2c and s2p	159
6.4.1	Uniqueness Between a Modulated Signal and its Dynamic Phasor	160
6.4.2	Computing the Analytic Signal Associated to y	161

6.4.3	Equivalence Between Synchronous Demodulation and Hilbert Transform	162
6.4.4	Modeling the Nonideal Synchronous Demodulation	165
6.4.5	On the Synchronous Demodulation with Time-Varying Frequency	166
6.5	Dynamic Phasor Control with Nonideal Operator $s2c$	167
6.6	Summary of the Chapter	172
7	Digital Implementation of the Direct Control Architecture	175
7.1	System Description and Problem Statement	176
7.2	Modeling the System and Dealing with its Nonidealities	178
7.2.1	System Modeling	178
7.2.2	Electrical Coupling Compensation	178
7.2.3	Dealing with the Input Nonlinearity	179
7.3	Continuous-Time Design of a Discrete-Time Controller	181
7.4	Design of a Parameter-Dependent \mathcal{H}_∞ Controller	183
7.4.1	Parameter-Dependent Control Design Problem	184
7.4.2	Solution in Continuous Time	185
7.4.3	Solution for Discrete-Time Implementation	186
7.5	Implementation Results on the Asygn's Platform	189
7.5.1	Controller Design	189
7.5.2	Validation of the Closed-Loop Performance Specifications	190
7.5.3	Tests on a Rotating Table	195
7.6	Summary of the Chapter	196
8	EM-$\Sigma\Delta$ Architecture: A Case Study	197
8.1	EM- $\Sigma\Delta$ Architecture and Control Problem	199
8.2	\mathcal{H}_∞ Synthesis for the EM- $\Sigma\Delta$ Architecture	201
8.2.1	An \mathcal{H}_∞ Criterion for the EM- $\Sigma\Delta$ Architecture	201
8.2.2	A Solution to the Unconstrained Case	204
8.2.3	A Solution to the Constrained Case	205
8.3	\mathcal{H}_∞ Synthesis for a Constrained EM- $\Sigma\Delta$ Controller	206
8.3.1	Rewriting the EM- $\Sigma\Delta$ Architecture in the General Form	206
8.3.2	Defining the Generalized Plant $\tilde{\mathbf{P}}$ and the Subset \mathcal{K}	207
8.3.3	Weighting Functions and Controller Design	208
8.4	Implementation Results	209
8.4.1	Measures at Rest	209
8.4.2	Global Performance Indicators	211
8.5	Summary	211
9	Conclusions and Perspectives	213
9.1	Summary of Results and Contributions	213
9.2	Future Works	215
9.2.1	Immediate or Short-Term Perspectives	215
9.2.2	Medium to Long-Term Perspectives	216
	References	217
A	Appendix of Chapter 2	227
A.1	Frequency-Domain Analysis of the Synchronous Demodulations	227
A.2	On the Mechanical Model of the MEMS Gyroscope with Endogenous Forces	228
B	Appendix of Chapter 3	231

B.1	Noiseless Analysis	231
B.1.1	Input Signals	231
B.1.2	Output Signals	232
B.1.3	Applying the Synchronous Demodulation	233
B.1.4	Compensating for the Scale Factor and Bias	235
B.1.5	Analysis of the SFNL	236
B.1.6	Analysis of the Bandwidth	237
B.2	Analysis with Respect to Noise	238
C	Appendix of Chapter 4	239
C.1	Families of Weighting Functions	239
C.1.1	Amplification Weighting Function	239
C.1.2	Attenuation Weighting Function	239
C.2	Numerical Values of Example 4.2 – 1DoF Control of the Drive Mode	240
C.3	Numerical Values of Example 4.3 – 2DoF Control of the Drive Mode	241
C.4	Numerical Values of Example 4.4 – 1DoF Control of the Sense Mode	241
C.5	Numerical Values of Example 4.5 – Multivariable Control (with $\hat{u}_{Cor,y} = -u_y$)	242
C.6	Numerical Values of Example 4.6 – Multivariable Control with Joint Estimation	242
C.7	Details of Section 4.4.1 – Quadratic Stability	243
D	Appendix of Chapter 5	245
D.1	Numerical Values of the LPV Controller of Section 5.4	245
E	Appendix of Chapter 6	249
E.1	Proof of Theorem 6.4	249
E.2	Proof of Theorem 6.5	250
E.2.1	Proof or Property (i)	250
E.2.2	Proof or Property (ii)	252
E.2.3	Proof or Property (iii)	252
E.3	Details of Example 6.6 – Nonideal Phasor Controller	255
F	Appendix of Chapter 7	257
F.1	On the Unstable Zeros of a PCT Model	257
F.2	On the “Normalizability” of the MEMS Gyroscope Model	258
F.3	Details on the PCT Model of a 2 nd -Order Resonator	258
F.4	Choice of the Fictitious Model of Example 7.1	260
F.5	Details on the SISO Controllers	260
F.5.1	2DoF Drive-Mode SISO Controller	260
F.5.2	1DoF Sense-Mode SISO Controller	262
F.6	Details on the MIMO Controller with Joint Estimation	264

List of Abbreviations

ADC	Analog-to-digital converter
ADRC	Active disturbance rejection control
AGC	Automatic gain control
ARE	Algebraic Ricatti equation
ARW	Angle-random walk
ASIC	Application-specific integrated circuit
BOT	Bias over temperature
BI	Bias instability
CA	Charge amplifier
CLTF	Closed-loop transfer function
CT	Continuous time
CVG	Coriolis vibrating gyroscope
DAC	Digital-to-analog converter
DoF	Degree(s) of freedom
DM	Drive mode
DPM	Dynamic phasor model
DT	Discrete time
DTG	Dynamically tuned gyroscope
EM- $\Sigma\Delta$	Electro-mechanical $\Sigma\Delta$
FOG	Fiber-optical gyroscope
FPGA	Field-programmable gate array
FS	Full scale
IEEE	Institute of Electrical and Electronics Engineers
IMP	Internal model principle
IQC	Integral quadratic constraint
LMI	Linear matrix inequality
LPV	Linear parameter-varying
LTI	Linear time-invariant
LTV	Linear time-varying
MEMS	Micro-electro-mechanical system
MIMO	Multiple-input and multiple-output
PCT	Pseudo-continuous time
PID	Proportional-integral-derivative
PLL	Phase-locked loop
PSD	Power spectral density
RLG	Ring-laser gyroscope
RRW	Rate random walk

SD	Synchronous demodulation
SF	Scale factor
SFNL	Scale factor nonlinearity
SFOT	Scale factor over temperature
SISO	Single-input and single-output
SM	Sense mode
SNR	Signal-to-noise ratio
USB	Universal serial bus
ZOH	Zero-order hold
ZRO	Zero-rate output

Notation

\mathbb{N}	Set of natural numbers
\mathbb{R}	Set of real numbers
\mathbb{R}^+	Set of nonnegative real numbers
\mathbb{C}	Set of complex numbers
j	Imaginary unit, <i>i.e.</i> , $j^2 = -1$
$\Re(v)$ or v_{\Re}	Real part of $v \in \mathbb{C}$
$\Im(v)$ or v_{\Im}	Imaginary part of $v \in \mathbb{C}$
\bar{v}	Complex conjugate of a complex variable v
u	Phasor of the sinusoidal signal u
I_n	Identity matrix of $\mathbb{R}^{n \times n}$ (subscripts may be omitted if obvious from the context)
$0_{n \times m}$	Zero matrix of $\mathbb{R}^{n \times m}$ (subscripts may be omitted)
$\text{diag}(A, B)$	Diagonal concatenation of two matrices A, B
$\text{col}(A, B)$	Column concatenation of two vectors a, b
A^T	Transpose of a matrix A
A^*	Conjugate transpose of a matrix A
A_{\perp}	Orthogonal complement of a matrix A , <i>i.e.</i> , $A^* A_{\perp} = 0$ and $[A^* \ A_{\perp}]$ is of maximum rank
$\lambda(M)$	Eigenvalue of a complex matrix M
$\sigma(M)$	Singular value of a complex matrix M
$\bar{\sigma}(M)$	Maximum singular value of a complex matrix M
$\underline{\sigma}(M)$	Minimum singular value of a complex matrix M
\diamond	In LMIs, represents terms that can be deduced from symmetry
\star	Redheffer (star) product
$*$	Convolution product
\circ	Composition of functions, <i>i.e.</i> , $(g \circ f)(x) = g(f(x))$
$T_{a \rightarrow b}$	Transfer from signal a to signal b
$\mathcal{F}[v]$	Fourier transform of a signal v
$\mathcal{L}[v]$	Laplace transform of a signal v
$\mathcal{Z}[v]$	Z-transform of a signal v
\mathcal{S}_v	Power spectral density of a signal v
$\ F\ _{\infty}$	\mathcal{H}_{∞} norm of an LTI system F
$\ v\ _2$	\mathcal{L}_2 norm of a signal v from \mathbb{R}^+ to \mathbb{C}^{n_v}
\mathcal{L}_2	Set of signals for which the \mathcal{L}_2 norm is bounded, defines the \mathcal{L}_2 space
$\ \Sigma\ _{i2}$	\mathcal{L}_2 gain of an operator Σ
\mathcal{L}_2^e	Extended \mathcal{L}_2 space
$\ \Sigma\ _{i2,e}$	\mathcal{L}_2^e gain of an operator Σ
$\ \Sigma\ _{i2}^q$	Quadratic \mathcal{L}_2 gain of an operator Σ

- v_I (resp v_Q) In-phase (resp. in-quadrature) term of a modulated signal v
- \hat{v} Estimate of the signal v
- $(\cdot)^c$ Indicates that the system (or matrices) is in continuous time
- $(\cdot)^d$ Indicates that the system (or matrices) is in discrete time
- $(\cdot)^p$ Indicates that the system (or matrices) is in pseudo-continuous time
- $(\cdot)_n$ Indicates that the system or signal are normalized in time/frequency

List of Symbols

$A_{x,m}$	Amplitude of the signal x_m	V
$A_{x,m}^{ref}$	Reference amplitude for the signal x_m	V
d	Mechanical damping matrix	kg/s
d_{xx} (resp. d_{yy})	Mechanical damping of the drive (resp. sense) mode	kg/s
d_{xy} and d_{yx}	Nonproportional damping coefficients	kg/s
$d_{Cor,x}$ (resp. $d_{Cor,y}$)	Exogenous disturbance representing the Coriolis force on the drive (resp. sense) mode	V
e_x (resp. e_y)	Zero-mean unit-variance white-noise signal	
F_s	Sampling frequency	Hz
F_{LP}	Low-pass filter of the synchronous demodulation	
f_{comp}	Compensation function	
G	To-be-controlled plant in direct approach	
G^{mech}	Mechanical model of the MEMS gyroscope	
H_{gyro}	Dynamic model of the entire MEMS gyroscope	
K	Controller	
k_0	Static gain of a dynamic system	
k	Mechanical stiffness matrix	kg/s ²
k_{xx} (resp. k_{yy})	Mechanical stiffness of the drive (resp. sense) mode	kg/s ²
k_{xy} and k_{yx}	Anisoelasticity coefficients	kg/s ²
k_{act}	Actuation gain	N/V ²
k_{lin}	Linearization gain (actuation)	V
k_{in}	Input (actuation and linearization) gain	N/V
k_{det}	Detection gain	F/m
k_{CA}	Charge-amplifier gain (for instrumentation)	V/F
k_{out}	Output (instrumentation) gain	V/m
k_{SF}	MEMS gyroscope scale factor	V/(rad/s)
k_{ZRO}	MEMS gyroscope bias of the measure	V
k_{SFNL}	Desired SFNL	
k_{ARW}	Desired ARW	°/√h
m	Matrix of mass	kg
m	Mass of the proof mass	kg
n_x (resp. n_y)	Process noise of the drive (resp. sense) mode	V
N_x (resp. N_y)	Process noise model for the drive (resp. sense) mode	
P	Weighted augmented plant for the \mathcal{H}_∞ /LPV synthesis	
\tilde{P}	Augmented plant (withouth weights) for the \mathcal{H}_∞ /LPV synthesis	

q_m	Image (in volts) of the proof-mass position	V
q_n	Measure (in volts) with noise of the proof-mass position	V
Q_x (resp. Q_y)	Quality factor of the drive (resp. sense) mode	
s	Complex Laplace variable and time-derivative operator	
s_p	Pseudo Laplace variable	
s_{If} (resp. s_{Qf})	In-phase (resp. in-quadrature) terms at the output of the synchronous demodulator	
t	Time variable	s
\mathbf{t}	Stands for the time variable t in the continuous-time context or the time sample k in the discrete-time context	
T_s	Sampling period	s
T_{int}	Internal temperature	K
u_x (resp. u_y)	Image of force applied on the drive (resp. sense) mode	V
$u_{Cor,x}$ (resp. $u_{Cor,y}$)	Image of the Coriolis force on the drive (resp. sense) mode	V
$u_{coup,x}$ (resp. $u_{coup,y}$)	Image of the mechanical coupling force on the drive (resp. sense) mode	V
u_P	Vector of control signals of the augmented plant	
v_{in}	Voltage applied to the MEMS gyroscope electrodes	V
V_{DC}	Offset (constant) voltage applied to the MEMS gyroscope electrodes	V
w	Vector of exogenous signals of the augmented plant	
W	Weighting functions	
x_m	Image of the proof-mass position on the \vec{x} -axis	V
x_m^{ref}	Drive-mode reference signal, in volts	V
x_n	Image with noise of the proof-mass position on the \vec{x} -axis	V
$\vec{x}, \vec{y}, \vec{z}$	Axes of the rotating reference frame (MEMS gyroscope)	
y_m	Image of the proof-mass position on the \vec{y} -axis	V
y_m^{ref}	Sense-mode reference signal, in volts	V
y_n	Image with noise of the proof-mass position on the \vec{y} -axis	V
y_P	Vector of measured output signals of the augmented plant	
z	Complex z-variable, $z = e^{j\omega T_s}$, and time-shift operator	
\mathbf{z}	Vector of controlled outputs of the augmented plant	
γ	Upper bound on the \mathcal{H}_∞ norm or $\mathcal{L}_2/\mathcal{L}_2^e$ gain of a system	
γ_p	Performance level for γ_p -tracking and γ_p -rejection	
$\hat{\gamma}_p, \hat{\gamma}_{p,T_0}$	Estimation of γ_p	
ΔE	Model uncertainties	
ΔM	Modulus margin	
Δ_{add}	Set of unstructured additive uncertainties	
ε_{SF}	Relative scale-factor error	
ε_{ZRO}	Residual bias	
ε_x	Drive-mode tracking error	V
$\check{\varepsilon}_x$	Upper bound of the drive-mode tracking error amplitude	V
ε_y	Sense-mode tracking/rejection error	V

$\check{\xi}_y$	Upper bound of the sense-mode tracking error amplitude	V
ε_{est}	Estimation error	V
$\check{\xi}_{est}$	Upper bound of the estimation error amplitude	V
θ	Known/measurable parameters	
λ_{SFNL}	Weighting factor used for SFNL-related specifications	
λ_{ARW}	Weighting factor used for ARW-related specifications	
ρ	Unknown/uncertain parameters	
τ	Independent integration variable	s
τ_A	Average time for the Allan deviation	s
ϕ_{exc}	Instantaneous excitation phase ($\dot{\phi}_{exc}(t) = \omega_{exc}(t)$)	rad
ω	Angular frequency	rad/s
$\omega_{0,x}$ (resp. $\omega_{0,y}$)	Resonance angular frequency of the drive (resp. sense) mode	rad/s
ω_{exc}	Excitation angular frequency	rad/s
ω_B	Bandwidth of the MEMS gyroscope	rad/s
ω_B^{des}	Desired bandwidth	rad/s
ω_c	Cutoff frequency of the low-pass filter F_{LP}	rad/s
ω_Ω	Bandwidth of the signal Ω_z	rad/s
ω_{ph}	Reference angular phase for the dynamic phasor modeling/control	rad/s
ϖ	“Pseudo-continuous” (angular) frequency	
Ω_z	Angular rate	rad/s
Ω_z^{FS}	Angular rate full scale	rad/s

Chapter 1

General Introduction

1.1 Context and Motivations

For the last years, micro-electro-mechanical (MEMS) inertial sensors have become ubiquitous (but usually unnoticed) in our daily life. Indeed, most of the smart phones are equipped with accelerometers and gyroscopes, which are very useful for image stabilization, health monitoring (*e.g.*, pedometers), navigation, gaming, etc. Actually, the field of application of MEMS inertial sensors is much wider. They are also found in drones and autonomous vehicles, in automotive safety systems (*e.g.*, airbags, electronic stability control, roll-over detection and prevention), in consumer electronics (*e.g.*, gaming systems, wearables, white goods), in guidance and navigation systems, in numerous industrial applications, in medical devices, and so on [AS09, Kem11, Sha13]. To illustrate their relevance in the modern society, in 2019, MEMS inertial sensors¹ represented a US\$ 3.19 billion market; and despite the COVID-19 pandemics and the economic crisis, this market is still expected to grow about 10% by 2025 [Yol20].

Inertial sensors make use of the effects of inertial forces to determine the dynamic compartment of objects. They can be classified as accelerometers if they are sensitive to linear inertial forces or as gyroscopes if they are sensitive to rotational inertial forces [Kem11]. Accelerometers measure the linear acceleration² of objects. On the other hand, gyroscopes measure the angular rate and/or orientation of objects. In this thesis, we focus our attention on the gyroscopes.

We can classify the gyroscopes into three main categories, depending on their working principle: rotary, optical and vibratory. Rotary gyroscopes represent the conventional mechanical gyroscopes, whose working principle relies on the gyroscopic effect of a spinning mass. Although this type of gyroscope presents an impressive accuracy, they are cumbersome and expensive. Nowadays, rotary gyroscopes are mainly represented by the dynamically tuned gyroscopes (DTG) [Apo16]. The optical gyroscopes take profit of the Sagnac effect to measure the angular rate (see, *e.g.*, [PCV⁺17] for further details on this technology). The main examples of this category are the fiber-optic gyroscope (FOG) and the ring-laser gyroscope (RLG). Optical gyroscopes are also very accurate and have the advantage to have no moving parts. However, they are also cumbersome and expensive.

Finally, we have the vibratory gyroscopes, which are also mechanical. Nevertheless, in contrast to the rotary ones, they do not have any rotating element. Indeed, vibratory gyroscopes rely on the oscillations/vibrations of a proof mass and on the so-called Coriolis force. For

¹Gyroscopes, accelerometers and inertial combos.

²As consequence, we can also determine the velocity and displacement, vibration, shocks or tilt (inclination).

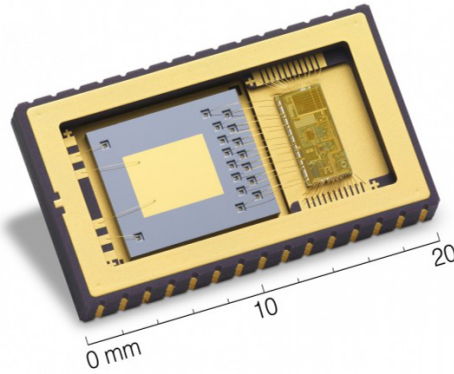


FIGURE 1.1: Picture of a commercial GYROPRO[®] MEMS gyroscope exposing its internal components: the micro-electro-mechanical part of the sensor at left, and the electronic part (ASIC) at right. Source: www.electronics-lab.com/gyro-high-performance-mems-gyroscopes.

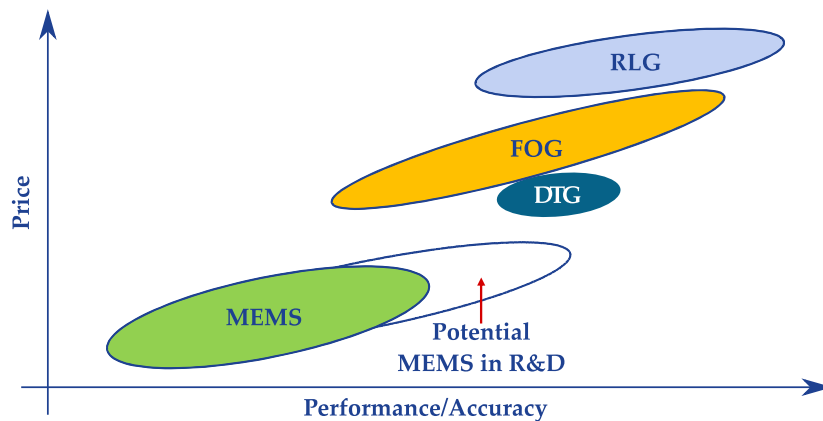


FIGURE 1.2: Price versus accuracy of different gyroscope technologies. Adapted from [LM14].

this reason, they are also known as Coriolis vibrating gyroscopes (CVG). Since the CVGs do not have rotating parts, they can be easily miniaturized through MEMS manufacturing techniques [AS09, Kem11, PCV⁺17]. Other types of CVG exist (see, *e.g.*, [Apo16]), however, in this thesis, we focus on the MEMS (Coriolis vibrating) gyroscopes.

MEMS gyroscopes have numerous advantages over other types of gyroscopes. They are much smaller (see Figure 1.1), cheaper, they consume much less energy and can be easily integrated into electronic devices. Nevertheless, because of their reduced size, MEMS devices are highly sensitive to fabrication imperfections, to environmental changes (*e.g.*, temperature, pressure) and to different sources of noise, what can quickly degrade their performance. For instance, in Figure 1.2, we present a comparison of price versus accuracy of different technologies, based on [LM14]. Thus, motivated by their low cost, a lot of effort has been put into enhancing the performance of MEMS gyroscopes, making them competitive with other technologies.

In this context, the project Next4MEMS was created with the main objective of developing a new generation of high-performance MEMS inertial sensor, enhancing the competitiveness of the French industry in the sector. This 20 M€ project was launched in 2016 and is supported by BPI France (the French bank for public investment) within the *Projets de Recherche et Développement Structurants pour la Compétitivité* (PSCS) funding scheme [Lab17].

The consortium is composed by the French leaders of the inertial sensor industry and two French research laboratories. This thesis is part of the project Next4MEMS and has a close collaboration with some of the industrial partners. Further details on this project will be given in Section 1.3.

As mentioned earlier, MEMS gyroscopes rely on Coriolis forces to measure the angular rate. The Coriolis forces are inertial forces that act on moving objects within a rotating reference frame. The gyroscope itself defines this reference frame. It is composed of a proof mass that is attached to the sensor by springs, which allow the mass to move along two perpendicular directions: the primary or drive direction, and the secondary or sense one. Micro actuators apply a force F_x on the proof mass, putting it into movement along the primary direction. Then, if the reference frame (gyroscope) is subjected to an angular rate Ω_z , which is orthogonal to the primary and secondary directions, a Coriolis force appears and produces oscillations along the secondary direction. This Coriolis force is given by

$$F_{Cor,y}(t) = -2m\Omega_z(t)\dot{x}(t), \quad (1.1)$$

where m is the mass of the moving object and x corresponds to its position along the primary axis. Now, if the proof mass describes a simple harmonic oscillation along the drive direction, x can be described by

$$x(t) = A_x \sin(\omega_{exc}t) \quad (1.2)$$

with amplitude A_x and a given frequency ω_{exc} , which is referred to as excitation frequency. This frequency has to be as close as possible to the resonance frequency of the spring-mass system along the primary direction, minimizing the required effort to put the proof mass into oscillation. Moreover, if A_x is equal to a given reference amplitude A_x^{ref} , (1.1) can be rewritten as

$$F_{Cor,y}(t) = -2mA_x^{ref}\omega_{exc}\Omega_z(t) \cdot \cos(\omega_{exc}t). \quad (1.3)$$

In this case, $F_{Cor,y}$ is an amplitude-modulated signal with carrier frequency ω_{exc} and amplitude proportional to Ω_z . Therefore, Ω_z can be obtained by estimating and demodulating $F_{Cor,y}$. One way to estimate $F_{Cor,y}$ is by applying a force F_y that counteracts the effects of $F_{Cor,y}$, compensating for the oscillations in the secondary direction. In this case, the estimation of $F_{Cor,y}$ becomes a disturbance rejection problem.

The performance of MEMS gyroscopes depends on how well controlled the primary oscillations are (ideally, $A_x = A_x^{ref}$) and how well the Coriolis force $F_{Cor,y}$ is estimated. Obviously, if there are no disturbances and the dynamic model of the MEMS gyroscope is perfectly known, the first goal can be achieved by inverting the model and applying the force F_x such that x tracks a reference signal

$$x^{ref}(t) = A_x^{ref} \sin(\omega_{exc}t); \quad (1.4)$$

and the second goal is achieved by measuring the secondary oscillations and computing $F_{Cor,y}$ that produces these oscillations. However, MEMS devices are highly sensitive to fabrication imperfections and to environmental changes. Therefore, to produce high-performance gyroscopes, the use of control loops is crucial [GBKN91, OAL⁺05, Zur15]. The main objective of these control loops is hence to ensure that the primary oscillations have a controlled amplitude and that the Coriolis force is precisely estimated. After obtaining the Coriolis force estimate, a post-processing stage is needed to recover the angular rate.

The entire MEMS gyroscope has two parts: the micro-electro-mechanical part and the electronic one. The former one corresponds to the MEMS itself, which constitutes the sensitive element of the sensor. For the sake of simplicity, we will refer to this part simply as mechanical

part. The electronic part is usually implemented in an application-specific integrated circuit (ASIC), which is usually mounted together with the MEMS in the same package, as shown in Figure 1.1. The ASIC has two main purposes: control the oscillations of the proof mass and estimate $F_{Cor,y}$; and process the estimate of $F_{Cor,y}$, providing the angular rate measure.

The mechanical part of the MEMS gyroscope can be modeled as two high quality-factor (very underdamped) resonators: one corresponding to the spring-mass system in the primary direction, and another corresponding to the spring-mass system in the secondary direction. These systems are respectively referred to as primary or drive mode and secondary or sense mode. In the ideal case, these two modes are only coupled by the Coriolis forces. Nevertheless, it is important to stress that a minor misalignment between the primary and secondary axes is enough to produce a mechanical coupling between drive and sense modes.

In the MEMS literature, the control architectures are usually based on the **complex envelope** (*i.e.*, amplitude and phase or direct and quadrature terms) of the oscillating signals. Since these envelopes are constant signal in steady state (while the oscillating signals are sinusoidal), simple PI or PID controllers can be employed to regulate, for instance, the amplitude and the phase of the oscillating signals [EMK12]. This solution has been widely used since the first MEMS gyroscope, presented in 1991 [GBKN91]. Indeed, the control architecture adopted nowadays in the commercial products of Zurich Instruments, see [Zur15], is basically the same as the one proposed by Lynch in 1998 [IEE04, Annex B], which is quite similar to the one presented in [GBKN91]. This fact points to the strength and acceptability of this control architecture in the MEMS industry. The drawback of the envelope-based architectures is that, in general, to measure the signal envelope, nonlinear elements have to be introduced in the control loop. Moreover, the dynamical couplings between amplitude and phase (or direct and quadrature terms), the couplings between the drive and sense modes, and the dependence on environmental conditions can be very hard to model and to take into account. Therefore, it is hard to provide, *a priori*, guarantees of stability and performance for the closed-loop system.

An alternative approach is to consider the classical feedback control architecture, which we refer to as **direct control architecture**, where the controller works directly with the harmonic signals instead of their complex envelope. For this architecture, advanced control techniques have been developed for vibration control of mechanical systems, see *e.g.*, [Wan19]. The potential interest is to explicitly take into account the different couplings and the dependence on the environmental condition, with formal guarantees of stability and performance. Nevertheless, their applicability to MEMS gyroscopes, including implementability, is still an open question. A possible reason is the inherent complexity of the controllers. Furthermore, in contrast to the design of PID controllers, which MEMS engineers are familiar to, the design of advanced controllers usually require an expertise in advanced control theory. This aspect might constitute an obstacle to the introduction of novel control strategies in the industry. Thus, an additional effort of making advanced control techniques more accessible is required.

1.2 Scope and Contributions

In this thesis, we aim to propose design methods for direct and envelope-based control architectures, and to experimentally validate the obtained controllers with real MEMS gyroscopes. The methods are expected to provide guarantees of stability and a certain performance level for the sensor. To achieve this purpose, we have to tackle four main problems, as follows.

The performance indicators of MEMS gyroscopes are related to the quality of the measure, they are not directly linked to the closed-loop behavior. Indeed, there is a post-processing

stage that uses the Coriolis force estimate to deduce the angular rate. Then, the first problem is: *how to relate the global performance specifications to specifications for the closed-loop system?* To answer this questions, we review the literature on MEMS gyroscopes and define the key performance indicators of the sensor. Then, by using an input-output approach, we establish the relationships between the performance indicators and the closed-loop behavior. These relationships are a valuable tool for the control design and constitute the first contribution of this thesis.

Based on these relationships, the problem is now: *how to design a controller for the direct control architecture?* First, we consider the case where the MEMS gyroscope works with a fixed operating condition and the excitation frequency ω_{exc} corresponds to the drive-mode resonance one. In this context, the control objectives include the tracking and rejection of sinusoidal signals, and the standard \mathcal{H}_∞ synthesis is applied for the controller design. The excitation frequency, however, may vary over time. Therefore, the control objectives of tracking/rejecting sinusoidal signals become the tracking/rejection of frequency-modulated signals, that is, the reference signal of (1.4) becomes a “time-varying-frequency sinusoidal” signal of the type

$$x_m^{ref}(t) = A_{x,m}^{ref} \sin(\phi_{exc}(t)) \quad \text{with} \quad \phi_{exc}(t) = \int_0^t \omega_{exc}(\tau) d\tau + \phi_{exc}^0, \quad (1.5)$$

where $\omega_{exc}(t)$ ranges arbitrarily in the interval $[\omega_{exc,1}, \omega_{exc,2}]$ and $\phi_{exc}^0 \in \mathbb{R}$. We reveal that this particular problem can be formulated as a weighted \mathcal{L}_2 criterion with a new class of weighting functions modeling the frequency-modulated signals. This result constitutes a second important contribution of the thesis.

In a third part, we consider the question: *how to design a controller for an envelope-based control architecture such that guarantees of stability and performance can be given?* To cope with this problem, we revisit the theory of complex envelopes, which allows us to define a formal framework for the analysis of the envelope-based control architectures. If the complex envelope is ideally measured in real time, we establish links between the direct control approach and the envelope-based ones. These links reveal that the performances achieved with both strategies are equivalent. When the signal envelope cannot be ideally measured, the same framework allows us to precisely model the nonidealities and to design controllers formally guaranteeing, at least, the stability of the closed-loop system. These results are also an important contribution of this thesis.

In the last part, the problem is: *how to properly design a controller for digital implementation?* Two cases are treated here. First, we consider a **flexible** platform developed by Asygn, which can implement complex control architectures, allowing to validate in practice different control strategies. The seconds case consists of a **dedicated** platform designed with the so-called electro-mechanical $\Sigma\Delta$ (EM- $\Sigma\Delta$), which is a particular control architecture that can be easily implemented in ASICs for MEMS gyroscopes. For both platforms, the practical results validate the proposed methods.

What is not treated in this thesis

Other aspects are also relevant, but are beyond the scope of this thesis.

Although the understanding of the working principles of the MEMS gyroscope is necessary for the controller design, the technological details concerning the design and fabrication of MEMS gyroscopes are not discussed in this document. Similarly, the design of the electronic

circuits and hardware needed for the implementation of the control loops, are also beyond the scope of this thesis.

In general, when designing a control system, three main stages are considered: *(i)* the modeling/identification of the to-be-controlled system, *(ii)* the controller design, and *(iii)* the analysis and performance validation of the closed-loop system. Along this document, we touch some basic aspects related to the modeling/identification, and analysis and performance validation in the MEMS gyroscope context. However, these subjects are treated with more details in other thesis within the scope of the same project, see [Col20, AC21].

Further than the closed-loop ensuring the proper operation of a MEMS gyroscope, external control loops or additional algorithms can also be used to estimate the drive-mode resonance frequency, as in [Mor21]; to compensate for mechanical couplings (see, *e.g.*, [Zur15]); or to change the behavior of the MEMS device (see, *e.g.*, [AOPB09]). For some results of this thesis, we consider that the drive-mode resonance frequency is known via the strategies of [Mor21], without presenting any fundamental details. Other external control loops are not considered in this work.

1.3 Project Next4MEMS

This thesis is within the scope of the project Next4MEMS, whose main objective is to develop a new generation of high-performance MEMS gyroscopes. Due to the complexity of the domain, the consortium is composed by French leaders of the inertial sensors industry – Tronics Microsystems, iXblue, Asygn –, and two French laboratories – Ampère and ONERA. ONERA and iXblue contribute with their expertise in the use of MEMS gyroscopes in high-performance applications. Tronics Microsystems and Asygn develop, respectively, the electro-mechanical part and the electronic circuits that compose the MEMS gyroscope. Finally, the laboratory Ampère collaborate with an expertise in Control Theory and its applications.

Within the scope of the same project, four theses were concomitantly developed at the laboratory Ampère, approaching the different facets of Control Theory in the MEMS gyroscope context. Further than the present thesis, the other three theses are briefly described below.

- “Data informativity for the prediction error identification of MIMO systems: identification of a MEMS gyroscope” by Kévin Colin [Col20], who proposes a systematic method for modeling and identifying the MEMS gyroscope. This method is based on the Prediction Error identification framework [Lju98], which, based on input and output data obtained through experiments, provides a model of the system. The main advantage of this framework is that, further than providing the system model, it also provides validation tools and uncertainty bounds, such that, with a certain (high) probability, we are sure that the obtained model is close enough to the real one. The model obtained through this method is used in the present thesis.
- “Performance validation of MEMS sensors using nonlinear uncertain models” by Jorge Ivan Ayala Cuevas [AC21], who proposes a computationally efficient method for the performance validation and stability analysis of the closed-loop system. This method adopts the μ -analysis [ZDG96] and integral quadratic constraints (IQC) [MR97] frameworks. Then, based on the model and uncertainties estimated by the method of [Col20] and on the controller design proposed in the present thesis, the method of [AC21] provide a worst-case estimation of the sensor performance. Moreover, it also indicates how the model accuracy and/or the controller design have to be improved to achieve a desired performance level.

- “Optimal identification experiment design: contributions to its robustification and to its use for dynamic network identification. Resonance Frequency Tracking” by Federico Morelli [Mor21]. The variation of the drive-mode resonance frequency is one of the major problems for MEMS gyroscopes. Therefore, [Mor21] proposes different techniques to track the variations of the drive-mode resonance frequency in real time. They are based on the Extremum-Seeking approach [ZO12] and Recursive identification [Lju98]. In some approaches proposed in the present thesis, the estimated resonance frequency is used to adapt the reference signal as well as the controller parameters.

Other works were also developed within the scope of the project Next4MEMS. A first bibliographic study on MEMS gyroscopes and traditional control architectures was realized by Roman Bohoslavets and Thomas Dehaeze within the scope of their undergraduate thesis at the beginning of the project, in 2017.

Later, and with the supervision of the author, other undergraduate thesis were also realized. A detailed study on the EM- $\Sigma\Delta$ architecture of the Tronics’ dedicated platform (see Section 2.3.2) was realized by Eva Markiewicz and allowed the development of a suited control design method (see Chapter 8). Thibault Vergez implemented, in a real MEMS gyroscope, a phasor-based controller, confirming some results of Chapter 6. Cécile Pernin set up a rotating table, proposed a test protocol and performed batteries of tests with the (flexible) Asygn’s platform (see 2.3.1), refining the identification and control design methods, and contributing to the practical results presented in Chapter 7.

Moreover, two research assistants/engineers also participated in the project and had the supervision/collaboration of the author. Anthony El Hajj realized practical tests with the EM- $\Sigma\Delta$ design method proposed in Chapter 8 and applied the same method to the design of the EM- $\Sigma\Delta$ architecture of MEMS accelerometers. At the time of writing, Cécile Pernin works on the implementation of traditional control architectures in the Asygn’s platform.

Finally, at the time of writing, Sarah Schmidt and Florian Coissac start their internship also with the supervision of the author. Sarah works toward the validation of the proposed EM- $\Sigma\Delta$ design method for MEMS accelerometers. Florian also works on the implementation of the traditional control architectures in the Asygn’s platform.

1.4 List of Publications and Collaborations

Conference Papers:

- (i) K. Colin, **F. Saggin**, C. Le Blanc, X. Bombois, A. Korniienko, G. Scorletti. “Identification-Based Approach for Electrical Coupling Compensation in a MEMS Gyroscope”, IEEE International Symposium on Inertial Sensors and Systems Proceedings, 2019 (Ref. [CSL+19]).
- (ii) J. Ayala-Cuevas, **F. Saggin**, G. Scorletti, A. Korniienko. “Stability Analysis of Time-Varying Systems with Harmonic Oscillations Using IQC Frequency Domain Multipliers”, IEEE Conference on Decision and Control (CDC), 2019 (Ref. [ACSKS19]).
- (iii) **F. Saggin**, G. Scorletti, A. Korniienko. “A Novel Phasor Control Design Method: Application to MEMS Gyroscopes”, American Control Conference (ACC), 2020 (Ref. [SSK20]).
- (iv) **F. Saggin**, J. Ayala-Cuevas, A. Korniienko, G. Scorletti. “Parameter-Dependent \mathcal{H}_∞ Control for MEMS Gyroscopes: Synthesis and Analysis”, IFAC World Conference, 2020 (Ref. [SACKS20]).

- (v) **F. Saggin**, A. Korniienko, G. Papin, E. Markiewicz, Y. David, A. El Hajj, G. Scorletti. “H-infinity Design of an EM- $\Sigma\Delta$ Feedback for MEMS Gyroscopes”, DGON Inertial Sensors and Systems (ISS), 2020 (Ref. [SKP+20]).
- (vi) **F. Saggin**, C. Pernin, A. Korniienko, G. Scorletti, C. Le Blanc. “Digital Control of MEMS Gyroscopes: a Robust Approach”, IEEE International Symposium on Inertial Sensors and Systems Proceedings, 2021 (Ref. [SPK+21]).

Project Reports and Softwares:

- (i) **F. Saggin**, K. Colin, J. Ayala-Cuevas, F. Morelli, A. Korniienko, G. Scorletti, X. Bombois. “Livrable 2.4 : Développement de Méthodes pour la Conception”, 2018 (Confidential).
- (ii) **F. Saggin**, K. Colin, J. Ayala-Cuevas, F. Morelli, E. Markiewicz, A. Korniienko, G. Scorletti, X. Bombois, A. El Hajj. “Livrable 2.6 Résultats Expérimentaux d’Application des Algorithmes de Conception sur la Plate-forme Considérée (Tronics/TDK)”, 2020 (Confidential).
- (iii) **F. Saggin**, A. Korniienko, A. El Hajj, G. Scorletti. “Software *Hinf_EMSD*”, 2020. Software for the design of the EM- $\Sigma\Delta$ parameters for a MEMS gyroscope.

Journal Papers (in preparation):

- (i) **F. Saggin**, G. Scorletti, A. Korniienko. “Tracking and Rejection of Signals with Time-Varying Frequency: a Suited Weighted \mathcal{L}_2 Criterion”.
- (ii) **F. Saggin**, J. Ayala-Cuevas, A. Korniienko, G. Scorletti. “Phasor Control in a Variable-Frequency Framework”.
- (iii) **F. Saggin**, A. Korniienko, A. El Hajj, G. Scorletti. “H-infinity Design of EM- $\Sigma\Delta$ Feedbacks: a Unified Approach for MEMS Accelerometers and Gyroscopes”.
- (iv) J. Ayala-Cuevas, G. Scorletti, A. Korniienko, A. Perodou, **F. Saggin**. “A Frequency Domain Integral Quadratic Constraints Approach for Robustness Analysis of Continuous Harmonically Time-Varying Systems”.

1.5 Organization of this Document

The remaining of this thesis is organized as follows.

Chapter 2 First, we give a background on MEMS gyroscopes. We start by presenting the working principles and the operation of an ideal MEMS gyroscope. Then, step-by-step, we introduce the nonidealities that are present in a real gyroscope and analyze how these nonidealities affect the measure of the angular rate. This analysis allows us to present the main performance indicators. Following this, we review the main control architectures reported in the literature, pointing to the strengths and limitations of each one. Then, we present the experimental setups in which the proposed solutions are to be implemented. All these ingredients are then used to formulate the research questions that guide the development of this thesis.

Chapter 3 Having presented all the blocks constituting a MEMS gyroscope as well as the main performance indicators in Chapter 2, we can now analyze how the behavior of the closed-loop system impacts the global performance indicators. This analysis is realized in a linear time-invariant (LTI) framework, which allows establishing frequency constraints

on the closed-loop transfer functions. Further than the performance specifications, the frequency constraints are also used to enforce the robust stability of the closed-loop system against different types of uncertainties. These frequency constraints define the closed-loop specifications considered for the controller design.

Chapter 4 In chapter 3, we show that the desired performances indicators can be translated into frequency constraints on the closed-loop transfer functions. In chapter 4, we present a design method that allows obtaining controllers satisfying these frequency constraints. The design method is based on the \mathcal{H}_∞ synthesis. Thus, we start the chapter by reviewing the \mathcal{H}_∞ synthesis, and, progressively, we propose different control strategies. Each proposed solution is followed by a numerical example. At the end of the chapter, the most interesting solutions are validated and illustrated through numerical simulation.

Chapter 5 In this chapter, we present one of the main theoretical contributions of this work: the definition of time-varying weighting functions that describe frequency-modulated signals. After presenting this interesting result, we apply it to design a MEMS gyroscope controller. The controller design is based on the standard linear parameter-varying (LPV) synthesis, in a polytopic approach. Numerical simulations demonstrate the effectiveness of the proposed approach.

Chapter 6 In this chapter, we revisit the theory of the complex envelopes, and we show that, although nonlinear elements are introduced in the control loops, the complex envelopes of the to-be-controlled system can be modeled as the signals of a linear system. This is true under the assumption that the complex envelopes could be perfectly measured in real time (ideality assumption). In this case, we establish links between the direct and the envelope-based control approaches, revealing that both approaches achieve exactly the same performance level. In reality, however, this ideality assumption is not satisfied and nonidealities are introduced in the control loop. Then, we proposed a control design method that takes these nonidealities into account, providing guarantees of stability. Part of these results were published in [SSK20].

Chapter 7 One of the messages of Chapter 6 is that, if possible to implement, the direct control architecture would be a better (linear) choice for the closed-loop operation of MEMS gyroscopes. Therefore, in Chapter 7, we detail the steps required for a digital implementation of the controller, still providing guarantees of stability and performance. The implementations results validate the proposed method and prove the implementability of the direct control architecture. Some results presented were published in [SACKS20] and [SPK⁺21].

Chapter 8 Here, we present a study case where the \mathcal{H}_∞ synthesis is applied to design the controller of a EM- $\Sigma\Delta$ architecture. Although the EM- $\Sigma\Delta$ can be almost considered as a direct control architecture, the particularity here is that, due to implementation constraints, only some parameters of the controller can be tuned. The controller is then said to be constrained. Therefore, we adapt the control method of Chapter 4. This method was implemented in the dedicated platform and allowed to enhance the performance of the sensor up to 40%, compared to the current solution adopted by the partner. The results of this chapter were presented in the conference paper [SKP⁺20] and are the core of the software *Hinf_EMSD*.

Chapter 9 Finally, in the last chapter, we draw the main conclusions of this thesis and indicate interesting directions for future works.

Chapter 2

MEMS Gyroscopes and the Control Challenges

MEMS gyroscopes are micromachined inertial sensors used to measure the angular rate of an object. They are composed of a tiny proof mass, which is able to move along two perpendicular axes. The proof mass is then driven to oscillate with a controlled amplitude along one axis. When subjected to an angular rate Ω_z , part of the energy of these oscillations is transmitted to the other axis through the Coriolis force, provoking oscillations along the second axis. The amplitude of the Coriolis force is proportional to the angular rate. Therefore, based on the secondary oscillations of the proof mass, one can estimate the Coriolis force and the angular rate.

It is important to note that to provide an accurate estimation of the angular rate, the primary oscillations has to be precisely controlled and the Coriolis force have to be accurately estimated. In general, these objectives are achieved through the use of control loops. Nevertheless, due to the reduced size of the MEMS devices and their sensitivity to environmental changes, the design and implementation of the control loops is very challenging. The main objective of this work is then to propose a systematic method to design controllers for MEMS gyroscopes, achieving high performance.

In this chapter, we aim at stating the research questions that guide the development of this thesis. We start the chapter by presenting the MEMS gyroscopes, its main performance indicators and the importance on operating these devices in closed loop. Then, in Section 2.2, we review the most relevant control architectures that are found in literature and in industry, evaluating their strengths and the potentials for improvement. These control architectures allow us to introduce, in Section 2.3, our experimental setups, which are used to validate the proposed methods. Finally, in Section 2.4, we state the research questions, fulfilling the objectives of this chapter.

2.1 A Background on MEMS Gyroscopes

In this section, we aim at providing some background on the multidisciplinary field of MEMS gyroscopes. Indeed, this fascinating subject borders the domains of Mechanics, Microelectronics, Signal Processing, Control Theory and Measurement, to cite a few [Kem11]. This thesis is mainly focused on the aspects related to the control of MEMS gyroscopes. However, before tackling the control problems, it is essential to provide a global view of the system to understand its capacities, limitations, and the role of the controller(s) in this complex framework.

In Section 2.1.1, we show that micro gyroscopes behave like a Foucault pendulum in microscopic scale, where, instead of measuring the rotation of Earth, MEMS gyroscopes measure their own angular rate. Moreover, instead of having a massive weight suspended by a string, micro gyroscopes have a tiny proof mass attached to their structure by springs, allowing the proof mass to oscillate.

In Section 2.1.2, the mechanical model of an **ideal** MEMS gyroscope is established. Based on this model, we discuss the closed-loop operation of the sensor. Obviously, to implement control loops, actuators and instrumentation are required. Thus, in Section 2.1.3, we describe the principles of actuation and instrumentation in micro scale. We also model their behavior and introduce the gyroscope model. Finally, we introduce the model of a MEMS gyroscope that will be used along with this thesis to illustrate our examples.

Most of the signals transiting in a MEMS gyroscope are quasi-sinusoidal. Indeed, these signals are related to the proof mass oscillations. However, the useful part of the information is contained in the amplitude and phase of these signals. For instance, “the **amplitude** of the Coriolis force is proportional to the angular rate”. Then, synchronous demodulation is employed to extract the amplitude (and phase) from this signal and to estimate the angular rate. Details on this important element are given in Section 2.1.4.

In Section 2.1.5, we introduce the main nonidealities that may appear in a real MEMS gyroscope. We also discuss how these nonidealities affect the operation of the device and its accuracy. Finally, in Section 2.1.6, the main performance specifications are presented. They are essential indicators of a real-sensor accuracy.

A wide literature on these topics is available. We base our review mainly on some textbooks, such as [AS09, AL10, Kem11, Apo16], the thesis [Sau08] and the rich literature review of [YAN98]. The aspects linked to the performance specifications are mainly based on the current IEEE (Institute of Electrical and Electronics Engineers) standards [IEE04, IEE06, IEE09, IEE19].

2.1.1 Working Principle: a Foucault Pendulum in a Chip

Let us introduce a bit of history to present the working principle of MEMS gyroscopes. For further details on this fascinating history, the curious reader is referred to the recent paper [Som17]. Since ancient times, philosophers and astronomers had suggested that Earth rotates on its own axis once every 24 hours. This suggestion was reinforced by Nicolaus Copernicus in his celebrated heliocentric theory. One century later, by the time of Galileo, even with no direct evidences, the academy was already convinced that Earth rotates on its axis. However, that was only in 1851 that Léon Foucault could demonstrate the rotation of Earth through the oscillations of a pendulum in his seminal work [Fou51]. This experiment is known today as Foucault pendulum.

To illustrate this interesting experiment, let us consider an oscillating pendulum on the North Pole, as shown in Figure 2.1. Note that the oscillations describe an oscillation plane, which is static in the space. Therefore, when the earth rotates on its axis from left to right, for an observer placed on the earth, the oscillation plane seems to rotate from right to left, as if there was an invisible force rotating that plane. This inertial – or virtual, or apparent – force is known as the Coriolis force. After 24 hours, the observer can note that the oscillation plane completes one rotation around the axis of the pendulum. Now, if the pendulum is placed in an intermediate latitude, the oscillation plane takes more time to complete a rotation (from the observer point of view). This period is proportional to the cosecant of the latitude in which the pendulum is placed. Indeed, if the pendulum is placed over the Equator Line (the

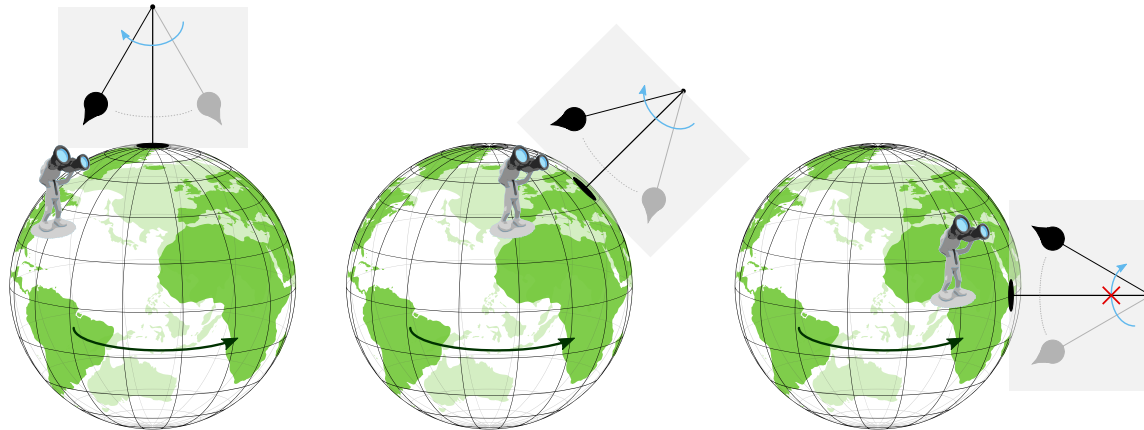


FIGURE 2.1: The Foucault pendulum on the North Pole, in an intermediate latitude and on the Equator Line. The (blue) arrow on the pendulum indicates the rotation of the oscillating plane from the observer point of view.

axis is perpendicular to the axis of Earth), there is no rotation of the pendulum around its own axis (always from the observer point of view).

That dependence on the cosecant of the latitude made hard for the public to understand the experiment. However, obsessed to demonstrate the rotation of Earth in a clearer way, Foucault used a device composed of a spinning wheel inside gimbals, which he named gyroscope [Fou52a], from the Greek roots “gyros” (rotation) and “scope” (to observe). Since the rotation axis of a rotating wheel is also static in space, it should rotate with respect to an observer on Earth. This fact was confirmed and published in *Comptes rendus hebdomadaires des séances de l’Académie des Sciences* in 1852 [Fou52b, Fou52a]. This description underlies the working principle of the mechanical high-precision gyroscopes discussed in Section 1.1.

Now, if we want to miniaturize high-precision gyroscopes, an important technological difficulty arises: the creation of rotating motion in MEMS devices [Kem11]. However, oscillating/vibrating motion can be easily produced in microdevices. Therefore, MEMS gyroscopes are built as mass-spring systems such that the mass can oscillate along two perpendicular axes: the primary (or \vec{x} -) axis, and the secondary (or \vec{y} -) axis. Figure 2.2 illustrates this description. Other designs can be considered, but different MEMS gyroscopes rely on the same principle: the Coriolis force. Thus, these gyroscopes are also classified as Coriolis vibrating gyroscopes (CVG). For further details, we refer the curious reader to one of the several textbooks on MEMS design [AS09, Kem11, Apo16] or microfabrication [AL10].

Coriolis vibrating gyroscopes can be classified into angle (Type I) or rate (Type II) gyroscopes. Type I CVGs are used to measure the angular position while Type II CVGs measure the angular rate of an object. Both types rely on the same principle – the Coriolis force – and can be built similarly. The main difference resides on the gyroscope operation. For Type I CVGs, the proof mass oscillates freely, just like a Foucault pendulum; thus, when the gyroscope rotates, the proof mass trajectory rotates in the opposite direction (always from the “structure” point of view). For Type II CVGs, the oscillations are always driven on the same direction. We describe this operation in the sequel. For a richer discussion on Types I and II CVGs, please refer to [Shk06, PZTS11]. The gyroscopes considered in this work are of Type II (angular rate).

Let us open a parenthesis and consider again the Foucault pendulum on the North Pole. Imagine now that the observer pushes the pendulum, such that the weight leaves and comes

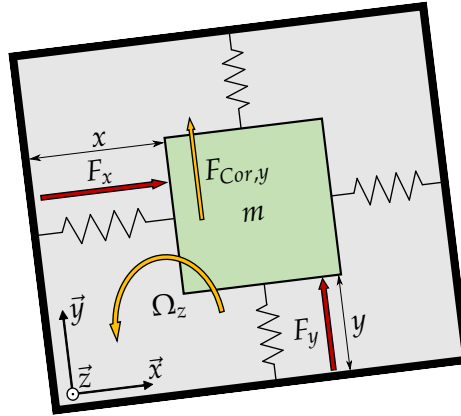


FIGURE 2.2: Mechanical representation of a MEMS gyroscope.

back to its hands. If we suppose that Earth does not rotate, he has to apply a minimum force in the forward direction, just enough to keep the oscillations with the same amplitude, compensating for energy losses (friction with the air, for instance). Now, if Earth starts rotating, the observer has to apply a perpendicular force to compensate for the Coriolis force. The Coriolis force is proportional to the angular rate Ω_z . Thus, based on this compensating force, the observer can estimate Ω_z .

MEMS gyroscopes work in the same way. Actuators apply a force F_x , driving primary oscillations of the proof mass along the \vec{x} -axis. Thus, when the device is subjected to an angular rate Ω_z (perpendicular to the $\vec{x}\vec{y}$ -plane), an oscillating Coriolis force appears along the secondary axis. The amplitude of the Coriolis force is proportional to the angular rate Ω_z , the amplitude and frequency of the primary oscillations, respectively A_x and ω_{exc} . Therefore, if we can apply a force F_y that compensates for the Coriolis force – *i.e.*, avoids oscillations along the \vec{y} -axis –, we can estimate the angular rate through the synchronous demodulation [Sau08]. Because of its role, the oscillation mode along the \vec{x} -axis is commonly called **drive mode**. Similarly, the oscillation mode along with the \vec{y} -axis, which is rather used to detect or sense the Coriolis force, is referred to as **sense mode**.

Note that for an accurate estimation of Ω_z , it is required to keep controlled oscillations on the drive mode, *i.e.*, the amplitude A_x and frequency of the primary oscillations ω_{exc} have to be regulated. Moreover, the Coriolis force has to be precisely compensated/estimated in the sense mode. Hence, the use of control loops is essential to design high-performance MEMS gyroscopes. In the sequel, we describe the model of an ideal MEMS gyroscope and introduce the closed-loop operation.

2.1.2 Ideal MEMS Gyroscope and Closed-Loop Operation

As discussed above, MEMS gyroscopes are conceived as mass-spring systems. Then, based on the second law of Newton, the dynamic behavior of an ideal gyroscope is described by the differential equation [Sau08]

$$\mathbf{m}\ddot{q}(t) + \mathbf{d}\dot{q}(t) + \mathbf{k}q(t) = F(t), \quad (2.1)$$

where $q = \begin{bmatrix} x \\ y \end{bmatrix}$, $F = \begin{bmatrix} F_x \\ F_y \end{bmatrix}$, $\mathbf{m} = \begin{bmatrix} m & 0 \\ 0 & m \end{bmatrix}$, $\mathbf{d} = \begin{bmatrix} d_{xx} & 0 \\ 0 & d_{yy} \end{bmatrix}$ and $\mathbf{k} = \begin{bmatrix} k_{xx} & 0 \\ 0 & k_{yy} \end{bmatrix}$. The variables x and y are respectively the positions of the proof mass in the \vec{x} - (drive mode) and \vec{y} -axes (sense mode) (see Figure 2.2), m represents the mass, F is the vector of applied forces, \mathbf{d} is the

mechanical damping matrix, and \mathbf{k} is the stiffness matrix. The indices x and y are associated with the drive and the sense modes, respectively.

Usually, MEMS resonators are characterized by their resonance frequency ω_0 and their quality factor Q . These parameters are related to the mechanical damping and stiffness coefficients, as follows¹:

$$\omega_{0,i} = \sqrt{\frac{k_{ii}}{m}} \quad \text{and} \quad Q_i = \frac{\sqrt{k_{ii}m}}{d_{ii}}.$$

with $i = \{x, y\}$. Therefore, by applying the Laplace transform to (2.1), the mechanical model of the MEMS gyroscope can be given by the transfer matrix

$$G^{mech}(s) = \begin{bmatrix} G_x^{mech}(s) & 0 \\ 0 & G_y^{mech}(s) \end{bmatrix}$$

with

$$G_x^{mech}(s) = \frac{x(s)}{F_x(s)} = \frac{k_{0,x}^{mech} \omega_{0,x}^2}{s^2 + \omega_{0,x}/Q_x \cdot s + \omega_{0,x}^2}, \quad (2.2)$$

$$G_y^{mech}(s) = \frac{y(s)}{F_y(s)} = \frac{k_{0,y}^{mech} \omega_{0,y}^2}{s^2 + \omega_{0,y}/Q_y \cdot s + \omega_{0,y}^2}, \quad (2.3)$$

$$k_{0,x}^{mech} = \frac{1}{m\omega_{0,x}^2} \quad \text{and} \quad k_{0,y}^{mech} = \frac{1}{m\omega_{0,y}^2}.$$

MEMS resonators are conceived to present a very high quality factor, usually ranging from the order of hundreds (e.g., [CCD⁺09]) to some millions (e.g., [PTS13]). This fact allows obtaining high gain around the resonance frequency, improving the performance of the device (signal to noise ratio, sensitivity, resolution, etc.) [YAN98]. On the other hand, the value of the resonance frequency ranges from some hundreds of hertz (e.g., [MV99]) to some hundreds of kilohertz (e.g., [WSNS⁺16]). Furthermore, typical MEMS gyroscopes are conceived such that the resonance frequencies of the drive and sense modes are very close [Sau08].

It is worth emphasizing that, despite the existence of different mechanical designs, the second-order behavior presented in equations (2.2) and (2.3) generalizes the dynamics of most of the (ideal) CVGs [Apo16, Chap. 2].

Let us go back to the mechanical model. When the MEMS gyroscope is subjected to an angular rate Ω_z (in rad s^{-1}) perpendicular to the $\vec{x}\vec{y}$ -plane, the Coriolis forces appear. They are given by

$$F_{Cor}(t) = \begin{bmatrix} F_{Cor,x}(t) \\ F_{Cor,y}(t) \end{bmatrix} = \Omega_z(t) \begin{bmatrix} 0 & 2m \\ -2m & 0 \end{bmatrix} \begin{bmatrix} \dot{x}(t) \\ \dot{y}(t) \end{bmatrix}. \quad (2.4)$$

Thus, by including F_{Cor} into (2.1), the following expression is obtained [Sau08, Apo16]:

$$\mathbf{m}\ddot{\mathbf{q}}(t) + \mathbf{d}\dot{\mathbf{q}}(t) + \mathbf{k}\mathbf{q}(t) = \mathbf{F}(t) + F_{Cor}(t) \quad (2.5)$$

¹Calling ω_0 the resonance frequency is an abuse of language. Indeed, if we denote the resonance frequency by ω_r , the natural frequency by ω_n and the damped natural frequency by ω_d , we have

$$\omega_d = \omega_n \sqrt{1 - \frac{1}{2Q}} \quad \text{and} \quad \omega_r = \omega_n \sqrt{1 - \frac{1}{Q}}.$$

However, because the quality factor of MEMS resonators is very high (i.e., $Q \gg 1$), we can consider $\omega_0 = \omega_n = \omega_r = \omega_d$ (similar to an undamped oscillator).

Since the Coriolis force appears as an additional force over the proof mass (see (2.5)), this force is commonly interpreted as a disturbance at the input of the mechanical system. Even if it is not the case, this disturbance is typically considered to be exogenous, such that the drive and sense modes can be considered as independent systems. For the moment, let us also make this assumption. In Section 2.2.3, we discuss the consequences of this hypothesis.

After having modeled an ideal MEMS gyroscope, let us discuss its operation. Note that the matrices \mathbf{m} , \mathbf{d} and \mathbf{k} in (2.5), as well as the transfer matrix G^{mech} , are diagonal. Then, the only coupling between the drive and sense modes is through the Coriolis forces.

Drive-Mode Operation As discussed earlier, the main objective of the drive mode is to allow the creation of a Coriolis force by keeping oscillations of the proof mass along the \vec{x} -axis. To this end, we apply a force F_x , producing steady-state oscillations of amplitude A_x and with excitation frequency ω_{exc} , *i.e.*, the signal x is of the form

$$x(t) = A_x \sin(\omega_{exc}t).$$

Obviously, the drive mode could operate in open loop. However, due to the disturbing Coriolis force $F_{Cor,x}$ and modeling errors, to regulate the amplitude A_x , a feedback loop and a controller, which we denote K_{DM} , are required. Based on the measures of x and on a given reference amplitude A_x^{ref} , such controller computes the force F_x to be applied so that $A_x = A_x^{ref}$, despite the presence of $F_{Cor,x}$. This feedback loop is depicted in Figure 2.3. Then, under ideal operation of the drive mode, we consider

$$x(t) = A_x^{ref} \sin(\omega_{exc}t). \quad (2.6)$$

Moreover, to minimize the applied force, it is also desired to use $\omega_{exc} \approx \omega_{0,x}$, taking advantage of the high gain of G_x^{mech} at its resonance frequency. The excitation frequency can be automatically set by an external loop, by the user or even implicitly by K_{DM} itself (see Section 2.2.1 for further details).

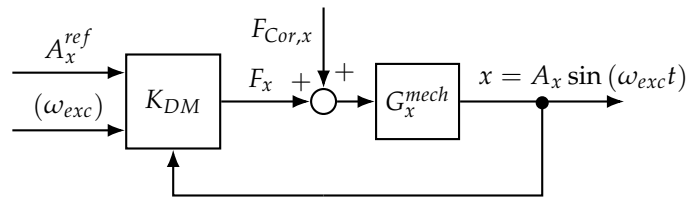


FIGURE 2.3: Closed-loop operation of the drive mode.

Sense-Mode Operation In its turn, the main objective of the sense mode is to estimate the Coriolis force acting on the sense mode, $F_{Cor,y}$, allowing for the computation of Ω_z (see (2.4)). The sense mode can be operated in two different modes: in open loop or in closed loop.

When operating in open loop, $F_y(t) \equiv 0$ and, for an ideal MEMS gyroscope, only the Coriolis force ($F_{Cor,y}$) produces oscillations on the sense mode. Then, based on the measures of y and on the model G_y^{mech} , $F_{Cor,y}$ can be estimated as $\hat{F}_{Cor,y}(s) = G_y^{mech}(s)^{-1}y(s)$, where $\hat{F}_{Cor,y}$ is the estimate of $F_{Cor,y}$. This approach is the simplest one to implement, since it is based only on the measurements of the position y and on posterior processing. However, the dynamics of the sense mode exclusively depends on its mechanical characteristics, which are often very

slow due to its high quality factor. Therefore, this operating mode is better suited for low-cost and low-performance applications.

On the other hand, the main idea behind the closed-loop operation is to implement a controller, K_{SM} , that computes the force F_y that, by keeping $y(t) \approx 0$, compensates for $F_{Cor,y}$. In this case, $F_y(t) \approx -F_{Cor,y}(t)$ and we define the estimate of the Coriolis force on the sense mode, $\hat{F}_{Cor,y}$, as $\hat{F}_{Cor,y}(t) = -F_y(t)$. Figure 2.4 illustrates this description with two equivalent schemes: one with the controller before the plant, as in a classical closed-loop system; and one with the controller after the plant, as commonly used for the closed-loop operation with the architecture known as electro-mechanical $\Sigma\Delta$ (EM- $\Sigma\Delta$), see Section 2.2.2.

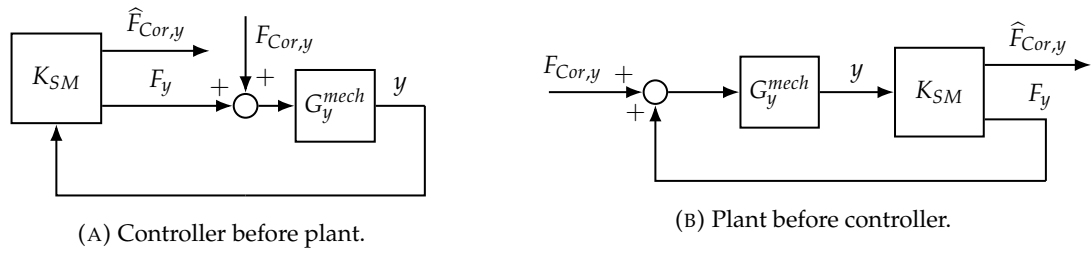


FIGURE 2.4: Closed-loop operation of the sense mode.

This closed-loop control strategy is also known as force-to-rebalance control and has two huge advantages over the open-loop operation.

- (i) The dynamics of the closed-loop system are determined by the sense mode and the controller, which can be designed to increase the bandwidth of the sensor [YAN98].
- (ii) Minimizing y implies the minimization of $F_{Cor,x}$, reducing disturbances on the drive mode. In addition, minimizing y also allows avoiding saturation on the sense-mode instrumentation circuits and reduce nonlinearities [RCRW09, CGZ⁺11].

Consequently, it is clear that, to design a high-performance gyroscope, the sense mode also has to operate in closed loop. Hence, in the remaining of this work, we focus on the closed-loop operation of the sense mode.

Finally, under ideal closed-loop operation, we consider that the controller K_{SM} produces

$$\hat{F}_{Cor,y}(t) = F_{Cor,y}(t) = -2m\Omega_z(t)\dot{x}(t). \quad (2.7)$$

Then, by plugging (2.6) into (2.7), we obtain

$$\hat{F}_{Cor,y}(t) = -\Omega_z(t) \cdot 2mA_x^{ref} \omega_{exc} \cos(\omega_{exc}t). \quad (2.8)$$

Please note that, because the sense-mode closed-loop operation also keeps $y(t) \approx 0$, we can neglect the Coriolis force acting on the drive mode, $F_{Cor,x}$. Then, even under a nonnull angular rate, we can still consider that (for ideal MEMS gyroscopes) the only coupling between the drive and sense modes is the Coriolis force acting on the sense one, *i.e.*, $F_{Cor,x}(t) \equiv 0$ and $F_{Cor,y}(t) = -2m\Omega_z(t)\dot{x}(t)$.

From the Coriolis Force to the Estimation of Ω_z Having estimated the Coriolis force, the last step consists in obtaining an estimate of Ω_z , which is denoted $\hat{\Omega}_z$. Note that $\hat{F}_{Cor,y}$ (see (2.8)) is a harmonic signal whose amplitude is modulated by $\Omega_z(t)$. Therefore, to compute the angular rate, it suffices to demodulate the signal $\hat{F}_{Cor,y}$. In general, the synchronous

demodulation (SD) is used to this purpose [Sau08]. This important element is presented in Section 2.1.4. This operation needs to know the phase of the signal to correctly determine the sign of Ω_z^2 . The phase $\omega_{exc}t$ can be obtained through x (or \dot{x}) or directly from ω_{exc} . Figure 2.5 synthesizes the general scheme used for the closed-loop operation of ideal MEMS gyroscopes.

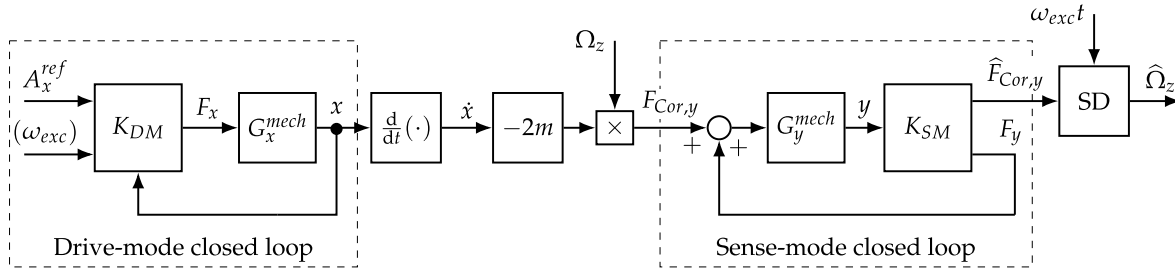


FIGURE 2.5: Closed-loop operation of an ideal MEMS gyroscope.

2.1.3 Actuation and Instrumentation

In the previous section, we described the mechanical part of the MEMS gyroscopes and its closed-loop operation. However, to operate in closed-loop, we need to use actuators and sensors. The present section aims at briefly describing the principles of actuators and sensors of MEMS devices, and how they impact the model and operation of the gyroscope.

Actuators are devices that convert an electrical signal (typically, a voltage) into a force. In MEMS devices, several technologies can be used for this purpose, such as electrostatic (capacitive), piezoelectric or electromagnetic mechanisms [Sau08, Kem11]. Similarly, sensors are elements that convert the position of the proof mass into an electrical signal. Here, the most common methods used for MEMS gyroscopes are capacitive, piezoelectric and piezoresistive detection [Sau08, Kem11].

In this work, we focus on the electrostatic actuation and capacitive detection, and on their simple modeling, which is sufficient for the control purposes. A deeper discussion on actuation and detection technologies can be found in [Kem11], for instance.

Electrostatic or Capacitive Actuation

Electrostatic or capacitive actuators rely on the attractive force created by an electric field between two electrodes. These electrodes form a capacitor of capacitance C_{el} , which depends on the geometry of the electrodes. These two electrodes can be conceived as a simple parallel-plate capacitor, as shown in Figure 2.6a, or as two comb structures that slide between each other, forming a comb-drive capacitor. This later structure is illustrated in Figure 2.6b. In both cases, one of the electrodes is built on the (fixed) base of the sensor, while the second one is built on the (moving) proof mass.

The electrostatic attractive force, denoted F_{es} , is given by

$$F_{es} = -\frac{1}{2} \frac{\partial C_{el}(d_{el})}{\partial d_{el}} v_{in}^2$$

²This reason explains the adjective “synchronous” in the name of this particular demodulator.

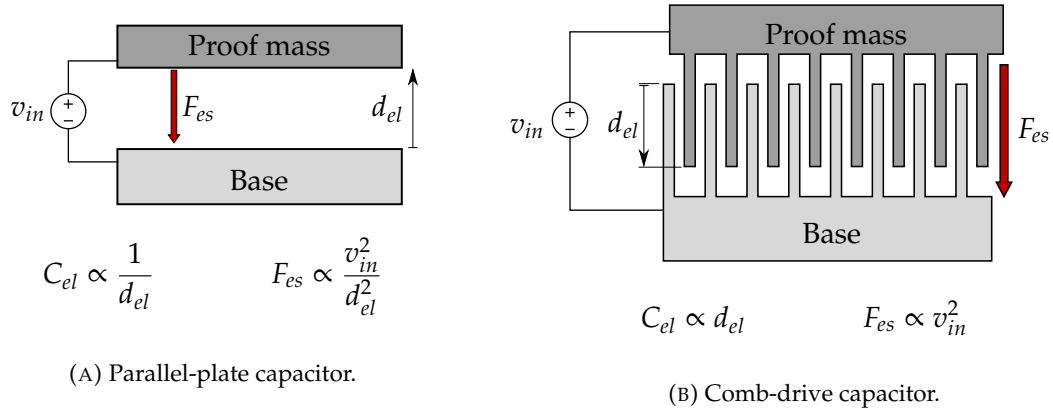


FIGURE 2.6: Capacitive transducers.

where v_{in} is the voltage between the electrodes and d_{el} is the gap between them in the case of parallel-plate capacitors or the variable dimension of the overlapping surface in the case of comb drives³ (see Figure 2.6).

As mentioned earlier, the capacitance C_{el} depends on the geometry of the electrodes, the electrical properties of the dielectric and on d_{el} . Let us then consider a constant k_{act} , which encapsulates all these contributions, except for d_{el} . In the case of parallel-plate actuator, the capacitance is given by $2k_{act}/d_{el}$. Therefore, the electrostatic force F_{es} is given by $k_{act}v_{in}^2/d_{el}^2$ and has a clear nonlinear dependence on d_{el} . If the displacements are small, this dependence can be linearized, providing a good approximation. Nevertheless, if the displacements are important, this approximation introduces nonnegligible errors, which can deteriorate the performance of the sensor.

The nonlinear dependence on d_{el} is eliminated by using comb-drive capacitors. In this case, the capacitance is given by $2k_{act}d_{el}$ and the electrostatic force is given by

$$F_{es}(t) = k_{act}v_{in}(t)^2. \quad (2.9)$$

Note that the force F_{es} of (2.9) is always positive (attractive). Then, to produce an “oscillating” force, two solutions can be considered [Sau08, AS09].

- (i) An offset voltage V_{DC} is added to a time-varying voltage u , i.e., $v_{in}(t) = V_{DC} + u(t)$. In this case, the electrostatic force is given by

$$F_{es}(t) = k_{act} (V_{DC} + u(t))^2 = k_{act} (V_{DC}^2 + 2V_{DC}u(t) + u(t)^2). \quad (2.10)$$

- (ii) Electrodes are built on the two sides (left and right, for instance) of the proof mass and a voltage $V_{DC} + u(t)$ is applied in one side, while a voltage $V_{DC} - u(t)$ is applied to the other side, as presented by the scheme of Figure 2.7, which is known as balanced or differential actuation scheme. In this case, the resulting electrostatic force is given by

$$F_{es}(t) = k_{act} \left((V_{DC} + u(t))^2 - (V_{DC} - u(t))^2 \right) = 4k_{act}V_{DC}u(t). \quad (2.11)$$

³In the case of the comb drive, the sign of F_{es} changes due to the modification on the sense (of the direction) of d_{el} . The electrostatic force is always attractive.

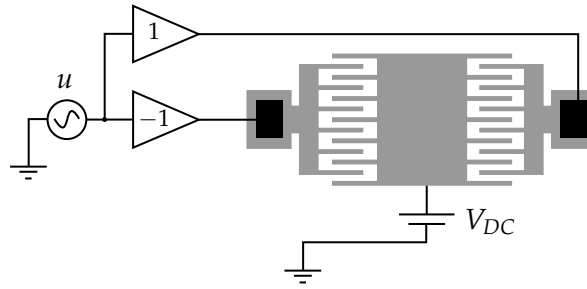


FIGURE 2.7: Balanced-actuation scheme [AS09].

Note that the electrostatic actuation introduces a square nonlinearity in the model: $F_{es} = k_{act}v_{in}^2$ (see (2.9)). Different methods can be considered to linearize this nonlinearity. The use of differential actuation (see Figure 2.7 and (2.11)) is one of the common methods to tackle this problem during the design of the MEMS device. However, when this solution is not implemented, which is the case in our work, other techniques can be used to linearize (2.10). We present one of these techniques in Section 7.2.3 (page 179). Regardless of the adopted method, we can therefore establish a linear relation between u and the electrostatic force:

$$F_{es}(t) = k_{in}u(t) \quad \text{with} \quad k_{in} = k_{act}k_{lin} \quad (2.12)$$

where k_{lin} is the linearization gain. Obviously, in the case of a balanced actuation (see (2.11)), $k_{lin} = 4V_{DC}$. For other linearization techniques, this constant can take other values, see Section 7.2.3 (page 179).

Capacitive Detection and Charge Amplifiers

Similar to the electrostatic actuation, by building electrodes on the fixed structure of the sensor and on the moving mass, we can measure the distance between them through the capacitance formed by them.

Let us consider a constant k_{det} , whose value depends on the shape of the electrodes and on the electrical properties of the dielectric separating them. Then, if the electrodes form a parallel-plate capacitor, the capacitance is given k_{det}/d_{el} , which is nonlinear with respect to d_{el} . Again, if the displacement amplitude is small with respect to the initial position, this nonlinear relation can be linearized with small error. Nevertheless, as the displacement amplitude becomes larger, the approximation error also gets larger. Now, if the electrodes form a comb drive, the capacitance is given by $k_{det}d_{el}$, which is linear with respect to d_{el} . In general, the parallel-plate configuration is used for the sense mode (small displacement), while the comb-drive structure is used for the drive mode (large displacement) [AS09].

Finally, to convert a capacitance into voltage, electronic circuits known as charge amplifiers are employed [Sau08]. These circuits are also usually modeled as constant gains, which we denote k_{CA} . Therefore, the relation between d_{el} and the output voltage is given by $v_{out} = k_{out}d_{el}$, where $k_{out} = k_{CA}k_{det}$.

Mechanical Model with Actuation and Instrumentation

Based on the above discussion, each mode of the MEMS gyroscope can be modeled by its respective mechanical model with the gains k_{in} and k_{out} at the input and output, modeling the actuation and instrumentation. Figure 2.8 illustrates the overall model of the drive mode. We also include the signal n_x , which represents the process and measurement noises,

(see Section 2.1.5, page 32, for a deeper discussion on the noise), defining the signals

$$x_m(t) = k_{out,x}x(t) \quad \text{and} \quad x_n(t) = x_m(t) + n_x(t). \quad (2.13)$$

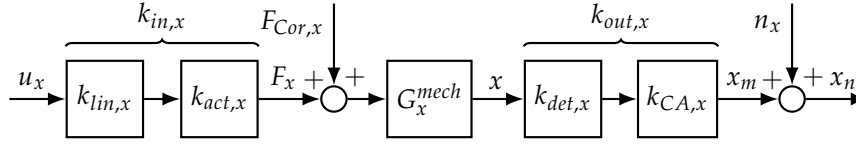


FIGURE 2.8: Overall model of the drive mode with actuation and instrumentation. For the sense mode, replace x by y .

The overall model can also be represented in the compact form of Figure 2.9, where

$$u_{Cor,x}(t) = \frac{F_{Cor,x}(t)}{k_{in,x}} \quad (2.14)$$

is the image of $F_{Cor,x}$ in volts. Therefore, the model of the drive mode of a MEMS gyroscope can be given by the transfer function

$$G_x(s) = \frac{x_m(s)}{u_x(s)} = \frac{k_{0,x}\omega_{0,x}^2}{s^2 + \omega_{0,x}/Q_x \cdot s + \omega_{0,x}^2}, \quad (2.15)$$

where $k_{0,x} = k_{out,x}k_{0,x}^{mech}k_{in,x}$.

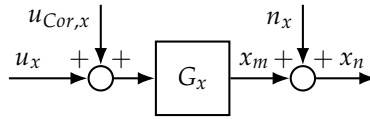


FIGURE 2.9: Compact linear model of the drive mode with actuation and instrumentation. For the sense mode, replace x by y .

When considering the ideal closed-loop operation, the output voltage x_m is given by

$$x_m(t) = A_{x,m}^{ref} \sin(\omega_{exc}t), \quad (2.16)$$

where $A_{x,m}^{ref} = k_{out,x}A_x^{ref}$ (see (2.6)).

Similarly, for the sense mode (see Figure 2.8 and Figure 2.9 replacing x by y), we define the measurement noise n_y and the signals

$$y_m(t) = k_{out,y}y(t) \quad \text{and} \quad y_n(t) = y_m(t) + n_y(t). \quad (2.17)$$

Hence, the model of the sense mode can be given by

$$G_y(s) = \frac{y_m(s)}{u_y(s)} = \frac{k_{0,y}\omega_{0,y}^2}{s^2 + \omega_{0,y}/Q_y \cdot s + \omega_{0,y}^2}. \quad (2.18)$$

Through this process, we also define

$$u_{Cor,y}(t) = \frac{F_{Cor,y}(t)}{k_{in,y}}, \quad (2.19)$$

which is an image of the actual Coriolis force $F_{Cor,y}$. For the closed-loop operation of a MEMS gyroscope, the controller does not apply directly F_y to compensate for $F_{Cor,y}$. It applies the signal u_y that compensates for $u_{Cor,y}$. Then, rather than working with $\hat{F}_{Cor,y}$, we use the signal $\hat{u}_{Cor,y}$ for the estimation of the angular rate Ω_z . In the ideal case, $\hat{u}_{Cor,y}$ is given by (see (2.8) and (2.16))

$$\hat{u}_{Cor,y}(t) = \frac{\hat{F}_{Cor,y}(t)}{k_{in,y}} = \frac{-\Omega_z(t) \cdot 2mA_{x,m}^{ref} \omega_{exc} \cos(\omega_{exc}t)}{k_{out,x}k_{in,y}}. \quad (2.20)$$

In the sequel, we introduce the models of the drive and sense modes which are used to illustrate the examples along this thesis.

Example 2.1 (Drive-mode model). *The behavior of the drive mode, including actuation and instrumentation, can be described by the transfer function G_x , presented in (2.15), with $\omega_{0,x} = 2\pi \cdot 11\,500 \text{ rad s}^{-1}$, $Q_x = 100\,000$ and $k_{0,x} = 2 \cdot 10^{-5}$. These values correspond to the typical values presented in Section 2.1.2. In particular, they correspond to the nominal characteristics of the MEMS gyroscopes of the family GYRO I (see Table 2.1).*

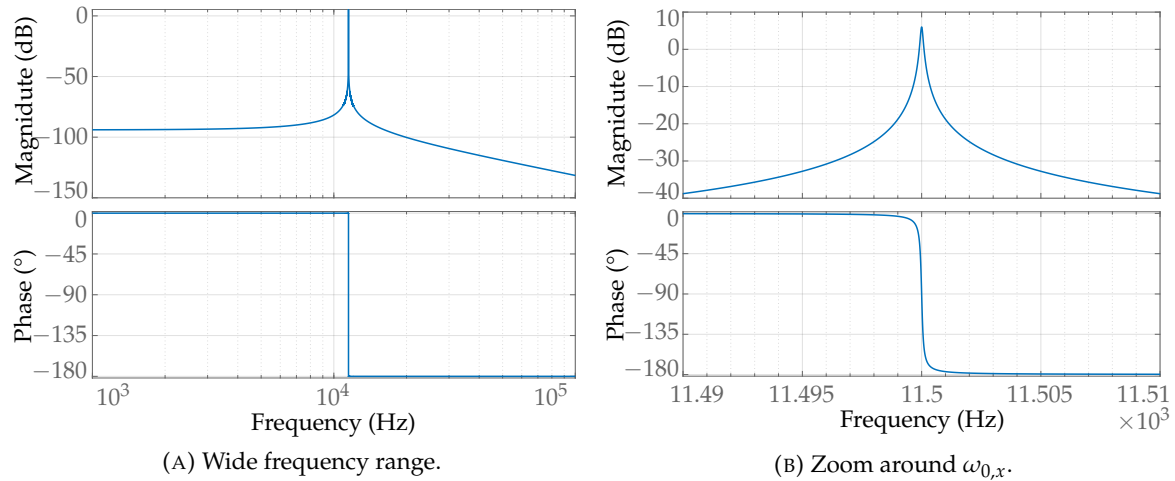


FIGURE 2.10: Bode diagram of the drive mode.

The Bode diagram of this model is presented in Figure 2.10. Observe that the magnitude presents a very narrow resonance peak at 11.5 kHz. That is, if we consider a frequency $\omega = \omega_{0,x} = 2\pi \cdot 11\,500 \text{ rad s}^{-1}$, we have $|G_x(j\omega)| = 2 \approx 6 \text{ dB}$; however, a slight change of ω drastically modifies $|G_x(j\omega)|$. For instance, with $\omega = 2\pi \cdot 11\,499 \text{ rad s}^{-1}$, $|G_x(j\omega)| \approx 0.15 \approx -19 \text{ dB}$.

Note that, for frequencies around the resonance frequency, the phase passes very quickly from close zero to around -180° , passing by -90° right at its resonance frequency. It is worth mentioning that some control strategies take advantage of this property to identify or track the resonance frequency (see Section 2.2.1 for further details).

Finally, the ratio between the gain at the resonance frequency and the static gain corresponds to the quality factor. Indeed,

$$\frac{|G_x(j\omega_{0,x})|}{|G_x(0)|} = \frac{2}{2 \cdot 10^{-5}} = 100\,000.$$

Example 2.2 (Sense-mode model). For the sense mode, we consider the plant given by

$$G_y(s) = \frac{k_{0,y}\omega_{0,y}^2}{s^2 + Q_y\omega_{0,y}s + \omega_{0,y}^2} \quad (2.21)$$

with $\omega_{0,y} = 2\pi \cdot 11\,550 \text{ rad s}^{-1}$, $Q_y = 10\,000$ and $k_{0,y} = 4 \cdot 10^{-3}$.

The Bode diagram of this model is presented in Figure 2.11. Similar to the previous example, G_y has important gains around the resonance frequency, $\omega_{0,y}$. However, due to a smaller quality factor, the resonance peak is wider for the sense mode. For instance, for $\omega = \omega_{0,y} = 2\pi \cdot 11\,550 \text{ rad s}^{-1}$, we have $|G_y(j\omega)| = 40 \approx 32 \text{ dB}$; and for $\omega = \omega_{0,x} = 2\pi \cdot 11\,500 \text{ rad s}^{-1}$, the magnitude of G_y is close to 0.5 (or -6 dB). For bigger mismatches, the loss of gain becomes more important. That is why MEMS gyroscopes are typically designed to have $\omega_{0,y}$ close to $\omega_{0,x}$.

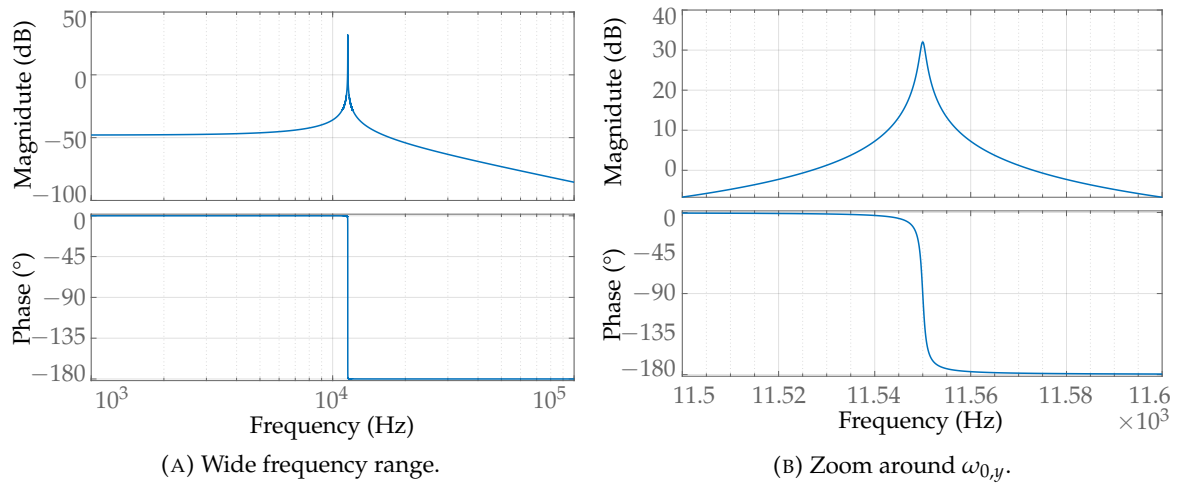


FIGURE 2.11: Bode diagram of the sense mode.

2.1.4 Ideal Synchronous Demodulation and Angular Rate Estimation

After estimating the Coriolis force, the angular rate is determined through the synchronous demodulation (SD), which is presented in this subsection. It is worth mentioning that the synchronous demodulation (also known as quadrature demodulation or synchronous detector) is an essential element in the operation of MEMS gyroscopes. Further than its use to compute the angular rate from the Coriolis force estimate, the synchronous demodulation can also be used to compute the amplitude and phase of a modulated signal. These features are very useful for some control architectures, see Section 2.2.

In this subsection, we introduce the synchronous demodulation in a general manner. Then, we apply this operation for the estimation of the angular rate of a MEMS gyroscope. Finally, we discuss how to use the synchronous demodulation to compute the amplitude and phase of a modulated signal.

Ideal Synchronous Demodulation: a General Case

Let us start by considering a quadrature amplitude-modulated signal $s_m(t) \in \mathbb{R}$ of the form

$$s_m(t) = s_I(t) \cos(\omega_{exc}t) - s_Q(t) \sin(\omega_{exc}t), \quad (2.22)$$

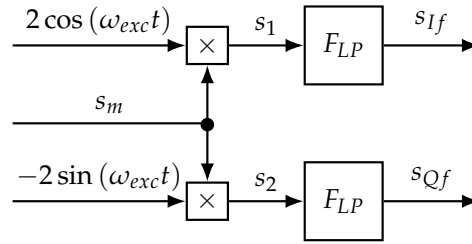


FIGURE 2.12: Block diagram of the synchronous demodulator.

where the signals $s_I(t) \in \mathbb{R}$ and $s_Q(t) \in \mathbb{R}$ define respectively the amplitude of the terms in phase and in quadrature (90° of phase shift) with $\cos(\omega_{exc}t)$. The signal s_m is also assumed to be a band-pass signal of bandwidth $2\omega_{exc}$ centered at ω_{exc} . This means that its power spectral density (PSD), \mathcal{S}_{s_m} , is such that,

$$\forall |\omega| \geq 2\omega_{exc}, \quad \mathcal{S}_{s_m}(\omega) = 0 \quad \text{and} \quad \mathcal{S}_{s_m}(0) = 0. \quad (2.23)$$

It is important to mention that any signal s_m that verifies (2.23) can be decomposed into in-phase and in-quadrature terms, as in (2.22). This decomposition is unique if s_I and s_Q are low-pass signals, *i.e.*, if their DSPs are such that

$$\forall |\omega| \geq \omega_{exc}, \quad \mathcal{S}_{s_I}(\omega) = 0 \quad \text{and} \quad \mathcal{S}_{s_Q}(\omega) = 0. \quad (2.24)$$

See, for instance, [Lat98, Sec. 11.5] for further details.

The synchronous demodulation of a modulated signal s_m corresponds to the extraction of the in-phase and in-quadrature terms, respectively s_I and s_Q [Sau08]. This operation can be performed by using the block diagram presented in Figure 2.12, where F_{LP} represents ideal low-pass filters, *i.e.*, filters whose frequency response is given by

$$F_{LP}(\omega) = \begin{cases} 1, & \forall |\omega| \leq \omega_{exc} \\ 0, & \text{otherwise} \end{cases}. \quad (2.25)$$

By plugging the signal s_m of (2.22) at the input of the synchronous demodulator, we have

$$s_1(t) = 2s_I(t) \cos(\omega_{exc}t)^2 - 2s_Q(t) \sin(\omega_{exc}t) \cos(\omega_{exc}t)$$

$$s_1(t) = s_I(t) (1 + \cos(2\omega_{exc}t)) - s_Q(t) \sin(2\omega_{exc}t)$$

and

$$s_2(t) = -2s_I(t) \cos(\omega_{exc}t) \sin(\omega_{exc}t) + 2s_Q(t) \sin(\omega_{exc}t)^2$$

$$s_2(t) = -s_I(t) \sin(2\omega_{exc}t) + s_Q(t) (1 - \cos(2\omega_{exc}t)).$$

Hence, after filtering out the high-frequency terms with F_{LP} , we obtain

$$s_{I_f}(t) = s_I(t) \quad \text{and} \quad s_{Q_f}(t) = s_Q(t),$$

fulfilling the objective of extracting the in-phase and in-quadrature terms. This is only possible because the low-frequency condition for the signals s_I and s_Q avoids the overlap between the spectra of the high-frequency terms (those with $\cos(2\omega_{exc}t)$ and $\sin(2\omega_{exc}t)$)

and the low-frequency terms. A detailed analysis of the synchronous demodulation in the frequency domain is provided in Appendix A.1.

Remark 2.1 (On the linearity of the synchronous demodulation). The synchronous demodulator is a linear time-varying (LTV) system, where the products by $2 \cos(\omega_{exc}t)$ and $-2 \sin(\omega_{exc}t)$ can be interpreted as time-varying gains. In general, the time-varying nature of the system could make the analysis in the frequency domain untractable or laborious. However, for the particular case where ω_{exc} is constant over time, an interesting property arises: multiplying a signal by $\cos(\omega_{exc}t)$ or $\sin(\omega_{exc}t)$ corresponds to the replication of its spectrum with a frequency shift of $+\omega_{exc}$ and $-\omega_{exc}$. For instance, if we consider the signal

$$s_1(t) = 2 \cos(\omega_{exc}t) \cdot s_m(t)$$

and the Fourier transform of s_m given by $\mathcal{F}[s_m]$, the Fourier transform of s_1 , $\mathcal{F}[s_1]$, is given by

$$\mathcal{F}[s_1](j\omega) = \mathcal{F}[s_m](j\omega + j\omega_{exc}) + \mathcal{F}[s_m](j\omega - j\omega_{exc}).$$

Therefore, despite its time-varying nature, the frequency-domain analysis of the synchronous demodulation (and systems with synchronous demodulation) is still possible.

Estimating the Angular Rate Through the Synchronous Demodulation

Let us consider again the ideal operation of a MEMS gyroscope. When subjected to an angular rate Ω_z , the Coriolis force acting on the sense mode can be determined through (2.20), which is recalled below:

$$\hat{u}_{Cor,y}(t) = -\frac{\Omega_z(t) \cdot 2mA_{x,m}^{ref}\omega_{exc}}{k_{out,x}k_{in,y}} \cos(\omega_{exc}t)$$

We assume that Ω_z is a low-pass signal, *i.e.*,

$$\forall |\omega| \geq \omega_{exc}, \quad \mathcal{S}_{\Omega_z}(\omega) = 0.$$

Therefore, by connecting $\hat{u}_{Cor,y}$, which is a pass-band signal (consequence of the assumption above), at the input of the synchronous demodulator ($s_m = \hat{u}_{Cor,y}$), we obtain

$$s_{If}(t) = k_{SF} \cdot \Omega_z(t) \quad \text{and} \quad s_{Qf}(t) = 0 \quad (2.26)$$

$$k_{SF} = -\frac{2mA_{x,m}^{ref}\omega_{exc}}{k_{out,x}k_{in,y}}, \quad (2.27)$$

where k_{SF} is referred to as the scale factor (SF) of the sensor.

It is worth mentioning that, in practice, the constant k_{SF} is not perfectly known, *i.e.*, cannot be accurately computed analytically because of the fabrication dispersion and modeling errors, and can vary as function of Ω_z . Hence, to obtain an accurate estimate for the scale factor, \hat{k}_{SF} , a calibration step is needed: the gyroscope is placed on a rotating table and different angular rates are applied; for each Ω_z , the value of s_{If} is read; then, \hat{k}_{SF} can be determined as the slope of the best line fitting the measured data (see Section 2.1.6 for further details). Therefore, \hat{k}_{SF} allows computing $\hat{\Omega}_z$ from s_{If} as follows:

$$\hat{\Omega}_z(t) = \frac{s_{If}(t)}{\hat{k}_{SF}} \approx \Omega_z(t).$$

Using the Synchronous Demodulation to Compute the Amplitude and Phase of a Signal

Let us come back to the general case of the synchronous demodulation. Please note that the signal s_m (2.22) can be rewritten in the form

$$s_m(t) = S_m(t) \cos(\omega_{exc}t + \phi_s(t)), \quad (2.28)$$

where $S_m(t) \in \mathbb{R}^+$ is the instantaneous amplitude or envelope of s_m , and $\phi_s(t) \in (-\pi, \pi]$ is the instantaneous phase shift with respect to the phase $\omega_{exc}t$. Then, the correspondence of S_m and ϕ_s with s_I and s_Q can be established through trigonometric identities, as follows.

$$s_I(t) = S_m(t) \cos(\phi_s(t)) \quad (2.29)$$

$$s_Q(t) = S_m(t) \sin(\phi_s(t)) \quad (2.30)$$

In the other direction, we have

$$S_m(t) = \sqrt{s_I(t)^2 + s_Q(t)^2} \quad (2.31)$$

and

$$\phi_s(t) = \arctan2(s_Q(t), s_I(t)), \quad (2.32)$$

where $\arctan2$ corresponds to the 2-argument arctangent function and returns a value in the interval $(-\pi, \pi]$. This function is defined, for two real scalars s_I and s_Q , as

$$\arctan2(s_Q, s_I) \triangleq 2 \cdot \arctan\left(\frac{s_Q}{\sqrt{s_I^2 + s_Q^2} + s_I}\right). \quad (2.33)$$

Hence, we can use the synchronous demodulator to extract the amplitude and phase shift of s_m (see (2.28)) as presented in Figure 2.13. That is, given a modulated signal s_m in the form of (2.28), or equivalently in the form of (2.22), the synchronous demodulator allows computing s_I and s_Q (s_{If} and s_{Qf} , respectively). These signals are then used to compute the amplitude, S_{mf} , and phase shift, ϕ_{sf} , of the signal, as follows:

$$S_{mf}(t) = \sqrt{s_{If}(t)^2 + s_{Qf}(t)^2} \quad \text{and} \quad \phi_{sf}(t) = \arctan2(s_{Qf}(t), s_{If}(t)). \quad (2.34)$$

Please note that, while spectral conditions on s_I and s_Q of (2.22) can be easily established to ensure $s_{If} = s_I$ and $s_{Qf} = s_Q$, simple conditions for S_m and ϕ_s of (2.28) cannot be established to ensure $S_{mf} = S_m$ and $\phi_{sf} = \phi_s$.

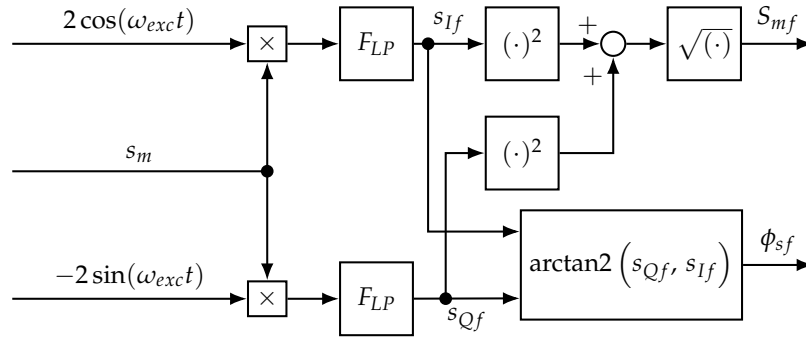


FIGURE 2.13: Block diagram of the synchronous demodulation for the computation of amplitude and phase of s_m .

2.1.5 Real (Nonideal) MEMS Gyroscopes

Up to this point, we have considered the gyroscope as ideal. In this section, we aim to present the main nonidealities found in real MEMS gyroscopes and discuss their effects on the angular rate estimation. These nonidealities can be splitted into some groups: mechanical coupling, error on the synchronous demodulation phase, noises, environmental sensitivity, parasitic electrical coupling, and nonlinearities.

To evaluate the impact of each group of nonidealities on the angular rate estimation, we consider a closed-loop operation in which:

- (i) K_{DM} enforces $x(t) = A_{x,m}^{ref}/k_{out,x} \cdot \sin(\omega_{exc}t)$ or, equivalently, $x_m(t) = A_{x,m}^{ref} \sin(\omega_{exc}t)$;
- (ii) K_{SM} enforces $y(t) \equiv 0$ by applying a control signal $u_y(t)$;
- (iii) the synchronous demodulator, based on $\hat{u}_{Cor,y}(t) = -u_y(t)$ and the phase $\omega_{exc}t$, computes $s_{I_f}(t)$, which is used afterward to determine $\hat{\Omega}_z$.

It is important to highlight that the controllers and synchronous demodulation are assumed to perfectly ensure the above requirements. Hence, we can isolate the effects of the gyroscope nonidealities from the effects of the operation nonidealities. The effects of the operation nonidealities are detailed in Chapter 3.

Mechanical Coupling: Anisoeasticity and Nonproportional Damping

During the fabrication process, a misalignment between the \vec{x} - and \vec{y} -axes (drive and sense modes) may occur. This imperfection gives origin to anisoeasticity and nonproportional damping effects. These effects appear in the model as nondiagonal terms in the matrices K and D , respectively (see [PSP⁺06, Sau08, Kem11] and references therein for further details). Thus, the dynamic behavior of the MEMS gyroscope is now described by the equation below:

$$\begin{bmatrix} m & 0 \\ 0 & m \end{bmatrix} \begin{bmatrix} \ddot{x} \\ \ddot{y} \end{bmatrix} + \begin{bmatrix} d_{xx} & d_{xy} \\ d_{yx} & d_{yy} \end{bmatrix} \begin{bmatrix} \dot{x} \\ \dot{y} \end{bmatrix} + \begin{bmatrix} k_{xx} & k_{xy} \\ k_{yx} & k_{yy} \end{bmatrix} \begin{bmatrix} x \\ y \end{bmatrix} = \begin{bmatrix} F_x \\ F_y \end{bmatrix} + \Omega_z \begin{bmatrix} 0 & 2m \\ -2m & 0 \end{bmatrix} \begin{bmatrix} \dot{x} \\ \dot{y} \end{bmatrix} \quad (2.35)$$

Note that we can define a coupling force vector F_{coup}

$$F_{coup}(t) = \begin{bmatrix} F_{coup,x}(t) \\ F_{coup,y}(t) \end{bmatrix} = - \begin{bmatrix} 0 & d_{xy} \\ d_{yx} & 0 \end{bmatrix} \begin{bmatrix} \dot{x}(t) \\ \dot{y}(t) \end{bmatrix} - \begin{bmatrix} 0 & k_{xy} \\ k_{yx} & 0 \end{bmatrix} \begin{bmatrix} x(t) \\ y(t) \end{bmatrix} \quad (2.36)$$

and rearrange (2.35) as

$$\begin{bmatrix} m & 0 \\ 0 & m \end{bmatrix} \begin{bmatrix} \ddot{x} \\ \ddot{y} \end{bmatrix} + \begin{bmatrix} d_{xx} & 0 \\ 0 & d_{yy} \end{bmatrix} \begin{bmatrix} \dot{x} \\ \dot{y} \end{bmatrix} + \begin{bmatrix} k_{xx} & 0 \\ 0 & k_{yy} \end{bmatrix} \begin{bmatrix} x \\ y \end{bmatrix} = \begin{bmatrix} F_x \\ F_y \end{bmatrix} + \begin{bmatrix} F_{Cor,x} \\ F_{Cor,y} \end{bmatrix} + \begin{bmatrix} F_{coup,x} \\ F_{coup,y} \end{bmatrix}, \quad (2.37)$$

which corresponds to (2.5), adding F_{coup} on right-hand side of the equation.

Therefore, the anisotropy and the nonproportional damping effects can be interpreted as the inclusion of a new force at the input of the drive and sense modes, mechanically coupling them. It is important to mention that, similar to the Coriolis forces, the coupling forces are sometimes interpreted as exogenous disturbances [Sau08, EMK12], despite their dependence on the internal signals (states). Let us now discuss the effects of the mechanical coupling on the operation of the sensor. In this nonideal framework, if the drive-mode controller works properly, it ensures the oscillation of x with the desired amplitude. In its turn, if the controller of the sense mode ensures $y(t) \equiv 0$, we have $F_{coup,x}(t) \equiv 0$ (see (2.36)) and

$$F_y(t) = -F_{Cor,y} - F_{coup,y} = (2m\Omega_z(t) + d_{yx}) \dot{x}(t) + k_{yx}x(t) \quad (2.38)$$

(see (2.37)). Now, by considering the actuation and instrumentation gains, we replace $x(t) = A_{x,m}^{ref} \sin(\omega_{exc}t) / k_{out,x}$ into (2.38) and with $u_y(t) = F_y(t) / k_{in,y}$, we obtain

$$u_y(t) = \frac{(2m\Omega_z(t) + d_{yx}) A_{x,m}^{ref} \omega_{exc}}{k_{out,x} k_{in,y}} \cos(\omega_{exc}t) + \frac{k_{yx} A_{x,m}^{ref}}{k_{out,x} k_{in,y}} \sin(\omega_{exc}t). \quad (2.39)$$

Then, with $\hat{u}_{Cor,y}(t) = -u_y(t)$ (ideal closed-loop operation), we have

$$\hat{u}_{Cor,y}(t) = -\frac{(2m\Omega_z(t) + d_{yx}) A_{x,m}^{ref} \omega_{exc}}{k_{out,x} k_{in,y}} \cos(\omega_{exc}t) - \frac{k_{yx} A_{x,m}^{ref}}{k_{out,x} k_{in,y}} \sin(\omega_{exc}t). \quad (2.40)$$

Therefore, after demodulating $\hat{u}_{Cor,y}$ through the synchronous demodulation, we obtain

$$s_{If}(t) = -\frac{(2m\Omega_z(t) + d_{yx}) A_{x,m}^{ref} \omega_{exc}}{k_{out,x} k_{in,y}} \quad (2.41)$$

and

$$s_{Qf}(t) = \frac{k_{yx} A_{x,m}^{ref}}{k_{out,x} k_{in,y}}. \quad (2.42)$$

We can then rewrite s_{If} as

$$s_{If}(t) = s_{If}^L(t) + s_{If}^0(t), \quad (2.43)$$

where s_{If}^L is proportional to Ω_z and s_{If}^0 is a constant value, that is,

$$s_{If}^L(t) = k_{SF} \cdot \Omega_z(t) \quad \text{and} \quad s_{If}^0(t) = k_{ZRO} \quad (2.44)$$

with k_{SF} given in (2.27) and $k_{ZRO} = -\frac{d_{yx} A_{x,m}^{ref} \omega_{exc}}{k_{out,x} k_{in,y}}$.

Note that, although the synchronous demodulation allows distinguishing part of the coupling force contributions present in $\hat{u}_{Cor,y}$, the estimate s_{If} is still perturbed by the nonproportional damping d_{yx} (term $s_{If}^0(t) = k_{ZRO}$). This nonideality is one of the main contributors of what is called a zero-rate output (ZRO) or bias. With the force-to-rebalance control, even under

ideal operation, this term is always present. The good news is that, even if k_{ZRO} may be not perfectly known, if its value is constant during the sensor operation, an estimation $\widehat{k}_{ZRO} \approx k_{ZRO}$ can be obtained in a calibration step and compensated afterward. Therefore, we can define a compensation function f_{comp} as

$$f_{comp}(s_{If}(t)) \triangleq \frac{s_{If}(t) - \widehat{k}_{ZRO}}{\widehat{k}_{SF}}, \quad (2.45)$$

such that $\widehat{\Omega}_z(t) = f_{comp}(s_{If}(t))$, and assuming $\widehat{k}_{SF} = k_{SF}$ and $\widehat{k}_{ZRO} = k_{ZRO}$, we obtain $\widehat{\Omega}_z(t) = \Omega_z(t)$.

Finally, it is worth mentioning that (2.42) can be useful to estimate the anisoelectricity term k_{yx} . In general, s_{Qf} can also be divided by \widehat{k}_{SF} , producing the so-called quadrature error Ω_Q , also given in $^\circ/s$, as in [RCRW09], for instance.

Synchronous Demodulation with a Phase Error

In Section 2.1.4, we considered that the synchronous demodulation uses the same phase $\omega_{exc}t$ to demodulate the signal s_m . However, it is possible that there exists a difference δ_ϕ between the phase used by the synchronous demodulation and that of s_m [SAH07], i.e., for s_m given in (2.22), the synchronous demodulation uses $2 \cos(\omega_{exc}t + \delta_\phi)$ and $-2 \sin(\omega_{exc}t + \delta_\phi)$ (instead of $2 \cos(\omega_{exc}t)$ and $-2 \sin(\omega_{exc}t)$) to obtain s_I and s_Q . Let us evaluate the consequence of this error on the angular rate estimation.

In this case, we have

$$\begin{aligned} s_1(t) &= 2s_I(t) \cos(\omega_{exc}t) \cos(\omega_{exc}t + \delta_\phi) - 2s_Q(t) \sin(\omega_{exc}t) \cos(\omega_{exc}t + \delta_\phi) \\ s_1(t) &= s_I(t) (\cos(2\omega_{exc}t + \delta_\phi) + \cos(\delta_\phi)) - s_Q(t) (\sin(2\omega_{exc}t + \delta_\phi) - \sin(\delta_\phi)) \end{aligned}$$

and

$$\begin{aligned} s_2(t) &= -2s_I(t) \cos(\omega_{exc}t) \sin(\omega_{exc}t + \delta_\phi) + 2s_Q(t) \sin(\omega_{exc}t) \sin(\omega_{exc}t + \delta_\phi) \\ s_2(t) &= -s_I(t) (\sin(2\omega_{exc}t + \delta_\phi) + \sin(\delta_\phi)) - s_Q(t) (\cos(2\omega_{exc}t + \delta_\phi) - \cos(\delta_\phi)). \end{aligned}$$

Thus, after filtering out the high-frequency terms, we obtain

$$\begin{bmatrix} s_{If}(t) \\ s_{Qf}(t) \end{bmatrix} = R(\delta_\phi) \begin{bmatrix} s_I(t) \\ s_Q(t) \end{bmatrix},$$

where $R(\delta_\phi)$ is a rotating matrix given by

$$R(\delta_\phi) = \begin{bmatrix} \cos(\delta_\phi) & \sin(\delta_\phi) \\ -\sin(\delta_\phi) & \cos(\delta_\phi) \end{bmatrix}.$$

Now, by considering $\delta_\phi \neq 0$ for the computation of s_{If} and $\widehat{\Omega}_z$ from $\widehat{u}_{Cor,y}$ (see (2.40)), we end up with

$$s_{If}(t) = -\frac{(2m\Omega_z(t) + d_{yx}) A_{x,m}^{ref} \omega_{exc}}{k_{out,x} k_{in,y}} \cos(\delta_\phi) + \frac{k_{yx} A_{x,m}^{ref}}{k_{out,x} k_{in,y}} \sin(\delta_\phi). \quad (2.46)$$

Again, s_{If} can be rewritten as in (2.43) and (2.44). However, the phase error modifies the values of k_{SF} and k_{ZRO} , as follows:

$$k_{SF} = -\frac{2mA_{x,m}^{ref}\omega_{exc}}{k_{out,x}k_{in,y}} \cos(\delta_\phi) \quad (2.47)$$

$$k_{ZRO} = -\frac{d_{yx}A_{x,m}^{ref}\omega_{exc}}{k_{out,x}k_{in,y}} \cos(\delta_\phi) + \frac{k_{yx}A_{x,m}^{ref}}{k_{out,x}k_{in,y}} \sin(\delta_\phi). \quad (2.48)$$

Finally, we can conclude that, if there exists a phase error on the synchronous demodulation, this error will produce a loss on the scale factor and an amplification on the bias. For this reason, it is always desired to have $\delta_\phi = 0$. Nevertheless, if this error is constant during the gyroscope operation, the actual values of k_{SF} and k_{ZRO} can be determined through calibration and compensated afterward with f_{comp} .

Environmental Sensitivity

In general, MEMS devices are very sensitive to environmental variations, such as variations of temperature, pressure or mechanical stress.

Temperature plays an important role on the mechanical properties of the MEMS gyroscope, modifying the resonance frequency and the quality factor of the resonators [XCWL09]. In practice, the sensitivity of the resonance frequency to the temperature is so clear that this property can be used to precisely measure the temperature of the chip [PTS13]. Similarly, ambient pressure and external mechanical stress may also modify the mechanical properties of MEMS resonators [XCWL09, TMF17].

Even if the variations of resonance frequency are not huge, because of the high quality factor, small drifts of the resonance frequency may cause enormous loss of gain, as illustrated in Example 2.1. This fact reinforces the need to maintain ω_{exc} as close as possible to $\omega_{0,x}$, which, in practice, varies during the operation of the sensor. On the other hand, variations on the quality factor are not so critical.

Please note that these nonidealities alter the mechanical properties of the MEMS gyroscope, hence the model of the to-be-controlled system. If the controllers are robust against these model variations, we shall not have problems related to the operation of the gyroscope itself. Nevertheless, even under ideal operation, the estimate $\hat{\Omega}_z$ is biased by the parameter d_{yx} , and this parameter may vary with temperature, pressure and/or mechanical stress. Then, it may turn out that the bias compensation can be less effective under environmental variations, degrading the quality of the measurement. Similarly, the scale factor compensation can also be degraded by those variations. Therefore, it is important to adapt the compensation function f_{comp} with respect to the environmental changes. In general, one of the major contributors for the variations of bias and scale factor is the temperature. Then, if the behavior of the bias and scale factor as function of the temperature is known, by measuring the temperature, f_{comp} can be adapted accordingly, see, e.g., [TWY17].

Parasitic Electrical Coupling

The wires linking the controller(s) to the MEMS gyroscope form distributed parasitic capacitances, creating alternative circuits for the electrical current. Then, part of the control signal may be fed through the detection circuits. These parasitic capacitances also appear between the drive and the sense modes, electrically coupling them. This effect is known

as parasitic electrical coupling, capacitive feed-through or crosstalk and can be modeled by a linear system E_{coup} , connecting the input voltage to the input of the charge amplifier, as presented in Figure 2.14 (in solid lines) [AS05, CSL⁺19].

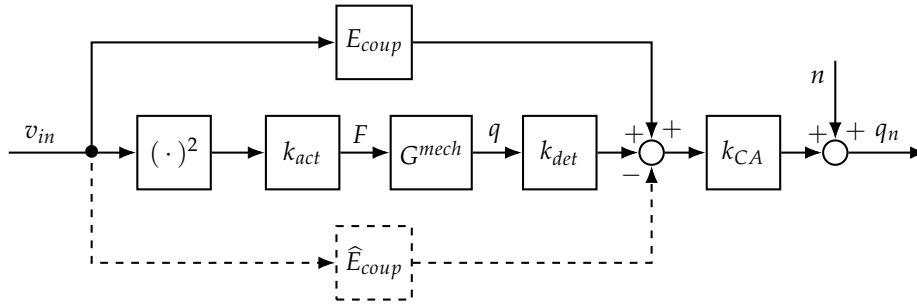


FIGURE 2.14: Model of the parasitic electrical coupling and compensation.

Concerning the presence of an electrical coupling in a MEMS gyroscope, two main problems can be listed.

- (i) This disturbing signal may saturate the charge amplifiers [CSL⁺19].
- (ii) The electrical coupling modifies the transfer between the input voltage and the measured signal. Thus, the closed-loop system may have its performance quickly deteriorated or even become unstable.

Therefore, it is essential to capture the behavior of E_{coup} and compensate for its effects [LS09, KAG⁺17]. In general, this compensation is made through the use of compensation capacitors, which mimic the parasitic capacitances and provide an alternative path for the current, minimizing the effect of this nonideality. For a better compensation, a digital filter can also be used, as discussed in our paper [CSL⁺19].

Nonlinearities: Spring Hardening and Spring Softening

In a real MEMS gyroscope, there exist several sources of nonlinearities, affecting the dynamic behavior of the system. However, most of them have in common the fact that, as consequence of the nonlinearity, the resonance frequency will depend on the amplitude of the input or output signal.

For some nonlinearities, the resonance frequency will increase when the signal amplitude increases, as if the stiffness coefficient (k_{ii}) had also increased. This is the case when the amplitude of oscillations is such that the nonlinear hardening of the silicon springs starts to appear. Hence, augmentation of the resonance frequency caused by a nonlinearity is usually called the spring hardening [You11]. On the other hand, nonlinearities provoking a reduction of the resonance frequency are said to soften the structure, the so-called spring-softening effect. This is typically the case of the nonlinearities linked to the electrostatic actuation and detection [AOPB09]. In general, when considering these nonlinear effects, the behavior of MEMS resonators (the drive and sense modes) can be described by the so-called Duffing equation [You11].

The spring-softening/hardening effects may be beneficial or not. In some specific cases, this feature is used to modify the resonance frequency of the device, compensating for changes due to temperature variations, for instance [AOPB09]. Nevertheless, in general, the spring-softening/hardening effects are avoided.

Concerning the estimation of the angular rate, the spring-softening/hardening effects can be considered as modifications on the model, similar to what happens with the environmental sensitivity.

For further details on the nonlinearities of MEMS devices, we refer the curious reader to the works [ABLN16, EKT⁺11, BRLS07, You11], for instance.

Noises

As any physical device, MEMS gyroscopes are also contaminated by noises from different origins or natures. We can cast as the principal sources of noise in MEMS gyroscopes the mechanical-thermal and electronic noises.

Due to their tiny dimensions, the moving parts of MEMS devices are susceptible to collisions with agitated molecules of a fluid (gas), provoking a random motion of these moving parts [Gab93]. This behavior is modeled by a random force, the mechanical-thermal noise, which appears at the input of the drive and sense modes. The power spectral density of this force (in N^2/Hz) is proportional to T_{int}/Q_i [Gab93, Sau08], where T_{int} is the absolute temperature (in K) and Q_i is the quality factor (Q_x and Q_y for the drive and sense modes, respectively). This relation justifies the necessity to conceive MEMS resonators with high quality factor to achieve a low-noise measure.

Similarly, electrical-thermal noises are generated in the components of the electronic circuits. Moreover, in the case of digital control implementation, analog-to-digital and digital-to-analog converters insert quantization errors, which are usually modeled as additive noise, disturbing the signal of interest [KM13].

From a system point of view, all these noises can be modeled as a single noise on the measures of the drive and sense modes. We call this noise the process noise and denote it $n = [n_x, n_y]$. This definition coincides with the one presented in Section 2.1.3 (see (2.13) and (2.17)). Moreover, we can define two linear systems, N_x and N_y , such that the PSD of n_x and n_y , respectively \mathcal{S}_{n_x} and \mathcal{S}_{n_y} , are given by

$$\mathcal{S}_{n_x}(\omega) = |N_x(j\omega)|^2 \mathcal{S}_{e_x}(\omega) \quad \text{and} \quad \mathcal{S}_{n_y}(\omega) = |N_y(j\omega)|^2 \mathcal{S}_{e_y}(\omega), \quad (2.49)$$

where \mathcal{S}_{e_x} and \mathcal{S}_{e_y} correspond to the PSD of unit-variance zero-mean white-noise signals e_x and e_y .

As consequence of the presence of noise in the closed-loop system, the output of the synchronous demodulator is also disturbed by an additive noise [KM13]. Therefore, by taking into consideration the effects of the noise and of the others nonidealities, we can write the output of the synchronous demodulator as

$$s_{If}(t) = s_{If}^L(t) + s_{If}^0(t) + s_{If}^n(t), \quad (2.50)$$

where the term s_{If}^n encapsulates the contribution of the different sources of noise.

Overall Model of a Nonideal MEMS Gyroscope

Having discussed the effects of the main nonidealities, we can now establish the overall model of a nonideal MEMS gyroscope.

The anisoelectricity and nonproportional damping produce a mechanical coupling between drive and sense modes. Then, the mechanical part of the MEMS gyroscope is a multivariable

system with two inputs and two outputs. In addition, the mechanical parameters of the gyroscope depend on the operating conditions, such as its temperature, pressure and mechanical stress. Therefore, the mechanical part of the gyroscope with actuation and instrumentation can be modeled by a linear parameter-varying (LPV) system $G^{\theta,\rho}$, whose parameters depend on θ and ρ . The vector $\theta \in \mathbb{R}^{n_\theta}$ represents the **known** variables, while the vector $\rho \in \mathbb{R}^{n_\rho}$ represents the **unknown** ones. That is, θ encapsulates the variables that can be measured in real time, as the internal temperature T_{int} , for instance; and ρ englobes the variable that are not measured in real time, *e.g.*, the mechanical stress and pressure. In general, those variables vary slowly, such that we can consider that, for each operating condition (θ, ρ) , $G^{\theta,\rho}$ is a linear time-invariant (LTI) or a frozen LPV system.

Similarly, the Coriolis force, which depends on the angular rate, also couples the drive and sense modes (see (2.35)). The dependence on Ω_z can be represented by a feedback loop (more details on this derivation are given in Appendix A.2), as illustrated in Figure 2.15a (see the mechanical part in the figure), where the matrix $C_{Cor}(\Omega_z)$ is given by

$$C_{Cor}(\Omega_z) = 2m\Omega_z \begin{bmatrix} 0 & \frac{1}{k_{in,x}k_{out,y}} \\ \frac{-1}{k_{in,y}k_{out,x}} & 0 \end{bmatrix}. \quad (2.51)$$

We denote G^{θ,ρ,Ω_z} the whole mechanical model (with actuation and instrumentation), indicating the dependence on the parameters θ and ρ as well as on the angular rate Ω_z .

Besides the mechanical part of the gyroscope, the parasitic electrical coupling also has to be considered. In general, the electrical coupling is compensated. However, the compensation is not perfect and a residual coupling ΔE_{coup} may exist. Therefore, the overall multivariable model of a nonideal MEMS gyroscope can be represented by the scheme of Figure 2.15a, where we recall that $u = \text{col}(u_x, u_y)$, $u_{Cor} = \text{col}(u_{Cor,x}, u_{Cor,y})$, $q_m = \text{col}(x_m, y_m)$, $q_n = \text{col}(x_n, y_n)$, $n = \text{col}(n_x, n_y)$ and $e = \text{col}(e_x, e_y)$. The measurement noise model is represented by $N = \text{diag}(N_x, N_y)$.

In general, the Coriolis force is considered to be exogenous and the dependence of the mechanical model on Ω_z is neglected. This simplification is often required to analyze the whole system in a tractable way. Moreover, the uncertainties related to the unknown parameters ρ and possible modeling errors of the mechanical part and electrical coupling can be encapsulated with ΔE_{coup} , defining an uncertain system ΔE . The overall model of the system is then simplified into the system presented in Figure 2.15b.

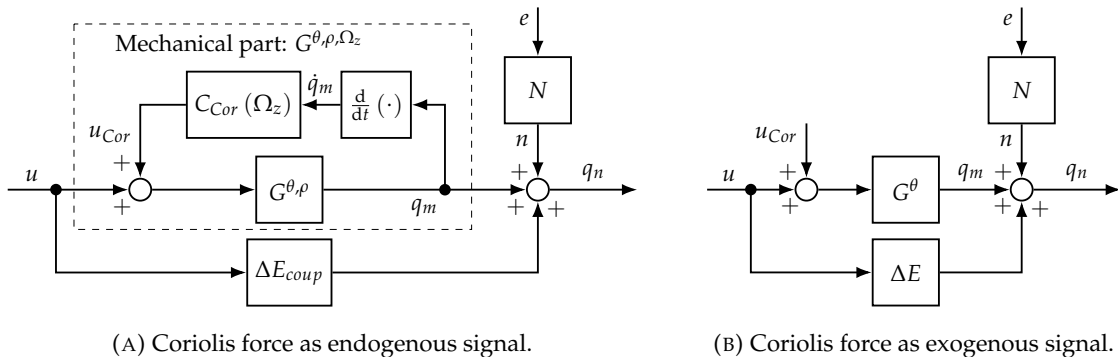


FIGURE 2.15: Overall model of a nonideal MEMS gyroscope.

The uncertain system ΔE can be defined through System Identification techniques [Lju98, BSG⁺04, Col20]. Qualitatively, since the signal-to-noise ratio (SNR) is better around the

resonance frequencies, the uncertainties are small in this frequency range and very important for low and high frequencies [Col20, AC21].

In the sequel, we present a multivariable model of a MEMS gyroscope, coupling the drive and sense modes of the examples 2.1 and 2.2.

Example 2.3 (Multiple-input multiple-output (MIMO) model). *In this example, we consider the drive and sense modes of the examples 2.1 and 2.2, adding anisoelasticity terms ($k_{xy} = k_{yx}$) such that the quadrature error is of $\Omega_Q = 30^\circ \text{s}^{-1}$. The nonproportional damping terms (d_{xy} and d_{yx}), usually negligible, are set to 0.*

Two cases are studied here. First, we consider $\Omega_z \equiv 0$. Then, we consider different values of $\Omega_z \in [-300, 300]^\circ/\text{s}$, evaluating the changes on the system behavior for different angular rates. In both cases, we consider the nominal system (with no uncertainties).

The magnitude frequency response of this model is presented in Figure 2.16 and Figure 2.17 (zoom). First, we note that the diagonal transfers correspond to the drive and sense modes of the previous examples. However, the mechanical coupling introduces off-diagonal transfers, which present two resonant peaks: at $\omega_{0,x}$ and at $\omega_{0,y}$. It is important to note that these cross-coupling transfers globally present magnitude smaller than the diagonal ones.

Concerning the variations of Ω_z on the system, increasing $|\Omega_z|$ mainly changes the gains of the cross-coupling terms around the resonance frequencies and in high frequencies. For this example, variations on the diagonal terms are negligible.

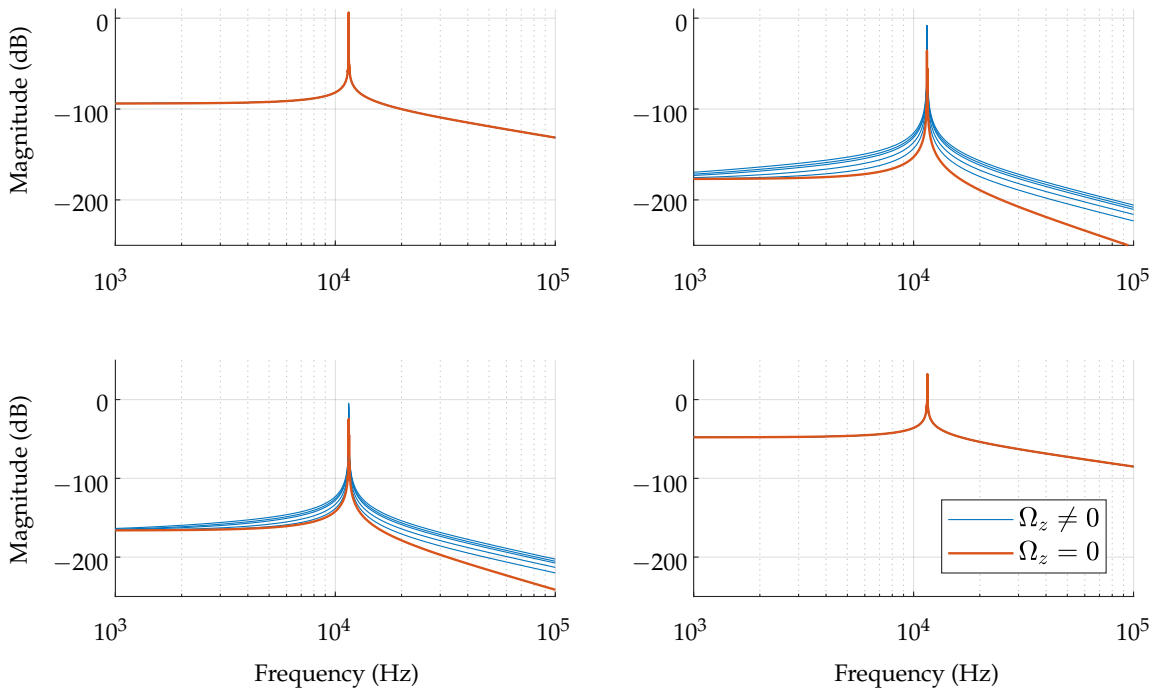


FIGURE 2.16: Bode diagram of the MEMS gyroscope for different values of Ω_z .

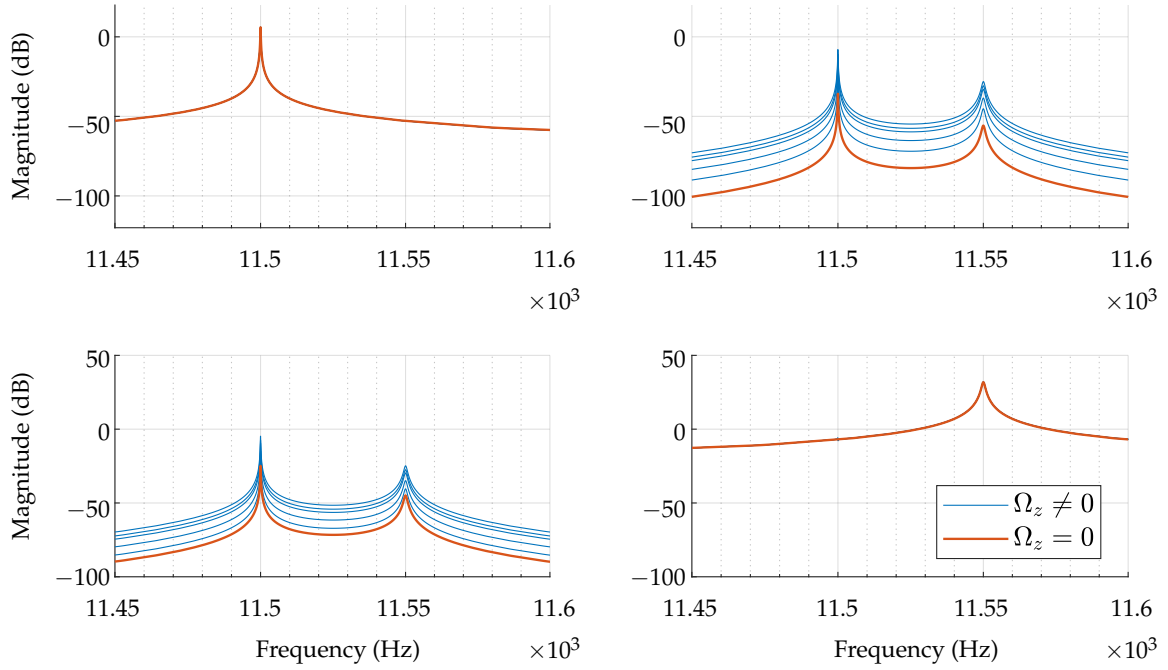


FIGURE 2.17: Bode diagram of the MEMS gyroscope for different values of Ω_z .
Zoom around $\omega_{0,x}$.

Model of the Angular Rate Estimate for a Nonideal MEMS Gyroscope

Recall that the scale factor and the bias depend on the parameters of the MEMS gyroscope. Now, if these parameters depend on θ and ρ , the scale factor and bias will also depend on θ and ρ . We denote them respectively $k_{SF}^{\theta,\rho}$ and $k_{ZRO}^{\theta,\rho}$. Therefore, the estimate $\hat{\Omega}_z$ is computed through the θ -dependent compensation function f_{comp}^θ , which is defined as

$$f_{comp}^\theta(s_{If}(t)) \triangleq \frac{s_{If}(t) - \hat{k}_{ZRO}^\theta}{\hat{k}_{SF}^\theta} \quad (2.52)$$

with \hat{k}_{SF}^θ and \hat{k}_{ZRO}^θ being respectively the estimates of $k_{SF}^{\theta,\rho}$ and $k_{ZRO}^{\theta,\rho}$. It is important to highlight the \hat{k}_{SF}^θ and \hat{k}_{ZRO}^θ can depend only on the known parameters θ (ρ represents the unknown parameters).

Let us now rewrite (2.50) as

$$s_{If}(t) = k_{SF}^{\theta,\rho} \Omega_z(t) + k_{ZRO}^{\theta,\rho} + s_{If}^n(t). \quad (2.53)$$

Therefore, we can compute $\hat{\Omega}_z$ through the compensation function f_{comp}^θ of (2.52), obtaining

$$\hat{\Omega}_z(t) = \frac{k_{SF}^{\theta,\rho} \Omega_z(t) + k_{ZRO}^{\theta,\rho} + s_{If}^n(t) - \hat{k}_{ZRO}^\theta}{\hat{k}_{SF}^\theta} \quad (2.54)$$

$$\hat{\Omega}_z(t) = \left(1 + \varepsilon_{SF}^{\theta,\rho}\right) \Omega_z(t) + \varepsilon_{ZRO}^{\theta,\rho} + \frac{s_{If}^n(t)}{\hat{k}_{SF}^\theta}, \quad (2.55)$$

where $\varepsilon_{SF}^{\theta,\rho}$ defines the relative error on the scale factor

$$\varepsilon_{SF}^{\theta,\rho} = \frac{k_{SF}^{\theta,\rho} - \widehat{k}_{SF}^\theta}{\widehat{k}_{SF}^\theta}, \quad (2.56)$$

and $\varepsilon_{ZRO}^{\theta,\rho}$ defines the residual bias, which is given by

$$\varepsilon_{ZRO}^{\theta,\rho} = \frac{k_{ZRO}^{\theta,\rho} - \widehat{k}_{ZRO}^\theta}{\widehat{k}_{SF}^\theta}. \quad (2.57)$$

Hence, the whole MEMS gyroscope can be represented by an operator with input Ω_z and output $\widehat{\Omega}_z$, as depicted in the scheme of Figure 2.18. Here, $\widetilde{H}_{gyro}^{\theta,\rho} = 1 + \varepsilon_{SF}^{\theta,\rho}$ and $\Omega_z^n(t) = \varepsilon_{ZRO}^{\theta,\rho} + s_{If}^n(t)/\widehat{k}_{SF}^\theta$ (see (2.55)).

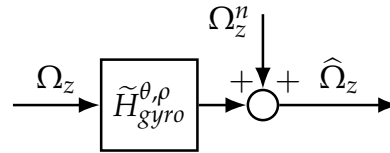


FIGURE 2.18: Model of the angular rate estimate $\widehat{\Omega}_z$.

2.1.6 Global Performance Indicators of MEMS Gyroscopes

In the previous section, the main nonidealities of MEMS gyroscopes are introduced and their effects on the final estimation of the angular rate are discussed. We show that, due to the presence of these nonidealities, the output of the synchronous demodulator is given by (2.53) or, after applying f_{comp}^θ , the angular rate estimate can be given by (2.55). Obviously, if $\varepsilon_{SF}^{\theta,\rho} = \varepsilon_{ZRO}^{\theta,\rho} = 0$, (2.55) can be rewritten as

$$\widehat{\Omega}_z(t) = \Omega_z(t) + \frac{s_{If}^n(t)}{\widehat{k}_{SF}^\theta}. \quad (2.58)$$

In this case, the only difference between $\widehat{\Omega}_z$ and Ω_z is due to the noise (s_{If}^n). Nevertheless, there might exist nonnull error on the scale factor and on the bias (i.e., $\varepsilon_{SF}^{\theta,\rho} \neq 0$ and $\varepsilon_{ZRO}^{\theta,\rho} \neq 0$). Indeed, because of the uncertainties on the parameters defining $k_{SF}^{\theta,\rho}$ and $k_{ZRO}^{\theta,\rho}$, the values of \widehat{k}_{SF}^θ and \widehat{k}_{ZRO}^θ are often determined through calibration and can only depend on θ . Therefore, the behavior of $\varepsilon_{SF}^{\theta,\rho}$ and $\varepsilon_{ZRO}^{\theta,\rho}$ through all the operating conditions determines how accurate the MEMS gyroscope is and define its global performance indicators, which we discuss in the sequel.

Scale Factor Performance Indicators

The scale factor is defined by standard as

“The ratio of a change in output to a change in the input intended to be measured. Scale factor is generally evaluated as the slope of the straight line that can be fitted by the method of least squares to input-output data.” [IEE19]

In general, the output of the synchronous demodulator is considered to be the gyroscope output, that is, the signal s_{If} . Then, considering $s_{If}(t) = k_{SF}^{\theta,\rho} \Omega_z(t)$ (see (2.53) with $s_{If}^n(t) \equiv 0$ and $k_{ZRO}^{\theta,\rho} = 0$) as the output signal for a given input Ω_z , the constant $k_{SF}^{\theta,\rho}$ determines that slope, defining the scale factor.

The main scale factor error specifications include.

- *Scale Factor Nonlinearity (SFNL)*: the systematic deviation from the straight line that defines the nominal input-output relationship [IEE19]. It is usually given in ppm of the full scale (FS). The SFNL indicates how far from Ω_z the estimate $\hat{\Omega}_z$ can be. This indicator is often evaluated at a given operating condition and for $\Omega_z \in [-\Omega_z^{FS}, \Omega_z^{FS}]$, where Ω_z^{FS} is the full scale or dynamic range of the sensor. Therefore, we adopt the definition

$$\text{SFNL} \triangleq \max_{\Omega_z \in [-\Omega_z^{FS}, \Omega_z^{FS}]} \left(\frac{|\hat{\Omega}_z - \Omega_z|}{\Omega_z^{FS}} \right). \quad (2.59)$$

- *Scale Factor Over Temperature (SFOT)*: indicates the scale-factor temperature sensitivity, that is, the change in the scale factor resulting from a temperature change [IEE19]. The SFOT represents the variation of the scale factor k_{SF}^{int} over the whole temperature range of operation $T_{\text{int}} \in [T_{\text{int},\text{min}}, T_{\text{int},\text{max}}]$, with respect to the scale factor at the nominal room temperature, $T_{\text{int},0}$. Thus, we adopt the definition

$$\text{SFOT} \triangleq \max_{T_{\text{int}} \in [T_{\text{int},\text{min}}, T_{\text{int},\text{max}}]} \left(\frac{|k_{SF}^{\text{int}} - k_{SF}^{\text{int},0}|}{k_{SF}^{\text{int},0}} \right). \quad (2.60)$$

Bias Error

If the gyroscope is at rest, *i.e.*, $\Omega_z = 0$, its output should remain null. However, due to the process noises, fabrication imperfections, numerical errors, aging and environmental changes (mainly linked to the temperature), the sensor produces a non-null output. The average of this measure over time is the bias or zero-rate output (ZRO). For further details, refer to [SASH06, SAH07], for instance.

The bias or ZRO is often compensated after calibration [TMF17]. Nevertheless, the problem is its sensitivity with respect to environmental variations and its stability over time. We consider the indicators below.

- *Bias Instability (BI)*: in this context, the stability is defined as “a measure of the ability of a specific mechanism or performance coefficient to remain invariant when continuously exposed to a fixed operating condition” [IEE19]. Obviously, if the sources of this instability can be measured and the relationship with the ZRO is known, compensation can be considered. However, if the sources are unknown or cannot be measured, they cannot be compensated and define the bias instability (BI). Due to its random (rather unknown) nature, this important performance parameter is related to the noise term (Ω_z^n), being presented with the noise indicators in the sequel.
- *Bias Over Temperature (BOT)*: indicates the bias temperature sensitivity, *i.e.*, the change in the bias resulting from a temperature change [IEE19]. Similar to the SFOT, the BOT represents the variation of the residual bias $\varepsilon_{ZRO}^{\text{int}}$ over the whole temperature range of operation $T_{\text{int}} \in [T_{\text{int},\text{min}}, T_{\text{int},\text{max}}]$, with respect to the bias at the nominal room

temperature, $T_{int,0}$. Hence, we adopt the definition

$$\text{BOT} \triangleq \max_{T_{int} \in [T_{int,min}, T_{int,max}]} \left(\left| \varepsilon_{ZRO}^{T_{int}} - \varepsilon_{ZRO}^{T_{int,0}} \right| \right). \quad (2.61)$$

Noise Performance Indicators: RMS Noise and Allan Variance

Giving sequence to the previous discussion, even when no angular rate is applied and the ZRO is compensated, the gyroscope produces a random signal at its output. This erratic output, after integration, may produce significant positioning/navigation error. Then, to characterize the performance of a MEMS gyroscope with respect to the different noises, some performance indicators are usually evaluated [IEE19], as follows.

- *RMS noise*: the power of the noise measured in the frequency range of interest.
- *Angle random walk (ARW)*: the angular error buildup with time that is due to white noise in angular rate and is typically expressed⁴ in $^\circ/\sqrt{\text{h}}$.
- *Bias instability (BI)*: the random variation in bias as computed over specified finite sample time and averaging time intervals. This nonstationary (evolutionary) process is characterized by a $1/f$ power spectral density. Typically expressed in $^\circ \text{h}^{-1}$.

While the interpretation of the RMS noise is straightforward, the interpretation of the other specifications is not. These last two parameters result from the Allan variance of the measured noise, which is a popular tool used to characterize the noise of inertial sensors [Fre15]. The Allan variance of the MEMS gyroscope is computed through the following steps [IEE06, Fre15].

- (i) The signal $\hat{\Omega}_z$ (see (2.55)) is measured with the gyroscope at rest (*i.e.*, $\Omega_z(t) \equiv 0$) and sampled with a sampling period τ_0 .
- (ii) A moving average filter of order $m \in \mathbb{N}$ is applied to the sampled signal. The order of the moving average filter defines the number of samples or the time $\tau_A = m\tau_0$ of the sample window.
- (iii) The variance of the averaged signal for a given τ_A is the Allan variance of $\hat{\Omega}_z$ for an average of length τ_A , denoted $\sigma_A^2(\tau_A)$.
- (iv) Steps (ii) and (iii) are repeated for different τ_A (or m).
- (v) The Allan deviation $\sigma_A(\tau_A)$ is then computed and plotted, producing a curve similar to the one presented in Figure 2.19.

This plot is interpreted as the standard deviation (of variance) of the noise after applying a moving average of length τ_A on $\hat{\Omega}_z$. The minimum value of $\sigma_A(\tau_A)$ defines the BI, which gives an idea on the minimal noise contribution on the measure. For the example of the figure, the standard deviation of the averaged noise samples can be as low as 0.8°h^{-1} . To achieve this value, a moving average of length of about 200 h has to be used. The ARW is defined as the value of a straight line for $\tau_A = 1 \text{ h}$. This line corresponds to the line that best fits $\sigma_A(\tau_A)$ with slope equal to -0.5 in a log-log scale [Fre15]. In this example, $\text{ARW} \approx 9^\circ/\sqrt{\text{h}}$.

⁴In general, the measures of a MEMS gyroscopes are expressed in $^\circ \text{s}^{-1}$, but they can also be expressed in $^\circ \text{h}^{-1}$, being $1^\circ \text{s}^{-1} = 3600^\circ \text{h}^{-1}$.

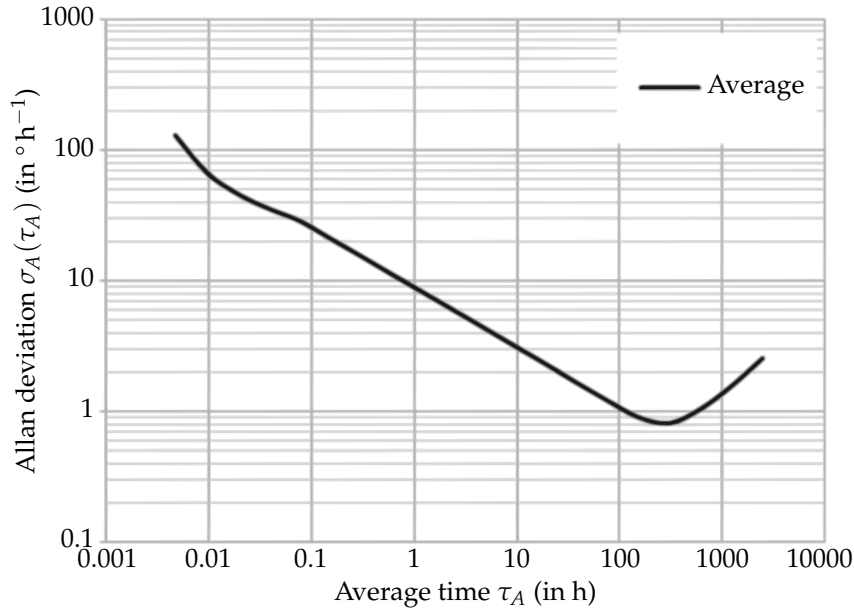


FIGURE 2.19: Example of Allan deviation plot (adapted from [Tro19]).

Dynamic Performance Indicator: the Bandwidth

The previous indicators determine how accurate are the measures of a gyroscope for a constant Ω_z . However, it is also important to characterize the behavior of the sensor to measure time-varying angular rates. The MEMS gyroscope can be seen as a dynamic operator whose input is the angular rate Ω_z and that produces the measure $\hat{\Omega}_z$ at its output (see Section 3.2.1 for further details). The frequency range in which the attenuation is smaller than 3 dB is defined as its bandwidth [IEE04].

2.2 Control Architectures in the Literature

In the previous section, a background on the MEMS gyroscopes was presented. At that point, it was shown how essential are the control loops for the operation of high-performance MEMS gyroscopes. However, no details on the control strategies were discussed. This section aims at reviewing the control architectures most used in the literature, their strengths and weaknesses.

In general, the drive and sense modes are considered to be independent single-input single-output (SISO) systems, and most of the control architectures have been developed under this assumption. Therefore, we start by reviewing the classical control architectures adopted to operate the drive and sense modes in closed loop in Section 2.2.1 and in Section 2.2.2, respectively. Then, in Section 2.2.3, we discuss the limitations of the “independence assumption” and present some recent works that consider a multiple-input multiple-output (MIMO) framework, integrating in a single controller the operation of the drive and sense modes.

2.2.1 Drive-Mode Control Architectures

The drive mode principal objective is to keep the proof mass oscillating so that in the presence of an angular rate, part of the oscillating energy is transferred to the sense mode through the Coriolis force. Because of the strong relationship between the Coriolis force and x (or \dot{x}), it is essential to control the amplitude of x , A_x , or of its velocity. Furthermore, if one can provoke

oscillations exactly at the resonance frequency, the power needed to keep the proof mass oscillating with a reasonable amplitude is minimal, and, most importantly, the signal-to-noise ratio (SNR) of the measure is maximized.

Note, however, that the resonance frequency of the drive mode can shift (due to temperature changes, for instance). Besides the issues related to the fluctuations of temperature, the performance of the gyroscope can be immensely degraded due to coupling effects, environmental variations, or aging. Therefore, the problem of the drive-mode control can be stated as follows.

Problem 2.1 (Drive-mode control problem). *To design a control system capable of producing and sustaining the proof mass oscillations with controlled amplitude and a frequency close to the resonance one, despite the disturbances and model changes.*

Thus, two main control objectives are pursued: regulate the amplitude of the oscillations, and track the resonance frequency. In the literature, different strategies are proposed to cope with this problem. We present the most common approaches in the sequel; their advantages and drawbacks are also discussed.

Automatic Gain Control (AGC) with Phase-Locked Loop (PLL)

Historically, to achieve the two control objectives above, two independent control loops are employed. One loop is conceived to control the oscillations amplitude: the automatic gain control (AGC) loop. The second one is based on the celebrated phase-locked loop (PLL) circuits, which allows to track the drive-mode resonance frequency by controlling the phase shift between the input and output signals. This strategy is motivated by the frequency response of a second-order resonator, as follows.

Let us consider the model of the drive mode, G_x . If we apply at the input a sinusoidal signal of amplitude U_x , *i.e.*,

$$u_x(t) = U_x \sin(\omega_{exc}t);$$

in steady-state, the output of the system is given by

$$x_m(t) = A_{x,m} \sin(\omega_{exc}t + \phi_{x,m}),$$

where $A_{x,m}$ is the amplitude or envelope of x_m , and $\phi_{x,m}$ is its phase shift with respect to the phase $\omega_{exc}t$ (phase of the input signal). They are respectively given by

$$A_{x,m} = |G_x(j\omega_{exc})| U_x \quad \text{and} \quad \phi_{x,m} = \arg(G_x(j\omega_{exc})).$$

Note that the amplitude of the input signal (U_x) has influence only on the amplitude of the output signal ($A_{x,m}$), while the excitation frequency ω_{exc} alters both $A_{x,m}$ and $\phi_{x,m}$. Even so, the excitation frequency is used to regulate $\phi_{x,m}$ and the input amplitude regulates the output one. Then, two (independent) control loops are designed to regulate the amplitude and phase shift of x_m .

For the amplitude control loop, the idea is to design a controller K_{amp} that, based on $A_{x,m}$ and a given reference amplitude $A_{x,m}^{ref}$, computes the amplitude U_x such that $A_{x,m} = A_{x,m}^{ref}$, see, for instance, [AH10, Sau08]. Note that the amplitudes ($A_{x,m}^{ref}$, $A_{x,m}$ and U_x) are constant signals when G_x is in (sinusoidal) steady-state. Hence, PI controllers are typically employed for this task.

For the phase loop, remember that the phase shift of G_x is equal to -90° or $-\pi/2$ rad when it operates at its resonance frequency, that is, $\arg(G_x(j\omega_{exc})) = -\pi/2$ rad (see Example 2.1). Moreover, this is the only case where a phase shift of $-\pi/2$ rad can be obtained. Thus, the idea here is to design a controller K_{ph} that, based on the measures of $\phi_{x,m}$, computes $\delta\omega$ and $\omega_{exc} = \delta\omega + \omega_{exc}^0$ such that $\phi_{x,m} = -\pi/2$ rad [KCV08, Sau08, RCRW09]. Note that, similar to the amplitude loop, when G_x is in steady-state, the input and output signals of the controller (respectively, $-\pi/2 - \phi_{x,m}$ and ω_{exc}) are also constant signals, justifying the use of a PI controller to close the phase loop.

Finally, the ideal synchronous demodulation (SD) can be employed to feedback the amplitude and phase shift of x_m , as presented in Section 2.1.4. The whole scheme of the control architecture with AGC and PLL is then presented in Figure 2.20.

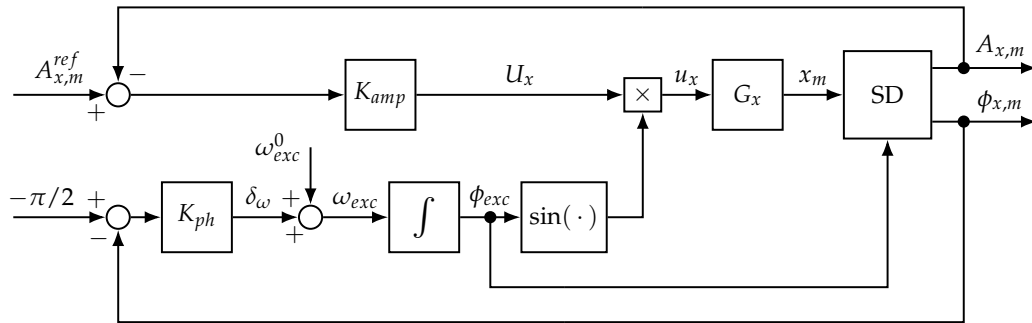


FIGURE 2.20: AGC+PLL architecture for the drive-mode operation.

This control strategy is very popular among the commercialized MEMS gyroscopes [Zur15], and even used as reference in the IEEE standard [IEE04]. Its success can be due to the simplicity behind its working principles and to the simplicity of the controllers (PI-like controller), providing an interesting solution for the drive-mode control problem. Moreover, as mentioned earlier, although the drive mode operates around its resonance frequency, the controller works with low-frequency signals (constant in steady-state). This fact may be very useful in the case of digital implementation of the controllers, for instance. In a certain extent, the modulation (product at the input of G_x) and the synchronous demodulation bring the dynamics of the plant from high-frequency range ($\omega \approx \omega_{0,x}$) to low-frequency range ($\omega \approx 0$). Then, if the modulation and demodulation processes (high-frequency) are implemented in hardware, the controllers can be implemented in a processor and operate with a sampling frequency that can be less than $\omega_{0,x}$. A deeper discussion on this topic is drawn in Chapter 6.

In addition to these interesting features, the architecture AGC+PLL presents several nonlinearities in the loops, making the to-be-controlled plants nonlinear. To design the controllers, the models are usually linearized around a particular operating point [EMK12]. The linearization does not allow to model the couplings between amplitude and phase. Hence, no formal guarantees of performance or stability are given *a priori*.

Nonlinear Automatic Gain Control (AGC) Architecture

A popular alternative to the AGC+PLL control architecture is the nonlinear AGC loop, which is presented in [MVG01]. Similar to the AGC+PLL architecture, the nonlinear AGC architecture presents two loops: one for regulating the amplitude of the oscillations and another for tracking the resonance frequency through the phase shift introduced by the drive mode. We call this strategy nonlinear AGC because the oscillations are not induced by a

PLL (as in the previous case), but by using a **nonlinear** control law ($u_x(t) = U_x(t) \cdot \dot{x}_m(t)$), as depicted in Figure 2.21, simplifying the phase loop. A synchronous demodulation (SD) is used to compute the amplitude of \dot{x}_m , $A_{v,m}$, and the amplitude controller K_{amp} computes the signal U_x such that $A_{v,m}$ tracks the reference $A_{v,m}^{ref}$.

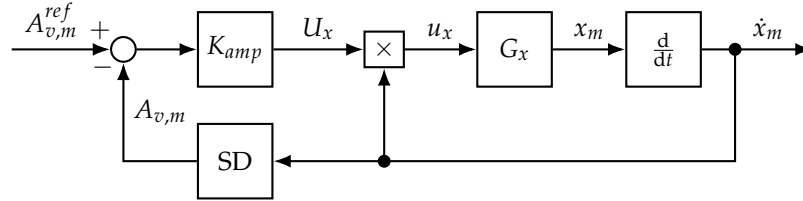


FIGURE 2.21: Nonlinear AGC architecture for the drive-mode operation.

The understanding of its principles is rather intuitive. Let us consider the differential equations of G_x (from (2.15))

$$\ddot{x}_m(t) + \frac{\omega_{0,x}}{Q_x} \dot{x}_m(t) + \omega_{0,x}^2 x_m(t) = k_{0,x} \omega_{0,x}^2 u_x(t). \quad (2.62)$$

Then, with the nonlinear control law $u_x(t) = U_x(t) \cdot \dot{x}_m(t)$, we obtain

$$\ddot{x}_m(t) + \underbrace{\left(\frac{1}{Q_x} - k_{0,x} \omega_{0,x} U_x(t) \right)}_{2\tilde{\zeta}_{ef}} \omega_{0,x} \dot{x}_m(t) + \omega_{0,x}^2 x_m(t) = 0. \quad (2.63)$$

At this point, we can define the effective damping factor $\tilde{\zeta}_{ef}$ as

$$\tilde{\zeta}_{ef} = \frac{1}{2Q_x} - \frac{k_{0,x} \omega_{0,x} U_x(t)}{2}.$$

The central idea of this architecture is to manipulate the effective damping factor $\tilde{\zeta}_{ef}$ such that the oscillations resulting from a nonnull initial condition converge to a sinusoidal signal with a desired amplitude [MVG01]. The amplitude controller K_{amp} computes the signal U_x so that $\tilde{\zeta}_{ef} > 0$ when $A_{v,m} > A_{v,m}^{ref}$, dampening the system and reducing the amplitude of the oscillations. On the other hand, when $A_{v,m} < A_{v,m}^{ref}$, the controller computes a signal U_x such that $\tilde{\zeta}_{ef} < 0$, what makes the system (transitorily) unstable, increasing the amplitude of the oscillations. To sustain oscillations with constant amplitude, the effective damping must be set to 0 by U_x . This condition is known in the literature as **Barkhausen's condition** [OAL⁺05]. In this case, the frequency of the oscillations, ω_{exc} , tracks the resonance frequency $\omega_{0,x}$.

The above description justifies the use of \dot{x}_m rather than x_m to control the system. Moreover, recall that the Coriolis force is proportional to Ω_z only if the product $\omega_{exc} A_x$ is constant (see Section 2.1.2). This product corresponds to the amplitude of the signal \dot{x} . Therefore, controlling \dot{x}_m rather than x_m allows maintaining the Coriolis force always proportional to Ω_z , despite the variations of ω_{exc} . Nevertheless, an important issue arises. In general, there are some noises on x_m , which are amplified by the time-derivative, specially in high frequencies, and injected in the loop. Therefore, instead of using \dot{x}_m , a phase shifter (all-pass filter) is used to introduce the required phase shift, as in [AH10, CYC⁺14], and illustrated in Figure 2.22.

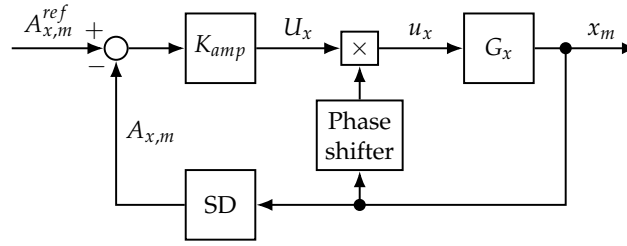


FIGURE 2.22: Nonlinear AGC architecture with a phase shifter.

The nonlinear AGC architecture is considered by numerous authors, such as in [MVG01, CMTB05, OAL⁺05, SSL⁺08, CCD⁺09, PSL⁺12]. In addition to provide a relatively simple structure, this approach ensures at the same time the amplitude control and the resonance frequency tracking. However, the nonlinearities present in the loop make it difficult to rigorously analyze the performance of the closed-loop system. The general approach consists in using averaging methods and linearization to analyze the equilibrium points and their stability (see [MVG01] and [CCD⁺09], for instance). Moreover, the resonance-frequency tracking is demonstrated only through experiments or simulations.

Direct Control Architecture

It has to be stressed that in the previous approaches, the controller does not work directly with x_m (nor \dot{x}_m). The controllers from the previous strategies operate based on the amplitude and phase of x_m . Moreover, these controllers do not compute the signal that is applied to the drive mode; they compute its amplitude and phase (or frequency). As discussed above, these approaches present interesting features for the operation of the drive mode; however, from the Control Theory perspective, it is not usual to introduce nonlinear functions (such as the synchronous demodulation) in the control loop. The major issue is that the inclusion of these nonlinearities makes harder to formally ensure stability or performance of the closed-loop system, even if the to-be-controlled plant G_x is linear. Thus, some authors have been proposing the use of classical control architecture for the drive-mode operation, e.g., [SHS⁺99, DA09, PHHN07, PK14]. We call this approach direct control since there are no modulation elements between the controller and the plant. Figure 2.23 illustrates this control architecture, in which the controller K_x , based on x_m and x_m^{ref} , computes u_x such that x_m tracks x_m^{ref} . The signal x_m^{ref} is of the form

$$x_m^{ref}(t) = A_{x,m}^{ref} \sin(\omega_{exc}t). \quad (2.64)$$

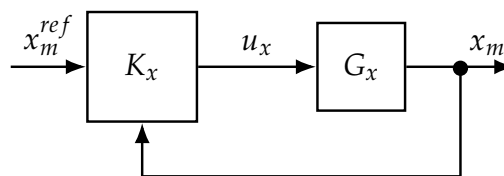


FIGURE 2.23: Direct control architecture for the drive-mode operation.

Since this architecture corresponds to the classical feedback loop, different control design methods can be considered, providing some formal guarantees, under the assumption that there are no interactions between the drive and sense modes. For instance, adaptive control

is applied in [SHS⁺99, PHHN07], model predictive control is used by [PK14], sliding mode control is employed in [BSK06] and active disturbance rejection control (ADRC) is the choice of [DA09].

The drawback of this approach is that the controller works with signals with a frequency content at least equal to ω_{exc} . Hence, in the case of digital implementation, the sampling frequency has to be sufficiently high to ensure a proper operation. Moreover, except for the ADRC solution, the effectiveness of the different control strategies is demonstrated only by simulation. This fact may indicate some difficulties for the implementation in a real MEMS gyroscope. The main drawback of the ADRC solution is that the controller is based on an observer that must have a bandwidth much higher than the resonance frequency of the drive mode. Hence, this solution may be suitable only for gyroscopes whose resonance frequencies are small.

Finally, we also have to mention that the operating frequency ω_{exc} is set by the reference signal (see (2.64)), which is supposed to be close to the resonance frequency of G_x , $\omega_{0,x}$. Nevertheless, if $\omega_{0,x}$ changes during the sensor operation, an external loop would be required to make ω_{exc} track $\omega_{0,x}$ automatically.

2.2.2 Sense-Mode Control Architectures

The sense mode can be considered as the main element of a MEMS gyroscope; it is where the Coriolis force will mainly act on. To operate the sense mode in closed loop, we can state the control problem as follows.

Problem 2.2 (Sense-mode control problem). *To design a control system capable of estimating the Coriolis force acting on the sense mode, despite the parasitic coupling forces, the variations of the environment or the device parameters.*

To tackle this problem in a closed-loop operation, the force-to-rebalance control strategy is considered, and the following control objective is defined: keep $y(t) \equiv 0$ by applying a force F_y that counteracts $F_{Cor,y}$. As discussed in Section 2.1.2, F_y (or, equivalently, u_y) can then be used as the estimate of the Coriolis force in an ideal gyroscope. This estimate is demodulated and allows computing the angular rate. From the Control Theory point of view, this problem can be interpreted as a classical disturbance rejection problem. For the case of a nonideal gyroscope, the same strategy is considered. However, we have to keep in mind that, in this case, the estimate of the Coriolis force is perturbed by the coupling forces, $F_{coup,y}$ (or, equivalently, $u_{coup,y}(t) = \frac{F_{coup,y}(t)}{k_{in,y}}$, see (2.19)). The synchronous demodulation and calibration/compensation are therefore needed to distinguish between those components (see Section 2.1.5) and to fully solve the problem.

Similar to the drive-mode control, different architectures are found in the literature for the force-to-rebalance control of the sense mode. In the sequel, we present the most important ones.

Envelope-Based Control Architecture (I/Q)

The first approach we consider is the envelope-based control architecture. Similar to the AGC+PLL architecture, two independent control loops are employed to achieve the control objective. In this case, to keep $y(t) = y_m(t) \equiv 0$, the idea is to null the in-phase and quadrature terms of the sense-mode displacement y , *i.e.*, its complex envelope. This concept

became popular with the work presented by Lynch in 1998, which is reproduced in [IEE04, Annex B].

To understand the idea behind the use of these two loops, let us consider that the drive and sense modes have the same resonance frequency, *i.e.*, $\omega_{0,x} = \omega_{0,y}$, and that the gyroscope operates at sinusoidal steady state with frequency $\omega_{exc} = \omega_{0,x}$. In this case, all the signals of the system are harmonic and can be decomposed into in-phase and quadrature terms (see Section 2.1.4). Then, the input u_y and the output y_m can be respectively written as

$$u_y(t) = u_{y,I} \cos(\omega_{exc}t) - u_{y,Q} \sin(\omega_{exc}t) \quad (2.65)$$

$$y_m(t) = y_{m,I} \cos(\omega_{exc}t) - y_{m,Q} \sin(\omega_{exc}t). \quad (2.66)$$

Recall that at $\omega = \omega_{0,x} = \omega_{0,y}$, the phase shift added by the sense mode is equal to -90° . Thus, the **in-phase** term of u_y , $u_{y,I}$, produces oscillations at the output, which are **in quadrature** with $\cos(\omega_{exc}t)$. Similarly, the **in-quadrature** term of u_y , $u_{y,Q}$, produces oscillations **in phase** with $\cos(\omega_{exc}t)$. This means that the term $y_{m,Q}$ only depends on $u_{y,I}$, as well as $y_{m,I}$ only depends on $u_{y,Q}$. Therefore, to achieve the original purpose (maintain $y_m(t) \equiv 0$), a controller $K_{y,Q}$ is designed to compensate for the quadrature forces by keeping $y_{m,I}(t) \equiv 0$, and a controller $K_{y,I}$ is designed to compensate for the in-phase forces by ensuring $y_{m,Q}(t) \equiv 0$ [LR02, Zur15]. The whole scheme of this control architecture is presented in Figure 2.24. In the case where $\omega_{0,x} \neq \omega_{0,y}$, the phase shift added by the sense mode at $\omega = \omega_{0,x}$ is equal to $-90^\circ + \delta\phi_y$ with $\delta\phi_y \neq 0$. The additional phase shift $\delta\phi_y$ is introduced on the synchronous demodulator such that the same reasoning holds when $\omega_{0,x} \neq \omega_{0,y}$ [Zur15].

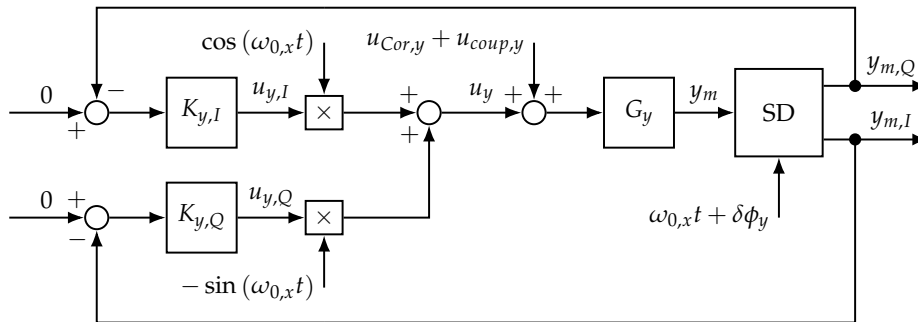


FIGURE 2.24: Envelope-based architecture for the sense-mode operation.

In this control architecture, if $y_m(t) \equiv 0$ and $x_m(t) = A_{x,m}^{ref} \sin(\omega_{exc}t)$, we also obtain (2.39), which is recalled below:

$$u_y(t) = \frac{(2m\Omega_z(t) + d_{yx}) A_{x,m}^{ref} \omega_{exc}}{k_{out,x} k_{in,y}} \cos(\omega_{exc}t) + \frac{k_{yx} A_{x,m}^{ref}}{k_{out,x} k_{in,y}} \sin(\omega_{exc}t).$$

Then, comparing this expression to that of (2.65), we obtain

$$u_{y,I}(t) = \frac{(2m\Omega_z(t) + d_{yx}) A_{x,m}^{ref} \omega_{exc}}{k_{out,x} k_{in,y}} \quad \text{and} \quad u_{y,Q}(t) = -\frac{k_{yx} A_{x,m}^{ref}}{k_{out,x} k_{in,y}}.$$

Therefore, $u_{y,I}$ corresponds to $-s_{If}$ in (2.41) and can be directly used to compute $\hat{\Omega}_z$ as $\hat{\Omega}_z(t) = f_{comp}(-u_{y,I}(t))$. Similarly, $u_{y,Q}$ corresponds to $-s_{Qf}$ in (2.42).

This control strategy is also popular [LR02, CGZ⁺11, EMK12, HZH⁺15, Zur15]. Similar to the AGC+PLL architecture, the simplicity of the controllers (PI-like controller) is an attractive feature provided by this control architecture, offering a simple solution for the sense-mode control problem. Moreover, the controllers also work with low-frequency signals.

On the other side, this architecture also presents several nonlinearities in the loops, making the to-be-controlled plant nonlinear. Then, to design the controllers, the models are often linearized around a particular operating point, and no formal guarantees of performance can be given. Moreover, the in-phase and quadrature loops are considered to be uncoupled. This case is found only under certain specific conditions, such as when the system is in steady state and $\omega_{0,x} = \omega_{0,y}$.

Direct Control Architecture

An alternative architecture to operate the sense mode is the classical feedback loop, which we also call direct control architecture and present in Figure 2.25. In this case, based on y_m , the controller K_y computes the signal u_y that compensates for the disturbances $u_{Cor,y}$ and $u_{coup,y}$ such that $y_m(t) \approx 0$.

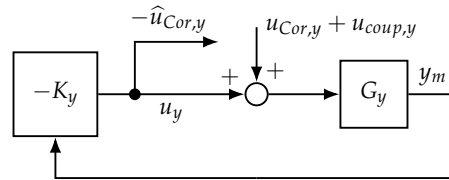


FIGURE 2.25: Direct control architecture for the sense-mode operation.

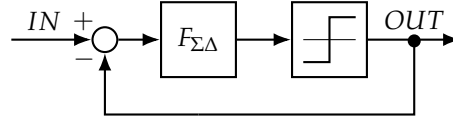
With this architecture, different control design methods can be considered. For instance, classical design methods are used in [PPK⁺04, SKL08] to obtain lead-lag compensator and PID-like controllers. More advanced design methods are also found in literature. We can cite some examples, such as the adaptive control used in [PH03] or the \mathcal{H}_∞ synthesis employed in [SLSK04, HLZ⁺15], obtaining controllers such that guarantees on the closed-loop system stability and performance can be given, under the assumption that there are no interactions between drive and sense modes.

EM- $\Sigma\Delta$ Architecture

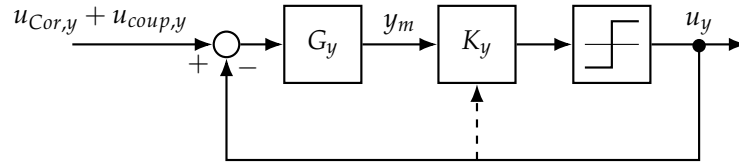
Last but not least, we present the electro-mechanical $\Sigma\Delta$ (EM- $\Sigma\Delta$) architecture. This architecture is inspired by the classical $\Sigma\Delta$ modulators [PB05, RRW08], which are widely used in analog-to-digital converters (ADC) and whose block diagram is illustrated in Figure 2.26. This circuit converts an analog signal at the input, IN , into a digital signal at the output, OUT . The output signal is coded into a single bit through the 1-bit quantizer, and the filter $F_{\Sigma\Delta}$ has three purposes:

- (i) minimize the effects of the quantization error on OUT , at least in the frequency range of the signal IN ;
- (ii) ensure that $OUT \approx IN$, at least in the frequency range of interest;
- (iii) ensure the stability of the closed-loop system.

In the EM- $\Sigma\Delta$ architecture, which is presented in Figure 2.27, the filter $F_{\Sigma\Delta}$ is replaced by a mechanical element – the sense mode – and an electronic filter or controller K_y . Therefore, the

FIGURE 2.26: Classical $\Sigma\Delta$ modulator.

input signal is replaced by $u_{Cor,y} + u_{coup,y}$. Then, if the controller works properly, the output signal u_y corresponds to the input one, at least in the frequency range of interest. For the case of a MEMS gyroscope, this interval comprises the frequencies around $\omega_{0,x}$.

FIGURE 2.27: EM- $\Sigma\Delta$ architecture for the sense-mode control.

Note that this control architecture is very similar to the direct control one. The only difference between these two approaches is that, in the EM- $\Sigma\Delta$ architecture, there exists a relay between the controller and the sense mode. This architecture is widely employed, see *e.g.*, [PB05, ESAES09, RCRW09, EEE+11, CYC+14, CLK16]. The use of a relay (1-bit quantizer) in the loop brings some interesting advantages over the other architectures, as follows.

- (i) The use of a bi-level actuation eliminates the problem with the nonlinear relationship between voltage and force, which is inherent to the electrostatic actuators.
- (ii) In the case of digital implementation of the controller, there is no need to use high-resolution digital-to-analog converter (DAC), reducing the costs of the system.
- (iii) The digital signal at the output is easily used by the signal processing stages (demodulation and compensation).

One of the main drawbacks of the EM- $\Sigma\Delta$ architecture is the presence of the relay in the loop. This relay is a strong nonlinearity. Hence, performance guarantees cannot be given [RRW08].

Another important drawback concerns the availability of design methods. In general, the control design methods of the EM- $\Sigma\Delta$ architecture are adapted from the electronic filter design of the classical $\Sigma\Delta$ modulators [PB05, RRW08]. The issue is that they are not fully suited for the particular problems of the EM- $\Sigma\Delta$ architecture.

2.2.3 Multivariable Control Architectures

So far, we have supposed that the operation of the drive and sense modes are independent, that is, the behavior of the drive-mode closed loop does not interfere on the behavior of the sense mode and vice-versa. Assuming that the drive and sense modes are two uncoupled SISO systems and that the Coriolis and coupling force are exogenous disturbance is convenient to understand the operation of MEMS gyroscope and to design simple controllers. However, this assumption does not hold in reality. Indeed, these forces couple the oscillating modes and, instead of a two-independent-SISO system, MEMS gyroscopes are MIMO systems. Therefore, to properly take into account the different interactions between the drive and sense modes, multivariable control techniques have to be used for the control design. Thus, we can define the following problem.

Problem 2.3 (Multivariable control problem). *To design a multivariable control system that solves, at the same time, Problem 2.1 and Problem 2.2.*

In the literature, works on the multivariable control of MEMS gyroscopes are rare. We can mention the works [PH04, YF13], tackling the problem through adaptive control; the work [PK14], where model predictive control is employed; and [DZG08], which proposes a solution based on the ADRC. These approaches have a common point: all of them use a direct control architecture. That is, based on the measures x_m and y_m , and on the reference signals x_m^{ref} and y_m^{ref} , the (single) controller K computes the signals u_x and u_y such that $x_m = x_m^{ref}$ and $y_m = y_m^{ref}$. This description is depicted in Figure 2.28.

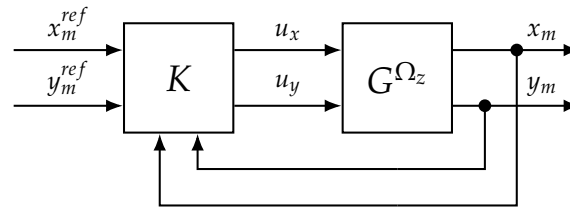


FIGURE 2.28: Multivariable direct control architecture for the gyroscope operation.

The works [PK14] and [DZG08] adopt a conventional closed-loop operation of the gyroscope, that is, x_m^{ref} is a sinusoidal signal and y_m^{ref} is set to 0; the signal u_y is then used to compute $\hat{\Omega}_z$. On the other hand, [PH04] proposes a mode of operation, in which y_m^{ref} is also a sinusoidal signal with a frequency different of that of x_m^{ref} . This strategy allows directly estimating the parameter Ω_z .

The biggest advantage of the MIMO approach is that the multivariable nature of the MEMS gyroscope is properly taken into account and strong nonlinear components are not present in the loop. Therefore, advanced multivariable control design methods can be applied, and formal guarantees of stability and performance can be given.

Some drawbacks of the MIMO approach also have to be mentioned. An important drawback is that these advanced methods require a certain expertise on Control Theory to design the controller and to implement the solution. Therefore, besides the efforts to demonstrate the interest on the use of MIMO approaches, further efforts have to be dispensed to make the solution accessible to the MEMS designers. Finally, as well as for the drive-mode direct control architectures, only works based on the ADRC solution present practical results.

2.2.4 Summary of the Control Architectures

Let us now summarize the main information on the control architectures presented in this section and compare their advantages and drawbacks. Note that the different control architectures can be regrouped into envelope-based, direct, and nonlinear architectures.

The control architectures based on the envelope of the signals comprise the AGC+PLL and the I/Q approaches. The main advantage of these strategies is that instead of operating with harmonic signals with frequency around $\omega_{0,x}$, the controllers can operate with low-frequency signals. The problem of tracking or rejecting sinusoidal signals becomes a problem of tracking or rejecting constant (or low-frequency) signals. Hence, simple PI controllers can be used to regulate amplitude and phase or the quadrature terms of the harmonic signals.

One issue of the envelope-based approaches is that, even if the gyroscope model is (mainly) linear, nonlinearities (modulation and demodulation) are included in the control loop, making the overall system nonlinear. Moreover, the coupling between amplitude and phase, or between the in-phase and the in-quadrature terms is neglected. Thus, no formal guarantees of stability or performance can be given *a priori*.

Alternatively, the direct control architectures can provide those guarantees. Furthermore, this is the only architecture used in the MIMO framework. Despite the rarity of implementation results in the literature, the few practical results indicate that the direct control architecture can be successfully implemented in a real MEMS gyroscope.

We have to mention, however, that controllers for the direct approach are, in general, more complex (higher order) than those used with envelope-based approaches, requiring more resources for their implementation. Another drawback of this approach is that the resonance frequency is not tracked. An external loop is needed to achieve this purpose. Finally, the design of a direct controller usually requires the system designer to have a good expertise on advanced control theory.

Finally, we have the nonlinear architectures AGC and EM- $\Sigma\Delta$. The strengths and weakness of these architectures are similar to those of the envelope-based ones. Globally, they are well-suited for the implementation on integrated circuits with low resources, thanks to their simplicity. Nevertheless, no formal guarantees of performance can be given due to the presence of strong nonlinearities in the loop (product $U_x(t) \times \dot{x}_m(t)$ in the AGC and relay in the EM- $\Sigma\Delta$ architecture).

2.3 Experimental Setups

For the proper operation of a MEMS gyroscope, some auxiliary systems are needed. Indeed, further than the MEMS itself, electronic circuits are used for actuation and detection, for the implementation of the controller(s), and for signal processing to compute the angular rate. In general, all these functionalities are implemented in an application-specific integrated circuit (ASIC), interfacing the MEMS gyroscope with the outside world. A typical system architecture, integrating MEMS and ASIC, is presented in Figure 2.29, where the variable capacitors represent the capacitive actuation and detection elements of the MEMS. In this example, the control loops of drive (DM) and sense (SM) modes are independent. Both loops are composed of: a charge amplifier (CA), which converts the varying detection capacitance into voltage; an analog-to-digital converter (ADC); a configurable digital controller; and a digital-to-analog converter (DAC). Then, based on the signals of the drive and sense modes, the angular rate can be estimated and compensated in function of the temperature. The estimation of the angular rate is then output through some communication protocol.

It is worth mentioning that ASICs are integrated circuits conceived to execute some specific task. Thus, the control loops implemented in an ASIC are often only configurable, that is, the control architecture is **fixed** and only some parameters can be changed in order to optimize the controllers to the different MEMS.

In some cases, the ASIC implements only the actuation and detection circuits. The controllers and the angular rate estimation are deported to an external field-programmable gate array (FPGA) or processor, where those elements are programmed in software, providing **flexibility** for the implementation of different control loops and estimation algorithms. This architecture is presented in Figure 2.30.

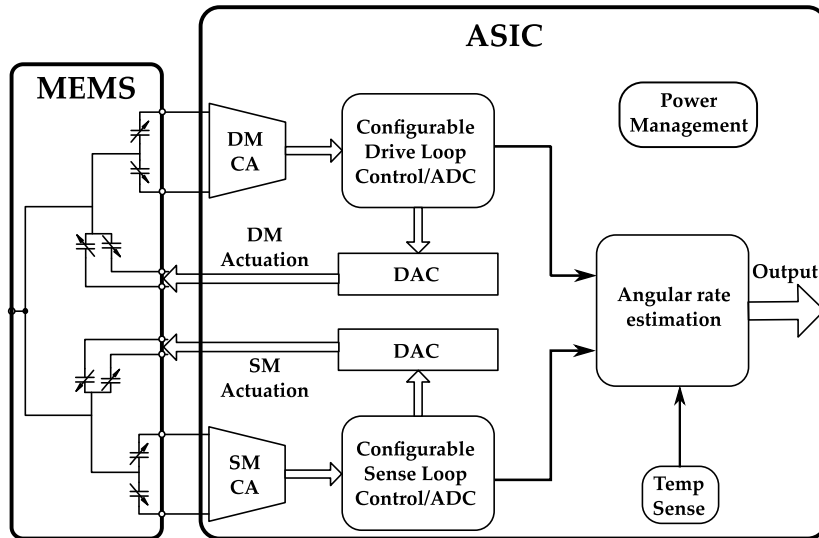


FIGURE 2.29: Integration of MEMS and ASIC. Adapted from [EEE⁺11].

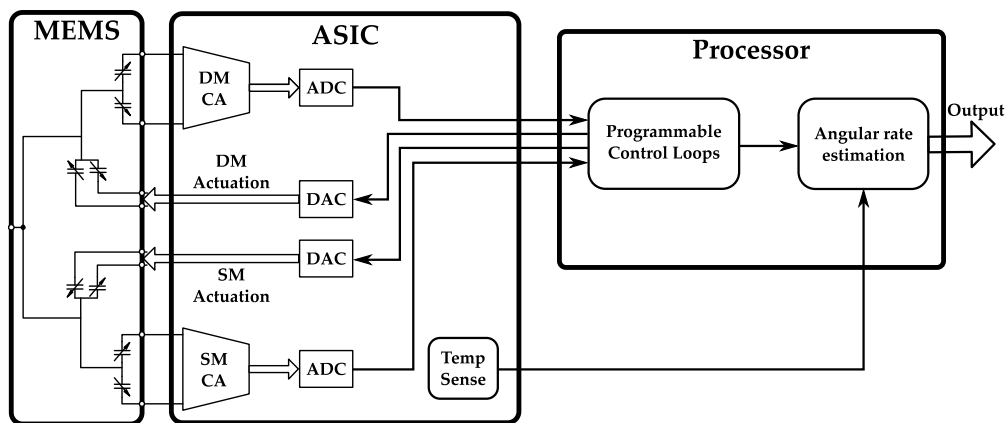


FIGURE 2.30: Integration of MEMS, ASIC and a processor.

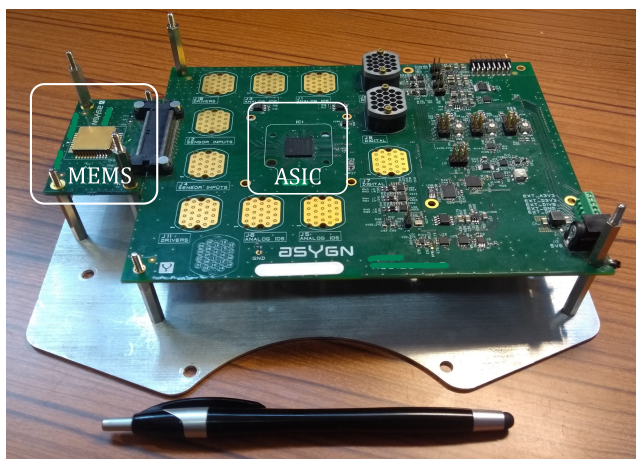
In this work, we consider both cases: the flexible architecture of Figure 2.30 and the dedicated one of Figure 2.29.

2.3.1 AS3125-SDK: a Flexible Sensor Development Kit

Part of the experimental tests are realized on the AS3125-SDK (Sensor Development Kit), which is conceived by ASYGN and whose picture is presented in Figure 2.31a. This development kit presents a system architecture similar to the one of Figure 2.30 and is mainly composed of:

- (i) an FPGA (Xilinx Zynq), which includes a micro processor, for the digital implementation of the control loop and estimation algorithms;
- (ii) a front-end ASIC (AS3125 “Idyle”) and ADCs to interface MEMS sensors with the FPGA;
- (iii) Universal serial bus (USB) ports for communication with external devices, *e.g.*, a computer.

The FPGA and the USB ports are on the bottom part of the development kit, being hidden in the picture.



(A) Development kit with a MEMS gyroscope.



(B) A MEMS gyroscope.

FIGURE 2.31: Pictures of the development kit and MEMS gyroscope.

The ASIC AS3125 “Idyle” is dedicated to interface the MEMS gyroscope to the FPGA and, in summary, integrates:

- (i) charge amplifiers with configurable gains (instrumentation circuits),
- (ii) 10-bits DACs,
- (iii) drivers or amplification circuits for actuation.

Moreover, the development kit also includes 18-bits ADCs operating at 1 MHz and second-order anti-aliasing filters F_{adc} with 100 kHz cutoff frequency,

The FPGA implements a micro processor in which the control loops and the estimation algorithms are coded in C++ language. The implemented processor allows the implementation of digital control loops with sampling frequency $F_s = 62.5$ kHz. To reduce the sampling frequency of the ADCs from 1 MHz to 62.5 kHz, a digital filter F_{ds} and a downsampling (or

decimation) by a factor 16 are implemented in hardware (FPGA). The FPGA also configures the ASIC and communicates with a computer through the USB ports.

The diagram of Figure 2.32 represents the overall control loop implemented in this development kit, illustrating the above description.

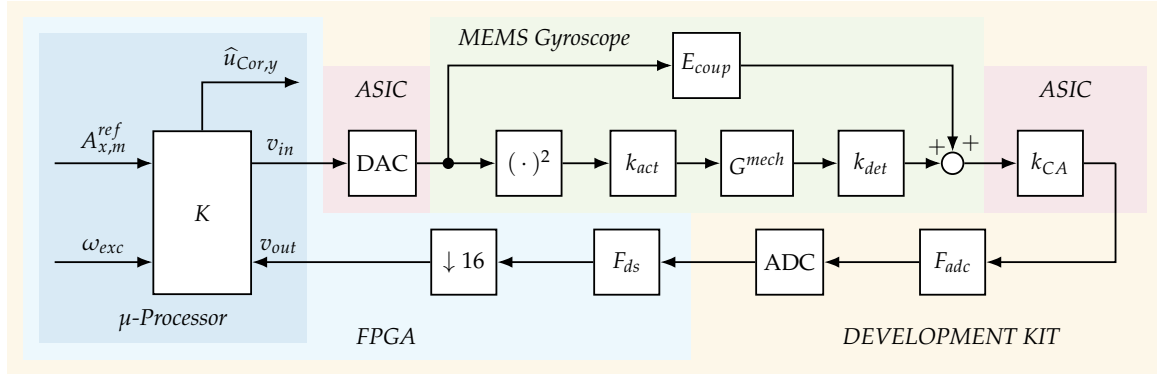


FIGURE 2.32: Overall control loop implemented in AS3125-SDK for the MEMS gyroscope operation.

On this development board, we use the MEMS gyroscopes of the family GYRO I, whose nominal main characteristics are listed in Table 2.1.

TABLE 2.1: Nominal characteristics of the MEMS gyroscopes of the family GYRO I.

Parameter	Drive mode ($i = x$)	Sense mode ($i = y$)
Resonance frequency ($\omega_{0,i}$)	11 500 Hz	11 550 Hz
Quality factor (Q_i)	$100 \cdot 10^3$	$10 \cdot 10^3$

2.3.2 Tronics' Platform with Dedicated ASIC

Another part of the experiments is realized on the platform of Tronics, which is a generic development board used to interface the MEMS gyroscopes and dedicated ASIC with a computer. The dedicated ASIC contains all the control loops and estimation process, and is implemented in the same chip of the MEMS with the system architecture of Figure 2.29.

The drive mode operates in closed loop in a nonlinear AGC architecture with phase shifter and a PI controller. An interesting feature of this platform is that the sampling frequency is locked with the resonance frequency of the drive mode, such that $F_s = 36 \cdot \omega_{0,x} / (2\pi)$. Then, when $\omega_{0,x}$ changes during the gyroscope operation, the sampling frequency changes accordingly, adapting the behavior of the digital elements.

The sense mode can operate in open or closed loop. As discussed in Section 2.1.2, we consider only the closed-loop operation. In this platform, the EM- $\Sigma\Delta$ architecture of Figure 2.33 is employed. We present, in the same figure, the elements of the actuation and instrumentation (see Section 2.1.3), indicating the key signals of the loop, as the Coriolis force ($F_{Cor,y}$, which is perturbed by the coupling force $F_{coup,y}$), the input voltage ($v_{in,y}$) and the output voltage (y_m). Some actuation and instrumentation gains, as well as the coefficients of the electronic filter, are programmable. They are identified in gray. The ADC has a resolution of 13 bits, while the DAC has a 1-bit resolution.

Please note that, in opposition to the previous platform, the parasitic electrical coupling (E_{coup}) is not represented here. Two facts justify its omission. First, because the MEMS and the ASIC are encapsulated in the same chip, the paths between them are short, reducing the parasitic electrical coupling.

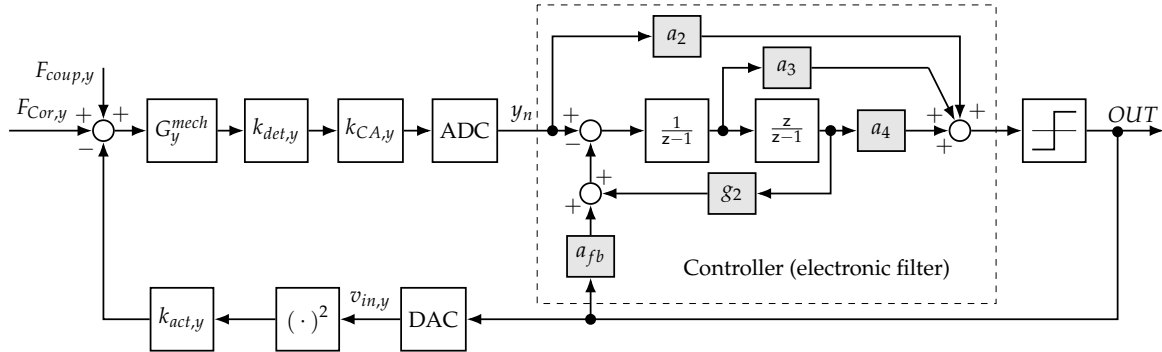


FIGURE 2.33: EM- $\Sigma\Delta$ architecture implemented in the dedicated ASIC. Configurable elements are represented in gray.

Finally, the angular rate estimation is implemented through the synchronous demodulation. The output bias (or ZRO) and the scale factor are compensated in function of the temperature.

A picture of the Tronics' platform with a MEMS gyroscope is presented in Figure 2.34. On this development board, we use the MEMS gyroscopes of the family GYRO II, whose sense-mode main nominal characteristics⁵ are $\omega_{0,y} = 1.004 \cdot \omega_{0,x}$ and $Q_y = 25 \cdot 10^3$.

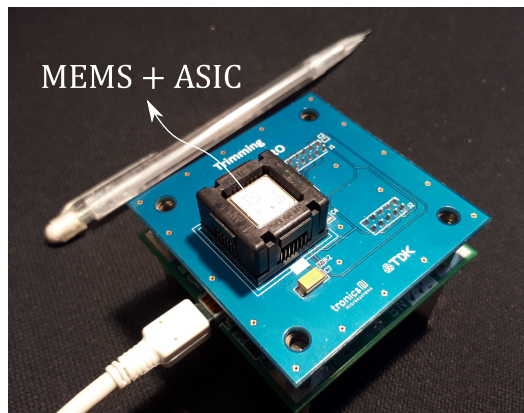


FIGURE 2.34: Picture of the Tronics' platform with a MEMS gyroscope.

2.4 Research Questions

In this chapter, the MEMS gyroscopes are presented and the most significant control architectures are discussed. Now, taking into account the nonidealities, implementation constraints and the different solutions considered in the literature, the main problem we want to address is: *how to choose a control architecture and design, in a systematic manner, a controller such that stability and performance guarantees can be given?*

Answering to that question is not an easy task. Indeed, in Section 2.2.4, we can note that, regarding the actual solutions, those which are typically implemented do not provide formal

⁵For confidentiality reasons, the frequencies are normalized to the drive-mode resonance frequency $\omega_{0,x}$.

guarantees of performance. Indeed, the control architectures are usually optimized in terms of cost and simple implementation. Nevertheless, the couplings between the drive and sense modes, the couplings between amplitude and phase (or in-phase and in-quadrature terms), as well as the dependence on environmental conditions, are not taken into account. On the other side, solutions based on the direct control architecture, for which formal performance guarantees can be given, are very rare in the literature. For this architecture, advanced control techniques have been developed for vibration control of mechanical systems, as in [Wan19], for instance. The main interest of this approach is to explicitly take into account the different couplings and the dependence on the environmental condition, with formal guarantees of stability and performance. Nevertheless, their applicability to MEMS gyroscopes, including implementability, is still an open question. A possible reason is the inherent complexity of the controllers.

Note that the performance indicators of MEMS gyroscopes are related to the quality of the measure and not (directly) to the closed-loop behavior. Indeed, the closed loop is a part of the whole gyroscope, and has an final objective to provide an estimate of the Coriolis force, which is treated afterward in a post-processing stage. Then, the first research question is:

(Q1) *how to relate the global performance specifications to specifications for the closed-loop system?*

Having defined the closed-loop specifications, the problem is: *how to design a controller for the direct control architecture that ensures the given closed-loop specifications?* As discussed in this chapter, the control objectives can be cast as to track or reject sinusoidal signals with the excitation frequency ω_{exc} . However, this frequency may vary over time. Therefore, two scenarios are considered, giving rise to the two research questions below.

(Q2) *Assuming that ω_{exc} is **constant** over time, how to design a direct controller with guarantees of stability and performance?*

(Q3) *Assuming that ω_{exc} **varies** over time, how to design a direct controller with guarantees of stability and performance?*

Although the traditional control architectures do not provide formal guarantees for the closed-loop system, they present interesting features from the implementation point of view. Then, we also want to find an answer to the question:

(Q4) *how to design a controller for an envelope-based control architecture such that guarantees of stability and performance can be given?*

Finally, we want to implement the proposed solution(s) in the platforms presented in Section 2.3: the flexible (see Section 2.3.1) and the dedicated one (see Section 2.3.2). In both cases, the controller is implemented in the discrete-time domain. Therefore, the two following questions arise.

(Q5) *How to properly design a controller for digital implementation in a **flexible** platform?*

(Q6) *How to properly design the EM- $\Sigma\Delta$ controller of a **dedicated** platform?*

The next chapters aim to answer each one of these research questions.

Chapter 3

From Global Performance Specifications to Closed-Loop Specifications

In Section 2.1.5, we investigated how the gyroscope nonidealities impact the estimate of Ω_z under the assumption of ideal operation, that is, when the system operates with a controller that ensures the perfect tracking of the reference signal and perfect estimation of the Coriolis force acting on the sense mode. Obviously, this ideal controller cannot be implemented in practice. However, that analysis gives important insights on how the quality of the measure is impacted by the nonidealities of the MEMS gyroscope. In this chapter, we go a little deeper in that direction. We consider that the gyroscope operates with a **real** (nonideal) controller. Then, we aim to define the conditions that a real controller has to fulfill in order to ensure a certain quality of the measure (*e.g.*, a given SFNL and/or bandwidth).

At this point, it is important to recall that the gyroscope global performance specifications pertain to the estimation of the angular rate, whereas the performance criterion of the control loops pertain to the behavior of the closed-loop system, before the synchronous demodulation. Therefore, it is crucial to translate the gyroscope global performance requirements into specifications for the closed-loop system. These specifications will be used in the next chapters to design the controller.

It is also worth recalling that the MEMS gyroscope is very sensitive to environmental changes and to fabrication imperfections, hence its model is not completely known. Then, in addition to pursue the performance specifications, we have to ensure that the closed-loop system is stable despite the modeling errors or changes on the model due to environmental changes, for instance. Based on this discussion, we can talk about four characteristics of a closed-loop system, as follows [SP01].

- (i) We talk about **nominal stability** when the nominal closed-loop system is stable. In this case, the model uncertainties are not taken into account.
- (ii) If the nominal system (with no uncertainties) achieves the performance specifications, we talk about **nominal performance**.
- (iii) **Robust stability** is the characteristic of the systems that are stable for all possible models around the nominal one.
- (iv) Finally, we talk about **robust performance** when the closed-loop system achieves the performance specifications for all possible models around the nominal one.

The main goal of this chapter is to define the closed-loop performance specifications such that the MEMS gyroscope global performance indicators are achieved. Here, the focus is given to the controller design. In general, we want this controller to ensure the robust performance of the system. However, the design of a controller that ensures robust performance is a problem reputed to be hard to solve [BYDM94]. On the other hand, the design of a controller that ensures nominal performance and robust stability is a problem that can be efficiently solved. We focus therefore on solving the latter problem. Once the controller is designed, the robust performance can be assessed by an *a posteriori* analysis, see, e.g., [AC21].

Hereafter, when talking about performance, we are referring to the nominal performance property; when talking about robustness, we are actually referring to the robust stability.

We start the chapter by presenting the main problem which we aim to solve here: determine the closed-loop specifications that ensure the desired (nominal) performance specification and robust stability. To tackle this problem, we first analyze the sensor output $\hat{\Omega}_z$ under nonideal operation. This analysis allows establishing the main links between the global and the closed-loop specifications. Then, we quantify, when possible, the closed-loop specifications for performance and robust stability. When it is not possible to quantify those specifications, we qualitatively indicate where and how to act for enhancing the global specification in question.

3.1 Problem Statement

In this section, we define the main problem to be tackled in this chapter. To this purpose, we start by recalling the closed-loop operation of the MEMS gyroscopes and the main control objectives. Then, we make some assumptions to tackle the problem in a tractable manner. Finally, the problem under investigation is stated.

3.1.1 System Description and Control Objectives

As intensively discussed in the previous chapter, to design a gyroscope that provides a good quality of measure, the use of control loops is required. Then, we consider the general multivariable direct control architecture of Figure 3.1. The plant G^{θ,ρ,Ω_z} represents the mechanical part of the MEMS gyroscope and all circuitry needed for actuation and detection. As discussed in Section 2.1.5 (page 32), the mechanical part of the gyroscope can be modeled by $G^{\theta,\rho}$ with a feedback loop, which represents the dependence on Ω_z . The controller is denoted by K^θ . The superscripts θ and ρ indicate that the system parameters may depend on θ and ρ . The variable θ corresponds to the **known** parameters, which can be measured and used by the controller. In its turn, ρ represents the **unknown** parameters. The block ΔE_{coup} models the residual electrical coupling.

In the considered control architecture, x_m^{ref} and y_m^{ref} denote the reference signal for the positions x_m and y_m of the proof mass along the \vec{x} - and the \vec{y} -axes, respectively; n_x (respectively n_y) corresponds to the noise on the measure of x_m (resp. y_m); $u_{Cor,x}$ (resp. $u_{Cor,y}$) denotes the Coriolis force acting on the drive (resp. sense) mode; and finally, $\hat{u}_{Cor,y}$ is the estimate of $u_{Cor,y}$.

As discussed in Section 2.1, the demodulation of $\hat{u}_{Cor,y}$ followed by the compensation function (f_{comp}^θ , defined in (2.52), page 35) leads to an exact estimate $\hat{\Omega}_z$ of the angular rate Ω_z if the conditions below are verified.

(C1) **Synchronous demodulation ideality condition:** the synchronous demodulation (SD) is ideal (*i.e.*, the low-pass filters F_{LP} are ideal and have cutoff frequency $\omega_c = \omega_{exc}$).

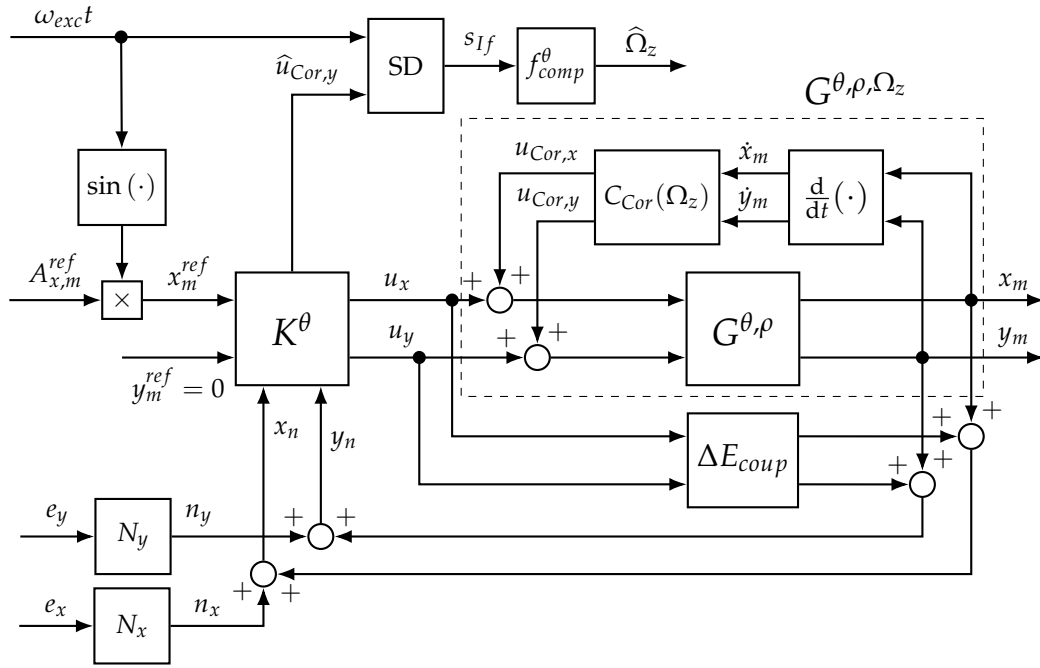


FIGURE 3.1: Control architecture for the MEMS gyroscope closed-loop operation.

- (C2) **Band-pass condition of $\hat{u}_{Cor,y}$:** the signal $\hat{u}_{Cor,y}$ is band-pass with bandwidth $2\omega_{exc}$ centered at ω_{exc} , that is,

$$\forall |\omega| \geq 2\omega_{exc}, \quad \mathcal{S}_{\hat{u}_{Cor,y}}(\omega) = 0 \quad \text{and} \quad \mathcal{S}_{\hat{u}_{Cor,y}}(0) = 0. \quad (3.1)$$

- (C3) **Coriolis force estimation condition:** the estimate of the Coriolis force acting on the sense mode is given by

$$\hat{u}_{Cor,y}(t) = k_{SF}\Omega_z(t) \cos(\omega_{exc}t) \quad (3.2)$$

with

$$k_{SF} = \frac{-2mA_{x,m}^{ref}\omega_{exc}}{k_{out,y}k_{in,y}}. \quad (3.3)$$

In this chapter, we focus on the behavior of the closed-loop system. Then, since the synchronous demodulation is outside the control loops, we make the following assumptions, regarding the conditions (C1) and (C2).

Assumption 3.1. The synchronous demodulation is ideal with filters whose cutoff frequency is $\omega_c = \omega_{exc}$.

Assumption 3.2. The bandwidth of the signal Ω_z , which is defined as ω_Ω such that

$$\forall |\omega| \geq \omega_\Omega, \quad \mathcal{S}_{\Omega_z}(\omega) = 0, \quad (3.4)$$

is smaller than ω_{exc} , that is, $\omega_\Omega < \omega_{exc}$.

The second assumption ensures that, if the condition (C3) is satisfied, the condition (C2) also holds (see Section 2.1.4, page 23).

The condition (C3) is ensured in steady state if there is a controller that achieves the following **control objectives**.

(O1) **Drive-mode reference tracking:** the signal x_m tracks the reference signal

$$x_m^{ref}(t) = A_{x,m}^{ref} \sin(\omega_{exc}t), \quad (3.5)$$

where $A_{x,m}^{ref}$ and ω_{exc} are constant values.

(O2) **Estimation of the Coriolis force:** the signal $\hat{u}_{Cor,y}$ is an accurate estimate of $u_{Cor,y}$, that is, $\hat{u}_{Cor,y}(t) = u_{Cor,y}(t)$.

(O3) **Sense-mode disturbance rejection:** the signal y_m tracks the reference signal $y_m^{ref}(t) \equiv 0$, rejecting the disturbances created by the Coriolis and coupling forces.

These control objectives are justified by the fact that the Coriolis force $u_{Cor,y}$ is defined as

$$u_{Cor,y}(t) = \frac{-2m\Omega_z(t)\dot{x}_m(t)}{k_{out,x}k_{in,y}}. \quad (3.6)$$

Hence, if the objectives (O1) and (O2) are fulfilled, the condition (C3) is promptly satisfied.

In order to improve the tracking of x_m^{ref} by x_m – control objective (O1) –, it is also interesting to have, in steady-state, $u_{Cor,x}(t) = 0$. Since

$$u_{Cor,x}(t) = \frac{2m\Omega_z(t)\dot{y}_m(t)}{k_{out,y}k_{in,x}}, \quad (3.7)$$

this goal can be achieved if y_m tracks $y_m^{ref}(t) \equiv 0$, which corresponds to the third control objective (O3).

In practice, however, it is not possible to implement a controller that perfectly achieves the above objectives. Thus, we can define the tracking errors $\varepsilon_x(t) \triangleq x_m^{ref}(t) - x_m(t)$ and $\varepsilon_y(t) \triangleq -y_m(t)$ as well as the estimation error $\varepsilon_{est}(t) \triangleq u_{Cor,y}(t) - \hat{u}_{Cor,y}(t)$ to quantify the closed-loop performance.

Remark 3.1 (On the amplitude of y_m). It is important to highlight that although we consider the model of the gyroscope as a linear system, the real gyroscope is actually nonlinear. Therefore, enforcing $y_m(t) = 0$ plays two important roles. The first one, as discussed above, is to eliminate (or at least attenuate) the disturbances on the drive mode provoked by $u_{Cor,x}$. The second one is to keep the gyroscope operating in a region where its behavior is rather linear.

It is also important to highlight that, in practice, the process noises also disturb the estimate $\hat{u}_{Cor,y}$. As discussed in Section 2.1.5, these noises are modeled by N_x , N_y and the signals e_x and e_y , which are assumed to be as follows.

Assumption 3.3. The signals e_x and e_y are assumed to be uncorrelated white noises with zero mean and unit variance, such that their PSD can be respectively given by

$$\mathcal{S}_{e_x}(\omega) = 1 \quad \text{and} \quad \mathcal{S}_{e_y}(\omega) = 1. \quad (3.8)$$

3.1.2 Analysis Model

In general, even if $G^{\theta,\rho}$, K^θ , F_{LP} , N_x and N_y are linear systems, it can be hard to evaluate the behavior of the whole system of Figure 3.1. This difficulty comes from:

- (i) the dependence of $G^{\theta,\rho}$ and K^θ on the parameters θ and ρ ,
- (ii) the time-varying nature of the synchronous demodulation and of the to-be-controlled plant (due to the dependence on Ω_z),
- (iii) the presence of the uncertain system ΔE .

As discussed in Section 2.1.5, the variations of the parameters θ and ρ are very slow with respect to the system dynamics. We can then make the following assumption.

Assumption 3.4. *The operating condition does not vary over time.*

This assumption implies that the parameters θ and ρ are fixed and the LPV systems $G^{\theta,\rho}$ and K^θ are frozen. In this case, $G^{\theta,\rho}$ and K^θ become LTI systems. Moreover, the uncertainties represented by ρ can be encapsulated with those represented by ΔE_{coup} into the uncertain system ΔE . Thus, we drop hereafter the dependence on θ and ρ to alleviate the notation.

In Section 2.1.4, we saw that even if the synchronous demodulation is based on multiplications by sinus and cosinus functions (modulation), in the special case where ω_{exc} is constant, frequency-domain analysis tools can be used (see Remark 2.1, page 25).

On the other hand, regarding the time-varying nature of the to-be-controlled plant (due to Ω_z), we consider that the Coriolis forces $u_{Cor,x}$ and $u_{Cor,y}$ are exogenous signals, which we hereafter denote $d_{Cor,x}$ and $d_{Cor,y}$ to distinguish from the endogenous signals $u_{Cor,x}$ and $u_{Cor,y}$. Neglecting the presence of noise, they are of the type

$$d_{Cor,x}(t) = \frac{2m\Omega_z(t)\omega_{exc}A_{y,m}}{k_{out,y}k_{in,x}} \cos(\omega_{exc}t), \quad (3.9)$$

$$d_{Cor,y}(t) = \frac{-2m\Omega_z(t)\omega_{exc}A_{x,m}}{k_{out,x}k_{in,y}} \cos(\omega_{exc}t), \quad (3.10)$$

where $A_{y,m} \in [0, \check{\epsilon}_y A_{x,m}^{ref}]$ and $A_{x,m} \in [(1 - \check{\epsilon}_x) A_{x,m}^{ref}, (1 + \check{\epsilon}_x) A_{x,m}^{ref}]$. The tracking error signals ϵ_x and ϵ_y are sinusoidal signals with frequency ω_{exc} . The variables $\check{\epsilon}_x \in \mathbb{R}_+$ and $\check{\epsilon}_y \in \mathbb{R}_+$ bound the amplitude of ϵ_x and ϵ_y with respect to $A_{x,m}^{ref}$, that is,

$$\forall t \in \mathbb{R}, \quad |\epsilon_x(t)| \leq \check{\epsilon}_x A_{x,m}^{ref} \quad \text{and} \quad |\epsilon_y(t)| \leq \check{\epsilon}_y A_{x,m}^{ref}.$$

The equations (3.9) and (3.10) follow from the definitions of $u_{Cor,y}$ and $u_{Cor,x}$ (see (3.6) and (3.7)) when

$$x_m(t) = A_{x,m}^{ref} \sin(\omega_{exc}t) - \epsilon_x(t) \quad \text{and} \quad y_m(t) = -\epsilon_y(t).$$

Therefore, the scheme of Figure 3.1 can be simplified into the scheme of Figure 3.2, where the closed-loop system is LTI. An additional assumption is made.

Assumption 3.5. *If the LTI closed-loop system of Figure 3.2 is stable and achieves some performance specifications (reference tracking and Coriolis force estimation), the system of Figure 3.1 is also stable and achieves the same performance specifications.*

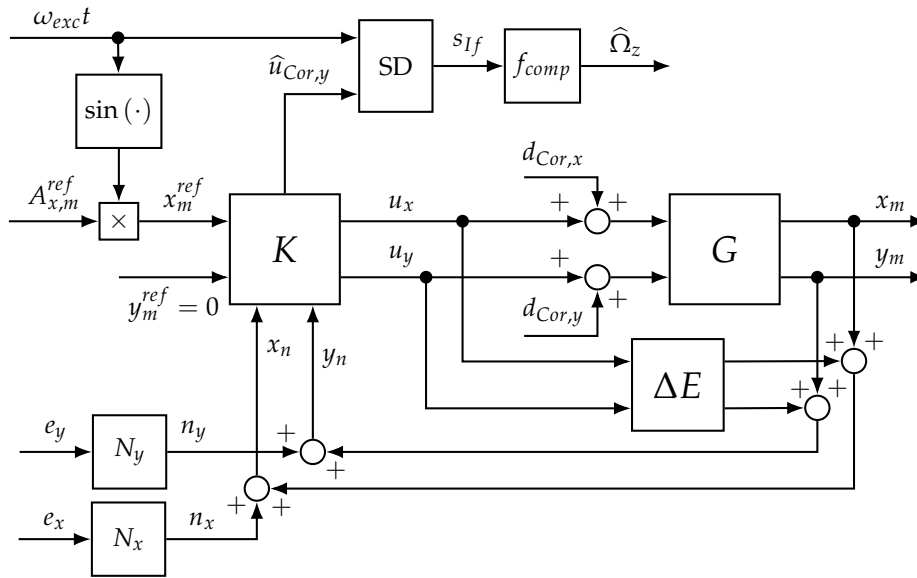


FIGURE 3.2: Simplified scheme of the closed-loop system under analysis.

With the assumption above, instead of analyzing the LTV system of Figure 3.1, we can extrapolate the results of the LTI system of Figure 3.2 to the former one. The attentive reader may be asking himself if we are not too optimistic. Indeed, this assumption carries a certain degree of optimism. However, we will show that, at least for the gyroscopes considered within the scope of this thesis, the level of optimism is very low.

Finally, remember that, in this chapter, we want to **separately** define the closed-loop specifications for nominal performance and for robust stability. Therefore, to evaluate the nominal performance and establish the closed-loop specifications, we consider the case where there are no uncertainties, *i.e.*, $\Delta E = 0$. The uncertainties ($\Delta E \neq 0$) are taken into consideration in a second time, establishing specifications for robust stability.

3.1.3 Analysis Problems

In Section 2.1.6, we claimed that a MEMS gyroscope can be modeled as a dynamic system that produces a measure $\hat{\Omega}_z$ of the angular rate Ω_z under which it is subject. Obviously, the measure is not perfect. Measurement errors can be introduced by the gyroscope itself. These errors can be related to the different sources of noise, to some inaccuracy or dysfunctioning of the sensor or to its dynamic response. Then, global performance indicators are used to characterize the quality of the measure of a given sensor. Here, we focus in some of the key indicators, as follows.

Accuracy: the accuracy of the sensor for a constant Ω_z can be given by the scale factor nonlinearity (SFNL). It indicates the maximum systematic error with respect to the full scale (or dynamic range) Ω_z^{FS} that can be committed by the sensor. These systematic errors can be originated from the nonlinearities of the system as well as by systematic errors committed by the controller, for instance. Here, in an LTI framework, we are only able to evaluate the second type of errors. We recall the SFNL definition below

$$\text{SFNL} \triangleq \max_{\Omega_z \in [-\Omega_z^{FS}, \Omega_z^{FS}]} \left(\frac{|\hat{\Omega}_z - \Omega_z|}{\Omega_z^{FS}} \right). \quad (3.11)$$

Bandwidth: the bandwidth of a MEMS gyroscope, denoted ω_B , is the frequency range in which its attenuation is smaller than 3 dB (equivalent to a gain of $\sqrt{2}/2$) [IEE04]. If the sensor has frequency response given by $H_{gyro}(j\omega)$, we define its bandwidth as the frequency ω_B such that

$$\forall |\omega| < \omega_B, \quad \left| 1 - \frac{H_{gyro}(j\omega)}{H_{gyro}(0)} \right| < 1 - \frac{\sqrt{2}}{2}. \quad (3.12)$$

Noise sensitivity: the noise sensitivity of the sensor is related to the **precision** (repeatability) of the measures. In general, different sources of noise are present in the system, producing different consequences on the quality of the measure. To characterize them, the Allan variation is usually used, defining different performance parameters. Here, we focus on the angle random walk (ARW). This choice is justified in Section 3.3.4.

Based on the above global performance parameters, we can finally state the main problem that we aim to solve in this chapter.

Problem 3.1. *Let us consider the system of Figure 3.2 with input signals x_m^{ref} , $d_{Cor,x}$ and $d_{Cor,y}$ given in (3.5), (3.9) and (3.10), respectively; with $y_m^{ref}(t) \equiv 0$; and with e_x and e_y satisfying Assumption 3.3. Then, which closed-loop specifications allow one to ensure the global performance specifications below?*

- (i) *The sensor SFNL is smaller than a given $k_{SFNL} > 0$.*
- (ii) *The sensor bandwidth ω_B is larger than a given $\omega_B^{des} > 0$, in rad s^{-1} .*
- (iii) *The sensor ARW is smaller than a given $k_{ARW} > 0$, in $^\circ / \sqrt{\text{h}}$.*

Obviously, prior to achieve a desired performance, the controller has to ensure the proper closed-loop operation of a real MEMS gyroscope. This means that the controller must fulfill, at best, the conditions and control objectives of Section 3.1.1 (reference tracking, estimation of the Coriolis force, disturbance rejection and band-pass condition). For a real controller, they can then be rewritten as the specifications below.

- (S1) **Drive-mode reference tracking:** the signal x_m tracks the reference signal x_m^{ref} , defined in (3.5), with a tracking error ε_x such that, in steady state, $|\varepsilon_x(t)| \leq \check{\varepsilon}_x A_{x,m}^{ref}$ with $0 < \check{\varepsilon}_x \ll 1$.
- (S2) **Estimation of the Coriolis force:** the signal $\hat{u}_{Cor,y}$ estimates $d_{Cor,y}$ of the form of (3.9) with an estimation error ε_{est} such that, in steady state, $|\varepsilon_{est}(t)| \leq \check{\varepsilon}_{est} A_{x,m}^{ref}$ with $0 < \check{\varepsilon}_{est} \ll 1$.
- (S3) **Sense-mode disturbance rejection:** the signal y_m tracks the reference signal $y_m^{ref}(t) \equiv 0$ with an error ε_y such that, in steady state, $|\varepsilon_y(t)| \leq \check{\varepsilon}_y A_{x,m}^{ref}$ with $0 < \check{\varepsilon}_y \ll 1$.
- (S4) **Band-pass condition:** the signal $\hat{u}_{Cor,y}$ is a band-pass signal centered at ω_{exc} with bandwidth smaller than $2\omega_{exc}$.
- (S5) **Robust stability:** the closed-loop system is stable against the uncertainties represented by ΔE .

Therefore, solving Problem 3.1 also requires the definition of closed-loop specification fulfilling the specifications (S1)–(S5). To solve this problem, we first need to compute the expression of the signals $\hat{u}_{Cor,y}$, x_m and y_m as functions of the input signals x_m^{ref} , $d_{Cor,x}$, $d_{Cor,y}$, e_x and e_y – specifications (S1) to (S4). To determine the accuracy and the bandwidth of the sensor –

specifications (i) and (ii), respectively –, we have to demodulate $\hat{u}_{Cor,y}$ and compute $\hat{\Omega}_z$ as function of the input angular rate Ω_z , neglecting the contributions of the different sources of noise. For the noise sensitivity – specification (iii) –, we have to compute the PSD of $\hat{\Omega}_z$, $\mathcal{S}_{\hat{\Omega}_z}$ with the sensor at rest (*i.e.*, $\Omega_z \equiv 0$). In this case, we consider the nominal system, *i.e.*, with $\Delta E = 0$. The uncertainties are taken into account for the robust stability specification (S5), being treated separately in an LTI framework in the end of the chapter.

3.2 Analysis of the Angular Rate Estimate $\hat{\Omega}_z$

Before proceeding with the solution of Problem 3.1, we have to analyze how the estimate of the angular rate, $\hat{\Omega}_z$, behaves under nonideal operation of the MEMS gyroscope. The analysis here presented is used in the next sections to determine the closed-loop specifications required to achieve the desired performance specifications.

Let us begin the analysis by defining x_m^{ref} , $d_{Cor,x}$, $d_{Cor,y}$, e_x and e_y as the inputs of interest of the closed-loop system of Figure 3.2, and x_m , y_m and $\hat{u}_{Cor,y}$ as its outputs of interest. Then, the frequency response of the closed-loop system can be given by (for the sake of clarity, the dependence on ω is omitted)

$$\begin{bmatrix} x_m \\ y_m \\ \hat{u}_{Cor,y} \end{bmatrix} = \begin{bmatrix} T_{x_m^{ref} \rightarrow x_m} & T_{d_{Cor,x} \rightarrow x_m} & T_{d_{Cor,y} \rightarrow x_m} \\ T_{x_m^{ref} \rightarrow y_m} & T_{d_{Cor,x} \rightarrow y_m} & T_{d_{Cor,y} \rightarrow y_m} \\ T_{x_m^{ref} \rightarrow \hat{u}_{Cor,y}} & T_{d_{Cor,x} \rightarrow \hat{u}_{Cor,y}} & T_{d_{Cor,y} \rightarrow \hat{u}_{Cor,y}} \end{bmatrix} \begin{bmatrix} T_{e_x \rightarrow x_m} & T_{e_y \rightarrow x_m} \\ T_{e_x \rightarrow y_m} & T_{e_y \rightarrow y_m} \\ T_{e_x \rightarrow \hat{u}_{Cor,y}} & T_{e_y \rightarrow \hat{u}_{Cor,y}} \end{bmatrix} \begin{bmatrix} x_m^{ref} \\ d_{Cor,x} \\ d_{Cor,y} \\ e_x \\ e_y \end{bmatrix}, \quad (3.13)$$

where we adopt the notation $T_{a \rightarrow b}$ to indicate the transfer from a signal a to a signal b . Note that the input signals x_m^{ref} , $d_{Cor,x}$ and $d_{Cor,y}$ are of deterministic nature, while the white-noise signals e_x and e_y are of stochastic nature. Indeed, x_m^{ref} , $d_{Cor,x}$ and $d_{Cor,y}$ are respectively given by (3.5), (3.9) and (3.10). On the other hand, e_x and e_y are uncorrelated stochastic processes with PSD given in (3.8) (see Assumption 3.3). Hence, we split this analysis into two parts, according to the nature of the input signals: a noiseless analysis and an analysis with respect to the noise.

3.2.1 Noiseless Analysis

Here, we present the main results regarding the noiseless analysis of the system. For the sake of clarity, the (cumbersome) calculation details are given in Appendix B.1.

Without the contributions of the different sources of noise, the estimated angular rate, $\hat{\Omega}_z$, can be given, in the frequency domain, by

$$\hat{\Omega}_z(j\omega) = \frac{k_{SF}}{\hat{k}_{SF}} H_{gyro}(j\omega) \Omega_z(j\omega) + \varepsilon_{ZRO} \cdot \delta(j\omega) \quad (3.14)$$

with δ being the Dirac delta function (impulse at $\omega = 0$) and

$$\varepsilon_{ZRO} = \frac{A_{x,m}^{ref} \mathfrak{S} \left(T_{x_m^{ref} \rightarrow \hat{u}_{Cor,y}}(j\omega_{exc}) \right) - \hat{k}_{ZRO}}{\hat{k}_{SF}}, \quad (3.15)$$

where $\Im(\cdot)$ is the imaginary part of (\cdot) . We recall that k_{SF} corresponds to the scale factor of the sensor (see (3.3)), and \widehat{k}_{SF} and \widehat{k}_{ZRO} are respectively the estimates of the scale factor and of the bias. The transfer H_{gyro} reads as

$$H_{gyro}(j\omega) = \frac{k_{ux}A_{y,m}}{2k_{SF}} \left(T_{d_{Cor,x} \rightarrow \widehat{u}_{Cor,y}}(j\omega - j\omega_{exc}) + T_{d_{Cor,x} \rightarrow \widehat{u}_{Cor,y}}(j\omega + j\omega_{exc}) \right) + \frac{A_{x,m}}{2A_{x,m}^{ref}} \left(T_{d_{Cor,y} \rightarrow \widehat{u}_{Cor,y}}(j\omega - j\omega_{exc}) + T_{d_{Cor,y} \rightarrow \widehat{u}_{Cor,y}}(j\omega + j\omega_{exc}) \right) \quad (3.16)$$

$$\text{with } k_{ux} = \frac{2m\omega_{exc}}{k_{out,y}k_{in,x}}.$$

The equations (3.14) and (3.16) confirm the claim that, from the input-output perspective and under the assumptions of Section 3.1, the MEMS gyroscope behaves as an LTI system. Its frequency response is given by $\frac{k_{SF}}{\widehat{k}_{SF}} H_{gyro}(j\omega)$ added by a residual bias ε_{ZRO} , as depicted in Figure 3.3. This frequency response determines the bandwidth and the accuracy (related to the SFNL) of the sensor. Thus, we want to have $\varepsilon_{ZRO} \approx 0$ and $\frac{k_{SF}}{\widehat{k}_{SF}} H_{gyro}(j\omega) \approx 1$, at least in the sensor bandwidth, *i.e.*, for $|\omega| \leq \omega_B$.

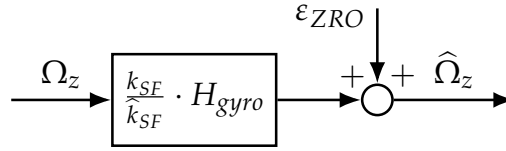


FIGURE 3.3: Block diagram representing the whole gyroscope without noise.

Now, if we consider the particular case of a constant angular rate input $\Omega_z(t) \equiv \Omega_z^\infty$, its estimate is given by $\widehat{\Omega}_z(t) = \widehat{\Omega}_z^\infty$ with

$$\widehat{\Omega}_z^\infty = \frac{k_{SF}}{\widehat{k}_{SF}} H_{gyro}(0) \Omega_z^\infty + \varepsilon_{ZRO}, \quad (3.17)$$

where

$$H_{gyro}(0) = \frac{k_{ux}A_{y,m}}{k_{SF}} \Re \left(T_{d_{Cor,x} \rightarrow \widehat{u}_{Cor,y}}(j\omega_{exc}) \right) + \frac{A_{x,m}}{A_{x,m}^{ref}} \Re \left(T_{d_{Cor,y} \rightarrow \widehat{u}_{Cor,y}}(j\omega_{exc}) \right), \quad (3.18)$$

where $\Re(\cdot)$ denotes the real part of (\cdot) . In this case, the scale factor error ε_{SF} is defined as

$$\varepsilon_{SF} = \frac{k_{SF}}{\widehat{k}_{SF}} \cdot H_{gyro}(0) - 1. \quad (3.19)$$

It is important to note that the expression of H_{gyro} depends on the closed-loop transfer functions $T_{d_{Cor,x} \rightarrow \widehat{u}_{Cor,y}}$ and $T_{d_{Cor,y} \rightarrow \widehat{u}_{Cor,y}}$, and on the tracking error upper bounds $\check{\varepsilon}_x$ and $\check{\varepsilon}_y$. Indeed, we recall that $A_{y,m} \in [0, \check{\varepsilon}_y A_{x,m}^{ref}]$ and $A_{x,m} \in [(1 - \check{\varepsilon}_x) A_{x,m}^{ref}, (1 + \check{\varepsilon}_x) A_{x,m}^{ref}]$.

In general, we want \widehat{k}_{SF} to be as close as possible to the real k_{SF} (ideally, $\widehat{k}_{SF} = k_{SF}$). Thus, the controller has to be designed such that $\check{\varepsilon}_x \ll 1$, $\check{\varepsilon}_y \ll 1$ and $T_{d_{Cor,y} \rightarrow \widehat{u}_{Cor,y}}(j\omega_{exc}) \approx 1$. These conditions correspond to the drive-mode reference tracking, sense-mode disturbance rejection and Coriolis force estimation objectives. In this context, (3.16) also shows that the

sensor bandwidth mainly depends on the bandwidth of $T_{d_{Cor,y} \rightarrow \hat{u}_{Cor,y}}$. In this case, the larger is the bandwidth of $T_{d_{Cor,y} \rightarrow \hat{u}_{Cor,y}}$ around $\omega = \omega_{exc}$, the larger is the bandwidth of H_{gyro} around $\omega = 0$.

It is worth mentioning that the measure is disturbed by ε_{ZRO} , given in (3.15). Although the contribution of $T_{x_m^{ref} \rightarrow \hat{u}_{Cor,y}}(j\omega_{exc})$ can be compensated by \hat{k}_{ZRO} , in practice, this compensation is not perfect and a residual appears. However, if the controller ensures $T_{x_m^{ref} \rightarrow \hat{u}_{Cor,y}}(j\omega_{exc}) \approx 0$, this residual tends to be smaller, producing a more accurate measure.

3.2.2 Analysis with Respect to the Noise

Here, in contrast to the previous section, we consider only the contributions of the stochastic signals e_x and e_y on the output signals of interest. The other input signals are set to zero. This point is justified by the fact that the noise effects on the gyroscope output are usually evaluated with the device at rest, *i.e.*, $\Omega_z(t) \equiv 0$. Under this condition, the only contributors for the noise on $\hat{u}_{Cor,y}$ are the signals e_x and e_y .

Recall that e_x and e_y are assumed to be uncorrelated white-noise signals with PSD equal to 1 (see Assumption 3.3). Hence, we can write the PSD of $\hat{u}_{Cor,y}$ as

$$\mathcal{S}_{\hat{u}_{Cor,y}}(\omega) = \left| T_{e_x \rightarrow \hat{u}_{Cor,y}}(j\omega) \right|^2 + \left| T_{e_y \rightarrow \hat{u}_{Cor,y}}(j\omega) \right|^2. \quad (3.20)$$

If the controller is such that the specification (S4) (page 61) is verified, the estimate $\hat{u}_{Cor,y}$ is a band-pass signal centered at ω_{exc} and of bandwidth smaller than $2\omega_{exc}$. Hence, after the synchronous demodulation and the compensation function f_{comp} , the PSD of $\hat{\Omega}_z$ reads as

$$\mathcal{S}_{\hat{\Omega}_z}(\omega) = \begin{cases} \frac{\mathcal{S}_{\hat{u}_{Cor,y}}(\omega + \omega_{exc}) + \mathcal{S}_{\hat{u}_{Cor,y}}(\omega - \omega_{exc})}{\hat{k}_{SF}^2}, & \forall |\omega| < \omega_{exc} \\ 0, & \text{otherwise.} \end{cases} \quad (3.21)$$

The calculation details are presented in Appendix B.2.

This result shows that the PSD of the noise that is present on the final measure depends on the closed-loop transfer functions $T_{e_x \rightarrow \hat{u}_{Cor,y}}$ and $T_{e_y \rightarrow \hat{u}_{Cor,y}}$, which depend on the process noise models and also on the controller. Thus, if possible, the controller shall be designed to shape these transfers, optimizing the noise sensitivity of the sensor, at least in the frequency range of interest.

We recall that for the synchronous demodulation to work properly, its input signal ($\hat{u}_{Cor,y}$) must be a band-pass signal (condition (C2) and specification (S4)). Then, in addition to the previous requirements, the controller also has to ensure this condition, eliminating (or attenuating) the components of frequency higher than $2\omega_{exc}$ and at $\omega = 0$. If, for any reason, the controller is not able to filter out these frequency components, a band-pass filter can be introduced between the controller and the synchronous demodulation (outside the closed-loop). This filter, however, may introduce a phase error on the synchronous demodulation (see discussion in Section 2.1.5, specially in page 29).

3.3 Closed-loop Specifications for Nominal Performance

In light of the results of the previous section, we can finally establish the links between the global performance specifications and the closed-loop ones. The specifications discussed in

this section are only related to the (nominal) performance of the gyroscope – specifications (S1)–(S4) and (i)–(iii) of Problem 3.1. Those related to the robustness (robust stability) of the system – specification (S5) – are discussed in the next section.

3.3.1 Closed-Loop Specifications for Conventional Closed-loop Operation

To ensure the conventional closed-loop operation, the controller has to fulfill the specifications (S1)–(S4). Globally, these specifications are expressed as the “size” of the estimation or tracking errors for the input signals x_m^{ref} of (3.5), $d_{Cor,x}$ of (3.9) and $d_{Cor,y}$ of (3.10). Then, we compute ε_x , ε_y and ε_{est} as function of the input signals in the frequency domain, as follows.

$$\begin{bmatrix} \varepsilon_x(j\omega) \\ \varepsilon_y(j\omega) \\ \varepsilon_{est}(j\omega) \end{bmatrix} = \begin{bmatrix} T_{x_m^{ref} \rightarrow \varepsilon_x}(j\omega) & T_{d_{Cor,x} \rightarrow \varepsilon_x}(j\omega) & T_{d_{Cor,y} \rightarrow \varepsilon_x}(j\omega) \\ T_{x_m^{ref} \rightarrow \varepsilon_y}(j\omega) & T_{d_{Cor,x} \rightarrow \varepsilon_y}(j\omega) & T_{d_{Cor,y} \rightarrow \varepsilon_y}(j\omega) \\ T_{x_m^{ref} \rightarrow \varepsilon_{est}}(j\omega) & T_{d_{Cor,x} \rightarrow \varepsilon_{est}}(j\omega) & T_{d_{Cor,y} \rightarrow \varepsilon_{est}}(j\omega) \end{bmatrix} \begin{bmatrix} x_m^{ref}(j\omega) \\ d_{Cor,x}(j\omega) \\ d_{Cor,y}(j\omega) \end{bmatrix}, \quad (3.22)$$

where

$$\begin{bmatrix} T_{x_m^{ref} \rightarrow \varepsilon_x} & T_{d_{Cor,x} \rightarrow \varepsilon_x} & T_{d_{Cor,y} \rightarrow \varepsilon_x} \\ T_{x_m^{ref} \rightarrow \varepsilon_y} & T_{d_{Cor,x} \rightarrow \varepsilon_y} & T_{d_{Cor,y} \rightarrow \varepsilon_y} \\ T_{x_m^{ref} \rightarrow \varepsilon_{est}} & T_{d_{Cor,x} \rightarrow \varepsilon_{est}} & T_{d_{Cor,y} \rightarrow \varepsilon_{est}} \end{bmatrix} = \begin{bmatrix} 1 - T_{x_m^{ref} \rightarrow x_m} & -T_{d_{Cor,x} \rightarrow x_m} & -T_{d_{Cor,y} \rightarrow x_m} \\ -T_{x_m^{ref} \rightarrow y_m} & -T_{d_{Cor,x} \rightarrow y_m} & -T_{d_{Cor,y} \rightarrow y_m} \\ -T_{x_m^{ref} \rightarrow \hat{u}_{Cor,y}} & -T_{d_{Cor,x} \rightarrow \hat{u}_{Cor,y}} & 1 - T_{d_{Cor,y} \rightarrow \hat{u}_{Cor,y}} \end{bmatrix}. \quad (3.23)$$

Drive-Mode Reference Tracking (S1)

In Section 3.2.1, we show that for the drive mode to operate properly, we have to ensure an accurate sinusoidal reference tracking of the drive mode, *i.e.*, $\check{\varepsilon}_x \ll 1$.

From (3.22), the tracking error signal ε_x is given by

$$\varepsilon_x(j\omega) = T_{x_m^{ref} \rightarrow \varepsilon_x}(j\omega)x_m^{ref}(j\omega) + T_{d_{Cor,x} \rightarrow \varepsilon_x}(j\omega)d_{Cor,x}(j\omega) + T_{d_{Cor,y} \rightarrow \varepsilon_x}(j\omega)d_{Cor,y}(j\omega). \quad (3.24)$$

In general, at $\omega = \omega_{exc}$, the most important contribution comes from the product $T_{x_m^{ref} \rightarrow \varepsilon_x} x_m^{ref}$. Then, we can consider

$$\left| T_{x_m^{ref} \rightarrow \varepsilon_x}(j\omega_{exc}) \right| < \check{\varepsilon}_x, \quad (3.25)$$

$$\left| T_{d_{Cor,x} \rightarrow \varepsilon_x}(j\omega_{exc}) \right| \approx 0, \quad (3.26)$$

$$\left| T_{d_{Cor,y} \rightarrow \varepsilon_x}(j\omega_{exc}) \right| \approx 0. \quad (3.27)$$

If there exists a controller that ensures the above conditions, it ensures a sinusoidal reference tracking with error bounded by $\check{\varepsilon}_x A_{x,m}^{ref}$ and three closed-loop specifications are therefore defined for specification (S1).

It is worth emphasizing that these specifications define constraints on the transfer functions only at $\omega = \omega_{exc}$, what is enough to ensure a good performance in steady state and with a constant angular rate, since all the input signals are sinusoidal with the same frequency. Now, if we want to extend this result to the case where Ω_z is time-varying, the disturbance signals $d_{Cor,x}$ and $d_{Cor,y}$ have a non-null PSD for $|\omega| \in [\omega_{exc} - \omega_\Omega, \omega_{exc} + \omega_\Omega]$. Then, rather

than considering (3.26) and (3.27), we consider

$$\forall |\omega| \in [\omega_{exc} - \omega_{\Omega}, \omega_{exc} + \omega_{\Omega}], \quad |T_{d_{Cor,x} \rightarrow \varepsilon_x}(j\omega)| \approx 0, \quad (3.28)$$

$$\forall |\omega| \in [\omega_{exc} - \omega_{\Omega}, \omega_{exc} + \omega_{\Omega}], \quad |T_{d_{Cor,y} \rightarrow \varepsilon_x}(j\omega)| \approx 0. \quad (3.29)$$

Estimation of $d_{Cor,y}$ (S2)

One of the requirements for the MEMS gyroscope to operate properly in closed-loop is that the controller is able to produce an accurate estimate of $d_{Cor,y}$, *i.e.*, $\hat{u}_{Cor,y} \approx d_{Cor,y}$ or, equivalently, $\check{\varepsilon}_{est} \ll 1$.

From (3.22), the estimation error signal ε_{est} is given by

$$\varepsilon_{est}(j\omega) = T_{x_m^{ref} \rightarrow \varepsilon_{est}}(j\omega)x_m^{ref}(j\omega) + T_{d_{Cor,x} \rightarrow \varepsilon_{est}}(j\omega)d_{Cor,x}(j\omega) + T_{d_{Cor,y} \rightarrow \varepsilon_{est}}(j\omega)d_{Cor,y}(j\omega). \quad (3.30)$$

In general, at $\omega = \omega_{exc}$, the most important contributions for ε_{est} come from the terms $T_{x_m^{ref} \rightarrow \varepsilon_{est}}x_m^{ref}$ and $T_{d_{Cor,y} \rightarrow \varepsilon_{est}}d_{Cor,y}$. Then, we consider

$$\left| T_{x_m^{ref} \rightarrow \varepsilon_{est}}(j\omega_{exc}) \right| < \lambda_{est} \cdot \check{\varepsilon}_{est}, \quad (3.31)$$

$$\left| T_{d_{Cor,x} \rightarrow \varepsilon_{est}}(j\omega_{exc}) \right| \approx 0, \quad (3.32)$$

$$\left| T_{d_{Cor,y} \rightarrow \varepsilon_{est}}(j\omega_{exc}) \right| < \frac{(1 - \lambda_{est})\check{\varepsilon}_{est}A_{x,m}^{ref}}{|k_{SF}\Omega_z|} \quad (3.33)$$

with $\lambda_{est} \in [0, 1]$.

Thus, if there is a controller ensuring the above conditions, we achieve the specification (S2), defining three closed-loop specifications in steady state and with a constant angular rate.

Now, if we want to extend this result to the case where Ω_z is time-varying, rather than considering (3.32) and (3.33), we consider

$$\forall |\omega| \in [\omega_{exc} - \omega_{\Omega}, \omega_{exc} + \omega_{\Omega}], \quad |T_{d_{Cor,x} \rightarrow \varepsilon_{est}}(j\omega)| \approx 0, \quad (3.34)$$

$$\forall |\omega| \in [\omega_{exc} - \omega_{\Omega}, \omega_{exc} + \omega_{\Omega}], \quad \left| T_{d_{Cor,y} \rightarrow \varepsilon_{est}}(j\omega) \right| < \frac{(1 - \lambda_{est})\check{\varepsilon}_{est}A_{x,m}^{ref}}{|k_{SF}\Omega_z|}. \quad (3.35)$$

Sense-Mode Disturbance Rejection (S3)

As discussed in Section 3.1.1, to enhance the reference tracking on the drive mode and to reduce the effects of nonlinearities of the real gyroscope (see Remark 3.1), we have to ensure a good disturbance rejection on the sense mode, *i.e.*, $\check{\varepsilon}_y \ll 1$.

From (3.22), the error signal ε_y is given by

$$\varepsilon_y(j\omega) = T_{x_m^{ref} \rightarrow \varepsilon_y}(j\omega)x_m^{ref}(j\omega) + T_{d_{Cor,x} \rightarrow \varepsilon_y}(j\omega)d_{Cor,x}(j\omega) + T_{d_{Cor,y} \rightarrow \varepsilon_y}(j\omega)d_{Cor,y}(j\omega). \quad (3.36)$$

In general, at $\omega = \omega_{exc}$, the most important contributions for ε_y come from the products $T_{x_m^{ref} \rightarrow \varepsilon_y} \cdot x_m^{ref}$ and $T_{d_{Cor,y} \rightarrow \varepsilon_y} \cdot d_{Cor,y}$. Then, we consider

$$\left| T_{x_m^{ref} \rightarrow \varepsilon_y}(j\omega_{exc}) \right| < \lambda_y \cdot \check{\varepsilon}_y, \quad (3.37)$$

$$\left| T_{d_{Cor,x} \rightarrow \varepsilon_y}(j\omega_{exc}) \right| \approx 0, \quad (3.38)$$

$$\left| T_{d_{Cor,y} \rightarrow \varepsilon_y}(j\omega_{exc}) \right| < \frac{(1 - \lambda_y) \check{\varepsilon}_y A_{x,m}^{ref}}{|k_{SF} \Omega_z|} \quad (3.39)$$

with $\lambda_y \in [0, 1]$.

If there exists a controller that ensures the above conditions, then the sinusoidal disturbance rejection has error bounded by $\check{\varepsilon}_y A_{x,m}^{ref}$ and the specification (S3) is achieved, establishing three more closed-loop specifications.

Similar to the reference tracking case, these specifications are defined for $\omega = \omega_{exc}$, what is enough to ensure a good performance with a constant Ω_z . If we want to extend this result to the case where the angular rate is time-varying, instead of considering (3.38) and (3.39), we consider

$$\forall |\omega| \in [\omega_{exc} - \omega_\Omega, \omega_{exc} + \omega_\Omega], \quad \left| T_{d_{Cor,x} \rightarrow \varepsilon_y}(j\omega_{exc}) \right| \approx 0, \quad (3.40)$$

$$\forall |\omega| \in [\omega_{exc} - \omega_\Omega, \omega_{exc} + \omega_\Omega], \quad \left| T_{d_{Cor,y} \rightarrow \varepsilon_y}(j\omega_{exc}) \right| < \frac{(1 - \lambda_y) \check{\varepsilon}_y A_{x,m}^{ref}}{|k_{SF} \Omega_z|}. \quad (3.41)$$

Band-pass condition of $\hat{u}_{Cor,y}$ (S4)

For the synchronous demodulation to operate properly, its input signal, $\hat{u}_{Cor,y}$, has to be a band-pass signal centered at ω_{exc} and with bandwidth smaller than $2\omega_{exc}$, *i.e.*, it satisfies (3.1). Since the input signals x_m^{ref} , $d_{Cor,x}$ and $d_{Cor,y}$ are also band-pass signals with the required characteristic and the closed-loop system is LTI, only the noise signals e_x and e_y can produce frequency terms outside the allowed frequency range. Then, in this case, we evaluate the contributions of these signals on the DSP of $\hat{u}_{Cor,y}$, $\mathcal{S}_{\hat{u}_{Cor,y}}$.

From (3.20), $\mathcal{S}_{\hat{u}_{Cor,y}}$ is given by

$$\mathcal{S}_{\hat{u}_{Cor,y}}(\omega) = \left| T_{e_x \rightarrow \hat{u}_{Cor,y}}(j\omega) \right|^2 + \left| T_{e_y \rightarrow \hat{u}_{Cor,y}}(j\omega) \right|^2. \quad (3.42)$$

Thus, if there is a controller ensuring

$$\forall |\omega| \geq 2\omega_{exc}, \quad \left| T_{e_x \rightarrow \hat{u}_{Cor,y}}(j\omega) \right| = 0 \quad \text{and} \quad \left| T_{e_x \rightarrow \hat{u}_{Cor,y}}(0) \right| = 0 \quad (3.43)$$

and

$$\forall |\omega| \geq 2\omega_{exc}, \quad \left| T_{e_y \rightarrow \hat{u}_{Cor,y}}(j\omega) \right| = 0 \quad \text{and} \quad \left| T_{e_y \rightarrow \hat{u}_{Cor,y}}(0) \right| = 0, \quad (3.44)$$

the specification (S4) is fulfilled, defining two additional closed-loop specifications.

3.3.2 Closed-Loop Specifications for SFNL

The nominal scale factor of a MEMS gyroscope can be given by k_{SF} (see (3.3)). However, systematic errors may appear, degrading the accuracy of the sensor. The scale factor non-linearity (SFNL) indicates how far from Ω_z the estimate $\hat{\Omega}_z$ can be, giving a measure of the sensor accuracy. This indicator is evaluated for a given operating condition and for $\Omega_z \in [-\Omega_z^{FS}, \Omega_z^{FS}]$, where Ω_z^{FS} is the full scale or dynamic range of the sensor. The definition of the SFNL is given in (3.11).

The analytic computation of the SFNL can be very complicated or even impossible, since the modeling of all the contributing phenomena may be complex. Its exact modeling is beyond the scope of this thesis. Nevertheless, we discuss here how to analyze this performance indicator in a simplified LTI framework.

First, we recall the definition of the estimation error ε_{est} :

$$\varepsilon_{est} \triangleq d_{Cor,y} - \hat{u}_{Cor,y}, \quad (3.45)$$

which can be computed, in the frequency domain, as

$$\varepsilon_{est}(j\omega) = \begin{bmatrix} T_{x_m^{ref} \rightarrow \varepsilon_{est}}(j\omega) & T_{d_{Cor,x} \rightarrow \varepsilon_{est}}(j\omega) & T_{d_{Cor,y} \rightarrow \varepsilon_{est}}(j\omega) \end{bmatrix} \begin{bmatrix} x_m^{ref}(j\omega) \\ d_{Cor,x}(j\omega) \\ d_{Cor,y}(j\omega) \end{bmatrix} \quad (3.46)$$

$$\text{with } \begin{bmatrix} T_{x_m^{ref} \rightarrow \varepsilon_{est}} & T_{d_{Cor,x} \rightarrow \varepsilon_{est}} & T_{d_{Cor,y} \rightarrow \varepsilon_{est}} \end{bmatrix} = \begin{bmatrix} -T_{x_m^{ref} \rightarrow \hat{u}_{Cor,y}} & -T_{d_{Cor,x} \rightarrow \hat{u}_{Cor,y}} & 1 - T_{d_{Cor,y} \rightarrow \hat{u}_{Cor,y}} \end{bmatrix}.$$

Then, we rewrite the definition of the SFNL (see (3.11)), replacing $\hat{\Omega}_z$ by $k_{SF}H_{gyro}(0)\Omega_z/\hat{k}_{SF}$ (the bias is supposed to be constant and known, such that $\varepsilon_{ZRO} = 0$):

$$\text{SFNL} = \max_{\Omega_z \in [-\Omega_z^{FS}, \Omega_z^{FS}]} \left(\frac{|\Omega_z|}{\Omega_z^{FS}} \cdot \left| \frac{k_{SF}H_{gyro}(0) - \hat{k}_{SF}}{\hat{k}_{SF}} \right| \right). \quad (3.47)$$

Since the scale factor error ε_{SF} is defined as $\frac{k_{SF}H_{gyro}(0) - \hat{k}_{SF}}{\hat{k}_{SF}}$ (see (3.19)) and $|\Omega_z|/\Omega_z^{FS} \leq 1$, we can compute an upper bound of the SFNL, as follows:

$$\text{SFNL} \leq \max_{\Omega_z \in [-\Omega_z^{FS}, \Omega_z^{FS}]} (|\varepsilon_{SF}|) = |\varepsilon_{SF}|. \quad (3.48)$$

Now, considering $\hat{k}_{SF} = k_{SF}$ and a proper operation of the MEMS gyroscope (*i.e.*, $\check{\varepsilon}_x \ll 1$, $\check{\varepsilon}_y \ll 1$ and $|T_{d_{Cor,y} \rightarrow \varepsilon_{est}}(j\omega_{exc})| \ll 1$), we can approximate the absolute value of the scale factor relative error, ε_{SF} , as

$$|\varepsilon_{SF}| \approx \left| \Re \left(T_{d_{Cor,y} \rightarrow \varepsilon_{est}}(j\omega_{exc}) \right) + 1 - \frac{A_{x,m}}{A_{x,m}^{ref}} \right| \quad (3.49)$$

and define the upper bound

$$|\varepsilon_{SF}| \leq \left| T_{d_{Cor,y} \rightarrow \varepsilon_{est}}(j\omega_{exc}) \right| + \check{\varepsilon}_x. \quad (3.50)$$

See the calculation details in Appendix B.1.5.

Note that, in (3.48), $|\varepsilon_{SF}|$ itself defines an upper bound on the SFNL. Therefore, by making

$$\left| T_{d_{Cor,y} \rightarrow \varepsilon_{est}}(j\omega_{exc}) \right| \leq k_{SFNL} - \check{\varepsilon}_x \quad (3.51)$$

with a constant $k_{SFNL} > 0$, we can determine how accurate the estimation of $d_{Cor,y}$ and the reference tracking have to be such that the MEMS gyroscope achieves a given SFNL. Indirectly, this constraint also imposes a condition on $\check{\varepsilon}_x$, which has to be smaller than k_{SFNL} . We can then respectively rewrite (3.25) and (3.51) as

$$\left| T_{x_m^{ref} \rightarrow \varepsilon_x}(j\omega_{exc}) \right| < \lambda_{SFNL} k_{SFNL} \quad (3.52)$$

$$\left| T_{d_{Cor,y} \rightarrow \varepsilon_{est}}(j\omega_{exc}) \right| \leq (1 - \lambda_{SFNL}) k_{SFNL}, \quad (3.53)$$

where $\lambda_{SFNL} \in [0, 1]$. Therefore, if there is a controller that verifies (3.52) and (3.53), the specification (i) of Problem 3.1 is satisfied.

We recall that in this analysis, we adopt an LTI framework and the nonlinearities of a real gyroscope are not considered. Thus, the results in practice may differ from this theoretical analysis. One of the ways to reduce the nonlinear effects is by reducing oscillations of the sense mode.

Without a complete nonlinear model, it is impossible to establish precise constraints to ensure a given SFNL. It is important to stress, however, that this analysis gives important insights on how the constraints can be modified to improve the SFNL, as follows.

- (i) The better is the reference tracking (*i.e.*, $\check{\varepsilon}_x \rightarrow 0$), the smaller is the SFNL upper bound. The tolerated tracking error $\check{\varepsilon}_x$ has to be at most of the same order of magnitude as k_{SFNL} .
- (ii) The better is the estimation of $d_{Cor,y}$ (*i.e.*, $\check{\varepsilon}_{est} \rightarrow 0$ or $\left| T_{d_{Cor,y} \rightarrow \varepsilon_{est}}(j\omega_{exc}) \right| \rightarrow 0$), the smaller is the SFNL upper bound. The magnitude of $T_{d_{Cor,y} \rightarrow \varepsilon_{est}}(j\omega_{exc})$ has to be at most of the same order of magnitude as the k_{SFNL} .
- (iii) The better is the sense-mode disturbance rejection (*i.e.*, $\check{\varepsilon}_y \rightarrow 0$), the smaller is the SFNL upper bound. Moreover, a good disturbance rejection also avoids nonlinear effects in a real gyroscope.

3.3.3 Closed-Loop Specifications for Bandwidth

The bandwidth ω_B of the sensor corresponds to the bandwidth of the transfer H_{gyro} (see (3.16)), which is defined as the frequency range in which the attenuation is smaller than 3 dB [IEE04]. This means that the bandwidth ω_B is such that,

$$\forall |\omega| < \omega_B, \quad \left| 1 - \frac{H_{gyro}(j\omega)}{H_{gyro}(0)} \right| < 1 - \frac{\sqrt{2}}{2}. \quad (3.54)$$

Similar to the SFNL, it can be very difficult to compute analytically the bandwidth of the whole MEMS gyroscope. The main difficulty here comes from the term on the left-hand side of (3.54). However, a good approximation of this term can be obtained when we have a good disturbance rejection ($\check{\varepsilon}_y \ll 1$) and an accurate estimation of $d_{Cor,y}$ (*i.e.*, $\left| T_{d_{Cor,y} \rightarrow \varepsilon_{est}}(j\omega_{exc}) \right| \ll$

1), as follows (see calculation details in Appendix B.1.6):

$$\left| 1 - \frac{H_{gyro}(j\omega)}{H_{gyro}(0)} \right| \approx \left| \frac{1}{2} \left(T_{d_{Cor,y} \rightarrow \varepsilon_{est}}(j\omega - j\omega_{exc}) + T_{d_{Cor,y} \rightarrow \varepsilon_{est}}(j\omega + j\omega_{exc}) \right) \right|.$$

Then, we can consider an upper bound on this term:

$$\left| 1 - \frac{H_{gyro}(j\omega)}{H_{gyro}(0)} \right| \leq \left| \frac{T_{d_{Cor,y} \rightarrow \varepsilon_{est}}(j\omega - j\omega_{exc})}{2} \right| + \left| \frac{T_{d_{Cor,y} \rightarrow \varepsilon_{est}}(j\omega + j\omega_{exc})}{2} \right|,$$

such that, given $\omega_B^{\text{des}} \in \mathbb{R}_+$, if

$$\forall |\omega| < \omega_B^{\text{des}}, \quad \left| \frac{T_{d_{Cor,y} \rightarrow \varepsilon_{est}}(j\omega - j\omega_{exc})}{2} \right| + \left| \frac{T_{d_{Cor,y} \rightarrow \varepsilon_{est}}(j\omega + j\omega_{exc})}{2} \right| < 1 - \frac{\sqrt{2}}{2}, \quad (3.55)$$

the condition (3.54) holds with $\omega_B \geq \omega_B^{\text{des}}$. Finally, by considering equal contributions of the two terms of the left-hand side, (3.55) is implied by

$$\forall |\omega| \in [\omega_{exc} - \omega_B^{\text{des}}, \omega_{exc} + \omega_B^{\text{des}}], \quad \left| T_{d_{Cor,y} \rightarrow \varepsilon_{est}}(j\omega) \right| < \frac{2 - \sqrt{2}}{2} \approx 0.2929, \quad (3.56)$$

defining a bandwidth ω_B larger than a given ω_B^{des} . This inequality defines a frequency constraint on $T_{d_{Cor,y} \rightarrow \varepsilon_{est}}$. Therefore, if there is a controller that ensures a good disturbance rejection and (3.56), the specification (ii) of Problem 3.1 is fulfilled.

3.3.4 Closed-Loop Specifications Related to Noise

In general, the specification indicators related to the noise are evaluated through the Allan variance σ_A^2 (or Allan deviation σ_A) of $\hat{\Omega}_z$ for $\Omega_z(t) \equiv 0$. The interpretation of the Allan variance or Allan deviation plot is recalled in Section 2.1.6. From the piecewise representation of a typical Allan deviation, as the one presented in Figure 3.4a, some performance indicators are deduced. For the sake of clarity, we also present its equivalence with the PSD of $\hat{\Omega}_z$, presented in Figure 3.4b [IEE06]. The most important noise-related performance indicators are listed below.

- (i) Angle Random Walk (ARW) or rate white noise: corresponds to the value, at the averaging time $\tau_A = 1$, of the straight line fitting the section of the Allan deviation with gradient -0.5 . It gives the minimum level of noise in the PSD of $\hat{\Omega}_z$.
- (ii) Bias Instability (BI): corresponds to the flat region around the minimum value of the Allan deviation plot and measures how the bias changes over a given period of time τ_A . In general, these changes happen in the long-term (high τ_A). When looking to the PSD, it has the behavior of a flicker noise ($1/f$) and appears in the very-low frequency range.
- (iii) Rate Random Walk (RRW): is a long-term (even slower than BI) phenomenon of unknown origin [IEE06] and appears on the Allan deviation plot as a slope with gradient $+0.5$.
- (iv) Quantization noise (Q): is a short-term (or high-frequency) phenomenon that results from the limited resolution of the sensor. It appears in the Allan deviation plot as a slope of gradient -1 and is preponderant for small values of τ_A . On the other hand, the quantization noise effects appears on the PSD in the high-frequency range.

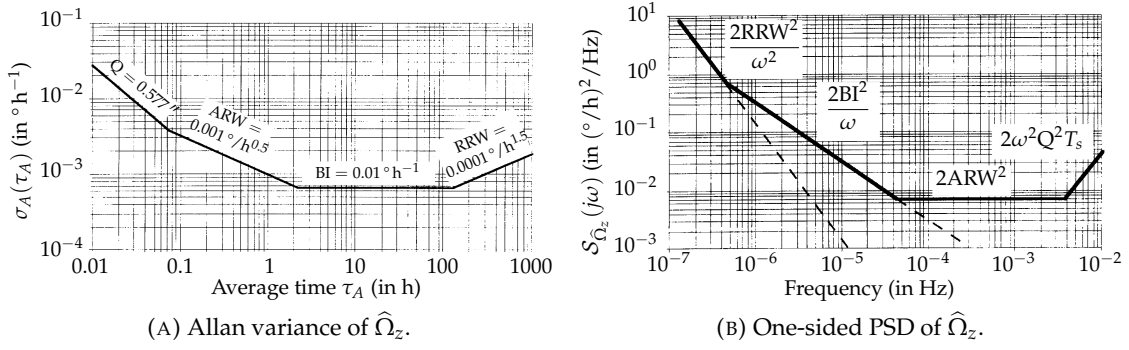


FIGURE 3.4: Piecewise representation (adapted from [IEE06]).

It is important to note that, among the above indicators, the controller plays an important role mainly for the ARW. Indeed, the quantization error depends on the choice of the sensor resolution and sampling period T_s and the BI and RRW are rather related to the residual bias error. Therefore, focusing on the controller design, we consider only the specification related to the ARW.

Note that, by bounding the PSD of $\hat{\Omega}_z$, an upper bound of the ARW can be obtained, that is, the inequality

$$\forall \omega \in \mathbb{R}, \quad \mathcal{S}_{\hat{\Omega}_z}(\omega) \leq k_{\text{ARW}}^2 \quad (3.57)$$

ensures $\text{ARW} \leq k_{\text{ARW}}$. This inequality (see (3.21)) is equivalent to

$$\forall |\omega| < \omega_{\text{exc}}, \quad \mathcal{S}_{\hat{u}_{\text{Cor},y}}(\omega + \omega_{\text{exc}}) + \mathcal{S}_{\hat{u}_{\text{Cor},y}}(\omega - \omega_{\text{exc}}) \leq (\hat{k}_{\text{SF}} \cdot k_{\text{ARW}})^2.$$

Then, if

$$\forall |\omega| \in (0, 2\omega_{\text{exc}}], \quad \mathcal{S}_{\hat{u}_{\text{Cor},y}}(\omega) \leq \frac{1}{2} (\hat{k}_{\text{SF}} \cdot k_{\text{ARW}})^2. \quad (3.58)$$

the inequality of (3.57) also holds. Finally, since $\mathcal{S}_{e_x}(\omega) = \mathcal{S}_{e_y}(\omega) = 1$ and through (3.20), (3.58) can be recast as frequency constraints on the transfers $T_{e_x \rightarrow \hat{u}_{\text{Cor},y}}$ and $T_{e_y \rightarrow \hat{u}_{\text{Cor},y}}$, as follows:

$$\forall |\omega| \in (0, 2\omega_{\text{exc}}], \quad |T_{e_x \rightarrow \hat{u}_{\text{Cor},y}}(j\omega)|^2 \leq \frac{\lambda_{\text{ARW}}}{2} (\hat{k}_{\text{SF}} \cdot k_{\text{ARW}})^2 \quad (3.59)$$

$$\forall |\omega| \in (0, 2\omega_{\text{exc}}], \quad |T_{e_y \rightarrow \hat{u}_{\text{Cor},y}}(j\omega)|^2 \leq \frac{(1 - \lambda_{\text{ARW}})}{2} (\hat{k}_{\text{SF}} \cdot k_{\text{ARW}})^2 \quad (3.60)$$

with $\lambda_{\text{ARW}} \in [0, 1]$.

Therefore, if there is a controller that ensures (3.59) and (3.60), the ARW of the sensor is bounded by k_{ARW} , and the specification (iii) of Problem 3.1 is fulfilled.

3.4 Closed-loop Specifications for Robust Stability

Further than the closed-loop specifications related to the performance, the controller must ensure the stability of the system, despite its inherent uncertainties. Here, we focus on dealing with unstructured or dynamic uncertainties, represented by ΔE .

Similar to the closed-loop specifications related to the performance, the specifications for robust stability are also expressed in terms of upper bounds on the frequency response magnitude of some transfer functions.

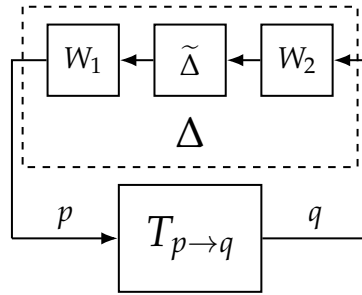


FIGURE 3.5: Interconnection for the weighted small gain theorem.

3.4.1 Weighted Small Gain Theorem

Here, we describe the weighted small gain theorem, which is a fundamental tool for evaluating the stability of a multivariable closed-loop system against unstructured or dynamic uncertainties. Further details on this important tool can be found in [ZDG96], for instance.

Let us first define an uncertainty set Δ :

$$\Delta = \left\{ \Delta(s) \mid \Delta(s) = W_1(s)\tilde{\Delta}(s)W_2(s) \text{ with } \|\tilde{\Delta}\|_{\infty} \leq 1 \right\}, \quad (3.61)$$

where W_1 and W_2 are stable transfer matrices. These matrices are used to determine the size of the unstructured uncertainties Δ . The weighted small gain theorem [ZDG96] claims therefore that, for a given stable transfer matrix $T_{p \rightarrow q}$, the system of Figure 3.5 is stable $\forall \Delta \in \Delta$ if and only if

$$\|W_2 T_{p \rightarrow q} W_1\|_{\infty} < 1. \quad (3.62)$$

3.4.2 Robust Stability Against Additive Uncertainties

Now, if we come back to the closed-loop system of Figure 3.2, we can note that the whole to-be-controlled system is $G + \Delta E$, which is naturally different from the nominal model G . In this context, the uncertain block ΔE represents thus an additive uncertainty. Here, we focus our analysis on this type of uncertainty. However, other types of uncertainties could be considered by following the same methodology.

Following the weighted small gain theorem, if we want the closed-loop system to be stable against additive uncertainties $\Delta E \in \Delta_{\text{add}}$, where, given stable transfer matrices $W_{\text{add},1}$ and $W_{\text{add},2}$,

$$\Delta_{\text{add}} = \left\{ \Delta E(s) \mid \Delta E(s) = W_{\text{add},1}(s)\tilde{\Delta}(s)W_{\text{add},2}(s) \text{ with } \|\tilde{\Delta}\|_{\infty} \leq 1 \right\}, \quad (3.63)$$

the transfer $T_{n \rightarrow u}$ must be such that

$$\|W_{\text{add},2} T_{n \rightarrow u} W_{\text{add},1}\|_{\infty} < 1. \quad (3.64)$$

Note that in the configuration of Figure 3.2, ΔE is in parallel with G (neglecting u_{Cor}), having the same input signals $u = \text{col}(u_x, u_y)$ and summing up with $\text{col}(x_m, y_m)$, at the same point as $n = \text{col}(n_x, n_y)$.

Therefore, if there is a controller that ensures (3.64), the closed-loop system is stable against uncertainties $\Delta E \in \Delta_{\text{add}}$, finally fulfilling the specification (S5).

Note that for (3.64) to hold, qualitatively, the $\bar{\sigma}(T_{n \rightarrow u}(j\omega))$ (reduces to $|T_{n \rightarrow u}(j\omega)|$ in the SISO case) has to be small in the frequency range where the uncertainties are important. Therefore, even if, *a priori*, we do not have constraints on the control signal(s), improving the robust stability against additive uncertainties implies the limitation of the noise effects on the control signal(s).

3.5 Summary of the Chapter

In this chapter, we first provide an analysis on the angular rate estimation of a MEMS gyroscope when it is operated by a nonideal controller. This analysis allows us to establish frequency constraints on the closed-loop transfer functions such that global performance specifications are achieved. Furthermore, by means of the small gain theorem, we can also determine frequency constraints on the closed-loop transfer functions that ensure the robust stability of the system against unstructured uncertainties.

In the next chapter, based on these frequency constraints, we design some controllers for the MEMS gyroscope. The most relevant frequency constraints are summarized in the sequel.

Global performance specifications (from Problem 3.1):

- (i) For $\text{SFNL} \leq k_{\text{SFNL}}$, see Section 3.3.2 (page 68), equations (3.52) and (3.53):

$$\left| T_{x_m^{ref} \rightarrow \varepsilon_x}(j\omega_{exc}) \right| < \lambda_{\text{SFNL}} k_{\text{SFNL}},$$

$$\left| T_{d_{Cor,y} \rightarrow \varepsilon_{est}}(j\omega_{exc}) \right| \leq (1 - \lambda_{\text{SFNL}}) k_{\text{SFNL}}.$$

Moreover, reducing $\check{\varepsilon}_y$ also improves the SFNL.

- (ii) For a bandwidth ω_B larger than ω_B^{des} , see Section 3.3.3 (page 69) and equation (3.56):

$$\forall |\omega| \in [\omega_{exc} - \omega_B^{\text{des}}, \omega_{exc} + \omega_B^{\text{des}}], \quad \left| T_{d_{Cor,y} \rightarrow \varepsilon_{est}}(j\omega) \right| < \frac{2 - \sqrt{2}}{2} \approx 0.2929.$$

- (iii) For $\text{ARW} < k_{\text{ARW}}$, see Section 3.3.4 (page 70) and equations (3.59) and (3.60):

$$\forall |\omega| \in (0, 2\omega_{exc}], \quad \left| T_{e_x \rightarrow \hat{u}_{Cor,y}}(j\omega) \right|^2 \leq \frac{\lambda_{\text{ARW}}}{2} (\hat{k}_{\text{SF}} \cdot k_{\text{ARW}})^2$$

$$\forall |\omega| \in (0, 2\omega_{exc}], \quad \left| T_{e_y \rightarrow \hat{u}_{Cor,y}}(j\omega) \right|^2 \leq \frac{(1 - \lambda_{\text{ARW}})}{2} (\hat{k}_{\text{SF}} \cdot k_{\text{ARW}})^2$$

Specifications for conventional closed-loop operation:

- (S1) **Drive-mode reference tracking:** the reference tracking of x_m^{ref} by x_m , see Section 3.3.1 (page 65), is mainly ensured by the constraints related to the SFNL. To improve the reference tracking, the equations (3.25), (3.28) and (3.29) can be considered.
- (S2) **Estimation of the Coriolis force:** similarly, the estimation of $d_{Cor,y}$ by $\hat{u}_{Cor,y}$, see Section 3.3.1 (page 66), is mainly ensured by the constraints related to the SFNL. To enhance the estimation, the equations (3.31), (3.34) and (3.35) can also be considered.
- (S3) **Sense-mode disturbance rejection:** the tracking of y_m^{ref} by y_m , see Section 3.3.1 (page 66), is not a crucial specification in the LTI framework. However, it can be very useful to keep

the real gyroscope operating in a linear region. To improve the disturbance rejection, the equations (3.37), (3.40) and (3.41) can be taken into account.

- (S4) **Band-pass condition of $\hat{u}_{Cor,y}$:** this condition, see Section 3.3.1 (page 67), is required to ensure that the synchronous demodulation works properly. The related constraints are given by equations (3.43) and (3.44):

$$\begin{aligned} \forall |\omega| \geq 2\omega_{exc}, \quad & \left| T_{e_x \rightarrow \hat{u}_{Cor,y}}(j\omega) \right| = 0 \quad \text{and} \quad \left| T_{e_x \rightarrow \hat{u}_{Cor,y}}(0) \right| = 0 \\ \forall |\omega| \geq 2\omega_{exc}, \quad & \left| T_{e_y \rightarrow \hat{u}_{Cor,y}}(j\omega) \right| = 0 \quad \text{and} \quad \left| T_{e_y \rightarrow \hat{u}_{Cor,y}}(0) \right| = 0, \end{aligned}$$

Closed-loop specifications for robust stability:

- (S5) For additive uncertainties ΔE defined by $W_{add,1}$ and $W_{add,2}$ according to (3.63), see Section 3.4 (page 71), equation (3.64):

$$\|W_{add,2}T_{n \rightarrow u}W_{add,1}\|_{\infty} < 1.$$

Chapter 4

Direct Control I: A Robust Approach

The main objective of this chapter is to propose a systematic method for designing a controller for the closed-loop operation of MEMS gyroscopes.

As discussed in Chapter 3, for the gyroscope to achieve the desired performance specification, the controller has to ensure that some key closed-loop transfer functions behave in a certain way. This behavior is given by the closed-loop specifications, which are naturally expressed as upper bounds on the frequency response magnitude of those key transfer functions.

In this context, the most suitable method for the controller design is the \mathcal{H}_∞ synthesis [SP01, SF09]. Indeed, the \mathcal{H}_∞ synthesis is a flexible and powerful design method that allows formulating the controller design problem as an optimization problem subject to mathematical constraints. These constraints express upper bounds on the magnitude of the frequency response of the closed-loop transfer functions, providing guarantees of stability and performance for the system.

Here, we consider the direct control architecture under different configurations. For the sake of pedagogy, we first consider the design of a SISO controller for the drive mode. Then, we design a SISO controller for the sense mode. In a first time, they are assumed to be uncoupled. In a second time, the mechanical coupling between these modes is also taken into consideration. Then, a multivariable (MIMO) approach is proposed.

For the SISO approach, two important assumptions are made: the mechanical coupling forces and the Coriolis forces are considered as exogenous input signals. When considering the MIMO approach, the mechanical coupling is properly taken into account for the controller design. However, the Coriolis force is still assumed to be exogenous. To validate the proposed solutions, numerical simulations are then performed.

In this chapter, we also consider that the to-be-controlled system is frozen, that is, the operating condition, represented by θ and ρ (see Section 2.1.5), is fixed. Therefore, the to-be-controlled system is LTI. For the sake of clarity, the superscripts θ and ρ are hence omitted along this chapter.

We start the chapter by presenting the principles of the \mathcal{H}_∞ synthesis in Section 4.1. Then, we apply this technique to design some controller(s) for MEMS gyroscopes under different configurations. Numerical examples are presented along the chapter and the most relevant solutions are validated through simulations.

4.1 \mathcal{H}_∞ Synthesis: Principles

In this section, we present the principles of the celebrated \mathcal{H}_∞ synthesis. The discussions drawn in this section are mainly based on the textbooks [ZDG96, SP01, SF09].

The beginning of the \mathcal{H}_∞ synthesis is often credited to the seminal paper [Zam81], in which G. Zames shows that, for LTI systems, the control design problem can be tackled as the optimization of a weighted \mathcal{H}_∞ -norm criterion. The main strength of the \mathcal{H}_∞ synthesis resides on the definition of the so-called \mathcal{H}_∞ criterion, which enforces upper bounds on the frequency response magnitude of the closed-loop system. In a certain extent, it allows shaping the closed-loop transfer functions. Therefore, in contrast to other modern control design methods (*e.g.*, LQG, \mathcal{H}_2), through the choice of an adequate \mathcal{H}_∞ criterion, the \mathcal{H}_∞ synthesis allows to ensure the robustness of the closed-loop system against some classes of uncertainties.

In the remaining of this section, we define the standard \mathcal{H}_∞ control problem, which is the core of the method. To solve this optimization problem, an adequate \mathcal{H}_∞ criterion has to be defined and an efficient optimization algorithm has to be used. These two key points are also presented in the sequel.

4.1.1 Standard \mathcal{H}_∞ Control Problem

Before introducing the \mathcal{H}_∞ control problem, let us first recall the definition of the \mathcal{H}_∞ norm.

Definition 4.1 (\mathcal{H}_∞ norm [SP01]). The \mathcal{H}_∞ norm of a proper stable system H is defined as

$$\|H\|_\infty = \sup_{\Re(s)>0} \bar{\sigma}(H(s)) = \sup_{\omega \in \mathbb{R}} \bar{\sigma}(H(j\omega)), \quad (4.1)$$

where the notation $\bar{\sigma}(H(s))$ indicates the largest singular value of $H(s)$.

The \mathcal{H}_∞ norm corresponds to the maximum gain of the system for all frequencies. For the particular case of SISO transfer functions, we have the property: $\bar{\sigma}(H(s)) = \underline{\sigma}(H(s)) = |H(s)|$ with $\underline{\sigma}(H(s))$ indicating the smallest singular value of $H(s)$. Thus, for a proper stable SISO system H , (4.1) can be rewritten as

$$\|H\|_\infty = \sup_{\Re(s)>0} \bar{\sigma}(H(s)) = \sup_{\omega \in \mathbb{R}} |H(j\omega)|. \quad (4.2)$$

Similar to modern control design methods (*e.g.*, LQG, \mathcal{H}_2), the general control configuration of Figure 4.1 is considered for the \mathcal{H}_∞ synthesis [SP01]. In this configuration, P is the so-called generalized or augmented plant, which admits the minimal state-space realization

$$P : \begin{cases} \dot{x}_P(t) &= A_P x_P(t) + B_w w(t) + B_u u_P(t) \\ z(t) &= C_z x_P(t) + D_{zw} w(t) + D_{zu} u_P(t) \\ y_P(t) &= C_y x_P(t) + D_{yw} w(t) + D_{yu} u_P(t) \end{cases} \quad (4.3)$$

with $x_P(t) \in \mathbb{R}^{n_P}$, $u_P(t) \in \mathbb{R}^{n_{u_P}}$, $y_P(t) \in \mathbb{R}^{n_{y_P}}$, $w(t) \in \mathbb{R}^{n_w}$, $z(t) \in \mathbb{R}^{n_z}$ and matrices of adequate dimensions. The vector w represents the exogenous inputs, z is the vector of controlled outputs, and u_P and y_P are respectively the control signals and measured outputs.

The controller K is given by

$$K : \begin{cases} \dot{x}_K(t) = A_K x_K(t) + B_K y_P(t) \\ u_P(t) = C_K x_K(t) + D_K y_P(t) \end{cases}, \quad (4.4)$$

where $x_K(t) \in \mathbb{R}^{n_K}$ with $n_K = n_P$ and the matrices have adequate dimensions. We can therefore state the standard \mathcal{H}_∞ control problem.

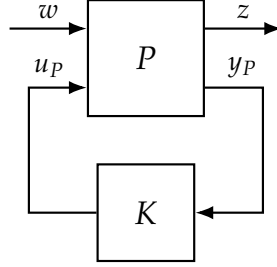


FIGURE 4.1: General control configuration.

Problem 4.1 (Standard \mathcal{H}_∞ control problem). *Given a plant P in the form of (4.3) and a performance level $\gamma > 0$, compute a controller K in the form of (4.4), if there exists any, such that the closed-loop system $P \star K$ is stable and*

$$\|P \star K\|_\infty < \gamma, \quad (4.5)$$

where $P \star K$ denotes the Redheffer product of P and K , that is, the closed-loop system defined by (4.3) and (4.4).

The equation (4.5) introduces the so-called \mathcal{H}_∞ criterion. It is important to emphasize that this criterion is defined through the choice of the augmented plant P , which is composed of the to-be-controlled system itself and weighting filters attributing different weights to the signals of interest, w and z .

The choice of the \mathcal{H}_∞ criterion is one of the crucial points of the \mathcal{H}_∞ synthesis. Indeed, the proper choice of the input and output signals and the design of the weighting functions can enforce the desired specifications and provide formal guarantees of robust stability and performance. Another crucial point is how to solve Problem 4.1, *i.e.*, how to compute a controller that ensures the stability of the closed-loop system and verifies (4.5). These two aspects are discussed in the sequel.

4.1.2 Defining an \mathcal{H}_∞ Criterion

As discussed earlier, the choice of the \mathcal{H}_∞ criterion, directly linked to the augmented plant P , is one of the most important steps of the \mathcal{H}_∞ synthesis. Indeed, properly defining the \mathcal{H}_∞ criterion allows to enforce constraints on the frequency response of the closed-loop transfer functions. This aspect is one of the biggest strengths of the \mathcal{H}_∞ synthesis. In this section, we present then how to properly define an \mathcal{H}_∞ criterion.

In general, weights are attributed to the different signals of interest through the so-called weighting filters (or weighting functions) W_{in} and W_{out} , as illustrated in Figure 4.2 [SP01]. These weighting filters are often diagonal, *i.e.*,

$$W_{\text{in}} = \text{diag}(W_{\text{in},1}, \dots, W_{\text{in},k}, \dots, W_{\text{in},n_w})$$

$$W_{\text{out}} = \text{diag}(W_{\text{out},1}, \dots, W_{\text{out},l}, \dots, W_{\text{in},n_z}),$$

and define $\tilde{w} = W_{\text{in}}w$ and $\tilde{z} = W_{\text{out}}^{-1}z$. In this case, the vector w represents the weighted or normalized exogenous inputs and \tilde{w} corresponds to the input signals of the system, such as the reference signal, disturbances and noises. Similarly, z represents the weighted or normalized controlled outputs and \tilde{z} consists of the controlled outputs, *e.g.*, the tracking and the estimation errors. It is worth mentioning that the signals of interest \tilde{w} and \tilde{z} do not have to be physical. They can, for instance, represent a non-measurable signal or a combination of signals.

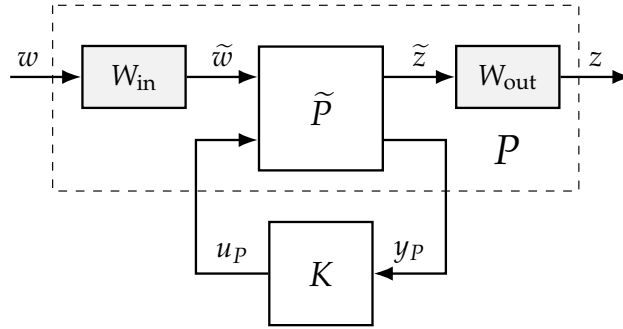


FIGURE 4.2: General control configuration with weighting filters.

Considering the weighting functions, the closed-loop system $T_{w \rightarrow z} = P \star K$ can be rewritten, in the Laplace domain, as

$$T_{w \rightarrow z}(s) = W_{\text{out}}(s)T_{\tilde{w} \rightarrow \tilde{z}}(s)W_{\text{in}}(s). \quad (4.6)$$

Then, if there exists a controller that ensures the stability of $T_{w \rightarrow z}$ and $\|T_{w \rightarrow z}\|_{\infty} < \gamma$, the stability of $T_{\tilde{w} \rightarrow \tilde{z}}$ and the condition

$$\|W_{\text{out}}T_{\tilde{w} \rightarrow \tilde{z}}W_{\text{in}}\|_{\infty} < \gamma \quad (4.7)$$

are also ensured. We highlight that the controller cannot stabilize the weighting functions in (4.6). Hence, the chosen weighting functions are required to be stable.

At this point, it is important to recall that the \mathcal{H}_{∞} norm of a matrix upper bounds the \mathcal{H}_{∞} norm of each of its elements [SP01]. Hence, (4.7) implies that

$$\forall l \in \{1, \dots, n_z\}, \forall k \in \{1, \dots, n_w\}, \quad \|W_{\text{out},l}T_{\tilde{w}_k \rightarrow \tilde{z}_l}W_{\text{in},k}\|_{\infty} < \gamma, \quad (4.8)$$

which is equivalent to

$$\forall l \in \{1, \dots, n_z\}, \forall k \in \{1, \dots, n_w\}, \forall \omega \in \mathbb{R}, \quad |T_{\tilde{w}_k \rightarrow \tilde{z}_l}(j\omega)| < \frac{\gamma}{|W_{\text{out},l}(j\omega)W_{\text{in},k}(j\omega)|}. \quad (4.9)$$

Furthermore, if $\gamma \leq 1$, (4.7) implies that the frequency response magnitude of each transfer $T_{\tilde{w}_k \rightarrow \tilde{z}_l}$ is upper bounded by the inverse of the product $W_{\text{out},l}W_{\text{in},k}$, see (4.9). The adequate choice of the weighting functions enforces therefore frequency constraints on $T_{\tilde{w}_k \rightarrow \tilde{z}_l}$ and expresses the desired closed-loop specifications.

Please note that these frequency constraints only act on the gain or magnitude of the frequency responses. The \mathcal{H}_{∞} criterion does not carry information on the phase of the frequency

responses. Furthermore, only upper bounds on the magnitude of the frequency response can be defined.

In this context, we always look for $\gamma \approx 1$. Indeed, if the terms $|W_{\text{out},l}W_{\text{in},k}|^{-1}$ define upper bounds on $|T_{\tilde{w}_k \rightarrow \tilde{z}_l}|$, having $\gamma < 1$ implies that all $|T_{\tilde{w}_k \rightarrow \tilde{z}_l}|$ are way below (by a factor γ) the given upper bounds and the desired closed-loop specifications are easily achieved by the controller. In this case, the designer can optimize the closed-loop specifications (for instance, constraining the control signal even further or enhancing the stability margins). On the other hand, if $\gamma > 1$, (4.7) does not imply that there is a transfer $T_{\tilde{w}_k \rightarrow \tilde{z}_l}$ that exceeds its upper bound. It rather indicates that one of the transfers **may** exceed its upper bound by a factor γ . Then, even with γ slightly larger than 1, the individual constraints may be satisfied¹. The individual transfers have then to be checked *a posteriori* by the designer. Finally, $\gamma \gg 1$ indicates that the enforced frequency constraints cannot be achieved. The \mathcal{H}_∞ criterion (or the closed-loop specifications) has to be reviewed in this case.

The choice of an \mathcal{H}_∞ criterion is nonunique. For instance, since the constraints on $|T_{\tilde{w}_k \rightarrow \tilde{z}_l}|$ are expressed through the product $W_{\text{out},l}W_{\text{in},k}$, to obtain the same product, different combinations of $W_{\text{out},l}$ and $W_{\text{in},k}$ can be considered. Moreover, note that $W_{\text{out},l}$ (resp. $W_{\text{in},k}$) appears on all the upper bounds of the transfers to the outputs \tilde{z}_l (resp. from the inputs \tilde{w}_k). Then, each weighting function acts not only on a given transfer function, but on all the transfers related to the given output (resp. input) signal.

Although very flexible, the choice of the \mathcal{H}_∞ criterion is nontrivial. Recall that, in general, all the closed-loop transfer function are interlinked. Then, when constraining one of them, we can be indirectly imposing some constraint on other transfers. We illustrate this point through the following example.

Example 4.1 (\mathcal{H}_∞ criterion and structural constraints). *Let us consider the control scheme of Figure 4.3, where the controller is represented by K and the to-be-controlled plant by G . The main objective here is to qualitatively define an \mathcal{H}_∞ criterion enforcing:*

- (i) reference tracking of low-frequency signals, i.e., for $|\omega| < \omega_b$, $T_{r \rightarrow y}(j\omega) \approx 1$;
- (ii) minimization of the control signal u .

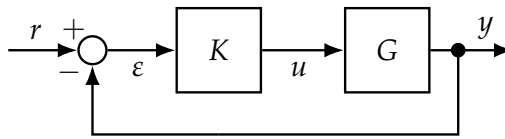


FIGURE 4.3: Control scheme for Example 4.1.

First, we have to define the signals of interest as well as the control signal and measured output. Clearly, the control signal is u and the measured output is ε ; then, under the general control configuration of the figures 4.1 and 4.2, $u_p = u$ and $y_p = \varepsilon$. In a first time, let us consider as signals of interest $\tilde{w} = r$ and $\tilde{z} = \text{col}(\varepsilon, u, y)$. Then, we compute the transfer $T_{\tilde{w} \rightarrow \tilde{z}}$:

$$T_{\tilde{w} \rightarrow \tilde{z}}(s) = \begin{bmatrix} T_{r \rightarrow \varepsilon}(s) \\ T_{r \rightarrow u}(s) \\ T_{r \rightarrow y}(s) \end{bmatrix} = \begin{bmatrix} S(s) \\ K(s)S(s) \\ T(s) \end{bmatrix}, \quad (4.10)$$

¹To illustrate this statement, let us consider $W_{\text{out}} = 1$, $W_{\text{in}} = I_2$ and $T_{\tilde{w} \rightarrow \tilde{z}} = [0.8 \quad j0.9]$. In this case, $\|W_{\text{out}}T_{\tilde{w} \rightarrow \tilde{z}}W_{\text{in}}\|_\infty = 1.2042 \implies \gamma > 1.2042$, $\|T_{\tilde{w}_1 \rightarrow \tilde{z}}\|_\infty = 0.8$ and $\|T_{\tilde{w}_2 \rightarrow \tilde{z}}\|_\infty = 0.9$. Note that even if $\gamma > 1$, the individual transfers $T_{\tilde{w}_1 \rightarrow \tilde{z}}$ and $T_{\tilde{w}_2 \rightarrow \tilde{z}}$ are still smaller than their upper bounds (equal to one).

where $S(s) = (1 + K(s)G(s))^{-1}$ and $T(s) = K(s)G(s)S(s) = 1 - S(s)$.

One of the objectives is to make $T(j\omega) \approx 1$ in a given frequency range (reference tracking). As discussed above, this constraint cannot be directly enforced through the \mathcal{H}_∞ criterion, since lower bounds cannot be directly imposed. Nevertheless, structurally, $T = 1 - S$. Then, enforcing $|S(j\omega)| \ll 1$ for $|\omega| < \omega_b$ implies that $T(j\omega) \approx 1$ in the same frequency range, as desired. The second objective is to minimize $T_{r \rightarrow u}$ wherever it is possible.

Let us now evaluate where and how these transfers can be minimized. Please note that the only way to have $|S(j\omega)| \ll 1$ is with $|K(j\omega)G(j\omega)| \gg 1$. However, $|K(j\omega)G(j\omega)| \gg 1$ implies that $|K(j\omega)S(j\omega)| \approx |G(j\omega)|^{-1}$. If $|K(j\omega)G(j\omega)| \ll 1$, we have that $S(j\omega) \approx 1$ and $|K(j\omega)S(j\omega)| \approx |K(j\omega)|$. This means that, in the frequency range in which the reference tracking is required ($|\omega| < \omega_b$), the control signal cannot be minimized. In contrast, for $|\omega| \geq \omega_b$, the control signal can be as small as the controller gain. In the sequel, we see how these structural constraints can be taken into account when defining the \mathcal{H}_∞ criterion.

Note that only the transfers $T_{r \rightarrow u} = KS$ and $T_{r \rightarrow \varepsilon} = S$ have to be upper bounded to achieve the control objectives. Therefore, to define the \mathcal{H}_∞ criterion, we recast the output signals of interest as $\tilde{z} = \text{col}(\varepsilon, u)$ and include the weighting functions W_r , W_ε and W_u , as presented in Figure 4.4.

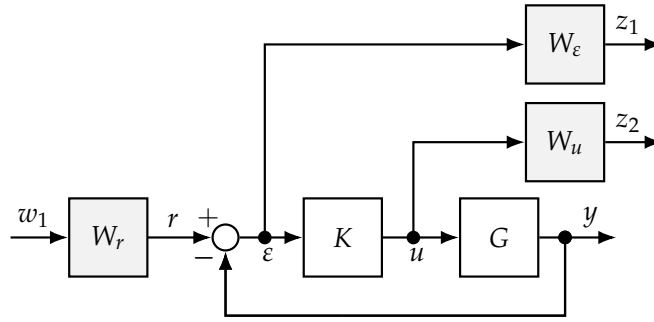


FIGURE 4.4: \mathcal{H}_∞ criterion for Example 4.1.

The \mathcal{H}_∞ control problem is thus to compute a controller K such that, for a given $\gamma > 0$,

$$\|T_{w \rightarrow z}\|_\infty = \left\| \begin{bmatrix} W_\varepsilon T_{r \rightarrow \varepsilon} W_r \\ W_u T_{r \rightarrow u} W_r \end{bmatrix} \right\|_\infty < \gamma. \quad (4.11)$$

If there is a solution for this problem with $\gamma \leq 1$, (4.11) implies that, $\forall \omega \in \mathbb{R}$,

$$|T_{r \rightarrow \varepsilon}(j\omega)| < \frac{1}{|W_\varepsilon(j\omega)W_r(j\omega)|} \quad \text{and} \quad |T_{r \rightarrow u}(j\omega)| < \frac{1}{|W_u(j\omega)W_r(j\omega)|}.$$

Therefore, $|W_\varepsilon(j\omega)W_r(j\omega)|$ must be as large as possible for $|\omega| < \omega_b$. Similarly, $|W_u(j\omega)W_r(j\omega)|$ should be as large as possible across all the frequency range. However, because of the structural constraint presented above, $|W_u(j\omega)W_r(j\omega)|$ can be large only for $|\omega| > \omega_b$. For $|\omega| < \omega_b$, $|W_u(j\omega)W_r(j\omega)|$ has to be smaller than $|G(j\omega)|$.

Finally, each weighting function has to be defined, recalling that this choice is nonunique. In this case, a possible choice would be $W_r(j\omega) \equiv 1$, and W_ε with high gain for $|\omega| < \omega_b$ (similar to a low-pass filter) and W_u with high gain for $|\omega| > \omega_b$ (similar to a high-pass filter).

Finally, it is important to highlight that the order of the controller is equal to the order of the to-be-controlled system added by the order of all the weighting functions. If the resulting

controller has a high order, model reduction can be performed [SP01, SF09]. The issue is that the stability and performance guarantees can be lost. Then, an *a posteriori* analysis is required to check for those properties. So, to avoid unnecessary model order reduction, the weighting functions should be as simple (low order) as possible.

4.1.3 Solving the Standard \mathcal{H}_∞ Control Problem

In general, the solution for the \mathcal{H}_∞ control problem can be obtained through two different approaches: (i) one based on the solution of algebraic Riccati equations (ARE) [DGKF89], and (ii) another one, based on linear matrix inequalities (LMIs) [GA94, IS94]. The \mathcal{H}_∞ control problem has an analytical solution that can be computed through two coupled ARE. This is the simplest and most reliable approach from the numerical computation point of view. Nevertheless, the augmented plant has to present some specific properties, which are not so restrictive, but limit the applicability of this approach [DGKF89, GA94]. On the other hand, LMI-based approaches are based on the optimization of a convex problem with constraints, being numerically more complex than ARE-based ones. However, no particular properties are required for the augmented plant and efficient convex optimization algorithms are widely available. Therefore, LMI-based approaches provide a general framework for the solution of Problem 4.1. For this reason, in this thesis, we privilege the LMI-based approaches.

The LMI-based approaches compute the \mathcal{H}_∞ controller in two steps. First, the existence of a solution for the problem is assessed. Then, if there exists a solution, a controller K that stabilizes $P \star K$ and ensures $\|P \star K\|_\infty < \gamma$ is computed.

In practice, the *Robust Control Toolbox* of Matlab[®] [BCPS20] can be employed to solve Problem 4.1 through the function `hinfsyn`.

We recall that in our application, the to-be-controlled plant (the drive and sense modes of a MEMS gyroscope) is a resonant systems with very-high quality factor. Then, to reduce numerical problems, the control synthesis is based on the frequency-normalized model of the to-be-controlled plant, where ω_{exc} is taken as the normalization frequency. In this normalized-frequency space, the operating frequency is then equal to the unity. Further details on the frequency normalization will be given in Chapter 7.

4.1.4 \mathcal{H}_∞ Synthesis: Summary

Having presented the \mathcal{H}_∞ synthesis, we can now summarize the method in some steps.

- (i) Given a control scheme and a to-be-controlled plant, define the signals of interest \tilde{w} and \tilde{z} as well as the controller input and output vectors (respectively y_P and u_P in the general control configuration).
- (ii) Compute, analytically, the closed-loop transfer functions, *i.e.*, $T_{\tilde{w} \rightarrow \tilde{z}}$, and check for equivalent transfers and structural constraints.
- (iii) Express the closed-loop specifications as upper bounds on the frequency response magnitude of the transfer functions of interest.
- (iv) Define the \mathcal{H}_∞ criterion, according to the specifications and structural constraints.
- (v) Solve the standard \mathcal{H}_∞ problem.
- (vi) Check the solution. If it is OK, continue; otherwise, go back to steps (i), (iii) or (iv).
- (vii) Implement the solution.

The steps (i)–(iv) are illustrated in Example 4.1 and the solution for the standard \mathcal{H}_∞ problem, step (v), is discussed in Section 4.1.3. When talking about checking the solution in step (vi), we mean that the closed-loop specifications are OK either with $\gamma < 1$ or with $\gamma \approx 1$ and an *a posteriori* analysis of the individual transfers is needed. A deeper analysis can be performed in this step, see [AC21] for further details on the performance validation for MEMS gyroscopes. Obviously, in step (vi), numerical simulations can also be considered.

4.2 SISO Control Architectures

In this section, we apply the \mathcal{H}_∞ synthesis to design a controller for the closed-loop operation of MEMS gyroscopes. For the controller design, we assume that there is no mechanical coupling between the drive and sense modes. Therefore, the two control loops are independent. We consider the direct control approach for the drive and sense modes. Thanks to the flexibility of the \mathcal{H}_∞ synthesis, the procedure adopted in this section is extended to a multivariable (MIMO) approach in Section 4.3.

We recall that the main objective of the drive-mode control is to ensure that the MEMS gyroscope proof mass oscillates along the \vec{x} -axis, describing a sinusoidal trajectory imposed by the reference signal x_m^{ref} (sinusoidal reference tracking). When the device is submitted to an angular rate Ω_z , a Coriolis force, whose amplitude is proportional to Ω_z , appears on the sense mode. Then, the main objective of the sense-mode control is to provide an accurate estimate of the Coriolis force (estimation of a sinusoidal signal), which is afterwards demodulated to obtain an estimate of $\hat{\Omega}_z$ (see Section 2.1).

For the drive mode, we consider two control configurations: with 1 degree of freedom (1DoF) and with 2 degrees of freedom (2DoF). We will see that the 1DoF control configuration presents some structural constraints linking the reference tracking and the noise rejection properties of the closed-loop system. One of the main interests on using a 2DoF control configuration is that this structural constraint can be avoided. For the sense mode, where the reference signal to be tracked is null, we consider only the 1DoF control architecture.

4.2.1 Drive-Mode Control

Besides the reference tracking objective, the drive-mode controller has to fulfill secondary control objectives so that the whole gyroscope achieves the desired global performance level. In the SISO approach, the drive-mode controller must be such that the following performance- and the robustness-related constraints are verified.

Drive-mode nominal performance constraints:

- (i) **SFNL and reference tracking:** for the SFNL (see (3.52), page 69), which implies the reference tracking, we consider

$$\left| T_{x_m^{ref} \rightarrow \varepsilon_x}(j\omega_{exc}) \right| \leq \lambda_{\text{SFNL}} k_{\text{SFNL}}. \quad (4.12)$$

- (ii) **Disturbance rejection:** in the SISO approach, to improve the reference tracking, we also reject the disturbance signal $d_{Cor,x}$. Then, from (3.28) (page 66), we consider,

$$\forall |\omega| \in (\omega_{exc} - \omega_\Omega, \omega_{exc} + \omega_\Omega), \quad \left| T_{d_{Cor,x} \rightarrow \varepsilon_x}(j\omega) \right| \leq k_{x1}, \quad (4.13)$$

where $k_{x1} \in \mathbb{R}_+$ is to be minimized.

Drive-mode robust stability constraint:

- (i) **Unmodeled dynamics:** to enforce the robustness against additive uncertainties $\Delta E_{xx} \in \mathbf{\Delta}_{\text{add}}$, which is defined by $W_{\text{add},1}$ and $W_{\text{add},2} = 1$ (see (3.63), page 72), we shall minimize at best $|T_{n_x \rightarrow u_x}(j\omega)|$, mainly in the frequency range where $|W_{\text{add},1}|$ is important. Indeed, the weighted small gain theorem ensures stability against this kind of uncertainty if

$$\forall \omega \in \mathbb{R}, \quad |T_{n_x \rightarrow u_x}(j\omega)| < \frac{1}{|W_{\text{add},1}(j\omega)|}. \quad (4.14)$$

In general, $|W_{\text{add},1}|$ is considered to be high in low and high frequencies, and small around $\omega_{0,x}$. Indeed, because of the low gain of the drive mode in low and high frequencies, the measurement noises hide the behavior of the system in these frequency ranges.

1DoF control configuration

Let us consider the classical 1 degree-of-freedom (1DoF) control configuration of Figure 4.5, where K_x represents the controller and G_x is the drive-mode model. The main objective here is to ensure an accurate tracking of the sinusoidal reference signal, *i.e.*, $x_m(t) \approx x_m^{\text{ref}}(t)$. To quantify the tracking error, we define $\varepsilon_x \triangleq x_m^{\text{ref}} - x_m$. We also define the signals of interest $\tilde{w} = \text{col}(x_m^{\text{ref}}, d_{\text{Cor},x}, n_x)$ and $\tilde{z} = \text{col}(\varepsilon_x, u_x, v_x)$. The transfer function matrix of this closed-loop system can then be given by (dropping the dependence on s)

$$\begin{bmatrix} T_{x_m^{\text{ref}} \rightarrow \varepsilon_x} & T_{d_{\text{Cor},x} \rightarrow \varepsilon_x} & T_{n_x \rightarrow \varepsilon_x} \\ T_{x_m^{\text{ref}} \rightarrow u_x} & T_{d_{\text{Cor},x} \rightarrow u_x} & T_{n_x \rightarrow u_x} \\ T_{x_m^{\text{ref}} \rightarrow v_x} & T_{d_{\text{Cor},x} \rightarrow v_x} & T_{n_x \rightarrow v_x} \end{bmatrix} = \begin{bmatrix} S_x & -G_x S_x & T_x \\ K_x S_x & -T_x & -K_x S_x \\ K_x S_x & S_x & -K_x S_x \end{bmatrix}, \quad (4.15)$$

where $S_x = (1 + K_x G_x)^{-1}$ is the sensitivity function, and $T_x = 1 - S_x = K_x G_x S_x$ is the complementary sensitivity function.

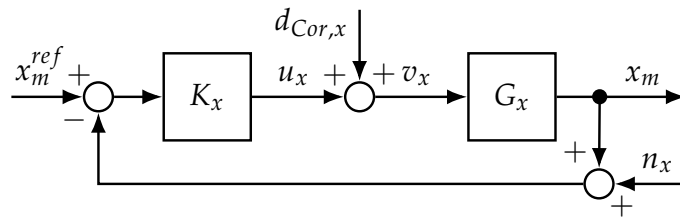


FIGURE 4.5: 1DoF control configuration for the drive-mode operation.

Please note that some of the transfers of (4.15) are equivalent. Indeed, $|T_{x_m^{\text{ref}} \rightarrow \varepsilon_x}| = |T_{d_{\text{Cor},x} \rightarrow v_x}|$, $|T_{d_{\text{Cor},x} \rightarrow u_x}| = |T_{n_x \rightarrow \varepsilon_x}|$ and $|T_{x_m^{\text{ref}} \rightarrow u_x}| = |T_{n_x \rightarrow u_x}| = |T_{x_m^{\text{ref}} \rightarrow v_x}| = |T_{n_x \rightarrow v_x}|$. Let us focus on the equivalence $|T_{n_x \rightarrow u_x}| = |T_{x_m^{\text{ref}} \rightarrow u_x}|$. To ensure a certain robustness level against additive uncertainties, $T_{n_x \rightarrow u_x}$ has to be upper bounded, see (4.14). On the other hand, the upper bound on the magnitude of the transfer $T_{x_m^{\text{ref}} \rightarrow u_x}$ implies limiting the control signal energy that is available for tracking the reference signal. In general, the higher the $|T_{x_m^{\text{ref}} \rightarrow u_x}|$ is, the

quicker the to-be-controlled system tracks the reference signal and higher the control signal amplitudes can be (mainly during the transient state). With a 1DoF controller, the robustness against additive uncertainties and the “available control signal energy” are expressed through the same transfer: $K_x S_x$. This structural constraint can be more or less restrictive depending on the to-be-controlled system and on the closed-loop specifications. Later, we will see that the 2DoF control configuration allows avoiding this structural constraint.

Also note that only three of the transfers of (4.15) have to be constrained to achieve the desired performance: $T_{x_m^{ref} \rightarrow \varepsilon_x}$, $T_{d_{Cor,x} \rightarrow \varepsilon_x}$ and $T_{n_x \rightarrow u_x}$. Moreover, most of them are equivalent. Thus, to express the performance- and robustness-related frequency constraints, we consider the block diagram of Figure 4.6, where, because of the equivalence between the transfers, the signals n_x and v_x are suppressed. Furthermore, without these signals, the tracking error coincides with the signal at the controller input. This scheme can be represented in the general control configuration of Figure 4.1 or Figure 4.2 with $\tilde{w} = \text{col}(x_m^{ref}, d_{Cor,x})$ and $\tilde{z} = \text{col}(\varepsilon_x, u_x)$, $W_{in} = \text{diag}(W_r, W_d)$, $W_{out} = \text{diag}(W_\varepsilon, W_u)$, $u_p = u_x$, and $y_p = \varepsilon_x$.

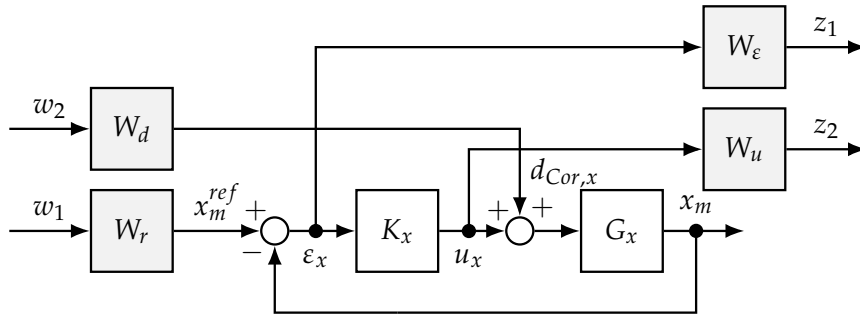


FIGURE 4.6: Block diagram for the 1DoF drive-mode control design.

The \mathcal{H}_∞ problem is therefore recast as to compute the controller K_x , if there is any, such that

$$\|T_{w \rightarrow z}\|_\infty = \left\| \begin{bmatrix} W_\varepsilon T_{x_m^{ref} \rightarrow \varepsilon_x} W_r & W_\varepsilon T_{d_{Cor,x} \rightarrow \varepsilon_x} W_d \\ W_u T_{x_m^{ref} \rightarrow u_x} W_r & W_u T_{d_{Cor,x} \rightarrow u_x} W_d \end{bmatrix} \right\|_\infty < \gamma. \quad (4.16)$$

Furthermore, if there is a solution for this problem with $\gamma \leq 1$, then (4.16) implies that, $\forall \omega \in \mathbb{R}$,

$$\begin{aligned} |T_{x_m^{ref} \rightarrow \varepsilon_x}(j\omega)| &< \frac{1}{|W_\varepsilon(j\omega)W_r(j\omega)|}, & |T_{d_{Cor,x} \rightarrow \varepsilon_x}(j\omega)| &< \frac{1}{|W_\varepsilon(j\omega)W_d(j\omega)|}, \\ |T_{x_m^{ref} \rightarrow u_x}(j\omega)| &< \frac{1}{|W_u(j\omega)W_r(j\omega)|}, & |T_{d_{Cor,x} \rightarrow u_x}(j\omega)| &< \frac{1}{|W_u(j\omega)W_d(j\omega)|}. \end{aligned}$$

The reference-tracking specification (see (4.12)) is achieved by constraining $|T_{x_m^{ref} \rightarrow \varepsilon_x}(j\omega)|$ to be small around $\omega = \omega_{exc}$. This restriction is enforced via the product $W_\varepsilon W_r$, which has to present a gain larger than $(\lambda_{SFNL} k_{SFNL})^{-1}$ at $\omega = \omega_{exc}$. Similarly, for the specification of disturbance rejection (see (4.13)), the product $W_\varepsilon W_d$ must present a gain larger than $1/k_{x1}$ around ω_{exc} . Finally, for the specification of robust stability against additive uncertainties (see (4.14)), $|W_u W_r|$ must be larger than $1/|W_{add,1}|$ across all the frequencies. It is also important to note that, since $|T_{d_{Cor,x} \rightarrow u_x}| = |1 - T_{x_m^{ref} \rightarrow \varepsilon_x}|$ ($|-T_x| = |1 - S_x|$), when we enforce

$|T_{x_m^{ref} \rightarrow \varepsilon_x}(j\omega)| \ll 1$ for $\omega \approx \omega_{exc}$, we also have $|T_{d_{Cor,x} \rightarrow u_x}(j\omega)| \approx 1$. This structural constraint has to be taken into consideration for the design of W_u and W_d .

In general, the condition (4.14) is enough to ensure the robust stability of the system against additive uncertainties. However, the designer may want to adopt more traditional stability margins, as the gain and phase margins. In this case, the requirement of a minimum modulus margin, which is closely related to the traditional stability margins [SP01], can be introduced on the original specifications, enhancing the overall system robustness. A minimal modulus margin ΔM can be enforced by constraining

$$\|S_x\|_\infty = \left\| T_{x_m^{ref} \rightarrow \varepsilon_x} \right\|_\infty < \frac{1}{\Delta M}. \quad (4.17)$$

This constraint is also enforced through the choice of W_ε and W_r .

As discussed in Section 4.1.2, the choice of the weighting functions is nonunique. In the sequel, we present a numerical example to illustrate the \mathcal{H}_∞ synthesis for the closed-loop operation of the drive mode of a MEMS gyroscope.

Example 4.2 (1DoF direct control of the drive mode). *Let us consider the drive-mode plant of Example 2.1 and the following specifications.*

- (i) **SFNL and reference tracking:** SFNL smaller than 500 ppm, i.e., reference tracking of a sinusoidal signal with relative error $\xi_x < 0.5k_{SFNL} = 250 \cdot 10^{-6}$ ($\lambda_{SFNL} = 0.5$) for $\omega_{exc} = \omega_{0,x}$.
- (ii) **Disturbance rejection:** minimize the disturbance effects, i.e., minimize k_{x1} .
- (iii) **Robustness against additive uncertainties:** minimize $|T_{x_m^{ref} \rightarrow u_x}|$ where $|W_{add,1}|$ is important (low and high frequencies).
- (iv) **Modulus margin (optional):** additionally, ensure a modulus margin $\Delta M > 0.5$.

Based on the \mathcal{H}_∞ synthesis, we want to design a 1DoF controller to operate the drive mode ensuring the above specifications. For this purpose, we consider the \mathcal{H}_∞ criterion defined by the scheme of Figure 4.6 and weighting functions that enforce the upper bounds presented in the figures 4.7 and 4.8. The weighting functions are first chosen to ensure the “hard” specifications – reference tracking and modulus margin (see transfer from x_m^{ref} to ε_x). The other weighting functions are iteratively chosen to minimize k_{x1} and $|T_{x_m^{ref} \rightarrow u_x}|$, respectively enhancing the disturbance rejection and the robustness against additive uncertainties. Their expressions and numerical values are given in Appendix C.2.

Then, by solving the standard \mathcal{H}_∞ problem with $\gamma = 0.9745$, we obtain the 6th-order controller whose Bode diagram is presented in Figure 4.9. Its numerical values are also given in Appendix C.2. Since $\gamma < 1$, all the specifications are satisfied. Indeed, all the closed-loop transfer functions satisfy the upper bounds in Figure 4.7 and Figure 4.8.

Globally, the controller has high gains around ω_{exc} and small gains in low and high frequencies (see Figure 4.9). These properties are indeed necessary to respectively ensure (i) that the transfer $T_{x_m^{ref} \rightarrow \varepsilon_x} = S_x$ has small gain around ω_{exc} (see Example 4.1), and (ii) that the transfer $T_{x_m^{ref} \rightarrow u_x} = K_x S_x$ has low gains in low and high frequencies. Indeed,

- if $|K_x(j\omega)G_x(j\omega)| \gg 1$, $|S_x(j\omega)| \approx 1/|K_x(j\omega)G_x(j\omega)|$;
- if $|K_x(j\omega)G_x(j\omega)| \ll 1$, $|K_x(j\omega)S_x(j\omega)| \approx |K_x(j\omega)|$.

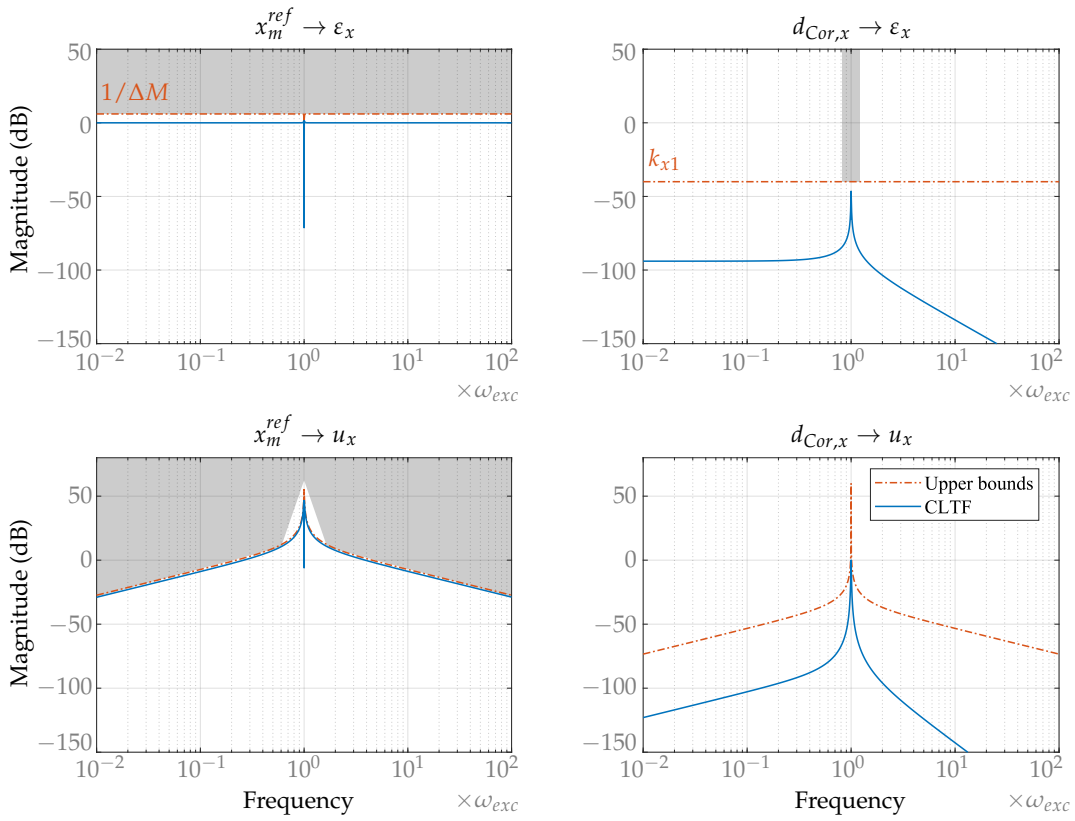


FIGURE 4.7: Upper bounds and closed-loop frequency responses for Example 4.2.

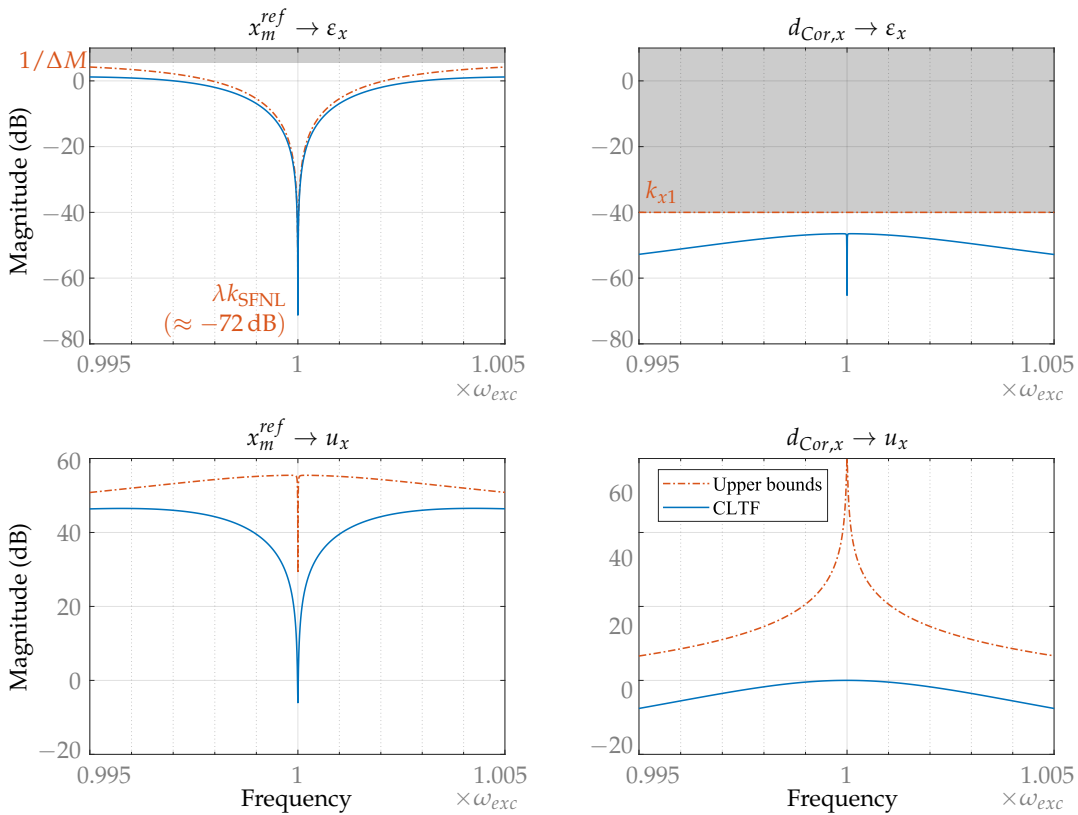


FIGURE 4.8: Upper bounds and closed-loop frequency responses for Example 4.2. Zoom around ω_{exc} .

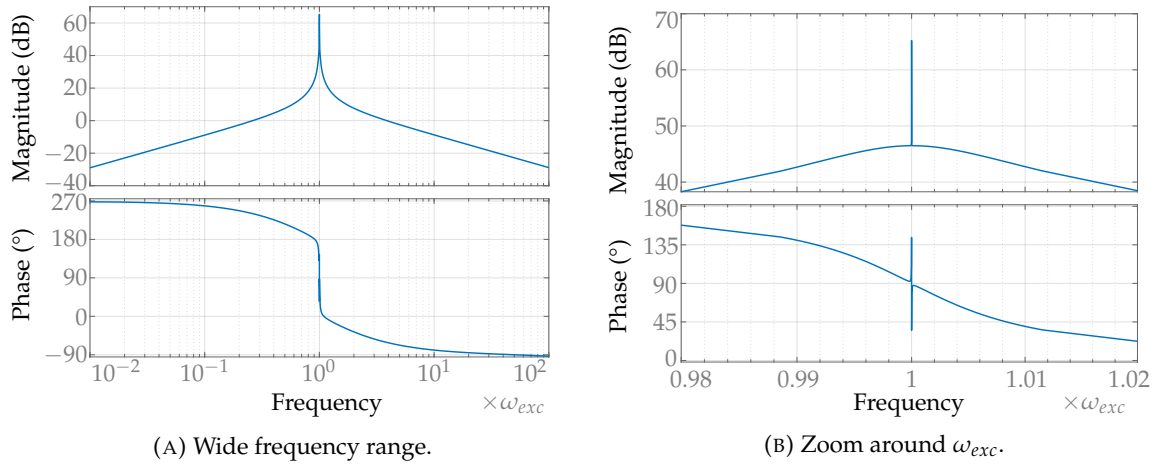


FIGURE 4.9: Bode diagrams of the controller obtained in Example 4.2.

Now, if we zoom the Bode diagram around ω_{exc} (see Figure 4.9b), we can note that the controller has a salient resonance peak at ω_{exc} , ensuring an accurate reference tracking. Moreover, the controller adds at least 20° of phase lead for $0.98\omega_{exc} < \omega < 1.02\omega_{exc}$, ensuring that, even with the 180° phase lag of the plant, the closed-loop system has a sufficient phase to ensure good stability margins.

2DoF Control Configuration

We have just seen that the 1DoF control configuration imposes a particular structural constraint: $|T_{x_m^{ref} \rightarrow u_x}| = |T_{n_x \rightarrow u_x}|$. Now, we present the 2DoF control configuration, which allows avoiding this constraint. The 2DoF control configuration is presented in Figure 4.10, where the controller $K_x = [K_{x1}, K_{x2}]$ has two inputs (x_m^{ref} and x_n) and one output (u_x). That is, the 2DoF controller is composed of a feedforward controller K_{x1} and a positive-feedback controller K_{x2} . The tracking error is still defined as $\varepsilon_x = x_m^{ref} - x_m$ and the signals of interest are $\tilde{w} = \text{col}(x_m^{ref}, d_{Cor,x}, n_x)$ and $\tilde{z} = \text{col}(\varepsilon_x, u_x, v_x)$. Now, the transfer function matrix of this closed-loop system is given by

$$\begin{bmatrix} T_{x_m^{ref} \rightarrow \varepsilon_x} & T_{d_{Cor,x} \rightarrow \varepsilon_x} & T_{n_x \rightarrow \varepsilon_x} \\ T_{x_m^{ref} \rightarrow u_x} & T_{d_{Cor,x} \rightarrow u_x} & T_{n_x \rightarrow u_x} \\ T_{x_m^{ref} \rightarrow v_x} & T_{d_{Cor,x} \rightarrow v_x} & T_{n_x \rightarrow v_x} \end{bmatrix} = \begin{bmatrix} 1 - K_{x1}G_xS_x & -G_xS_x & T_x \\ K_{x1}S_x & -T_x & K_{x2}S_x \\ K_{x1}S_x & S_x & K_{x2}S_x \end{bmatrix}, \quad (4.18)$$

where $S_x = (1 - K_{x2}G_x)^{-1}$ is the sensitivity function, and $T_x = 1 - S_x = -K_{x2}G_xS_x$ is the complementary sensitivity function. Please note that, as claimed, there is no more equivalence between the transfers $T_{x_m^{ref} \rightarrow u_x}$ and $T_{n_x \rightarrow u_x}$. Then, $|T_{x_m^{ref} \rightarrow u_x}|$ can be different of $|T_{n_x \rightarrow u_x}|$.

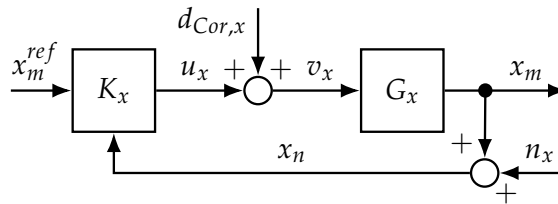


FIGURE 4.10: 2DoF control configuration for the drive-mode operation.

To express the desired performance- and robustness-related frequency constraints, we consider the block diagram of Figure 4.11, which can be represented in the general control configuration of Figure 4.1 or Figure 4.2 with $\tilde{w} = \text{col}(x_m^{ref}, d_{Cor,x}, n_x)$ and $\tilde{z} = \text{col}(\varepsilon_x, u_x)$, $W_{in} = \text{diag}(W_r, W_d, W_n)$, $W_{out} = \text{diag}(W_\varepsilon, W_u)$, $u_P = u_x$, and $y_P = \text{col}(x_m^{ref}, x_n)$.

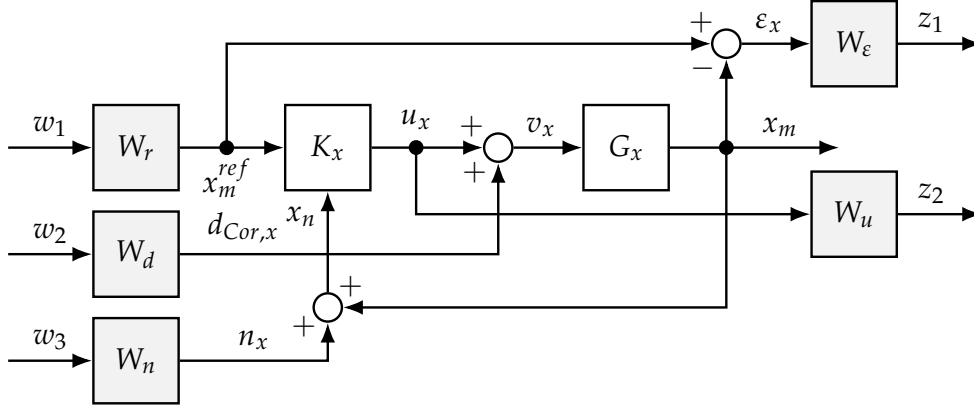


FIGURE 4.11: Block diagram for the 2DoF drive-mode control design.

The \mathcal{H}_∞ problem is then recast as to compute the controller $K_x = [K_{x1}, K_{x2}]$, if there is any, such that

$$\|T_{w \rightarrow z}\|_\infty = \left\| \begin{bmatrix} W_\varepsilon T_{x_m^{ref} \rightarrow \varepsilon_x} W_r & W_\varepsilon T_{d_{Cor,x} \rightarrow \varepsilon_x} W_d & W_\varepsilon T_{n_x \rightarrow \varepsilon_x} W_n \\ W_u T_{x_m^{ref} \rightarrow u_x} W_r & W_u T_{d_{Cor,x} \rightarrow u_x} W_d & W_u T_{n_x \rightarrow u_x} W_n \end{bmatrix} \right\|_\infty < \gamma. \quad (4.19)$$

If there exists a solution for this problem with $\gamma \leq 1$, then, $\forall \omega \in \mathbb{R}$,

$$\begin{aligned} |T_{x_m^{ref} \rightarrow \varepsilon_x}| &< \frac{1}{|W_\varepsilon W_r|}, & |T_{d_{Cor,x} \rightarrow \varepsilon_x}| &< \frac{1}{|W_\varepsilon W_d|}, & |T_{n_x \rightarrow \varepsilon_x}| &< \frac{1}{|W_\varepsilon W_n|}, \\ |T_{x_m^{ref} \rightarrow u_x}| &< \frac{1}{|W_u W_r|}, & |T_{d_{Cor,x} \rightarrow u_x}| &< \frac{1}{|W_u W_d|}, & |T_{n_x \rightarrow u_x}| &< \frac{1}{|W_u W_n|}. \end{aligned}$$

As well as for the previous case (1DoF), the specification of reference tracking (see (4.12)) can be achieved by constraining $|T_{x_m^{ref} \rightarrow \varepsilon_x}|$ to be small around $\omega = \omega_{exc}$. This restriction is enforced via the product $W_\varepsilon W_r$, which has to present a gain larger than $(\lambda_{SFNL} k_{SFNL})^{-1}$ at $\omega = \omega_{exc}$. For the specification of disturbance rejection (see (4.13)), the product $W_\varepsilon W_d$ must present a gain larger than $1/k_{x1}$ around ω_{exc} . Finally, for the specification of robust stability against additive uncertainties (see (4.14)), $|W_u W_n|$ must be larger than $|W_{add,1}|$.

It is important to mention that we could opt to consider v_x instead of u_x as signal of interest. This would allow us, if required, to upper bound the transfer $T_{d_{Cor,x} \rightarrow v_x} = S_x$, enforcing a minimal modulus margin.

Example 4.3 (2DoF direct control of the drive mode). *Let us consider again the drive-mode plant of Example 2.1 and the following specifications.*

- (i) **SFNL and reference tracking:** SFNL smaller than 500 ppm, i.e., reference tracking of a sinusoidal signal with relative error $\check{\varepsilon}_x < 0.5k_{SFNL} = 250 \cdot 10^{-6}$ ($\lambda_{SFNL} = 0.5$) for $\omega_{exc} = \omega_{0,x}$.
- (ii) **Disturbance rejection:** minimize the disturbance effects, i.e., minimize k_{x1} .

(iii) **Robustness against additive uncertainties:** minimize $|T_{n_x \rightarrow u_x}|$ where $|W_{add,1}|$ is important (low and high frequencies).

Based on the \mathcal{H}_∞ synthesis, we want to design a 2DoF controller to operate the drive mode ensuring the above specifications. To this end, we consider the \mathcal{H}_∞ criterion defined by the scheme of Figure 4.11 and weighting functions that enforce the upper bounds of the figures 4.12 and 4.13. Similar to Example 4.2, we start by choosing the weighting functions defining the “hard constraints” – in this case, the reference tracking (see transfer from x_m^{ref} to ε_x). The other weighting functions are iteratively chosen to minimize k_{x1} and the magnitude of $T_{n_x \rightarrow u_x}$ (mainly in low and high frequencies). Their numerical values are given in Appendix C.3.

Please note that, in contrast to the 1DoF case, here, the transfers $T_{x_m^{ref} \rightarrow u_x}$ and $T_{n_x \rightarrow u_x}$ have different magnitude. Then, the upper bound on $T_{x_m^{ref} \rightarrow u_x}$ can be relaxed, allowing to have a quicker reference tracking (if needed). The transfer $T_{n_x \rightarrow u_x}$ is still used for the robust stability specification.

Then, by solving the standard \mathcal{H}_∞ problem with $\gamma = 1.1634$, we obtain the 8th-order controller whose Bode diagram is presented in Figure 4.14 and numerical values are given in Appendix C.3. First, note that in this case, $\gamma > 1$. By observing the obtained closed-loop transfer functions in Figure 4.13, we can realize that $|T_{n_x \rightarrow \varepsilon_x}|$ is slightly higher than its upper bound. Similarly, $|T_{n_x \rightarrow u_x}|$ is also slightly higher than its upper bound. Even though, the main closed-loop specifications (reference tracking and disturbance rejection) are fulfilled.

The modulus margin is verified a posteriori. We obtain $\|S_x\|_\infty = 1.0347 \approx 0.2963$ dB, which gives $\Delta M = 0.9665 > 0.5$.

Globally, K_{x1} has high gains across all the frequency range. Since its input signal is x_m^{ref} , which is a sinusoidal signal (spectrum concentrated around ω_{exc}), the high gains in low and high frequency ranges is not an issue. On the other hand, K_{x2} is similar to the 1DoF controller of Example 4.2, that is, it has important gains around ω_{exc} and lower gains in low and high frequencies, ensuring low gain for $T_{n_x \rightarrow u_x}$ in these frequencies. Two main differences can be observed. Due to the positive feedback, the phase of K_{x2} presents an additional 180° phase lead, but it still ensures a sufficient phase for stability. The second difference consists on the absence of the “salient” resonance peak. In the 1DoF case, this resonance peak was needed to ensure an accurate reference tracking. Here, the feedforward controller K_{x1} also helps to achieve an accurate reference tracking, such that this resonance peak becomes unnecessary.

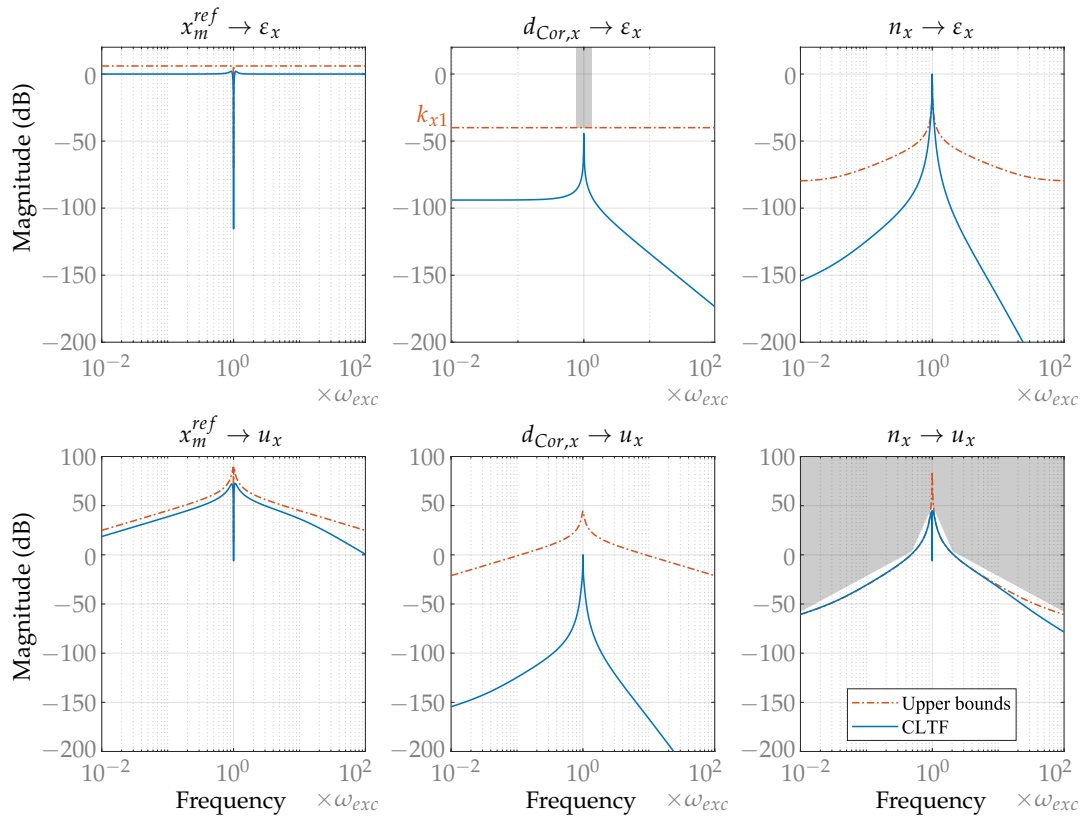


FIGURE 4.12: Upper bounds and closed-loop frequency responses for Example 4.3.

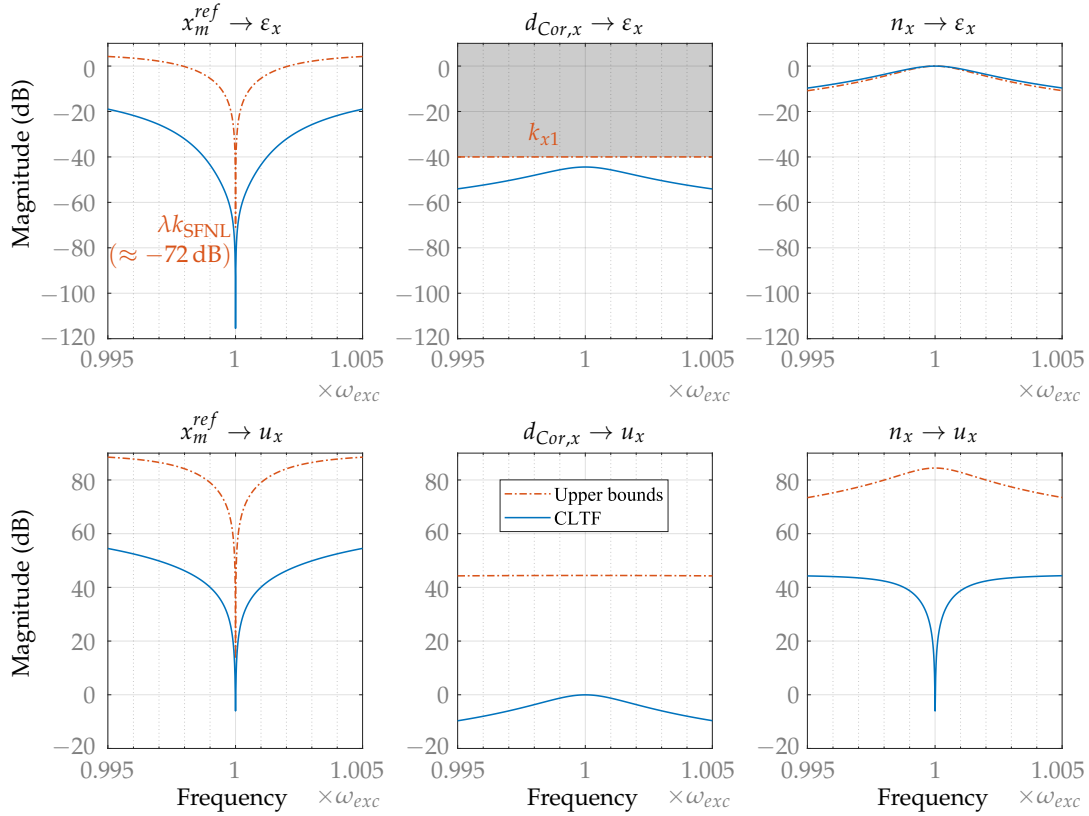


FIGURE 4.13: Upper bounds and closed-loop frequency responses for Example 4.3. Zoom around ω_{exc} .

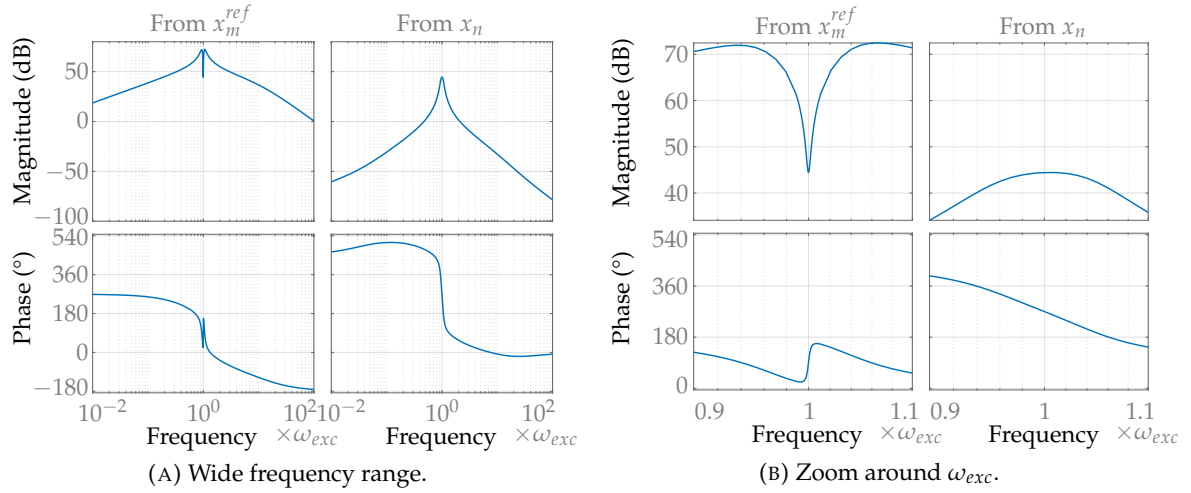


FIGURE 4.14: Bode diagrams of the controller obtained in Example 4.3.

4.2.2 Sense-Mode Control

Besides the main objective of estimating the Coriolis force, the sense-mode controller also has to fulfill secondary control objectives so that the whole gyroscope achieves the desired global performance level. In the SISO approach, the sense-mode controller has to be such that the frequency constraints below are satisfied.

Sense-mode nominal performance constraints:

- (i) **SFNL and estimation of the Coriolis force:** for the SFNL (see (3.53), page 69), which also implies an accurate estimation of $d_{Cor,y}$, we consider

$$\left| T_{d_{Cor,y} \rightarrow \varepsilon_{est}}(j\omega_{exc}) \right| \leq (1 - \lambda_{SFNL}) k_{SFNL}. \quad (4.20)$$

- (ii) **Disturbance rejection:** in the SISO approach, for the minimization of y_m (or equivalently, ε_y), we consider (3.41) (page 67):

$$\forall |\omega| \in [\omega_{exc} - \omega_{\Omega}, \omega_{exc} + \omega_{\Omega}], \quad \left| T_{d_{Cor,y} \rightarrow y_m}(j\omega) \right| = \left| T_{d_{Cor,y} \rightarrow \varepsilon_y}(j\omega) \right| < k_{y2}, \quad (4.21)$$

where $k_{y2} \in \mathbb{R}_+$ is to be minimized.

- (iii) **Bandwidth:** to ensure a bandwidth ω_B larger than ω_B^{des} (see (3.56), page 70),

$$\forall |\omega| \in [\omega_{exc} - \omega_B^{\text{des}}, \omega_{exc} + \omega_B^{\text{des}}], \quad \left| T_{d_{Cor,y} \rightarrow \varepsilon_{est}}(j\omega) \right| < \frac{2 - \sqrt{2}}{2} \approx 0.2929. \quad (4.22)$$

- (iv) **Angle random walk (ARW):** in the SISO approach, $T_{e_x \rightarrow \hat{u}_{Cor,y}} = 0$ (no coupling between the drive and sense modes); then, we rewrite (3.60) (page 71) with $\lambda_{ARW} = 0$ as

$$\forall |\omega| \in (0, 2\omega_{exc}], \quad \left| T_{e_y \rightarrow \hat{u}_{Cor,y}}(j\omega) \right| = \left| N_y(j\omega) T_{n_y \rightarrow \hat{u}_{Cor,y}}(j\omega) \right| \leq \frac{\sqrt{2}}{2} \hat{k}_{SF} k_{ARW} \quad (4.23)$$

and consider

$$\forall |\omega| \in (0, 2\omega_{exc}], \quad \left| T_{n_y \rightarrow \hat{u}_{Cor,y}}(j\omega) \right| \leq \frac{k_n}{|N_y(j\omega)|}, \quad (4.24)$$

where $k_n = \frac{\sqrt{2} \cdot \hat{k}_{SF} k_{ARW}}{2}$ is to be minimized and N_y defines the power spectral density of the noise (see (2.49), page 32).

- (v) **Band-pass condition of $\hat{u}_{Cor,y}$:** in the SISO approach, to ensure the band-pass condition of $\hat{u}_{Cor,y}$, the controller has to ensure (see (3.44), page 67)

$$\forall |\omega| \geq 2\omega_{exc}, \quad \left| T_{e_y \rightarrow \hat{u}_{Cor,y}}(j\omega) \right| \ll 1 \quad \text{and} \quad \left| T_{e_y \rightarrow \hat{u}_{Cor,y}}(0) \right| \ll 1. \quad (4.25)$$

Sense-mode robust stability constraint:

- (i) **Unmodeled dynamics:** to enforce the robustness against additive uncertainties $\Delta E_{yy} \in \Delta_{add}$, which is defined by $W_{add,1}$ and $W_{add,2} = 1$ (see (3.63), page 72), we shall minimize at best $|T_{n_y \rightarrow u_y}(j\omega)|$, mainly in the frequency range where $|W_{add,1}|$ is important. Indeed, the weighted small gain theorem ensures stability against this kind of uncertainty if

$$\forall \omega \in \mathbb{R}, \quad \left| T_{n_y \rightarrow \hat{u}_{Cor,y}}(j\omega) \right| = |T_{n_y \rightarrow u_y}(j\omega)| < \frac{1}{|\Delta W_{add,1}(j\omega)|}. \quad (4.26)$$

Similar to the drive mode, $|W_{add,1}|$ is assumed to be important in low and high frequencies, and small around $\omega_{0,x}$ and $\omega_{0,y}$.

For the sense mode, we consider only the 1DoF control configuration. Since the sense-mode control objective is rather a regulation (or disturbance rejection) problem, there are no significant advantages on using the 2DoF control configuration. Here, we consider the control scheme of Figure 4.15, where K_y represents the controller and G_y is the sense-mode model. The main objective is to provide an accurate estimate of the signal $d_{Cor,y}$. This estimate is given by $\hat{u}_{Cor,y} = -u_y$. In addition, we define the estimation error $\varepsilon_{est} = d_{Cor,y} - \hat{u}_{Cor,y} = d_{Cor,y} + u_y$. We also define the signals of interest $\tilde{w} = \text{col}(d_{Cor,y}, n_y)$ and $\tilde{z} = \text{col}(\varepsilon_{est}, \hat{u}_{Cor,y}, y_m)$. This closed-loop system can then be given by the following transfer functions:

$$\begin{bmatrix} T_{d_{Cor,y} \rightarrow \varepsilon_{est}} & T_{n_y \rightarrow \varepsilon_{est}} \\ T_{d_{Cor,y} \rightarrow \hat{u}_{Cor,y}} & T_{n_y \rightarrow \hat{u}_{Cor,y}} \\ T_{d_{Cor,y} \rightarrow y_m} & T_{n_y \rightarrow y_m} \end{bmatrix} = \begin{bmatrix} S_y & K_y S_y \\ T_y & -K_y S_y \\ G_y S_y & -T_y \end{bmatrix}, \quad (4.27)$$

where $S_y = (1 - K_y G_y)^{-1}$ is the sensitivity function, and $T_y = 1 - S_y = -K_y G_y S_y$ is the complementary sensitivity function.

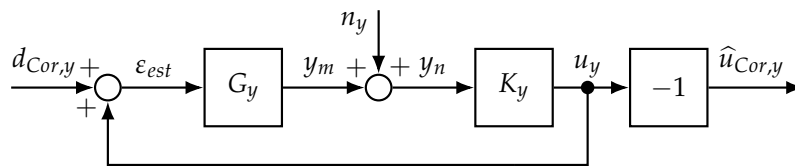


FIGURE 4.15: 1DoF control configuration for the sense-mode operation.

Please note that the magnitudes of some transfer functions of (4.27) are equal:

$$\left| T_{n_y \rightarrow \hat{u}_{Cor,y}} \right| = |T_{n_y \rightarrow \varepsilon_{est}}| = |K_y S_y| \quad \text{and} \quad |T_{n_y \rightarrow y_m}| = \left| T_{d_{Cor,y} \rightarrow \hat{u}_{Cor,y}} \right| = |T_y|.$$

Then, to express the performance- and robustness-related frequency constraints, we consider the block diagram of Figure 4.16, where, because of the equivalence between the transfer

functions mentioned above, the signal $\hat{u}_{Cor,y}$ is not considered as a signal of interest. In this case, $\tilde{w} = \text{col}(d_{Cor,y}, n_y)$ and $\tilde{z} = \text{col}(\varepsilon_{est}, y_m)$, $W_{in} = \text{diag}(W_d, W_n)$, $W_{out} = \text{diag}(W_\varepsilon, W_y)$, $u_p = u_y$, and $y_p = y_n$.

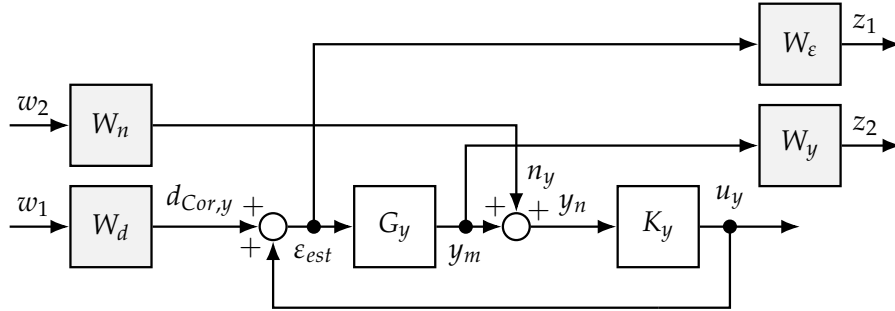


FIGURE 4.16: Block diagram for the 1DoF sense-mode control design.

The \mathcal{H}_∞ problem is then recast as to compute the controller K_y , if there is any, such that

$$\|T_{w \rightarrow z}\|_\infty = \left\| \begin{bmatrix} W_\varepsilon T_{d_{Cor,y} \rightarrow \varepsilon_{est}} W_d & W_\varepsilon T_{n_y \rightarrow \varepsilon_{est}} W_n \\ W_y T_{d_{Cor,y} \rightarrow y_m} W_d & W_y T_{n_y \rightarrow y_m} W_n \end{bmatrix} \right\|_\infty < \gamma. \quad (4.28)$$

If the problem above has a solution with $\gamma \leq 1$, then (4.28) implies that, $\forall \omega \in \mathbb{R}$,

$$\begin{aligned} |T_{d_{Cor,y} \rightarrow \varepsilon_{est}}| &< \frac{1}{|W_\varepsilon W_d|}, & |T_{n_y \rightarrow \varepsilon_{est}}| &< \frac{1}{|W_\varepsilon W_n|}, \\ |T_{d_{Cor,y} \rightarrow y_m}| &< \frac{1}{|W_y W_d|}, & |T_{n_y \rightarrow y_m}| &< \frac{1}{|W_y W_n|}. \end{aligned}$$

The specification for SFNL (accurate estimation) and bandwidth (respectively, (4.20) and (4.22)) can be achieved by constraining $|T_{d_{Cor,y} \rightarrow \varepsilon_{est}}|$. These constraints are enforced through the product $W_\varepsilon W_d$, which has to present a gain larger than $((1 - \lambda_{\text{SFNL}})k_{\text{SFNL}})^{-1}$ at $\omega = \omega_{exc}$ and higher than $1/0.2929$ for $|\omega| \in (\omega_{exc} - \omega_B, \omega_{exc} + \omega_B)$.

Similarly, for the disturbance rejection (or minimization of y_m – see (4.21)), the product $W_y W_d$ must present a gain larger than $1/k_{y2}$ around ω_{exc} . Finally, the specifications for ARW, band-pass condition of $\hat{u}_{Cor,y}$ and robust stability against additive uncertainties (respectively (4.24), (4.25) and (4.26)) are enforced through $|W_\varepsilon W_n|$, which must be larger than $|N_y(j\omega)|/k_n$ (ARW) and larger than $|W_{add,1}|$ (robustness) across all the frequencies. Moreover, to fulfill the band-pass condition, $|W_\varepsilon W_n|$ must present a very high gain at $\omega = 0$ and for $|\omega| \geq 2\omega_{exc}$.

It is also important to note that, since $T_y = 1 - S_y$, when enforcing $|T_{d_{Cor,y} \rightarrow \varepsilon_{est}}(j\omega)| < (1 - \lambda_{\text{SFNL}})k_{\text{SFNL}} \ll 1$, we have $|T_{n_y \rightarrow y_m}(j\omega)| \approx 1$ (recalling that $|T_{d_{Cor,y} \rightarrow \varepsilon_{est}}| = |S_y|$ and $|T_{n_y \rightarrow y_m}| = |T_y|$). This structural constraint has also to be taken into consideration for the design of W_y and W_n .

If needed, a minimal modulus margin ΔM can also be enforced by constraining $T_{d_{Cor,y} \rightarrow \varepsilon_{est}}$ through $W_\varepsilon W_d$, to present magnitude smaller than $1/\Delta M$ across all the frequencies, similar to the drive mode.

Let us now present an example to illustrate the \mathcal{H}_∞ synthesis for the design of a controller for the sense-mode closed-loop operation.

Example 4.4 (Direct control of the sense mode). *Let us consider the sense-mode plant of Example 2.2 and the following specifications.*

- (i) **SFNL and Coriolis force estimation:** SFNL smaller than 500 ppm, i.e., estimation of a sinusoidal signal with relative error $\xi_{est} < 0.5k_{SFNL} = 250 \cdot 10^{-6}$ ($\lambda_{SFNL} = 0.5$) for $\omega_{exc} = \omega_{0,x}$.
- (ii) **Disturbance rejection:** minimize the displacement of the proof mass along the \bar{y} -axis, i.e., minimize k_{y2} .
- (iii) **Bandwidth:** $\omega_B \geq \omega_B^{des} = 2\pi 200 \text{ rad s}^{-1}$.
- (iv) **ARW:** minimize the ARW, i.e., minimize k_n .
- (v) **Band-pass condition:** ensure the band-pass condition of $\hat{u}_{Cor,y}$.
- (vi) **Robustness against additive uncertainties:** minimize $|T_{n_y \rightarrow \epsilon_{est}}|$ where $|W_{add,1}|$ is important (low and high frequencies).
- (vii) **Modulus margin (optional):** additionally, ensure a modulus margin $\Delta M > 0.5$.

Based on the \mathcal{H}_∞ synthesis, we aim to design a controller for the sense mode that ensures the above specifications. To achieve this objective, we consider the \mathcal{H}_∞ criterion defined by the scheme of Figure 4.16 and weighting functions that enforce the upper bounds of the figures 4.17 and 4.18.

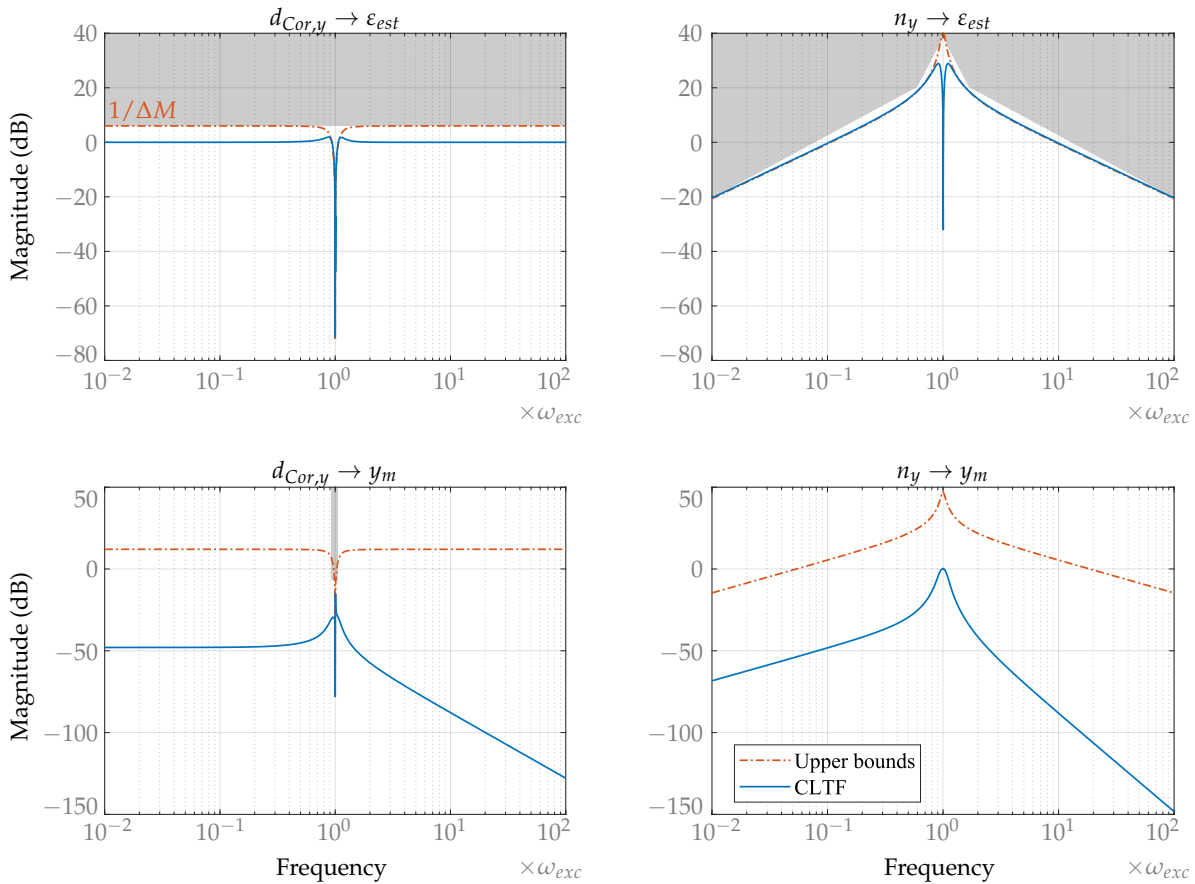


FIGURE 4.17: Upper bounds and closed-loop frequency responses for Example 4.4.

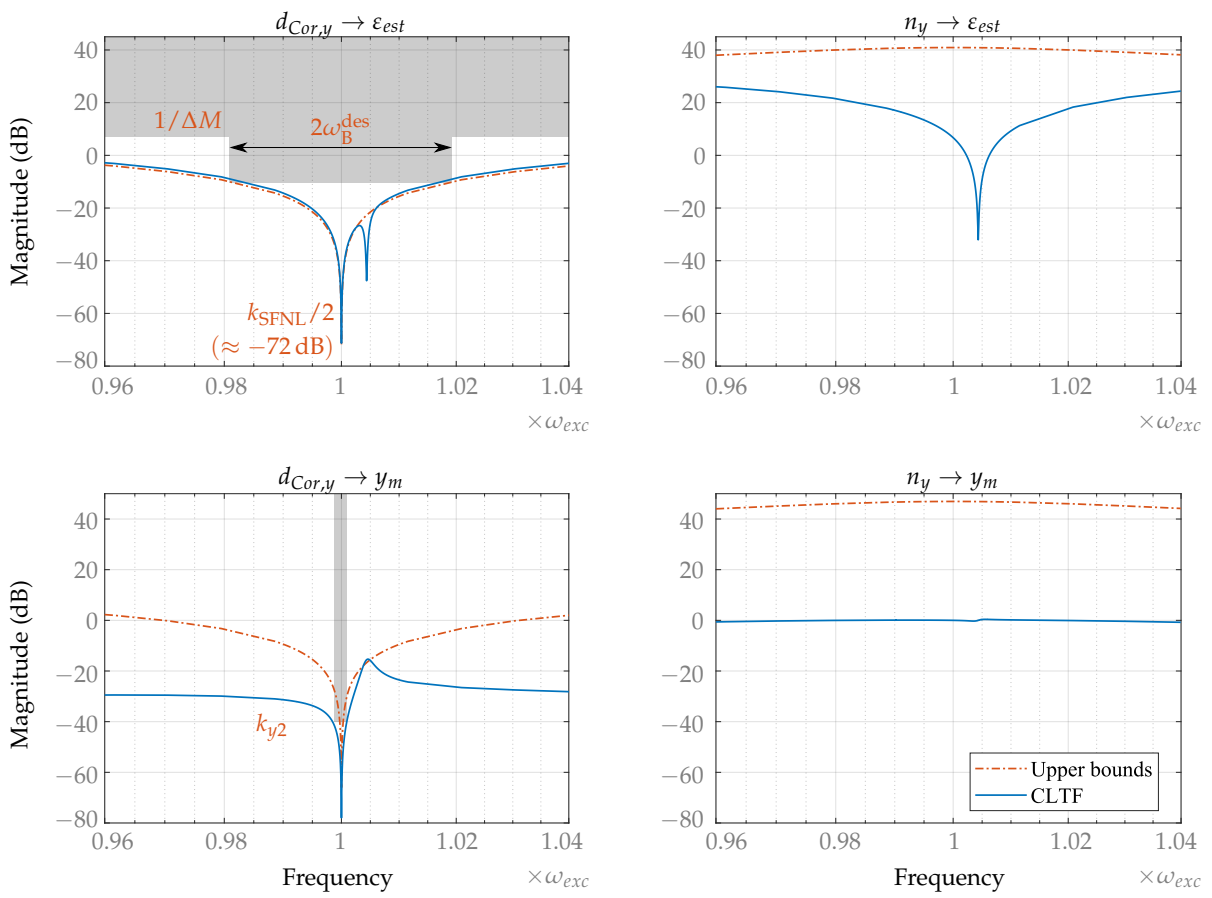


FIGURE 4.18: Upper bounds and closed-loop frequency responses for Example 4.4. Zoom around ω_{exc} .

As well as for the previous examples, the weighting functions are chosen first to enforce the “hard constraints” – the accurate estimation (SFNL), the bandwidth and the modulus margin (all of them related to the transfer from $d_{Cor,y}$ to ε_{est}). In particular, we chose to place the dynamic weighting function enforcing low gain for $\omega = \omega_{exc}$ rather on the input signal ($d_{Cor,y}$) than on the output signal (ε_{est}). Putting this weighting function on ε_{est} would impose an upper bound with low gain at $\omega = \omega_{exc}$ on the transfer $T_{n_y \rightarrow \varepsilon_{est}}$. This constraint cannot be enforced because $|T_{d_{Cor,y} \rightarrow \varepsilon_{est}}(j\omega_{exc})| \ll 1$ implies $|K_y(j\omega_{exc})| \gg 1$, which, in its turn, implies that $|T_{n_y \rightarrow \varepsilon_{est}}(j\omega_{exc})| = |K_y(j\omega_{exc})S_y(j\omega_{exc})| \approx |G_y(j\omega_{exc})|^{-1}$. The same argument is used to justify a trade-off between the bandwidth and the ARW: the larger (better) is the bandwidth, the higher (worse) is the ARW. Indeed, the transfer $T_{n_y \rightarrow \varepsilon_{est}}$ cannot be minimized by the controller in the frequency range where $|K_y(j\omega)G_y(j\omega)| \gg 1$, which is the case when $|T_{d_{Cor,y} \rightarrow \varepsilon_{est}}(j\omega)| = |S_y(j\omega)| \ll 1$ (e.g., in the bandwidth). The other weighting functions are iteratively chosen to enforce the rest of the specifications. Their numerical values are given in Appendix C.4.

By solving the standard \mathcal{H}_∞ problem with $\gamma = 1.1422$, we obtain the 6th-order controller whose Bode diagram is presented in Figure 4.19 and numerical values are also given in Appendix C.4. Similar to Example 4.3, we also have γ slightly larger than 1. Note that, in Figure 4.17 and Figure 4.18, the upper bound violations arise mainly on the transfer $T_{d_{Cor,y} \rightarrow \varepsilon_{est}}$ and correspond to the bandwidth specification, which may be somewhat conservative. Thus, even with a small violation of the upper bounds, the required bandwidth shall be observed².

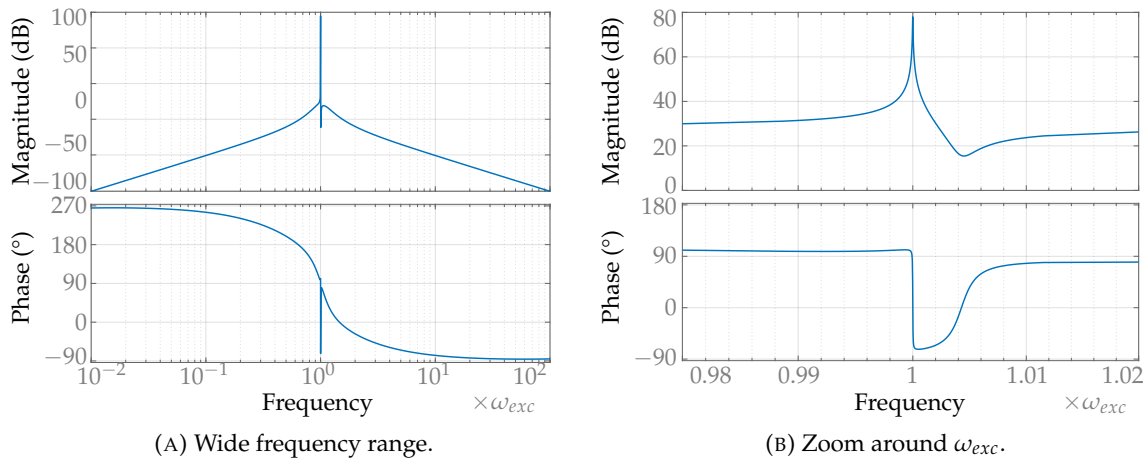


FIGURE 4.19: Bode diagrams of the controller obtained in Example 4.4.

Globally, the controller has high gains around ω_{exc} to ensure an accurate estimation of $d_{Cor,y}$ with a given bandwidth, and low gain in low and high frequencies, ensuring the robust stability against unmodeled dynamics in these frequency ranges (see Figure 4.19a).

When we zoom its Bode diagram around ω_{exc} (see Figure 4.19b), we can note the presence of an important resonance peak at ω_{exc} , which is followed by an antiresonance. The main role of this antiresonance is to add a phase lead before the sense mode adds a 180° phase lag, ensuring a sufficient phase for the closed-loop system stability. We recall that the sense-mode resonance frequency is equal to $11.55 \text{ kHz} \approx 1.004\omega_{exc}$.

²As well as for the other specifications, a deeper performance analysis must be performed to validate the proposed controller.

4.3 MIMO Control Architectures

Up to this point, we have considered independent SISO controllers to operate the MEMS gyroscope in closed loop. However, besides the coupling produced by the Coriolis force, the drive and sense modes might be mechanically coupled through anisoelectricity and nonproportional damping. Moreover, the design of SISO controllers for a multivariable system does not provide any guarantee of stability nor performance. Therefore, in this section, we aim to propose a multivariable approach for the closed-loop operation of MEMS gyroscopes, properly taking into consideration the mechanical coupling between the drive and sense modes. As well as for the SISO approach, we consider the \mathcal{H}_∞ synthesis for the controller design.

Two different strategies are considered here. We start by considering a control configuration that is inspired by the SISO approach presented in the previous section. In that configuration, the estimate $\hat{u}_{Cor,y}$ is directly linked to the control signal u_y , *i.e.*, $\hat{u}_{Cor,y} = -u_y$. Then, thanks to the fact that the controller acts on the drive and sense modes, we can introduce a novel control configuration, where the controller is designed with a third output signal, which is directly used as $\hat{u}_{Cor,y}$, avoiding the direct links between the signals $\hat{u}_{Cor,y}$ and u_y .

4.3.1 MIMO 2DoF Control Architecture (with $\hat{u}_{Cor,y} = -u_y$)

Let us first consider the 2DoF control configuration of Figure 4.20, in which we recall that $u = \text{col}(u_x, u_y)$, $v = \text{col}(v_x, v_y)$, $q_m = \text{col}(x_m, y_m)$, $q_n = \text{col}(x_n, y_n)$, $d_{Cor} = \text{col}(d_{Cor,x}, d_{Cor,y})$ and $n = \text{col}(n_x, n_y)$. Moreover, for the sake of symmetry, we define a reference vector $r = \text{col}(x_m^{ref}, y_m^{ref})$. Then, the tracking error vector is given by $\varepsilon = \text{col}(\varepsilon_x, \varepsilon_y) = r - q_m$. The estimate of $d_{Cor,y}$ is obtained through $\hat{u}_{Cor,y} = -u_y$, such that the estimation error can be given by $\varepsilon_{est} = d_{Cor,y} + u_y$, which is equal to v_y . Similar to the SISO approach, the 2DoF controller is given by $K = [K_1, K_2]$, where K_1 is a feedforward controller with r as input signal, and K_2 is a positive-feedback controller with $q_n = q_m + n$ as input signal.

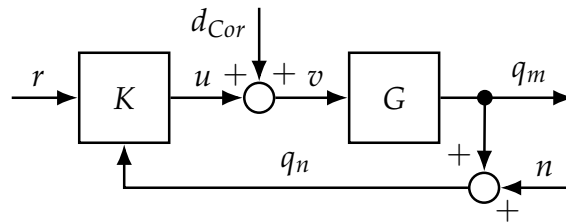


FIGURE 4.20: Multivariable 2DoF control configuration.

By defining the signals of interest $\tilde{w} = \text{col}(r, d_{Cor}, n)$ and $\tilde{z} = \text{col}(\varepsilon, u, v)$, the above closed-loop system defines the following transfer matrix:

$$\begin{bmatrix} T_{r \rightarrow \varepsilon} & T_{d_{Cor} \rightarrow \varepsilon} & T_{n \rightarrow \varepsilon} \\ T_{r \rightarrow u} & T_{d_{Cor} \rightarrow u} & T_{n \rightarrow u} \\ T_{r \rightarrow v} & T_{d_{Cor} \rightarrow v} & T_{n \rightarrow v} \end{bmatrix} = \begin{bmatrix} I - SGK_1 & -SG & T \\ S_I K_1 & -T_I & K_2 S \\ S_I K_1 & S_I & K_2 S \end{bmatrix}, \quad (4.29)$$

where $S = (I - GK_2)^{-1}$ is the output sensitivity function, $T = I - S = -SGK_2 = -GK_2S$ is the output complementary sensitivity function, $S_I = (I - K_2G)^{-1}$ is the input sensitivity function and $T_I = I - S_I$ is the input complementary sensitivity function.

To express the desired performance- and robustness-related frequency constraints of Chapter 3, we consider the block diagram of Figure 4.21, which can be represented in the general control configuration of Figure 4.1 or Figure 4.2 with $\tilde{w} = \text{col}(x_m^{ref}, d_{Cor}, n)$ and $\tilde{z} = \text{col}(\varepsilon, u, v_y)$, $W_{in} = \text{diag}(W_{r1}, W_d, W_n)$ with $W_d = \text{diag}(W_{d1}, W_{d2})$ and $W_n = \text{diag}(W_{n1}, W_{n2})$, and $W_{out} = \text{diag}(W_\varepsilon, W_u, W_{est})$ with $W_\varepsilon = \text{diag}(W_{\varepsilon1}, W_{\varepsilon2})$ and $W_u = \text{diag}(W_{u1}, W_{u2})$, $u_P = \text{col}(u_x, u_y)$, and $y_P = \text{col}(x_m^{ref}, 0, x_n, y_n)$.

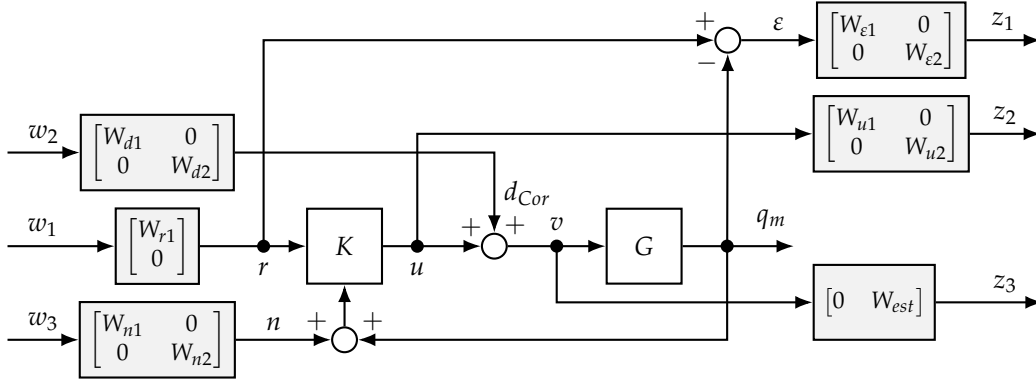


FIGURE 4.21: Block diagram for the 2DoF MIMO control design.

The \mathcal{H}_∞ problem is then to compute the controller $K = [K_1, K_2]$, if there is any, such that

$$\|T_{w \rightarrow z}\|_\infty = \left\| \begin{bmatrix} W_\varepsilon T_{x_m^{ref} \rightarrow \varepsilon} W_{r1} & W_\varepsilon T_{d_{Cor} \rightarrow \varepsilon} W_d & W_\varepsilon T_{n \rightarrow \varepsilon} W_n \\ W_u T_{x_m^{ref} \rightarrow u} W_{r1} & W_u T_{d_{Cor} \rightarrow u} W_d & W_u T_{n \rightarrow u} W_n \\ W_{est} T_{x_m^{ref} \rightarrow \varepsilon_{est}} W_{r1} & W_{est} T_{d_{Cor} \rightarrow \varepsilon_{est}} W_d & W_{est} T_{n \rightarrow \varepsilon_{est}} W_n \end{bmatrix} \right\|_\infty < \gamma. \quad (4.30)$$

In contrast to the SISO approach, where all frequency constraints are defined on SISO transfer functions, in a MIMO approach, the frequency constraints can be defined on SISO or on MIMO transfer functions. In our case, all the performance-related constraints are based on SISO transfer functions, while the robustness-related frequency constraints are defined on MIMO transfer functions.

Let us first consider the performance-related constraints. If there exists a solution for the problem above with $\gamma \leq 1$, then (4.30) implies that the \mathcal{H}_∞ norm of each individual element of the matrix is also upper bounded by 1. Thus, $\forall \omega \in \mathbb{R}$,

$$\begin{aligned} |T_{x_m^{ref} \rightarrow \varepsilon_x}| &< \frac{1}{|W_{\varepsilon1} W_{r1}|}, & |T_{d_{Cor,x} \rightarrow \varepsilon_x}| &< \frac{1}{|W_{\varepsilon1} W_{d1}|}, & |T_{d_{Cor,y} \rightarrow \varepsilon_x}| &< \frac{1}{|W_{\varepsilon1} W_{d2}|}, \\ |T_{x_m^{ref} \rightarrow \varepsilon_y}| &< \frac{1}{|W_{\varepsilon2} W_{r1}|}, & |T_{d_{Cor,x} \rightarrow \varepsilon_y}| &< \frac{1}{|W_{\varepsilon2} W_{d1}|}, & |T_{d_{Cor,y} \rightarrow \varepsilon_y}| &< \frac{1}{|W_{\varepsilon2} W_{d2}|}, \\ |T_{x_m^{ref} \rightarrow \varepsilon_{est}}| &< \frac{1}{|W_{est} W_{r1}|}, & |T_{d_{Cor,x} \rightarrow \varepsilon_{est}}| &< \frac{1}{|W_{est} W_{d1}|}, & |T_{d_{Cor,y} \rightarrow \varepsilon_{est}}| &< \frac{1}{|W_{est} W_{d2}|}, \\ |T_{n_x \rightarrow \varepsilon_{est}}| &< \frac{1}{|W_{est} W_{n1}|}, & |T_{n_y \rightarrow \varepsilon_{est}}| &< \frac{1}{|W_{est} W_{n2}|}. \end{aligned}$$

Similar to the SISO approach, the performance-related specifications are enforced through the choice of the corresponding weighting functions.

Let us now consider the robustness-related constraints, which are based on the frequency response of MIMO transfer functions. For instance, for additive uncertainties $\Delta E \in \Delta_{\text{add}}$, defined by the matrices $W_{\text{add},1}$ and $W_{\text{add},2}$, the closed-loop system has to present the following property (see (3.64)):

$$\|W_{\text{add},2}T_{n \rightarrow u}W_{\text{add},1}\|_{\infty} = \sup_{\omega \in \mathbb{R}} \bar{\sigma}(W_{\text{add},2}(j\omega)T_{n \rightarrow u}(j\omega)W_{\text{add},1}(j\omega)) < 1. \quad (4.31)$$

Note that, if $\gamma \leq 1$, (4.30) implies that $\|W_u T_{n \rightarrow u} W_n\|_{\infty} < 1$. Therefore, if W_u and W_n are such that $\|W_{\text{add},2}T_{n \rightarrow u}W_{\text{add},1}\|_{\infty} \leq \|W_u T_{n \rightarrow u} W_n\|_{\infty}$, (4.31) holds and the stability against all $\Delta E \in \Delta_{\text{add}}$ is ensured.

Before to proceed with a numerical example, it is important to mention a limitation of this control architecture. Demanding an accurate estimation of $d_{\text{Cor},y}$ is contradictory to the minimization of the displacements along the \vec{y} axis. To justify this claim, let us partition

$G = \begin{bmatrix} G_{xx} & G_{xy} \\ G_{yx} & G_{yy} \end{bmatrix}$. In the frequency domain, its output vector can be given by

$$\begin{bmatrix} x_m(j\omega) \\ y_m(j\omega) \end{bmatrix} = \begin{bmatrix} G_{xx}(j\omega) & G_{xy}(j\omega) \\ G_{yx}(j\omega) & G_{yy}(j\omega) \end{bmatrix} \begin{bmatrix} v_x(j\omega) \\ v_y(j\omega) \end{bmatrix}.$$

Hence, if all the closed-loop transfers to $\varepsilon_{\text{est}} = v_y$ have small gains around $\omega = \omega_{\text{exc}}$ (requirement for an accurate estimation) and $x_m \approx x_m^{\text{ref}}$ (accurate reference tracking), in this frequency range, we have $v_y(j\omega_{\text{exc}}) \approx 0$ and $v_x(j\omega_{\text{exc}}) \approx x_m^{\text{ref}}(j\omega_{\text{exc}})/G_{xx}(j\omega_{\text{exc}})$, which leads to

$$y_m(j\omega_{\text{exc}}) \approx \frac{G_{yx}(j\omega_{\text{exc}})}{G_{xx}(j\omega_{\text{exc}})} x_m^{\text{ref}}(j\omega_{\text{exc}}).$$

Since $T_{x_m^{\text{ref}} \rightarrow y_m}(j\omega_{\text{exc}}) = y_m(j\omega_{\text{exc}})/x_m^{\text{ref}}(j\omega_{\text{exc}})$, the accurate estimation and reference tracking requirements impose

$$\left| T_{x_m^{\text{ref}} \rightarrow \varepsilon_y}(j\omega_{\text{exc}}) \right| = \left| T_{x_m^{\text{ref}} \rightarrow y_m}(j\omega_{\text{exc}}) \right| \approx \left| \frac{G_{yx}(j\omega_{\text{exc}})}{G_{xx}(j\omega_{\text{exc}})} \right|, \quad (4.32)$$

showing that, under these conditions and for $\omega \approx \omega_{\text{exc}}$, the controller cannot minimize $\left| T_{x_m^{\text{ref}} \rightarrow y_m} \right|$ further than $|G_{yx}/G_{xx}|$. Obviously, by relaxing the requirements for reference tracking and accurate estimation, $\left| T_{x_m^{\text{ref}} \rightarrow y_m} \right|$ can be reduced and a trade-off can be made. In the next subsection, however, we show how to avoid this structural constraint.

Example 4.5 (2DoF multivariable control design for a MEMS gyroscope). *Let us consider the plant of Example 2.3 and the following specifications.*

- (i) **SFNL (drive-mode reference tracking and estimation of the Coriolis force):** SFNL smaller than 500 ppm, i.e., reference tracking of a sinusoidal signal with relative error smaller than $\check{\xi}_x < 0.5k_{\text{SFNL}} = 250 \cdot 10^{-6}$ and estimation of a sinusoidal signal with relative error $\check{\xi}_{\text{est}} < 0.5k_{\text{SFNL}} = 250 \cdot 10^{-6}$ ($\lambda_{\text{SFNL}} = 0.5$) for $\omega_{\text{exc}} = \omega_{0,x}$.
- (ii) **Sense-mode disturbance rejection:** minimize the displacement of the proof mass along the \vec{y} -axis, i.e., minimize k_{y2} .
- (iii) **Bandwidth:** $\omega_B \geq \omega_B^{\text{des}} = 2\pi 200 \text{ rad s}^{-1}$.
- (iv) **ARW:** minimize the ARW, i.e., minimize k_n .

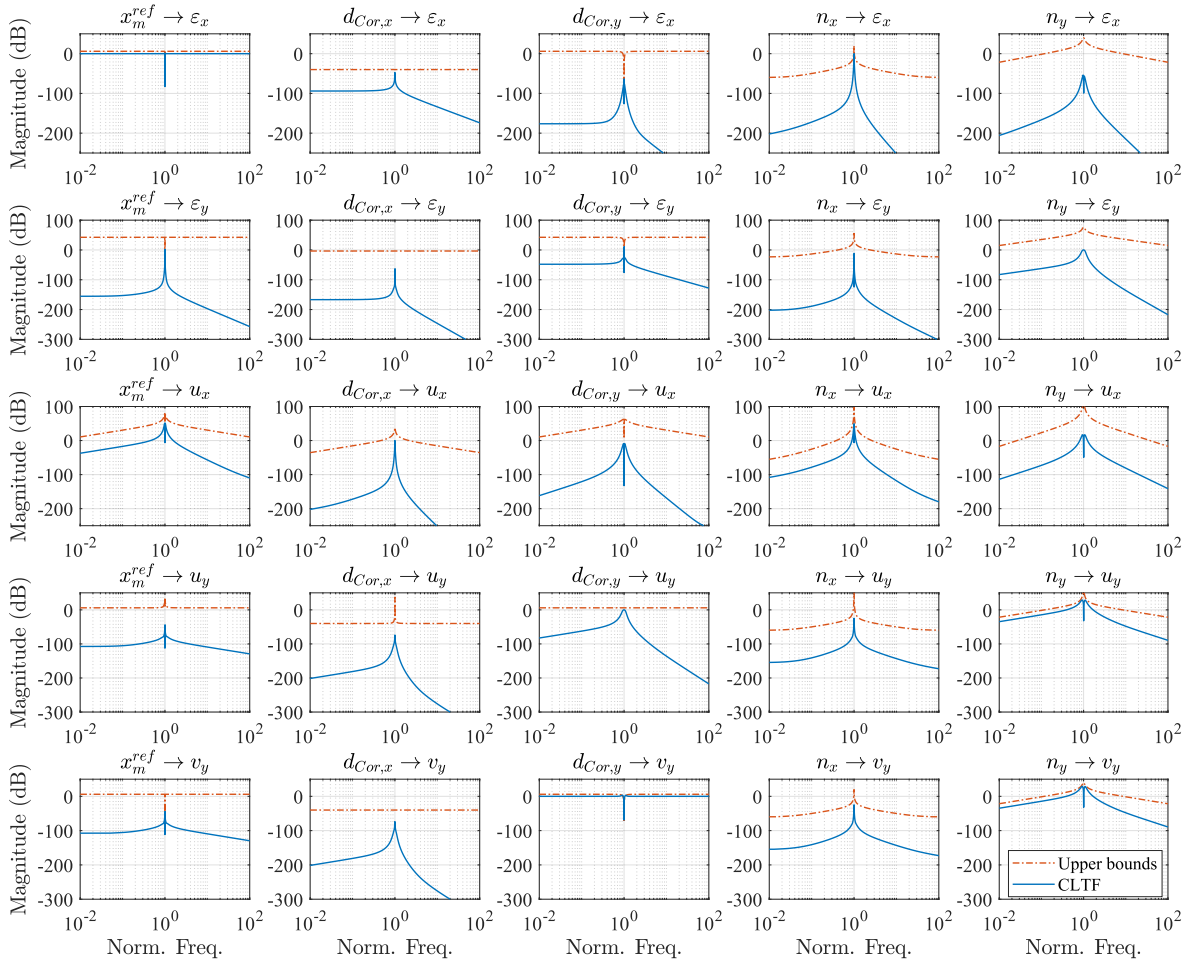


FIGURE 4.22: Upper bounds and closed-loop frequency responses for Example 4.5.

(v) **Band-pass condition:** ensure the band-pass condition of $\hat{u}_{Cor,y}$.

(vi) **Robustness against additive uncertainties:** minimize $\bar{\sigma}(T_{n_y \rightarrow \epsilon_{est}})$ where $\bar{\sigma}(W_{add,1})$ is important (low and high frequencies).

Based on the \mathcal{H}_∞ synthesis, we aim to design a multivariable controller for a MEMS gyroscopes that ensures the above specifications. To this purpose, we consider the \mathcal{H}_∞ criterion defined by the scheme of Figure 4.21 and weighting functions that enforce the upper bounds of the figures 4.22 and 4.23.

As well as for the previous examples, the weighting functions are chosen first to enforce the “hard constraints” – reference tracking, accurate estimation and bandwidth. The other weighting functions are iteratively chosen to enforce the rest of the specifications. Their expression and numerical values are given in Appendix C.5.

By solving the standard \mathcal{H}_∞ problem with $\gamma = 1.7245$, we obtain the 16th-order controller whose Bode diagram is presented in Figure 4.25 and numerical values are also given in Appendix C.5. Concerning the closed-loop frequency responses given in Figure 4.22 and Figure 4.23, let us focus on the transfer from x_m^{ref} to ϵ_y (see the second row of the first column in Figure 4.23). Even if the weighting functions enforce this transfer to have a gain smaller than $1/60 \approx -36$ dB for $\omega \approx \omega_{exc}$ (we would like to minimize even further), due to the structural constraint of (4.32), this value cannot be achieved.

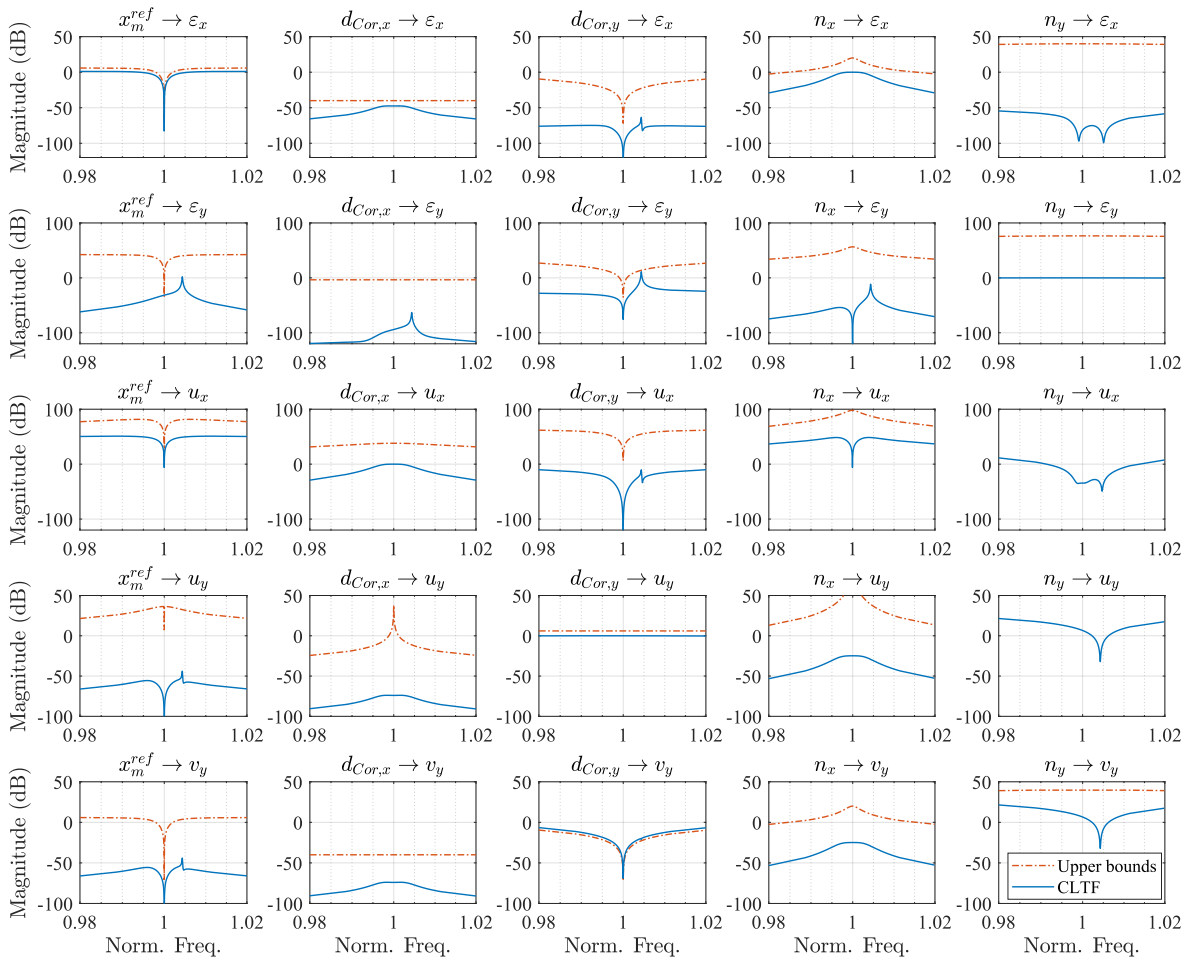


FIGURE 4.23: Upper bounds and closed-loop frequency responses for Example 4.5. Zoom around ω_{exc} .

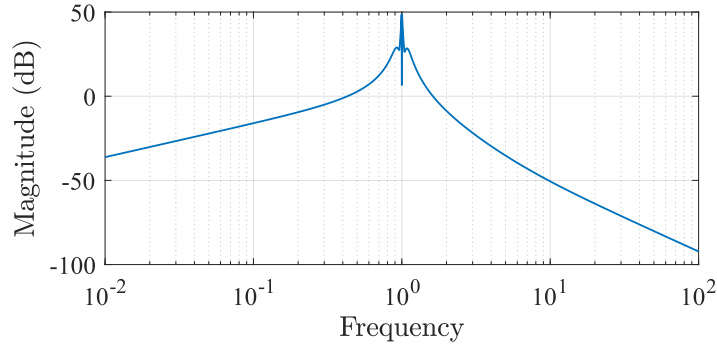


FIGURE 4.24: Largest singular value of $T_{n \rightarrow u}$ for Example 4.5.

Indeed, in this example, $\left| G_{yx}(j\omega_{exc}) / G_{xx}(j\omega_{exc}) \right| = 0.02184 \approx -31 \text{ dB}$, which also corresponds to the value of $\left| T_{x_m^{ref} \rightarrow \varepsilon_y}(j\omega_{exc}) \right|$, confirming the discussion related to this structural constraint.

The robustness of the closed-loop system against additive uncertainties is optimized by reducing at best the magnitude of the individual transfers of $T_{n \rightarrow u} = \begin{bmatrix} T_{n_x \rightarrow u_x} & T_{n_y \rightarrow u_x} \\ T_{n_x \rightarrow u_y} & T_{n_y \rightarrow u_y} \end{bmatrix}$ in low and high frequencies through the choice of W_n . A measure of the robustness can be given by $\bar{\sigma}(T_{n \rightarrow u})$, which is represented in Figure 4.24 (see discussion in Section 3.4.2). Therefore, this controller ensures the stability of the system even if the model uncertainties are important in low and high frequencies. However, the model is required to be precise around the resonance frequency.

Finally, the Bode diagram of the controller is presented in Figure 4.25a and Figure 4.25b. Since the second input of the controller is set to zero, we can eliminate this input. The controller is then partitioned as $K = \begin{bmatrix} K_{11} & K_{12} & K_{13} \\ K_{21} & K_{22} & K_{23} \end{bmatrix}$ with the input vector $\text{col}(x_m^{ref}, x_n, y_n)$ and output vector $\text{col}(u_x, u_y)$. We can note that K_{11} and K_{12} are similar to the drive-mode controller of Example 4.3 and K_{23} is similar to the sense-mode controller of Example 4.4. The other terms correspond to the cross-coupling and allow the controller to properly take the gyroscope mechanical coupling into account.

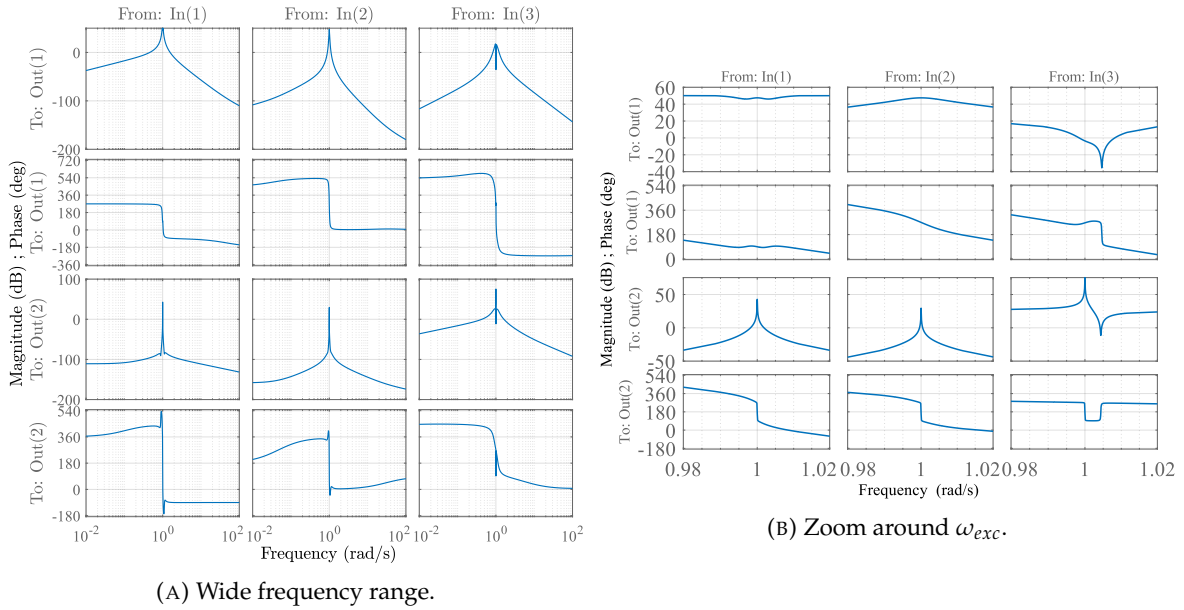


FIGURE 4.25: Bode diagrams of the controller obtained in Example 4.5.

4.3.2 MIMO 2DoF Control Architecture with Joint Estimation

We have just discussed that in the MIMO approach of Section 4.3.1, we cannot have a controller that ensures at the same time an accurate reference tracking, a precise estimation of $d_{Cor,y}$ and the minimization of $\left| T_{x_m^{ref} \rightarrow y_m} \right|$ beyond a certain value. In this subsection, we present a novel control architecture that allows avoiding this constraint.

We consider the control configuration of Figure 4.26, which is similar to the control configuration of Figure 4.20. The difference is that now the controller has a third output: $\hat{u}_{Cor,y}$. The controller is now given by $K = \begin{bmatrix} K_1 & K_2 \\ K_3 & K_4 \end{bmatrix}$, where K_1 and K_2 are still feedforward and positive-feedback controllers, respectively; and $K_{est} = [K_3, K_4]$ behaves like a filter that, based on the signals $x_m^{ref}, y_m^{ref}, x_n$ and y_n and on the plant model G , directly estimates $d_{Cor,y}$.

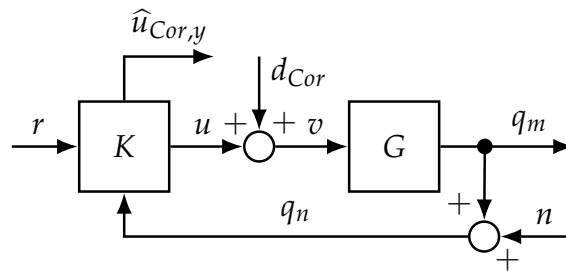


FIGURE 4.26: Multivariable 2DoF control configuration with joint estimation.

By defining the signals of interest $\tilde{w} = \text{col}(r, d_{Cor}, n)$ and $\tilde{z} = \text{col}(\varepsilon, u, v, \varepsilon_{est})$ with $\varepsilon = r - q_m$ and $\varepsilon_{est} = d_{Cor,y} - \hat{u}_{Cor,y}$, the above closed-loop system defines the following transfer

matrix:

$$\begin{bmatrix} T_{r \rightarrow \varepsilon} & T_{d_{Cor} \rightarrow \varepsilon} & T_{n \rightarrow \varepsilon} \\ T_{r \rightarrow u} & T_{d_{Cor} \rightarrow u} & T_{n \rightarrow u} \\ T_{r \rightarrow v} & T_{d_{Cor} \rightarrow v} & T_{n \rightarrow v} \\ T_{r \rightarrow \varepsilon_{est}} & T_{d_{Cor} \rightarrow \varepsilon_{est}} & T_{n \rightarrow \varepsilon_{est}} \end{bmatrix} = \begin{bmatrix} I - SGK_1 & -SG & T \\ S_I K_1 & -T_I & K_2 S \\ S_I K_1 & S_I & K_2 S \\ (K_4 SG + K_3) K_1 & I - K_4 SG & -K_4 S \end{bmatrix}, \quad (4.33)$$

where the sensitivity functions are the same of (4.29). Moreover, we note that the difference between (4.29) and (4.33), as claimed at the beginning of this section, is that in the latter equation, the transfers to ε_{est} (last line) are, in a certain extent, independent from those to v (third line).

To express the desired performance- and robustness-related frequency constraints of Chapter 3, we consider the block diagram of Figure 4.27, which can be represented in the general control configuration of Figure 4.1 or Figure 4.2 with $\tilde{w} = \text{col}(x_m^{ref}, d_{Cor}, n)$ and $\tilde{z} = \text{col}(\varepsilon, u, \varepsilon_{est})$, $W_{in} = \text{diag}(W_{r1}, W_d, W_n)$ with $W_d = \text{diag}(W_{d1}, W_{d2})$ and $W_n = \text{diag}(W_{n1}, W_{n2})$, $W_{out} = \text{diag}(W_\varepsilon, W_u, W_{est})$ with $W_\varepsilon = \text{diag}(W_{\varepsilon1}, W_{\varepsilon2})$ and $W_u = \text{diag}(W_{u1}, W_{u2})$, $u_P = \text{col}(u_x, u_y, \hat{u}_{Cor,y})$, and $y_P = \text{col}(x_m^{ref}, 0, x_n, y_n)$.

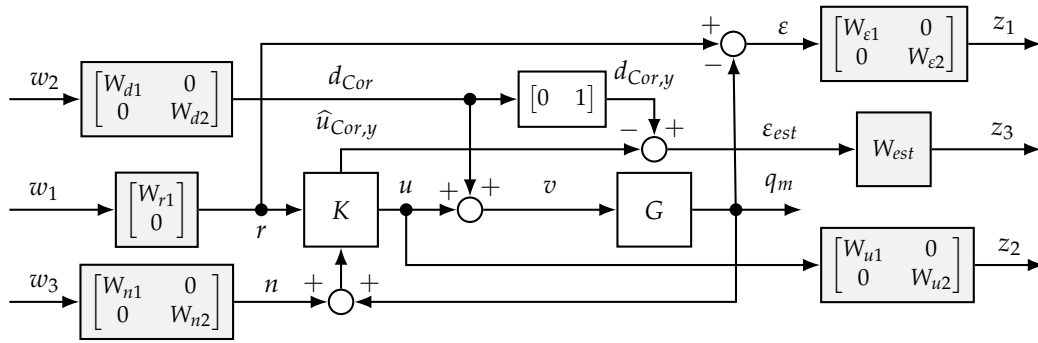


FIGURE 4.27: Block diagram for the 2DoF MIMO control design with joint estimation.

The \mathcal{H}_∞ problem is then to compute the controller K , if there is any, such that

$$\|T_{w \rightarrow z}\|_\infty = \left\| \begin{bmatrix} W_\varepsilon T_{x_m^{ref} \rightarrow \varepsilon} W_{r1} & W_\varepsilon T_{d_{Cor} \rightarrow \varepsilon} W_d & W_\varepsilon T_{n \rightarrow \varepsilon} W_n \\ W_u T_{x_m^{ref} \rightarrow u} W_{r1} & W_u T_{d_{Cor} \rightarrow u} W_d & W_u T_{n \rightarrow u} W_n \\ W_{est} T_{x_m^{ref} \rightarrow \varepsilon_{est}} W_{r1} & W_{est} T_{d_{Cor} \rightarrow \varepsilon_{est}} W_d & W_{est} T_{n \rightarrow \varepsilon_{est}} W_n \end{bmatrix} \right\|_\infty < \gamma, \quad (4.34)$$

Example 4.6 (2DoF multivariable control design for a MEMS gyroscope with joint estimation). Let us consider the plant, noise models and the specifications of Example 4.5. Then, based on the \mathcal{H}_∞ synthesis, we want to design a multivariable controller with joint estimation for a MEMS gyroscopes, ensuring the given specifications.

We consider the \mathcal{H}_∞ criterion defined by the scheme of Figure 4.27 and weighting functions that enforce the upper bounds of the figures Figure 4.28 and Figure 4.29. The weighting functions are first chosen to enforce the “hard constraints” – reference tracking, accurate estimation and bandwidth. The other weighting functions are iteratively chosen to enforce the other specifications. Their expression and numerical values are given in Appendix C.6.

By solving the standard \mathcal{H}_∞ problem with $\gamma = 1.1037$, we obtain a 14th-order controller whose Bode diagram is presented in Figure 4.31 and Figure 4.32. Its numerical values are also given

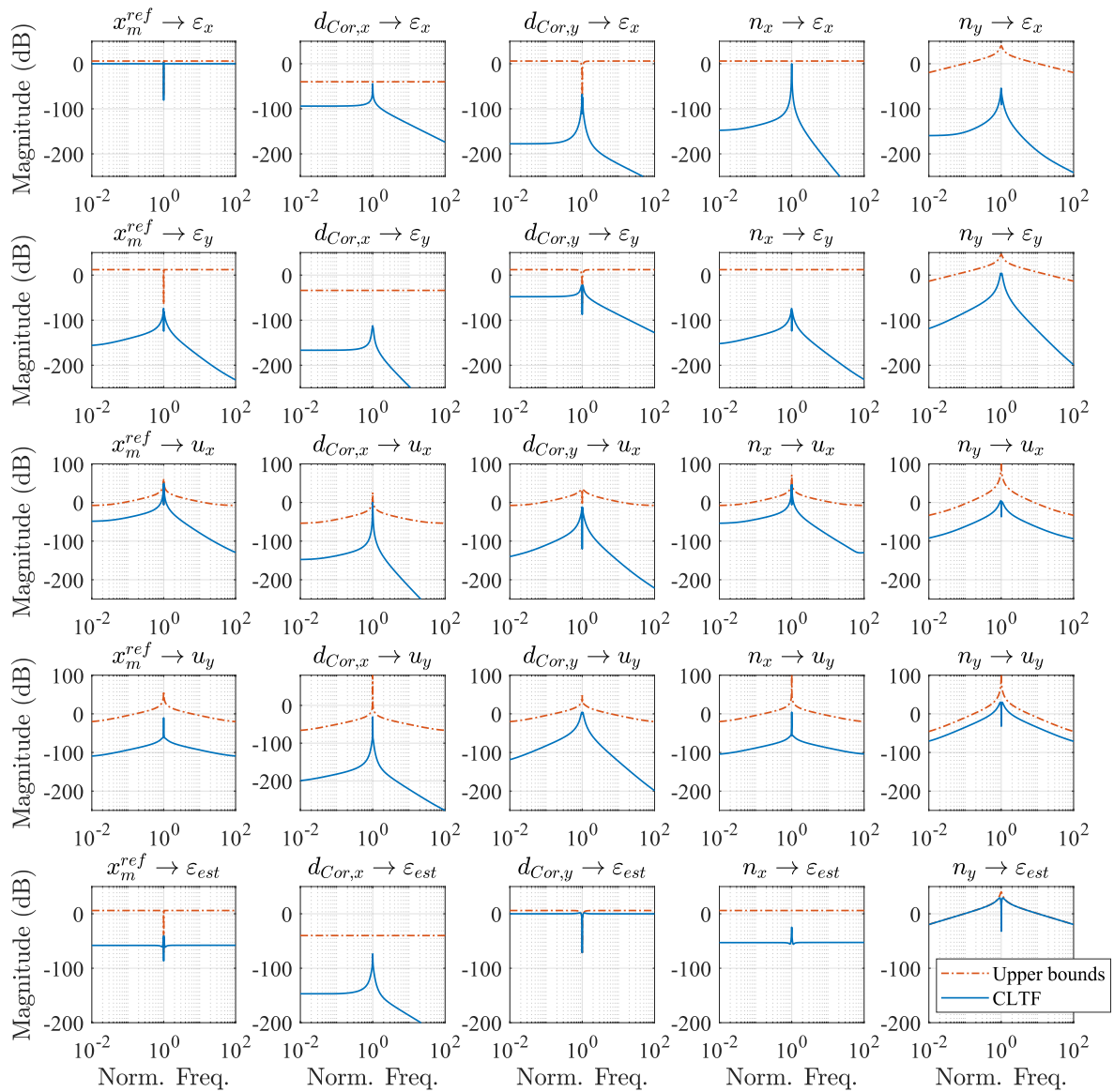


FIGURE 4.28: Upper bounds and closed-loop frequency responses for Example 4.6.

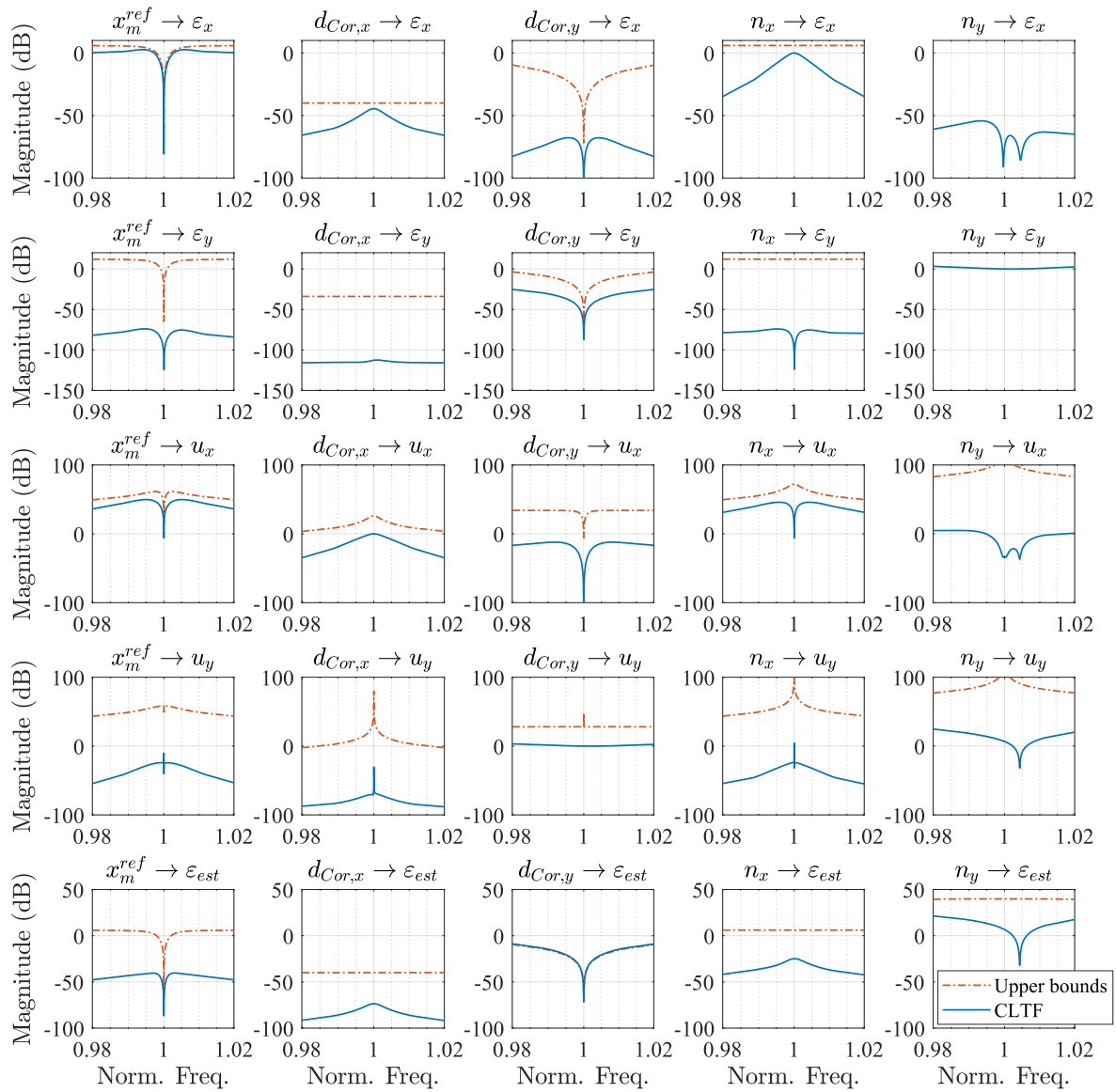


FIGURE 4.29: Upper bounds and closed-loop frequency responses for Example 4.6. Zoom around $\omega_{exc}(= 1)$.

in Appendix C.6. Concerning the closed-loop frequency responses given in Figure 4.28 and Figure 4.29, the results obtained in this example are globally similar to those of Example 4.5. The main difference appears on the transfer from x_m^{ref} to ε_y , whose magnitude at ω_{exc} is smaller than -120 dB, whereas in the previous example, it cannot be made smaller than -31 dB.

The robustness of the closed-loop system against additive uncertainties can be verified through the largest singular values of $T_{n \rightarrow u}$, presented in Figure 4.30. The results here are, again, very similar to those of Example 4.5.

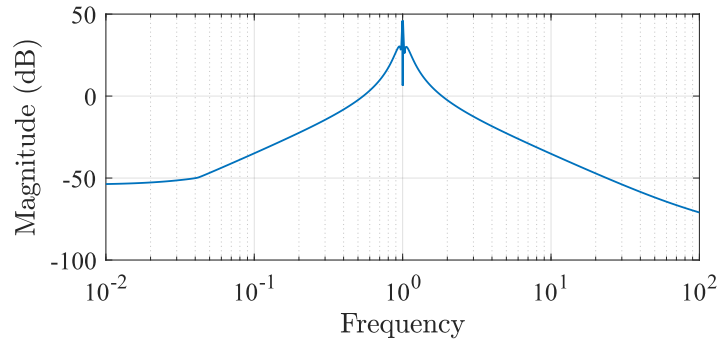


FIGURE 4.30: Largest singular value of $T_{n \rightarrow u}$ for Example 4.6.

Finally, the Bode diagram of the controller is presented in Figure 4.31 and Figure 4.32. The main difference of this controller, compared to that of Example 4.5, is that it presents a third output, which directly produces the estimate of the Coriolis force $\hat{u}_{Cor,y}$. Otherwise, the other elements of the controller are similar to the previous example. We recall that the second input of the controller is eliminated since it is set to zero. Therefore, the input vector of the controller is $\text{col}(x_m^{ref}, x_n, y_n)$ and its output vector is $\text{col}(u_x, u_y, \hat{u}_{Cor,y})$.

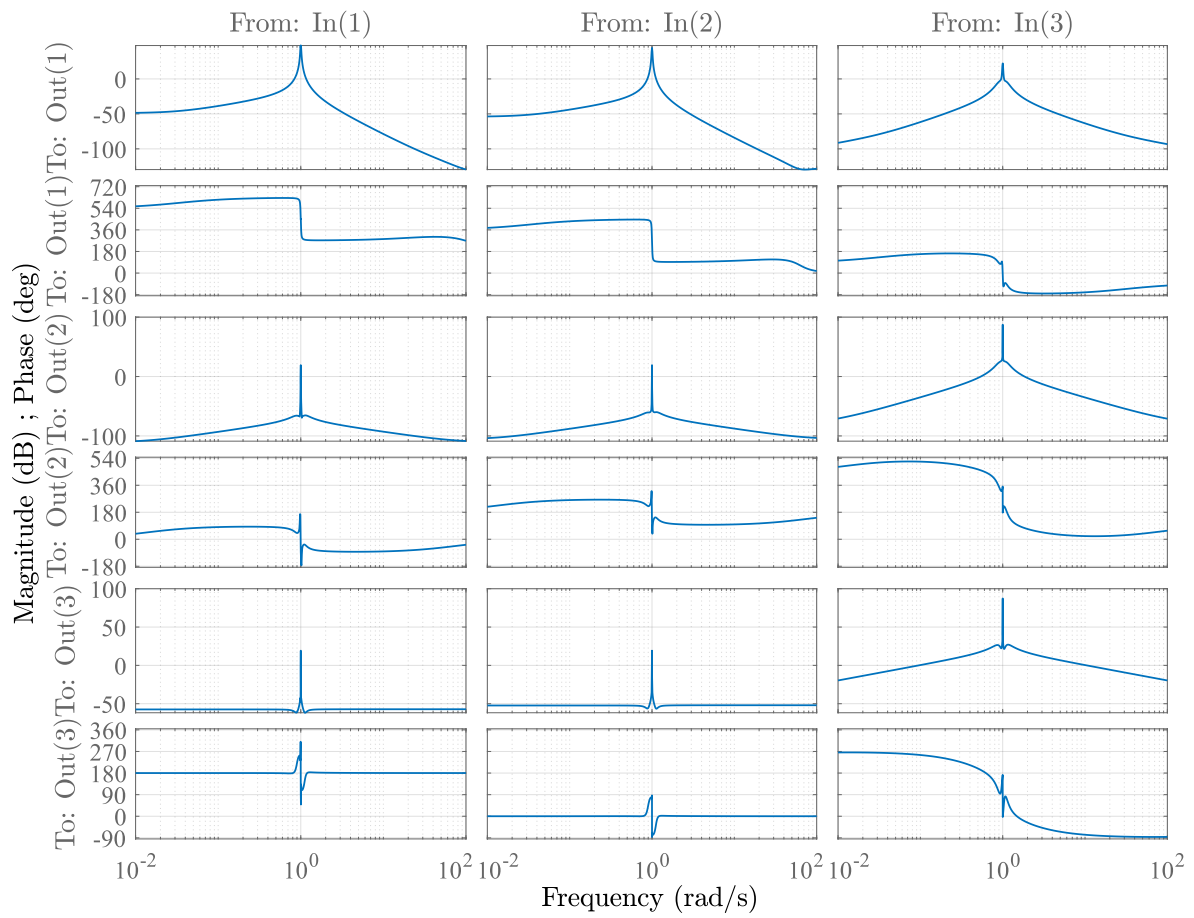


FIGURE 4.31: Bode diagram of the controller of Example 4.6.

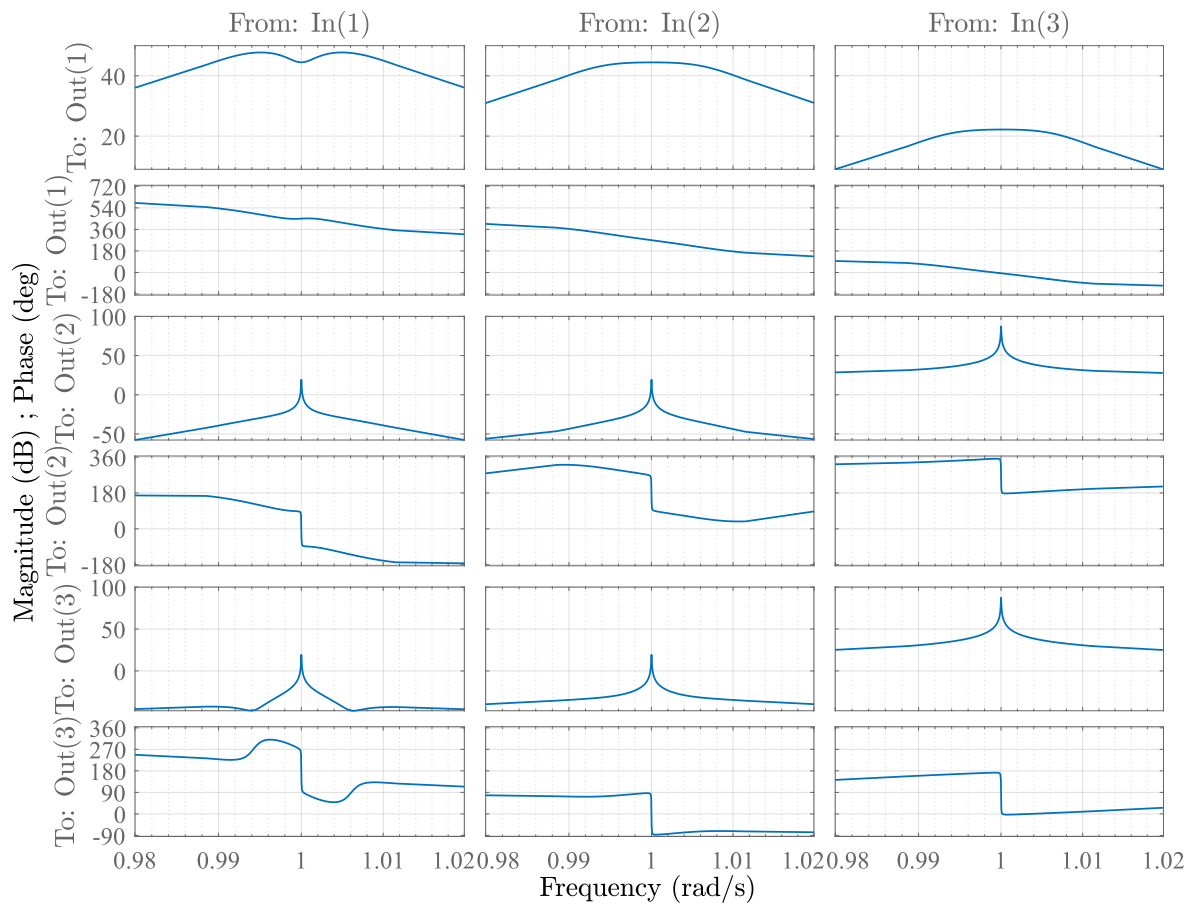


FIGURE 4.32: Bode diagram of the controller of Example 4.6. Zoom around $\omega_{exc}(= 1)$.

4.4 Validation of the Proposed Solutions

Since Chapter 3, and in the present chapter, we have made the important assumption that the Coriolis forces are exogenous to the MEMS gyroscope. This assumption is crucial to consider LTI design methods for the controller design (as the \mathcal{H}_∞ synthesis). Nevertheless, it is known that these forces are internal to the system and change its dynamics. In this section, we aim to show that, even if the effects of the Coriolis forces are not fully taken into account for the controller design, for the system under study, the designed controllers behave well when the Coriolis forces are properly considered. This means that the stability and performance obtained with the complete LTV model are the same as those obtained with the simplified LTI model, verifying Assumption 3.5 (page 59).

In this section, we want then to validate and compare two of the approaches proposed in this chapter.

SISO approach: the drive mode is in closed loop with the 2DoF controller of Example 4.3 and the sense mode with the 1DoF controller of Example 4.4. In this case, the overall controller K is given by

$$K = \begin{bmatrix} K_{x1} & K_{x2} & 0 \\ 0 & 0 & K_y \end{bmatrix} \quad (4.35)$$

and the estimate $\hat{u}_{Cor,y}$ is defined as $\hat{u}_{Cor,y} = -u_y$.

MIMO approach: the drive and sense modes are in closed loop with the MIMO controller with joint estimation of Example 4.6. In this case, the estimate $\hat{u}_{Cor,y}$ is directly computed by the controller (third output).

For both approaches, the controller design is based on the nominal model of the gyroscope (see the model of Example 2.1 and of Example 2.2 for the SISO approach, and that of Example 2.3 for the MIMO approach).

The validation for each approach is realized in two steps. First, we assess the stability of the closed-loop system. This analysis consists in solving a feasibility problem under LMI constraints. Then, a numerical simulation is performed to confirm and illustrate the results. Finally, we compare the simulation results of the considered approaches.

4.4.1 Assessing the Stability of the Closed-Loop System

Here, we want to assess the stability of the closed-loop system composed of an LTI controller (SISO or MIMO controller) and the full nominal model of the MEMS gyroscope, which depends on Ω_z . For this purpose, we adopt a standard polytopic approach, as follows.

First, we compute the state-space representation of the closed-loop system. As discussed in Section 2.1.5 (page 27), the MEMS gyroscope can be modeled (neglecting the dependence on θ and ρ) by G^{Ω_z} , which admits the representation below

$$G^{\Omega_z} : \begin{cases} \dot{x}_G(t) &= A_G(\Omega_z(t))x_G(t) + B_G u(t) \\ q_m(t) &= C_G x_G(t) \end{cases}, \quad \Omega_z(t) \in [\Omega_{z,1}, \Omega_{z,2}], \quad (4.36)$$

where $\Omega_{z,1} = -\Omega_z^{FS}$, $\Omega_{z,2} = \Omega_z^{FS}$ and the dependence of A_G on $\Omega_z(t)$ is affine. The state-space matrices are detailed in Appendix C.7. In their turn, the LTI controllers (SISO or MIMO)

admit the following state-space representation

$$K : \begin{cases} \dot{x}_K(t) &= A_K x_K(t) + B_K [r(t) \ q_m(t)] \\ u(t) &= C_K x_K(t) + D_K [r(t) \ q_m(t)] \end{cases} . \quad (4.37)$$

Therefore, the closed-loop system can be written in the form

$$H^{\Omega_z} : \begin{cases} \dot{x}_H(t) &= A_H(\Omega_z(t)) x_H(t) + B_H r(t) \\ q_m(t) &= C_H x_H(t) \end{cases} , \quad \Omega_z(t) \in [\Omega_{z,1}, \Omega_{z,2}] , \quad (4.38)$$

with $x_H = \text{col}(x_G, x_K)$,

$$A_H(\Omega_z(t)) = \begin{bmatrix} A_G(\Omega_z(t)) + B_G D_K C_G & B_G C_K \\ B_K C_G & A_K \end{bmatrix} , \quad B_H = \begin{bmatrix} B_G D_K \\ B_K \end{bmatrix} \quad \text{and} \quad C_H = [C_G \ 0] .$$

The stability of this closed-loop system can be assessed through the following feasibility problem: let a system H^{Ω_z} be given by (4.38) with $\Omega_z(t) \in [\Omega_{z,1}, \Omega_{z,2}]$; if there exists a single symmetric matrix $X \succ 0$ such that

$$A_H(\Omega_{z,1})^\top X + X A_H(\Omega_{z,1}) \prec 0 \quad \text{and} \quad A_H(\Omega_{z,2})^\top X + X A_H(\Omega_{z,2}) \prec 0 ,$$

then H^{Ω_z} is asymptotically stable for all $\Omega_z(t) \in [\Omega_{z,1}, \Omega_{z,2}]$. This result follows immediately from the definition of quadratic stability for polytopic systems [AGB95]. Further details on the quadratic stability will be given in Section 5.3.1.

For the SISO and the MIMO approaches considered in this section, the above problem has a solution, proving the quadratic stability of the closed-loop system for all $\Omega_z(t) \in [-\Omega_z^{FS}, \Omega_z^{FS}]$. In the case of the SISO approach, this result also proves the stability of the system with respect to the mechanical couplings (neglected for the controller desing).

4.4.2 Validation Through Simulation

In this section, we simulate the control scheme of Figure 4.33, where the to-be-controlled system G^{Ω_z} is the same of Example 2.3 and the controllers are defined according to the chosen (SISO or MIMO) approach.

For both approaches, the reference signal is given by $x_m^{ref}(t) = A_{x,m}^{ref} \cdot \sin(\omega_{exc} t)$ with $A_{x,m}^{ref} = 0.5$ and $\omega_{exc} = \omega_{0,x}$. The filters of the synchronous demodulation (SD) are implemented with a 4th-order low-pass filter with cutoff frequency³ $\omega_c = 2\pi \cdot 3000 \text{ rad s}^{-1}$.

We start the system at rest (*i.e.*, $\Omega_z(t) = 0$). Then, we check if the drive mode operates properly. We apply the sinusoidal reference signal and observe the output x_m . This result is presented in Figure 4.34, where we can observe an accurate tracking of the reference signal for the SISO and MIMO approaches. Indeed, all the signals are superposed.

At 0.5 s, we apply an angular rate $\Omega_z(t) = 300^\circ \text{ s}^{-1}$ (which is also the full scale angular rate) and observe the other signals of the system. These signals are presented in Figure 4.35 and in Figure 4.36 for the SISO and MIMO approaches, respectively. First, it is important to note that, even when Ω_z varies, the closed-loop system is still stable in both cases. The first line of the figures presents the signals of the drive mode, where we can note that the

³Recall that, in contrast to an ideal filter (*e.g.*, see (2.25), page 24), a real filter has a transition band. Then, to properly attenuate the high-frequency terms of the synchronous demodulation, its cutoff frequency has to be quite smaller than ω_{exc} .

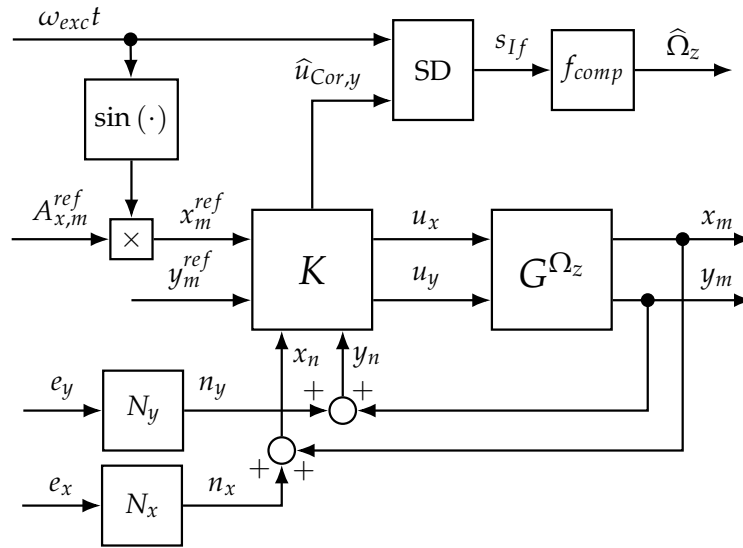


FIGURE 4.33: Control scheme considered for the simulations.

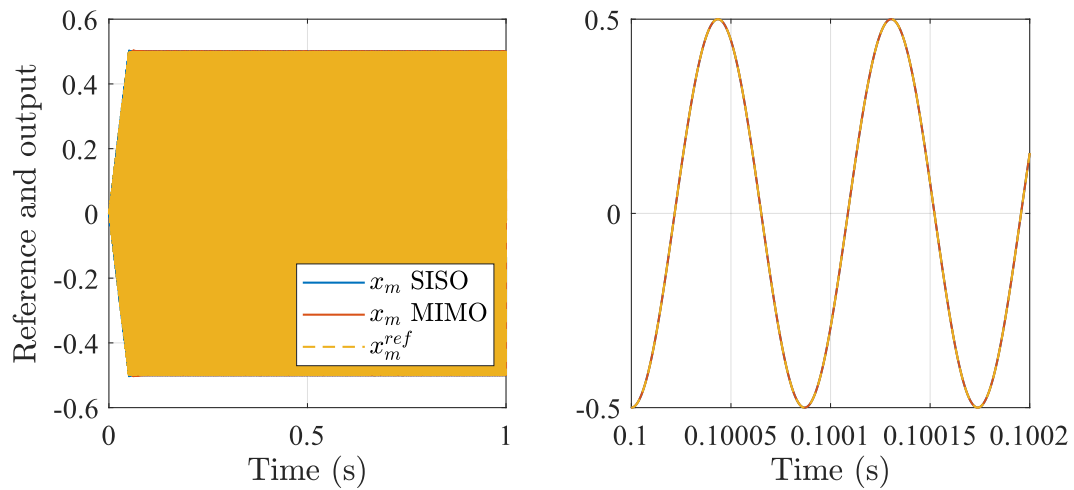


FIGURE 4.34: Simulation results for reference tracking (drive mode).

control signal u_x is practically not disturbed by the variation of Ω_z . The tracking error ε_x suffers a small disturbance, which quickly vanishes. Even if the tracking error of the MIMO approach is bigger than that of the SISO one, both of them achieve the desired performance (for $A_{x,m}^{ref} = 0.5$, $|\varepsilon_x| < 1.25 \cdot 10^{-4} = \xi_x \cdot A_{x,m}^{ref}$). Moreover, it is interesting to note that the amplitude of the control signal is slightly smaller for the MIMO approach. This is justified by the fact that with a multivariable approach, the controller uses at the same time the signals u_x and u_y to make $x_m \approx x_m^{ref}$ and to keep $y_m \approx 0$.

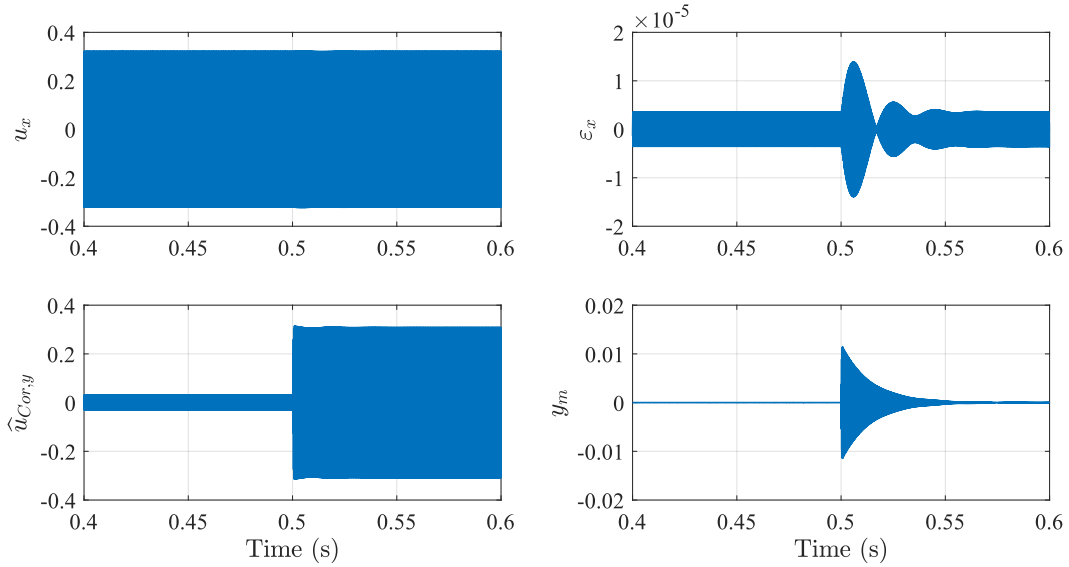


FIGURE 4.35: Signals of the closed-loop system for a variation of Ω_z for the SISO approach.

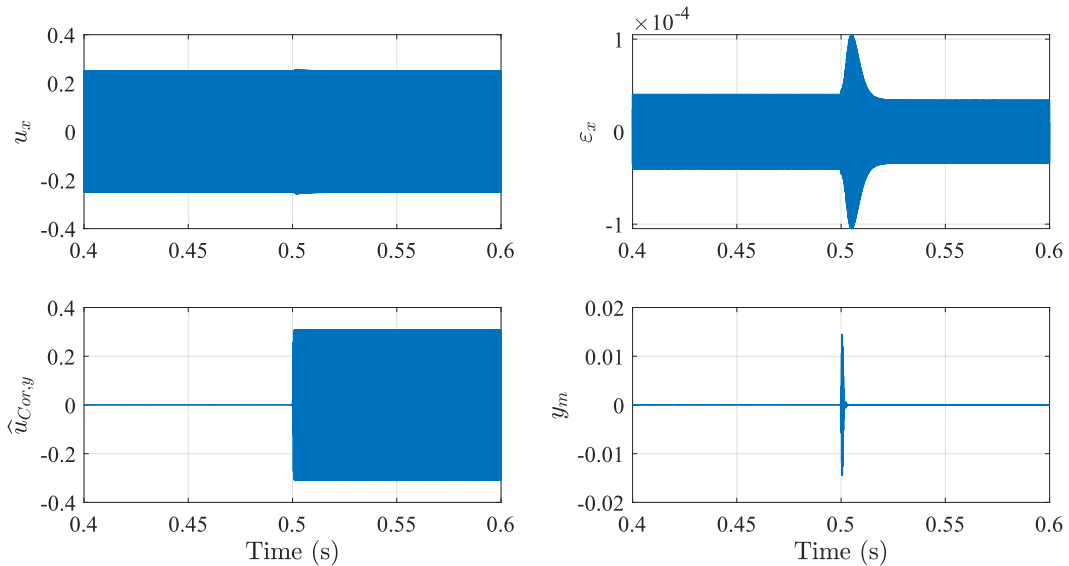


FIGURE 4.36: Signals of the closed-loop system for a variation of Ω_z for the MIMO approach.

Now, when we observe the sense-mode signals (second line of the figures), we observe that oscillations appear on y_m when there is a variation of the angular rate. However, these oscillations are quickly attenuated by the controller with a steady-state amplitude which is always smaller than $1 \cdot 10^{-4}$. However, the multivariable controller is able to reject them

much quicker. Finally, for the SISO approach, the amplitude of $\hat{u}_{Cor,y}$ rapidly passes from 0.03 to around 0.3 at 0.5 s. The amplitude of 0.03 corresponds to the compensation of the mechanical coupling forces, which disturb the sense mode. The 0.3 amplitude represents the contributions of the Coriolis force and the mechanical coupling ones. On the other hand, the MIMO controller estimates only the Coriolis force. Based on the MIMO model of the MEMS gyroscope, the controller is able to distinguish between the Coriolis and the mechanical coupling forces. Moreover, the estimate of the MIMO controller achieves the steady-state much quicker than the SISO controller. This analysis is confirmed when we look the synchronous demodulation output signals in Figure 4.37. The in-phase term s_{If} mainly represents the contributions of the Coriolis force, while the quadrature term s_{Qf} represents the contributions of the mechanical coupling forces⁴.

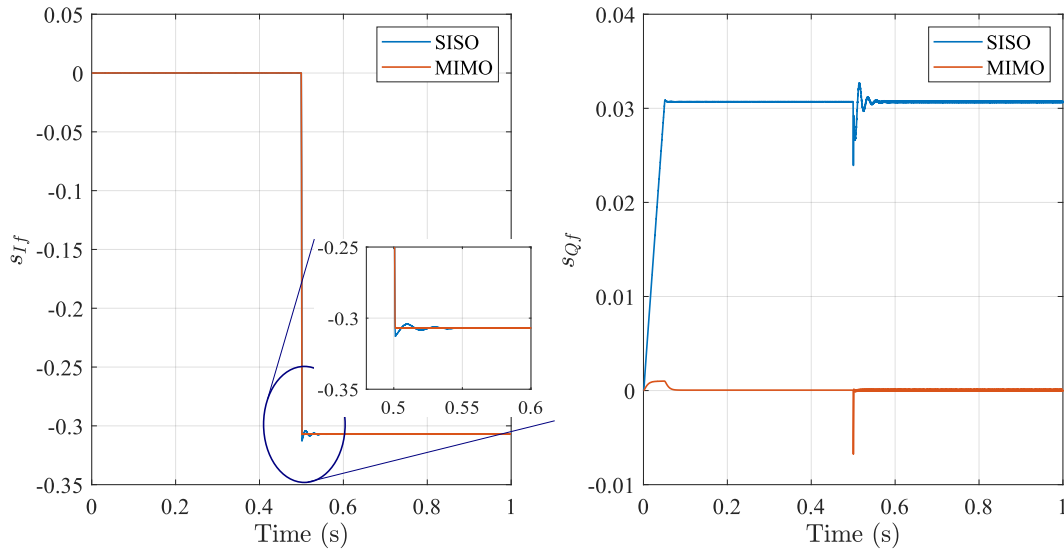


FIGURE 4.37: Synchronous demodulation output signals for a variation of Ω_z .

We repeat the same test with different values of Ω_z and evaluate how the steady-state value of s_{If} is related to Ω_z . We obtain the behavior of Figure 4.38 and Figure 4.39 for the SISO and MIMO approaches, respectively. Moreover, from the simulation data, we fit the best straight line, determining the scale factor and the zero-rate output (ZRO or bias) of the simulated system. For the SISO approach, we obtain

$$k_{SF} = -1.0234 \cdot 10^{-3} \text{units}/(^{\circ}/\text{s}) \quad \text{and} \quad k_{ZRO} = -7.5912 \cdot 10^{-7} \text{units}.$$

Moreover, based on the residue, *i.e.*, the difference between the simulated data and the linear fit, we can compute the SFNL, which in this case gives SFNL = 0.03 ppm. For the MIMO approach, we obtain

$$k_{SF} = -1.0234 \cdot 10^{-3} \text{units}/(^{\circ}/\text{s}), \quad k_{ZRO} = 8.0131 \cdot 10^{-5} \text{units} \quad \text{and} \quad \text{SFNL} = 0.04 \text{ppm}.$$

Please note that both approaches present similar performance and largely achieve the desired specification of SFNL (smaller than 500 ppm, value considered in the examples). These excellent results can be justified by some facts, as follows.

- The closed-loop specifications related to the SFNL, such as presented in Chapter 3, present a certain conservatism. Indeed, in Chapter 3, we consider that $\hat{k}_{SF} = k_{SF}$.

⁴The ramp at the beginning is linked to the ramp amplitude of x_m .

However, in these simulations, we estimate k_{SF} through the best straight line fitting the measures.

- In simulation, the presence of nonlinearities of actuation and instrumentation are not taken into account.

We highlight that these results are reassuring, since the real system may present some unmodeled behavior, which tend to degrade the SFNL.

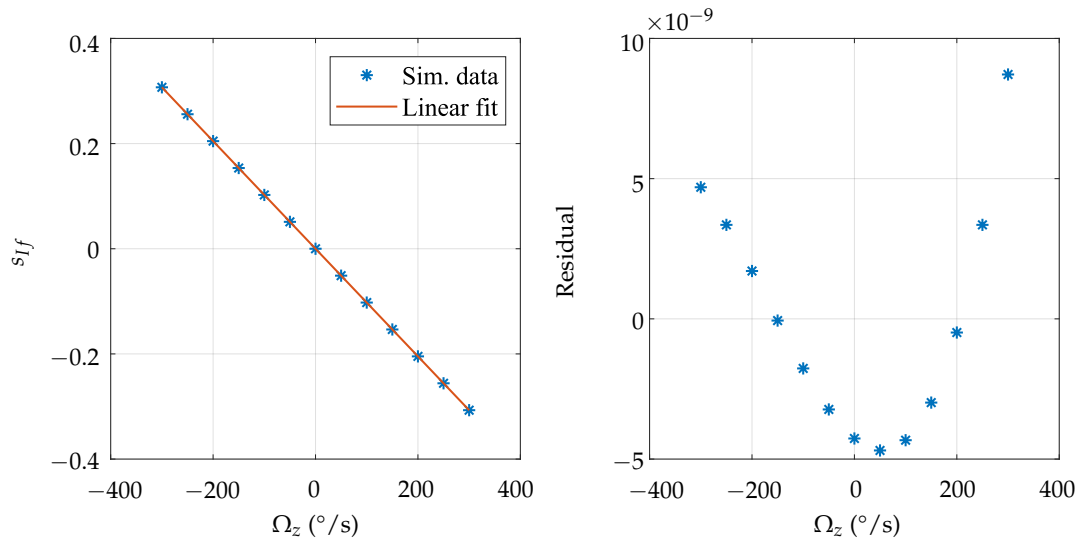


FIGURE 4.38: Evolution of s_{If} with respect to Ω_z for SISO approach and residual.

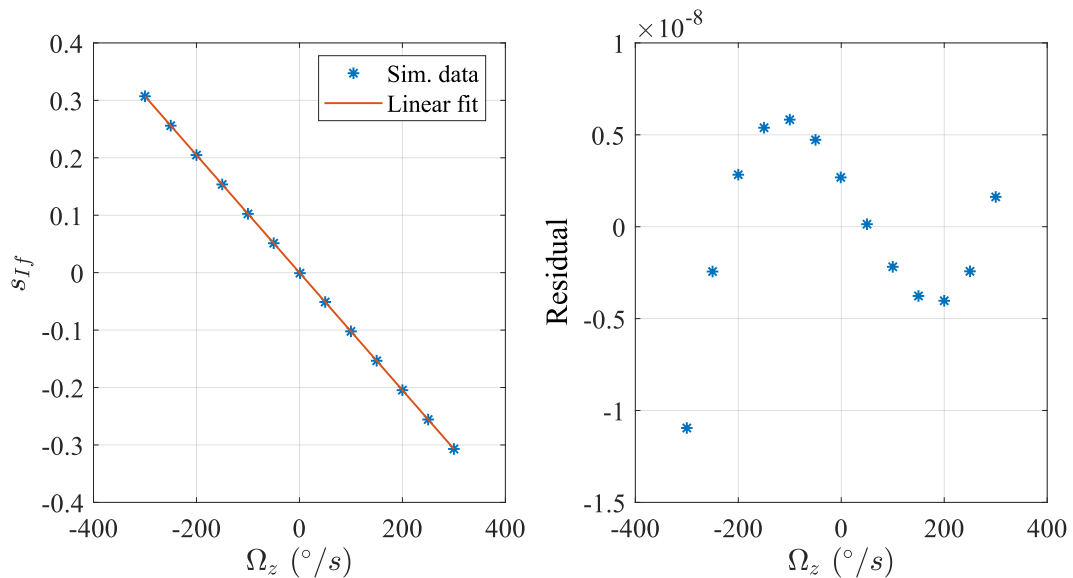


FIGURE 4.39: Evolution of s_{If} with respect to Ω_z for MIMO approach and residual.

4.5 Summary of the Chapter

In this chapter, we presented a control design method that allows to compute, in a flexible and systematic manner, controllers for the closed-loop operation of MEMS gyroscopes. This

method is based on the \mathcal{H}_∞ synthesis, which provides a powerful framework for the design of controllers ensuring a certain level of performance and robustness for LTI systems. The strength of the \mathcal{H}_∞ synthesis relies on the so-called \mathcal{H}_∞ criterion. Indeed, the proper choice of the \mathcal{H}_∞ criterion allows expressing closed-loop frequency constraints through weighting functions. As discussed in Chapter 3, the main global performance indicators of a MEMS gyroscope can be translated into frequency constraints on some of the closed-loop transfer functions, making the \mathcal{H}_∞ synthesis the natural choice for the control design.

Adopting the direct control approach, different control architectures are progressively presented. First, we consider a SISO approach, in which the drive- and sense-mode controllers are designed independently, considering the coupling forces as exogenous signals. For the drive mode, two architectures are presented: with a 1DoF and with a 2DoF controller. The main advantage of the 2DoF control configuration is that it allows distinguishing the reference tracking performance from those related to the robustness against additive uncertainties ($|T_{x_m^{ref} \rightarrow u_x}| \neq |T_{n_x \rightarrow u_x}|$). For the sense-mode control, only the 1DoF control configuration is considered.

In a second time, a MIMO approach is considered. The main strength of this approach is that the multivariable nature of the MEMS gyroscope (mechanical coupling between modes) is properly taken into account for the controller design, providing some guarantees of performance and robust stability. This is not possible with the SISO approach⁵. Moreover, the MIMO approach with joint estimation allows to directly compute $d_{Cor,y}$, allowing the signal u_y to be used for the minimization of y_m .

Regardless of the approach (SISO or MIMO), two important assumptions are considered along this chapter: (i) the Coriolis force is considered as an exogenous signal; and (ii) the ambient conditions (e.g., temperature, pressure) are steady. Under these assumptions, the MEMS gyroscope can be considered as an LTI system. Through some simulation results, we have shown that the proposed controllers behave well even when the angular rate slightly alters the dynamics of the system.

⁵Indeed, for the gyroscope considered in this chapter, by increasing the mechanical coupling, we can make the closed-loop system with SISO approach unstable.

Chapter 5

Direct Control II: Toward a Time-Varying Solution

In the previous chapter, we present a systematic method that allows us to design a controller for MEMS gyroscopes, fulfilling the specifications of Chapter 3. In both chapters, we consider that the operating conditions (such as the temperature and pressure) are fixed. Then, the main control specifications are cast as the tracking, rejection or estimation of sinusoidal signals with a constant excitation frequency¹, ω_{exc} .

In the direct control approach considered in Chapter 4, the excitation frequency is imposed by the reference signal and is assumed to be equal (or very close) to the resonance frequency of the drive mode $\omega_{0,x}$, taking advantage of its high gain at this frequency and requiring the minimal control effort. However, as discussed in Chapter 2, the operating conditions may change during the operation of the device, modifying $\omega_{0,x}$. Then, to keep the excitation frequency always close to $\omega_{0,x}$, an external loop is required. This external loop estimates $\omega_{0,x}$ and adapts ω_{exc} accordingly. In the scope of our project, two strategies are considered: Extremum Seeking and Recursive Identification. In both strategies, ω_{exc} is a signal which can be decomposed into two parts: a slow- and a fast-varying (or low- and high-frequency) term. The slow-varying term corresponds to the actual value of $\omega_{0,x}$, which varies slowly². On the other hand, the fast-varying term corresponds to the disturbances introduced by these algorithms. More details on these strategies and the first results can be found in the thesis [Mor21].

Obviously, when ω_{exc} changes, the reference signal is also modified. Moreover, since the performance specifications are parameterized by ω_{exc} , we also want to design a controller whose gains depend on this parameter, ensuring the best performance level in all operating conditions. Therefore, the main problem is to track/reject signals of the type

$$r(t) = A_r \sin \left(\int_0^t \omega_{exc}(\tau) d\tau + \phi_r^0 \right), \quad (5.1)$$

where the frequency ω_{exc} is known and can arbitrarily vary in a given range.

Here, we focus on the control of the drive mode in which we want to ensure the tracking/rejection of signals in the form of (5.1). Moreover, in this chapter, we consider only the case of fast variations of ω_{exc} . Under this condition, the model of the MEMS gyroscope does

¹Actually, to be precise, the Coriolis force is an amplitude-modulated signal with a constant-frequency carrier.

²The main factor contributing to variations of $\omega_{0,x}$ is usually the internal temperature, which, indeed, varies slowly.

not change and can be considered as an LTI system. The case of slow variations will be treated in Section 7.4 (page 183).

Although we focus on the MEMS gyroscope application, we highlight that the problem of tracking/rejecting signals of the type of (5.1) is also found in other applications, such as in the control of power converters or in electric machinery, see, e.g., [ZH03, PSSF17, RSPC17, CSF⁺17]. In general, these solutions consist in employing the internal model principle (IMP) and computing a controller that optimizes a generic performance criterion.

In this chapter, we propose a design method based on the standard LPV synthesis and on a novel performance criterion, which is specific for signals of the type of (5.1). Similar to the \mathcal{H}_∞ synthesis, weighting functions are used to express the control specifications. The main difficulty is, due to the time-varying nature of ω_{exc} , how to design weighting functions defining signals in the form of (5.1). An important contribution of this work is a new class of weighting functions that properly describe this type of signal.

The remaining of this chapter is organized as follows. Section 5.1 states the problem under investigation. In Section 5.2, we present our main result, allowing to recast the original problem as an LPV control problem. In this control problem, a new class of weighting functions is used to properly describe signals in the form of (5.1). In Section 5.3, we then present a solution to the LPV control problem. A numerical example and simulation results demonstrate the effectiveness of the proposed approach.

Before proceeding with the problem statement, let us recall some important definitions.

Some Useful Definitions

First, we introduce the definition of the \mathcal{L}_2 norm of a signal, which also defines an \mathcal{L}_2 space.

Definition 5.1 (\mathcal{L}_2 norm of a signal and \mathcal{L}_2 space [Hil13]). The \mathcal{L}_2 norm of a signal v from \mathbb{R}_+ to \mathbb{C}^{n_v} is defined as

$$\|v\|_2^2 = \int_0^\infty v(t)^* v(t) dt.$$

The set of signals for which the \mathcal{L}_2 norm is bounded is denoted \mathcal{L}_2 and defines the \mathcal{L}_2 space.

Please note that important classes of signals, such as a constant (nonnull) or periodic ones, are not included in the \mathcal{L}_2 space. Indeed, the \mathcal{L}_2 space includes only energy signals (or finite-energy signals). Then, to consider power signals (or finite-power signals), as a sinusoidal one, the extended \mathcal{L}_2 norm and space, denoted \mathcal{L}_2^e , are defined. Their definition rely on the truncation operator, defined as follows.

Definition 5.2 (Truncation operator [Hil13]). The time (causal) truncation of a signal v from \mathbb{R}_+ to \mathbb{C}^{n_v} at a given time $T > 0$ is defined as

$$P_T(v(t)) = v_T(t) = \begin{cases} v(t), & \forall t \leq T \\ 0, & \text{otherwise.} \end{cases}$$

Definition 5.3 (\mathcal{L}_2^e space [Hil13]). The extended \mathcal{L}_2 space, denoted \mathcal{L}_2^e space, is the set of signals v from \mathbb{R}_+ to \mathbb{C}^{n_v} such that $\forall T > 0, \|P_T(v)\|_2 < \infty$.

Finally, based on the definitions of \mathcal{L}_2 and \mathcal{L}_2^e , we can define the induced norms or gains of operators.

Definition 5.4 (\mathcal{L}_2 gain of an operator [Hil13]). The \mathcal{L}_2 gain or \mathcal{L}_2 -induced norm, of an operator Σ is defined as

$$\|\Sigma\|_{i_2} = \sup_{v \in \mathcal{L}_2, v \neq 0} \frac{\|\Sigma(v)\|_2}{\|v\|_2}.$$

Definition 5.5 (\mathcal{L}_2^e gain of an operator [Wil71]). The \mathcal{L}_2^e gain or \mathcal{L}_2^e -induced norm, of an operator Σ is defined as

$$\|\Sigma\|_{i_{2,e}} = \sup_{v \in \mathcal{L}_2^e, v \neq 0, T > 0} \frac{\|\Sigma(v)\|_{2,T}}{\|v\|_{2,T}}.$$

5.1 Problem Statement

Let us consider the 2DoF control configuration of Figure 5.1, where the to-be-controlled plant G is an LTI system and admits the state-space representation

$$G : \begin{cases} \dot{x}(t) &= Ax(t) + Bv(t) \\ y(t) &= Cx(t) + Dv(t) \end{cases} \quad (5.2)$$

with $x(t) \in \mathbb{R}^{n_G}$, $v(t) \in \mathbb{R}$, $y(t) \in \mathbb{R}$, and $A \in \mathbb{R}^{n_G \times n_G}$, $B \in \mathbb{R}^{n_G \times 1}$, $C \in \mathbb{R}^{1 \times n_G}$ and $D \in \mathbb{R}$. The signals d and n respectively represent a disturbance at the input of the plant and the measurement noise, defining

$$v(t) \triangleq u(t) + d(t) \quad \text{and} \quad y_n(t) \triangleq y(t) + n(t). \quad (5.3)$$

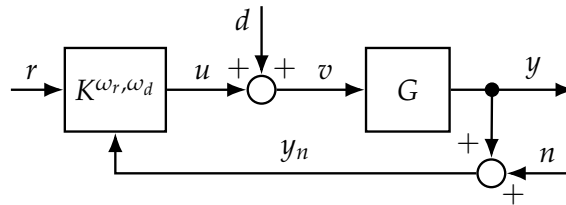


FIGURE 5.1: 2DoF control configuration.

The **original control objective** is to compute a control signal u such that, based on the reference signal r and the measure y_n , the following goals are achieved.

- (i) *Reference tracking*: the output signal y tracks the reference signals $r \in \mathcal{R}[\omega_{r,1}, \omega_{r,2}]$, which is defined as follows. Given $\omega_{r,2} \geq \omega_{r,1} > 0$ and the set

$$\Omega_r[\omega_{r,1}, \omega_{r,2}] = \{\omega_r \mid \forall t \in \mathbb{R}_+, \omega_r(t) \in [\omega_{r,1}, \omega_{r,2}]\}, \quad (5.4)$$

the set \mathcal{R}_{ω_r} is defined for $\omega_r \in \Omega_r[\omega_{r,1}, \omega_{r,2}]$ as

$$\mathcal{R}_{\omega_r} = \left\{ r \mid \exists A_r \in \mathbb{R}_+, \exists \phi_r^0 \in \mathbb{R}, \forall t \in \mathbb{R}_+, r(t) = A_r \sin \left(\int_0^t \omega_r(\tau) d\tau + \phi_r^0 \right) \right\} \quad (5.5)$$

where the variable A_r is the amplitude, ϕ_r^0 is the phase at the origin, and the measurable function $\omega_r(t)$ is referred to as the instantaneous (angular) frequency of r . The

instantaneous frequency defines the instantaneous phase of r , ϕ_r , which reads

$$\phi_r(t) = \int_0^t \omega_r(\tau) d\tau + \phi_r^0. \quad (5.6)$$

The reference signal set is then defined as

$$\mathcal{R}[\omega_{r,1}, \omega_{r,2}] = \bigcup_{\omega_r \in \Omega_r[\omega_{r,1}, \omega_{r,2}]} \mathcal{R}_{\omega_r}.$$

- (ii) *Disturbance rejection*: the disturbance signals $d \in \mathcal{D}[\omega_{d,1}, \omega_{d,2}]$, which is defined as follows. Given $\omega_{d,2} \geq \omega_{d,1} > 0$ and the set

$$\Omega_d[\omega_{d,1}, \omega_{d,2}] = \{\omega_d \mid \forall t \in \mathbb{R}_+, \omega_d(t) \in [\omega_{d,1}, \omega_{d,2}]\}, \quad (5.7)$$

the set \mathcal{D}_{ω_d} is defined for $\omega_d \in \Omega_d[\omega_{d,1}, \omega_{d,2}]$ as

$$\mathcal{D}_{\omega_d} = \left\{ d \mid \exists A_d \in \mathbb{R}_+, \exists \phi_d^0 \in \mathbb{R}, \forall t \in \mathbb{R}_+, d(t) = A_d \sin \left(\int_0^t \omega_d(\tau) d\tau + \phi_d^0 \right) \right\}, \quad (5.8)$$

where the variable A_d is the amplitude, ϕ_d^0 is the phase at the origin, and the measurable function $\omega_d(t)$ is the instantaneous frequency of d and defines the instantaneous phase of d , ϕ_d , as

$$\phi_d(t) = \int_0^t \omega_d(\tau) d\tau + \phi_d^0. \quad (5.9)$$

The disturbance signal set is then defined as

$$\mathcal{D}[\omega_{d,1}, \omega_{d,2}] = \bigcup_{\omega_d \in \Omega_d[\omega_{d,1}, \omega_{d,2}]} \mathcal{D}_{\omega_d}.$$

- (iii) *Robust stability against LTI additive uncertainties*: the closed-loop system is robustly stable against additive uncertainties $\Delta E \in \Delta_{\text{add}}$, where the set of uncertainties Δ_{add} is defined as, given stable transfer functions $W_{\text{add},1}$ and $W_{\text{add},2}$,

$$\Delta_{\text{add}} = \left\{ \Delta E \mid \exists \tilde{\Delta}, \|\tilde{\Delta}\|_{i2} \leq 1, \Delta E = W_{\text{add},1} \tilde{\Delta} W_{\text{add},2} \right\}. \quad (5.10)$$

The transfers $W_{\text{add},1}$ and $W_{\text{add},2}$ define the size of the uncertainty ΔE .

Regarding the reference tracking and the disturbance rejection goals, we adopt the following definitions, based on [DW80, Zam81, Hil13].

Definition 5.6 (γ_p -tracking). For a given performance level $\gamma_p \in (0, 1)$, the closed-loop system is said to γ_p -track the set of signals $\mathcal{R}[\omega_{r,1}, \omega_{r,2}]$ if³:

$$\forall \omega_r \in \Omega_r[\omega_{r,1}, \omega_{r,2}], \forall r \in \mathcal{R}_{\omega_r}, \forall T > 0, \quad \|r - y\|_{2,T} \leq \gamma_p \|r\|_{2,T}. \quad (5.11)$$

³Since $\forall \omega_r \in \Omega_r[\omega_{r,1}, \omega_{r,2}], \mathcal{R}_{\omega_r} \in \mathcal{L}_2^e$, $\|r\|_{2,T}$ is well-defined.

Definition 5.7 (γ_p -rejection). For a given performance level $\gamma_p \in (0, 1)$, the closed-loop system is said to γ_p -reject the set of signals $\mathcal{D} [\omega_{d,1}, \omega_{d,2}]$ if⁴:

$$\forall d \in \mathcal{D} [\omega_{d,1}, \omega_{d,2}], \forall r \in \mathcal{R} [\omega_{r,1}, \omega_{r,2}], \forall T > 0, \quad \|y_{r,d} - y_{r,0}\|_{2,T} \leq \gamma_p \|d\|_{2,T}. \quad (5.12)$$

where $y_{r,d}$ denotes the output of the closed-loop system with the reference signal r and the disturbance signal d .

Note that the reference and disturbance signals depend on their instantaneous frequency, respectively $\omega_r(t)$ and $\omega_d(t)$. Since these parameters are assumed to be measured in real time, we consider, for all $\omega_r \in \Omega_r [\omega_{r,1}, \omega_{r,2}]$ and for all $\omega_d \in \Omega_d [\omega_{d,1}, \omega_{d,2}]$, a controller of the form

$$K^{\omega_r, \omega_d} : \begin{cases} \dot{x}_K(t) &= A_K(\omega_r(t), \omega_d(t))x_K(t) + B_K(\omega_r(t), \omega_d(t))y_P(t) \\ u(t) &= C_K(\omega_r(t), \omega_d(t))x_K(t) + D_K(\omega_r(t), \omega_d(t))y_P(t) \end{cases}, \quad (5.13)$$

where $x_K \in \mathbb{R}^{n_K}$, $y_P = \text{col}(r, y_n)$, and the matrices have appropriate dimensions and depend on the instantaneous frequencies ω_r and ω_d .

Now, we can state the main objective of this chapter as follows.

Problem 5.1. Given the to-be-controlled plant G (see (5.2) and (5.3)), compute for all $\omega_r \in \Omega_r [\omega_{r,1}, \omega_{r,2}]$ and for all $\omega_d \in \Omega_d [\omega_{d,1}, \omega_{d,2}]$, a controller K^{ω_r, ω_d} in the form of (5.13) such that the closed-loop system defined by (5.2), (5.3) and (5.13):

- (i) γ_p -tracks reference signals r belonging to $\mathcal{R} [\omega_{r,1}, \omega_{r,2}]$ and γ_p -rejects disturbance signals d that belong to $\mathcal{D} [\omega_{d,1}, \omega_{d,2}]$;
- (ii) is stable for any function $\omega_r \in \Omega_r [\omega_{r,1}, \omega_{r,2}]$ and for any function $\omega_d \in \Omega_d [\omega_{d,1}, \omega_{d,2}]$;
- (iii) is stable against LTI additive uncertainties $\Delta E \in \Delta_{\text{add}}$ (see (5.10)).

To solve this problem, we adopt an approach similar to the \mathcal{H}_∞ synthesis, where we define a criterion and the desired behavior of the closed-loop system is expressed through weighting functions. Usually, for the \mathcal{H}_∞ synthesis, the design of the weighting functions is realized in the frequency domain and can follow two different methodologies: the transfer function shaping approach and the signal-based one [SP01]. In Chapter 4, we rather adopt the former approach, in which the weighting functions are chosen to shape the frequency response magnitude of the transfer functions of interest. The second approach consists in using the weighting functions to describe the signals of interest⁵. Since we cannot define (LTI) transfer functions because of the time-varying nature of the controller, we adopt the second approach in this chapter.

The main challenge here is how to define weighting functions that finely describe signals $r \in \mathcal{R}_{\omega_r}$ for all $\omega_r \in \Omega_r [\omega_{r,1}, \omega_{r,2}]$ and $d \in \mathcal{D}_{\omega_d}$ for all $\omega_d \in \Omega_d [\omega_{d,1}, \omega_{d,2}]$. In the next section, we tackle this particular problem, what allows us to formulate a criterion adapted to this kind of signals. Then, we discuss how to compute the desired controller.

⁴Since $\mathcal{D} [\omega_{d,1}, \omega_{d,2}] \in \mathcal{L}_2^e$, $\|d\|_{2,T}$ is well-defined.

⁵In an LTI framework, the weighting functions describe the frequency content of the signals.

5.2 Main Result: \mathcal{L}_2 Criterion and LTV Weighting Functions

In this section, we show that the computation of a controller solving Problem 5.1 can be recast as the solution of an LPV control problem. In this new problem, the control specifications are expressed through an \mathcal{L}_2 criterion with LPV weighting functions.

5.2.1 The \mathcal{L}_2 Criterion

Based on the control configuration of Figure 5.1 and on the control objectives announced in Section 5.1, we define the input signals of interest $\tilde{w} = \text{col}(r, d, n)$ as well as the output signals of interest $\tilde{z} = \text{col}(\varepsilon, u)$, where $\varepsilon \triangleq r - y$. Then, to describe these signals, we include weighting functions $W_{\text{in}}^{\omega_r, \omega_d} = \text{diag}(W_r^{\omega_r}, W_d^{\omega_d}, W_n)$ on the input signals and $W_{\text{out}} = \text{diag}(W_\varepsilon, W_u)$ on the output signals, as depicted in Figure 5.2. These weighting functions define $w = W_{\text{in}}^{\omega_r, \omega_d^{-1}} \tilde{w}$ and $z = W_{\text{out}} \tilde{z}$. Here, we denote $T_{a \rightarrow b}$ the **operator** mapping the input signals a to the output signals b . In particular, the operator $T_{\tilde{w} \rightarrow \tilde{z}}$ can be given by $\tilde{P} \star K^{\omega_r, \omega_d}$, where the augmented plant \tilde{P} reads as

$$\tilde{P} = \begin{bmatrix} 1 & 0 & 0 & 0 \\ 0 & 0 & 0 & 1 \\ 1 & 0 & 0 & 0 \\ 0 & 0 & 1 & 0 \end{bmatrix} + \begin{bmatrix} -1 \\ 0 \\ 0 \\ 1 \end{bmatrix} G [0 \quad 1 \quad 0 \quad 1]. \quad (5.14)$$

Similarly, the operator $T_{w \rightarrow z}$ can be given by $P^{\omega_r, \omega_d} \star K^{\omega_r, \omega_d} = W_{\text{out}} \left(\tilde{P} \star K^{\omega_r, \omega_d} \right) W_{\text{in}}^{\omega_r, \omega_d}$. In this case, the weighted augmented plant P^{ω_r, ω_d} is given by $P^{\omega_r, \omega_d} = \begin{bmatrix} W_{\text{out}} & 0 \\ 0 & I_2 \end{bmatrix} \tilde{P} \begin{bmatrix} W_{\text{in}}^{\omega_r, \omega_d} & 0 \\ 0 & 1 \end{bmatrix}$.

Now, we present part of the solution for Problem 5.1. The following theorem establishes a mathematical criterion that allows us to determine whether an LTV controller (see (5.13)) achieves the desired performance specifications.

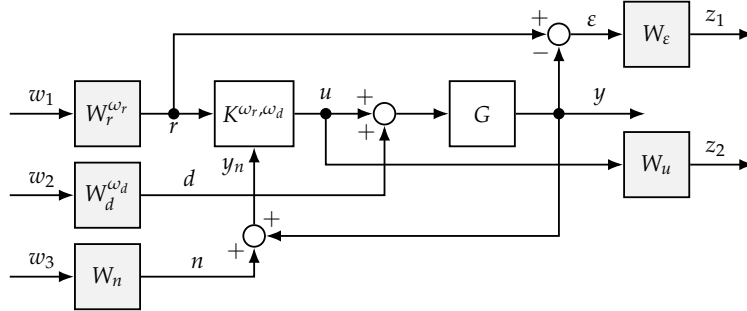


FIGURE 5.2: \mathcal{L}_2 criterion for the considered control problem.

Theorem 5.1. *Let us consider $\omega_{r,2} \geq \omega_{r,1} > 0$ and $\omega_{d,2} \geq \omega_{d,1} > 0$, stable transfer functions $W_{add,1}$ and $W_{add,2}$ and the augmented plant \tilde{P} (see (5.14)). If a given controller K^{ω_r, ω_d} (see (5.13)) is such that, for all $\omega_r \in \Omega_r [\omega_{r,1}, \omega_{r,2}]$ and for all $\omega_d \in \Omega_d [\omega_{d,1}, \omega_{d,2}]$,*

$$\left\| W_{\text{out}} \left(\tilde{P} \star K^{\omega_r, \omega_d} \right) W_{\text{in}}^{\omega_r, \omega_d} \right\|_{i_2} \leq 1, \quad (5.15)$$

where $W_{\text{in}}^{\omega_r, \omega_d} = \text{diag}(W_r^{\omega_r}, W_d^{\omega_d}, W_n)$ and $W_{\text{out}} = \text{diag}(W_\varepsilon, W_u)$ with

(i) for all $\omega_r \in \Omega_r [\omega_{r,1}, \omega_{r,2}]$, $W_r^{\omega_r}$ being stable, inversely stable and such that

$$\mathcal{R}_{\omega_r} \subset \left\{ r \in \mathcal{L}_2^e \mid \forall T > 0, \left\| W_r^{\omega_r^{-1}}(r) \right\|_{2,T} \leq \|r\|_{2,T} \right\}; \quad (5.16)$$

(ii) for all $\omega_d \in \Omega_d [\omega_{d,1}, \omega_{d,2}]$, $W_d^{\omega_d}$ being stable, inversely stable and such that

$$\mathcal{D}_{\omega_d} \subset \left\{ d \in \mathcal{L}_2^e \mid \forall T > 0, \left\| W_d^{\omega_d^{-1}}(d) \right\|_{2,T} \leq \|d\|_{2,T} \right\}; \quad (5.17)$$

(iii) W_n being a stable LTI system defined such as

$$\forall \omega \in \mathbb{R}, \quad |W_n(j\omega)| \geq |W_{add,1}(j\omega)|; \quad (5.18)$$

(iv) $W_\varepsilon = \gamma_p^{-1}$;

(v) W_u being a stable LTI system defined such as

$$\forall \omega \in \mathbb{R}, \quad |W_u(j\omega)| \geq |W_{add,2}(j\omega)|; \quad (5.19)$$

then, the closed-loop system $\tilde{P} \star K^{\omega_r, \omega_d}$ has the γ_p -tracking and γ_p -rejection properties, is stable for any functions $\omega_r \in \Omega_r [\omega_{r,1}, \omega_{r,2}]$ and $\omega_d \in \Omega_d [\omega_{d,1}, \omega_{d,2}]$, and is stable against LTI additive uncertainties $\Delta E \in \mathbf{\Delta}_{add}$ (defined by $W_{add,1}$ and $W_{add,2}$, see (5.10)).

Note that this theorem defines an \mathcal{L}_2 criterion, see (5.15), in which the weighting functions describe the signals of interest and the uncertainty ΔE . Indeed, the input weights $W_r^{\omega_r}$ and $W_d^{\omega_d}$ must define the sets of signals in which $\mathcal{R} [\omega_{r,1}, \omega_{r,2}]$ and $\mathcal{D} [\omega_{d,1}, \omega_{d,2}]$ are respectively included. In this case, W_ε defines the tracking and rejection performance level γ_p . On the other hand, the weighting functions W_n and W_u are used to express the size of the additive uncertainty $\Delta E \in \mathbf{\Delta}_{add}$. In our case, ΔE is considered to be important in low and high frequencies, and small around $\omega_{0,x}$. Please note that, as discussed in Chapter 4, enhancing the robustness against additive uncertainties also corresponds to improving the noise attenuation and reducing the control energy.

Proof. γ_p -tracking: for all $\omega_r \in \Omega_r [\omega_{r,1}, \omega_{r,2}]$, equation (5.15) is equivalent [Wil71, Theorem 2.1, page 15] to

$$\left\| W_{out} T_{\tilde{w} \rightarrow \tilde{z}} W_{in}^{\omega_r, \omega_d} \right\|_{i2,e} \leq 1. \quad (5.20)$$

In its turn, as $T_{\tilde{w}_1 \rightarrow \tilde{z}_1} = T_{r \rightarrow \varepsilon}$, (5.20) implies that

$$\left\| W_\varepsilon T_{r \rightarrow \varepsilon} W_r^{\omega_r} \right\|_{i2,e} \leq 1. \quad (5.21)$$

Now, since $W_\varepsilon = \gamma_p^{-1}$ and $\gamma_p > 0$, for all $w_1 \in \mathcal{L}_2^e$,

$$\forall T > 0, \quad \left\| T_{r \rightarrow \varepsilon} (W_r^{\omega_r}(w_1)) \right\|_{2,T} \leq \gamma_p \|w_1\|_{2,T}. \quad (5.22)$$

With $w_1 = W_r^{\omega_r^{-1}}(r)$, we have

$$\forall T > 0, \quad \left\| T_{r \rightarrow \varepsilon}(r) \right\|_{2,T} \leq \gamma_p \left\| W_r^{\omega_r^{-1}}(r) \right\|_{2,T}. \quad (5.23)$$

Since

$$\mathcal{R}_{\omega_r} \subset \left\{ r \in \mathcal{L}_2^e \mid \forall T > 0, \left\| W_r^{\omega_r^{-1}}(r) \right\|_{2,T} \leq \|r\|_{2,T} \right\},$$

we have for all $\omega_r \in \Omega_r [\omega_{r,1}, \omega_{r,2}]$,

$$\forall r \in \mathcal{R}_{\omega_r}, \forall T > 0, \quad \|T_{r \rightarrow \varepsilon}(r)\|_{2,T} \leq \gamma_p \|r\|_{2,T}, \quad (5.24)$$

which corresponds to the γ_p -tracking definition (see Definition 5.6 and (5.11)).

γ_p -rejection: by following the same procedure of the γ_p -tracking proof, we obtain for all $\omega_d \in \Omega_d [\omega_{d,1}, \omega_{d,2}]$,

$$\forall d \in \mathcal{D}_{\omega_d}, \forall T > 0, \quad \|T_{d \rightarrow \varepsilon}(d)\|_{2,T} \leq \gamma_p \|d\|_{2,T}. \quad (5.25)$$

Since the closed-loop system is linear and $y_{0,d} = T_{d \rightarrow \varepsilon}(d)$, we have $y_{0,d} = y_{r,d} - y_{r,0}$, that is, (5.25) is equivalent to (5.12) and the γ_p -rejection property is assessed (see Definition 5.7).

Stability for all $\omega_r \in \Omega_r [\omega_{r,1}, \omega_{r,2}]$ and for all $\omega_d \in \Omega_d [\omega_{d,1}, \omega_{d,2}]$: the system stability is directly implied by the existence of an induced- \mathcal{L}_2 norm for the closed-loop system (see (5.15)).

Stability against $\Delta E \in \Delta_{\text{add}}$: similar to the γ_p -tracking case, (5.15) also implies that

$$\|W_u T_{n \rightarrow u} W_n\|_{i2,e} \leq 1. \quad (5.26)$$

Moreover, with (5.18) and (5.19), (5.26) implies that

$$\|W_{\text{add},1} T_{n \rightarrow u} W_{\text{add},2}\|_{i2,e} \leq 1, \quad (5.27)$$

which, through the (nonlinear) weighted small gain theorem [Vid02], ensures the system stability for all $\Delta E \in \Delta_{\text{add}}$. \square

The problem now is how to define the weighting functions W_r and W_d satisfying (5.16) and (5.17). We tackle this problem in the sequel.

5.2.2 A New Class of LTV Weighting Functions

Theorem 5.1 establishes an \mathcal{L}_2 criterion that allows to solve Problem 5.1. However, for this result to be used, it is necessary to define a class of LTV weighting functions that, for $\omega_r \in \Omega_r [\omega_{r,1}, \omega_{r,2}]$ and for $\omega_d \in \Omega_d [\omega_{d,1}, \omega_{d,2}]$, describes the sets of reference and disturbance signals associated to ω_r and ω_d , respectively \mathcal{R}_{ω_r} and \mathcal{D}_{ω_d} (see (5.5) and (5.8)). This important class of weighting functions is defined in the following lemma.

Lemma 5.1 (LTV weighting functions). *Let us consider:*

- $\omega_{\eta,2} \geq \omega_{\eta,1} > 0$,
- a set $\Omega_\eta [\omega_{\eta,1}, \omega_{\eta,2}]$ of measurable functions ω_η defined as

$$\Omega_\eta [\omega_{\eta,1}, \omega_{\eta,2}] = \left\{ \omega_\eta \mid \forall t \in \mathbb{R}_+, \omega_\eta(t) \in [\omega_{\eta,1}, \omega_{\eta,2}] \right\}, \quad (5.28)$$

- for $\omega_\eta \in \Omega_\eta [\omega_{\eta,1}, \omega_{\eta,2}]$, the set $\mathcal{W}_{\omega_\eta}$ of signals η defined as

$$\mathcal{W}_{\omega_\eta} = \left\{ \eta \mid \exists A_\eta \in \mathbb{R}_+, \exists \phi_\eta^0 \in \mathbb{R}, \forall t \in \mathbb{R}_+, \eta(t) = A_\eta \sin \left(\int_0^t \omega_\eta(\tau) d\tau + \phi_\eta^0 \right) \right\}. \quad (5.29)$$

Then, the LTV system W^{ω_η} , defined as

$$W^{\omega_\eta} : \begin{cases} \dot{x}_W(t) &= \omega_\eta(t) A_W x_W(t) + \omega_\eta(t) B_W v(t) \\ \eta(t) &= C_W x_W(t) + D_W v(t) \end{cases}, \quad (5.30)$$

with $A_W = \begin{bmatrix} 0 & 1 \\ -1 & -2\tilde{\xi}_0 \end{bmatrix}$, $B_W = \begin{bmatrix} 2(\tilde{\xi}_1 - \tilde{\xi}_0) \\ -4\tilde{\xi}_0(\tilde{\xi}_1 - \tilde{\xi}_0) \end{bmatrix}$, $C_W = \begin{bmatrix} \tilde{\xi}_0 \\ \tilde{\xi}_1 \end{bmatrix}$, $D_W = \frac{\tilde{\xi}_0}{\tilde{\xi}_1}$ and $\tilde{\xi}_1 \gg \tilde{\xi}_0 > 0$, has the following properties:

- (i) W^{ω_η} and $W^{\omega_\eta^{-1}}$ are stable;
- (ii) $\mathcal{W}_{\omega_\eta} \subset \left\{ \eta \in \mathcal{L}_2^e \mid \forall T > 0, \left\| W^{\omega_\eta^{-1}}(\eta) \right\|_{2,T} \leq \|\eta\|_{2,T} \right\}$;
- (iii) $\left\| W^{\omega_\eta^{-1}} \right\|_{i2} \geq \frac{\tilde{\xi}_1}{\tilde{\xi}_0} \gg 1$;
- (iv) $\left\{ \eta \in \mathcal{L}_2^e \mid \forall T > 0, \left\| W^{\omega_\eta^{-1}}(\eta) \right\|_{2,T} \leq \|\eta\|_{2,T} \right\} \neq \mathcal{L}_2^e$.

The property (i) is essential for the use of the LTV system W^{ω_η} as a weighting function since it ensures the stability of W^{ω_η} as well as the stability of its inverse, $W^{\omega_\eta^{-1}}$. The property (ii) claims that the set of signals $\mathcal{W}_{\omega_\eta}$ is a subset of the whole class of signals that can be described by W^{ω_η} .

Although the properties (i) and (ii) are crucial for a weighting function, they are not sufficient to accurately describe the set of signals of interest. Indeed, any constant gain larger than 1 would satisfy these two properties. The properties (iii) and (iv) indicate then the selectiveness of the weighting function. The property (iii) reveals that there exists a class of signals that is attenuated by W^{ω_η} or, equivalently, a class of signals that is highly amplified by $W^{\omega_\eta^{-1}}$. Therefore, the set of signals defined by W^{ω_η} cannot be equal to the entire space \mathcal{L}_2^e . This last description corresponds to the property (iv).

Let us now introduce a useful lemma.

Lemma 5.2 (Time-normalization lemma). *Let be a system H given by the state-space representation*

$$H : \begin{cases} \dot{x}_H(t) &= \dot{\phi}_H(t) A_H x_H(t) + \dot{\phi}_H(t) B_H u_H(t) \\ y_H(t) &= C_H x_H(t) + D_H u_H(t) \end{cases}, \quad (5.31)$$

where $x_H(t) \in \mathbb{R}^{n_H}$, $u_H(t) \in \mathbb{R}^{n_{u_H}}$, $y_H(t) \in \mathbb{R}^{n_{y_H}}$ and ϕ_H is differentiable strictly increasing function from \mathbb{R} to \mathbb{R} , that is, $\forall t \in \mathbb{R}, \dot{\phi}_H(t) > 0$. Then, the normalized version of H , denoted H_n , reads as

$$H_n : \begin{cases} \dot{x}_{Hn}(t_n) &= A_H x_{Hn}(t_n) + B_H u_{Hn}(t_n) \\ y_{Hn}(t_n) &= C_H x_{Hn}(t_n) + D_H u_{Hn}(t_n) \end{cases}, \quad (5.32)$$

where x_{Hn} , u_{Hn} and y_{Hn} respectively denote the signals x_H , u_H and y_H with the new time variable, that is, $x_{Hn} = x_H \circ \phi_H^{-1}$ and similarly for the other signals. In this normalized-time space, the time variable is defined as $t_n \triangleq \phi_H(t)$.

Proof of Lemma 5.2. This proof is based on the chain rule. First, we define a new “time” variable $t_n \triangleq \phi_H$ and the normalized-time signal x_{Hn} such that $x_H(t) = (x_{Hn} \circ \phi_H)(t) = x_{Hn}(\phi_H(t)) = x_{Hn}(t_n)$. By applying the chain rule to \dot{x}_H , we have $\dot{x}_H = (\dot{x}_{Hn} \circ \phi_H) \cdot \dot{\phi}_H$. Then, by replacing this expression in (5.31) and with $y_H(t) = (y_{Hn} \circ \phi_H)(t)$ and $u_H(t) = (u_{Hn} \circ \phi_H)(t)$, we promptly obtain (5.32). \square

At this point, we can prove Lemma 5.1, as follows.

Proof of Lemma 5.1. Property (i): to prove this property, we have to assess the stability of W^{ω_η} , compute $W^{\omega_\eta^{-1}}$ and assess its stability.

Since $\xi_0 > 0$, the matrix A_W is Hurwitz. Then, there exists a symmetric matrix $X \succ 0$ such that

$$A_W^\top X + X A_W \prec 0. \quad (5.33)$$

Moreover, since ω_η is strictly positive for all $\omega_\eta \in \Omega_\eta[\omega_{\eta,1}, \omega_{\eta,2}]$, we have

$$\forall \omega_\eta \in \Omega_\eta[\omega_{\eta,1}, \omega_{\eta,2}], \quad \omega_\eta(t) \left(A_W^\top X + X A_W \right) \prec 0,$$

which is equivalent to (5.33) and ensures the quadratic stability of W^{ω_η} for all $\omega_\eta \in \Omega_\eta[\omega_{\eta,1}, \omega_{\eta,2}]$ (see Definition 5.8 and Remark 5.1 in page 130).

The state-space representation of $W^{\omega_\eta^{-1}}$ is given by:

$$W^{\omega_\eta^{-1}} : \begin{cases} \dot{x}_{Wi}(t) &= \omega_\eta(t) A_{Wi} x_{Wi}(t) + \omega_\eta(t) B_{Wi} \eta(t) \\ v(t) &= C_{Wi} x_{Wi}(t) + D_{Wi} \eta(t) \end{cases}, \quad (5.34)$$

with $A_{Wi} = \begin{bmatrix} 0 & 1 \\ -1 & -2\xi_1 \end{bmatrix}$, $B_{Wi} = \begin{bmatrix} 2(\xi_0 - \xi_1) \\ -4\xi_1(\xi_0 - \xi_1) \end{bmatrix}$, $C_{Wi} = \begin{bmatrix} \xi_1 & 0 \\ \xi_0 & \end{bmatrix}$, $D_{Wi} = \frac{\xi_1}{\xi_0}$, which corresponds to the state-space representation of W^{ω_η} with the parameters ξ_0 and ξ_1 being exchanged. Since $\xi_1 > 0$, $W^{\omega_\eta^{-1}}$ is also quadratically stable.

Property (ii): here, we have to prove that the signals of $\mathcal{W}_{\omega_\eta}$ are included in the set

$$\left\{ \eta \in \mathcal{L}_2^e \mid \forall T > 0, \left\| W^{\omega_\eta^{-1}}(\eta) \right\|_{2,T} \leq \|\eta\|_{2,T} \right\}, \quad (5.35)$$

which represents the set of signals that can be described by W^{ω_η} . To this purpose, let us consider $\eta \in \mathcal{W}_{\omega_\eta}$, that is,

$$\exists A_\eta \in \mathbb{R}_+, \exists \phi_\eta^0 \in \mathbb{R}, \forall t \in \mathbb{R}_+, \eta(t) = A_\eta \sin(\phi_\eta(t)) \quad \text{with} \quad \phi_\eta(t) = \int_0^t \omega_\eta(\tau) d\tau + \phi_\eta^0.$$

Now, we apply Lemma 5.2 with $t_n \triangleq \phi_\eta$, such that the state-space representation of W^{ω_η} in this new time domain is given by

$$W_n^{\omega_\eta} : \begin{cases} \dot{x}_{Wn}(t_n) &= A_W x_{Wn}(t_n) + B_W v_n(t_n) \\ \eta_n(t_n) &= C_W x_{Wn}(t_n) + D_W v_n(t_n) \end{cases}, \quad (5.36)$$

where x_{W_n} , η_n and v_n respectively denote the signals x_W , η and v with the new time variable, that is, $x_{W_n} = x_W \circ \phi_\eta^{-1}$ and similarly for the other signals. Please note that in this normalized-time domain, the system $W_n^{\omega_\eta}$ is LTI and has as transfer function

$$W_n^{\omega_\eta}(s_n) = \frac{\zeta_0 s_n^2 + 2\zeta_1 s_n + 1}{\zeta_1 s_n^2 + 2\zeta_0 s_n + 1}, \quad (5.37)$$

where s_n denotes the Laplace variable associated to t_n . Similarly, its inverse, $W_n^{\omega_\eta^{-1}}$, has the following transfer function

$$W_n^{\omega_\eta^{-1}}(s_n) = \frac{\zeta_1 s_n^2 + 2\zeta_0 s_n + 1}{\zeta_0 s_n^2 + 2\zeta_1 s_n + 1}. \quad (5.38)$$

Then, for the input $\eta(t) = A_\eta \sin(\phi_\eta(t))$, the output of $W_n^{\omega_\eta^{-1}}$ is $v(t) = A_v \sin(\phi_\eta(t))$. Indeed, in the normalized-time domain, the input signal $\eta(t) = A_\eta \sin(\phi_\eta(t))$ corresponds to $\eta_n(t_n) = A_\eta \sin(t_n)$ and the output signal corresponds to $v_n(t_n) = A_v \sin(t_n)$, where $A_v = A_\eta \left| W_n^{\omega_\eta^{-1}}(j1) \right| = A_\eta$. Moreover, the amplification of $W_n^{\omega_\eta^{-1}}$ (resp. $W_n^{\omega_\eta}$) is minimal (resp. maximal) and equal to one⁶ when $s_n = j1$. Thus, in this particular case ($v(t) = \eta(t) = A_\eta \sin(\phi_\eta(t))$), we have

$$\forall T > 0, \quad \left\| W_n^{\omega_\eta^{-1}}(\eta) \right\|_{2,T} \leq \|\eta\|_{2,T} \quad (5.39)$$

that is condition (ii). For the most of other signals belonging to \mathcal{L}_2^ℓ , this condition does not hold.

The magnitude plot of $W_n^{\omega_\eta}$ and a discussion on the inclusion of $\mathcal{W}_{\omega_\eta}$ in (5.35) are presented after this proof.

Property (iii): now, in order to prove that $\left\| W_n^{\omega_\eta^{-1}} \right\|_{i2} \geq \frac{\zeta_1}{\zeta_0}$, let us recall that

$$\left\| W_n^{\omega_\eta^{-1}} \right\|_{i2} = \left\| W_n^{\omega_\eta^{-1}} \right\|_{i2,\ell} = \sup_{\eta \neq 0, T > 0} \frac{\left\| W_n^{\omega_\eta^{-1}}(\eta) \right\|_{2,T}}{\|\eta\|_{2,T}}.$$

Now, let us consider $\eta(t) = \eta_0$, which corresponds to $\eta_n(t_n) = \eta_0$ in the normalized-time domain. Then, it is easy to prove that $W_n^{\omega_\eta^{-1}}(\eta) = \eta_0 \frac{\zeta_1}{\zeta_0}$ where $\frac{\zeta_1}{\zeta_0}$ is the static gain of $W_n^{\omega_\eta^{-1}}$ (see (5.38)). Hence, $\left\| W_n^{\omega_\eta^{-1}} \right\|_{i2,\ell} \geq \frac{\zeta_1}{\zeta_0}$.

The last part of this property ($\frac{\zeta_1}{\zeta_0} \gg 1$) follows immediately from $\zeta_1 \gg \zeta_0$.

Property (iv): is a direct consequence of property (iii). □

Based on the proof of the property (ii), a frequency-domain-like analysis of $W_n^{\omega_\eta}$, associated to $W_n^{\omega_\eta}$, can be realized (see Lemma 5.2 and (5.37)). This analysis is of fundamental interest for the choice of the parameters ζ_0 and ζ_1 . In Figure 5.3 we present the magnitude plot of $W_n^{\omega_\eta}$ for different values of ζ_0 and ζ_1 . First, let us focus on the interpretation of the x-axis. The normalized time t_n , which is associated to the Laplace variable s_n , is defined as a function of

⁶The phase shift induced by $W_n^{\omega_\eta^{-1}}$ or $W_n^{\omega_\eta}$ is null for $s_n = j1$.

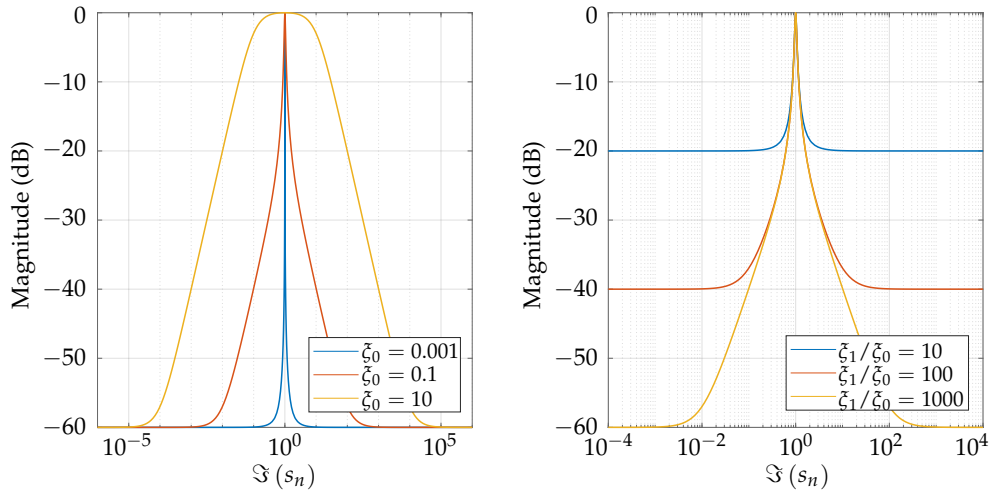


FIGURE 5.3: Magnitude plot of $W_n^{\omega_\eta}$ for different values of ζ_0 and ζ_1 . On the left, the ratio ζ_1/ζ_0 is constant and equal to 1000. On the right, ζ_0 is constant and equal to 0.1.

a given trajectory $\omega_\eta \in \Omega_\eta [\omega_{\eta,1}, \omega_{\eta,2}]$. Then, a signal of the type

$$\eta'(t) = A_{\eta'} \sin(k' \phi_\eta(t))$$

with $A_{\eta'} \in \mathbb{R}_+$ and $k' \in \mathbb{R}_+$, in normalized time, is rewritten as

$$\eta'_n(t_n) = A_{\eta'} \sin(k' t_n). \quad (5.40)$$

Note, in (5.40), that k' corresponds to a frequency-like variable and corresponds to the x-axes of Figure 5.3. We can say that $W_n^{\omega_\eta}$ acts as a band-pass filter for signals in the form of η' . The bandwidth of this filter is determined by ζ_0 , and the attenuation in the rejection band is given by the ratio ζ_0/ζ_1 . We can also note that for very selective filters, only signals with $k' \approx 1$ can pass through, reducing the set of signals that can be described by the system. Therefore, we can infer that the more selective $W_n^{\omega_\eta}$ is, the tighter is the inclusion of $\mathcal{W}_{\omega_\eta}$ in the whole set of signals described by W^{ω_η} .

Finally, some remarks related to this class of LTV weighting functions are important to be made. First, in the case of usual sinusoidal signal with frequency ω_η in $[\omega_{\eta,1}, \omega_{\eta,2}]$, the weighting functions W^{ω_η} boils down to the usual \mathcal{H}_∞ weighting function. Another important remark is that we here focus on signals of $\mathcal{W}^{\omega_\eta}$. Nevertheless, the same approach can be extended to a wider set of signals, such as, for a given $N_H \in \mathbb{N}$, for all $\omega_\eta \in \Omega_\eta [\omega_{\eta,1}, \omega_{\eta,2}]$:

$$\mathcal{W}_{N_H}^{\omega_\eta} = \left\{ \eta_H \left| \begin{array}{l} \exists A_{\eta,i} \in \mathbb{R}_+^{N_H}, \exists \phi_{\eta,i}^0 \in \mathbb{R}^{N_H}, \forall t \in \mathbb{R}_+, \\ \eta_H(t) = \sum_{i=1}^{N_H} A_{\eta,i} \sin \left(\int_0^t i \omega_\eta(\tau) d\tau + \phi_{\eta,i}^0 \right) \end{array} \right. \right\}, \quad (5.41)$$

which describes “periodic” signals whose fundamental frequency can vary over time.

5.2.3 LPV Control Problem

Now, based on Lemma 5.1, we can define LPV weighting functions $W_r^{\Omega_r}$ and $W_d^{\Omega_d}$ (whose parameters depend on the measurable functions ω_r and ω_d) that fulfill the conditions of Theorem 5.1 for all $\omega_r \in \Omega_r [\omega_{r,1}, \omega_{r,2}]$ and for all $\omega_d \in \Omega_d [\omega_{d,1}, \omega_{d,2}]$, as follows.

- Being the set of reference signals r given by (5.5), the weighting function $W_r^{\omega_r}$ is then defined as

$$W_r^{\omega_r} : \begin{cases} \dot{x}_{W_r}(t) &= \omega_r(t)A_{W_r}x_{W_r}(t) + \omega_r(t)B_{W_r}w_1(t) \\ r(t) &= C_{W_r}x_{W_r}(t) + D_{W_r}w_1(t) \end{cases}, \quad (5.42)$$

with $A_{W_r} = \begin{bmatrix} 0 & 1 \\ -1 & -2\xi_{0r} \end{bmatrix}$, $B_{W_r} = \begin{bmatrix} 2(\xi_{1r} - \xi_{0r}) \\ -4\xi_{0r}(\xi_{1r} - \xi_{0r}) \end{bmatrix}$, $C_{W_r} = \begin{bmatrix} \xi_{0r} & 0 \\ \xi_{1r} & 0 \end{bmatrix}$, $D_{W_r} = \frac{\xi_{0r}}{\xi_{1r}}$, $\xi_{1r} \gg \xi_{0r} > 0$.

- Being the set of disturbance signals d given by (5.8), the weighting function $W_d^{\omega_d}$ is hence given by

$$W_d^{\omega_d} : \begin{cases} \dot{x}_{W_d}(t) &= \omega_d(t)A_{W_d}x_{W_d}(t) + \omega_d(t)B_{W_d}w_2(t) \\ d(t) &= C_{W_d}x_{W_d}(t) + D_{W_d}w_2(t) \end{cases}, \quad (5.43)$$

with $A_{W_d} = \begin{bmatrix} 0 & 1 \\ -1 & -2\xi_{0d} \end{bmatrix}$, $B_{W_d} = \begin{bmatrix} 2(\xi_{1d} - \xi_{0d}) \\ -4\xi_{0d}(\xi_{1d} - \xi_{0d}) \end{bmatrix}$, $C_{W_d} = \begin{bmatrix} \xi_{0d} & 0 \\ \xi_{1d} & 0 \end{bmatrix}$, $D_{W_d} = \frac{\xi_{0d}}{\xi_{1d}}$, $\xi_{1d} \gg \xi_{0d} > 0$.

Finally, Problem 5.1 can be recast as the following control problem.

Problem 5.2. For the to-be-controlled plant G given by (5.2) and the configuration of Figure 5.2, compute for all $\omega_r \in \Omega_r [\omega_{r,1}, \omega_{r,2}]$ and for all $\omega_d \in \Omega_d [\omega_{d,1}, \omega_{d,2}]$ a controller K^{ω_r, ω_d} in the form of (5.13), if there exists any, such that for all $\omega_r \in \Omega_r [\omega_{r,1}, \omega_{r,2}]$ and for all $\omega_d \in \Omega_d [\omega_{d,1}, \omega_{d,2}]$, the closed-loop system is stable and

$$\left\| W_{\text{out}} \left(\tilde{P} \star K^{\omega_r, \omega_d} \right) W_{\text{in}}^{\omega_r, \omega_d} \right\|_{i2} \leq 1, \quad (5.44)$$

where $W_{\text{in}}^{\omega_r, \omega_d} = \text{diag} (W_r^{\omega_r}, W_d^{\omega_d}, W_n)$, $W_{\text{out}} = \text{diag} (W_\varepsilon, W_u)$, $W_r^{\omega_r}$ is given in (5.42), $W_d^{\omega_d}$ in (5.43), W_n in (5.18), $W_\varepsilon = \gamma_p^{-1}$ and W_u is defined in (5.19).

This problem is actually an LPV control problem since it is equivalent to compute a controller such that $\left(\tilde{P} \star K^{\Omega_r, \Omega_d} \right)$ is stable and

$$\left\| W_{\text{out}} \left(\tilde{P} \star K^{\Omega_r, \Omega_d} \right) W_{\text{in}}^{\Omega_r, \Omega_d} \right\|_{i2} \leq 1,$$

where $W_{\text{out}} \left(\tilde{P} \star K^{\Omega_r, \Omega_d} \right) W_{\text{in}}^{\Omega_r, \Omega_d}$ is defined as

$$\left\{ W_{\text{out}} \left(\tilde{P} \star K^{\omega_r, \omega_d} \right) W_{\text{in}}^{\omega_r, \omega_d}, \omega_r \in \Omega_r [\omega_{r,1}, \omega_{r,2}], \omega_d \in \Omega_d [\omega_{d,1}, \omega_{d,2}] \right\}.$$

A solution is presented in the sequel.

5.3 Solving the LPV Control Problem: a Polytopic Approach

To solve Problem 5.2 and compute a controller K^{Ω_r, Ω_d} that fulfills the desired specifications, we adopt a polytopic approach. This solution is presented in Section 5.3.2. However, before presenting it, we recall some important definitions in the polytopic LPV framework.

5.3.1 Some Definitions in the LPV Framework

Let us consider the polytopic LPV system below

$$H^\Theta : \begin{cases} \dot{x}_H(t) &= A_H(\theta(t))x_H(t) + B_H(\theta(t))u_H(t) \\ y_H(t) &= C_H(\theta(t))x_H(t) + D_H(\theta(t))u_H(t) \end{cases}, \quad \theta(\cdot) \in \Theta \quad (5.45)$$

where $\theta(t) \in \mathbb{R}^{n_\theta}$ ranges over a fixed polytope Θ and the dependence of the state-space matrices is affine on θ . The polytope Θ is defined by its $N_\theta = 2^{n_\theta}$ vertices θ_i , where $i \in \{1, \dots, N_\theta\}$. In this case, the state-space matrices of H^Θ are of the form

$$\begin{bmatrix} A_H(\theta(t)) & B_H(\theta(t)) \\ C_H(\theta(t)) & D_H(\theta(t)) \end{bmatrix} = \sum_{i=1}^{N_\theta} \alpha_i(\theta(t)) \begin{bmatrix} A_{H,i} & B_{H,i} \\ C_{H,i} & D_{H,i} \end{bmatrix}$$

with $\begin{bmatrix} A_{H,i} & B_{H,i} \\ C_{H,i} & D_{H,i} \end{bmatrix} = \begin{bmatrix} A_H(\theta_i) & B_H(\theta_i) \\ C_H(\theta_i) & D_H(\theta_i) \end{bmatrix}$, $\sum_{i=1}^{N_\theta} \alpha_i(\theta(t)) = 1$ and $\alpha_i(\theta(t)) \geq 0$.

Now, we can define the important properties of quadratic stability and quadratic \mathcal{L}_2 gain for this class of system, as follows.

Definition 5.8 (Quadratic stability [AGB95]). The LPV system H^Θ given in (5.45) is quadratically stable if and only if, for all trajectories of $\theta \in \Theta$, there exists a single symmetric matrix $X \succ 0$ such that

$$\forall \theta \in \Theta, \quad A_H(\theta(t))^\top X + XA_H(\theta(t)) \prec 0. \quad (5.46)$$

Definition 5.9 (Quadratic \mathcal{L}_2 gain [AGB95]). The LPV system H^Θ (5.45) is stable and has quadratic \mathcal{L}_2 gain smaller than $\gamma > 0$ if and only if there exists a single symmetric matrix $X \succ 0$ such that

$$\forall \theta \in \Theta, \quad \begin{bmatrix} A_H(\theta(t))^\top X + XA_H(\theta(t)) & XB_H(\theta(t)) & C_H(\theta(t))^\top \\ B_H(\theta(t))^\top X & -\gamma I & D_H(\theta(t))^\top \\ C_H(\theta(t)) & D_H(\theta(t)) & -\gamma I \end{bmatrix} \prec 0. \quad (5.47)$$

The quadratic \mathcal{L}_2 gain of a system H^Θ is denoted $\|H^\Theta\|_{\mathcal{L}_2}^q$.

In the special case where (5.45) is polytopic, which is indeed our case, the infinite constraints on (5.46) and (5.47) can be simplified to a finite number of LMIs. Thanks to the vertex property of polytopic systems [AGB95], the inequalities (5.46) and (5.47) hold for all $\theta \in \Theta$ if and only if they hold at the vertices θ_i . Therefore, to assess the quadratic stability of (5.45), it suffices to solve a feasibility problem: find $X \succ 0$ such that

$$\forall i \in \{1, \dots, N_\theta\}, \quad A_{H,i}^\top X + XA_{H,i} \prec 0. \quad (5.48)$$

Remark 5.1. If a symmetric matrix X is solution of (5.48), all matrices of the form $\tilde{X} = \tilde{k}X$ with $\tilde{k} \in \mathbb{R}_+$ are also solution of (5.48).

Similarly, the condition (5.47) is equivalent to

$$\forall i \in \{1, \dots, N_\theta\}, \quad \begin{bmatrix} A_{H,i}^\top X + XA_{H,i} & XB_{H,i} & C_{H,i}^\top \\ B_{H,i}^\top X & -\gamma I & D_{H,i}^\top \\ C_{H,i} & D_{H,i} & -\gamma I \end{bmatrix} \prec 0. \quad (5.49)$$

It is worth highlighting that the quadratic \mathcal{L}_2 gain of a system implies its quadratic stability. The solution of (5.47) for a given $\gamma > 0$ also defines an upper bound on the \mathcal{L}_2 gain of a system, that is, $\|H^\Theta\|_{i_2} \leq \|H^\Theta\|_{i_2}^q < \gamma$. As we will see in the sequel, this property plays a crucial role in the proposed solution to Problem 5.2. Indeed, a controller that ensures $\|W_{\text{out}} \left(\tilde{P} \star K^{\Omega_r, \Omega_d} \right) W_{\text{in}}^{\Omega_r, \Omega_d}\|_{i_2}^q \leq 1$ also ensures $\|W_{\text{out}} \left(\tilde{P} \star K^{\Omega_r, \Omega_d} \right) W_{\text{in}}^{\Omega_r, \Omega_d}\|_{i_2} \leq 1$, which corresponds to the condition (5.44).

We also have to mention that in the particular case where $\Theta = \{\theta_0\}$ with θ_0 constant, the LPV system H^Θ becomes an LTI system. Then, $\|H^\Theta\|_\infty = \|H^\Theta\|_{i_2} = \|H^\Theta\|_{i_2}^q$.

5.3.2 The Standard LPV Synthesis

Similar to the H_∞ synthesis, in the LPV framework, the controller design is also formulated as an optimization problem, as follows.

Problem 5.3 (Standard LPV control problem). *Let an augmented polytopic plant P^Θ be given by*

$$P^\Theta : \begin{cases} \dot{x}_P(t) &= A_P(\theta(t))x_P(t) + B_w(\theta(t))w(t) + B_u u_P(t) \\ z(t) &= C_z(\theta(t))x_P(t) + D_{zw}(\theta(t))w(t) + D_{zu} u_P(t) \\ y_P(t) &= C_y x_P(t) + D_{yw} w(t) \end{cases}, \quad \theta(\cdot) \in \Theta \quad (5.50)$$

with $x_P(t) \in \mathbb{R}^{n_P}$, $u_P(t) \in \mathbb{R}^{n_{u_P}}$, $w(t) \in \mathbb{R}^{n_w}$, $y_P(t) \in \mathbb{R}^{n_{y_P}}$, $z(t) \in \mathbb{R}^{n_z}$. The parameter $\theta(t) \in \mathbb{R}^{n_\theta}$ is measured in real time and ranges over a fixed polytope Θ . Therefore, for a given $\gamma > 0$, we want to compute a polytopic LPV controller

$$K^\Theta : \begin{cases} \dot{x}_K(t) &= A_K(\theta(t))x_K(t) + B_K(\theta(t))y_P(t) \\ u_P(t) &= C_K(\theta(t))x_K(t) + D_K(\theta(t))y_P(t) \end{cases}, \quad \theta(\cdot) \in \Theta \quad (5.51)$$

with $x_K(t) \in \mathbb{R}^{n_P}$, if there exists any, such that,

$$\|P^\Theta \star K^\Theta\|_{i_2}^q < \gamma. \quad (5.52)$$

Similar to the \mathcal{H}_∞ synthesis, the desired control specifications can also be expressed through the choice of the augmented plant P^Θ , which includes the weighting functions and defines the closed-loop transfers of interest. It is important to highlight that only the matrices A_P , B_w , C_z and D_{zw} can be dependent on θ . This condition is required so that this problem can be formulated as a convex optimization problem. Although it may seem restrictive, this condition can be easily fulfilled by introducing stable LTI filter(s) between the controller and the to-be-controlled plant. This technique slightly modifies the augmented plant such that the input matrices B_u and D_{zu} as well as the output matrices C_y and D_{yw} have no dependence on θ . For further details, see, e.g., [AGB95].

The existence of a controller that solves the problem above is assessed by the theorem below.

Theorem 5.2 ([AGB95]). *Given the augmented LPV system of (5.50), there exists an LPV controller in the form of (5.51), such that $\|P^\Theta \star K^\Theta\|_{i_2}^q < \gamma$ for all trajectories of $\theta(t)$ in the polytope Θ , defined by the N_θ vertices θ_i , if and only if there are symmetric matrices $R, S \in \mathbb{R}^{n_P \times n_P}$ such that for all*

$i \in \{1, \dots, N_\theta\}$,

$$[\diamond]^\top \begin{bmatrix} SA_{P,i}^\top + A_{P,i}S & B_{w,i} & SC_{z,i}^\top \\ B_{w,i}^\top & -\gamma I & D_{zw,i}^\top \\ C_{z,i}S & D_{zw,i} & -\gamma I \end{bmatrix} \begin{bmatrix} B_u^\top & 0 & D_{zu}^\top \end{bmatrix}_\perp \prec 0, \quad (5.53)$$

$$[\diamond]^\top \begin{bmatrix} A_{P,i}^\top R + RA_{P,i} & RB_{w,i} & C_{z,i}^\top \\ B_{w,i}^\top R & -\gamma I & D_{zw,i}^\top \\ C_{z,i} & D_{zw,i} & -\gamma I \end{bmatrix} \begin{bmatrix} C_y & D_{yw} & 0 \end{bmatrix}_\perp \prec 0 \quad (5.54)$$

$$\text{and} \quad \begin{bmatrix} R & I \\ I & S \end{bmatrix} \succ 0 \quad (5.55)$$

$$\text{with} \quad \begin{bmatrix} A_{P,i} & B_{w,i} \\ C_{z,i} & D_{zw,i} \end{bmatrix} = \begin{bmatrix} A_P(\theta_i) & B_w(\theta_i) \\ C_z(\theta_i) & D_{zw}(\theta_i) \end{bmatrix}.$$

Based on the solution of (5.53), (5.54) and (5.55), the state-space matrices of the controller at the vertices θ_i are computed. The state-space matrices of K^Θ at a given $\theta \in \Theta$ are obtained through the convex combination of K^Θ evaluated at each of the vertices θ_i . For further details on the controller computation, see [AGB95] and references therein.

In practice, as well as for the \mathcal{H}_∞ problem, the *Robust Control Toolbox* of Matlab[®] [BCPS20] can be employed to solve the LPV control problem through the function `hinfgs`.

5.3.3 Solution to Problem 5.1

Now, we have all the elements needed to solve Problem 5.1, as summarized below.

- (i) Theorem 5.1 establishes an \mathcal{L}_2 criterion that allows us to assess if a given controller solves Problem 5.1.
- (ii) The \mathcal{L}_2 criterion is defined through LTI weighting functions and the LTV weighting functions presented in Lemma 5.1.
- (iii) These two points allow us to recast Problem 5.1 as an LPV control problem, see Problem 5.2.
- (iv) Finally, Theorem 5.2 with $\gamma \leq 1$ allows us to assess the existence of a controller solving Problem 5.2 and, as consequence, Problem 5.1. Based on the solution of the LMIs (see (5.53), (5.54) and (5.55)), the LPV controller is then computed.

In our case, the augmented plant \tilde{P} is given by (5.14) and the weighted augmented plant P^{Ω_r, Ω_d} is given by $P^{\Omega_r, \Omega_d} = \begin{bmatrix} W_{\text{out}} & 0 \\ 0 & I_2 \end{bmatrix} \tilde{P} \begin{bmatrix} W_{\text{in}}^{\Omega_r, \Omega_d} & 0 \\ 0 & 1 \end{bmatrix}$, which can be written as P^Θ of (5.50) with $\theta = \text{col}(\omega_r, \omega_d)$, defining a polytope Θ whose vertices are given by $\theta_1 = \text{col}(\omega_{r,1}, \omega_{d,1})$, $\theta_2 = \text{col}(\omega_{r,1}, \omega_{d,2})$, $\theta_3 = \text{col}(\omega_{r,2}, \omega_{d,1})$ and $\theta_4 = \text{col}(\omega_{r,2}, \omega_{d,2})$; the independence of the matrices B_u , D_{zu} , C_y and D_{yw} on ω_r and ω_d follows immediately from the fact that only the input weights are dependent on these parameters. Similarly, the controller K^{ω_r, ω_d} of (5.13) corresponds to the one of (5.51) also with $\theta = \text{col}(\omega_r, \omega_d)$ and $\theta(t) \in \Theta$.

5.4 Numerical Results and Simulation

In this section, we apply the results of this chapter to design a controller for the drive mode of a MEMS gyroscope, whose model is given in Example 2.1 (page 22). We recall that this model

corresponds to a second-order resonator with a quality factor $Q_x = 100\,000$ and resonance frequency $\omega_{0,x} = 2\pi \cdot 11\,500 \text{ rad s}^{-1}$. The main control objectives are then:

- (i) to ensure that its output x_m , here denoted y , γ_p -tracks the reference signal

$$r(t) = A_r \sin \left(\int_0^t \omega_r(\tau) d\tau \right) \quad (5.56)$$

with $\omega_r(t) \in [2\pi \cdot 11\,498, 2\pi \cdot 11\,502]$ (in rad s^{-1});

- (ii) to ensure that disturbances of the type

$$\forall A_d \in \mathbb{R}_+, \forall \phi_d^0 \in \mathbb{R}, \quad d(t) = A_d \sin \left(\int_0^t \omega_d(\tau) d\tau + \phi_d^0 \right),$$

where $\omega_d = \omega_r$, are γ_p -rejected by the closed-loop system;

- (iii) to ensure the robust stability of the closed-loop system against additive uncertainties in low and high frequencies.

In particular, we consider as specification $\gamma_p = 250 \cdot 10^{-6}$. If we were in the particular case where $\omega_r(t) \equiv \omega_{0,x}$, this specification would be equivalent to ensuring a relative tracking error smaller than $250 \cdot 10^{-6}$, as in Example 4.3 (page 88), for instance.

To achieve the above objectives, we consider the control configuration of Figure 5.1 and the \mathcal{L}_2 criterion of Figure 5.2, where

- (i) W_r is given in (5.42) with $\xi_{1r} = 7.2 \cdot 10^{-3}$ and $\xi_{0r} = 9 \cdot 10^{-7}$;

- (ii) W_d is given in (5.43) with $\xi_{1d} = 7.2 \cdot 10^{-3}$ and $\xi_{0d} = 9 \cdot 10^{-7}$;

- (iii) W_n is given by

$$W_n(s) = M_n \frac{(s/\omega_n)^2 + (s/\omega_n) \alpha_n A_n / M_n + 1}{(s/\omega_n)^2 + (s/\omega_n) \alpha_n + 1} \quad (5.57)$$

with $A_n = 1.25 \cdot 10^{-4}$, $M_n = 125$, $\alpha_n = 5.565 \cdot 10^4$ and $\omega_n = \omega_{0,x}$;

- (iv) $W_\varepsilon = \gamma_p^{-1} = 4000$;

- (v) W_u is given by

$$W_u(s) = M_u \frac{(s/\omega_u)^2 + (s/\omega_u) \alpha_u A_u / M_u + 1}{(s/\omega_u)^2 + (s/\omega_u) \alpha_u + 1} \quad (5.58)$$

with $A_u = 1.6 \cdot 10^{-3}$, $M_u = 400$, $\alpha_u = 4.687 \cdot 10^4$ and $\omega_u = \omega_{0,x}$.

The controller is computed with $\gamma = 0.9954$. For the sake of illustration⁷, the weighting functions can be interpreted as upper bounds on the closed-loop transfers functions frozen at the vertices $\omega_{r,1} = 2\pi \cdot 11\,498 \text{ rad s}^{-1}$ and $\omega_{r,2} = 2\pi \cdot 11\,502 \text{ rad s}^{-1}$, as shown in Figure 5.4 and Figure 5.5. These figures also present the magnitude of the closed-loop transfers frozen at the same vertices. Note that the weighting functions enforce low gains for the transfers $T_{n \rightarrow u}$ in low and high frequencies, ensuring good stability margins against additive uncertainties in these frequency ranges. The upper bounds also enforce the transfers $T_{r \rightarrow \varepsilon}$ and $T_{d \rightarrow \varepsilon}$ to have low gains at ω_r . Indeed, at the vertex $\omega_{r,1}$, $T_{r \rightarrow \varepsilon}$ and $T_{d \rightarrow \varepsilon}$ have very small gains at the frequency $\omega_{r,1}$. The same happens at the vertex $\omega_{r,2}$.

⁷Actually, this analysis in the frequency domain is valid only for LTI systems or frozen LPV ones, which is the case when ω_r is constant. This interpretation cannot be considered when ω_r varies over time.

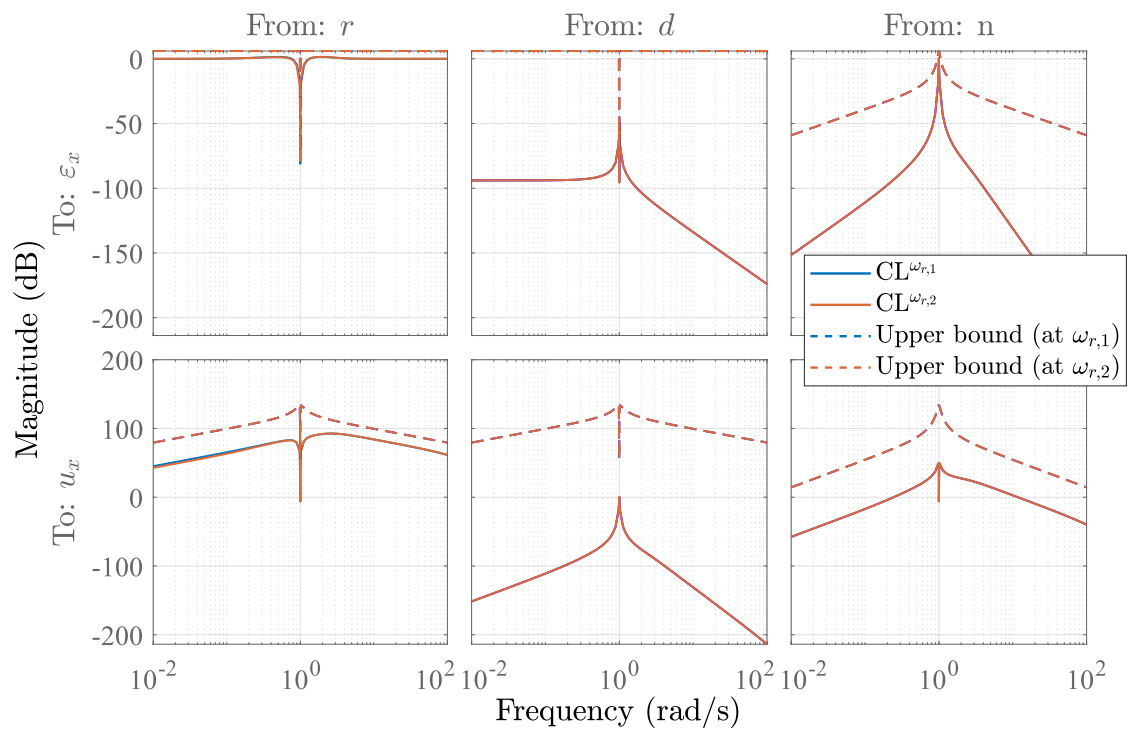


FIGURE 5.4: Closed-loop transfers (CL) at the vertices $\omega_{r,1}$ and $\omega_{r,2}$ (superposed in the figure) and upper bounds (superposed).

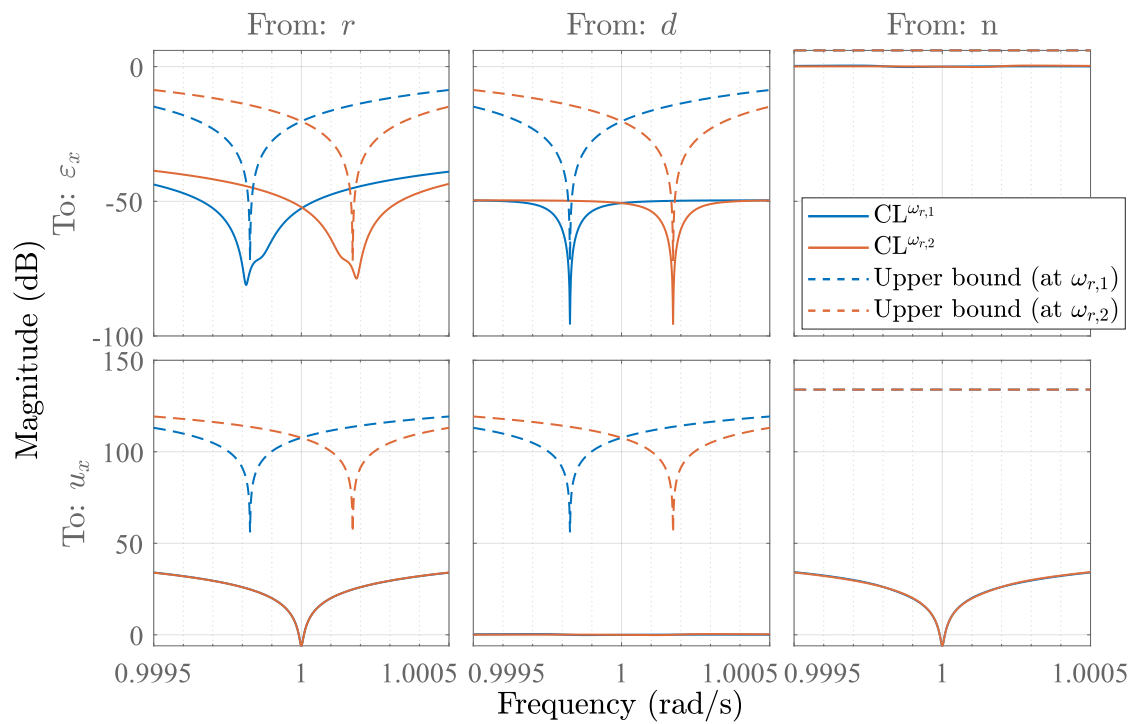


FIGURE 5.5: Closed-loop transfers (CL) at the vertices $\omega_{r,1}$ and $\omega_{r,2}$ and upper bounds. Zoom around $\omega_{0,x}$.

The Bode diagrams of the controller frozen at the vertices are presented in Figure 5.6 and Figure 5.7 (zoom). The expression and numerical values of the controller are given in Appendix D.1. Here, it is important to note that the controller presents resonance peaks at ω_r to ensure the reference tracking and disturbance rejection at this frequency, and low gains in low and high frequencies to enhance the robustness against uncertainties in these frequency ranges.

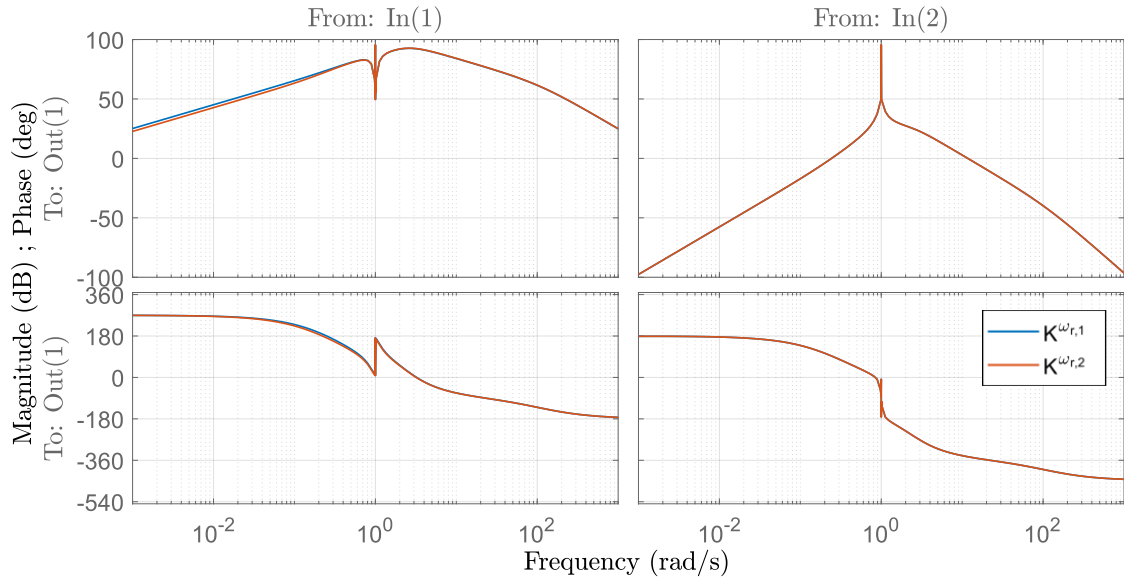


FIGURE 5.6: Controller at the vertices $\omega_{r,1}$ and $\omega_{r,2}$ (superposed in the figure).

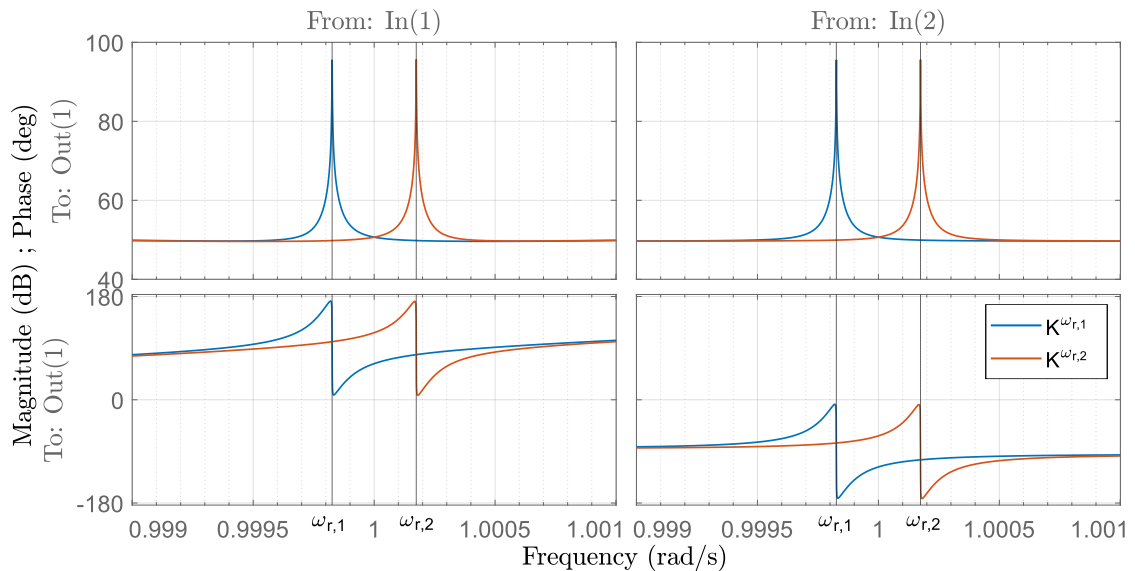


FIGURE 5.7: Controller at the vertices $\omega_{r,1}$ and $\omega_{r,2}$. Zoom around $\omega_{0,x}$.

The whole closed-loop system is then simulated with the reference signal of (5.56), where the function $\omega_r(t)$ is presented in Figure 5.8. Different types of signal are considered here, as presented in Table 5.1. The system starts from its (sinusoidal) steady state with $\omega_r(t) = \omega_{0,x}$. The tracking error and the control signal are presented, respectively, in Figure 5.9 and Figure 5.10. We recall that the reference amplitude A_r is equal to 1.

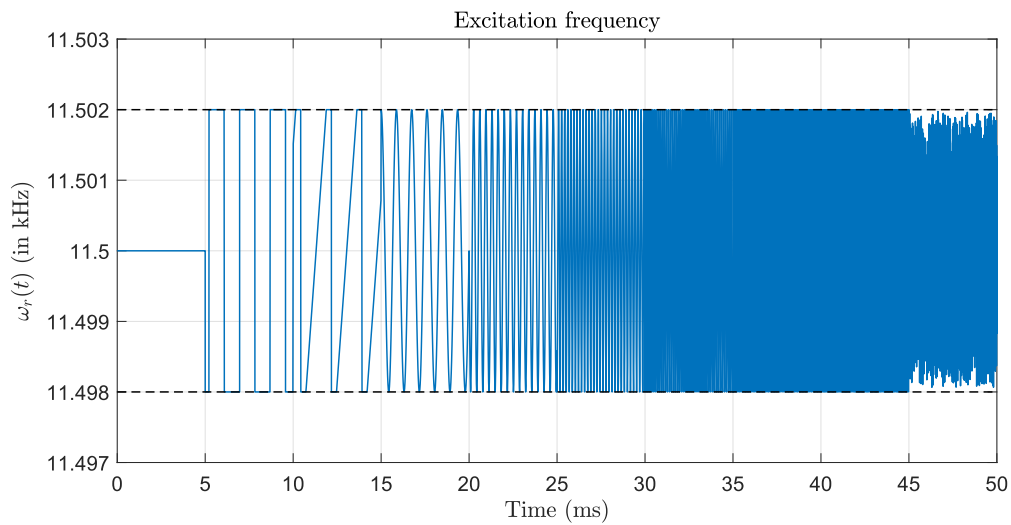


FIGURE 5.8: Excitation frequency $\omega_r(t)$. Details are provided in Table 5.1.

TABLE 5.1: Types of signal defining $\omega_r(t)$.

Time t (in ms)	Signal type	Range/Value	Fundamental frequency
[0, 5)	Constant	$\omega_{0,x}$	—
[5, 10)	Square	$[\omega_{r,1}, \omega_{r,2}]$	$0.05 \cdot \omega_{0,x}$
[10, 15)	Sawtooth	$[\omega_{r,1}, \omega_{r,2}]$	$0.05 \cdot \omega_{0,x}$
[15, 20)	Sinusoidal	$[\omega_{r,1}, \omega_{r,2}]$	$0.10 \cdot \omega_{0,x}$
[20, 25)	Sinusoidal	$[\omega_{r,1}, \omega_{r,2}]$	$0.25 \cdot \omega_{0,x}$
[25, 30)	Sinusoidal	$[\omega_{r,1}, \omega_{r,2}]$	$0.50 \cdot \omega_{0,x}$
[30, 35)	Sinusoidal	$[\omega_{r,1}, \omega_{r,2}]$	$0.75 \cdot \omega_{0,x}$
[35, 40)	Sinusoidal	$[\omega_{r,1}, \omega_{r,2}]$	$1.00 \cdot \omega_{0,x}$
[40, 45)	Sinusoidal	$[\omega_{r,1}, \omega_{r,2}]$	$1.50 \cdot \omega_{0,x}$
[45, 50)	Random	$[\omega_{r,1}, \omega_{r,2}]$	—

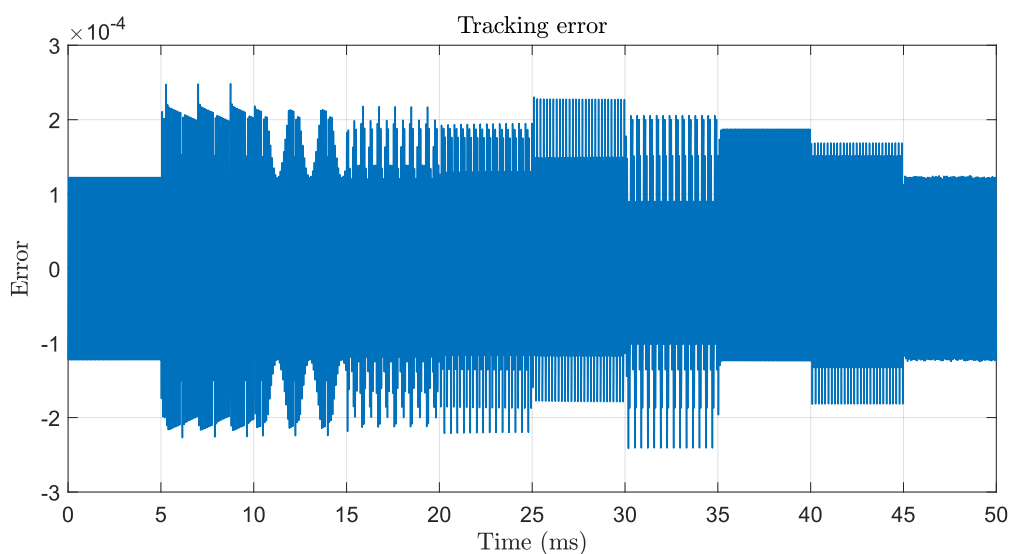


FIGURE 5.9: Tracking error $\varepsilon(t)$ for reference amplitude $A_r = 1$.

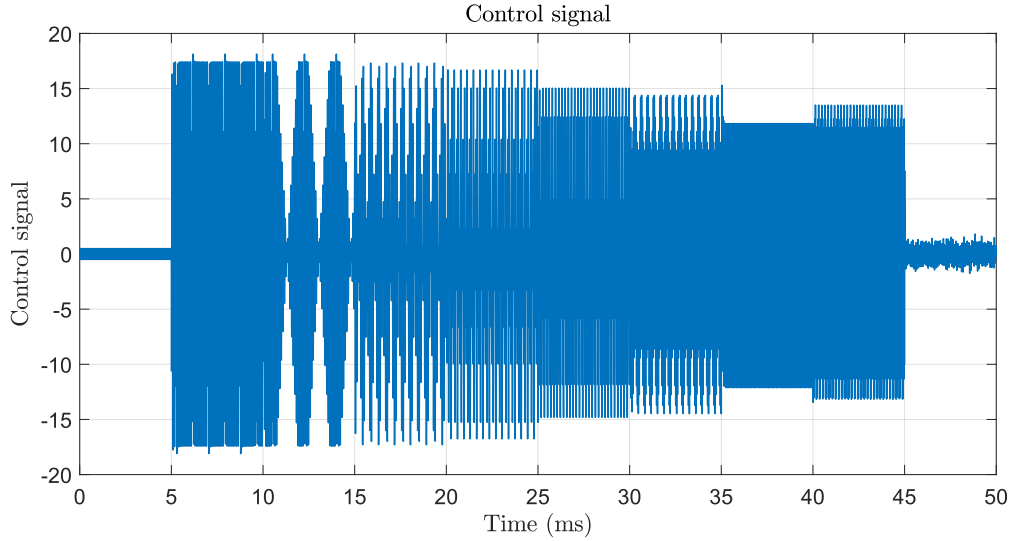


FIGURE 5.10: Control signal $u(t)$ for reference amplitude $A_r = 1$.

It is important to highlight that, despite the arbitrary variations of ω_r , the tracking error is always bounded by a value close to $2.5 \cdot 10^{-4}$ (for reference amplitude $A_r = 1$). This is possible because the controller is able to adapt itself according to ω_r . See, for instance, the control signal at $t = 5$ ms. At this instant, ω_r passes from $\omega_{0,x}$ (frequency where the gain of G is maximum) to $\omega_{r,1}$ (frequency where the gain of G is much smaller). The controller immediately compensates for the loss of gain (of G) by increasing the amplitude of the control signal, keeping $y(t) \approx r(t)$ and $\varepsilon \approx 0$.

Finally, to evaluate the γ_p -tracking property, we compute two performance indicators, denoted $\hat{\gamma}_{p,T_0}$ and $\hat{\gamma}_p$, which are respectively defined as

$$\hat{\gamma}_{p,T_0}(t) \triangleq \sqrt{\frac{\int_{t-T_0}^t \varepsilon(\tau)^2 d\tau}{\int_{t-T_0}^t r(\tau)^2 d\tau}} \quad \text{and} \quad \hat{\gamma}_p(t) \triangleq \sqrt{\frac{\int_0^t \varepsilon(\tau)^2 d\tau}{\int_0^t r(\tau)^2 d\tau}}. \quad (5.59)$$

Note that $\hat{\gamma}_{p,T_0}$ is related to the power of the signals ε and r in a moving time horizon of a fixed width T_0 . This indicator allows detecting fast variations of the system performance. On the other hand, $\hat{\gamma}_p$ corresponds to the definition of γ_p (see (5.11)) with $T = t$. With $T_0 = 1.5 \cdot 2\pi/\omega_{0,x}$, the evolution of $\hat{\gamma}_{p,T_0}$ and $\hat{\gamma}_p$ over time is plotted in Figure 5.11 and compared to the specified value of $\gamma_p = 2.5 \cdot 10^{-4}$. In this figure, we can confirm that, as expected, $\hat{\gamma}_{p,T_0}$ and $\hat{\gamma}_p$ are always smaller than the required value of $\gamma_p = 2.5 \cdot 10^{-4}$, validating the proposed solution.

For the sake of comparison, in Figure 5.12, we also present the performance indicators $\hat{\gamma}_{p,T_0}$ and $\hat{\gamma}_p$ obtained with an alternative approach. In this alternative approach, the LTV controller $K_0^{\omega_r}$ is split into two parts, as depicted in Figure 5.13: a resonant controller $K_{res}^{\omega_r}$ and a stabilizing controller K_{st} . The part $K_{res}^{\omega_r}$ is a second-order resonator known as a Proportional-Resonant controller of the form

$$K_{res}^{\omega_r} : \begin{cases} \dot{x}_{res}(t) &= \omega_r(t) \begin{bmatrix} -\zeta_{res} & -1 \\ 1 & -\zeta_{res} \end{bmatrix} x_{res}(t) + \omega_r(t) \begin{bmatrix} 1 \\ -1 \end{bmatrix} \sqrt{\frac{k_r}{2}} u_{res}(t) \\ u(t) &= \begin{bmatrix} 1 & -1 \end{bmatrix} \sqrt{\frac{k_r}{2}} x_{res}(t) + \begin{bmatrix} k_p \end{bmatrix} u_{res}(t) \end{cases}, \quad (5.60)$$

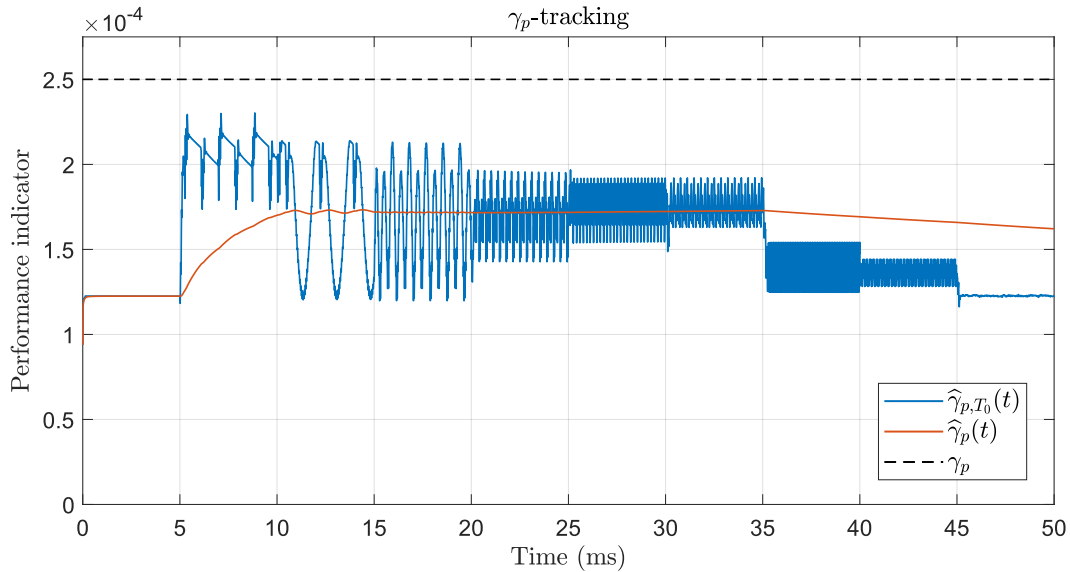


FIGURE 5.11: Performance indicator $\hat{\gamma}_p$ and $\hat{\gamma}_{p,T_0}$ with $T_0 = 1.5 \cdot 2\pi/\omega_{0,x}$ (see (5.59)). Proposed LPV controller.

where $k_p > 0$ corresponds to the proportional gain, $k_r > 0$ is the resonant gain and $0 < \zeta_{res} \ll 1$ is the damping factor (ideally, $\zeta_{res} = 0$). The resonance frequency of $K_{res}^{\omega_r}$ is given by ω_r , such that, if the closed-loop system is stable, it asymptotically ensures the tracking and rejection of sinusoidal signals with frequency ω_r . The LTI controller K_{st} ensures the quadratic stability of the system for all $\omega_r \in \Omega_r [\omega_{r,1}, \omega_{r,2}]$. What is important to note here is that, although this approach provides guarantees of quadratic stability, the tracking of signals in $\mathcal{R} [\omega_{r,1}, \omega_{r,2}]$ is ensured only when ω_r tends to a constant value (or varies slowly). Indeed, in this example, we obtain performance indicators $\hat{\gamma}_{p,T_0}$ and $\hat{\gamma}_p$ that are at least 50 and 10 times higher than the desired specification, respectively. This is mainly due to the fast variations of ω_r .

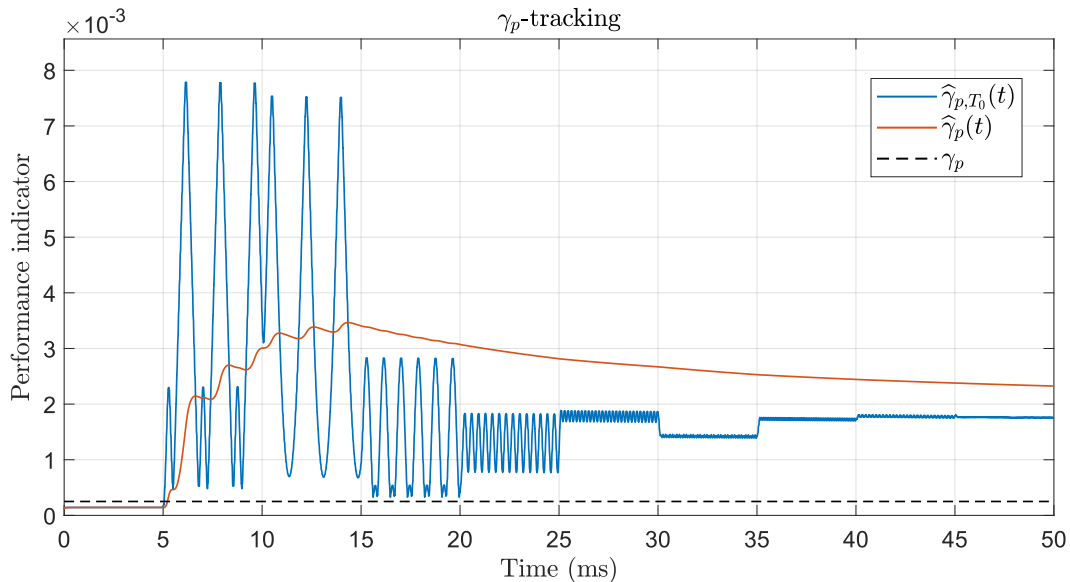


FIGURE 5.12: Performance indicator $\hat{\gamma}_p$ and $\hat{\gamma}_{p,T_0}$ with $T_0 = 1.5 \cdot 2\pi/\omega_{0,x}$ (see (5.59)). Alternative approach.

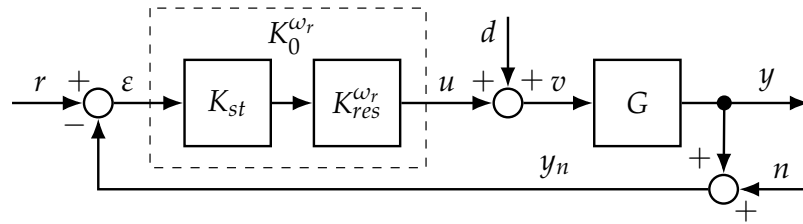


FIGURE 5.13: Alternative control configuration.

5.5 Summary and Conclusions of the Chapter

In this chapter, we propose a new approach for the design of controllers whose objective is to ensure, with a guaranteed performance level, the tracking or rejection of frequency-modulated signals. This control problem can be found in MEMS gyroscopes when an external loop is used to adapt/disturb the instantaneous excitation frequency ω_{exc} for identification purposes, for instance. We highlight however that this problem is also of main interest in other domains, such as in the control of wind turbines or power converters.

In particular, we demonstrate that the original problem of tracking or rejecting frequency-modulated signals can be formulated as a mathematical \mathcal{L}_2 criterion in which weighting functions are used to describe the signals of interest. Nevertheless, different from periodic signals, the time-varying nature of the frequency-modulated signals make it difficult the design of weighting functions in the frequency domain, as is the case in the \mathcal{H}_∞ synthesis, for instance. We thus propose a new class of LTV weighting functions, which formally describes this type of signals.

Based on the LTV weighting functions, the original control problem can then be formulated as a standard polytopic LPV problem. The solution of this problem provides a polytopic controller whose parameters depend on the (measured) instantaneous frequency of the signals of interest. Moreover, this controller formally ensures the tracking/rejection with a certain performance level. This performance level is defined as function of the power of the reference/disturbance and the tracking error signals.

Simulation results confirm the main results of this chapter and illustrate the benefits of our approach against a standard design methods: the guaranteed performance, even under arbitrary variations of ω_r over time.

Chapter 6

Envelope-Based Control: Bringing the Dynamics to Low Frequency

As discussed in Section 2.2, for the closed-loop operation of MEMS gyroscopes, most of the works focus on the envelope-based control architectures, mainly represented by the architectures AGC with PLL for the drive mode (see page 40) and envelope-based (I/Q) for the sense mode (see page 44). The main interest in the use of these approaches comes from the fact that the amplitude and phase or the in-phase and in-quadrature terms are constant or low-frequency signals in steady-state. Hence, we can use PID controllers to track the (constant or low-frequency) reference amplitude and phase shift of the drive mode oscillations, and to compensate for the (constant or low-frequency) in-phase and in-quadrature terms related to the (oscillating) Coriolis and coupling forces, see [IEE04, EMK12, Zur15]. Moreover, the use of PID controllers comes together with accessible design methods and easy implementation (in analog as well as in digital domain), providing an attractive solution for the industry.

Despite all the interesting features of the envelope-based control architectures, we also have to mention some downsides of this approach. Even if the original system (MEMS gyroscope) is mainly linear, nonlinearities (modulators and demodulators) are included in the loop to compute the amplitude and phase shift or in-phase and in-quadrature terms of the modulated signals, making the overall to-be-controlled system nonlinear. The conventional approach is then to establish an envelope model of the system, linearize it around operating points and design independent controllers for the regulation of amplitude and phase or rejection of in-phase and in-quadrature terms [Sau08, EMK12], leading to controllers that are not guaranteed to ensure the performance nor stability of the closed-loop system *a priori*.

In this chapter, we propose a control architecture and a design method that allow us to combine the main advantage of the envelope-based architectures (work with low-frequency signals) with the main strengths of the direct control architecture (guarantees of stability and performance).

The remaining of the chapter is organized as follows. In Section 6.1, we state the problem under investigation. In Section 6.2, we model the nonlinear to-be-controlled system through dynamic phasors (presented in the sequel). Then, we reveal that the to-be-controlled system is actually linear if an adequate representation of the dynamic phasors is considered. In Section 6.3, this fact allows us to apply an \mathcal{H}_∞ /LPV approach to synthesize a controller with stability and performance guarantees. Moreover, with this formalism, we reveal that the best achievable performance of an envelope-based controller is equivalent to the best achievable

performance of a direct controller, under the assumption that the amplitude and phase (or in-phase and in-quadrature terms) of a signal can be perfectly measured in real time. In Section 6.4, we show that this assumption cannot be met in a real application. Nevertheless, we also demonstrate that, in practice, the best way to obtain the amplitude and phase (or in-phase and in-quadrature terms) of a signal is through synchronous demodulators. The drawback is that they introduce filters and nonlinearities in the loop. Then, a novel control design method, which takes these nonidealities into account, is proposed in Section 6.5.

Dynamic Phasor Definitions

Before proceeding with the problem statement, let us introduce some key concepts for the development of this chapter. Let us consider a sinusoidal signal in the form of

$$v(t) = V \cos(\omega_{ph}t + \phi_v),$$

where V defines the amplitude and ϕ_v is the phase shift with respect to a reference phase $\omega_{ph}t$. By using the Euler formula, we can rewrite v as

$$v(t) = \Re \left(\underline{v} e^{j\omega_{ph}t} \right),$$

where the amplitude and phase are represented by a single complex quantity $\underline{v} = V e^{j\phi_v}$, called **phasor**. Thus, the sinusoidal signal v can be interpreted as the projection, over the real-axis, of the phasor \underline{v} rotating on the complex plane with an angular frequency ω_{ph} . The same phasor can be equivalently represented by its real and imaginary parts, *i.e.*, $\underline{v} = \underline{v}_R + j\underline{v}_I$. This form is called **Cartesian** or **rectangular** representation, while the form $\underline{v} = V e^{j\phi_v}$ is called **exponential** or **polar** representation.

The main interest on their use relies on the fact that the phasor \underline{v} of a sinusoidal signal v is directly related to its Fourier transform¹. Then, they can be used to simply describe sinusoidal signals. Phasors are widely used in different fields. In Control Theory, they are particularly used to compute the (steady-state) output of a linear system to sinusoidal inputs.

Now, if the amplitude, the phase shift and the reference frequency ω_{ph} are allowed to vary over time, that is,

$$v(t) = V(t) \cos(\phi_{ph}(t) + \phi_v(t)) \quad \text{with} \quad \phi_{ph}(t) = \int_0^t \omega_{ph}(\tau) d\tau,$$

we can rewrite v as $v(t) = \Re \left(\underline{v}(t) e^{j\phi_{ph}(t)} \right)$. Then, similar to the phasor definition, the complex signal $\underline{v}(t) = V(t) e^{j\phi_v(t)}$ should be referred to as the complex envelope associated with v [Rub09], which are directly related to the in-phase and in-quadrature terms of a modulated signal (see Section 2.1.4, page 23). Indeed, the in-phase and in-quadrature terms respectively correspond to \underline{v}_R and \underline{v}_I (with $\omega_{ph} = \omega_{exc}$). We have to mention, however, that the term complex envelope (or in-phase and in-quadrature terms) presupposes that the

¹Indeed,

$$\mathcal{F}[v](j\omega) = \frac{\underline{v} \cdot \delta(j\omega - j\omega_{ph}) + \bar{\underline{v}} \cdot \delta(j\omega + j\omega_{ph})}{2}.$$

If we consider only the positive frequencies (recalling that real-valued signals have a symmetric spectrum, and considering only the positive frequencies is sufficient to represent the whole signal), we have $\mathcal{F}[v](j\omega) = \underline{v} \cdot \delta(j\omega - j\omega_{ph}) / 2$

variations of \underline{v} are slow and that ω_{ph} is constant over time² (see Section 2.1.4, page 23). Then, to get rid of these inherent assumptions, in this document, we rather use the appellation **dynamic phasors** to describe the complex signal \underline{v} , which can be interpreted as a time-varying phasor and represents the instantaneous amplitude V (or envelope) and the instantaneous phase shift of the signal v with respect to a given reference phase ϕ_{ph} .

6.1 Problem Statement

In this section, we state the problem under investigation.

The main strength of the envelope-based architectures, such as the AGC+PLL and I/Q architectures (see Figure 2.20, page 41, and Figure 2.24, page 45), relies on the use of amplitude and phase or in-phase and in-quadrature terms of an amplitude-modulated signal. Here, we consider the control architecture presented in Figure 6.1, which is based on the amplitude and phase of the signals. The plant is represented by G , and K_{ap} corresponds to the amplitude-and-phase controller. The operator $s2p$ allows extracting the amplitude and phase shift from a modulated signal, while $p2s$ generates a modulated signal from a given amplitude and phase shift. The phase shifts are defined with respect to a given reference phase ϕ_{ph} , which is defined as

$$\phi_{ph}(t) = \int_0^t \omega_{ph}(\tau) d\tau + \phi_{ph}^0 \quad (6.1)$$

with $\phi_{ph}^0 \in \mathbb{R}$ and the instantaneous reference frequency ω_{ph} belonging to a set of measurable functions $\Omega_{ph}[\omega_{ph,1}, \omega_{ph,2}]$, which is defined as, given $\omega_{ph,2} \geq \omega_{ph,1} > 0$,

$$\Omega_{ph}[\omega_{ph,1}, \omega_{ph,2}] = \{\omega_{ph} \mid \forall t \in \mathbb{R}, \omega_{ph}(t) \in [\omega_{ph,1}, \omega_{ph,2}]\}. \quad (6.2)$$

Since ω_{ph} is known, it can be used by the controller.

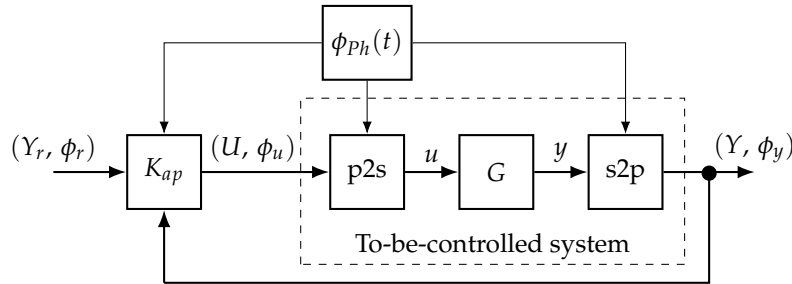


FIGURE 6.1: Amplitude-and-phase control architecture.

In this context, the control problem consists in computing the amplitude U and phase shift ϕ_u of the control signal u such that the amplitude Y and phase shift ϕ_y of the output signal y track the amplitude Y_r and phase shift ϕ_r related to a sinusoidal reference signal y_r . All the phase shifts are defined with respect to a given reference phase³ ϕ_{ph} . The reference signal is, for a given reference phase ϕ_{ph} , defined as

$$y_r(t) = Y_r(t) \cos(\phi_{ph}(t) + \phi_r(t)). \quad (6.3)$$

²In Section 6.4, we will see that these assumptions are related to the practical realization of an operator that allows extracting the complex envelope of a signal.

³Not to be confused with the phase of the reference signal, which would be given by $\phi_{ph}(t) + \phi_r(t)$ (see (6.3)).

Although this architecture can be used in other applications, in the MEMS gyroscope context, G would represent the drive mode and/or the sense mode. For the sake of simplicity, we focus on the use of this architecture for the drive mode. Thus, G represents the drive-mode model. In the same context, as discussed in the previous chapters, the reference signal is usually given by

$$y_r(t) = A_r \sin(\phi_{exc}(t)) \quad (6.4)$$

with $\phi_{exc}(t) = \int_0^t \omega_{exc}(\tau) d\tau + \phi_r^0$ (see, e.g., (5.1), page 117) and defines the operating frequency of the gyroscope, ω_{exc} (we recall that this frequency is supposed to be as close as possible to the actual drive-mode resonance frequency, $\omega_{0,x}$). The reference phase ϕ_{ph} is not necessarily linked to ϕ_{exc} . Nevertheless, if we consider the special case where

$$\phi_{ph}(t) = \int_0^t \omega_{exc}(\tau) d\tau, \quad \phi_r(t) = \phi_r^0 + \pi/2 \quad \text{and} \quad Y_r(t) = A_r, \quad (6.5)$$

(6.3) and (6.4) are equivalent, and the signals to be tracked (Y_r and ϕ_r) are constant over time. Therefore, we consider that these conditions hold hereafter.

Note that, with respect to a direct control architecture, the operators p2s and s2p are introduced in the control loop. The operator p2s is a modulator that computes u from a given amplitude U and phase shift ϕ_u with respect to a given phase ϕ_{ph} , that is,

$$u(t) = U(t) \cos(\phi_{ph}(t) + \phi_u(t)). \quad (6.6)$$

In its turn, the operator s2p, based on the same phase ϕ_{ph} , allows extracting the couple (Y , ϕ_y) from the modulated signal

$$y(t) = Y(t) \cos(\phi_{ph}(t) + \phi_y(t)). \quad (6.7)$$

Please note that, while it is clear how to build u from a given couple (U , ϕ_u) (see (6.6)), the same cannot be said on how to build a couple (Y , ϕ_y) from a given signal y (see (6.7)). By the moment, let us assume that there exists an operator s2p that, somehow, does that. In Section 6.4, we show that an approximation of this operator can be implemented in practice through the synchronous demodulation.

Finally, the main problem of this chapter can be formulated as follows.

Problem 6.1 (Amplitude-and-phase control problem). *Let us consider an LTI system G and the control architecture of Figure 6.1. Given $\omega_{ph,2} \geq \omega_{ph,1} > 0$, let the reference phase ϕ_{ph} be given by (6.1) with $\omega_{ph} \in \Omega_{ph}[\omega_{ph,1}, \omega_{ph,2}]$. Then, we want to design a controller K_{ap} , based on a given couple of reference amplitude and phase shift (Y_r , ϕ_r) and on the couple (Y , ϕ_y), computes the amplitude and phase shift of the control signal (U , ϕ_u) such that (Y , ϕ_y) tracks constant signals (Y_r , ϕ_r), for all $Y_r \in \mathbb{R}_+$ and for all $\phi_y \in \mathbb{R}$. The phase shifts are defined with respect to $\phi_{ph}(t)$.*

We split this problem into four parts, as follows.

- (i) Let us assume that the operators s2p and p2s exist and can be implemented in practice, i.e., Y , ϕ_y can be instantaneously measured from y . Then, how to model the to-be-controlled system (composed of the plant G , and the operators s2p and p2s)?
- (ii) How to design a controller solving Problem 6.1 under the assumptions above?
- (iii) How can we implement in practice the operator s2p?
- (iv) How to solve Problem 6.1 considering an implementable operator s2p?

Each of these questions is answered in each of the following sections.

6.2 System Modeling Through Dynamic Phasors

In this section, we aim to model the to-be-controlled system, which is composed of the plant G and the operators $p2s$ and $s2p$. The plant is defined by the linear system below

$$G : \begin{cases} \dot{x}(t) &= Ax(t) + Bu(t) \\ y(t) &= Cx(t) + Du(t) \end{cases} \quad (6.8)$$

with state vector $x(t) \in \mathbb{R}^n$, input vector $u(t) \in \mathbb{R}^{n_u}$, output vector $y(t) \in \mathbb{R}^{n_y}$, and the real matrices A , B , C and D of appropriate dimensions. Remember that the operator $p2s$ constrains each element of the input vector to be in the form of (6.6), and the output signals are assumed to be in the form of (6.7), such that the operator $s2p$ can extract its instantaneous amplitude and phase shift. Thus, given a function ϕ_{ph} with $\omega_{ph} \in \Omega_{ph}[\omega_{ph,1}, \omega_{ph,2}]$, the to-be-controlled system can be defined by

$$G_{ap} : \begin{cases} \dot{x}(t) &= Ax(t) + BU(t) \cos(\phi_{ph}(t) + \phi_u(t)) \\ \begin{bmatrix} Y(t) \\ \phi_y(t) \end{bmatrix} &= s2p(Cx(t) + DU(t) \cos(\phi_{ph}(t) + \phi_u(t))) \end{cases} \cdot \quad (6.9)$$

Note that the operator $s2p$ is nonlinear and the input signal is a nonlinear function of U and ϕ_u . Then, it is clear that replacing the input and output signals of G by their amplitude and phase (dynamic phasors in the polar representation) makes the to-be-controlled system G_{ap} nonlinear. However, in the sequel, we show that if the signals of G are instead replaced by their

system whose state-space matrices are affine functions of $\omega_{ph}(t)$.

Although we rather consider the original plant as an LTI system (6.8), we show that the same results are easily extended to any LPV system of the form

$$G^\Theta : \begin{cases} \dot{x}(t) &= A(\theta(t))x(t) + B(\theta(t))u(t) \\ y(t) &= C(\theta(t))x(t) + D(\theta(t))u(t) \end{cases}, \quad \theta(\cdot) \in \Theta \quad (6.10)$$

with $x(t) \in \mathbb{R}^n$, $u(t) \in \mathbb{R}^{n_u}$, $y(t) \in \mathbb{R}^{n_y}$, $\theta(t) \in \mathbb{R}^{n_\theta}$ ranges over a fixed polytope Θ and the dependence of the state-space matrices is affine on θ (as in (5.45), page 130). This extension will be of main interest in Section 6.3 for the design of the controller.

6.2.1 Dynamic Phasor Modeling

The following theorem introduces a linear model of the nonlinear plant G_{ap} . This modeling is based on the dynamic phasors associated with the signals of the original plant G .

Theorem 6.1 (Dynamic phasor model). *Let a reference phase $\phi_{ph}(t)$ be given by (6.1) with $\omega_{ph} \in \Omega_{ph}[\omega_{ph,1}, \omega_{ph,2}]$, and consider a couple $(U(t), \phi_u(t))$ and the system G , see (6.8). Then, for the input signal of the form $u(t) = U(t) \cos(\phi_{ph}(t) + \phi_u(t))$, the output of G is given by*

$$y(t) = Y(t) \cos(\phi_{ph}(t) + \phi_y(t)),$$

where $Y(t) = |\underline{y}(t)|$, $\phi_y(t) = \arg(\underline{y}(t))$, and \underline{y} is the output of the system $\underline{G}^{\omega_{ph}}$, defined by

$$\underline{G}^{\omega_{ph}} : \begin{cases} \dot{\underline{x}}(t) &= (A - j\omega_{ph}(t)I)\underline{x}(t) + B\underline{u}(t) \\ \underline{y}(t) &= C\underline{x}(t) + D\underline{u}(t) \end{cases} \quad (6.11)$$

for the input $\underline{u}(t) = U(t)e^{j\phi_u(t)}$.

Proof. Let $\underline{y}(t)$ and $\underline{x}(t)$ be the solution of (6.11) for the input $\underline{u}(t) = U(t)e^{j\phi_u(t)}$. Then, we multiply (6.11) by $e^{j\phi_{ph}(t)}$. By recalling that $\dot{\phi}_{ph}(t) = \omega_{ph}(t)$ (see (6.1)) and since

$$\frac{d}{dt} \left(\underline{x}(t)e^{j\phi_{ph}(t)} \right) = \left(\frac{d\underline{x}(t)}{dt} + j\omega_{ph}(t)\underline{x}(t) \right) e^{j\phi_{ph}(t)},$$

we obtain, with $\omega_{ph} \in \Omega_{ph} [\omega_{ph,1}, \omega_{ph,2}]$,

$$\begin{cases} \frac{d}{dt} \left(\underline{x}(t)e^{j\phi_{ph}(t)} \right) &= A\underline{x}(t)e^{j\phi_{ph}(t)} + B\underline{u}(t)e^{j\phi_{ph}(t)} \\ \underline{y}(t)e^{j\phi_{ph}(t)} &= C\underline{x}(t)e^{j\phi_{ph}(t)} + D\underline{u}(t)e^{j\phi_{ph}(t)} \end{cases} \quad (6.12)$$

By taking the real part of the equations above, we obtain, with $\omega_{ph} \in \Omega_{ph} [\omega_{ph,1}, \omega_{ph,2}]$,

$$\begin{cases} \frac{d}{dt} \left(\Re \left(\underline{x}(t)e^{j\phi_{ph}(t)} \right) \right) &= A\Re \left(\underline{x}(t)e^{j\phi_{ph}(t)} \right) + B\Re \left(\underline{u}(t)e^{j\phi_{ph}(t)} \right) \\ \Re \left(\underline{y}(t)e^{j\phi_{ph}(t)} \right) &= C\Re \left(\underline{x}(t)e^{j\phi_{ph}(t)} \right) + D\Re \left(\underline{u}(t)e^{j\phi_{ph}(t)} \right) \end{cases}, \quad (6.13)$$

which corresponds to (6.8) with $u(t) = U(t) \cos(\phi_{ph}(t) + \phi_u(t))$, $x(t) = \Re \left(\underline{x}(t)e^{j\phi_{ph}(t)} \right)$ and $y(t) = \Re \left(\underline{y}(t)e^{j\phi_{ph}(t)} \right)$. \square

The system $\underline{G}^{\omega_{ph}}$, see (6.11), computes, for a given reference phase ϕ_{ph} defined by $\omega_{ph} \in \Omega_{ph} [\omega_{ph,1}, \omega_{ph,2}]$, the dynamic phasors associated with x and y (respectively \underline{x} and \underline{y}) from the dynamic phasor associated with the input u (\underline{u}). In other words, from the instantaneous amplitude and phase shift of the input signal u (respectively U and ϕ_u), (6.11) governs the behavior of the instantaneous amplitude and phase shift of y (respectively Y and ϕ_y). Thus, we refer to $\underline{G}^{\omega_{ph}}$ as the Dynamic Phasor Model (DPM) of G with respect to the reference phase ϕ_{ph} . The DPM $\underline{G}^{\omega_{ph}}$ is a system whose state matrices and signals are complex-valued. Nevertheless, by splitting the signals into real and imaginary parts, this system can be equivalently represented by the following real-valued one:

$$\underline{G}_{dp}^{\omega_{ph}} : \begin{cases} \dot{x}_{dp}(t) &= A_{dp}(\omega_{ph}(t))x_{dp}(t) + B_{dp}u_{dp}(t) \\ y_{dp}(t) &= C_{dp}x_{dp}(t) + D_{dp}u_{dp}(t) \end{cases} \quad (6.14)$$

with $x_{dp} = \text{col}(\underline{x}_{\Re}, \underline{x}_{\Im})$, $u_{dp} = \text{col}(\underline{u}_{\Re}, \underline{u}_{\Im})$, $y_{dp} = \text{col}(\underline{y}_{\Re}, \underline{y}_{\Im})$,

$$A_{dp}(\omega_{ph}(t)) = \begin{bmatrix} A & \omega_{ph}(t)I \\ -\omega_{ph}(t)I & A \end{bmatrix},$$

$B_{dp} = \text{diag}(B, B)$, $C_{dp} = \text{diag}(C, C)$ and $D_{dp} = \text{diag}(D, D)$. In general, when simply referring to DPM, we refer to its real representation, $\underline{G}_{dp}^{\omega_{ph}}$. Otherwise, if we want to distinguish between the real and complex representations, we shall refer to $\underline{G}^{\omega_{ph}}$ as the Complex DPM of G . In contrast, $\underline{G}_{dp}^{\omega_{ph}}$ is referred to as the Real DPM of G .

Technically, there are no issues in dealing with complex-valued systems. For instance, classical Control Theory tools, such as Bode diagram, Nyquist criterion, and root locus, can be easily adapted and applied to this class of system. The main difference is that, in contrast to real-valued systems, complex-valued ones do not have the symmetric frequency response property. Moreover, complex poles or zeros may not present a conjugated pair. Then, these classical tools would have to be adapted for the use with complex-valued system. On the other hand, the real representation of a complex-valued system doubles the order and size of the input and output vectors. Thus, multivariable tools shall be considered for the analysis even if the original system is SISO. An interesting discussion on the use of complex-valued systems in control can be found in the recent work [TBR17].

All complex-valued systems can be represented by a real-valued one. However, the opposite is not valid. The opposite is valid only for a particular class of real-valued systems, called rotational-invariant systems (also referred to as symmetric or isotropic systems) [Bod14, TBR17]. This point is further discussed in Section 6.2.2.

We also highlight that the DPM (real or complex representation) is an LTV system whose state matrix linearly depends on the (time-varying) reference frequency ω_{ph} . In the literature, ω_{ph} is often considered as constant. Nevertheless, with Theorem 6.1, we demonstrate that the DPM is valid for any function $\omega_{ph} \in \Omega_{ph} [\omega_{ph,1}, \omega_{ph,2}]$. In the sequel, we present, through an example, the accuracy of our approach to describe the envelope of the signals.

Example 6.1. Here, we want to illustrate the application of Theorem 6.1 for modeling the envelope of a signal generated by an LTI system. To this end, we consider the plant G_x of Example 2.1, which admits a state-space representation with the matrices

$$A = \begin{bmatrix} 0 & 1 \\ -\omega_{0,x}^2 & -\omega_{0,x}/Q_x \end{bmatrix}, \quad B = \begin{bmatrix} 0 \\ k_{0,x}\omega_{0,x} \end{bmatrix}, \quad C = [1 \ 0] \quad \text{and} \quad D = 0,$$

recalling that $\omega_{0,x} = 2\pi 11500 \text{ rad s}^{-1}$, $Q_x = 100\,000$ and $k_{0,x} = 2 \cdot 10^{-5}$. We also consider the input signal u given in (6.6) with $U(t) = 0$ for $t < 1\text{s}$, $U(t) = 1$ otherwise, and $\phi_u(t) \equiv 0$. The reference phase ϕ_{ph} , which also corresponds to the excitation one ϕ_{exc} , is given by $\phi_{ph}(t) = \int_0^t \omega_{ph}(\tau) d\tau$ for the function ω_{ph} presented in Figure 6.2 (top).

The signal u is then applied to G , obtaining the output y , which is presented in Figure 6.2 (middle). To compute its envelope, we apply the phasor $\underline{u}(t) = U(t)e^{j\phi_u(t)} = \underline{u}_{\Re}(t) + j\underline{u}_{\Im}(t)$ to the DPM of G_x , which we denote $G_{x,dp}^{\omega_{ph}}$ (computed through (6.14) with $u_{dp} = \text{col}(\underline{u}_{\Re}, \underline{u}_{\Im})$). Also in Figure 6.2 (middle), we can observe that the signal $Y(t) = |\underline{y}(t)| = \sqrt{\underline{y}_{\Re}(t)^2 + \underline{y}_{\Im}(t)^2}$, computed through the DPM, precisely corresponds to the envelope of the signal y , as expected. This fact reveals the accuracy of this model to describe the signal envelope during transient state ($t \geq 1\text{s}$) as well as for time-varying excitation frequencies ($2 < t < 22\text{s}$).

For the sake of completeness, we also present in Figure 6.2 the phase shift $\phi_y(t) = \arg(\underline{y}(t)) = \arctan2(\underline{y}_{\Im}(t), \underline{y}_{\Re}(t))$ (middle) and the real and imaginary parts of \underline{y} (bottom). All these signals are computed through the DPM.

Note that, since

$$u(t) = U(t) \cos(\phi_{ph}(t) + \phi_u(t)) = \underline{u}_{\Re}(t) \cos(\phi_{ph}(t)) - \underline{u}_{\Im}(t) \sin(\phi_{ph}(t)), \quad (6.15)$$

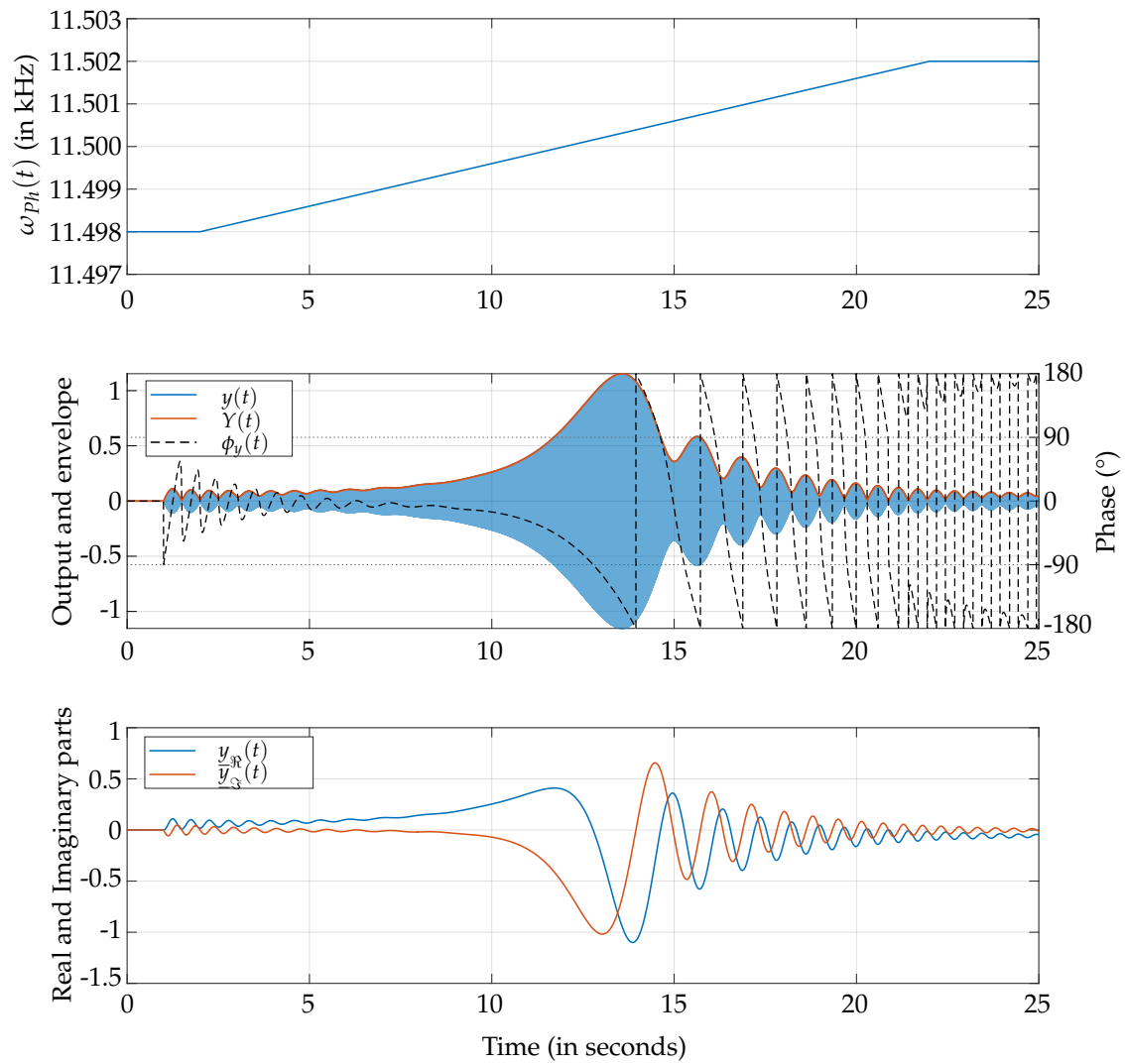


FIGURE 6.2: Simulation of the original system and its DPM with time-varying excitation frequency.

the Real DPM, $G_{dp}^{\omega_{ph}}$, can be rewritten as

$$\begin{cases} \dot{x}(t) &= Ax(t) + B [\cos(\phi_{ph}(t)) & -\sin(\phi_{ph}(t))] u_{dp}(t) \\ y_{dp}(t) &= s2c(Cx(t) + D [\cos(\phi_{ph}(t)) & -\sin(\phi_{ph}(t))] u_{dp}(t)) \end{cases}, \quad (6.16)$$

where x is the state vector of G_{ap} (see (6.9)), and $s2c$ is an operator that associates y_{dp} with y . The only difference between G_{ap} (see (6.9)) and $G_{dp}^{\omega_{ph}}$ (equivalently in (6.14) and (6.16)) is the representation of the dynamic phasors: while G_{ap} uses a polar representation, the latter one takes into consideration the Cartesian representation of the same phasor. Thus, as claimed at the beginning of the section, if we consider the rectangular representation instead of the polar one, for a given $\phi_{ph}(t)$, the to-be-controlled system (6.9) is modeled by an LTV system: $G_{dp}^{\omega_{ph}}$, defined in (6.14).

Extension of the Dynamic Phasor Modeling for an LPV System Note that the only assumption made on the original plant (6.8) is that it must be linear, that is, the original model can be either an LTI or an LPV system. In the LPV case, in which the system matrices depend on a parameter vector θ belonging to a set Θ , the DPM matrices will depend on θ and also on $\omega_{ph}(t)$. That is, for the LPV system (6.10), its DPM is given by, for $\omega_{ph} \in \Omega_{ph}[\omega_{ph,1}, \omega_{ph,2}]$,

$$\underline{G}^{\Theta, \omega_{ph}} : \begin{cases} \dot{\underline{x}}(t) &= (A(\theta(t)) - j\omega_{ph}(t)I) \underline{x}(t) + B(\theta(t)) \underline{u}(t) \\ \underline{y}(t) &= C(\theta(t)) \underline{x}(t) + D(\theta(t)) \underline{u}(t) \end{cases}, \quad \theta(\cdot) \in \Theta, \quad (6.17)$$

or

$$G_{dp}^{\Theta, \omega_{ph}} : \begin{cases} \dot{x}_{dp}(t) &= A_{dp}(\theta(t), \omega_{ph}(t)) x_{dp}(t) + B_{dp}(\theta(t)) u_{dp}(t) \\ y_{dp}(t) &= C_{dp}(\theta(t)) x_{dp}(t) + D_{dp}(\theta(t)) u_{dp}(t) \end{cases}, \quad \theta(\cdot) \in \Theta \quad (6.18)$$

with

$$A_{dp}(\theta(t), \omega_{ph}(t)) = \begin{bmatrix} A(\theta(t)) & \omega_{ph}(t)I \\ -\omega_{ph}(t)I & A(\theta(t)) \end{bmatrix},$$

$B_{dp}(\theta(t)) = \text{diag}(B(\theta(t)), B(\theta(t)))$, $C_{dp}(\theta(t)) = \text{diag}(C(\theta(t)), C(\theta(t)))$ and $D_{dp}(\theta(t)) = \text{diag}(D(\theta(t)), D(\theta(t)))$.

Remark 6.1. Up to this point, there are no particular assumptions on the signals of interest. The only assumptions for this modeling to hold are summarized below.

- (i) The plant G is linear.
- (ii) The operators $s2c$ or $s2p$ are ideal, that is, it is possible to instantly obtain a couple $(Y(t), \phi_y(t))$ or $(\underline{y}_{\Re}(t), \underline{y}_{\Im}(t))$ from the measurement of $y(t)$ and a given $\phi_{ph}(t)$.

In the sequel, we present some essential properties of the Dynamic Phasor Model.

6.2.2 Properties of the Dynamic Phasor Model

For a better understanding of the dynamic phasor model, we evaluate some of its properties. We consider two different cases. First, we consider a particular case where the reference frequency is constant, *i.e.*, $\omega_{ph,1} = \omega_{ph,2} = \omega_{ph}^{\infty}$. This special case arises, for instance, when we want to track a sinusoidal signal y_r of frequency $\omega_{ph}^{\infty} = \omega_{exc}$. In this context, we can discuss the stability, the dynamics, the frequency response and the \mathcal{H}_{∞} norm of the DPM in an LTI framework. In the second case, the reference frequency is time-varying, that is, $\omega_{ph,2} > \omega_{ph,1}$ and $\omega_{ph} \in \Omega_{ph}[\omega_{ph,1}, \omega_{ph,2}]$. This general case arises when we consider the

problem of tracking “variable-frequency sinusoidal” reference signals, as in (6.3). We assess the quadratic \mathcal{L}_2 -gain stability of the DPM in this second case.

Particular Case: Constant Reference Frequency and LTI System

Let us start by considering an LTI system G , whose Complex DPM is given by $\underline{G}^{\omega_{ph}^\infty}$ and Real DPM is given by $G_{dp}^{\omega_{ph}^\infty}$, respectively from (6.11) and (6.14) with $\omega_{ph}(t) \equiv \omega_{ph}^\infty$. The first property to which we bring our attention is the stability equivalence, stated as follows.

Theorem 6.2 (Stability equivalence). *Let G be an LTI system. $\underline{G}^{\omega_{ph}^\infty}$ and $G_{dp}^{\omega_{ph}^\infty}$ are respectively the Complex DPM and Real DPM of G with $\omega_{ph}(t) \equiv \omega_{ph}^\infty$. Then, the DPMs ($\underline{G}^{\omega_{ph}^\infty}$ and $G_{dp}^{\omega_{ph}^\infty}$) are stable if and only if G is stable.*

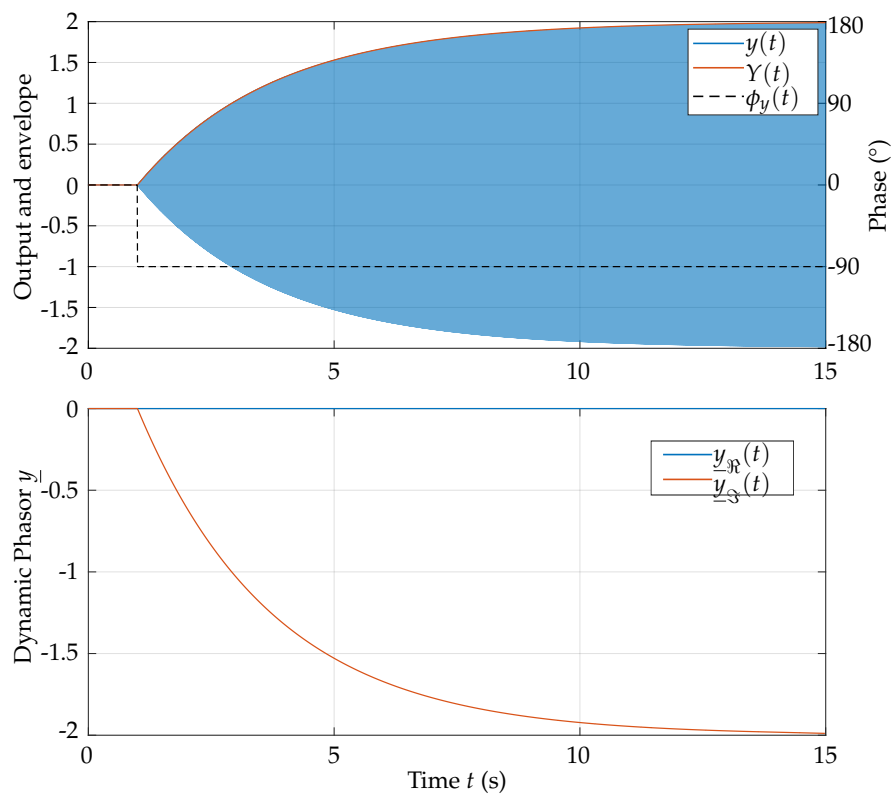
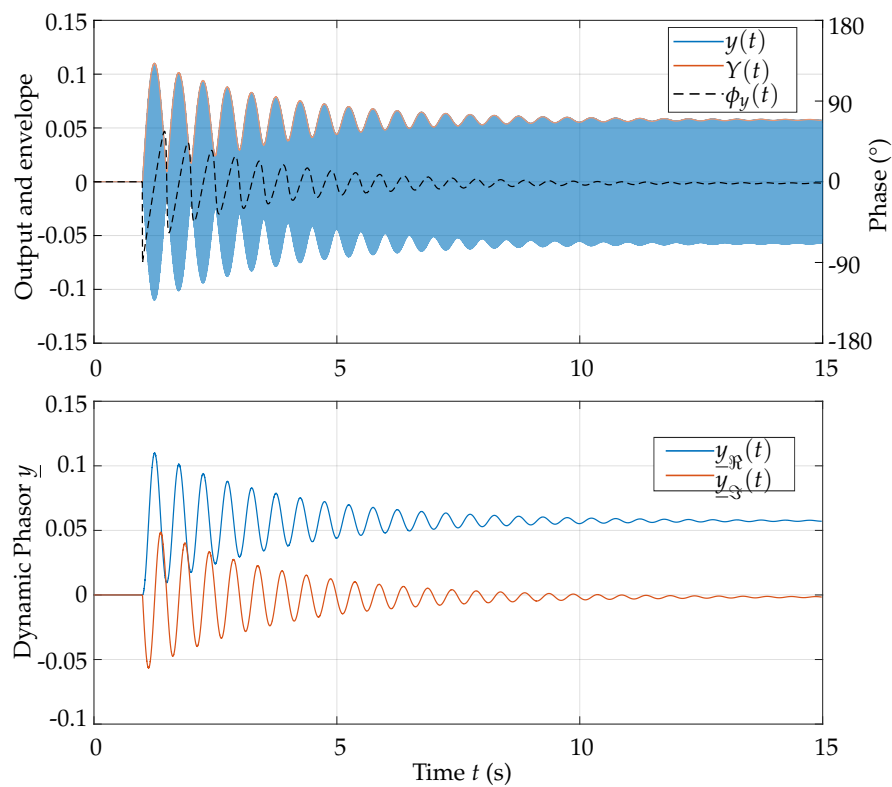
Proof. To prove the equivalence between the stability of the G , $\underline{G}^{\omega_{ph}^\infty}$ and $G_{dp}^{\omega_{ph}^\infty}$, we evaluate the eigenvalues λ of their state matrices: A , $A - j\omega_{ph}^\infty I$ and A_{dp} . Being, for all $i \in \{1, \dots, n\}$, $\lambda_i(A - j\omega_{ph}^\infty I) = \lambda_i(A) - j\omega_{ph}^\infty$, $\lambda_i(A_{dp}) = \lambda_i(A) + j\omega_{ph}^\infty$ and $\lambda_{i+n}(A_{dp}) = \lambda_i(A) - j\omega_{ph}^\infty$, we have $\Re(\lambda_i(A)) = \Re(\lambda_i(A - j\omega_{ph}^\infty I)) = \Re(\lambda_i(A_{dp})) = \Re(\lambda_{i+n}(A_{dp}))$, concluding the proof. \square

It is clear that the dynamics of the DPM is different from the dynamics of the original system. Indeed, the former one depends on the reference frequency ω_{ph}^∞ , while the latter one does not. However, Theorem 6.2 reveals that, even if the DPM dynamics depends on ω_{ph}^∞ , it conserves the stability of the original system. This is illustrated in the next example.

Example 6.2. *Let us consider again the plant G_x , its DPM $G_{x,dp}^{\omega_{ph}^\infty}$, $\phi_u(t) \equiv 0$, and $U(t) = 0$ for $t < 1$ s and $U(t) = 1$ otherwise, as in Example 6.1. Here, we consider two different constant excitation/reference frequencies to show how ω_{ph}^∞ can impact the dynamics of the DPM.*

First, we consider the particular case $\omega_{ph}^\infty = \omega_{0,x}$, representing, in the case of a MEMS gyroscope, the operation of the drive mode with a (perfect) resonance-frequency tracking (ensured by a PLL, Extremum Seeking or closed-loop identification, for instance). We also consider a general case $\omega_{ph}^\infty \neq \omega_{0,x}$, which represents, in the case of a MEMS gyroscope, an operation with a mismatch between the excitation and the resonance frequencies. We choose $\omega_{ph}^\infty = 2\pi 11498 \text{ rad s}^{-1}$, representing a slight mismatch of less than 0.02%.

The simulation results are depicted in Figure 6.3 and Figure 6.4, where we show the real and imaginary parts of the output dynamic phasor as well as the instantaneous amplitude $Y(t) = |\underline{y}(t)|$ and phase $\phi_y(t) = \arg(\underline{y}(t))$ with \underline{y} computed through the DPM. The envelope Y is compared to the signal y , which is obtained at the output of G_x . In the first case (Figure 6.3), with $\omega_{ph}^\infty = \omega_{0,x}$, we can observe that the DPM mainly behaves like a typical first-order system with time constant $\tau_c \approx 3$ s. Moreover, when observing the real and imaginary parts of the phasor \underline{y} , only \underline{y}_{\Im} is modified by the chosen input, indicating that, since $\underline{u}_{\Re}(t) = U(t)$ and $\underline{u}_{\Im}(t) = 0$ (see (6.15) with $\phi_u(t) \equiv 0$), there is no coupling between \underline{u}_{\Re} and \underline{y}_{\Re} in this particular case. However, a slight modification of ω_{ph}^∞ produces an important change on the DPM behavior, see Figure 6.4. Indeed, we could say that the envelope Y behaves like the output of a lightly damped second-order system. In contrast to the first case, the impact of \underline{u}_{\Re} is more important on \underline{y}_{\Re} than on \underline{y}_{\Im} , which also indicates modifications on the transfers coupling \underline{u}_{\Re} to \underline{y}_{\Re} and \underline{y}_{\Im} .

FIGURE 6.3: Output of the DPM and original system for $\omega_{ph}^\infty = 2\pi 11500$.FIGURE 6.4: Output of the DPM and original system for $\omega_{ph}^\infty = 2\pi 11498$.

Let us now discuss the frequency responses of G , $\underline{G}^{\omega_{ph}^\infty}$ and $G_{dp}^{\omega_{ph}^\infty}$. To this purpose, we consider their transfer functions (matrices), which are respectively given by

$$G(s) = C(sI - A)^{-1}B + D, \quad (6.19)$$

$$\underline{G}^{\omega_{ph}^\infty}(s) = C(sI - A + j\omega_{ph}^\infty I)^{-1}B + D \quad (6.20)$$

and

$$G_{dp}^{\omega_{ph}^\infty}(s) = C_{dp}(sI - A_{dp})^{-1}B_{dp} + D_{dp}. \quad (6.21)$$

From (6.19) and (6.20), we have that $\underline{G}^{\omega_{ph}^\infty}(s) = G(s + j\omega_{ph}^\infty)$, and consequently,

$$\underline{G}^{\omega_{ph}^\infty}(j\omega) = G(j\omega + j\omega_{ph}^\infty). \quad (6.22)$$

Thus, the frequency response of the Complex DPM corresponds to a frequency shift of the frequency response of G by ω_{ph}^∞ . Note that evaluating the response of $\underline{G}^{\omega_{ph}^\infty}$ to a constant signal, *i.e.*, $\underline{G}^{\omega_{ph}^\infty}(0)$, is equivalent to evaluate the sinusoidal steady-state response of G to a sinusoidal signal of frequency ω_{ph}^∞ , *i.e.*, $G(j\omega_{ph}^\infty)$. Moreover, also note that, since G has real parameters, its frequency response is symmetric with respect to the frequencies. Then, after shifting, $\underline{G}^{\omega_{ph}^\infty}$ presents an asymmetric frequency response.

Let us now evaluate the frequency response of $G_{dp}^{\omega_{ph}^\infty}$. To this purpose, we develop (6.21) as

$$G_{dp}^{\omega_{ph}^\infty}(s) = \begin{bmatrix} \underline{G}_R(s, \omega_{ph}^\infty) & -\underline{G}_I(s, \omega_{ph}^\infty) \\ \underline{G}_I(s, \omega_{ph}^\infty) & \underline{G}_R(s, \omega_{ph}^\infty) \end{bmatrix}, \quad (6.23)$$

where the terms $\underline{G}_R(s, \omega_{ph}^\infty)$ and $\underline{G}_I(s, \omega_{ph}^\infty)$ are given by

$$\underline{G}_R(s, \omega_{ph}^\infty) = C(sI - A) ((s - j\omega_{ph}^\infty)I - A) ((s + j\omega_{ph}^\infty)I - A)^{-1} B + D \quad (6.24)$$

and

$$\underline{G}_I(s, \omega_{ph}^\infty) = -\omega_{ph}^\infty C ((s - j\omega_{ph}^\infty)I - A) ((s + j\omega_{ph}^\infty)I - A)^{-1} B. \quad (6.25)$$

Note that, as any real representation of a complex-valued system, there is a redundancy in $G_{dp}^{\omega_{ph}^\infty}$: the diagonal blocks are equal (\underline{G}_R), and the off-diagonal blocks are also equal but with opposite sign ($\pm \underline{G}_I$). Systems with this structure are known as isotropic or rotational-invariant systems [Bod14, TBR17]. Further than this property, the DPM also presents the identities below, which are directly derived from (6.24) and (6.25),

$$\underline{G}_R(s, -\omega_{ph}^\infty) = \underline{G}_R(s, \omega_{ph}^\infty) \quad (6.26)$$

and

$$\underline{G}_I(s, -\omega_{ph}^\infty) = -\underline{G}_I(s, \omega_{ph}^\infty). \quad (6.27)$$

Now, we consider a factorization of $G_{dp}^{\omega_{ph}^\infty}$ with unitary matrices⁴, yielding to

$$G_{dp}^{\omega_{ph}^\infty} = \mathcal{I}_y \begin{bmatrix} \underline{G}_R(s, \omega_{ph}^\infty) - j\underline{G}_I(s, \omega_{ph}^\infty) & 0 \\ 0 & \underline{G}_R(s, \omega_{ph}^\infty) + j\underline{G}_I(s, \omega_{ph}^\infty) \end{bmatrix} \mathcal{I}_u, \quad (6.28)$$

⁴A complex square matrix \mathcal{I} is said to be unitary if and only if $\mathcal{I}^* \mathcal{I} = \mathcal{I} \mathcal{I}^* = I$. They have the important property: $\underline{\sigma}(\mathcal{I}) = \overline{\sigma}(\mathcal{I}) = 1$.

where

$$\mathcal{I}_y = \frac{1}{\sqrt{2}} \begin{bmatrix} -jI & jI \\ I & I \end{bmatrix} \quad \text{and} \quad \mathcal{I}_u = \frac{1}{\sqrt{2}} \begin{bmatrix} jI & I \\ -jI & I \end{bmatrix}.$$

Hence, from (6.22), (6.26) and (6.27), the frequency response of $G_{dp}^{\omega_{ph}^\infty}$ can be given by

$$G_{dp}^{\omega_{ph}^\infty} = \mathcal{I}_y \begin{bmatrix} G(j\omega - j\omega_{ph}^\infty) & 0 \\ 0 & G(j\omega + j\omega_{ph}^\infty) \end{bmatrix} \mathcal{I}_u. \quad (6.29)$$

Thus, the frequency response of each element of $G_{dp}^{\omega_{ph}^\infty}$ is a combination of the original system frequency response shifted by $+j\omega_{ph}^\infty$ and $-j\omega_{ph}^\infty$. Moreover, if we evaluate the extremum singular values of $G_{dp}^{\omega_{ph}^\infty}$, because $\sigma(\mathcal{I}_y) = \sigma(\mathcal{I}_u) = 1$, we obtain

$$\begin{aligned} \underline{\sigma}(G_{dp}^{\omega_{ph}^\infty}) &= \min(\underline{\sigma}(G(j\omega - j\omega_{ph}^\infty)), \underline{\sigma}(G(j\omega + j\omega_{ph}^\infty))) \\ \bar{\sigma}(G_{dp}^{\omega_{ph}^\infty}) &= \max(\bar{\sigma}(G(j\omega - j\omega_{ph}^\infty)), \bar{\sigma}(G(j\omega + j\omega_{ph}^\infty))). \end{aligned} \quad (6.30)$$

These singular values define the bounds of the $G_{dp}^{\omega_{ph}^\infty}$ frequency response. An illustration will be presented in Example 6.3.

In Chapter 3, we express the performance specifications of a MEMS gyroscope through an \mathcal{H}_∞ criterion. Then, for considering the use of the dynamic phasor framework for this application, assessing the \mathcal{H}_∞ norm of the DPM is also of central concern.

Theorem 6.3 (\mathcal{H}_∞ -norm equivalence). *Let G be a given LTI system. $\underline{G}^{\omega_{ph}^\infty}$ and $G_{dp}^{\omega_{ph}^\infty}$ are respectively the Complex DPM and Real DPM of G with $\omega_{ph}(t) \equiv \omega_{ph}^\infty$. Then, the \mathcal{H}_∞ norm of the DPMs ($\underline{G}^{\omega_{ph}^\infty}$ and $G_{dp}^{\omega_{ph}^\infty}$) is equal to the \mathcal{H}_∞ norm of G , that is,*

$$\|G\|_\infty = \|\underline{G}^{\omega_{ph}^\infty}\|_\infty = \|G_{dp}^{\omega_{ph}^\infty}\|_\infty. \quad (6.31)$$

This result shows that the DPMs conserve the \mathcal{H}_∞ norm of the original LTI system, regardless of the representation (real or complex) and the constant reference frequency ω_{ph}^∞ .

Proof of Theorem 6.3. From the \mathcal{H}_∞ -norm definition (Definition 4.1, page 76) and the frequency response of $\underline{G}^{\omega_{ph}^\infty}$ (see (6.22)), it follows immediately that $\|\underline{G}^{\omega_{ph}^\infty}\|_\infty = \|G\|_\infty$. From (6.30), it follows that $\|G_{dp}^{\omega_{ph}^\infty}\|_\infty = \|G\|_\infty$, completing the proof. \square

Example 6.3 (Continuation and end). *In Figure 6.5, we plot the Bode diagrams of each transfer of the DPM for the two reference frequencies considered in Example 6.2. At a first glance, we note that the diagonal terms are equal and that the off-diagonal elements are equal in magnitude and have a difference of 180° in phase, as expected (see (6.23)).*

As presented in Example 2.1, the Bode diagram of G_x presents a strong resonance peak at $\omega_{0,x}$, see Figure 2.10 (page 22). Then, when considering its DPM with $\omega_{ph}^\infty = \omega_{0,x}$, this resonance peak is shifted to $\omega = 0$ and to $\omega = 2\omega_{0,x}$. Now, if we neglect the high-frequency resonance peaks and focus on the transfers from $\underline{u}_{\mathcal{R}}$, we note that the transfer from $\underline{u}_{\mathcal{R}}$ to $\underline{y}_{\mathcal{R}}$ has very small gains (in general, smaller than -100 dB), while the transfer from $\underline{u}_{\mathcal{R}}$ to $\underline{y}_{\mathcal{S}}$ is similar to a first-order low-pass filter with a cutoff frequency close to 0.05 Hz and a gain close to 2 in low-frequencies.

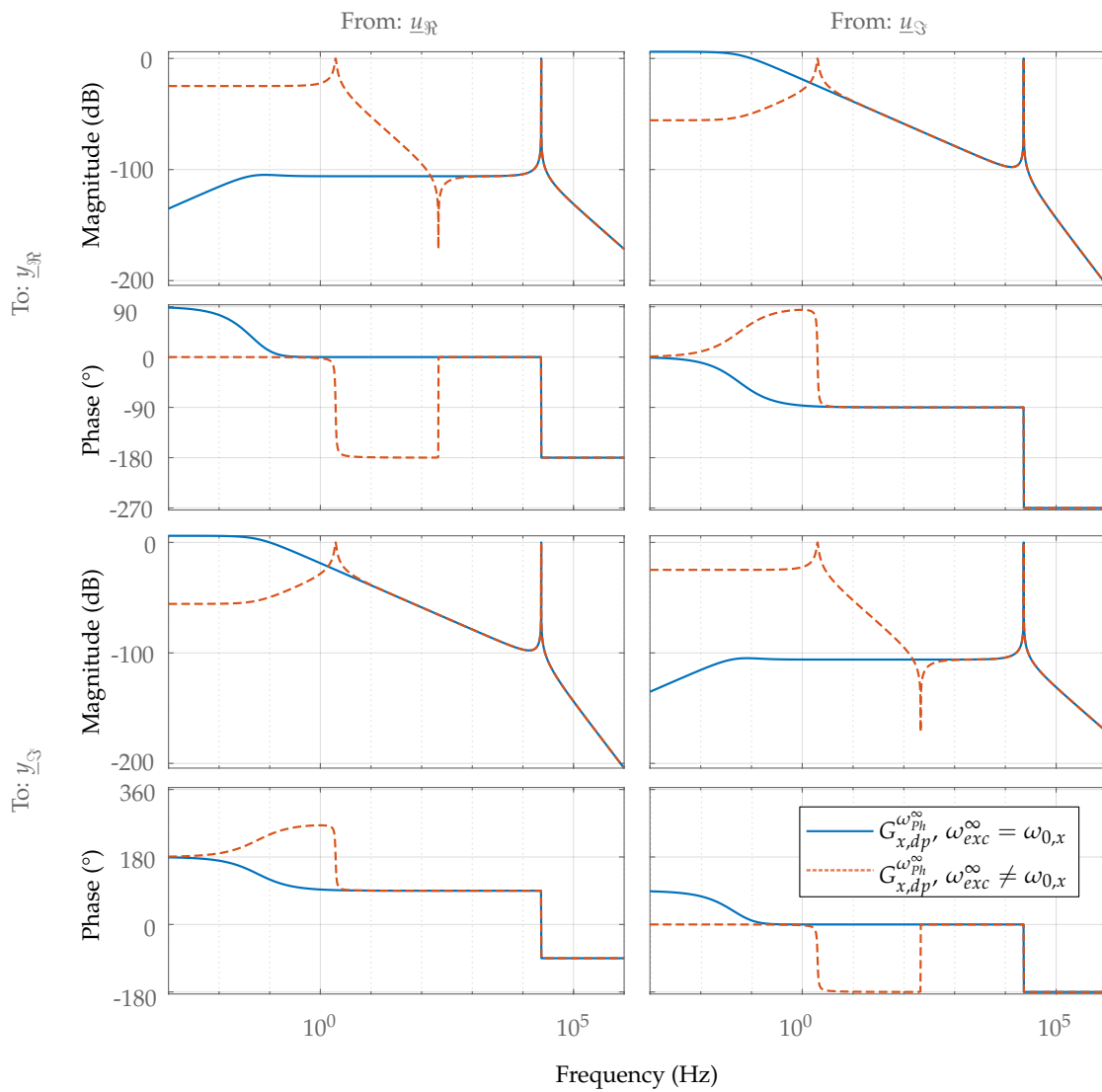


FIGURE 6.5: Bode diagrams of $G_{x,dp}^{\omega_{ph}^{\infty}}$ for $\omega_{ph}^{\infty} = 2\pi 11500 = \omega_{0,x}$ and for $\omega_{ph}^{\infty} = 2\pi 11498 \neq \omega_{0,x}$.

When considering the DPM with $\omega_{ph}^\infty \neq \omega_{0,x}$, the resonance peak of the system is shifted to $\omega = \omega_{0,x} - \omega_{ph}^\infty$ and to $\omega = \omega_{0,x} + \omega_{ph}^\infty$. If we proceed with a similar interpretation, we note that in this case the transfer from \underline{u}_R to \underline{y}_R behaves as a low-pass filter with a gain close to 0.06 in low-frequencies and with a resonance peak close to 2 Hz, justifying the oscillations found in Example 6.2. In its turn, the transfer from \underline{u}_R to \underline{y}_S behaves like a band-pass filter, attenuating low and high frequencies. Both analyses are coherent with the results of Example 6.2.

In Figure 6.6, we present the singular values of the DPM for the two reference frequencies. Further than the behavior described above, note that in both cases, the maximum value of the maximum singular values is equal to 6 dB, which corresponds to $\|G_x\|_\infty = 2$, as expected.

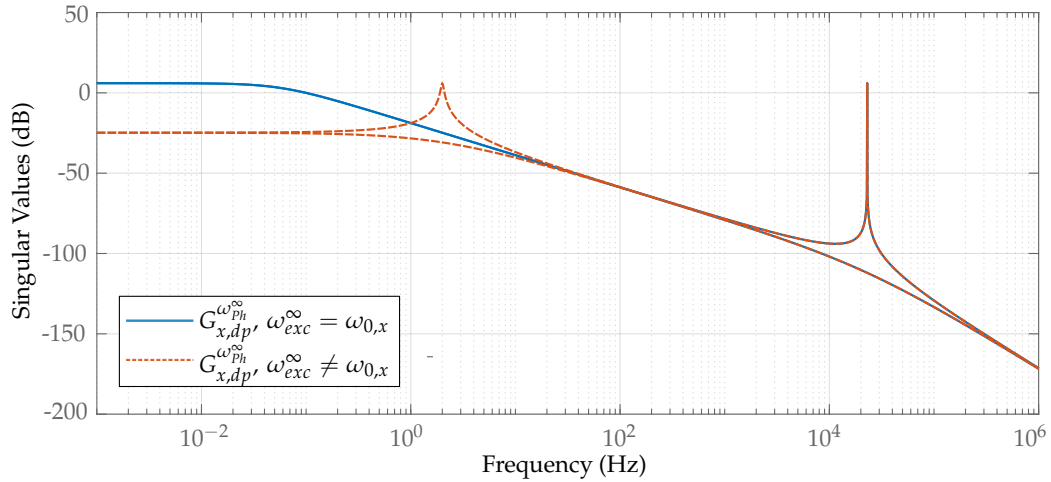


FIGURE 6.6: Singular values of $G_{x,dp}^{\omega_{ph}^\infty}$ for $\omega_{ph}^\infty = 2\pi 11500 = \omega_{0,x}$ and for $\omega_{ph}^\infty = 2\pi 11498 \neq \omega_{0,x}$.

Remark 6.2 (On the DPM high-frequency modes). In general, we may be interested only on the (dominant) low-frequency dynamics of the DPM. Indeed, in Example 6.2, the effects of the high-frequency resonance peaks cannot be noticed. Then, these high-frequency resonance peaks are often neglected for practical reasons, see, e.g., [EK10]. Nevertheless, for the sake of formalism, in this work, we keep these modes in the DPM.

General Case: Time-Varying Reference Frequency and LPV System

We now consider a more general case: with the original system G , we investigate the link between the properties of G and of its DPMs $\underline{G}^{\omega_{ph}}$ and $G_{dp}^{\omega_{ph}}$ (see (6.8), (6.11) and (6.14), respectively) for all $\omega_{ph} \in \Omega_{ph} [\omega_{ph,1}, \omega_{ph,2}]$. In particular, we consider the quadratic \mathcal{L}_2 -gain stability of these systems.

Please note that evaluating the quadratic \mathcal{L}_2 -gain stability of the LTV systems $\underline{G}^{\omega_{ph}}$ and $G_{dp}^{\omega_{ph}}$ for all $\omega_{ph} \in \Omega_{ph} [\omega_{ph,1}, \omega_{ph,2}]$ is equivalent to evaluating the quadratic \mathcal{L}_2 -gain stability of the LPV systems $\underline{G}^{\Omega_{ph}}$ and $G_{dp}^{\Omega_{ph}}$, which are defined as follows:

$$\underline{G}^{\Omega_{ph}} = \{ \underline{G}^{\omega_{ph}}, \omega_{ph} \in \Omega_{ph} [\omega_{ph,1}, \omega_{ph,2}] \}$$

$$G_{dp}^{\Omega_{ph}} = \{ G_{dp}^{\omega_{ph}}, \omega_{ph} \in \Omega_{ph} [\omega_{ph,1}, \omega_{ph,2}] \}.$$

Since we enter in the LPV framework, we also generalize the original system to the LPV plant G^Θ . Therefore, we want to investigate the link between the quadratic \mathcal{L}_2 -gain stability of G^Θ

(see (6.10)) and that of $\underline{G}^{\Theta, \Omega_{Ph}}$ and $G_{dp}^{\Theta, \Omega_{Ph}}$, where

$$\begin{aligned}\underline{G}^{\Theta, \Omega_{Ph}} &= \left\{ \underline{G}^{\Theta, \omega_{Ph}}, \omega_{Ph} \in \Omega_{Ph} [\omega_{Ph,1}, \omega_{Ph,2}] \right\} \\ G_{dp}^{\Theta, \Omega_{Ph}} &= \left\{ G_{dp}^{\Theta, \omega_{Ph}}, \omega_{Ph} \in \Omega_{Ph} [\omega_{Ph,1}, \omega_{Ph,2}] \right\}\end{aligned}$$

with $\underline{G}^{\Theta, \omega_{Ph}}$ and $G_{dp}^{\Theta, \omega_{Ph}}$ respectively given in (6.17) and (6.18).

The following result allows then to generalize the results of the particular case, where $\omega_{Ph}(t) \equiv \omega_{Ph}^{\infty}$ and G is LTI, to the general LPV case, where G^{Θ} is LPV and we consider all $\omega_{Ph} \in \Omega_{Ph} [\omega_{Ph,1}, \omega_{Ph,2}]$.

Theorem 6.4 (Quadratic \mathcal{L}_2 -gain stability equivalence). *Let us consider the LPV system G^{Θ} , its Complex DPM $\underline{G}^{\Theta, \Omega_{Ph}}$ and Real DPM $G_{dp}^{\Theta, \Omega_{Ph}}$. Then,*

$$\left\| G^{\Theta} \right\|_{i_2}^q = \left\| \underline{G}^{\Theta, \Omega_{Ph}} \right\|_{i_2}^q = \left\| G_{dp}^{\Theta, \Omega_{Ph}} \right\|_{i_2}^q. \quad (6.32)$$

Sketch of proof. This proof is based on the definition of the quadratic \mathcal{L}_2 -gain stability (Definition 5.9). First, we prove that the solution to the LMI (5.47) applied to G^{Θ} generates a solution for the same problem when applied to $G_{dp}^{\Theta, \Omega_{Ph}}$. The same procedure is applied in the other direction. The complete proof is given in Appendix E.1. \square

Since the \mathcal{H}_{∞} norm of an LTI system is equal to its \mathcal{L}_2 gain, if G is an LTI system, (6.32) reduces to

$$\|G\|_{\infty} = \left\| \underline{G}^{\Omega_{Ph}} \right\|_{i_2}^q = \left\| G_{dp}^{\Omega_{Ph}} \right\|_{i_2}^q. \quad (6.33)$$

In addition to considering an LTI system G , if $\Omega_{Ph} = \{\omega_{Ph}^{\infty}\}$, (6.32) simplifies to (6.31). Moreover, since the quadratic \mathcal{L}_2 -gain stability property of an LTI system implies internal stability, this theorem unifies and generalizes Theorems 6.2 and 6.3.

6.3 Dynamic Phasor Control

In the previous section, we have revealed that the *a priori* nonlinear to-be-controlled system G_{ap} (see (6.9)) is actually linear if, instead of using the polar representation of the dynamic phasors (amplitude and phase), the signals are represented by their corresponding dynamic phasor in the rectangular representation (see (6.14)). Therefore, with a change on the dynamic phasor representation, the control scheme of Figure 6.1 can be equivalently replaced by the one presented in Figure 6.7, which we denote dynamic phasor control architecture. Having said that, the (nonlinear) amplitude-and-phase control problem (Problem 6.1) can be recast as follows.

Problem 6.2 (Dynamic phasor control problem). *Given the DPM of G ($G_{dp}^{\omega_{Ph}}$), design a controller $\underline{K}^{\omega_{Ph}}$ with state-space matrices $\underline{A}(\omega_{Ph})$, $\underline{B}(\omega_{Ph})$, $\underline{C}(\omega_{Ph})$, $\underline{D}(\omega_{Ph})$, which, based on y_{dp} and on a reference phasor $y_{r,dp}$, computes u_{dp} such that y_{dp} tracks $y_{r,dp}$ for all $\omega_{Ph} \in \Omega_{Ph} [\omega_{Ph,1}, \omega_{Ph,2}]$.*

Similar to Chapter 5), solving this LTV control problem for all $\omega_{Ph} \in \Omega_{Ph} [\omega_{Ph,1}, \omega_{Ph,2}]$ is equivalent to solving a standard LPV problem. Obviously, if Ω_{Ph} reduces to a singleton (*i.e.*, $\Omega_{Ph} = \{\omega_{Ph}^{\infty}\}$), this control problem can be solved in an LTI framework through the \mathcal{H}_{∞} synthesis.

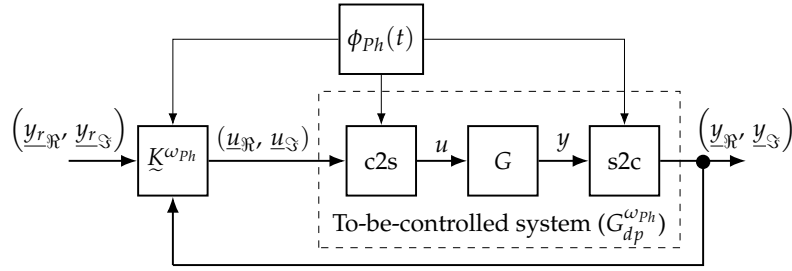


FIGURE 6.7: Dynamic phasor control architecture.

In this section, we aim to answer two main questions.

- (i) Considering the direct control architecture presented in Chapter 5 and the dynamic phasor control approach, does any of them ensure a better performance level?

In this context, we consider an LPV augmented plant P^\ominus in the form of (5.50) (page 131) with n_{u_p} control signals, n_w exogenous input signals, n_{y_p} measured outputs and n_z controlled outputs. This augmented plant is composed of the original to-be-controlled system G and weighting functions, which are used to enforce the desired closed-loop specification and depend on the excitation frequency ω_{exc} . The controller K^\ominus is of the form of (5.51) (page 131) and also depends on ω_{exc} . The performance level γ represents an upper bound on $\|P^\ominus \star K^\ominus\|_{i2'}^q$, that is, $\|P^\ominus \star K^\ominus\|_{i2'}^q < \gamma$.

Note that P^\ominus expresses the desired control specifications in the direct control approach. To express the same specifications in the dynamic phasor framework, we use the DPM of P^\ominus for all $\omega_{ph} \in \Omega_{ph} [\omega_{ph,1}, \omega_{ph,2}]$, denoted $P_{dp}^{\ominus, \Omega_{ph}}$. Furthermore, we consider that the reference frequency, ω_{ph} , is equal to the excitation frequency, that is, $\omega_{ph} = \omega_{exc}$.

- (ii) In Chapters 4 and 5, we see how to design a direct controller fulfilling specifications that are related to the global performance of the MEMS gyroscope. However, for practical implementation reasons, it can be preferred to use an envelope-based architecture. In this context, is it possible to transform a direct controller into a dynamic phasor one? If so, how?

6.3.1 Connections Between Direct Control and Dynamic Phasor Control

We now investigate the links between the direct control problem and the complex phasor one. These links will allow us to evaluate the performance levels obtained with each approach. However, before proceeding, let us define the permutation matrices \mathcal{P}_{in} and \mathcal{P}_{out} , given by

$$\mathcal{P}_{in} = \begin{bmatrix} I_{n_w} & 0 & 0 & 0 \\ 0 & 0 & I_{n_{u_p}} & 0 \\ 0 & I_{n_w} & 0 & 0 \\ 0 & 0 & 0 & I_{n_{u_p}} \end{bmatrix} \quad \text{and} \quad \mathcal{P}_{out} = \begin{bmatrix} I_{n_z} & 0 & 0 & 0 \\ 0 & 0 & I_{n_z} & 0 \\ 0 & I_{n_{y_p}} & 0 & 0 \\ 0 & 0 & 0 & I_{n_{y_p}} \end{bmatrix}.$$

These matrices are used to permute the inputs and outputs of the DPM of the augmented system P^\ominus , such that the Redheffer (star) product can be correctly applied. Now, we are ready to state one of the main results of the chapter.

Theorem 6.5. Let P^\ominus be the augmented plant defined by (5.50) and K^\ominus the controller defined by (5.51). Moreover, let $P_{dp}^{\ominus, \Omega_{ph}}$, $K_{dp}^{\ominus, \Omega_{ph}}$ and $(P^\ominus \star K^\ominus)_{dp}^{\Omega_{ph}}$ be respectively the DPM of P^\ominus , K^\ominus and $P^\ominus \star K^\ominus$ for all $\omega_{ph} \in \Omega_{ph}[\omega_{ph,1}, \omega_{ph,2}]$, and define $\mathcal{P}_{dp}^{\ominus, \Omega_{ph}} \triangleq \mathcal{P}_{out} P_{dp}^{\ominus, \Omega_{ph}} \mathcal{P}_{in}$. Then, given $\gamma > 0$,

$$(i) (P^\ominus \star K^\ominus)_{dp}^{\Omega_{ph}} = \mathcal{P}_{dp}^{\ominus, \Omega_{ph}} \star K_{dp}^{\ominus, \Omega_{ph}};$$

$$(ii) \text{ if } K^\ominus \text{ is such that } \|P^\ominus \star K^\ominus\|_{i2}^q < \gamma \text{ then } \|\mathcal{P}_{dp}^{\ominus, \Omega_{ph}} \star K_{dp}^{\ominus, \Omega_{ph}}\|_{i2}^q < \gamma;$$

(iii) there exists an LPV controller $\underline{K}^{\ominus, \Omega_{ph}}$ such that $\|\mathcal{P}_{dp}^{\ominus, \Omega_{ph}} \star \underline{K}^{\ominus, \Omega_{ph}}\|_{i2}^q < \gamma$ if and only if there exists K^\ominus such that $\|P^\ominus \star K^\ominus\|_{i2}^q < \gamma$.

The first property states that the DPM of the interconnection $P^\ominus \star K^\ominus$ is equal to the interconnection of their DPMs.

The second property claims that if a direct controller K^\ominus achieves a given performance level γ , then the DPM $K_{dp}^{\ominus, \Omega_{ph}}$ of K^\ominus is a solution of the dynamic phasor control problem, ensuring the same performance level γ . Put differently, if a direct controller K^\ominus achieves a given performance level, a phasor controller can be directly computed through Theorem 6.1, i.e., $K_{dp}^{\ominus, \Omega_{ph}}$, and this controller ensures the same performance level γ .

The third property is the most interesting result. It reveals that if $\underline{K}^{\ominus, \Omega_{ph}}$ (solution to the dynamic phasor control problem) achieves a given performance level then, necessarily, the same level of performance can be obtained by a direct control law and vice-versa. In other words, even with an augmented degree of freedom (number of variables), the phasor controller cannot achieve a better performance level than that of a direct controller.

Sketch of proof. (Details are provided in Appendix E.2)

Property (i): By writing the state-space representation of $(P^\ominus \star K^\ominus)_{dp}^{\Omega_{ph}}$ and $\mathcal{P}_{dp}^{\ominus, \Omega_{ph}} \star K_{dp}^{\ominus, \Omega_{ph}}$ from those of P^\ominus and K^\ominus , and by observing that they are equal, one proves Property (i).

Property (ii): Follows from Property (i) and Theorem 6.4.

Property (iii): The proof consists in applying the LPV problem associated to the direct control problem. The existence of K^\ominus such that $\|P^\ominus \star K^\ominus\|_{i2}^q < \gamma$ is equivalent to the existence of a solution to the feasibility problem defined by Theorem 5.2 (page 131). Then, the solution of this problem is used to construct the solution of the feasibility problem defined by Theorem 5.2 when it is applied to the dynamic phasor control problem, implying the existence of $\underline{K}^{\ominus, \Omega_{ph}}$ such that $\|\mathcal{P}_{dp}^{\ominus, \Omega_{ph}} \star \underline{K}^{\ominus, \Omega_{ph}}\|_{i2}^q < \gamma$. The same procedure is applied in the other sense, changing the direct problem by the dynamic phasor problem and vice-versa. \square

The following example illustrates how a direct controller can be implemented in a phasor control architecture, obtaining the same results that it would have in the direct control architecture.

Example 6.4. In this example, we consider the model and the direct controller of Section 5.4 (page 132). The controller is transformed into a phasor controller $K_{dp}^{\ominus, \Omega_{ph}}$ through (6.18) and implemented according to the phasor-based architecture of Figure 6.7. Since the operator $s2c$ cannot be ideally implemented in practice (this point is detailed in the next section), we use the DPM of G , $G_{dp}^{\Omega_{ph}}$, to model the to-be-controlled system.

To evaluate the tracking performance of the system (γ_p -tracking), we apply a reference signal with the same amplitude $A_r = 1$ and the same time-varying frequency as in Section 5.4 (see Figure 5.8, page 136). The performance indicators are computed as

$$\widehat{\gamma}_{p,T_0}(t) \triangleq \sqrt{\frac{\int_{t-T_0}^t \varepsilon_{dp}(\tau)^\top \varepsilon_{dp}(\tau) d\tau}{\int_{t-T_0}^t y_{r,dp}(\tau)^\top y_{r,dp}(\tau) d\tau}} \quad \text{and} \quad \widehat{\gamma}_p(t) \triangleq \sqrt{\frac{\int_0^t \varepsilon_{dp}(\tau)^\top \varepsilon_{dp}(\tau) d\tau}{\int_0^t y_{r,dp}(\tau)^\top y_{r,dp}(\tau) d\tau}}. \quad (6.34)$$

The evolution of these indicators over time is illustrated in Figure 6.8 and corresponds to the same indicators obtained in the previous chapter for the direct approach (see Figure 5.11, page 138). This fact confirms the property (ii) of Theorem 6.5.

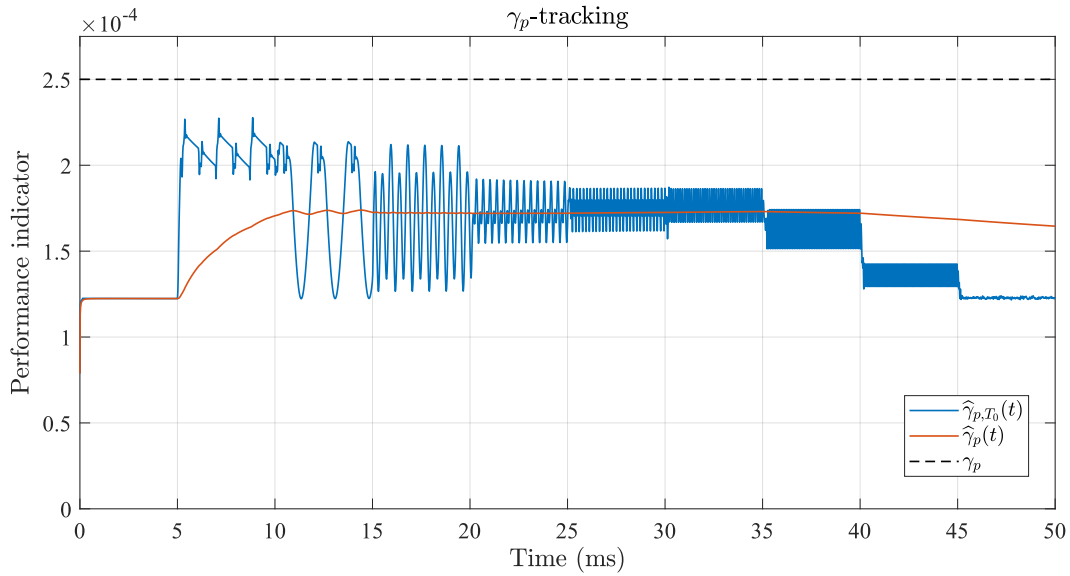


FIGURE 6.8: Performance indicator $\widehat{\gamma}_p$ and $\widehat{\gamma}_{p,T_0}$ with $T_0 = 1.5 \cdot 2\pi/\omega_{0,x}$ (see (6.34)). LPV phasor controller.

In Figure 6.9, we present the tracking error of both strategies. For the sake of clarity, we illustrate only the time interval $t \in [5, 20]$ ms, but the conclusions hold for the whole simulation. We observe that, as expected, the tracking error in the phasor control approach corresponds exactly to the envelope of the tracking error obtained in the direct approach.

The above results are based on the fact that G_{ap} (see (6.9)) is exactly described by $G_{dp}^{\Omega_{ph}}$ (with different representation of the dynamic phasors). Nonetheless, we will discuss in the next section that the ideal operators s2c and s2p cannot be implemented in practice. To extract amplitude and phase of a signal (or equivalently the real and imaginary parts of the phasor), nonlinear operators and filters are introduced in the loop. These additional elements, that were not taken into consideration in this section, may drastically degrade the performance of the closed-loop system or even make it unstable. Thus, in the next section, we present how to implement the operator s2c and how to model its nonidealities. Then, we propose an approach to take into account these nonidealities during the control design.

6.4 Implementation of the Operators s2c and s2p

Up to this point, we have considered the blocks s2p and s2c as operators that allow extracting from a sinusoidal signal y the couples (Y, ϕ_y) and $(\underline{y}_{\Re}, \underline{y}_{\Im})$, respectively (*i.e.*, the components

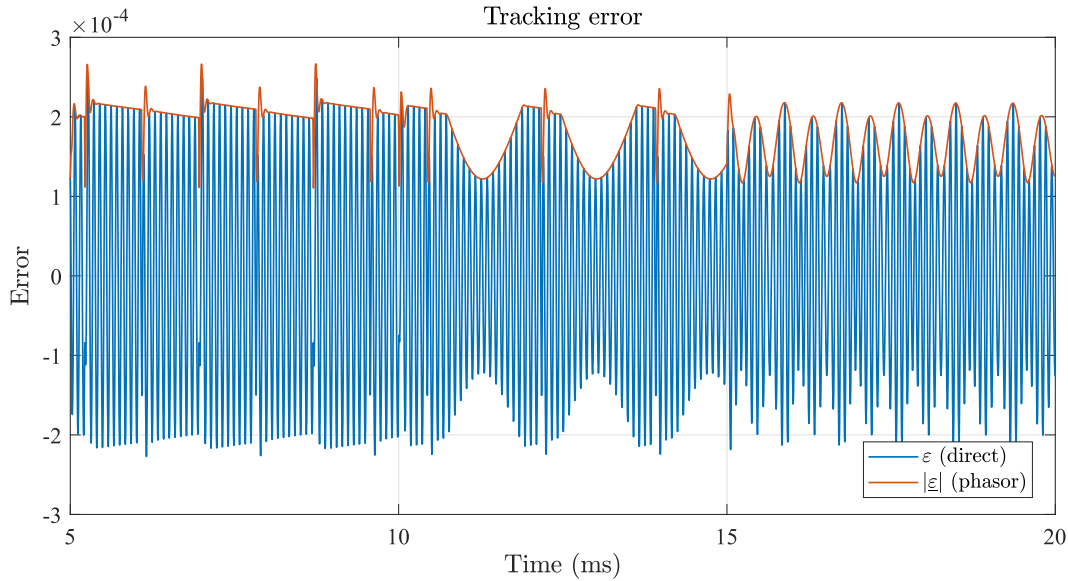


FIGURE 6.9: Tracking error of direct control and phasor control architectures.

of the associated dynamic phasor \underline{y}). In this section, we show that these operators cannot be ideally implemented in practice due to an ambiguity problem. However, if spectral constraints are imposed on the signals of interest, a real s2c can be implemented by the synchronous demodulation. The study is realized in a constant-frequency framework, *i.e.*, $\omega_{ph}(t) \equiv \omega_{ph}^\infty$. At the end of the section, a discussion on the time-varying frequency case is drawn.

6.4.1 Uniqueness Between a Modulated Signal and its Dynamic Phasor

The main problem concerning the implementation of the operators s2c and the s2p is related to the so-called **ambiguity problem**, which we describe as follows. Let us consider a signal y of the form

$$y(t) = \Re \left(\underline{y}(t) e^{j\omega_{ph}^\infty t} \right) \quad \text{with} \quad \underline{y}(t) = Y(t) e^{j\phi_y(t)}. \quad (6.35)$$

The question is: given $y(t)$ and ω_{ph}^∞ , is it possible to compute a unique dynamic phasor \underline{y} associated with y ? Unfortunately, the answer is no. If we consider, for example,

$$y(t) = 10 \cos(\omega_{ph}^\infty t + \pi/4), \quad (6.36)$$

one could promptly define $Y(t) \equiv 10$ and $\phi_y(t) \equiv \pi/4$. However, $Y(t) = 10 \cos(\omega_{ph}^\infty t + \pi/4)$ and $\phi_y(t) = -\omega_{ph}^\infty t$ is also a valid couple⁵. In fact, an infinite number of dynamic phasors \underline{y} (or couples $(Y(t), \phi_y(t))$) define the same signal y .

The ambiguity problem is recurrent in the literature and comes from the fact that only the real part of $\underline{y}(t) e^{j\omega_{ph}^\infty t}$ defines y . Note that the actual problem is then how to properly define the imaginary part of $\underline{y}(t) e^{j\omega_{ph}^\infty t}$. In general, the solution is based on the classical notion of analytic signal (or pre-envelope) [Gab46, VV77, Ven94, Pic97], whose definition is given below.

⁵Recall that (6.35) can be written as $y(t) = Y(t) \cos(\omega_{ph}^\infty t + \phi_y(t))$.

Definition 6.1 (Analytic signal). A signal $\tilde{v}(t) \in \mathbb{C}$ is said to be an analytic signal if its spectrum is null for nonpositive frequencies⁶, that is,

$$\forall \omega \leq 0, \quad \mathcal{F}[\tilde{v}](\omega) = 0. \quad (6.37)$$

Moreover, $\tilde{v}(t)$ is said to be associated to a signal $v(t) \in \mathbb{R}$ if $\Re(\tilde{v}(t)) = v(t)$.

Based on the above definition, if we define $\underline{y}(t)e^{j\omega_{ph}^\infty t}$ as the analytic signal \tilde{y} associated to y , \underline{y} can be unambiguously computed as

$$\underline{y}(t) = \tilde{y}(t)e^{-j\omega_{ph}^\infty t}, \quad (6.38)$$

solving the ambiguity problem.

Let us apply this result to our example. First, we rewrite (6.36) as

$$y(t) = \frac{10}{2} \left(e^{j\omega_{ph}^\infty t + j\pi/4} + e^{-j\omega_{ph}^\infty t - j\pi/4} \right).$$

In this particular case, we can obtain \tilde{y} by eliminating the term $e^{-j\omega_{ph}^\infty t - j\pi/4}$ (nonpositive frequency) and by multiplying the remaining term by 2 (so that $\Re(\tilde{y}(t)) = y(t)$):

$$\tilde{y}(t) = 10e^{j\omega_{ph}^\infty t + j\pi/4} = 10e^{j\pi/4}e^{j\omega_{ph}^\infty t}.$$

Then, through (6.38), we obtain $\underline{y}(t) \equiv 10e^{j\pi/4}$, which unambiguously corresponds to $Y(t) \equiv 10$ and $\phi_y(t) \equiv \pi/4$.

Remark 6.3. Other solutions could be considered. However, it has been shown that only methods based on the analytic signals satisfy physical conditions on the dynamic phasor (or complex envelope) of the signals, such as continuity and differentiability, phase independence and harmonic correspondence. See, e.g., [VV77, Vak96] for further details on these physical conditions.

6.4.2 Computing the Analytic Signal Associated to y

The problem now is how to compute the analytic signal \tilde{y} associated to y . The solution is based on the Hilbert transform and is presented as follows. Further (interesting) details can be found in [Gab46, VV77], for instance.

By Definition 6.1, \tilde{y} is such that $\mathcal{F}[\tilde{y}](\omega) = 0$ for $\omega \leq 0$ and $\Re(\tilde{y}(t)) = y(t)$. Thus, we can write the analytic signal associated to y as $\tilde{y}(t) = \tilde{y}_{\Re}(t) + j\tilde{y}_{\Im}(t)$ with $\tilde{y}_{\Re}(t) = y(t)$ and $\tilde{y}_{\Im}(t) \in \mathbb{R}$. In the frequency domain, it gives

$$\mathcal{F}[\tilde{y}](\omega) = \mathcal{F}[y](\omega) + j\mathcal{F}[\tilde{y}_{\Im}](\omega).$$

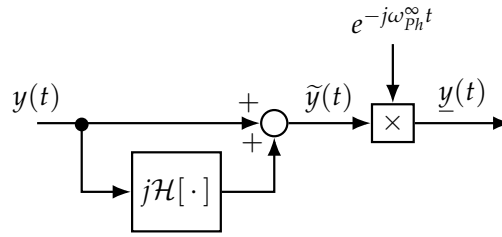
Now, recall that the spectrum $\mathcal{F}[y]$ of a real-valued signal y is symmetric, that is,

$$\mathcal{F}[y](\omega) = \overline{\mathcal{F}[y]}(-\omega).$$

Then, to obtain $\mathcal{F}[\tilde{y}](\omega) = 0$, the signal \tilde{y}_{\Im} must be such that

$$\mathcal{F}[\tilde{y}_{\Im}](\omega) = -j \operatorname{sgn}(\omega) \mathcal{F}[y](\omega), \quad (6.39)$$

⁶In general, the analytic signal has null spectrum for negative frequencies. However, to avoid indefinities at $\omega = 0$, we also consider $\mathcal{F}[\tilde{v}](0) = 0$.

FIGURE 6.10: Computing \tilde{y} and \underline{y} through the Hilbert transform.

where sgn denotes the sign function.

Note, in (6.39), that $\tilde{y}_{\mathfrak{S}}$ can be obtained by passing y through a filter F_H whose frequency response is given by

$$F_H(\omega) = -j \text{sgn}(\omega). \quad (6.40)$$

We can then define, in the time domain, $\tilde{y}_{\mathfrak{S}}(t) = f_H * y(t)$, where f_H is the impulse response of F_H and is given by $f_H(t) = 1/(\pi t)$. This special convolution product is called the **Hilbert transform** and is defined, for a real signal y , as

$$\mathcal{H}[y](t) \triangleq f_H * y(t) = \frac{1}{\pi} \int_{-\infty}^{\infty} \frac{y(\tau)}{t - \tau} d\tau. \quad (6.41)$$

Therefore, based on the Hilbert transform, the analytic signal \tilde{y} is computed from y as

$$\tilde{y}(t) = y(t) + j\mathcal{H}[y](t) \quad (6.42)$$

and the dynamic phasor \underline{y} can be obtained through (6.38), as depicted in Figure 6.10.

The definition of the Hilbert transform may not provide, at a first glance, a clear understanding of this operation. However, by evaluating (6.40), we can note that the Hilbert transform does not modify the spectrum magnitude of the signal y . It only shifts the spectrum of the signal by $-\pi/2$ rad (or $+\pi/2$ rad for negative frequencies), creating a signal in quadrature with the input signal (y). It behaves like an ideal phase shifter, shifting the phase of the input signal by $\pm\pi/2$ rad. Indeed, some basic and useful Hilbert transforms are [VV77]

$$\mathcal{H}[\cos(\omega_{ph}^\infty \bullet)](t) = \sin(\omega_{ph}^\infty t) \quad \text{and} \quad \mathcal{H}[\sin(\omega_{ph}^\infty \bullet)](t) = -\cos(\omega_{ph}^\infty t). \quad (6.43)$$

Let us come back to our example of Section 6.4.1. First, we compute \tilde{y} associated with y of (6.36) (see (6.42) and (6.43)), yielding to

$$\tilde{y}(t) = 10 \cos(\omega_{ph}^\infty t + \pi/4) + j10 \sin(\omega_{ph}^\infty t + \pi/4) = 10e^{j\omega_{ph}^\infty t + j\pi/4} = 10e^{j\pi/4} e^{j\omega_{ph}^\infty t}.$$

Then, by applying (6.38), we obtain $\underline{y}(t) \equiv 10e^{j\pi/4}$, which corresponds to $Y(t) \equiv 10$ and $\phi_y(t) \equiv \pi/4$.

6.4.3 Equivalence Between Synchronous Demodulation and Hilbert Transform

The main issue of the method described above is that the Hilbert transform (or the filter F_H , see (6.40)) cannot be implemented in real time. Indeed, by definition (see (6.41)), the computation of $\mathcal{H}[y]$ at time t depends on the whole signal y , *i.e.*, for $t \in (-\infty, \infty)$. In this section, we show that the ideal synchronous demodulation can be used to compute the

dynamic phasor associated with a modulated signal, keeping the same properties of the Hilbert transform. To this purpose, we consider the signal

$$y(t) = y_a(t) \cos(\omega_{ph}^\infty t) - y_b(t) \sin(\omega_{ph}^\infty t), \quad (6.44)$$

which is such that

$$\forall |\omega| \geq 2\omega_{ph}^\infty, \quad \mathcal{F}[y](\omega) = 0 \quad \text{and} \quad \mathcal{F}[y](0) = 0. \quad (6.45)$$

As discussed in Section 2.1.4 (page 23), any band-pass signal that satisfies (6.45) can be written in the form of (6.44). Moreover, the signals y_a and y_b are low-pass signals, that is,

$$\forall |\omega| \geq \omega_{ph}^\infty, \quad \mathcal{F}[y_a](\omega) = 0 \quad \text{and} \quad \mathcal{F}[y_b](\omega) = 0. \quad (6.46)$$

Then, we use the Hilbert transform to extract a dynamic phasor y from y (as summarized in Figure 6.10), we apply y to an ideal synchronous demodulation, and we compare the results obtained with both approaches, showing that they are equivalent.

Method Based on the Hilbert Transform

The first step consists in computing the analytic signal \tilde{y} . Recall that, $\tilde{y}_{\Re}(t) = y(t)$ and $\tilde{y}_{\Im}(t) = \mathcal{H}[y(t)]$. The latter one is developed as

$$\begin{aligned} \tilde{y}_{\Im}(t) &= \mathcal{H}[y_a(\bullet) \cos(\omega_{ph}^\infty \bullet) - y_b(\bullet) \sin(\omega_{ph}^\infty \bullet)](t) \\ \tilde{y}_{\Im}(t) &= \mathcal{H}[y_a(\bullet) \cos(\omega_{ph}^\infty \bullet)](t) - \mathcal{H}[y_b(\bullet) \sin(\omega_{ph}^\infty \bullet)](t). \end{aligned}$$

At this point, let us open a parenthesis and introduce an important result concerning the Hilbert transform of a product.

Theorem 6.6 (Bedrosian's theorem [Bed63]). *Let $v_l(t)$ and $v_h(t)$ be real functions of time, such that $\mathcal{F}[v_l](\omega) = 0$ for $|\omega| \geq \omega_b$ and $\mathcal{F}[v_h](\omega) = 0$ for $|\omega| < \omega_b$. Then,*

$$\mathcal{H}[v_l \cdot v_h](t) = v_l(t) \cdot \mathcal{H}[v_h](t). \quad (6.47)$$

This theorem claims that the Hilbert transform of the product between a low-frequency (v_l) and a high-frequency signal (v_h), whose spectra do not overlap, is given by the product of the low-frequency signal with the Hilbert transform of the high-frequency one.

Let us close the parenthesis and come back to the computation of \tilde{y}_{\Im} . Since y_a and y_b are low-pass signals (see (6.46)) and do not overlap the spectra of $\cos(\omega_{ph}^\infty \bullet)$ and $\sin(\omega_{ph}^\infty \bullet)$, we can apply the Bedrosian's theorem, yielding to

$$\tilde{y}_{\Im}(t) = y_a(t) \mathcal{H}[\cos(\omega_{ph}^\infty \bullet)](t) - y_b(t) \mathcal{H}[\sin(\omega_{ph}^\infty \bullet)](t).$$

Hence, with the Hilbert transforms of the sine and cosine functions (see (6.43)), we have

$$\tilde{y}_{\Im}(t) = y_a(t) \sin(\omega_{ph}^\infty t) + y_b(t) \cos(\omega_{ph}^\infty t).$$

Finally, with $\tilde{y}(t) = y(t) + j\tilde{y}_{\Im}(t)$, we obtain

$$\tilde{y}(t) = (y_a(t) + jy_b(t)) e^{j\omega_{ph}^\infty t},$$

yielding to the dynamic phasor

$$\underline{y}(t) = \tilde{y}(t)e^{-j\omega_{ph}^{\infty}t} = y_a(t) + jy_b(t).$$

Note that $y_a = \underline{y}_{\Re}$ and $y_b = \underline{y}_{\Im}$.

Remark 6.4 (The dynamic phasors and the complex envelopes). As claimed in the beginning of the chapter, if the conditions (6.45) and (6.46) are verified, the dynamic phasors correspond to the classical definition of complex envelopes, see, e.g., [Rub09].

Ideal Synchronous Demodulation

The ideal synchronous demodulation is presented in Section 2.1.4, but we recall the main principles here. Its structure is depicted in Figure 6.11, where F_{LP} are ideal low-pass filters with cutoff frequency $\omega_c = \omega_{ph}^{\infty}$. At the input of the synchronous demodulation, we plug the signal y of (6.44).

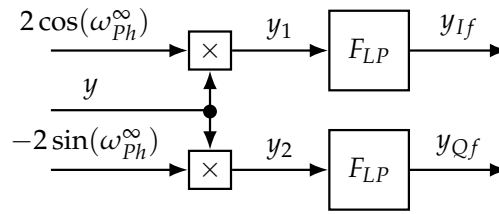


FIGURE 6.11: Block diagram of the synchronous demodulation.

The signals $y_1(t) = 2y(t) \cos(\phi_{ph}(t))$ and $y_2(t) = -2y(t) \sin(\phi_{ph}(t))$ are rewritten as

$$y_1(t) = y_a(t) + \overbrace{(y_a(t) \cos(2\phi_{ph}(t)) - y_b(t) \sin(2\phi_{ph}(t)))}^{\delta y_I(t)} \quad (6.48)$$

$$y_2(t) = y_b(t) - \underbrace{(y_a(t) \sin(2\phi_{ph}(t)) + y_b(t) \cos(2\phi_{ph}(t)))}_{\delta y_Q(t)}. \quad (6.49)$$

Note that, y_1 and y_2 are composed of low-frequency terms y_a and y_b and of high-frequency terms δy_I and δy_Q . Because of (6.46), the spectra of $\delta y_I(t)$ and $\delta y_Q(t)$ are nonnull for $|\omega| \in (\omega_{ph}^{\infty}, 3\omega_{ph}^{\infty})$. As consequence, since F_{LP} is an ideal low-pass filter with cutoff frequency $\omega_c = \omega_{ph}^{\infty}$, the high-frequency terms δy_I and δy_Q are eliminated, and we obtain $y_{If}(t) = y_a(t)$ and $y_{Qf}(t) = y_b(t)$.

Finally, under the assumptions that y is a band-pass signal and that the low-pass filter of the synchronous demodulation are ideal, the in-phase and the in-quadrature terms y_{If} and y_{Qf} correspond to the terms y_a and y_b of y , just like in the method based on the Hilbert transform. Under the same conditions, y_{If} and y_{Qf} respectively correspond to the real and imaginary parts of the phasor \underline{y} , that is, $y_{If} = \underline{y}_{\Re}$ and $y_{Qf} = \underline{y}_{\Im}$. Therefore, as claimed earlier, the ideal synchronous demodulation implements the ideal operator s2c. Similarly, the ideal operator s2p can be implemented by computing amplitude and phase from the in-phase and in-quadrature terms, as depicted in Figure 2.13 (page 27).

6.4.4 Modeling the Nonideal Synchronous Demodulation

In practice, the low-pass filters of the synchronous demodulation are not ideal. Indeed, they have a transition band between the passband and the stopband. Then, to better attenuate the high-frequency components (δy_I and δy_Q), the cutoff frequency must be lower than ω_{ph}^∞ . Moreover, ideal filters have a real-valued frequency response, which is unitary within the bandwidth and null outside. In contrast, real filters have a complex-valued frequency response, whose magnitude is close to the unity within the passband and close to zero otherwise, and whose phase is non-null.

If the synchronous demodulation is used in a control loop, as is the case in the dynamic phasor control architecture with a real s2c (a real/nonideal synchronous demodulation), the differences between ideal and real filters can dramatically change the behavior of the closed-loop system, which can even become unstable. This point is illustrated in the next example.

Example 6.5. *In this example, we take the controller designed in Example 6.4 and implement it in the phasor control architecture of Figure 6.7. However, at this time, the operator s2p is implemented through a synchronous demodulation with (nonideal) Butterworth low-pass filters with cutoff frequency $\omega_c < \omega_{0,x}$ and order N_F . Three cases are considered:*

Case I: $\omega_c = 0.1\omega_{0,x}$ and $N_F = 5$,

Case II: $\omega_c = 0.01\omega_{0,x}$ and $N_F = 5$,

Case III: $\omega_c = 0.1\omega_{0,x}$ and $N_F = 2$.

In Case I, we obtain a stable closed-loop system providing performance indicators that are similar to the ones obtained in Example 6.4 (see Figure 6.8). The signal y_{dp} does not exist in this control architecture. Then, we use the signals $y_{If} \approx \underline{y}_{\mathcal{R}}$ and $y_{Qf} \approx \underline{y}_{\mathcal{S}}$ (at the output of the operator s2c) and redefine the tracking error as $\varepsilon_{dp} = y_{r,dp} - \hat{y}_{dp}$ with $\hat{y}_{dp} = \text{col}(y_{If}, y_{Qf})$. The performance indicators are defined as in (6.34) and presented in Figure 6.12. In this figure, we can observe that $\hat{\gamma}_{p,T_0}$ slightly exceeds the value of γ_p , indicating a slight performance degradation. For the fast variations of $\omega_{ph} = \omega_{exc}$ ($t > 20$ ms), the synchronous demodulation low-pass filters end up by attenuating the fast variations of the error, producing performance indicators that tend to the value in steady state ($t < 5$ ms).

In Case II and Case III, the closed-loop system is **unstable**.

Because of the multivariable and nonlinear nature of the to-be-controlled system (G_{dp} with nonideal s2c), it is hard to determine *a priori* if the controller designed from the direct controller will ensure the stability and performance of the closed-loop system. Therefore, when using the dynamic phasor control architecture with a real synchronous demodulation, one of the two actions have to be considered.

- (i) Evaluate the effect of the nonideal s2c after designing the controller through the method of Section 6.3, which assumes that the operator s2c is ideal. This *a posteriori* analysis is investigated in our paper [ACSKS19] and detailed in [AC21].
- (ii) Take the nonidealities of the real synchronous demodulation into account for the controller design. This second point is developed in Section 6.5 and requires an accurate model of the s2c nonidealities. This model is presented in the sequel.

The question here is how to model the nonideal s2c, *i.e.*, the synchronous demodulation with nonideal F_{LP} . From (6.48) and (6.49) and with $y_a = \underline{y}_{\mathcal{R}}$ and $\underline{y}_b = y_{\mathcal{S}}$, the signals y_1 and y_2 can

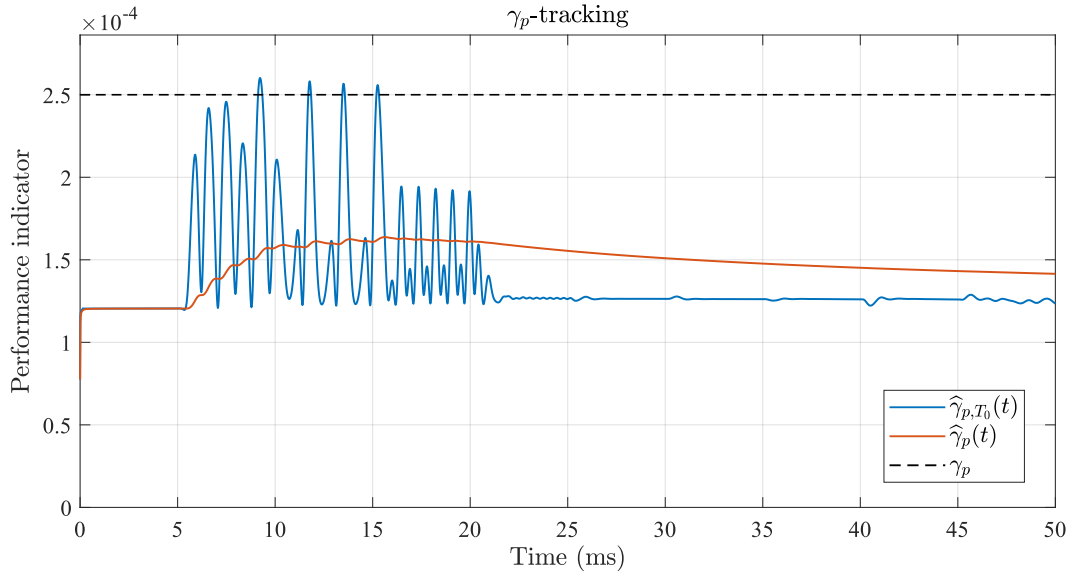


FIGURE 6.12: Case I - Performance indicators with K_{dp} of Example 6.4 and nonideal (real) s2c.

be rewritten in matrix form as

$$\begin{bmatrix} y_1(t) \\ y_2(t) \end{bmatrix} = (I + \Delta(\phi_{ph}(t))) \begin{bmatrix} y_{\mathcal{R}}(t) \\ y_{\mathcal{I}}(t) \end{bmatrix} \quad (6.50)$$

with

$$\Delta(\phi_{ph}(t)) = \begin{bmatrix} \cos(2\phi_{ph}(t)) & -\sin(2\phi_{ph}(t)) \\ -\sin(2\phi_{ph}(t)) & -\cos(2\phi_{ph}(t)) \end{bmatrix}. \quad (6.51)$$

Hence, the nonideal s2c (real synchronous demodulation) can be modeled as the interconnection of an ideal s2c, the block $(I + \Delta(\phi_{ph}(t)))$ and the nonideal filters F_{LP} . In the case of the phasor control architecture, the strong interest of this modeling is that the to-be-controlled system is represented as an interconnection of the DPM and the nonidealities (F_{LP} and $\Delta(\phi_{ph}(t))$) of the operator s2c, as illustrated in Figure 6.13. In this case, the outputs of the synchronous demodulation correspond to approximations (or estimates) of the actual phasor \underline{y} . We denote this approximation $\hat{\underline{y}}$.

6.4.5 On the Synchronous Demodulation with Time-Varying Frequency

So far, we have considered the excitation frequency as a constant parameter. However, this frequency might change during the system operation. Indeed, in the case of MEMS gyroscopes, ω_{ph} is often equal to ω_{exc} , which is usually linked to the drive-mode resonance frequency. Thus, it is essential to evaluate the impact of these variations on the synchronous demodulation. In this section, two points are discussed.

- (i) What can be ensured in the case where ω_{ph} varies arbitrarily?
- (ii) What are the implications on the synchronous demodulation when considering a slow time-varying ω_{ph} ?

Synchronous demodulation and arbitrarily time-varying ω_{ph} : it is important to note that the equations (6.48) and (6.49) are always valid, even in the case of time-varying ω_{ph} . The

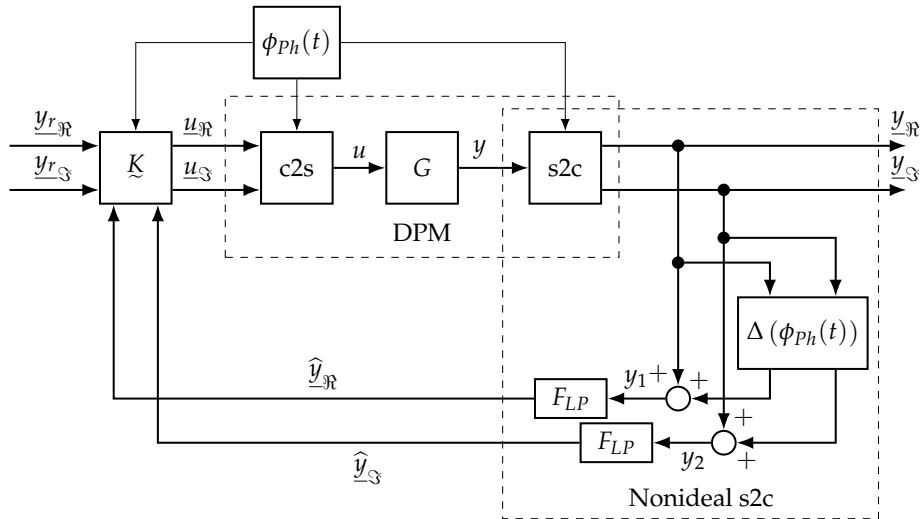


FIGURE 6.13: Block diagram of the dynamic phasor control architecture with nonideal s2c.

main issue here is that, since ω_{ph} is now time-varying, the power spectrum support of the high-frequency terms (δy_I and δy_Q) is, in general, not bounded, overlapping the power spectrum support of \underline{y}_{\Re} and \underline{y}_{\Im} (equivalently y_a and y_b), even if the low-pass filters are ideal. Hence, the estimates $\hat{\underline{y}}_{\Re}$ and $\hat{\underline{y}}_{\Im}$ do not correspond anymore to \underline{y}_{\Re} and \underline{y}_{\Im} . Nevertheless, even if $\hat{\underline{y}}_{\Re}$ and $\hat{\underline{y}}_{\Im}$ may be corrupted, the whole model of the to-be-controlled plant (DPM and nonideal s2c) is still valid.

Synchronous demodulation and slow time-varying ω_{ph} : there is a particular case in which the results of the synchronous demodulation can be extended to a time-varying framework. This is possible when ω_{ph} is assumed to vary slowly, see, for instance, [Fel06]. In this case, the results converge to the results of the constant-frequency framework, as follows. For $\omega_{ph}^{\infty} \in [\omega_{ph,1}, \omega_{ph,2}]$, if the power spectrum support of \underline{y}_{\Re} and \underline{y}_{\Im} is in the range $(0, \omega_{ph,1}^{\infty})$, and the ideal low-pass filter has cutoff frequency $\omega_c = \omega_{ph,1}^{\infty}$, then $\hat{\underline{y}}_{\Re}(t) = \underline{y}_{\Re}(t)$ and $\hat{\underline{y}}_{\Im}(t) = \underline{y}_{\Im}(t)$, as required.

6.5 Dynamic Phasor Control with Nonideal Operator s2c

In this section, we propose another solution to the dynamic phasor control problem. In contrast to the previous approach, where we transform a direct controller into a phasor one, now we design the controller directly the “dynamic phasor domain”. At this time, we take into account the nonideal operator s2c. Two similar approaches can be considered here. If the reference frequency ω_{ph} is constant (*i.e.*, $\omega_{ph}(t) = \omega_{ph}^{\infty}$) and the original to-be-controlled system is LTI, we consider the \mathcal{H}_{∞} synthesis. On the other hand, if ω_{ph} varies over time in a given interval $[\omega_{ph,1}, \omega_{ph,2}]$ or the original to-be-controlled plant is LPV, we consider the LPV synthesis. Remember that the \mathcal{H}_{∞} synthesis is a particular case of the LPV synthesis. Consequently, this section is rather presented in an LPV framework.

The closed-loop system has to achieve the performance specifications below.

- (i) **Reference tracking:** ensure the tracking of **constant** reference signals $(\underline{y}_{r\Re}, \underline{y}_{r\Im})$.

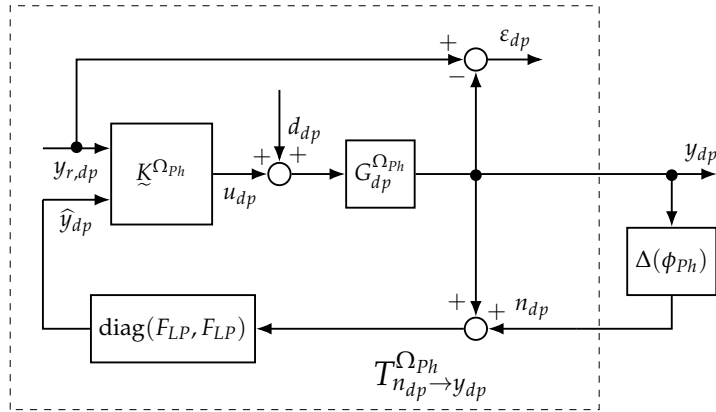


FIGURE 6.14: Simplified block diagram of the dynamic phasor control architecture with nonideal s2c.

- (ii) **Low-pass condition of the control signal:** minimize the PSD of the control signal for $\omega > \omega_{Ph,1}$, ensuring that the conditions for uniqueness are satisfied.
- (iii) **Robust stability:** ensure the stability of the closed-loop system against the nonidealities of the s2c.

To solve this problem, we consider the control architecture presented in Figure 6.14, which is a simplified version of Figure 6.13. The vector $y_{r,dp} = \text{col}(\underline{y}_{r_{\mathcal{R}}}, \underline{y}_{r_{\mathcal{S}}})$ represents the reference signal to be tracked, $\epsilon_{dp} = \text{col}(\epsilon_{\mathcal{R}}, \epsilon_{\mathcal{S}})$ is the tracking error vector, $d_{dp} = \text{col}(\underline{d}_{\mathcal{R}}, \underline{d}_{\mathcal{S}})$ corresponds to input disturbances and $n_{dp} = \text{col}(\underline{n}_{\mathcal{R}}, \underline{n}_{\mathcal{S}})$ represents the signals at the output of the time-varying matrix $\Delta(\phi_{exc}(t))$. The two elements of the nonideal operator s2c are taken into account as follows.

Nonideal filters F_{LP} : although these filters represent nonidealities of the s2c, they can be easily considered for the controller synthesis. In general, the low-pass filters F_{LP} are LTI systems. Therefore, if we consider the \mathcal{H}_{∞} or the LPV synthesis (see Chapter 4 or Chapter 5, respectively), it suffices to include these filter in the augmented plant and normally proceed with the controller synthesis.

Time-varying matrix $\Delta(\phi_{Ph}(t))$: note that the nonideal closed-loop system presented in Figure 6.14 can be rewritten as the interconnection of $T_{n_{dp} \rightarrow y_{dp}}^{\Omega_{Ph}}$ and $\Delta(\phi_{Ph}(t))$. Thus, the small gain theorem can be applied to assess the stability of this interconnection [Vid02], that is, the system is stable if,

$$\left\| T_{n_{dp} \rightarrow y_{dp}}^{\Omega_{Ph}} \right\|_{i_2} \left\| \Delta(\phi_{Ph}(t)) \right\|_{i_2} < 1,$$

recalling that $\omega_{Ph}(t) = \dot{\phi}_{Ph}(t)$. Since

$$\forall t \in \mathbb{R}_+, \forall \phi_{Ph}(t) \in \mathbb{R}, \quad \bar{\sigma}(\Delta(\phi_{Ph}(t))) \leq 1,$$

we have that

$$\left\| \Delta(\phi_{Ph}(t)) \right\|_{i_2} \leq 1.$$

Therefore, if

$$\left\| T_{n_{dp} \rightarrow y_{dp}}^{\Omega_{Ph}} \right\|_{i_2} < 1, \tag{6.52}$$

the stability of the overall interconnected system is ensured.

Based on the above discussion, we define the signals of interest $\tilde{w} = \text{col}(y_{r,dp}, d_{dp}, n_{dp})$ and $\tilde{z} = \text{col}(\varepsilon_{dp}, u_{dp}, y_{dp})$. Then, the closed-loop system under study defines the following operators (omitting the dependence on Ω_{ph}):

$$\begin{bmatrix} T_{y_{r,dp} \rightarrow \varepsilon_{dp}} & T_{d_{dp} \rightarrow \varepsilon_{dp}} & T_{n_{dp} \rightarrow \varepsilon_{dp}} \\ T_{y_{r,dp} \rightarrow u_{dp}} & T_{d_{dp} \rightarrow u_{dp}} & T_{n_{dp} \rightarrow u_{dp}} \\ T_{y_{r,dp} \rightarrow y_{dp}} & T_{d_{dp} \rightarrow y_{dp}} & T_{n_{dp} \rightarrow y_{dp}} \end{bmatrix} = \begin{bmatrix} I - SGK_1 & -SG & T \\ S_I K_1 & -T_I & K_2 S \\ SGK_1 & SG & -T \end{bmatrix}, \quad (6.53)$$

where $S = (I - GK_2 F_{LP})^{-1}$, $T = I - S = -SGK_2 F_{LP} = -GK_2 F_{LP} S$, $S_I = (I - K_2 F_{LP} G)^{-1}$ and $T_I = I - S_I$.

Note that $\|T_{n_{dp} \rightarrow \varepsilon_{dp}}\|_{i_2} = \|T_{n_{dp} \rightarrow y_{dp}}\|_{i_2}$. Hence, to express the desired specifications, we consider the block diagram of Figure 6.15.

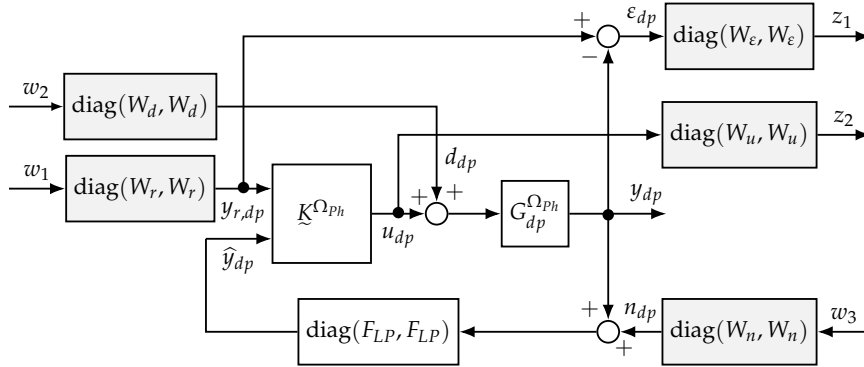


FIGURE 6.15: Considered criterion for the LPV synthesis.

The problem is then to compute the controller $\underline{K}^{\Omega_{ph}} = \left[\underline{K}_1^{\Omega_{ph}}, \underline{K}_2^{\Omega_{ph}} \right]$, if there is any, such that (for the sake of clarity, the dependence of the closed-loop transfers on Ω_{ph} is omitted),

$$\left\| \begin{bmatrix} W_\varepsilon T_{y_{r,dp} \rightarrow \varepsilon_{dp}} W_r & W_\varepsilon T_{d_{dp} \rightarrow \varepsilon_{dp}} W_d & W_\varepsilon T_{n_{dp} \rightarrow \varepsilon_{dp}} W_n \\ W_u T_{y_{r,dp} \rightarrow u_{dp}} W_r & W_u T_{d_{dp} \rightarrow u_{dp}} W_d & W_u T_{n_{dp} \rightarrow u_{dp}} W_n \end{bmatrix} \right\|_{i_2} < \gamma. \quad (6.54)$$

It is important to mention that if W_ε and W_n are constant and such that $W_\varepsilon W_n = 1$, if $\gamma < 1$, (6.54) implies that $\|T_{n_{dp} \rightarrow \varepsilon_{dp}}\|_{i_2} < 1$ and, as consequence, (6.52) holds and the stability against the time-varying block $\Delta(\phi_{ph}(t))$ is ensured.

It is also worth remarking that, in contrast to the LPV synthesis considered in Chapter 5, the weighting functions are now LTI. Thus, their design can be made to express the frequency content of the signals that they describe, similar to the \mathcal{H}_∞ synthesis. For instance, we here consider constant (or low-frequency) signals. In this case, the reference weighting function W_r can be defined as a low-pass filter with high gains in low frequency and small gains in high frequencies. The main particularity here (compared to a standard \mathcal{H}_∞ synthesis) is that since the closed-loop system is time-varying, the input weights cannot be commuted with the output ones.

Finally, we also have to point out that in this approach, the constraints are on the real and imaginary parts of the phasors, what may introduce some conservatism. For instance, if we

want to constrain the amplitude of the tracking error signal ε to have an amplitude smaller than a given $\check{\varepsilon} > 0$ at ω_{ph} , we have to constrain the corresponding phasor $\underline{\varepsilon}$ to be such that $|\underline{\varepsilon}| = \sqrt{\varepsilon_{\Re}^2 + \varepsilon_{\Im}^2} \leq \check{\varepsilon}$. To achieve this condition, we consider the worst case, in which ε_{\Re} can be equal to ε_{\Im} , yielding to

$$\varepsilon_{\Re} \leq \frac{\sqrt{2}\check{\varepsilon}}{2} \quad \text{and} \quad \varepsilon_{\Im} \leq \frac{\sqrt{2}\check{\varepsilon}}{2},$$

which implies that $\sqrt{\varepsilon_{\Re}^2 + \varepsilon_{\Im}^2} \leq \check{\varepsilon}$.

The choice of weighting functions and the effectiveness of this approach are illustrated in the next example.

Example 6.6. *In this example, we aim to design a phasor controller that is robust against the nonidealities of the nonideal operators s2c. For the sake of clarity, we consider a simple case, where $\omega_{ph}(t) \equiv \omega_{ph}^{\infty} = \omega_{0,x}$ and the to-be-controlled plant is the drive mode of a MEMS gyroscope (see Example 2.1, page 22) at a given operating condition. Then, the \mathcal{H}_{∞} synthesis can be used to design the phasor controller. We highlight however that the same procedure can be applied to an LPV synthesis in the case where ω_{ph} varies over time or the to-be-controlled plant is LPV.*

Here, we consider the phasor control architecture of Figure 6.7 with a nonideal s2c. This operator is implemented through a synchronous demodulator with a second-order Butterworth low-pass filter with cutoff frequency $\omega_c = 0.1\omega_{0,x}$. This case corresponds to Case III of Example 6.5, in which the closed-loop system happens to be unstable.

The main control specifications are as follows.

- (i) **Reference tracking:** to track constant reference signals with relative errors ε_{\Re} and ε_{\Im} smaller than $\lambda_{\text{SFNL}}k_{\text{SFNL}}/\sqrt{2} \approx 176.8 \cdot 10^{-6} \approx -75$ dB ($\lambda_{\text{SFNL}} = 0.5$ and $k_{\text{SFNL}} = 500 \cdot 10^{-6}$).
- (ii) **Low-pass condition of the control signal:** minimize the PSD of u_{dp} for $\omega \geq \omega_{ph}^{\infty}$.
- (iii) **Robust stability:** ensure the stability of the closed-loop system against the s2c nonidealities.

To this end, we consider the \mathcal{H}_{∞} criterion defined by the scheme of Figure 6.15 and weighting functions that enforce the upper bounds presented in Figure 6.16. Similar to the examples of Chapter 4, we start by choosing the weighting functions defining the “hard constraints” – in this case, the reference tracking and stability against the block $\Delta(\phi_{ph}(t))$ (see transfers from $y_{r,dp}$ to ε_{dp} and from n_{dp} to ε_{dp} , respectively). The other weighting functions are iteratively chosen to minimize u_{dp} . Their numerical values are given in Appendix E.3.

Then, by solving the standard \mathcal{H}_{∞} problem with $\gamma = 0.9851$, we obtain the 12th-order controller whose magnitude Bode diagram is presented in Figure 6.17. First, note that in this case, $\gamma < 1$. Then, since we consider $W_n = W_e = 1$, the stability against the time-varying block $\Delta(\phi_{ph}(t))$ is ensured. Moreover, the magnitude of all the transfers from $y_{r,dp}$ to ε_{dp} are smaller than -75 dB in low frequencies. This fact shall ensure the tracking of constant signals, as required. Finally, note that the transfers to u_{dp} also have small magnitude for $\omega > \omega_{ph}^{\infty} = \omega_{0,x} \approx 7.2 \cdot 10^4 \text{rad s}^{-1}$.

Finally, the whole system is simulated according to the phasor control architecture of Figure 6.7. This system is composed of real c2s and s2c operators (modulator and nonideal synchronous demodulation), the original to-be-controlled system G and the phasor controller \underline{K} . The tracking errors for $y_{r,\Re} = 1$ and $y_{r,\Im} = 0$, in steady state, are given in Figure 6.18. In this figure, we present the real and imaginary parts of the tracking error phasor, respectively ε_{\Re} and ε_{\Im} , as well as their mean value. For the sake of

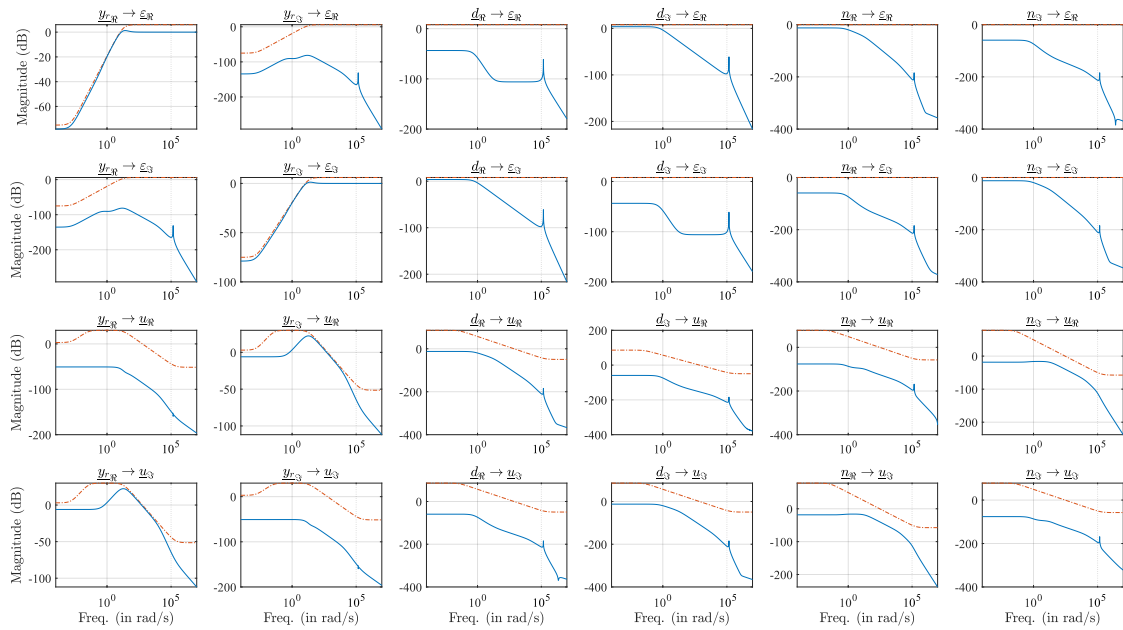


FIGURE 6.16: Upper bounds and closed-loop frequency responses for Example 6.6.

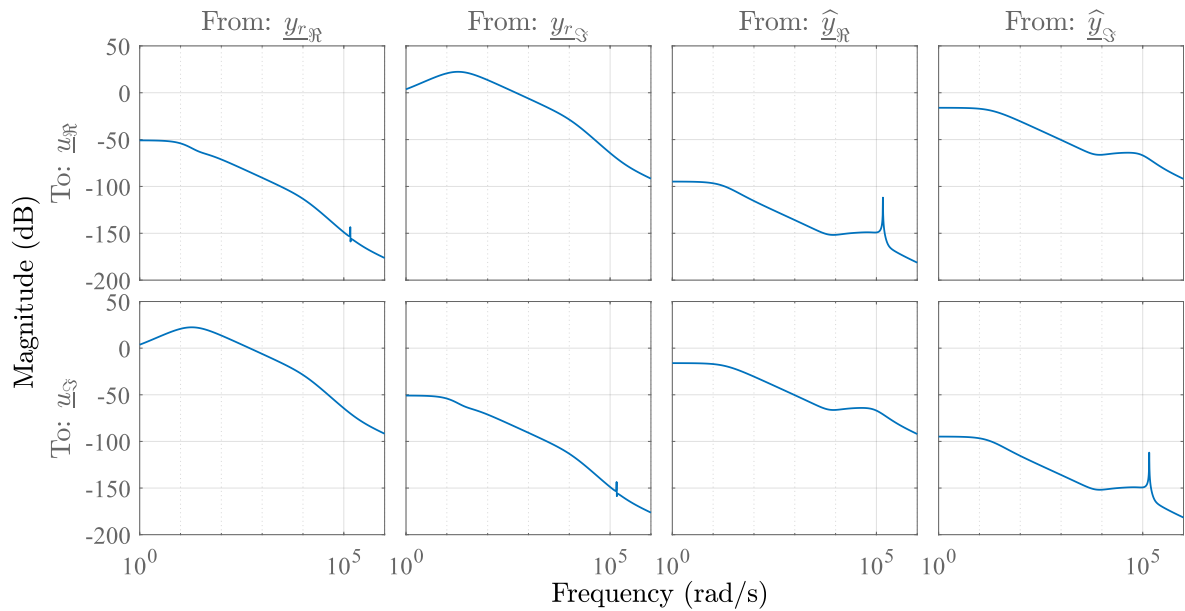


FIGURE 6.17: Magnitude Bode diagram of the phasor controller of Example 6.6.

comparison, we also present the results, denoted “Only filter”, for a fictitious system composed of \mathbb{K} , G_{dp} and the nonideal filters F_{LP} . In this case, the time-varying block $\Delta(\phi_{ph}(t))$ does not exist.

Note that when we consider the complete nonideal system, $\underline{\varepsilon}_{\mathbb{R}}$ and $\underline{\varepsilon}_{\mathbb{S}}$ oscillate with a fundamental frequency equal to $2\omega_{ph}^{\infty}$. Moreover, their mean value (which can be related to the performance at $\omega = 0$) is higher than the desired value ($0.5 \cdot 10^{-4} > 0.18 \cdot 10^{-4}$). However, if we look to the results of the fictitious system, the required specifications are fulfilled. This fact indicates that, even if the controller ensures the stability of the system, the presence of the time-varying block $\Delta(\phi_{ph}(t))$ can produce a performance degradation. Indeed, only the robust stability is guaranteed and not the robust performance.

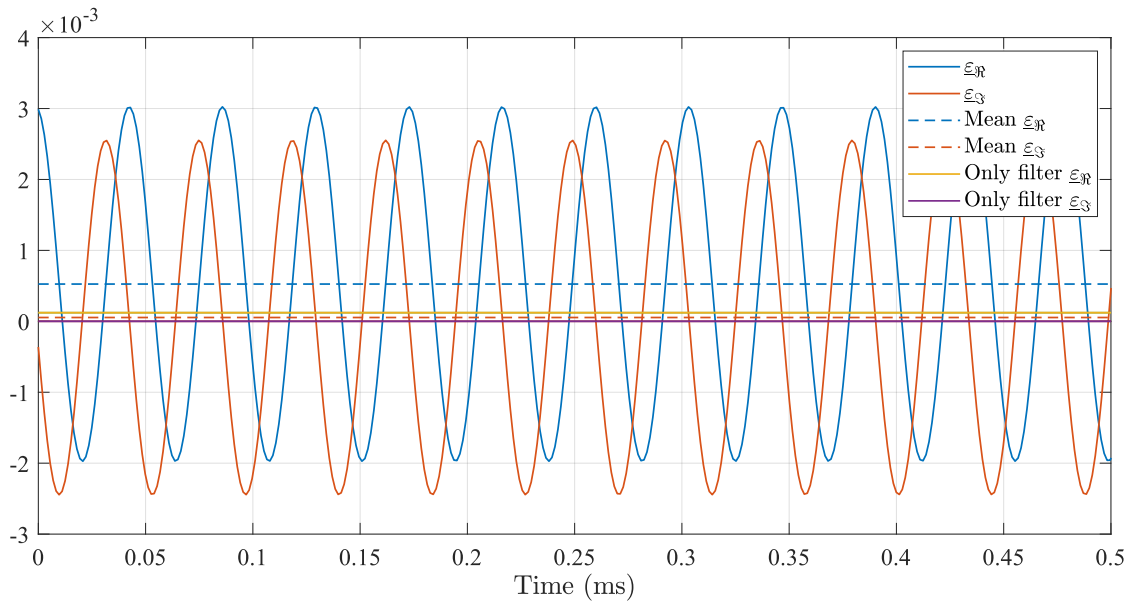


FIGURE 6.18: Simulation results for the tracking error of Example 6.6 for $\underline{y}_{r_{\mathbb{R}}} = 1$ and $\underline{y}_{r_{\mathbb{S}}} = 0$.

6.6 Summary of the Chapter

The use of an envelope-based architecture may be attractive for the control of MEMS gyroscopes. The main interest comes from the fact that the envelope of the signals evolves much slower than the signals themselves. Moreover, in steady-state, the envelopes are often constant signals. Then, classical (PID-like) controllers can be employed, for instance, to regulate the amplitude of oscillations. Nevertheless, to implement this approach, modulators and demodulators have to be included in the control loop. Hence, linearization is performed and, in contrast with the direct approach, performance and stability guarantees cannot be provided.

In this chapter, we demonstrate that it is possible to merge the main features of the envelope-based architecture with those of the direct architectures, *i.e.*, “low-frequency” controllers with formal performance and stability guarantees. The dynamic phasor model, presented in Section 6.2, shows that the nonlinear nature of the to-be-controlled plant comes from the representation of the so-called dynamic phasor. Then, if considering the rectangular representation instead of the polar one, the to-be-controlled plant becomes linear. Thus, the original nonlinear control problem can be recast as a linear one, and the \mathcal{H}_{∞} /LPV synthesis can be employed to design a controller, ensuring stability and some performance level.

We also demonstrate in Section 6.3 that if ideal operators $s2c$ exist, in addition to the equivalence between direct and phasor-based controllers, the achievable performance levels are the same. Then, choosing a phasor-based or a direct control architecture does not allow obtaining a better performance of the device.

Even if it is possible to design a direct controller and then to convert it into a phasor controller, an essential message of this chapter is that, due to the nonidealities of the $s2c$, presented in Section 6.4, the phasor controller shall be designed in the phasor space, taking into account the nonidealities of a real operator $s2c$ (synchronous demodulation). In Section 6.5, we present a design method where the nonidealities of the $s2c$ are taken into account.

The final message of this chapter is that implementation constraints shall guide the choice of the control architecture. That is, the use of direct control architecture is recommended when the controller can operate at frequencies higher than the resonance frequency of the drive mode. On the other hand, the use of phasor control architecture is to be considered when the resonance frequency of the device is higher than the maximum frequency at which the controller can operate. In this case, modulators and demodulators ($c2s$ and $s2c$) allow shifting the dynamics of the system to lower frequencies, where the controller can therefore operate.

Chapter 7

Digital Implementation of the Direct Control Architecture

In Chapter 2, we pointed to the lack of implementation results in the literature concerning the use of direct control architectures for the operation of MEMS gyroscopes. In this chapter, our main objective is then to demonstrate the implementability of a digital (direct) controller to operate a real MEMS gyroscope. To this purpose, we consider the \mathcal{H}_∞ synthesis, as presented in Chapter 4. Further than the lack of implementation results, the points highlighted in the sequel also motivate the choice of the direct control architecture to be implemented.

Up to this point, we have proposed two linear approaches for the operation of MEMS gyroscopes. First, the direct control architecture, in which the controller works with high-frequency modulated signals. The foremost advantage of this approach relies on the fact that the to-be-controlled system, the MEMS gyroscope, is (mainly) linear. Therefore, linear controllers can ensure the tracking and rejection of modulated signals with formal stability and performance guarantees. An inherent drawback of this approach is that, if we consider a digital implementation, the controller has to work with a sampling frequency higher than the operating frequency, which is usually equal to the drive-mode resonance frequency. This drawback can quickly become an obstacle if the resonance frequencies are high. Indeed, the digital controller may not have enough time to compute and update the control signal within a sampling period.

A solution for the cases where the direct control architecture cannot be employed (due to high resonance frequency) is to use an envelope-based (low-frequency) control architecture. In Chapter 6, we have shown that, under the assumption that the envelopes can be perfectly measured, linear control architectures implemented in high (direct control architectures) or in low frequency (envelope-based architectures) present the same performance level. In practice, however, this assumption does not hold¹ and the performance can be worse for low-frequency approaches. Thus, if the digital controller can operate with a high sampling frequency (with respect to the resonance frequencies), the direct control architecture would be a better (linear) solution.

In order to implement the proposed solution in a real prototype, several practical aspects, which were not considered in the previous chapters, have to be taken into consideration. These aspects are mainly related to the nonidealities of the MEMS gyroscope and to the digital nature of the controller. Then, in this chapter, we present the solutions to these practical issues.

¹Indeed, we recall that the low-pass filters of the synchronous demodulation (operators $s2c$) are not ideal, and the high-frequency terms (generated by the demodulation process and represented by the time-varying block $\Delta(\phi_{pi}(t))$) degenerate the system performance.

Up to this point, we considered the gyroscope as a linear system. However, it is known that the relation between the voltage applied on the actuation circuits and the effective force applied to the proof mass is nonlinear (see Section 2.1.3, page 18). Moreover, the MEMS gyroscopes are also disturbed by parasitic electrical coupling (see Section 2.1.3, page 18). In this chapter, we reveal that these nonidealities can be compensated, such that the resulting system is indeed linear and the previous results apply.

To implement the direct control architecture, we use the development kit presented in Section 2.3.1 (page 51), in which the controller is programmed in C++ language. The controller is hence implemented in discrete time (DT). In Chapter 4, we presented the \mathcal{H}_∞ synthesis in a continuous-time (CT) framework. Indeed, the CT domain is more suited for frequency-domain design methods, as the \mathcal{H}_∞ synthesis. Then, in this chapter, we also present the procedure adopted to properly design a DT controller based on a CT design method, having the same guarantees in both domains.

Another important characteristic of MEMS gyroscopes is the sensitivity to the temperature, which changes the resonance frequencies and can quickly degrade the performance of the sensor. In this chapter, we reveal that, if the resonance frequency variations are (very) slow and can be measured, we can take advantage of the model structure and design a simple parameter-dependent controller, which can be updated in real time, ensuring high performance even under temperature variations.

Finally, the complete design solution is implemented in the development kit, and tests are realized at rest (with $\Omega_z = 0$) and on a rotating table, allowing to validate the design method and to demonstrate the implementability of our solution.

This chapter is organized as follows. In Section 7.1, we describe the development kit and formalize the problem under investigation. In Section 7.2, we present the modeling approach and how to deal with the system nonidealities (input nonlinearity and parasitic electrical coupling). Then, in Section 7.3, the design method for a digital controller is discussed. In Section 7.4, we extend the \mathcal{H}_∞ synthesis for the design of gyroscope controllers whose parameters vary as function of the drive-mode resonance frequency. Finally, the implementation results are presented in Section 7.5 and conclusions are drawn in Section 7.6.

7.1 System Description and Problem Statement

In this chapter, we consider the Asygn's platform, presented in Section 2.3.1. Its block diagram is recalled in Figure 7.1. The system is basically composed of a MEMS gyroscope, an FPGA and a front-end ASIC. The MEMS gyroscope is composed of its mechanical part (G^{mech}) and the actuation and detection circuitry (for further details, see Section 2.1.5, page 27). The expected (nominal) resonance frequencies and quality factors of the drive and sense modes are given in Table 7.1. Moreover, the nonideal MEMS gyroscope also presents a parasitic electrical coupling, which can be modeled by E_{coup} .

TABLE 7.1: Nominal characteristics of the MEMS gyroscopes of the family GYRO I.

Parameter	Drive mode ($i = x$)	Sense mode ($i = y$)
Resonance frequency ($\omega_{0,i}$)	11 500 Hz	11 550 Hz
Quality factor (Q_i)	$100 \cdot 10^3$	$10 \cdot 10^3$

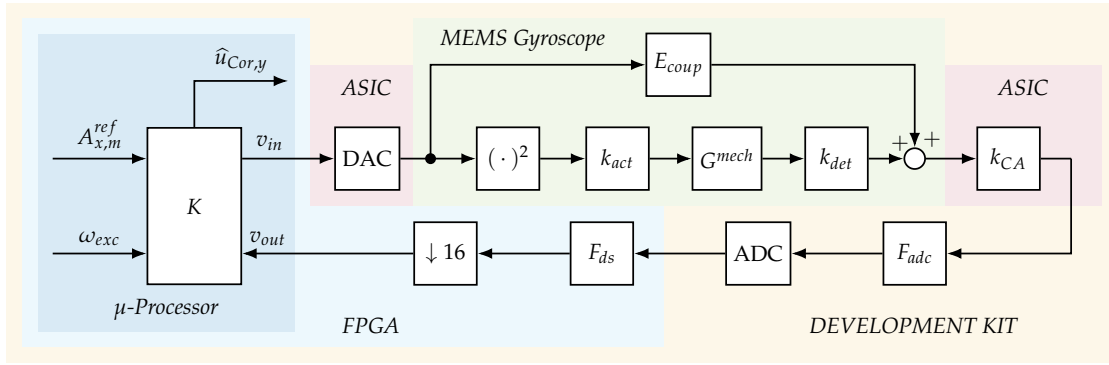


FIGURE 7.1: Block diagram of the development kit used in this chapter.

The front-end ASIC makes the interface between the MEMS gyroscope and the FPGA. It is composed of 10-bit digital-to-analog converters (DAC) and charge amplifiers (k_{CA}). The DACs convert the digital signals received from the FPGA into voltages that are applied to the sensor. Due to implementation constraints, these voltages have to be in the range $[0, 2]$ V. The charge amplifiers convert the capacitance (proportional to the positions x and y) into voltage. Moreover, external anti-aliasing filters F_{adc} and analog-to-digital converters (ADC) convert the signals obtained from the charge amplifiers into digital signals that are communicated to the FPGA. These ADCs operate with a 1 MHz sampling frequency and have a 18-bit resolution.

Finally, the FPGA implements a microprocessor, which is programmed in C++ language. The processor uses double-precision floating-point format to perform the mathematical operations. We denote $v_{in} = \text{col}(v_{in,x}, v_{in,y})$ the signals that the processor sends to the DACs, and $v_{out} = \text{col}(v_{out,x}, v_{out,y})$ the signals after decimation. Hence, the system “seen” by the processor corresponds to the system between the signals v_{in} and v_{out} . The control-related routines are executed every $16 \mu\text{s}$, what is equivalent to a sampling frequency $F_s = 62.5 \text{ kHz}$. To downsample the signal issued from the ADCs at 1 MHz, a digital low-pass filter F_{ds} and a decimator with downsampling factor equal to 16 are implemented in hardware in the same FPGA.

Note that the sampling frequency is 5 to 6 times higher than the expected resonance frequencies. This ratio is enough to implement a direct control architecture in discrete time, providing that the sampling and holding operations of the converters are taken into account in the control design. Our main objective is then to implement a digital direct controller, operating with $F_s = 62.5 \text{ kHz}$, that fulfills the same specifications of Example 4.5. The most important specifications are recalled below.

- (i) **Drive-mode reference tracking:** reference tracking of a sinusoidal signal with relative error smaller than $\check{\epsilon}_x < 0.5k_{\text{SFNL}} = 250 \cdot 10^{-6}$ for $\omega_{exc} = \omega_{0,x}$.
- (ii) **Estimation of the Coriolis force:** estimation of a sinusoidal signal with relative error $\check{\epsilon}_{est} < 0.5k_{\text{SFNL}} = 250 \cdot 10^{-6}$ ($\lambda_{\text{SFNL}} = 0.5$) for $\omega_{exc} = \omega_{0,x}$.

Problem 7.1. *Given the model of the MEMS gyroscope and the closed-loop performance specifications, design and implement a digital controller that ensures the desired closed-loop performance.*

Before proceeding with this problem, we have to obtain a model of the MEMS gyroscope. This point is treated in the sequel.

7.2 Modeling the System and Dealing with its Nonidealities

In this section, we show how to model the overall system and how to deal with the main non-idealities of the MEMS gyroscope: the parasitic electrical coupling and the input nonlinearity.

7.2.1 System Modeling

The first step for the controller design consists in defining the model of the to-be-controlled system. In general, three approaches can be considered here: the so-called white-box, black-box and gray-box modeling. In the white-box modeling, the model is determined through first principles (*e.g.*, fundamental equations of motion). In contrast to the white-box modeling, the black-box modeling only uses experimental data collected from the system. Finally, in the gray-box modeling, experimental data is used to determine the parameters of first-principle models. In the scope of the Next4MEMS project, we consider the latter approach. For more details on modeling and identification techniques for MEMS gyroscopes, we refer the reader to the thesis [Col20].

In [Col20, Chapter 7], it is shown that the overall system seen by the controller can be modeled by three discrete-time subsystems – G_{ID}^d , E_{ID}^d and N_{ID}^d –, as presented in Figure 7.2. The mechanical part of the MEMS gyroscope and all the circuitry are encapsulated in G_{ID}^d with a square nonlinearity at the input (due to the nonlinear relationship between voltage and electrostatic force, see Section 2.1.3, page 18). The parasitic electrical coupling is modeled by E_{ID}^d . Finally, all the noise sources (*e.g.*, thermal noise, electrical noise and quantization error) are modeled as white-noise signals $e = \text{col}(e_x, e_y)$ filtered by N_{ID}^d .

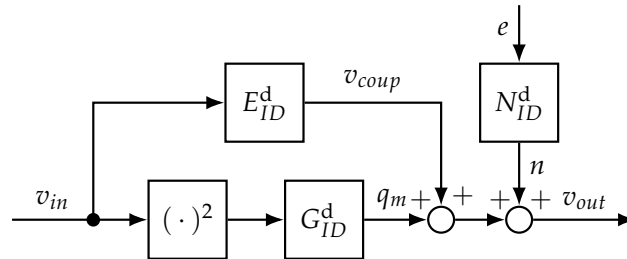


FIGURE 7.2: Block diagram of the identified model seen by the controller.

7.2.2 Electrical Coupling Compensation

As discussed in Section 2.1.5 (page 27), the parasitic electrical coupling is one of the sources of error in MEMS gyroscopes. Nevertheless, its disturbing effects can be digitally compensated, as follows.

Note that the output signal v_{out} has several contributions. Indeed, as illustrated in Figure 7.2,

$$v_{out}(t) = v_{coup}(t) + q_m(t) + n(t),$$

where $q_m = \text{col}(x_m, y_m)$ is proportional to the positions x and y of the gyroscope proof mass, $n = \text{col}(n_x, n_y)$ is the contribution of the different sources of noise and $v_{coup} = \text{col}(v_{coup,x}, v_{coup,y})$ corresponds to a disturbance generated by the electrical coupling. Since v_{in} is generated by the processor and E_{ID}^d is known, we can then compute v_{coup} and define

$$q_n(t) \triangleq v_{out}(t) - v_{coup}(t),$$

such that we obtain

$$q_n(t) = q_m(t) + n(t),$$

compensating for the parasitic electrical coupling contributions. This procedure is depicted in Figure 7.3, where the dashed elements represent the operations digitally realized by the processor. Further details on the electrical coupling modeling and compensation can be found in our paper [CSL⁺19] and in the thesis [Col20].

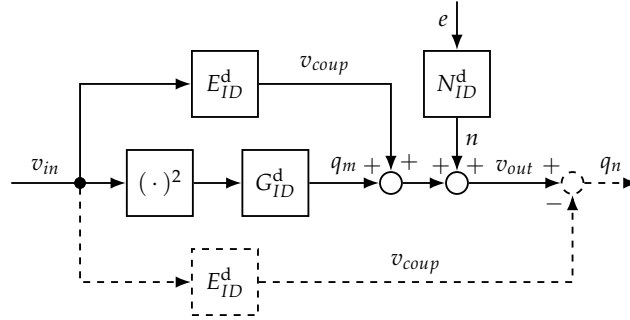


FIGURE 7.3: Block diagram of the identified model with electrical coupling compensation. Elements in dashed line are digitally implemented in the micro-processor.

7.2.3 Dealing with the Input Nonlinearity

Depending on the actuation technique used for the MEMS gyroscope, a square nonlinearity can appear at its input, see Section 2.1.3 (page 18). For the gyroscope considered here, this nonlinearity is in fact present. To deal with this nonlinearity, we extend a technique that is widely used for MEMS gyroscopes, see, *e.g.*, [Sau08, Section 4.1]. We will see that, as claimed in Section 2.1.3, the square nonlinearity can be replaced by a constant gain $k_{lin} \in \mathbb{R}^{2 \times 2}$ and the to-be-controlled system is modeled by the linear system $G^d = G_{ID}^d k_{lin}$.

Let us assume that the input voltages, $v_{in} = \text{col}(v_{in,x}, v_{in,y})$, are of the form

$$v_{in}(t) = V_{DC} + u(t) \quad (7.1)$$

with $V_{DC} = \text{col}(V_{DC,x}, V_{DC,y})$, $V_{DC,x} \in \mathbb{R}$ and $V_{DC,y} \in \mathbb{R}$. By developing (7.1), the signal at the input of G_{ID}^d reads as

$$\begin{bmatrix} v_{in,x}(t)^2 \\ v_{in,y}(t)^2 \end{bmatrix} = \begin{bmatrix} V_{DC,x}^2 \\ V_{DC,y}^2 \end{bmatrix} + \begin{bmatrix} 2V_{DC,x}u_x(t) \\ 2V_{DC,y}u_y(t) \end{bmatrix} + \begin{bmatrix} u_x^2(t) \\ u_y^2(t) \end{bmatrix}. \quad (7.2)$$

Let us also assume that u_x and u_y are band-pass signals centered at ω_u with bandwidth $2\omega_{bu}$, that is, with $i \in \{x, y\}$

$$\forall |\omega| \leq \omega_u - \omega_{bu} \quad \text{and} \quad \forall |\omega| \geq \omega_u + \omega_{bu}, \quad \mathcal{F}[u_i](\omega) = 0. \quad (7.3)$$

In this case, the spectrum of u_i^2 can be given by $\mathcal{F}[u_i^2](\omega) = \mathcal{F}[u_i] * \mathcal{F}[u_i](\omega)$, which is null for $2\omega_{bu} \leq |\omega| \leq 2\omega_u - 2\omega_{bu}$ and for $|\omega| \geq 2\omega_u + 2\omega_{bu}$. Finally, since the spectrum of $v_{in,i}^2$ is a combination of the spectra of u_i , u_i^2 and $V_{DC,i}^2$ (Dirac delta function at $\omega = 0$), we can represent its spectrum as illustrated in Figure 7.4. Please note that if $\omega_{bu} < \omega_u/3$ the spectrum of u_i does not overlap the one of u_i^2 .

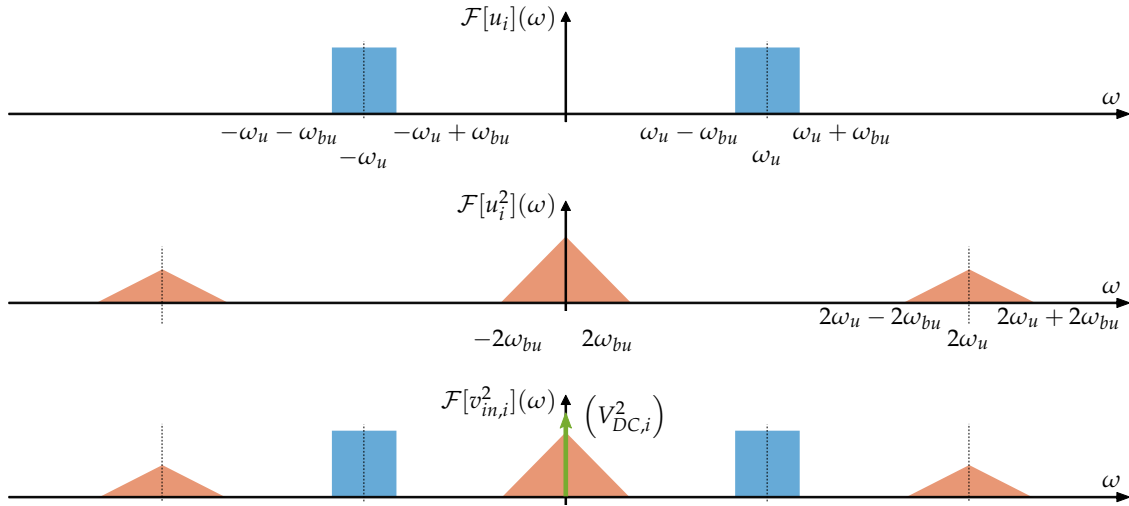


FIGURE 7.4: Illustrative example of the spectrum of the signals u_i , u_i^2 and $v_{in,i}^2$ with $i \in \{x, y\}$.

Recall that the MEMS gyroscope behaves as a very selective band-pass filter around the drive-mode² resonance frequency $\omega_{0,x}$. This means that only the effects of the components around these frequencies will be seen at the gyroscope (compensated) output q_n . Therefore, if $\omega_u = \omega_{exc} \approx \omega_{0,x}$ and $\omega_{bu} < \omega_u/3$ (to avoid overlapping the spectrum contributions related to u_i and to u_i^2), only the contribution of $2V_{DC,i}u_i$ appears on q_n , as depicted in Figure 7.5. In this case, we can approximate

$$G_{ID}^d(z)v_{in}^2(t) \approx \underbrace{G_{ID}^d(z)k_{lin}}_{\triangleq G^d(z)} u(t)$$

with $k_{lin} = \text{diag}(k_{lin,x}, k_{lin,y})$, $k_{lin,i} = 2V_{DC,i}$ and two abuses of notation: $v_{in}^2 = \text{col}(v_{in,x}^2, v_{in,y}^2)$, and z representing, at the same time, the shift operator and the complex variable of the z -transform.

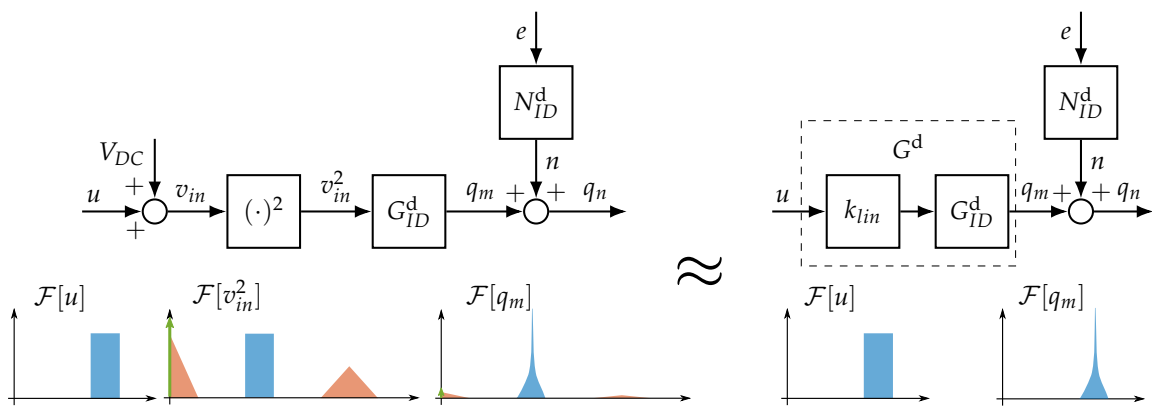


FIGURE 7.5: Full compensated model (left) and linear compensated model (right) with an illustrative example of the spectrum of the main signals.

²The sense-mode resonance frequency is often very close to $\omega_{0,x}$ so that we can consider $\omega_{0,y} = \omega_{0,x}$ in this reasoning.

In [Sau08, Section 4.1], u_i is considered to be of the form $u_i(t) = V_{AC,i} \cos(\omega_{exc}t)$ with $V_{AC,i} \in \mathbb{R}_+$. This form would rather correspond to the actuation signal in steady state. Our approach extends this result for the transient state.

7.3 Continuous-Time Design of a Discrete-Time Controller

In the previous section, we obtained a linear model of the MEMS gyroscope, and the control design methods proposed in this thesis could then be applied. However, this model and the to-be-implemented controller are in discrete time (DT), whereas we have rather considered the controller and to-be-controlled plant as continuous-time (CT) systems. In this section, we present a traditional (but sometimes forgotten) procedure to design a DT controller based on a CT method.

The common procedure to design a DT controller through frequency-domain methods (as the \mathcal{H}_∞ synthesis) is illustrated in Figure 7.6 and described in the sequel [JLN55, ÅW97].

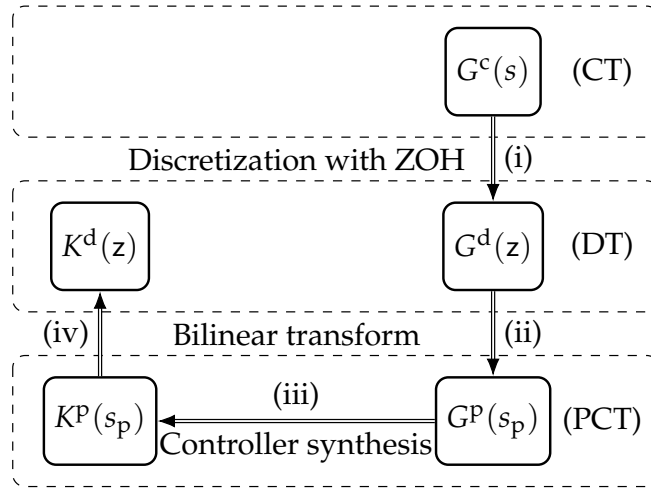


FIGURE 7.6: Procedure for the synthesis of a DT controller based on a CT design method.

- (i) **Discretization of the CT system:** let us consider a CT system G^c with state-space matrices (A, B, C, D) . The ADC is modeled by a sampler with sampling period T_s and the DAC is modeled by a zero-order hold (ZOH) with the same sampling period. The corresponding DT system G^d is computed by the step-invariant method, which gives

$$G^d(z) = (1 - z^{-1}) \mathcal{Z} \left[\mathcal{L}^{-1} \left[\frac{G^c(s)}{s} \right] \right]. \quad (7.4)$$

Recall that, by definition, $z = e^{sT_s}$. Then, since G^d is a rational function of z , G^d is a nonrational function of s . As consequence, the frequency response of G^d , which is given by $G^d(e^{j\omega T_s})$, is also a nonrational function of ω .

If the DT state-space representation is considered, G^d is defined by the state-space matrices (A^d, B^d, C^d, D^d) , which read as

$$\begin{aligned} A^d &= e^{AT_s} \\ B^d &= A^{-1} (e^{AT_s} - I) B \\ C^d &= C \\ D^d &= D. \end{aligned} \quad (7.5)$$

We highlight that when using DT identification, G^d is directly obtained and includes the ZOH. In this case, the matrices (A^d, B^d, C^d, D^d) are given and this step can be skipped.

- (ii) **Defining a CT-like system:** to use frequency-domain control design methods, we have to define an equivalent CT system that also takes into account the ZOH. To this purpose, we should replace z by e^{sT_s} . The problem here is that, as discussed earlier, the obtained transfer would not be a rational function of s and the current CT design methods could not be used. Instead, we define a new variable s_p , such that,

$$z = e^{sT_s} = \frac{1 + s_p T_s / 2}{1 - s_p T_s / 2}. \quad (7.6)$$

Hence, the CT-like plant that represents G^c with the ZOH is given by

$$G^p(s_p) = G^d(z) \Big|_{z = \frac{2/T_s + s_p}{2/T_s - s_p}}. \quad (7.7)$$

In state-space representation, if -1 is not an eigenvalue of A^d , G^p is defined by the state-space matrices (A^p, B^p, C^p, D^p) , which read as

$$\begin{aligned} A^p &= \frac{2}{T_s} (A^d - I) (A^d + I)^{-1} \\ B^p &= \frac{4}{T_s} (A^d + I)^{-1} B^d \\ C^p &= C^d (A^d + I)^{-1} \\ D^p &= D^d - C^d (A^d + I)^{-1} B^d. \end{aligned} \quad (7.8)$$

Note that when $sT_s \ll 1$, $s_p \approx s$. Indeed, $e^{sT_s} = \frac{e^{sT_s/2}}{e^{-sT_s/2}} \approx \frac{1+sT_s/2}{1-sT_s/2}$. This approximation is known as trapezoidal or Tustin's approximation or bilinear transform. The complex variable s_p represents a "pseudo Laplace variable" that is related to s through

$$s_p = \frac{2}{T_s} \frac{e^{sT_s} - 1}{e^{sT_s} + 1} = \frac{2}{T_s} \tanh\left(\frac{sT_s}{2}\right). \quad (7.9)$$

In the literature, the variable s_p is usually denoted w and defines the so-called w -plane (see, e.g., [ÅW97, Section 8.4]). It is important to highlight that when $s = j\omega$, we obtain $s_p = j\omega$ with

$$\omega = g(\omega) \triangleq \frac{2}{T_s} \tan\left(\frac{\omega T_s}{2}\right), \quad (7.10)$$

where ω defines what we call the pseudo-continuous frequency. Its reciprocal would be the "pseudo-time" variable. For this reason, we call G^p the pseudo continuous-time (PCT) model. Equation (7.10) means that the frequency response (in ω) of a linear

system is distorted in the pseudo-continuous frequency space (in ω). Moreover, note that this distortion is a nonlinear function of ω .

Finally, it is important to highlight that a PCT model obtained through the bilinear transform, as presented here, will always have unstable zeros at $s_p = 2/T_s$, bounding the bandwidth of the closed-loop system, see, *e.g.*, [FL85] and [SP01, Chapter 5]. Further details on the unstable zeros of PCT models are discussed in Appendix F.1.

- (iii) **Controller synthesis in PCT:** a PCT controller K^P is computed through a CT design method, such as the \mathcal{H}_∞ synthesis. The resulting controller is then assumed to be defined by the state-space matrices $(A_K^P, B_K^P, C_K^P, D_K^P)$.
- (iv) **Controller discretization:** the last step consists in discretizing the controller with the sampling period T_s . To this purpose, we apply the bilinear transform in the other sense, that is,

$$K^d(z) = K^P(s_p) \Big|_{s_p = \frac{2}{T_s} \frac{z-1}{z+1}}.$$

In state-space representation, K^d is therefore defined by the matrices $(A_K^d, B_K^d, C_K^d, D_K^d)$, which are finally given by

$$\begin{aligned} A_K^d &= \left(\frac{2I}{T_s} + A_K^P \right) \left(\frac{2I}{T_s} - A_K^P \right)^{-1} \\ B_K^d &= 2 \frac{2}{T_s} \left(\frac{2I}{T_s} - A_K^P \right)^{-1} B_K^P \\ C_K^d &= C_K^P \left(\frac{2I}{T_s} - A_K^P \right)^{-1} \\ D_K^d &= D_K^P + C_K^P \left(\frac{2I}{T_s} - A_K^P \right)^{-1} B_K^P. \end{aligned} \tag{7.11}$$

The main strength of this procedure relies on the stability equivalence property ensured by the bilinear transform. This means that the DT closed-loop system (composed of G^d and K^d) is stable if and only if the PCT closed-loop system (composed of G^P and K^P) is also stable. Moreover, the bilinear transform also conserves the \mathcal{H}_∞ norm of the systems³, that is, $\|G^P\|_\infty = \|G^d\|_\infty$.

7.4 Design of a Parameter-Dependent \mathcal{H}_∞ Controller

The design of a parameter-dependent controller for a parameter-dependent plant can be addressed by the so-called linear parameter-varying (LPV) approaches (such as the polytopic method presented in Section 5.3.2, page 131). In the particular case treated in this chapter, these approaches lead to conservative solutions or to a parameterization which can be too complex to be implemented in real time. The conservatism of the LPV approaches comes from the fact that the parameter of interest is assumed to vary arbitrarily [Pac94, SE98], whereas ω_0 is assumed to be constant (or slow varying). On the other hand, [DSFM05] proposes a nonconservative design method for constant parameter-dependent controller. However, the proposed controller parametrization is, in general, too complicated to be implemented in a limited-cost embedded processor.

³This claim can be easily proven through (7.6), (7.7) and the \mathcal{H}_∞ -norm definitions

$$\|G^P\|_\infty \triangleq \sup_{s_p > 0} \bar{\sigma}(G^P(s_p)) \quad \text{and} \quad \|G^d\|_\infty \triangleq \sup_{|z| > 1} \bar{\sigma}(G^d(z)).$$

In this section, we present, for the particular problem of MEMS gyroscopes (and similar ones), a parameter-dependent \mathcal{H}_∞ controller design method. Our approach provides performance guarantees, reduced conservatism, and simple parameterization in the case where ω_{exc} is measured and constant. We propose two design methods: for a CT controller, and for a DT controller. The former one is suitable for analog implementations or for digital implementation where the sampling period T_s is so small that the discretization effects (sampling and holding) can be neglected. The main interest on considering the design of a CT controller is that this approach also gives important insights on the controller parametrization. The second method is suitable for digital implementations where the discretization effects have to be taken into consideration, which is often the case for MEMS gyroscopes.

It is important to highlight that the assumption of ω_{exc} constant is used for the controller design. However, in practice, this condition can be relaxed to slow variations of ω_{exc} , see, e.g., our paper [SACKS20].

7.4.1 Parameter-Dependent Control Design Problem

Let us assume that the MEMS gyroscope model can be written as a particular type of LPV systems of the form

$$G^{\omega_0} : \begin{cases} \dot{x}(t) = \omega_0 Ax(t) + \omega_0 Bu(t) \\ y(t) = Cx(t) + Du(t) \end{cases} \quad (7.12)$$

with $x(t) \in \mathbb{R}^{n_G}$, $u(t) \in \mathbb{R}^{n_{u_G}}$, $y(t) \in \mathbb{R}^{n_{y_G}}$ and matrices of adequate dimensions. The parameter $\omega_0 \in [\omega_{0,1}, \omega_{0,2}]$ is supposed to be known in real time. We also consider the control objectives of Section 7.1, which consist in tracking or rejecting sinusoidal signals of frequency $\omega_{exc} = \omega_{0,x} = \omega_0$ with $\omega_0 \in [\omega_{0,1}, \omega_{0,2}]$. Our objective is then to design a controller that fulfills the control objectives and whose gains are dependent on ω_0 .

With the standard \mathcal{H}_∞ synthesis (see Section 4.1, page 76), for each ω_0 , the design of the controller is formulated as an optimization problem. Based on the control objectives, we define signals of interest $\tilde{w} \in \mathbb{R}^{n_w}$ and $\tilde{z} \in \mathbb{R}^{n_z}$. These signals, together with the to-be-controlled system G^{ω_0} , define an augmented plant \tilde{P}^{ω_0} . Weighting functions $W_{in}^{\omega_0}$ and $W_{out}^{\omega_0}$, which also depend on ω_0 , are introduced on the signals of interest, defining the weighted augmented plant P^{ω_0} , as shown in Figure 7.7. The \mathcal{H}_∞ problem is then to find, for each $\omega_0 \in [\omega_{0,1}, \omega_{0,2}]$, a controller K^{ω_0} , if there is any, such that the weighted closed-loop transfer functions are stable and meet a given performance level γ , that is, $\|P^{\omega_0} \star K^{\omega_0}\|_\infty < \gamma$.

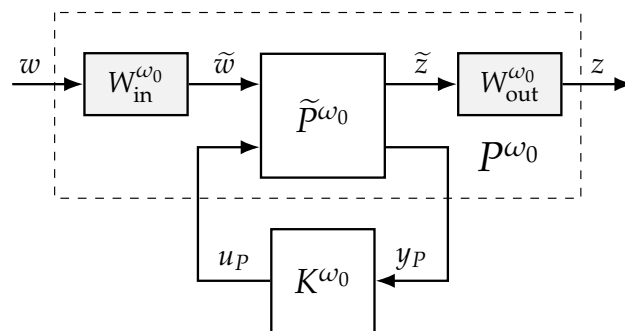


FIGURE 7.7: General control configuration with ω_0 -dependent weighting filters.

Note that computing all the controllers K^{ω_0} through the standard \mathcal{H}_∞ synthesis implies solving an infinite number of optimization problems. However, based on the \mathcal{H}_∞ synthesis, we can formulate the following control design problem.

Problem 7.2 (Parameter-dependent control design problem). *Assume that ω_0 is constant and measured in real time. Given the ω_0 -dependent augmented plant P^{ω_0} and a performance level $\gamma > 0$, find a single (and simple-to-implement) controller K^{ω_0} whose gains depend on ω_0 , if there is any, such that, $\forall \omega_0 \in [\omega_{0,1}, \omega_{0,2}]$, $\|P^{\omega_0} \star K^{\omega_0}\|_\infty < \gamma$.*

A similar problem is treated in [DSFM05]. However, as mentioned before, the proposed controller parametrization is in general too complicated to be implemented in a limited-cost embedded processor. In the sequel, we reveal that, in the case of MEMS gyroscope (and similar applications) a simple parametrization, suited for real-time implementation, is obtained.

7.4.2 Solution in Continuous Time

Here, we present a solution in continuous-time (CT) domain, which provides the central elements for the solution in DT.

Let us also assume that the weighting functions can also be written in the form of (7.12). Thus, the augmented plant P^{ω_0} admits the state-space representation:

$$P^{\omega_0} : \begin{cases} \dot{x}_P(t) &= \omega_0 A_P x_P(t) + \omega_0 B_w w(t) + \omega_0 B_u u(t) \\ z(t) &= C_z x_P(t) + D_{zw} w(t) + D_{zu} u(t) \\ y_P(t) &= C_y x_P(t) + D_{yw} w(t) \end{cases}, \quad (7.13)$$

where $x_P(t) \in \mathbb{R}^{n_P}$, $y_P(t) \in \mathbb{R}^{n_y}$, $w(t) \in \mathbb{R}^{n_w}$, $z(t) \in \mathbb{R}^{n_z}$ and whose matrices do not depend on ω_0 .

At this point, we can then define a normalized Laplace variable $s_n = s/\omega_0$ and a normalized time $t_n = \omega_0 t$, such that the normalized version of P^{ω_0} , denoted P_n , is cast as

$$P_n : \begin{cases} \dot{x}_{P,n}(t_n) &= A_P x_{P,n}(t_n) + B_w w_n(t_n) + B_u u_n(t_n) \\ z_n(t_n) &= C_z x_{P,n}(t_n) + D_{zw} w_n(t_n) + D_{zu} u_n(t_n) \\ y_{P,n}(t_n) &= C_y x_{P,n}(t_n) + D_{yw} w_n(t_n) \end{cases} \quad (7.14)$$

with $x_{P,n}(t_n) = x_P(t_n/\omega_0)$ and similarly for the other signals. Note that the state-space matrices of P_n do not depend on ω_0 . Moreover, since $P^{\omega_0}(s) = P_n(s_n)$, $\|P^{\omega_0}\|_\infty = \|P_n\|_\infty$. Thus, the solution of Problem 7.2 is the solution of the standard \mathcal{H}_∞ problem: given a normalized augmented plant P_n (7.14) and a performance level $\gamma > 0$, compute a normalized controller K_n , if there exists any, in the form of

$$K_n : \begin{cases} \dot{x}_{K,n}(t_n) &= A_K x_{K,n}(t_n) + B_K y_{P,n}(t_n) \\ u_n(t_n) &= C_K x_{K,n}(t_n) + D_K y_{P,n}(t_n) \end{cases}, \quad (7.15)$$

where $x_{K,n}(t_n) \in \mathbb{R}^{n_K}$, such that $\|P_n \star K_n\|_\infty < \gamma$. Hence, the CT ω_0 -dependent controller K^{ω_0} is given by

$$K^{\omega_0} : \begin{cases} \dot{x}_K(t) &= \omega_0 A_K x_K(t) + \omega_0 B_K y_P(t) \\ u_P(t) &= C_K x_K(t) + D_K y_P(t) \end{cases}. \quad (7.16)$$

Please note that the new (denormalized) controller K^{ω_0} ensures the stability of the closed-loop system and $\|P^{\omega_0} \star K^{\omega_0}\|_\infty < \gamma$ for all $\omega_0 \in [\omega_{0,1}, \omega_{0,2}]$, i.e., solves Problem 7.2.

Remark 7.1 (On the realism of the model and weighting functions “normalizability” assumption). Note that the to-be-controlled plant G^{ω_0} and the weighting functions are assumed to be an LPV system in the form of (7.12), that is, the state and input matrices are linear functions of ω_0 . As consequence, the augmented plant P^{ω_0} has the same structure. These assumptions allow us to use the frequency normalization and model the LPV system P^{ω_0} for all $\omega_0 \in [\omega_{0,1}, \omega_{0,2}]$ as a single LTI system P_n , whose parameters (in the “normalized-time” space with $t_n = \omega_0 t$) do not depend on ω_0 .

At this point, the reader may be asking himself: “how realistic are these assumptions?”. If we consider the \mathcal{H}_∞ design examples considered in Chapter 4, note that controller synthesis is already made in a normalized-frequency space. Thus, if we consider the same normalized weighting functions for all $\omega_0 \in [\omega_{0,1}, \omega_{0,2}]$, in the original (denormalized) frequency space, the weighting functions are indeed in the form of (7.12).

Regarding the MEMS gyroscope model, for the sake of simplicity, we only consider the drive mode (for further discussion on this assumption for the whole gyroscope model, see Appendix F.2). Note that the drive-mode transfer function (see (2.15), page 21) can be rewritten as

$$G^{\omega_{0,x}}(s) = \frac{x_m(s)}{u_x(s)} = \frac{k_{0,x}}{(s/\omega_{0,x})^2 + (s/\omega_{0,x})/Q_x + 1}, \quad (7.17)$$

and admits the state-space representation of (7.12) with $\omega_0 = \omega_{0,x}$ and

$$A = \begin{bmatrix} 0 & 1 \\ -1 & -1/Q_x \end{bmatrix}, \quad B = \begin{bmatrix} 0 \\ 1 \end{bmatrix}, \quad C = [k_{0,x} \ 0] \quad \text{and} \quad D = 0.$$

Then, if the variations of $\omega_{0,x}$ do not change the values of Q_x and $k_{0,x}$, the referred assumption holds.

7.4.3 Solution for Discrete-Time Implementation

We now discuss the design of a discrete-time (DT) controller whose gains depend on ω_0 and for which the discretization effects (sampling and holding) cannot be neglected. Obviously, the first idea would be to adopt the procedure of Section 7.3 with the parameter-dependent design proposed in Section 7.4.2. However, observe that the controller is designed in the PCT space, based on a PCT model of G^{ω_0} . Then, before applying the approach of Section 7.4.2, we need to check if the PCT model of G^{ω_0} can be expressed as in (7.12).

By following the procedure illustrated in Figure 7.6, for a CT system $G^c = G^{\omega_0}$ given by the state-space matrices $(\omega_0 A, \omega_0 B, C, D)$, its PCT model G^p is given by the state-space matrices (A^p, B^p, C^p, D^p) , which, for the sampling period T_s , read as (see (7.5) and (7.8))

$$\begin{aligned} A^p &= \frac{2}{T_s} (e^{\omega_0 A T_s} - I) (e^{\omega_0 A T_s} + I)^{-1} \\ B^p &= \frac{4}{T_s} (e^{\omega_0 A T_s} + I)^{-1} A^{-1} (e^{\omega_0 A T_s} - I) B \\ C^p &= C (e^{\omega_0 A T_s} + I)^{-1} \\ D^p &= D - C (e^{\omega_0 A T_s} + I)^{-1} A^{-1} (e^{\omega_0 A T_s} - I) B. \end{aligned} \quad (7.18)$$

Please note that, this time, the dependence of the state matrices on ω_0 is nonlinear and the approach of Section 7.4.2 cannot be directly applied to G^p . However, for some particular cases (such as for high quality factor resonators, which is indeed the case of MEMS gyroscopes), the PCT model can be approximated by a fictitious system H^{p,ω_0} with state

matrices $(\omega_0 A_H, \omega_0 B_H, C_H, D_H)$, where $\omega_0 = g(\omega_0)$ (see (7.10)). This point is illustrated in the following example.

Example 7.1 (On the fictitious model of $G^{\omega_{0,x}}$). *The main objective of this example is to show that a 2^{nd} -order resonator whose model parameters depend on $\omega_{0,x} \in [\omega_{0,x,1}, \omega_{0,x,2}]$ in CT (or DT) will have a PCT model whose parameters depend linearly on $\omega_{0,x} = g(\omega_{0,x})$.*

For the system $G^{\omega_{0,x}}$ given in (7.17), its model in PCT, with $Q_x \gg 1$, can be given by (further details are given in Appendix F.3):

$$G^{P,\omega_{0,x}}(s_p) = \frac{k_{0,x} (1 - (s_p/\omega_{0,x}) \omega_{0,x} T_s/2) (1 + (s_p/\omega_{0,x}) / (2Q_x))}{(s_p/\omega_{0,x})^2 + (s_p/\omega_{0,x}) / (Q_x \text{sinc}(\omega_{0,x} T_s)) + 1}, \quad (7.19)$$

which can be approximated by the fictitious system

$$H^{P,\omega_{0,x}}(s_p) = \frac{k_{0,x} (1 - (s_p/\omega_{0,x}) / z_u)}{(s_p/\omega_{0,x})^2 + (s_p/\omega_{0,x}) / (Q_x \text{sinc}(\omega_{0,x,2} T_s)) + 1} \quad (7.20)$$

with $z_u = \tan(\omega_{0,x,2} T_s/2)^{-1}$, which admits the state-space matrices $(\omega_{0,x} A_H, \omega_{0,x} B_H, C_H, D_H)$, where

$$A_H = \begin{bmatrix} 0 & 1 \\ -1 & -1/(Q_x \text{sinc}(\omega_{0,x,2} T_s)) \end{bmatrix}, \quad B_H = \begin{bmatrix} 0 \\ 1 \end{bmatrix}, \quad C_H = \begin{bmatrix} k_{0,x} & \frac{-k_{0,x}}{z_u} \end{bmatrix} \quad \text{and} \quad D_H = 0.$$

Details on the choice of this specific fictitious model are also provided in Appendix F.4. It is important to highlight however that the choice of a fictitious model is not unique. The main objective is to define a model that approximates $G^{P,\omega_{0,x}}$ and such that in the normalized space, it is represented by a single LTI system.

Now, since the fictitious system can be normalized with respect to $\omega_0 = g(\omega_0)$, we can design a controller for H^{P,ω_0} with the approach of Section 7.4.2. The DT controller is then obtained through the bilinear transform.

To summarize this method, we present Figure 7.8, which completes the scheme of Figure 7.6. The new steps are described as follows.

- (i) Instead of designing the controller in PCT, we define a fictitious model, H^{P,ω_0} , from the set of G^{P,ω_0} for $\omega_0 \in [g(\omega_{0,1}), g(\omega_{0,2})]$.
- (ii) H^{P,ω_0} is normalized by ω_0 , giving origin to a normalized pseudo-continuous time (nPCT) model H_n^P .
- (iii) Then, a normalized PCT controller K_n^P is designed by solving a standard \mathcal{H}_∞ problem, where P_n is defined by normalized weighting functions and H_n^P .
- (iv) This controller is thus denormalized by ω_0 , generating K^{P,ω_0} .
- (v) Finally, the DT controller K^{d,ω_0} is obtained by the bilinear transform of K^{P,ω_0} .

For an nPCT controller K_n^P given by the state-space matrices (A_K, B_K, C_K, D_K) , the PCT controller K^{P,ω_0} has the state-space matrices $(\omega_0 A_K, \omega_0 B_K, C_K, D_K)$. Then, recalling that $\omega_0 = g(\omega_0)$, the DT controller K^{d,ω_0} is defined by the matrices $(A_K^d(\omega_0), B_K^d(\omega_0), C_K^d(\omega_0), D_K^d(\omega_0))$

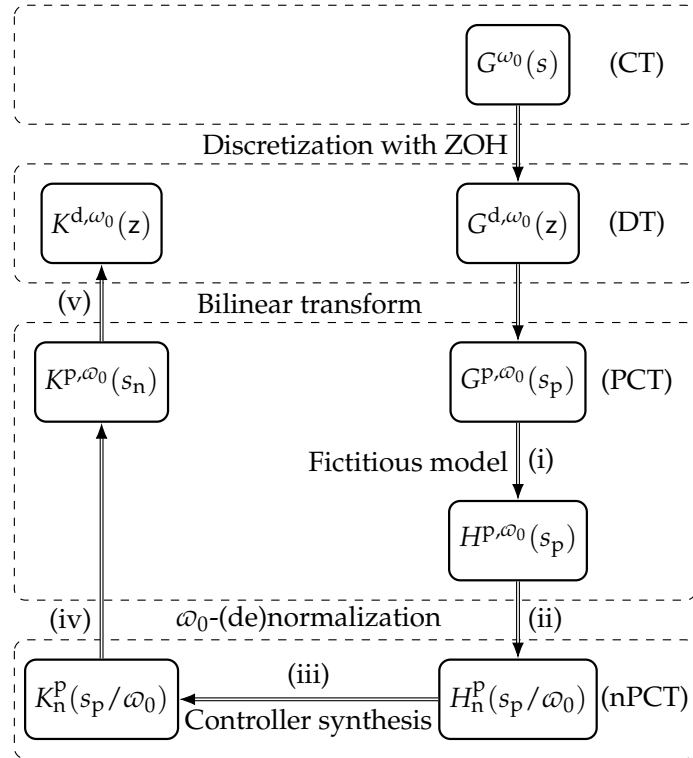


FIGURE 7.8: Procedure for the design of a parameter-dependent DT controller.

with

$$\begin{aligned}
 A_K^d(\omega_0) &= (2I/T_s + \omega_0 A_K)(2I/T_s - \omega_0 A_K)^{-1} \\
 B_K^d(\omega_0) &= 4/T_s (2I/T_s - \omega_0 A_K)^{-1} \omega_0 B_K \\
 C_K^d(\omega_0) &= C_K (2I/T_s - \omega_0 A_K)^{-1} \\
 D_K^d(\omega_0) &= D_K + C_K (2I/T_s - \omega_0 A_K)^{-1} \omega_0 B_K.
 \end{aligned} \tag{7.21}$$

Remark 7.2 (On the digital controller with ω_0 -dependent sampling period). The solution presented in this section provides a controller whose state-space matrices depend on given matrices A_K , B_K , C_K , D_K , the sampling period T_s and $\omega_0 = g(\omega_0)$ (see (7.21)). Then, if the sampling period T_s is fixed and the parameter ω_0 changes, the controller matrices have to be updated. However, the same result can be obtained if, instead of updating the controller matrices, we link the sampling period T_s with the parameter ω_0 in a proper way, as we reveal in the sequel.

The matrices of (7.21) can be rewritten as

$$\begin{aligned}
 A_K^d(\omega_0) &= (2I + \omega_0 T_s A_K)(2I - \omega_0 T_s A_K)^{-1} \\
 B_K^d(\omega_0) &= 4\omega_0 T_s (2I - \omega_0 T_s A_K)^{-1} B_K \\
 C_K^d(\omega_0) &= C_K (2I - \omega_0 T_s A_K)^{-1} \\
 D_K^d(\omega_0) &= D_K + C_K (2I - \omega_0 T_s A_K)^{-1} B_K.
 \end{aligned} \tag{7.22}$$

Then, by defining a constant $\alpha_{T_s} \triangleq \omega_0 T_s$, the same controller can be implemented by the constant matrices

$$\begin{aligned} A_K^d &= (2I + \alpha_{T_s} A_K) (2I - \alpha_{T_s} A_K)^{-1} \\ B_K^d &= 4\alpha_{T_s} (2I - \alpha_{T_s} A_K)^{-1} B_K \\ C_K^d &= C_K (2I - \alpha_{T_s} A_K)^{-1} \\ D_K^d &= D_K + C_K (2I - \alpha_{T_s} A_K)^{-1} B_K \end{aligned} \quad (7.23)$$

and the ω_0 -dependent sampling period $T_s(\omega_0) = \alpha_{T_s} / g(\omega_0)$, such that its frequency response varies according to ω_0 , solving the Problem 7.2 as well. Finally, it is worth noting that, if $T_s \ll 1/\omega_0$, we can approximate $\omega_0 = g(\omega_0) \approx \omega_0$ (see (7.10)) and $\alpha_{T_s} \approx \omega_0 T_s$.

In the MEMS gyroscope context, this strategy is used to link the drive-mode resonance frequency $\omega_{0,x}$ to the sampling frequency, ensuring good performance of the sensor under variations of $\omega_{0,x}$ (due to temperature changes, for instance), see [EEE⁺11, CXZ⁺21]. Although this approach has been used in the literature and in the industry, no theoretical results endorsing this approach could be found. The framework that we propose here validates the approach.

Given that the controller design is based on the the fictitious system H^{P,ω_0} , which is an approximation of G^{P,ω_0} , the stability and performance of the actual closed-loop system has to be evaluated *a posteriori*. For further details on this analysis procedure, please refer to our paper [SACKS20] or to the thesis [AC21].

7.5 Implementation Results on the Asygn's Platform

In this section, we illustrate the whole procedure for the design and implementation of a digital direct controller on the (flexible) Asygn's platform, presented in Section 2.3.1. Moreover, tests are made to evaluate the implementation of the control loops and their efficiency. In particular, we verify the reference tracking and the Coriolis force estimation specifications of Section 7.1.

The tests are realized at room temperature, keeping the operating conditions as steady as possible, such that in the controller is not frequency-dependent in this section.

7.5.1 Controller Design

Identified model: the first step consists in identifying the to-be-controlled system. Here, we follow the approach of [Col20]. The Bode diagram representing the MEMS gyroscope at rest ($\Omega_z = 0$), G_{ID}^d is given in Figure 7.9 and in Figure 7.10. For a clearer explanation, let us partition G_{ID}^d as

$$G_{ID}^d = \begin{bmatrix} G_{ID,xx}^d & G_{ID,xy}^d \\ G_{ID,yx}^d & G_{ID,yy}^d \end{bmatrix}.$$

As expected (see Example 2.3, page 34), the diagonal transfers $G_{ID,xx}^d$ and $G_{ID,yy}^d$, which represent respectively the drive and sense modes, behave as resonators. Their resonance frequencies and quality factors are given below

$$\begin{aligned} \omega_{0,x} &= 2\pi 11.5864 \cdot 10^3 \text{ rad/sec}, & \omega_{0,y} &= 2\pi 11.6785 \cdot 10^3 \text{ rad/sec}, \\ Q_x &= 88.116 \cdot 10^3 \approx 99 \text{ dB} & \text{and} & & Q_y &= 7.992 \cdot 10^3 \approx 78 \text{ dB}. \end{aligned}$$

The off-diagonal terms $G_{ID,yx}^d$ and $G_{ID,yx}^d$ model the mechanical coupling between the drive and sense modes. Note that $G_{ID,yx}^d$ has low gains compared to the diagonal terms, indicating a weak coupling between those modes. Possibly because of the weak coupling, the transfer $G_{ID,xy}^d$ could not be accurately identified. Then, it is considered to be null. Still on $G_{ID,yx}^d$, we can note two resonance peaks, at $\omega_{0,x}$ and $\omega_{0,y}$, as expected.

Now, if we look to the phases of the same transfers, at the resonance peaks, they are not close to -90° or -270° . Indeed, they are rather close to 0° or -180° . This shift in phase is due to the presence of the additional filters and of the ZOH in the loop.

In Figure 7.11, we present the Bode diagram of the identified E_{ID}^d , which represents the parasitic electrical coupling and is expected to behave as a high-pass filter. This is the behavior observed in Figure 7.11.

Electrical coupling compensation: having identified the to-be-controlled system, we implement E_{ID}^d in the processor to compensate for the parasitic electrical coupling, see Figure 7.3.

Dealing with the input nonlinearity: here, we consider the method presented in Section 7.2.3 with $V_{DC,x} = V_{DC,y} = 1$ V. Therefore, we define $G^d = 2G_{ID}^d$. This model will be used in the sequel for the controller synthesis.

Controller synthesis: based on G^d and on the desired performance specifications, we apply the procedure presented in Section 7.4.3 with $H^{P,\omega_0} = G^{P,\omega_0}$ (since the operating conditions are steady). Two different strategies are considered: the SISO and the MIMO approaches of Chapter 4, as in the examples 4.3 and 4.4 for the SISO approach, and Example 4.6 for the MIMO approach. The details on the controller synthesis are given in Appendix F.5 and Appendix F.6.

7.5.2 Validation of the Closed-Loop Performance Specifications

Here, we aim to validate the main closed-loop performance specifications: the reference tracking and the Coriolis force estimation.

Test Protocol: the first test is performed on the experimental platform with the gyroscope at rest (Ω_z) and the results are presented in Figure 7.12. In this figure, we present the main signals of the closed-loop: x_n , the measured output of the drive mode; y_n , the measured output of the sense mode; u_x , the control signal of the drive mode; and $\hat{u}_{Cor,y}$, the Coriolis force estimate, which, in the SISO approach, is given by $\hat{u}_{Cor,y} = -u_y$ and, in the MIMO approach, corresponds directly to the third output of the controller. We apply a reference signal of the form of

$$x_m^{ref}(t) = A_{x,m}^{ref}(t) \sin(\omega_{exc}t)$$

with amplitude $A_{x,m}^{ref}$ and frequency $\omega_{exc} = \omega_{0,x}$. We also add an artificial disturbance of the form

$$\tilde{u}_{Cor,y}(t) = A_{Cor,y}(t) \sin(\omega_{exc}t) \quad (7.24)$$

on the sense-mode control signal. The whole test presents five different stages, as follows.

- (i) For $0 \leq t < 0.5$ s: the system is open loop, *i.e.*, $u_x(t) = u_y(t) = 0$. In this interval, x_n and y_n mainly correspond to the measurement noises n_x and n_y (since $x_m = y_m = 0$). Here, we obtain $\sigma_x^2 \approx 2 \cdot 10^{-5}$ and $\sigma_y^2 \approx 1 \cdot 10^{-5}$.

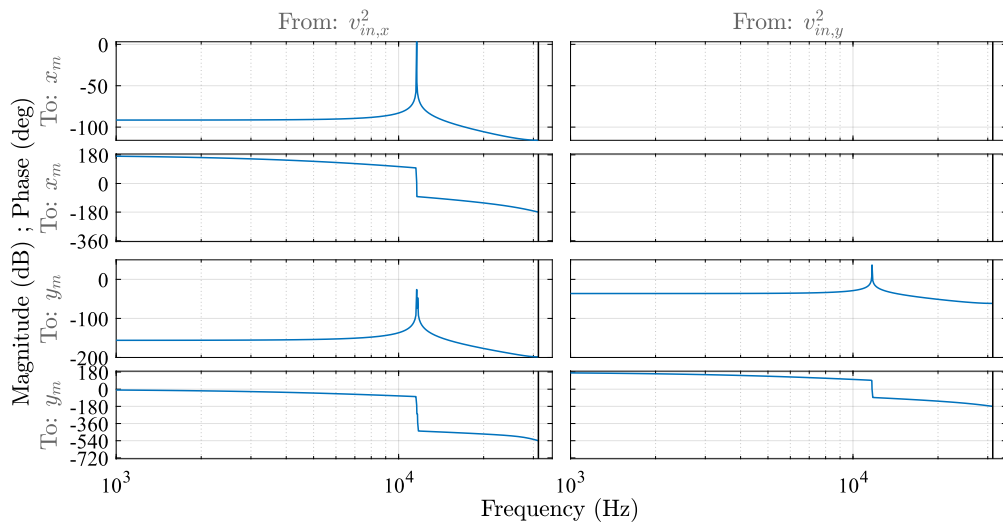


FIGURE 7.9: Bode diagram of the identified model G_{ID}^d .

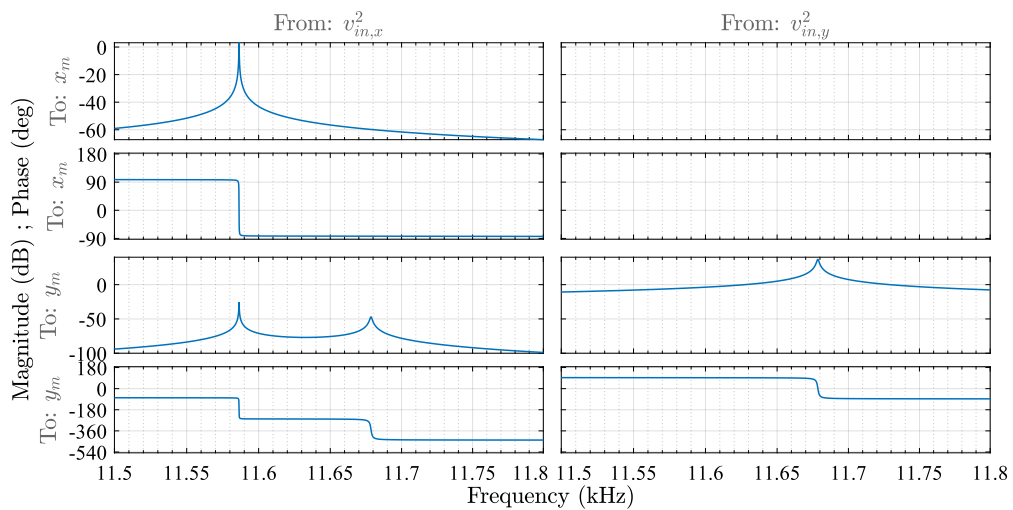


FIGURE 7.10: Bode diagram of the identified model G_{ID}^d . Zoom around the resonance frequencies.

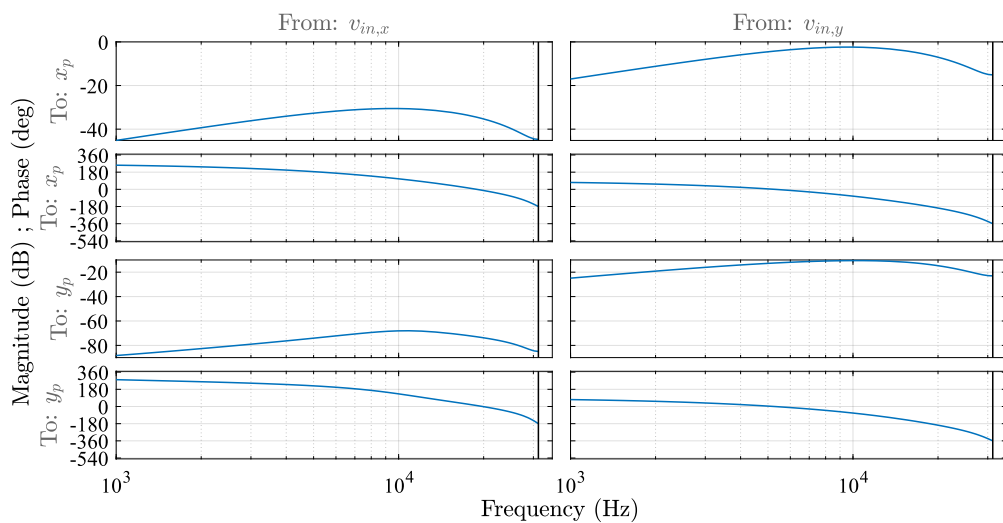


FIGURE 7.11: Bode diagram of the identified model E_{ID}^d .

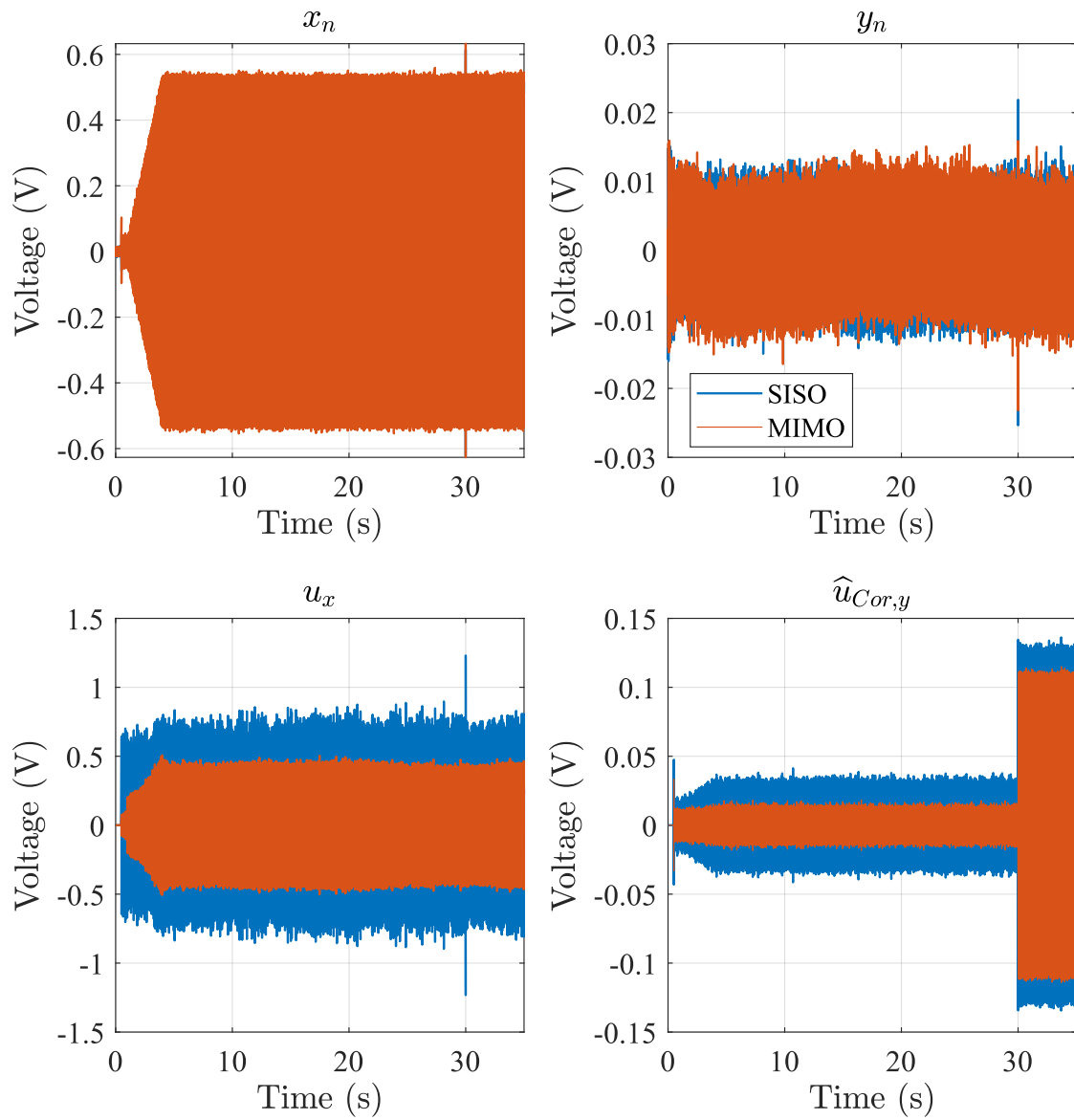
- (ii) For $0.5 \text{ s} \leq t < 1 \text{ s}$: the loops are closed, $A_{x,m}^{ref}(t) = A_{Cor,y}(t) = 0$. Then, the measures within this interval correspond to the contribution of the noises on the signals.
- (iii) For $1 \text{ s} \leq t < 4 \text{ s}$: the amplitude $A_{x,m}^{ref}$ increases linearly, achieving the maximum value of 0.5 V at $t = 4 \text{ s}$. The slope of $A_{x,m}^{ref}$ allows avoiding saturation of the actuators at the start. The artificial disturbance is null.
- (iv) For $4 \text{ s} \leq t < 30 \text{ s}$: in this interval, $A_{x,m}^{ref}(t) = 0.5 \text{ V}$ and $A_{Cor,y}(t) = 0$. Here, we can evaluate the reference tracking performance. We can already note that the measured oscillations (x_n) have an amplitude close to 0.5 V for both approaches (SISO and MIMO are almost superposed in the figure), what indicates that, qualitatively, the specification is fulfilled. Details on the reference tracking performance evaluation will be given in the sequel.
- (v) For $30 \text{ s} \leq t < 35 \text{ s}$: in this last interval, we apply a step on $A_{Cor,y}$, such that $A_{Cor,y}(t) = 0.1 \text{ V}$, emulating a Coriolis force acting on the sense mode. Thus, we can evaluate the estimation performance. $A_{x,m}^{ref}$ is still equal to 0.5 V . We can observe that the Coriolis force estimate $\hat{u}_{Cor,y}$ suffers an important impact of about 0.1 V , qualitatively indicating the achievement of the estimation performance specification. It is also interesting to note that at $t = 30 \text{ s}$, the variation of $A_{Cor,y}$ also disturbs the other signals, even the drive mode ones (slightly). This fact may indicate a non-modeled coupling from the sense mode into the drive mode.

Validation of the Reference Tracking: to evaluate the reference tracking specification, we compute $\varepsilon_x = x_m^{ref} - x_n$, which, for the interval $25 < t < 27$ is presented in Figure 7.13. The main contributions of the tracking error come from the measurement noises. To evaluate the performance at $\omega = \omega_{0,x}$, we estimate the power spectral densities of ε_x and x_m^{ref} , $\mathcal{S}_{\varepsilon_x}$ and $\mathcal{S}_{x_m^{ref}}$, respectively. The ratio $\mathcal{S}_{\varepsilon_x} / \mathcal{S}_{x_m^{ref}}$ gives an estimate of $\left| T_{x_m^{ref} \rightarrow \varepsilon_x} \right|^2$ and allows to better evaluate the reference tracking specification. At the frequency $\omega = \omega_{0,x}$, Figure 7.13 reveals that this gain is around -96 dB (which corresponds to 16 ppm , for the specification 250 ppm) and -76 dB (which corresponds to 160 ppm , for the specification 250 ppm) for the SISO and MIMO approaches, respectively, largely fulfilling the required specification in both cases.

Validation of the Coriolis Force Estimation: to evaluate this specification, we have to compute the error between a given/known Coriolis force, $\tilde{u}_{Cor,y}$ (see (7.24)) and its estimate. However, recall that other disturbances exist in the system and produce a nonnull estimate $\hat{u}_{Cor,y}$ (in general, due to the couplings between the drive and the sense modes and to different noises). Therefore, to take into account only the contributions of $\tilde{u}_{Cor,y}$, we define $\hat{u}_{Cor,y}^0$ as sinusoidal signal of frequency ω_{exc} that fits $\hat{u}_{Cor,y}$ in the interval $5 \text{ s} < t < 30 \text{ s}$ (where $\tilde{u}_{Cor,y}(t) = 0$). Thus, we redefine the estimation error as

$$\varepsilon_{est}(t) = \tilde{u}_{Cor,y}(t) - \left(\hat{u}_{Cor,y}(t) - \hat{u}_{Cor,y}^0(t) \right).$$

The obtained results are also presented in Figure 7.13, where we can observe a good estimation of this artificial disturbance. We can also note that the MIMO approach, thanks to the additional output, produces an estimate much quicker (less than 1 ms) than the SISO one (more than 2 ms). Similar to the reference tracking evaluation, we estimate the PSD of ε_{est} and $\tilde{u}_{Cor,y}$, $\mathcal{S}_{\varepsilon_{est}}$ and $\mathcal{S}_{\tilde{u}_{Cor,y}}$, respectively; and estimate $\left| T_{\tilde{u}_{Cor,y} \rightarrow \varepsilon_{est}} \right|^2$ as the ratio $\mathcal{S}_{\varepsilon_{est}} / \mathcal{S}_{\tilde{u}_{Cor,y}}$, which is presented in Figure 7.13 as well. This ratio reveals a gain close to -62 dB (which corresponds

FIGURE 7.12: Main signals measured at rest ($\Omega_z = 0$).

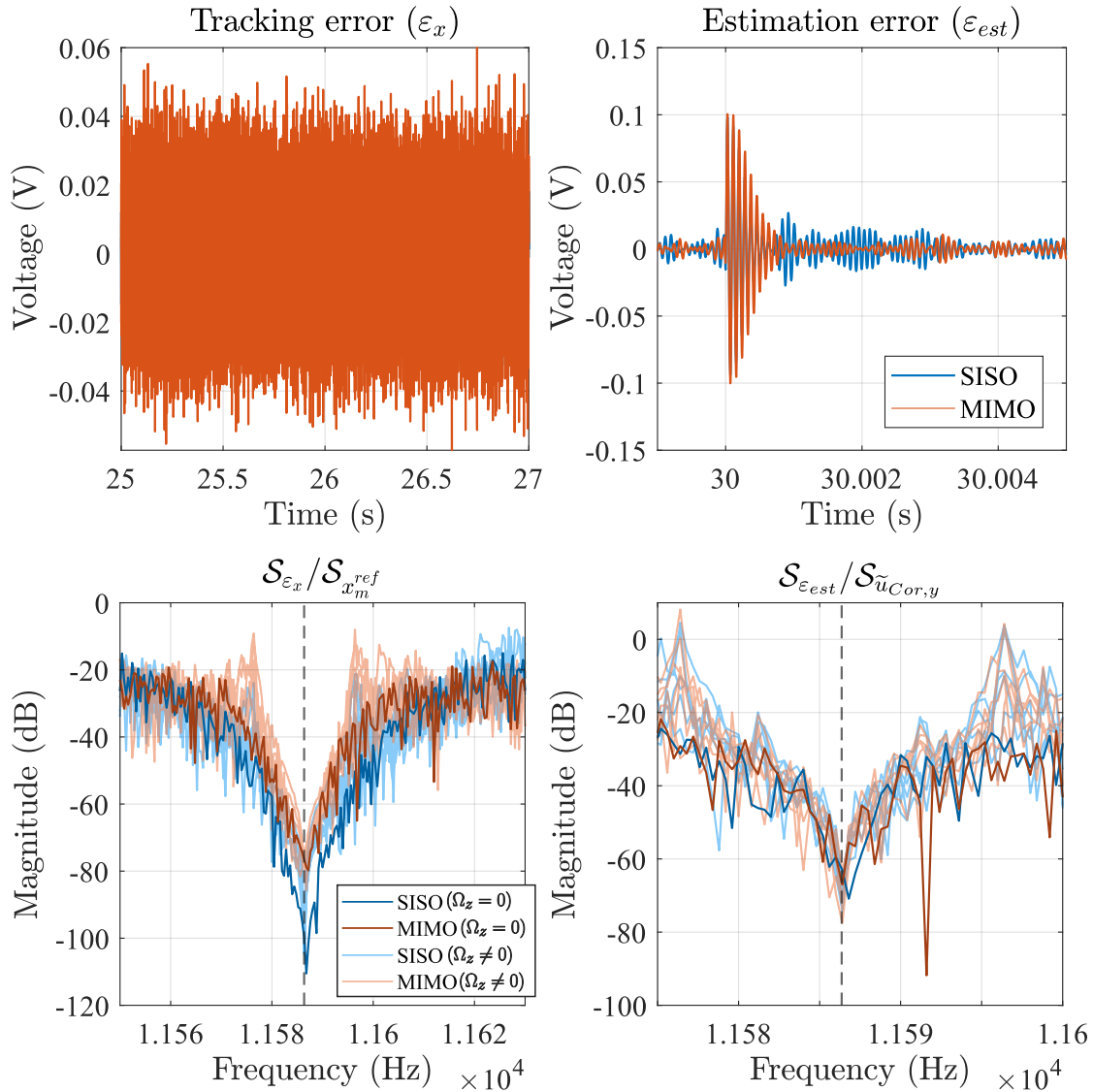


FIGURE 7.13: Performance evaluation.

to 790 ppm, for the specification 250 ppm) and -66 dB (which corresponds to 500 ppm, for the specification 250 ppm) at ω_{exc} for the SISO and MIMO approaches, respectively. Therefore, in practice this tight estimation specification was not fulfilled in both cases.

Some factors may justify this results, but the main candidate would be the resonance-frequency variations associated to neglected nonlinearities. As discussed throughout this thesis, variations of the drive-mode resonance frequency are a crucial factor on the MEMS gyroscope performance. At the time of writing, experimental tests are being made on the same experimental setup. Preliminary, they show that, even under a “steady” operating condition, variations of the drive-mode resonance frequency occur. Then, due to the enormous quality factor, minimal differences between ω_{exc} and $\omega_{0,x}$ cause an important loss of gain of the resonator, which requires stronger control signals to achieve the same reference signal. In a linear system, this would not be an important problem. Nevertheless, neglected nonlinear effects linked to the input voltage amplitude (as the spring-hardening/softening effects) alter the dynamics and couplings of the system. This fact reinforces the need to use resonance-frequency tracking mechanism.

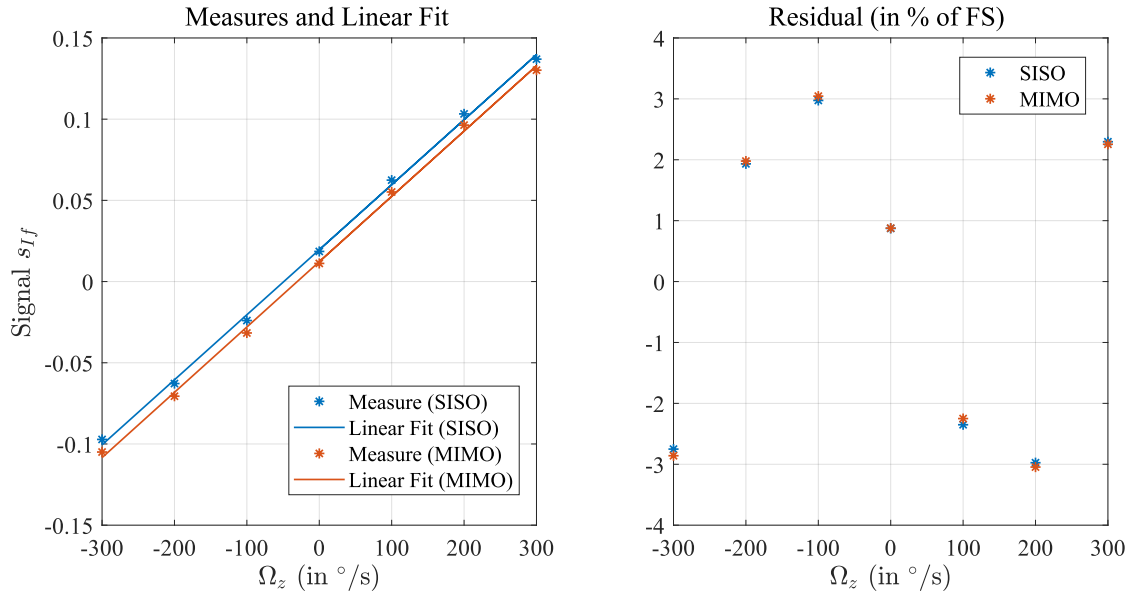


FIGURE 7.14: Measures on rotating table.

7.5.3 Tests on a Rotating Table

Here, we aim to validate the main closed-loop performance specifications when the gyroscope is submitted to nonnull angular rates. The main objectives are to verify if the relevant Assumption 3.5 (page 59), which assumes that the performance and stability of the closed-loop system is the same at rest and under different Ω_z .

Test Protocol: we consider the same protocol of Section 7.5.2. The only difference is that the gyroscope is now placed on a rotating table, and we realize different tests with $\Omega_z \in \{-300, -200, -100, 100, 200, 300\}^\circ/\text{s}$.

Performance Validation: further than the stability, which is conserved, regarding the reference tracking and the estimation specifications for different angular rates, the results are similar to those with $\Omega_z = 0$, that is, for all the considered angular rates, we have a reference tracking with relative error smaller than -72 dB at ω_{exc} and estimation with relative error smaller than -60 dB.

Measures of Ω_z finally, the Coriolis force estimate $\hat{u}_{Cor,y}$ is demodulated and filtered, obtaining s_{If} , which is compared to the actual Ω_z in Figure 7.14. Although the estimation lacks of linearity (SFNL $\approx 3\%$), these experiments prove the implementability of the direct control architecture and the validity of the proposed design approach. The nonlinear behavior of the measure may have some origins: the variations of the drive-mode resonance frequency, a nonlinear behavior of the MEMS gyroscope (modeled as a linear system), modeling errors (such as a coupling from sense to drive mode). The good news is that the designed controllers operate as expected, even if the actual MEMS gyroscopes might present differences with respect to the obtained model.

7.6 Summary of the Chapter

In this chapter, we propose a complete design method for digital direct controllers of MEMS gyroscopes. The proposed approach is based on the \mathcal{H}_∞ synthesis. Further than the \mathcal{H}_∞ design method already presented in Chapter 4, we consider the main aspects related to the practical implementation: the nonlinear input of the MEMS gyroscope, the presence of parasitic electrical coupling, the digital implementation of the controller and the dependence of the gyroscope model on the temperature.

In this chapter, we reveal that the square input nonlinearity can be treated as a simple gain if the input signal is a bandpass signal centered at $\omega_{0,x}$ and with bandwidth smaller than $\omega_{0,x}/3$. This result allows us then to consider the gyroscope as a linear system. Moreover, we also indicate how to proceed with the digital compensation of the parasitic electrical coupling.

The discrete-time nature of the controller is also considered. In order to design the digital controller, additional steps are introduced in the control design method and the controller synthesis is performed in the so-called normalized PCT (nPCT) space. The use of this space provides some benefits, as follows.

- (i) The design of a DT controller is realized in a CT-like space (nPCT), which is better suited for the use of frequency-domain design methods (such as the \mathcal{H}_∞ synthesis) and takes into account the presence of the ZOH.
- (ii) Since the design is realized in a normalized-frequency space and since this space is defined by $\omega_{0,x}$, the design of ω_0 -dependent controllers is straightforward.

The implementation results validate the proposed method and prove the implementability of the direct control architecture. Further investigation is needed to justify the nonlinear behavior of the angular rate measures.

Chapter 8

EM- $\Sigma\Delta$ Architecture: A Case Study

In this chapter, we present a study case consisting of a MEMS gyroscope in which the sense mode operates in closed-loop with an electro-mechanical $\Sigma\Delta$ (EM- $\Sigma\Delta$) architecture. The main purpose here is to present a control design method based on the \mathcal{H}_∞ synthesis and the direct control architecture (see Chapter 4, page 75). This approach is applied to the EM- $\Sigma\Delta$ architecture implemented in the Tronics' dedicated platform, presented in Section 2.3.2, whose block diagram is recalled in Figure 8.1. Practical results are also presented in this chapter and demonstrate the effectiveness of our approach.

In this experimental setup, the drive mode operates in closed loop with a nonlinear self-oscillating AGC control architecture (see Figure 2.22, page 43), producing oscillations with controlled amplitude and at the drive-mode resonance frequency, that is, $\omega_{exc} = \omega_{0,x}$. We can then assume that the drive mode operates adequately, and we focus on the sense-mode operation. Moreover, in this platform, the sampling frequency F_s is given by $F_s = 36\omega_{0,x}/(2\pi)$.

As introduced in Section 2.2.2 (page 46), the EM- $\Sigma\Delta$ architecture has been widely employed, such as in [PB05, ESAES09, RCRW09, EEE⁺11, CYC⁺14, CLK16], thanks to its interesting benefits. First, like other closed-loop strategies, the bandwidth, linearity, dynamic range, and robustness of the sensor are improved. Second, the use of a relay (1-bit quantizer) for the actuation avoids problems linked to the nonlinear relationship between voltage and force of electrostatic actuators, improving the linear behavior of the device. Finally, being the output signal coded into a single bit, the interface with the digital processing circuits

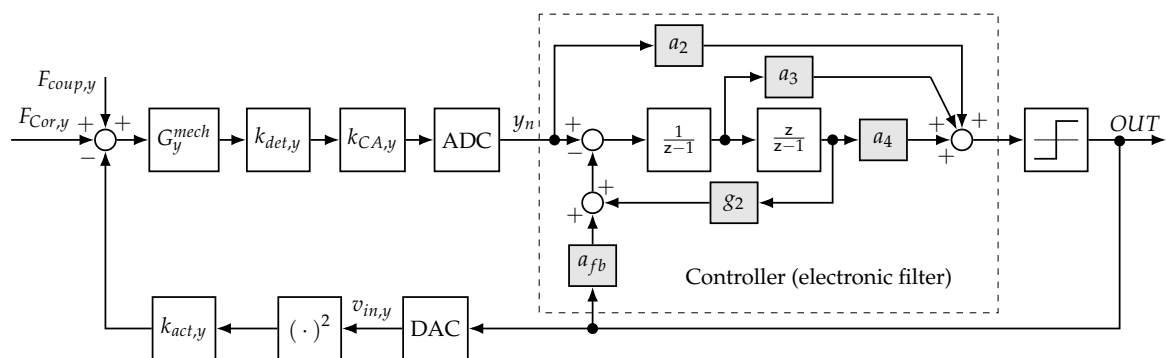


FIGURE 8.1: EM- $\Sigma\Delta$ architecture under study. Configurable elements are represented in gray.

is straightforward. Nevertheless, despite these interesting features, the relay introduces a strong nonlinearity in the loop, prohibiting the (direct) use of linear design tools.

The EM- $\Sigma\Delta$ architecture is inspired by the classical $\Sigma\Delta$ modulators, which are widely used in ADCs, especially when high resolution is required [RRW08]. The strength of the classical $\Sigma\Delta$ modulators comes from the use of oversampling and feedback loops. The oversampling allows achieving an interesting signal-to-noise ratio (SNR), even when coding the signal with a single bit. On the other hand, the feedback loops are composed of filters that are designed to achieve three primary goals.

- (i) Shape the power spectral density (PSD) of the quantization error (difference between the input and output signals of the relay), minimizing its influence on the output signal, at least in the frequency range of interest.
- (ii) Ensure that the output signal tracks the input one, at least in the frequency range of interest.
- (iii) Ensure the stability of the closed-loop system.

In the classical $\Sigma\Delta$ modulators, these noise-shaping filters are fully configurable by the designer. There exist well-established methods and numerical tools, allowing for an efficient modulator design (see [ST04] and references therein for further details). Nevertheless, the noise-shaping filter of the EM- $\Sigma\Delta$ is composed of an electronic filter and an electro-mechanical element – the sense mode –, which is not configurable, implying strong structural constraints. Then, while the design of classical $\Sigma\Delta$ modulators is well established, the design of the EM- $\Sigma\Delta$ modulator may be a difficult task [RRW08].

In addition to the structural constraints (imposed by the non-configurable sense mode), other issues arise in an EM- $\Sigma\Delta$ architecture.

Model uncertainties: the model of the sense mode is often uncertain due to fabrication dispersion, environmental variation as well as imperfect modeling. Moreover, the electrostatic comb fingers can create high-frequency resonant modes, adding an extra phase lag to the system, compromising its stability [CLK16].

Additional sources of noise: the sense mode also introduces noise (mechanical-thermal and electronic noise) in the loop [PB06].

Thus, further than the standard $\Sigma\Delta$ specifications (minimization of the quantization error and tracking of the input signal by the output one), the design of the EM- $\Sigma\Delta$ electronic filter, which we will rather call controller, has three more objectives to pursue, as follows.

- (i) Ensure the stability of the closed-loop system, despite the uncertainties related to the mechanical transfer, *i.e.*, robust stability.
- (ii) Minimize the effects of the different noises (in addition to the quantization error) on the output signal.
- (iii) Minimization of the proof mass displacement along the \vec{y} -axis [WK11]. As discussed in Chapter 3, minimizing these displacements is useful to improve the linear behavior of the sensor.

Some design methods for the EM- $\Sigma\Delta$ controller are proposed in the literature. They are mainly inspired by the design of classical $\Sigma\Delta$ modulators. In [PB05], the authors choose a controller composed of a second-order resonator associated with a lead-phase compensator. The resonator allows attenuating the quantization error in a certain frequency range, whereas

the compensator provides the required phase to ensure the stability of the closed-loop system. The effects of the electronic noises are evaluated afterward in [PB06]. In [RRW08], the authors show that with an additional feedback, the same design flow of the classical $\Sigma\Delta$ modulators can be applied for the EM- $\Sigma\Delta$ feedback, providing a systematic design methodology and ensuring a certain robustness against the relay. Nevertheless, the effects of all the noise sources are not considered for the controller design, and the robust stability is only partially ensured.

More recently, the use of genetic algorithms was also proposed [WK11, CYC⁺14]. The main advantage of this approach is that it allows choosing a multi-objective criterion to be optimized. In these works, the criterion consists of (i) minimizing the effect of the noises and the quantization error on the output signal; and (ii) minimizing the displacement of the proof mass. The main issue of this approach, however, is that the solutions do not provide guarantees of performance or robust stability. Usually, these properties are assessed through extensive simulations [WK11], which can be computationally expensive.

From the Control Theory point of view, one of the main challenges comes from the presence of the relay (1-bit quantizer), which is a strong nonlinearity, in the control loop. Another challenge arises from the fact that the configurable parameters of the EM- $\Sigma\Delta$ under study are bounded and have limited precision, conferring a constrained nature to the controller.

As usually considered for the design of $\Sigma\Delta$ modulators, the relay is modeled as an uncertain gain (similar to the describing-function method [GV68]) followed by a quantization noise, representing the quantization error [AP87], obtaining a linearized model of the system, see, e.g., [PB05, RRW08]. Then, we propose a systematic method to design the EM- $\Sigma\Delta$ controller, guaranteeing both performance and robust stability for the linearized model. This method is based on the \mathcal{H}_∞ synthesis and direct control architecture. The constrained nature of the controller is also taken into account.

The remaining of this chapter is organized as follows. In Section 8.1, we formalize the control objectives related to the EM- $\Sigma\Delta$ architecture and formulate the problem under investigation. In Section 8.2, we propose a design method based on the \mathcal{H}_∞ synthesis. The proposed method is then applied to the EM- $\Sigma\Delta$ architecture under study in Section 8.3. The solution is applied to the prototype and the practical results are presented in Section 8.4.

8.1 EM- $\Sigma\Delta$ Architecture and Control Problem

In this section, first we aim to describe the EM- $\Sigma\Delta$ architecture. Then, in a second time, we discuss the expected behavior of the closed-loop system, highlighting the main control objectives and defining the control problem we want to solve in this chapter.

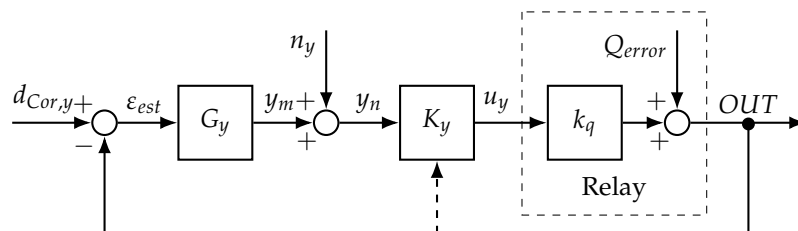


FIGURE 8.2: General block diagram of an EM- $\Sigma\Delta$ architecture.

Let us consider the general EM- $\Sigma\Delta$ architecture of Figure 8.2, which is basically composed of the sense mode G_y (mechanical part, actuation and instrumentation circuitry), a controller (or electronic filter) K_y , and a relay (or 1-bit quantizer). The signal $d_{Cor,y}$ is an image of the Coriolis and coupling forces acting on the sense mode. This signal is to be rebalanced by OUT . Hence, OUT is expected to be as close as possible to $d_{Cor,y}$ so that OUT is a good estimate of $d_{Cor,y}$ and, as consequence, of the Coriolis force (the coupling force is separated *a posteriori* thanks to the synchronous demodulation and post processing). To quantify the performance of the system, we then define the error between these signals, which corresponds to the estimation error: $\varepsilon_{est} \triangleq d_{Cor,y} - OUT$. At the output of G_y , y_m is an image of the proof mass displacement along the \vec{y} -axis. The signal n_y models process noises as well as any bias added by the instrumentation circuits. The measured signal is then given by $y_n = y_m + n_y$.

The relay is modeled as an uncertain gain k_q (similar to how relays are modeled in the describing function method, see [AP87]) followed by a quantization error, which is denoted Q_{error} and is usually modeled as a white-noise signal. This modeling is usually adopted for the design of classical $\Sigma\Delta$ modulators and for the EM- $\Sigma\Delta$ design [AP87, PB05, RRW08]. Finally, the relay produces the signal OUT , which can only assume the values $+1$ and -1 .

The EM- $\Sigma\Delta$ controller, K_y , is given by

$$K_y : \begin{cases} \sigma x_K(t) &= A_K x_K(t) + B_K y_P(t) \\ u_y(t) &= C_K x_K(t) + D_K y_P(t) \end{cases} \quad (8.1)$$

with $x_K(t) \in \mathbb{R}^{n_K}$, $y_P(t) \in \mathbb{R}^{n_{y_P}}$ and $u_y(t) \in \mathbb{R}$. We use σ to represent the time-derivative operator s for continuous-time (CT) systems and the time-shift operator z for discrete-time (DT) systems. Similarly, t stands for the time variable t in the CT case, and for the time samples k in the DT case. The controller may have one ($n_{y_P} = 1$) or two ($n_{y_P} = 2$) input signals. In the first case, it is said to be a one-degree-of-freedom (1DoF) controller, and we have $y_P = y_n$. With two inputs, we have a two-degrees-of-freedom (2DoF) controller and $y_P = \text{col}(y_n, OUT)$.

We also classify the controllers as unconstrained or constrained. Note that K_y can be rewritten as

$$K_y : \begin{cases} \begin{bmatrix} \sigma x_K(t) \\ u_y(t) \end{bmatrix} = \mathbf{K} \begin{bmatrix} x_K(t) \\ y_P(t) \end{bmatrix} \end{cases} \quad \text{with} \quad \mathbf{K} \triangleq \begin{bmatrix} A_K & B_K \\ C_K & D_K \end{bmatrix}. \quad (8.2)$$

Then, a controller is said to be n_K -**unconstrained** if $\mathbf{K} \in \mathbb{R}^{(n_K+1) \times (n_K+n_{y_P})}$. On the other hand, a controller is said to be n_K -**constrained** if $\mathbf{K} \in \mathcal{K}$, where $\mathcal{K} \subset \mathbb{R}^{(n_K+1) \times (n_K+n_{y_P})}$. The constrained nature of a controller may be originated from the limited resolution of its coefficients or by a predetermined choice of poles and zeros, for instance. More details on the unconstrained/constrained nature of the controller are given in Section 8.2.2 and Section 8.2.3.

Regardless of its structure (1DoF or 2DoF, constrained or unconstrained), we can enumerate the qualitative **control objectives** for the controller design:

- (O1) ensure the tracking of the input signal by the output one, *i.e.*, $OUT = d_{Cor,y}$ or $\varepsilon_{est} = 0$;
- (O2) minimize the displacement (y_m) of the proof mass;
- (O3) minimize the effects of Q_{error} on OUT ;
- (O4) minimize the effects of the different noises and bias (n_y) on OUT ;
- (O5) ensure the stability of the closed-loop system against the relay (nonlinearity);

- (O6) ensure the stability of the closed-loop system against the mechanical transfer uncertainties (e.g., unmodeled dynamics or environmental sensitivity).

Note that it may be impossible to completely achieve all these specifications. For instance, if we consider the first objective ($OUT = d_{Cor,y}$), it is clear that this equality holds only if $d_{Cor,y}(t) \in \{-1, 1\}$, which is clearly not the case for a MEMS gyroscope. However, it is possible to make them (approximately) equal, at least, in the frequency range around $\omega_{0,x}$. Therefore, like in the previous chapters, we want to fulfill the above objectives, at best, in the frequency range of interest. This point leads us, again, to translating the control objectives into closed-loop specifications in the frequency domain. Assuming it is done, we can thus state the general EM- $\Sigma\Delta$ design problem as follows.

Problem 8.1 (General EM- $\Sigma\Delta$ design problem). *Given G_y and k_q , compute the controller K_y (matrix \mathbf{K}) such that the closed-loop system of Figure 8.2 achieves the required closed-loop specifications.*

Since the closed-loop system of Figure 8.2 is LTI, this problem is solved through the \mathcal{H}_∞ synthesis and the controller design is formulated as an optimization problem (similar to the procedure of Chapter 4). In this context, two aspects are of crucial importance: the choice of an \mathcal{H}_∞ criterion and the resolution of the optimization problem. The proper choice of the \mathcal{H}_∞ criterion allows enforcing the desired behavior of the closed-loop system. The \mathcal{H}_∞ criterion is defined by the so-called augmented plant P , which includes the to-be-controlled plant and the weighting functions (see Section 4.1, page 76). In the case of the standard \mathcal{H}_∞ synthesis, where the controller is unconstrained, the optimization problem is convex. However, if the controller is constrained, the optimization problem becomes non-convex and different tools have to be used. In the next section, we define an \mathcal{H}_∞ criterion for the EM- $\Sigma\Delta$ architecture. Then, depending on the controller nature (constrained/unconstrained), we discuss how to solve the related optimization problems.

8.2 \mathcal{H}_∞ Synthesis for the EM- $\Sigma\Delta$ Architecture

In this section, we use the \mathcal{H}_∞ framework to design the EM- $\Sigma\Delta$ controller, solving Problem 8.1. First, we define an \mathcal{H}_∞ criterion, which express, through weighting functions, the desired control objectives. Then, we discuss how to solve the optimization problem for unconstrained and for constrained controllers.

8.2.1 An \mathcal{H}_∞ Criterion for the EM- $\Sigma\Delta$ Architecture

The first step to define the \mathcal{H}_∞ criterion related to the EM- $\Sigma\Delta$ architecture (see Figure 8.2) is to choose the signals of interest and compute the closed-loop transfer functions, defining the augmented plant \tilde{P} , just like in the standard \mathcal{H}_∞ synthesis, see Section 4.1 (page 76). Then, the control specifications are formulated as closed-loop frequency constraints that express the desired closed-loop behavior. Finally, weighting functions are designed to enforce these frequency constraints, defining the weighted augmented plant P . Here, we consider the general case where the controller is defined as $K_y = [K_{y,1}, K_{y,2}]$ (2DoF). In the case of a 1DoF controller, we consider the same results but with $K_{y,2} = 0$.

We start by selecting as input signals of interest the inputs $d_{Cor,y}$, n_y and Q_{error} , and the outputs ε_{est} , y_m and u_y . They define the input vector $\tilde{w} = \text{col}(d_{Cor,y}, n_y, Q_{error})$ and the

output vector $\tilde{z} = \text{col}(\varepsilon_{est}, y_m, u_y)$. Thus, the closed-loop transfer matrix $T_{\tilde{w} \rightarrow \tilde{z}}$ is given by

$$\begin{bmatrix} T_{d_{Cor,y} \rightarrow \varepsilon_{est}} & T_{n_y \rightarrow \varepsilon_{est}} & T_{Q_{error} \rightarrow \varepsilon_{est}} \\ T_{d_{Cor,y} \rightarrow y_m} & T_{n_y \rightarrow y_m} & T_{Q_{error} \rightarrow y_m} \\ T_{d_{Cor,y} \rightarrow u_y} & T_{n_y \rightarrow u_y} & T_{Q_{error} \rightarrow u_y} \end{bmatrix} = \begin{bmatrix} (1 - k_q K_{y,2}) S_1 & -k_q K_{y,1} S_1 & -S_1 \\ G_y (1 - k_q K_{y,2}) S_1 & -G_y k_q K_{y,1} S_1 & -G_y S_1 \\ G_y K_{y,1} S_1 & K_{y,1} S_1 & -T_1/k_q \end{bmatrix}, \quad (8.3)$$

where

$$S_1 = \frac{1}{1 + k_q (G_y K_{y,1} - K_{y,2})} \quad \text{and} \quad T_1 = 1 - S_1.$$

Let us now translate the control objectives of page 200 into mathematical constraints on the closed-loop frequency responses, as follows. Most of them yield to frequency constraints very similar to those considered in Section 4.2.2 (page 91).

Tracking of the input signal $d_{Cor,y}$ by OUT – (O1): this control objective pertains to the transfer $T_{d_{Cor,y} \rightarrow \varepsilon_{est}}$, which is directly related to the SFNL (estimation of the Coriolis force) and to the bandwidth of the sensor. Then, we consider

$$\left| T_{d_{Cor,y} \rightarrow \varepsilon_{est}}(j\omega_{exc}) \right| \leq k_{SFNL} \quad (8.4)$$

and

$$\forall \omega \in [\omega_{exc} - \omega_B^{\text{des}}, \omega_{exc} + \omega_B^{\text{des}}], \quad \left| T_{d_{Cor,y} \rightarrow \varepsilon_{est}}(j\omega) \right| < \frac{2 - \sqrt{2}}{2} \approx 0.2929, \quad (8.5)$$

ensuring $OUT \approx d_{Cor,y}$, at least for the frequency range around ω_{exc} .

Displacement minimization – (O2): this objective corresponds to the disturbance rejection specification of Section 4.2.2, in which the minimization of $\left| T_{d_{Cor,y} \rightarrow y_m}(j\omega) \right|$ for $\omega \in [\omega_{exc} - \omega_\Omega, \omega_{exc} + \omega_\Omega]$ is required, that is,

$$\forall \omega \in [\omega_{exc} - \omega_\Omega, \omega_{exc} + \omega_\Omega], \quad \left| T_{d_{Cor,y} \rightarrow y_m}(j\omega) \right| \ll 1. \quad (8.6)$$

As discussed in Chapter 3, we recall that reducing y_m tends to improve the linearity of the sensor.

Minimization of the effects of Q_{error} and n_y on OUT – (O3) and (O4): minimizing the effects of the quantization error Q_{error} and of the different noises n_y on OUT is equivalent to enforce,

$$\forall \omega \in (0, 2\omega_{exc}], \quad \left| T_{Q_{error} \rightarrow \varepsilon_{est}}(j\omega) \right| \ll 1 \quad \text{and} \quad \left| T_{n_y \rightarrow \varepsilon_{est}}(j\omega) \right| \ll 1. \quad (8.7)$$

These constraints are directly related to the performance of the sensor with respect to the noise (ARW, RMS noise, etc.).

Robustness against the relay – (O5): for the controller design, the quasi-linear model of the relay is adopted, *i.e.*, the relay is modeled as an uncertain gain with additive noise, as in [AP87, PB05, RRW08]. Then, to make the closed-loop system robust against this uncertain gain, the condition

$$\|T_{Q_{error} \rightarrow \varepsilon_{est}}\|_\infty < 2 \quad (8.8)$$

is generally considered for stability [RRW08]. Because $T_{Q_{error} \rightarrow \epsilon_{est}} = S_1$, which represents a sensitivity function, this condition corresponds to a modulus margin $\Delta M_1 > 0.5$, implying sufficient phase and gain margins (against the uncertain gain k_q). Strictly speaking, this condition is valid only for the quasi-linear model; it does not mathematically apply for the nonlinear system with the real relay. However, in the absence of a simple formal stability measure, this condition has been widely used in practice [RRW08]. In light of this discussion, it is also essential to keep the relay operating as close as possible to a “linear” behavior, avoiding saturation of the quantizer (see the upper part of Figure 8.7 for an illustration of this saturation). To this purpose, the bias (low-frequency components) at the relay input (signal u_y) has to be minimized, as well as its high-frequency components, that is,

$$\forall \omega \ll \omega_{exc}, \quad |T_{d_{Cor,y} \rightarrow u_y}(j\omega)| \ll 1, \quad |T_{n_y \rightarrow u_y}(j\omega)| \ll 1, \quad \text{and} \quad |T_{Q_{error} \rightarrow u_y}(j\omega)| \ll 1, \quad (8.9)$$

$$\forall \omega \gg \omega_{exc}, \quad |T_{d_{Cor,y} \rightarrow u_y}(j\omega)| \ll 1, \quad |T_{n_y \rightarrow u_y}(j\omega)| \ll 1, \quad \text{and} \quad |T_{Q_{error} \rightarrow u_y}(j\omega)| \ll 1. \quad (8.10)$$

Robustness against the model uncertainties – (O6): a typical choice to enforce good stability margins against model uncertainties is to choose a convenient modulus margin at the input or output of the gyroscope model G_y [SP01]. In this case, the sensitivity function is given by $S_2 = T_{d_{Cor,y} \rightarrow \epsilon_{est}}$. Then, the modulus margin is given by $\Delta M_2 = 1 / \|S_2\|_\infty$. So, by restricting the maximum value of $|S_2(j\omega)|$, a minimum modulus margin can be enforced. Further than the modulus margin ΔM_2 , additive and multiplicative uncertainties can be considered to take into account the high-frequency resonant modes of the comb fingers. Based on the small gain theorem (similar to Section 3.4, page 71), by bounding $|T_{n_y \rightarrow \epsilon_{est}}(j\omega)|$ and $|T_{n_y \rightarrow y_m}(j\omega)|$ in the frequency range where the high-frequency resonant modes are located, the robust stability of the closed-loop system against these high-frequency modes can be ensured.

As claimed earlier, the above closed-loop specifications are frequency dependent. To take into account this dependence, we add weighting filters on the signals of interest, as in Chapter 4. The closed-loop system with the weighting functions $W_{in} = \text{diag}(W_d, W_n, W_Q)$ and $W_{out} = \text{diag}(W_\epsilon, W_y, W_u)$ is then presented in Figure 8.3, defining the weighted signals of interest as $w = W_{in}^{-1} \tilde{w}$ and $z = W_{out} \tilde{z}$.

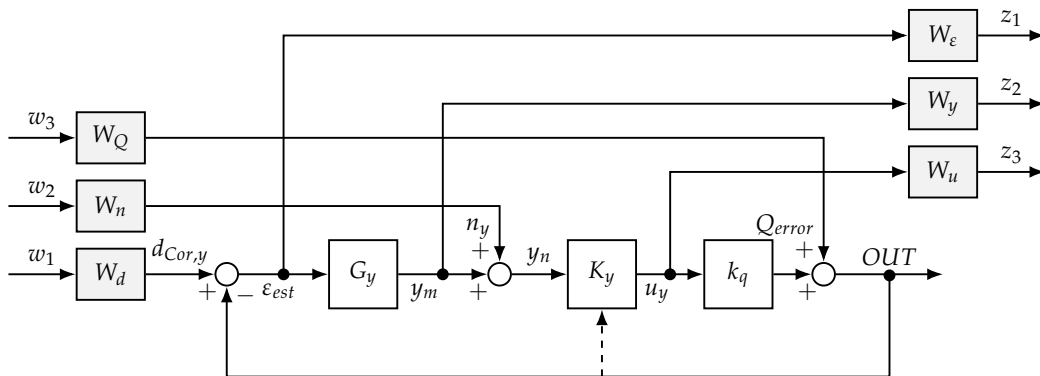


FIGURE 8.3: \mathcal{H}_∞ criterion for the EM- $\Sigma\Delta$ architecture.

In this context, if there exists a controller K_y such that, for a given $\gamma > 0$, satisfies the following \mathcal{H}_∞ criterion:

$$\|W_{\text{out}} T_{\tilde{w} \rightarrow \tilde{z}} W_{\text{in}}\|_\infty = \left\| \begin{bmatrix} W_\varepsilon T_{d_{\text{Cor},y} \rightarrow \varepsilon_{\text{est}}} W_d & W_\varepsilon T_{n_y \rightarrow \varepsilon_{\text{est}}} W_n & W_\varepsilon T_{Q_{\text{error}} \rightarrow \varepsilon_{\text{est}}} W_Q \\ W_y T_{d_{\text{Cor},y} \rightarrow y_m} W_d & W_y T_{n_y \rightarrow y_m} W_n & W_y T_{Q_{\text{error}} \rightarrow y_m} W_Q \\ W_u T_{d_{\text{Cor},y} \rightarrow u_y} W_d & W_u T_{n_y \rightarrow u_y} W_n & W_u T_{Q_{\text{error}} \rightarrow u_y} W_Q \end{bmatrix} \right\|_\infty < \gamma, \quad (8.11)$$

we also have that (omitting the frequency dependence), $\forall \omega \in \mathbb{R}$,

$$\begin{aligned} |T_{d_{\text{Cor},y} \rightarrow \varepsilon_{\text{est}}}| &< \frac{\gamma}{|W_\varepsilon W_d|}, & |T_{n_y \rightarrow \varepsilon_{\text{est}}}| &< \frac{\gamma}{|W_\varepsilon W_n|}, & |T_{Q_{\text{error}} \rightarrow \varepsilon_{\text{est}}}| &< \frac{\gamma}{|W_\varepsilon W_Q|}, \\ |T_{d_{\text{Cor},y} \rightarrow y_m}| &< \frac{\gamma}{|W_y W_d|}, & |T_{n_y \rightarrow y_m}| &< \frac{\gamma}{|W_y W_n|}, & |T_{Q_{\text{error}} \rightarrow y_m}| &< \frac{\gamma}{|W_y W_Q|}, \\ |T_{d_{\text{Cor},y} \rightarrow u_y}| &< \frac{\gamma}{|W_u W_d|}, & |T_{n_y \rightarrow u_y}| &< \frac{\gamma}{|W_u W_n|}, & |T_{Q_{\text{error}} \rightarrow u_y}| &< \frac{\gamma}{|W_u W_Q|}. \end{aligned} \quad (8.12)$$

Then, the proper choice of the weighting functions allows one to enforce the closed-loop constraints and, hence, the desired control specifications.

We emphasize that this \mathcal{H}_∞ criterion can be employed to any EM- $\Sigma\Delta$ architecture in the form of Figure 8.2, regardless of the controller structure (1DoF or 2DoF, constrained or unconstrained). The structure of the controller determines the optimization method that is used to solve the \mathcal{H}_∞ problem above. This point is discussed in the sequel.

Before proceeding, we recall that the \mathcal{H}_∞ criterion defines the weighted augmented plant P (see Section 4.1, page 76), which admits the state-space representation below:

$$P : \begin{cases} \sigma x_P(t) &= A_P x_P(t) + B_w w(t) + B_u u_y(t) \\ z(t) &= C_z x_P(t) + D_{zw} w(t) + D_{zu} u_y(t) \\ y_P(t) &= C_y x_P(t) + D_{yw} w(t) + D_{yu} u_y(t) \end{cases} \quad (8.13)$$

with $x_P(t) \in \mathbb{R}^{n_P}$ and n_P being the sum of the orders of G_y and of the weighting functions.

8.2.2 A Solution to the Unconstrained Case

An EM- $\Sigma\Delta$ controller is said to be n_K -unconstrained if it admits a state-space representation in the form of (8.2) with $\mathbf{K} \in \mathbb{R}^{(n_K+1) \times (n_K+n_{y_P})}$. In particular, when simply referring to unconstrained controller, we mean the full-order controller, *i.e.*, $n_K = n_P$. In this case, computing the matrix \mathbf{K} (or controller K_y of (8.2)) is equivalent to the standard \mathcal{H}_∞ control problem. Indeed, the closed-loop system formed by (8.13) and (8.1) can be written as

$$P \star K_y : \begin{cases} \sigma x_P(t) &= A_{cl} x_P(t) + B_{cl} w(t) \\ z(t) &= C_{cl} x_P(t) + D_{cl} w(t) \end{cases} \quad (8.14)$$

with $x_P = \text{col}(x_P, x_K)$,

$$\begin{aligned} A_{cl} &= \underbrace{\begin{bmatrix} A_P & 0 \\ 0 & 0 \end{bmatrix}}_A + \underbrace{\begin{bmatrix} 0 & B_u \\ I & 0 \end{bmatrix}}_{B_u} \underbrace{\begin{bmatrix} A_K & B_K \\ C_K & D_K \end{bmatrix}}_K \underbrace{\begin{bmatrix} 0 & I \\ C_y & 0 \end{bmatrix}}_{C_y}, & B_{cl} &= \underbrace{\begin{bmatrix} B_w \\ 0 \end{bmatrix}}_{B_w} + \underbrace{\begin{bmatrix} 0 & B_u \\ I & 0 \end{bmatrix}}_{B_u} \underbrace{\begin{bmatrix} A_K & B_K \\ C_K & D_K \end{bmatrix}}_K \underbrace{\begin{bmatrix} 0 \\ D_{yw} \end{bmatrix}}_{D_{yw}}, \\ C_{cl} &= \underbrace{\begin{bmatrix} C_z & 0 \end{bmatrix}}_{C_z} + \underbrace{\begin{bmatrix} 0 & D_{zu} \\ 0 & 0 \end{bmatrix}}_{D_{zu}} \underbrace{\begin{bmatrix} A_K & B_K \\ C_K & D_K \end{bmatrix}}_K \underbrace{\begin{bmatrix} 0 & I \\ C_y & 0 \end{bmatrix}}_{C_y}, & D_{cl} &= \underbrace{\begin{bmatrix} D_{wz} \\ 0 \end{bmatrix}}_{D_{wz}} + \underbrace{\begin{bmatrix} 0 & D_{zu} \\ 0 & 0 \end{bmatrix}}_{D_{zu}} \underbrace{\begin{bmatrix} A_K & B_K \\ C_K & D_K \end{bmatrix}}_K \underbrace{\begin{bmatrix} 0 \\ D_{yw} \end{bmatrix}}_{D_{yw}}. \end{aligned}$$

The closed-loop system can be interpreted as the static output feedback of \mathbf{P} (plant P augmented with the n_K states of K_y)

$$\mathbf{P} : \begin{cases} \sigma x_{\mathbf{P}}(t) &= \mathbf{A}x_{\mathbf{P}}(t) + \mathbf{B}_w w(t) + \mathbf{B}_u \mathbf{u}(t) \\ z(t) &= \mathbf{C}_z x_{\mathbf{P}}(t) + \mathbf{D}_{zw} w(t) + \mathbf{D}_{zu} \mathbf{u}(t) \\ \mathbf{y}(t) &= \mathbf{C}_y x_{\mathbf{P}}(t) + \mathbf{D}_{yw} w(t) + \mathbf{D}_{yu} \mathbf{u}(t) \end{cases} \quad (8.15)$$

with $\mathbf{u}(t) = \mathbf{K}\mathbf{y}(t)$, where $\mathbf{y} = \text{col}(x_K, y_p)$ and $\mathbf{u} = \text{col}(\sigma x_K, u_y)$, that is, $P \star K_y = \mathbf{P} \star \mathbf{K}$.

Therefore, for the case of an unconstrained controller, finding \mathbf{K} that solves Problem 8.1 is recast as the \mathcal{H}_∞ problem below.

Problem 8.2 (\mathcal{H}_∞ -based unconstrained EM- $\Sigma\Delta$ design problem). *Given the plant \mathbf{P} (defined by G_y, k_q and weighting functions W_{in} and W_{out}) and a performance level $\gamma > 0$, compute a matrix $\mathbf{K} \in \mathbb{R}^{(n_p+1) \times (n_p+n_{y_p})}$, if there exists any, that stabilizes $T_{w \rightarrow z} = \mathbf{P} \star \mathbf{K}$ and ensures $\|T_{w \rightarrow z}\|_\infty < \gamma$.*

This \mathcal{H}_∞ problem is convex and can be efficiently solved [AGB95], in the same way as presented in Section 4.1 (page 76).

8.2.3 A Solution to the Constrained Case

In most of the EM- $\Sigma\Delta$ architectures, the controller structure is constrained. Indeed, the matrix \mathbf{K} defining the controller in (8.2) belongs to a subset of $\mathbb{R}^{(n_K+1) \times (n_K+n_{y_p})}$, denoted \mathcal{K} . Moreover, the order of the controller, n_K , is commonly smaller than the order of the augmented plant, n_p . These limitations are mainly related to implementation constraints, such as the limited resolution of the coefficients, and a predetermined (fixed) choice of the controller order (n_K) or of some poles and zeros.

The good news is that in this constrained framework, the closed-loop system can still be written in the form of (8.14) and (8.15) with the control law $\mathbf{u}(t) = \mathbf{K}\mathbf{y}(t)$. The only difference is that $\mathbf{K} \in \mathcal{K}$ and $\mathcal{K} \subset \mathbb{R}^{(n_K+1) \times (n_K+n_{y_p})}$. The exact definition of the augmented plant \mathbf{P} and the subset \mathcal{K} depends on the controller structure and related implementation constraints. We illustrate this point in Section 8.3.

In the case of a constrained controller, finding K_y that solves Problem 8.1 can then be recast as the structured \mathcal{H}_∞ problem below.

Problem 8.3 (\mathcal{H}_∞ -based constrained EM- $\Sigma\Delta$ design problem). *Given the plant \mathbf{P} (defined by G_y, k_q and weighting functions W_{in} and W_{out}), a subset $\mathcal{K} \subset \mathbb{R}^{(n_K+1) \times (n_K+n_{y_p})}$ and a performance level $\gamma > 0$, compute a matrix $\mathbf{K} \in \mathcal{K}$, if there exists any, that stabilizes $T_{w \rightarrow z} = \mathbf{P} \star \mathbf{K}$ and ensures $\|T_{w \rightarrow z}\|_\infty < \gamma$.*

The Problem 8.3 corresponds to a structured \mathcal{H}_∞ synthesis problem. In this case, the optimization problem is no longer convex [AN06]. Then, the solution may depend on the initial point and, even if there exists a solution to the problem, there are no guarantees that this solution will be found. However, with good initialization, this problem can be tackled by available optimization methods [AN06].

In practice, Problem 8.3 can also be solved via the *Robust Control Toolbox* of Matlab[®] [BCPS20] with the function `hinfstruct`.

8.3 \mathcal{H}_∞ Synthesis for a Constrained EM- $\Sigma\Delta$ Controller

In this section, we apply the proposed method to design the controller parameters of the particular EM- $\Sigma\Delta$ architecture of Figure 8.1. We emphasize however that the procedure here applied can be extended to other EM- $\Sigma\Delta$ architectures.

The objective here is then to compute the parameters a_2, a_3, a_4, a_{fb} and g_2 such that the closed-loop system is stable and verifies, at best, the control objectives (O1–O6) of page 200. Thus, we apply the following steps:

- (i) the first step is to rewrite the scheme of Figure 8.1 as the general EM- $\Sigma\Delta$ scheme of Figure 8.2;
- (ii) an augmented plant $\tilde{\mathbf{P}}$ (the weighting functions are not included in the augmented plant at this step) and the subset \mathcal{K} are then defined;
- (iii) the weighting functions are designed to enforce the desired specifications and introduced in the augmented plant $\tilde{\mathbf{P}}$, producing $\mathbf{P} = \text{diag}(W_{\text{out}}, 1) \tilde{\mathbf{P}} \text{diag}(W_{\text{in}}, I_{n_{yp}})$;
- (iv) finally, the controller parameters are computed by solving Problem 8.3 with the plant \mathbf{P} and the subset \mathcal{K} defined in the previous steps.

These steps are detailed in the sequel.

8.3.1 Rewriting the EM- $\Sigma\Delta$ Architecture in the General Form

The first step for the EM- $\Sigma\Delta$ controller design consists in rewriting the given EM- $\Sigma\Delta$ architecture (see Figure 8.1) in the general form of Figure 8.2. In other words, we have to identify the three main blocks of the EM- $\Sigma\Delta$ architecture: the sense-mode model (G_y), the controller (K_y) and the relay.

Obtaining the Sense-Mode Model

The mechanical part of the sense mode, including the actuation and instrumentation circuitry ($k_{act,y}, G_y^{mech}, k_{det,y}, k_{CA,y}$) can be modeled by a continuous-time (CT) system G_y^c , whose transfer function is given by

$$G_y^c(s) = \frac{k_{0,y}\omega_{0,y}^2}{s^2 + s \cdot \omega_{0,y}/Q_y + \omega_{0,y}^2}, \quad (8.16)$$

where $k_{0,y}$ is the static gain, $\omega_{0,y}$ is the resonance frequency and Q_y is the quality factor of the sense mode. We highlight that identification techniques can be used to define each one of these parameters. In our case, $k_{0,y} = 0.0759$, $\omega_{0,y} = 1.004 \cdot \omega_{0,x}$ and $Q_y = 23.4 \cdot 10^3$, recalling that $\omega_{0,x}$ is the resonance frequency of the drive mode¹.

We also consider the ADC and DAC as part of the sense-mode model. As discussed in Chapter 7, taking the effects of these converters (sampling and holding effects) into account is crucial to provide guarantees of performance and stability of the closed-loop system. To this purpose, we apply the same procedure of Chapter 7 (see (7.4), page 181) to G_y^c , obtaining

¹For confidentiality reasons, in this chapter, the frequencies are normalized to $\omega_{exc} = \omega_{0,x}$.

the equivalent discrete-time model

$$G_y^d(z) = (1 - z^{-1}) \mathcal{Z} \left[\mathcal{L}^{-1} \left[\frac{G_y^c(s)}{s} \right] \right]. \quad (8.17)$$

In the architecture under study, all the digital elements work with the sampling period T_s , which is synchronized with the excitation frequency ($\omega_{exc} = \omega_{0,x}$) thanks to an external PLL so that $T_s = 2\pi / (36\omega_{0,x})$. This choice is justified by Remark 7.2 (page 188).

The Constrained Controller

The output signal u_y of the controller of Figure 8.1 can be given in the z-domain as

$$u_y(z) = \left(a_2 + \frac{(a_3 + a_4)z - a_3}{z^2 + (g_2 - 2)z + 1} \right) y_n(z) - a_{fb} \frac{(a_3 + a_4)z - a_3}{z^2 + (g_2 - 2)z + 1} OUT(z), \quad (8.18)$$

defining, in discrete time (DT),

$$K_y^d(z) = \begin{bmatrix} K_{y,1}^d(z) & K_{y,2}^d(z) \end{bmatrix} = \begin{bmatrix} a_2 + \frac{(a_3 + a_4)z - a_3}{z^2 + (g_2 - 2)z + 1} & -a_{fb} \frac{(a_3 + a_4)z - a_3}{z^2 + (g_2 - 2)z + 1} \end{bmatrix}. \quad (8.19)$$

Note that this controller is constrained. Indeed, it is of order 2, *i.e.*, $n_K = 2$. If any of the weighting functions of the \mathcal{H}_∞ criterion has an order larger than zero, since G_y^d is also of order 2, the order of the generalized plant is larger than 2. Moreover, due to the predefined structure of the controller, its poles and zeros cannot be placed arbitrarily. Indeed, this structure fixes the z-domain poles p_{z1} and p_{z2} such that $p_{z1} \cdot p_{z2} = 1$, constraining the set of implementable controllers.

This controller can also be represented in the state space as in (8.2) with

$$\mathbf{K} = \left[\begin{array}{c|c} A_K & B_K \\ \hline C_K & D_K \end{array} \right] = \left[\begin{array}{cc|cc} 1 & 1 & 0 & 0 \\ -g_2 & 1 - g_2 & 1 & -a_{fb} \\ \hline a_4 & a_3 + a_4 & a_2 & 0 \end{array} \right]. \quad (8.20)$$

The Relay

As discussed in Section 8.1, we model the relay as an uncertain gain k_q followed by the quantization error Q_{error} . In particular, we consider $k_q = 1$ for the controller design.

8.3.2 Defining the Generalized Plant $\tilde{\mathbf{P}}$ and the Subset \mathcal{K}

The next step is to define the generalized plant $\tilde{\mathbf{P}}$ and the subset \mathcal{K} . To this purpose, we isolate the unit delay blocks (z^{-1}), which define the controller states, defining a discrete-time augmented plant $\tilde{\mathbf{P}}^d$, as illustrated in Figure 8.4. The signals entering the matrix \mathbf{K} define the vector $\mathbf{y} = \text{col}(x_{K,1}, x_{K,2}, y_n, OUT)$ and the signals delivered by these parameters define $\mathbf{u} = \text{col}(zx_{K,1}, zx_{K,2}, u_y)$.

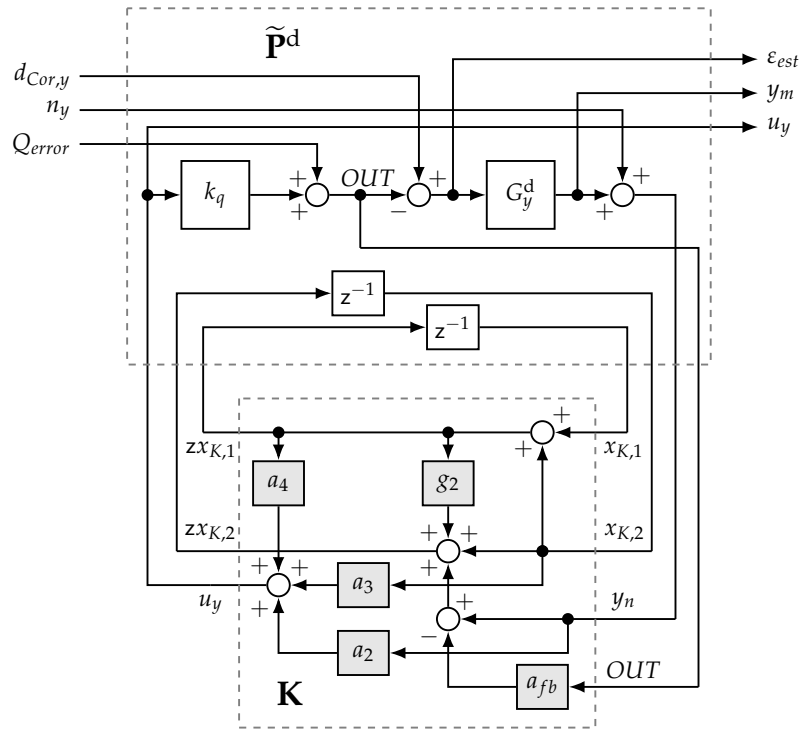


FIGURE 8.4: EM- $\Sigma\Delta$ architecture with constrained controller in the general control configuration for static output feedback.

Note that $\mathbf{u} = \mathbf{K}\mathbf{y}$ with \mathbf{K} given in (8.20). Therefore, we define, for this particular EM- $\Sigma\Delta$ architecture, the subset \mathcal{K} as

$$\mathcal{K} \triangleq \left\{ \mathbf{K} \left| \begin{array}{l} \exists a_2 \in [a_2, \bar{a}_2], \exists a_3 \in [a_3, \bar{a}_3], \exists a_4 \in [a_4, \bar{a}_4], \\ \exists a_{fb} \in [a_{fb}, \bar{a}_{fb}], \exists g_2 \in [g_2, \bar{g}_2], \\ \mathbf{K} = \left[\begin{array}{cc|cc} 1 & 1 & 0 & 0 \\ -g_2 & 1-g_2 & 1 & -a_{fb} \\ \hline a_4 & a_3+a_4 & a_2 & 0 \end{array} \right] \end{array} \right. \right\}. \quad (8.21)$$

The notations $\underline{(\cdot)}$ and $\overline{(\cdot)}$ indicate the lower and upper bounds of (\cdot) , respectively.

Finally, note that the generalized plant $\tilde{\mathbf{P}}^d$ is in discrete-time. Although it is possible to make the design in discrete-time, for frequency-domain design methods (as the \mathcal{H}_∞ synthesis), it is more convenient to use equivalent (pseudo) continuous-time models, see discussion in Section 7.3 (page 181). The main reason is that in continuous time, conventional frequency-domain techniques can be used. The equivalent continuous-time model (or its PCT model) is obtained through the bilinear (or Tustin) transform of $\tilde{\mathbf{P}}^d$, as follows

$$\tilde{\mathbf{P}}(s_p) = \tilde{\mathbf{P}}^d(z) \Big|_{z = \frac{2/T_s + s_p}{2/T_s - s_p}}$$

8.3.3 Weighting Functions and Controller Design

The weighting functions, thanks to (8.11) and (8.12), define upper bounds on $T_{\tilde{w} \rightarrow \tilde{z}}$ and, therefore, are used to enforce the control objectives of Section 8.1. The controller constraints are also taken into account. Hence, we design the continuous-time weighting functions

such that the frequency constraints correspond to the upper bounds presented in Figure 8.5 and Figure 8.6. The latter one presents a zoom around $\omega_{0,x}$ (the resonance frequency of the drive mode), which normalizes the frequency axis. The proposed method is applied, obtaining closed-loop transfers whose frequency responses are identified as **CL_new**. For the sake of comparison, we also present the frequency responses obtained with a set of parameters currently used by the industrial partner, which are computed through a method based on [EEE⁺11]. These transfers are identified as **CL_old**.

Please note that, globally, **CL_old** and **CL_new** have similar frequency responses around $\omega_{0,x}$ (normalized frequency equal to 1) and for higher frequencies. The main difference appears in low frequencies. This behavior is justified by the choice of the weighting functions (upper bounds), which, to ensure that the relay operates “linearly” (see constraint of (8.9)), enforce the transfers to u_y (the relay input) to have low gains in low frequencies, reducing the offset at the relay input. Moreover, we obtain $\|T_{Q_{error} \rightarrow \varepsilon_{est}}\|_{\infty} < 1.3$, ensuring good stability margins against the uncertain gain k_q . We also obtain $\|S_2\|_{\infty} < 4.4$, providing an adequate stability margin with respect to the model uncertainties. Because of the controller constraints, this value cannot be further reduced.

Note that the upper bound on $|T_{Q_{error} \rightarrow \varepsilon_{est}}|$ shapes the referred transfer such that the quantification error on the signal *OUT* is minimized around $\omega_{0,x}$. Also note that **CL_new** reduces the effects of n_y on *OUT* (equivalent to $T_{n_y \rightarrow \varepsilon_{est}}$), specially in low frequency. Due to the controller constraints (chosen architecture), the gains of the transfers $T_{d_{Cor,y} \rightarrow \varepsilon_{est}}$, $T_{d_{Cor,y} \rightarrow y_m}$, $T_{n_y \rightarrow \varepsilon_{est}}$ and $T_{n_y \rightarrow y_m}$ cannot be minimized around $\omega_{0,x}$. Even though, the proposed approach allows enhancing the global behavior of the closed-loop system (reducing the magnitude of the closed-loop transfers, at least where the structural constraints allows so).

8.4 Implementation Results

In this section, we present the practical results obtained with the proposed approach in the Tronics’ dedicated platform, always comparing with the performance obtained with the parameters denoted **CL_old**. Two types of test are realized. First, we evaluate the behavior of the MEMS gyroscope at rest with the parameters **CL_new**. The objective of this test is to check if the system behaves as expected with the new parameters.

Having validated the design approach, the same procedure is used to compute a set of parameters **CL_new** for other five gyroscopes. Then, a full battery of tests is realized on a rotating table in a temperature-controlled chamber. These tests allow to characterize the main performance indicators of these gyroscopes with the parameters **CL_old** and with the parameters **CL_new** (applied to the same gyroscope). The performance indicators here evaluated are the scale-factor nonlinearity (SFNL), the RMS noise, the angle random walk (ARW), bias instability (BI), the scale factor over temperature (SFOT) and the bias over temperature (BOT). The definition of these indicators is given in Section 2.1.6 (page 36).

8.4.1 Measures at Rest

First, we measure the signal *OUT* with the two different sets of parameters (**CL_old** and **CL_new**) with the gyroscope at rest and with the drive mode normally operating. The results are presented in Figure 8.7. Please note that with **CL_old**, the relay output seems to be saturated. Then, the quasi-linear model of the relay cannot be considered for this set of parameters. Indeed, when the output stays at 1, the closed-loop system behaves as if it was in open-loop operation. On the other hand, with **CL_new**, the signal *OUT* is more balanced

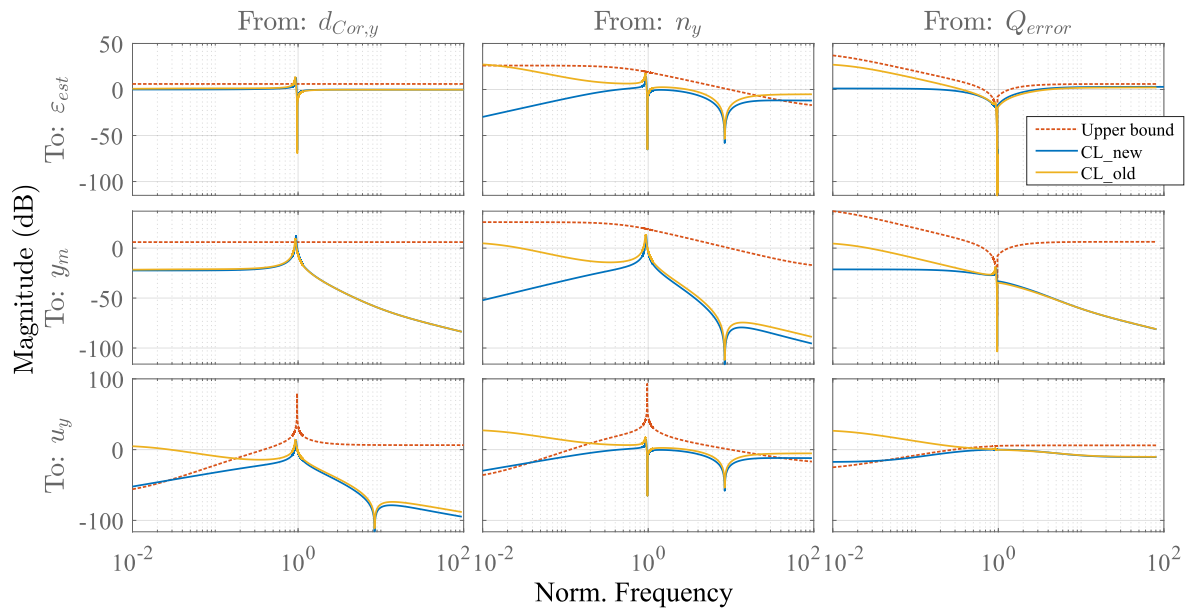


FIGURE 8.5: Closed-loop transfer functions.

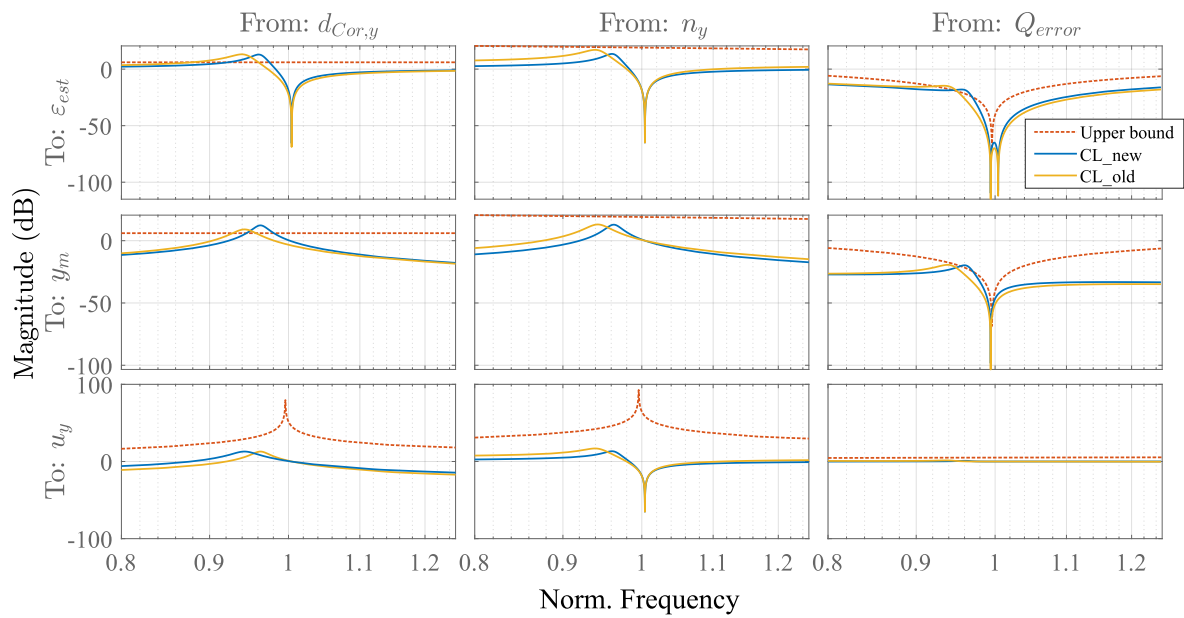


FIGURE 8.6: Closed-loop transfer functions. Zoom around the resonance frequency $\omega_{0,x}$.

TABLE 8.1: Results for a set of six gyroscopes.

Parameter	SFNL (ppm)	RMS noise (°/s)	ARW (°/√h)	BI (°/h)	SFOT (%)	BOT (°/s)
CL_old	259	0.035	0.148	0.317	0.032	0.013
CL_new	150	0.020	0.097	0.302	0.029	0.010
Improvement	32%	43%	34%	5%	10%	22%

(with an average close to zero). This improvement is achieved through the attenuation of the offset (or low-frequency) signals on u_y .

When comparing the PSD of *OUT* for the two sets of parameters – see Figures 8.8 and 8.9 –, we can note a substantial reduction of the low-frequency components (up to 70 dB attenuation). The noise level is also reduced in almost all the frequency range, especially around $\omega_{0,x}$. The peak that appears at $\omega = 1$ corresponds to the coupling force, which transfers part of the oscillations from the drive mode to the sense one (parasitic mechanical coupling).

8.4.2 Global Performance Indicators

The same design approach is applied to six different gyroscopes of the same family. These gyroscopes are then placed on a rotating table in a temperature-controlled chamber to perform some characterization tests. These tests consist in varying the temperature from -40°C up to 85°C . For each temperature, the scale factor and the bias are measured. Thus, SFOT and BOT can be computed. The SFNL, the RMS noise and the Allan variance, which defines the ARW and the BI, are measured at room temperature.

The average results are presented in Table 8.1, where we can observe a significant improvement of more than 30% on the SFNL, the RMS noise, and the ARW. These parameters are mainly linked to the linear behavior of the sensor (SFNL) and the noise on the signal *OUT*. As discussed earlier, these aspects are greatly enhanced with **CL_new**. Moreover, although the (more) modest performance improvement on the SFOT and BOT, our approach demonstrates to be as robust as the established one for temperature changes. Regarding the BI, the performance of both approaches are similar.

8.5 Summary

In this chapter, a new method for designing the electronic filter of an EM- $\Sigma\Delta$ feedback was presented. This approach is based on the \mathcal{H}_∞ synthesis. The choice of an adequate \mathcal{H}_∞ criterion is one of the crucial points of the \mathcal{H}_∞ synthesis. Then, we propose an \mathcal{H}_∞ criterion that is suited for any EM- $\Sigma\Delta$ architecture, regardless of the controller structure. The main strength of this method is that the desired specifications are expressed through the weighting functions, which can be adapted by the designer. Another crucial point is the computation of the controller. Here, two cases arise: the unconstrained and the constrained cases. We focus on the latter one, which represents most of the controllers in EM- $\Sigma\Delta$ feedbacks.

To illustrate the use of our method, we consider a given EM- $\Sigma\Delta$ architecture. A new electronic filter is designed and compared to an established one for the same gyroscope. The flexibility of our method allows us to better manage the nonlinearities of the relay, despite the controller constraints, reflecting in a consistent improvement of the global performance of a set of gyroscopes.

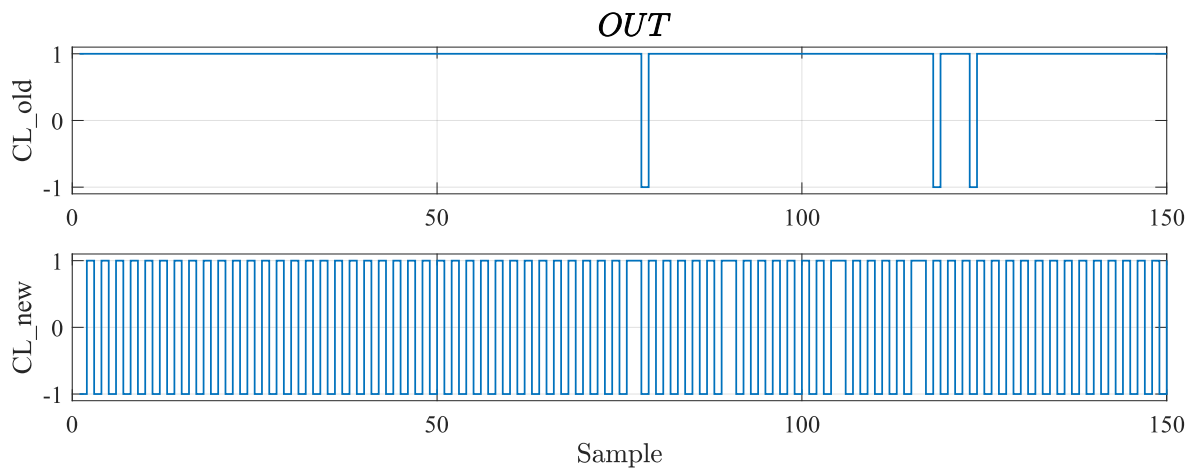


FIGURE 8.7: Measures of the signal *OUT* for the two approaches.

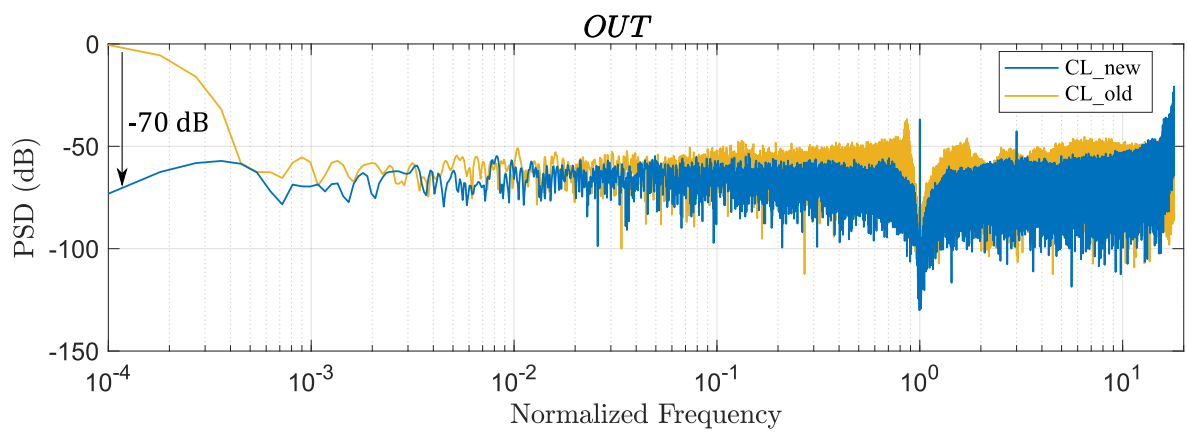


FIGURE 8.8: PSD of the measures of the signal *OUT* for the two approaches.

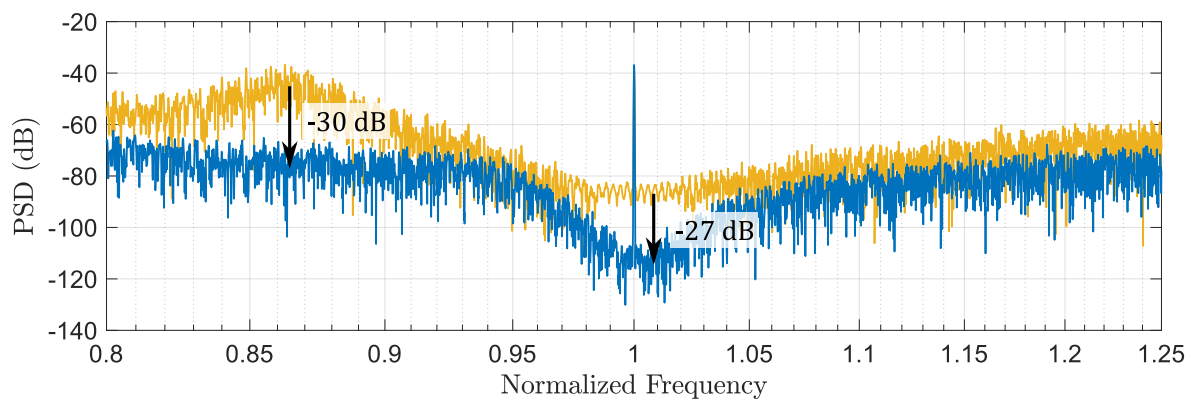


FIGURE 8.9: PSD of the measures of the signal *OUT* for the two approaches. Zoom around $\omega_{0,x}$.

Chapter 9

Conclusions and Perspectives

In this document, we have developed systematic and flexible methods for the design of controller(s) for MEMS gyroscopes under different (linear) architectures. The main obtained results and contributions are summarized in the sequel, answering to most of the research questions of Section 2.4 (page 53). All the questions could not find a complete answer, and new interesting questions arised. Therefore, indications of future works are given in the second part of this final chapter.

9.1 Summary of Results and Contributions

The first step to design a control system is to specify the desired closed-loop specifications. For the case of the MEMS gyroscopes, defining these specifications is not trivial. Indeed, the performance indicators of the device are based on the quality of the angular rate measure and are not directly related to the behavior of the closed loop, which is only a constituting part of the device. To cope with this issue, we proposed an LTI input-output framework that allowed us to express the key performance indicators as frequency constraints on the closed-loop transfers. This contribution is presented in Chapter 3, answers to the research question (Q1) and is used to determine the closed-loop specifications for the design of MEMS gyroscope controllers.

Two main families of control architectures were considered in this thesis: those based on the complex envelope of the oscillating signals, called the envelope-based control architectures; and those based on the oscillating signals themselves, called the direct control architectures. The foremost advantage of the former one is that the complex envelope of oscillating signals is constant in steady state, allowing the use of simple PI-like controllers to regulate the amplitude and phase of the oscillating signals. Thanks to its simplicity, this solution has been widely used in the industry. The main drawback is that nonlinear elements are introduced in the closed-loop system, the different couplings (mechanical couplings between the drive and sense modes, and coupling between the amplitude and phase loops or in-phase and in-quadrature loops) and dependence on the environmental conditions are not considered. Then, guarantees of stability and performance cannot be given *a priori*. On the other side, with direct control architectures these aspects can be considered and formal guarantees of stability and performance can be provided *a priori*. Here, the main challenges are: to provide a systematic, flexible and accessible design method; and to demonstrate the implementability of the solution.

The design of a direct controller was split into two parts. In Chapter 4, we considered the case where the drive-mode resonance frequency $\omega_{0,x}$ was constant over time and known, corresponding to the research question (Q2). In this case, the standard \mathcal{H}_∞ synthesis was

applied and different strategies with different complexities were considered (with one or two degrees of freedom, SISO, MIMO and MIMO with explicit estimation of the Coriolis force). The simulation results validated the proposed method. The systematicness, flexibility and accessibility of the design method are provided by the \mathcal{H}_∞ synthesis and the use of the weighting functions. Indeed, after an \mathcal{H}_∞ criterion is defined, engineers with basic knowledge on classical control design methods can make adjustments on the weighting functions, adapting the \mathcal{H}_∞ criterion to new specifications or (slightly) different models.

In practice, however, $\omega_{0,x}$ varies (mainly due to temperature variations) and an external mechanism (see [Mor21]) is required to keep track of $\omega_{0,x}$. The same mechanism generates the excitation ω_{exc} , which is equal to the estimate of $\omega_{0,x}$. In this case, instead of tracking a sinusoidal reference signal, the control objective is to track a signal of the type

$$x_m^{ref}(t) = A_{x,m}^{ref} \sin(\phi_{exc}(t)) \quad \text{with} \quad \phi_{exc}(t) = \int_0^t \omega_{exc}(\tau) d\tau + \phi_{exc}^0, \quad (9.1)$$

where $\phi_{exc}^0 \in \mathbb{R}$ and $\omega_{exc}(t)$ ranges arbitrarily in the interval $[\omega_{exc,1}, \omega_{exc,2}]$. In Chapter 5, we revealed that this new control objective can be expressed through a weighted \mathcal{L}_2 criterion with a new class of LPV weighting functions, precisely describing x_m^{ref} with a time-varying excitation frequency. Therefore, standard LPV design methods were used to compute a controller whose gains depend on ω_{exc} , achieving the required control objective with guaranteed performance (e.g., γ_p -tracking), providing an answer to (Q3). Numerical simulations confirmed these results.

In Chapter 6, we established a framework for the analysis of envelope-based control architectures and for the design of suited controllers, giving a response to the research question (Q4). This framework relies on the so-called dynamic phasor modeling, which allows to exactly describe the dynamic behavior of the complex envelopes of the oscillating signals. Moreover, this framework allowed us to establish links between direct control architectures and envelope-based one, revealing that the performance achieved with both approaches are equivalent if the complex envelopes can be ideally measured. In practice, however, the complex envelopes are measured through the synchronous demodulation. Then, the ideality assumption does not hold and the performance of the direct control approaches happens to be superior. Nevertheless, if the use of envelope-based architectures is required (because of implementation constraints, for instance), we model the nonidealities of the synchronous demodulation, such that we can design a controller that ensures, at least, the robust stability of the closed-loop system.

The last part of the thesis was devoted to the digital implementation of the controllers. First, we considered the implementation of a digital controller in a flexible platform. Because of the better performance obtained with direct control architectures, we opted to implement this architecture in the flexible platform. Then, in Chapter 7, we discussed how to adapt the design method of Chapter 4 for the digital implementation of the controller, answering to (Q5). We also proposed an extension of the \mathcal{H}_∞ synthesis for the particular case where $\omega_{0,x}$ and ω_{exc} change very slowly in time. In this case, we took advantage of the particular structure of the system, such that the design of a parameter-dependent controller can be recast as a simple LTI control problem. This result, presented in Section 7.4, provides a simple parametrization of the controller. The practical results with a real prototype demonstrated the implementability of the direct control architectures. However, the high sensitivity of the MEMS gyroscope to temperature variations points to the necessity of a (more accurate) nonlinear modeling and the introduction of an external mechanism for the tracking of the

drive-mode resonance frequency.

Finally, we also considered the particular EM- $\Sigma\Delta$ architecture of the Tronics' platform, proposing a new design method for the controller design. Also based on the \mathcal{H}_∞ synthesis, the proposed method provides systematicness, flexibility and accessibility, giving an answer to (Q6). Moreover, the practical results showed an improvement of up to 40% of some key performance indicators. The proposed solution was embedded in a software and integrates nowadays the production line of the industrial partner.

9.2 Future Works

During this thesis, several interesting questions arose and can lead to future works. Let us classify them as immediate or short-term perspectives, and as medium to long-term ones.

9.2.1 Immediate or Short-Term Perspectives

Here, we can consider the immediate extensions of the presented results and implementation of the other control strategies, as follows.

Integration of the direct control architecture with a resonance-frequency tracking mechanism As widely discussed throughout this document, the direct control architecture requires an additional mechanism to keep track of the drive-mode resonance frequency [Mor21], providing then a complete solution for the control of MEMS gyroscopes. It is important to keep in mind that the implementation of this mechanism and the update of the controller in real time will require more computing power from the processor. Then, it is important to optimize the implementation code (by code optimization and model reduction of the dynamic systems) so that the controllers and the resonance-frequency tracking mechanism can run in real time.

Implementation of the envelope-based control architectures We have chosen to implement the direct control architecture in Chapter 7. However, the same platform allows the implementation of envelope-based control architectures. In this context, the controller can operate with a much smaller sampling frequency, which demands much less computing power. The integration with the resonance-frequency tracking mechanism may be easier under this configuration.

Use of the new class of LPV weighting functions in other applications The solution proposed in Chapter 5 is motivated by the MEMS gyroscope application, but can easily find applications in other domains. For instance, the potential is very interesting in the control of power converters connected to the grid, whose frequency varies around 50 Hz (or other values).

\mathcal{H}_∞ synthesis for the EM- $\Sigma\Delta$ feedback of MEMS accelerometers The EM- $\Sigma\Delta$ feedback architecture is also widely used for the control of MEMS accelerometers, where, instead of compensating for sinusoidal signals, the control objective is to compensate for constant (or low-frequency) signals: the linear acceleration of the device. Therefore, thanks to the flexibility provided by the \mathcal{H}_∞ synthesis, the solution of Chapter 8 also applies to MEMS accelerometers, constituting a unified approach for the design of EM- $\Sigma\Delta$ architectures.

Dynamic-phasor modeling of the AGC+PLL control architecture In Chapter 2, we presented the AGC+PLL control architecture, which is widely used in the industry. One of the issues of this architecture is that the couplings between the amplitude and phase/frequency are not taken into account. The dynamic-phasor modeling proposed in Chapter 6 allows to precisely model the nonlinear to-be-controlled plant under this configuration, including the couplings between amplitude and phase/frequency. Since this model is supposed to be more accurate, the performance of the closed-loop system can be improved.

9.2.2 Medium to Long-Term Perspectives

Other interesting perspectives can be envisaged for the medium to long term, opening the doors for new challenges from the Control Theory as well as from the MEMS gyroscope point of view.

Less conservative control design for phasor control with nonideal s2c In Section 6.5, we propose a solution for the design of a phasor control that ensures *a priori* the stability of the closed-loop system against the nonidealities of the s2c. In particular, to ensure the stability against the time-varying matrix $\Delta(\phi_{ph}(t))$, we considered the small gain theorem, which is a very conservative solution. The same time-varying matrix could be more precisely represented through weighting functions obtained by adequate multipliers, as the ones proposed in [ACSKS19] or [AC21], providing a less conservative solution.

Extension of the dynamic phasor framework for nonlinear systems In Chapter 6, we proposed a framework for the modeling and design of systems based on the so-called dynamic phasor. We focused on the linear systems (LTI or LPV). However, we can imagine to extend this results to a nonlinear framework.

LPV weighting functions for a wider class of signals At the end of Section 5.2.2, we pointed to the possibility of extending the LPV weighting functions to a wider class of signals: “periodic” signals that can be decomposed as a finite sum of “frequency-varying” sinusoidal signals.

Use of nonlinear control architectures for MEMS gyroscopes In this work, we rather focused on linear control techniques. However, the use of nonlinear elements can provide some features that linear elements cannot. For instance, the self-oscillating AGC as well as the AGC+PLL control architectures allow to track the drive-mode resonance frequency. This is not possible with purely linear control architectures. The problem is that, in general, it is difficult to provide guarantees of performance for a nonlinear closed-loop system. Nevertheless, some recent works have been tackling this problem through the notion of incremental \mathcal{L}_2 gain, see, for instance, [Hil13, SFH15, Wai18].

More accurate (nonlinear) model of the MEMS gyroscope Throughout this thesis, we consider that the mechanical part of the MEMS gyroscope with actuation and instrumentation circuits is modeled as a linear dynamic system. However, it is known that MEMS gyroscopes present plenty of nonlinear elements (nonlinear springs, nonlinear capacitances for actuation, nonlinear capacitances for detection/instrumentation, etc.) [You11]. Even if these nonlinear behaviors are rather weak, the specifications of high-performance may require these nonlinear effects to be precisely modeled.

References

- [ABLN16] R. Abdolvand, B. Bahreyni, J. Lee, and F. Nabki. Micromachined Resonators: A Review. *Micromachines*, 7(9):160, sep 2016. doi:10.3390/mi7090160.
- [AC21] J. I. Ayala-Cuevas. *Performance validation of MEMS sensors using nonlinear uncertain models*. Ph. D. thesis, Université de Lyon, 2021.
- [ACSKS19] J. Ayala-Cuevas, F. Saggin, A. Korniienko, and G. Scorletti. Stability Analysis of Time-Varying Systems with Harmonic Oscillations Using IQC Frequency Domain Multipliers. In *IEEE Conference on Decision and Control*, pages 5193–5198, Nice, 2019. IEEE. doi:10.1109/CDC40024.2019.9029738.
- [AGB95] P. Apkarian, P. Gahinet, and G. Becker. Self-scheduled \mathcal{H}_∞ control of linear parameter-varying systems: a design example. *Automatica*, 31(9):1251–1261, 1995. doi:10.1016/0005-1098(95)00038-X.
- [AH10] L. Aaltonen and K. A. I. Halonen. An analog drive loop for a capacitive MEMS gyroscope. *Analog Integrated Circuits and Signal Processing*, 63(3):465–476, 2010. doi:10.1007/s10470-009-9395-6.
- [AL10] T. M. Adams and R. A. Layton. *Introductory MEMS: Fabrication and applications*. 2010. doi:10.1007/978-0-387-09511-0.
- [AN06] P. Apkarian and D. Noll. Nonsmooth H-infinity Synthesis. *IEEE Transactions on Automatic Control*, 51(1):71–86, 2006. doi:10.1109/TAC.2005.860290.
- [AOPB09] R. Antonello, R. Oboe, L. Prandi, and F. Biganzoli. Automatic Mode Matching in MEMS Vibrating Gyroscopes Using Extremum-Seeking Control. *IEEE Transactions on Industrial Electronics*, 56(10):3880–3891, oct 2009. doi:10.1109/TIE.2009.2020707.
- [AP87] S. H. Ardalan and J. J. Paulos. An Analysis of Nonlinear Behavior in Delta-Sigma Modulators. *IEEE Transactions on Circuits and Systems*, 34(6):593–603, 1987. doi:10.1109/TCS.1987.1086187.
- [Apo16] V. Apostolyuk. *Coriolis Vibratory Gyroscopes*. Springer International Publishing, Cham, Switzerland, 2016. doi:10.1007/978-3-319-22198-4.
- [AS05] C. Acar and A. M. Shkel. An approach for increasing drive-mode bandwidth of MEMS vibratory gyroscopes. *Journal of Microelectromechanical Systems*, 14(3):520–528, jun 2005. doi:10.1109/JMEMS.2005.844801.
- [AS09] C. Acar and A. Shkel. *MEMS Vibratory Gyroscopes*. MEMS Reference Shelf. Springer US, Boston, MA, 2009. doi:10.1007/978-0-387-09536-3.
- [ÅW97] K. J. Åström and B. Wittenmark. *Computer-Controlled Systems: Theory and Design*. Prentice-Hall information and system sciences series. Prentice Hall, third edition, 1997.

- [BCPS20] G. Balas, R. Chiang, A. Packard, and M. Safonov. The robust control toolbox of matlab. Technical report, MathWork, 2020. URL: https://fr.mathworks.com/help/pdf_doc/robust/index.html.
- [Bed63] E. Bedrosian. A product theorem for Hilbert transforms. *Proceedings of the IEEE*, 51(5):868–869, 1963. doi:10.1109/PROC.1963.2308.
- [Bod14] M. Bodson. Design of controllers in the complex domain. In *IEEE Conference on Decision and Control*, number February, pages 4077–4082. IEEE, 2014. doi:10.1109/CDC.2014.7040023.
- [BRLS07] F. Braghin, F. Resta, E. Leo, and G. Spinola. Nonlinear dynamics of vibrating MEMS. *Sensors and Actuators A: Physical*, 134(1):98–108, feb 2007. doi:10.1016/j.sna.2006.10.041.
- [BSG⁺04] X. Bombois, G. Scorletti, M. Gevers, R. Hildebrand, and P. Van den Hof. Cheapest open-loop identification for control. In *IEEE Conference on Decision and Control*, pages 382–387 Vol.1. IEEE, 2004. doi:10.1109/CDC.2004.1428659.
- [BSK06] C. Batur, T. Sreeramreddy, and Q. Khasawneh. Sliding mode control of a simulated MEMS gyroscope. *ISA Transactions*, 45(1):99–108, jan 2006. doi:10.1016/S0019-0578(07)60069-X.
- [BYDM94] R. P. Braatz, P. M. Young, J. C. Doyle, and M. Morari. Computational complexity of μ calculation. *IEEE Transactions on Automatic Control*, 39(5):1000–1002, may 1994. doi:10.1109/9.284879.
- [CCD⁺09] J. Cui, X. Z. Chi, H. T. Ding, L. T. Lin, Z. C. Yang, and G. Z. Yan. Transient response and stability of the AGC-PI closed-loop controlled MEMS vibratory gyroscopes. *Journal of Micromechanics and Microengineering*, 19(12):17, dec 2009. doi:10.1088/0960-1317/19/12/125015.
- [CGZ⁺11] J. Cui, Z. Guo, Q. Zhao, Z. Yang, Y. Hao, and G. Yan. Force Rebalance Controller Synthesis for a Micromachined Vibratory Gyroscope Based on Sensitivity Margin Specifications. *Journal of Microelectromechanical Systems*, 20(6):1382–1394, dec 2011. doi:10.1109/JMEMS.2011.2167663.
- [CLK16] F. Chen, X. Li, and M. Kraft. Electromechanical Sigma-Delta Modulators ($\Sigma\Delta$) Force Feedback Interfaces for Capacitive MEMS Inertial Sensors: A Review. *IEEE Sensors Journal*, 16(17):6476–6495, 2016. doi:10.1109/JSEN.2016.2582198.
- [CMTB05] Y.-C. Chen, R. T. M’Closkey, T. A. Tran, and B. Blaes. A control and signal Processing integrated circuit for the JPL-boeing micromachined gyroscopes. *IEEE Transactions on Control Systems Technology*, 13(2):286–300, mar 2005. doi:10.1109/TCST.2004.839558.
- [Col20] K. Colin. *Data informativity for the prediction error identification of MIMO systems: identification of a MEMS gyroscope*. Ph. D. thesis, Université de Lyon, 2020. URL: <https://tel.archives-ouvertes.fr/tel-03114994>.
- [CSF⁺17] R. S. Castro, A. T. Salton, J. V. Flores, M. Kinnaert, and D. F. Coutinho. Variable frequency resonant controller for load reduction in wind turbines. *Control Engineering Practice*, 66(October 2016):76–88, sep 2017. doi:10.1016/j.conengprac.2017.06.007.

- [CSL⁺19] K. Colin, F. Saggin, C. Le Blanc, X. Bombois, A. Korniienko, and G. Scorletti. Identification-Based Approach for Electrical Coupling Compensation in a MEMS Gyroscope. In *IEEE International Symposium on Inertial Sensors and Systems (INERTIAL)*, pages 1–4. IEEE, apr 2019. doi:10.1109/ISISS.2019.8739573.
- [CXZ⁺21] F. Chen, D. Xu, W. Zhou, M. Kraft, and X. Li. A discrete-time self-clocking complex electromechanical $\Sigma\Delta$ gyroscope with quadrature error cancellation. *Sensors and Actuators A: Physical*, 317:112470, jan 2021. doi:10.1016/j.sna.2020.112470.
- [CYC⁺14] F. Chen, W. Yuan, H. Chang, G. Yuan, J. Xie, and M. Kraft. Design and Implementation of an Optimized Double Closed-Loop Control System for MEMS Vibratory Gyroscope. *IEEE Sensors Journal*, 14(1):184–196, jan 2014. doi:10.1109/JSEN.2013.2271586.
- [DA09] L. Dong and D. Avanesian. Drive-Mode Control for Vibrational MEMS Gyroscopes. *IEEE Transactions on Industrial Electronics*, 56(4):956–963, apr 2009. doi:10.1109/TIE.2008.2010088.
- [DGKF89] J.C. Doyle, K. Glover, P.P. Khargonekar, and B.A. Francis. State-space solutions to standard H_2 and H_∞ control problems. *IEEE Transactions on Automatic Control*, 34(8):831–847, 1989. doi:10.1109/9.29425.
- [DSFM05] M. Dinh, G. Scorletti, V. Fromion, and E. Magarotto. Parameter dependent H_∞ control by finite dimensional LMI optimization: application to trade-off dependent control. *Int. J. Robust Nonlin.*, 15(9):383–406, jun 2005.
- [DW80] C. Desoer and Y.-T. Wang. Foundations of feedback theory for nonlinear dynamical systems. *IEEE Transactions on Circuits and Systems*, 27(2):104–123, feb 1980. doi:10.1109/TCS.1980.1084787.
- [DZG08] L. Dong, Q. Zheng, and Z. Gao. On Control System Design for the Conventional Mode of Operation of Vibrational Gyroscopes. *IEEE Sensors Journal*, 8(11):1871–1878, nov 2008. doi:10.1109/JSEN.2008.2006451.
- [EEE⁺11] A. Elsayed, A. Elshennawy, A. Elmallah, A. Shaban, B. George, M. Elmala, A. Ismail, A. Wassal, M. Sakr, A. Mokhtar, M. Hafez, A. Hamed, M. Saeed, M. Samir, M. Hammad, M. Elkhoully, A. Kamal, M. Rabieah, A. Elghufaili, S. Shaibani, I. Hakami, and T. Alanazi. A self-clocked ASIC interface for MEMS gyroscope with 1m noise floor. In *IEEE Custom Integrated Circuits Conference*. IEEE, sep 2011. doi:10.1109/CICC.2011.6055369.
- [EK10] M. Egretzberger and A. Kugi. A dynamical envelope model for vibratory gyroscopes. *Microsystem Technologies*, 16(5):777–786, 2010. doi:10.1007/s00542-009-0979-y.
- [EKT⁺11] A. M. Elshurafa, K. Khirallah, H. H. Tawfik, A. Emira, A. K. S. Abdel Aziz, and S. M. Sedky. Nonlinear Dynamics of Spring Softening and Hardening in Folded-MEMS Comb Drive Resonators. *Journal of Microelectromechanical Systems*, 20(4):943–958, aug 2011. doi:10.1109/JMEMS.2011.2148162.
- [EMK12] M. Egretzberger, F. Mair, and A. Kugi. Model-based control concepts for vibratory MEMS gyroscopes. *Mechatronics*, 22(3):241–250, 2012. doi:10.1016/j.mechatronics.2011.06.003.

- [ESAES09] A. K. El-Shennawy, H. Aboushady, and A. El-Sayed. Design method for a $\Sigma\Delta$ -based closed loop gyroscope. *International Design and Test Workshop*, 2009. doi:10.1109/IDT.2009.5404085.
- [Fel06] M. Feldman. Time-varying vibration decomposition and analysis based on the Hilbert transform. *Journal of Sound and Vibration*, 295(3-5):518–530, 2006. doi:10.1016/j.jsv.2005.12.058.
- [FL85] J. Freudenberg and D. Looze. Right half plane poles and zeros and design tradeoffs in feedback systems. *IEEE Trans. Autom. Control*, 30(6):555–565, jun 1985.
- [Fou51] L. Foucault. Démonstration physique du mouvement de rotation de la terre au moyen du pendule. In *Comptes rendus hebdomadaires des séances de l'Académie des Sciences*, volume 32, pages 135–138, Paris, France, 1851. Académie des Sciences. URL: https://fr.wikisource.org/wiki/Démonstration_physique_du_mouvement_de_rotation_de_la_Terre_au_moyen_du_pendule.
- [Fou52a] L. Foucault. Sur les phénomènes d'orientation des corps tournants entraînés par un axe fixe à la surface de la Terre – Nouveaux signes sensibles du mouvement diurne. In *Comptes rendus hebdomadaires des séances de l'Académie des Sciences*, volume 35, pages 424–427, Paris, France, 1852. Académie des Sciences. URL: <https://gallica.bnf.fr/ark:/12148/bpt6k2992n/f428.image>.
- [Fou52b] L. Foucault. Sur une nouvelle démonstration expérimentale du mouvement de la Terre, fondée sur la fixité du plan de rotation. In *Comptes rendus hebdomadaires des séances de l'Académie des Sciences*, volume 35, pages 421–424, Paris, France, 1852. Académie des Sciences. URL: <https://gallica.bnf.fr/ark:/12148/bpt6k2992n/f425.image>.
- [Fre15] Freescale. Allan Variance: Noise Analysis for Gyroscopes, 2015. URL: <http://cache.freescale.com/files/sensors/doc/app{ }note/AN5087.pdf>.
- [GA94] P. Gahinet and P. Apkarian. A linear matrix inequality approach to H_∞ control. *International Journal of Robust and Nonlinear Control*, 4(4):421–448, 1994. doi:10.1002/rnc.4590040403.
- [Gab46] D. Gabor. Theory of communication. Part 1: The analysis of information. *Journal of the Institution of Electrical Engineers - Part III: Radio and Communication Engineering*, 93(26):429–441, 1946. doi:10.1049/ji-3-2.1946.0074.
- [Gab93] T. B. Gabrielson. Mechanical-thermal noise in micromachined acoustic and vibration sensors. *IEEE Transactions on Electron Devices*, 40(5):903–909, may 1993. doi:10.1109/16.210197.
- [GBKN91] P. Greiff, B. Boxenhorn, T. King, and L. Niles. Silicon monolithic micromechanical gyroscope. In *International Conference on Solid-State Sensors and Actuators*, pages 966–968. IEEE, 1991. doi:10.1109/SENSOR.1991.149051.
- [GV68] A. Gelb and W. E. Van der Velde. *Multiple input describing functions and nonlinear system design*. McGraw-Hill, New York, NY, 1968.
- [Hil13] S. D. Hillerin. *Commande robuste de systèmes non linéaires incertains*. Ph. D. thesis, Supelec, 2013.

- [HLZ⁺15] C. H. He, D. C. Liu, Q. C. Zhao, Y. F. En, Z. C. Yang, D. C. Zhang, and G. Z. Yan. A novel narrow-band force rebalance control method for the sense mode of MEMS vibratory gyroscopes. *Measurement*, 62:197–204, feb 2015. doi:10.1016/j.measurement.2014.11.009.
- [HZH⁺15] C. He, Q. Zhao, Q. Huang, D. Liu, Z. Yang, D. Zhang, and G. Yan. A MEMS Vibratory Gyroscope With Real-Time Mode-Matching and Robust Control for the Sense Mode. *IEEE Sensors Journal*, 15(4):2069–2077, apr 2015. doi:10.1109/JSEN.2014.2371456.
- [IEE04] IEEE Aerospace and Electronic Systems Society (institution). IEEE Standard Specification Format Guide and Test Procedure for Coriolis Vibratory Gyros. *IEEE Std 1431-2004*, 2004. doi:10.1109/IEEESTD.2001.93363.
- [IEE06] IEEE Aerospace and Electronic Systems Society (institution). IEEE Standard Specification Format Guide and Test Procedure for Single-Axis Laser Gyros. *IEEE Std 647-2006*, (September), 2006.
- [IEE09] IEEE Aerospace and Electronic Systems Society (institution). IEEE Standard for Inertial Systems Terminology. *IEEE Std 1559-2009*, (August), 2009. doi:10.1109/IEEESTD.2009.5226540.
- [IEE19] IEEE Aerospace and Electronic Systems Society (institution). IEEE Standard for Inertial Sensor Terminology. *IEEE Std 528-2019*, 2019. doi:10.1109/IEEESTD.2019.8863799.
- [IS94] T. Iwasaki and R.E. Skelton. All controllers for the general H_∞ control problem: LMI existence conditions and state space formulas. *Automatica*, 30(8):1307–1317, aug 1994. doi:10.1016/0005-1098(94)90110-4.
- [JLN55] G. W. Johnson, D. P. Lindorff, and C. G. A. Nordling. Extension of continuous-data system design techniques to sampled-data control systems. *Transactions of the American Institute of Electrical Engineers, Part II: Applications and Industry*, 74(4):252–263, sep 1955. doi:10.1109/TAI.1955.6366385.
- [KAG⁺17] M. Kangul, E. Aydin, F. Gokce, O. Zorlu, and H. Kulah. Analysis and Elimination of the Capacitive Feedthrough Current on Electrostatically Actuated and Sensed Resonance-Based MEMS Sensors. *Journal of Microelectromechanical Systems*, 26(6):1272–1278, dec 2017. doi:10.1109/JMEMS.2017.2729624.
- [KCV08] C. Kharrat, E. Colinet, and A. Voda. H_∞ Loop shaping control for PLL-based mechanical resonance tracking in NEMS resonant mass sensors. In *IEEE Sensors*, pages 1135–1138. IEEE, oct 2008. doi:10.1109/ICSENS.2008.4716641.
- [Kem11] V. Kempe. *Inertial MEMS - Principles and Practice*. Cambridge University Press, Cambridge, 2011.
- [KM13] D. Kim and R. T. M’Closkey. Spectral Analysis of Vibratory Gyro Noise. *IEEE Sensors Journal*, 13(11):4361–4374, nov 2013. doi:10.1109/JSEN.2013.2269797.
- [Lab17] Laboratoire Ampère (institution). NEXT4MEMS (2017-2020) : Capteurs Inertiels MEMS de Haute Performance, 2017. URL: <http://www.ampere-lab.fr/spip.php?article885>.
- [Lat98] B. P. Lathi. *Modern Digital and Analog Communication Systems*. Oxford University Press, Inc., New York, NY, 3rd edition, 1998.

- [Lju98] L. Ljung. *System identification: theory for the user*. Pearson Education, 2nd edition, 1998.
- [LM14] D. Lin and T. Miller. Robust MEMS gyroscope for oil and gas exploration. In Debbie G. Senesky and Sachin Dekate, editors, *Sensors for Extreme Harsh Environments*, volume 9113, page 91130I, jun 2014. doi:10.1117/12.2050613.
- [LR02] P. W. Loveday and C. A. Rogers. The influence of control system design on the performance of vibratory gyroscopes. *Journal of Sound and Vibration*, 255(3):417–432, aug 2002. doi:10.1006/jsvi.2001.4163.
- [LS09] J. E.-Y. Lee and A. A. Seshia. Parasitic feedthrough cancellation techniques for enhanced electrical characterization of electrostatic microresonators. *Sensors and Actuators A: Physical*, 156(1):36–42, nov 2009. doi:10.1016/j.sna.2009.02.005.
- [Mor21] F. Morelli. *Optimal identification experiment design: contributions to its robustification and to its use for dynamic network identification*. Resonance Frequency Tracking. Ph. D. thesis, Université de Lyon, 2021.
- [MR97] A. Megretski and A. Rantzer. System analysis via integral quadratic constraints. *IEEE Transactions on Automatic Control*, 42(6):819–830, jun 1997. doi:10.1109/9.587335.
- [MV99] R. T. M’Closkey and A. Vakakis. Analysis of a microsensor automatic gain control loop. In *American Control Conference*, volume 5, pages 3307–3311. IEEE, 1999. doi:10.1109/ACC.1999.782377.
- [MVG01] R. T. M’Closkey, A. Vakakis, and R. Gutierrez. Mode Localization Induced by a Nonlinear Control Loop. *Nonlinear Dynamics*, 25(1/3):221–236, 2001. doi:10.1023/A:1012934112137.
- [OAL⁺05] R. Oboe, R. Antonello, E. Lasalandra, G. Spinola Durante, and L. Prandi. Control of Z-Axis MEMS Vibrational Gyroscope. *IEEE/ASME Transactions on Mechatronics*, 10(4):364–370, 2005. doi:10.1109/TMECH.2005.852437.
- [Pac94] A. Packard. Gain scheduling via Linear Fractional Transformations. *Syst. Control Lett.*, 22(2):79–92, feb 1994.
- [PB05] V. P. Petkov and B. E. Boser. A fourth-order SigmaDelta interface for micromachined inertial sensors. *IEEE Journal of Solid-State Circuits*, 40(8):1602–1609, aug 2005. doi:10.1109/JSSC.2005.852025.
- [PB06] V. P. Petkov and B. E. Boser. High-order electromechanical Sigma-Delta modulation in micromachined inertial sensors. *IEEE Transactions on Circuits and Systems I: Regular Papers*, 53(5):1016–1022, may 2006. doi:10.1109/TCSI.2006.869901.
- [PCV⁺17] V. M. N. Passaro, A. Cuccovillo, L. Vaiani, M. De Carlo, and C. E. Campanella. Gyroscope Technology and Applications: A Review in the Industrial Perspective. *Sensors*, 17(10):2284, oct 2017. doi:10.3390/s17102284.
- [PH03] S. Park and R. Horowitz. Adaptive control for the conventional mode of operation of mems gyroscopes. *Journal of Microelectromechanical Systems*, 12(1):101–108, feb 2003. doi:10.1109/JMEMS.2002.807468.
- [PH04] S. Park and R. Horowitz. New Adaptive Mode of Operation for MEMS Gyroscopes. *Journal of Dynamic Systems, Measurement, and Control*, 126(4):800, 2004. doi:10.1115/1.1849252.

- [PHHN07] S. Park, R. Horowitz, S. K. Hong, and Y. Nam. Trajectory-Switching Algorithm for a MEMS Gyroscope. *IEEE Transactions on Instrumentation and Measurement*, 56(6):2561–2569, dec 2007. doi:10.1109/TIM.2007.908597.
- [Pic97] B. Picinbono. On instantaneous amplitude and phase of signals. *IEEE Transactions on Signal Processing*, 45(3):552–560, 1997. doi:10.1109/78.558469.
- [PK14] M. H. Pishrobat and J. Keighobadi. Model Predictive Control of MEMS Vibratory Gyroscope. *IFAC Proceedings Volumes*, 47(3):7278–7283, 2014. doi:10.3182/20140824-6-ZA-1003.02322.
- [PPK⁺04] Y. Park, S. Park, D. Kwak, H. Ko, T. Song, D. Cho, K. Huh, and J.-H. Park. Feedback Control of MEMS Gyroscope to Achieve the Tactical-Grade Specifications. *IFAC Proceedings Volumes*, 37(6):671–676, jun 2004. doi:10.1016/S1474-6670(17)32253-X.
- [PSL⁺12] S. Park, J. W. Song, B. Lee, H. Yoon, Y. J. Lee, and S. Sung. Autonomous Oscillation Control Loop Design for Amplitude Controlled, Frequency Read-Out-Type Resonant Sensors. *IEEE/ASME Transactions on Mechatronics*, 17(6):1009–1020, dec 2012. doi:10.1109/TMECH.2011.2157352.
- [PSP⁺06] A. S. Phani, A. A. Seshia, M. Palaniapan, R. T. Howe, and J. Yasaitis. Modal Coupling in Micromechanical Vibratory Rate Gyroscopes. *IEEE Sensors Journal*, 6(5):1144–1152, oct 2006. doi:10.1109/JSEN.2006.881432.
- [PSSF17] C. Peng, J. Sun, X. Song, and J. Fang. Frequency-Varying Current Harmonics for Active Magnetic Bearing via Multiple Resonant Controllers. *IEEE Transactions on Industrial Electronics*, 64(1):517–526, jan 2017. doi:10.1109/TIE.2016.2598723.
- [PTS13] I. P. Prikhodko, A. A. Trusov, and A. M. Shkel. Compensation of drifts in high-Q MEMS gyroscopes using temperature self-sensing. *Sensors and Actuators A: Physical*, 201:517–524, oct 2013. doi:10.1016/j.sna.2012.12.024.
- [PZTS11] I. P. Prikhodko, S. A. Zotov, A. A. Trusov, and A. M. Shkel. Foucault pendulum on a chip: angle measuring silicon MEMS gyroscope. In *IEEE International Conference on Micro Electro Mechanical Systems*, pages 161–164. IEEE, jan 2011. doi:10.1109/MEMSYS.2011.5734386.
- [RCRW09] J. Raman, E. Cretu, P. Rombouts, and L. Weyten. A Closed-Loop Digitally Controlled MEMS Gyroscope With Unconstrained Sigma-Delta Force-Feedback. *IEEE Sensors Journal*, 9(3):297–305, mar 2009. doi:10.1109/JSEN.2008.2012237.
- [RRW08] J. Raman, P. Rombouts, and L. Weyten. An Unconstrained Architecture for Systematic Design of Higher Order $\Sigma\Delta$ Force-Feedback Loops. *IEEE Transactions on Circuits and Systems I: Regular Papers*, 55(6):1601–1614, jul 2008. doi:10.1109/TCSI.2008.917998.
- [RSPC17] G. A. Ramos, R. A. Soto-Perez, and J. A. Cifuentes. A Varying Frequency LPV-Based Control Strategy for Three-Phase Inverters. *IEEE Transactions on Industrial Electronics*, 64(9):7599–7608, sep 2017. URL: <http://ieeexplore.ieee.org/document/7938404/>, doi:10.1109/TIE.2017.2703656.
- [Rub09] E. Rubiola. *Phase Noise and Frequency Stability in Oscillators*. Cambridge University Press, Cambridge, 2009.

- [SACKS20] F. Saggini, J. Ayala-Cuevas, A. Kornienko, and G. Scorletti. Parameter-dependent H_∞ control of a MEMS gyroscope: synthesis and analysis. volume 53, pages 7331–7337, 2020. doi:10.1016/j.ifacol.2020.12.990.
- [SAH07] M. Saukoski, L. Aaltonen, and K. A. I. Halonen. Zero-Rate Output and Quadrature Compensation in Vibratory MEMS Gyroscopes. *IEEE Sensors Journal*, 7(12):1639–1652, dec 2007. doi:10.1109/JSEN.2007.908921.
- [SASH06] M. Saukoski, L. Aaltonen, T. Salo, and K. Halonen. Readout and Control Electronics for a Microelectromechanical Gyroscope. In *IEEE Instrumentation and Measurement Technology Conference*, number April, pages 1741–1746. IEEE, apr 2006. doi:10.1109/IMTC.2006.328223.
- [Sau08] M. Saukoski. *System and Circuit Design for a Capacitive MEMS Gyroscope*. Ph. D. thesis, Helsinki University of Technology, 2008.
- [SE98] G. Scorletti and L. El Ghaoui. Improved linear matrix inequality conditions for gain scheduling. In *Proc. IEEE Conf. Decis. Control*, volume 4, pages 3626–3631, 1998.
- [SF09] G. Scorletti and V. Fromion. *Automatique fréquentielle avancée*. 2009. URL: <https://cel.archives-ouvertes.fr/cel-00423848v2>.
- [SFH15] G. Scorletti, V. Fromion, and S. D. Hillerin. Toward nonlinear tracking and rejection using LPV control. *IFAC-PapersOnLine*, 48(26):13–18, 2015. doi:10.1016/j.ifacol.2015.11.106.
- [Sha13] D. K. Shaeffer. MEMS inertial sensors: A tutorial overview. *IEEE Communications Magazine*, 51(4):100–109, apr 2013. doi:10.1109/MCOM.2013.6495768.
- [Shk06] A. M. Shkel. Type I and Type II Micromachined Vibratory Gyroscopes. In *IEEE/ION Position, Location and Navigation Symposium*, pages 586–593. IEEE, 2006. doi:10.1109/PLANS.2006.1650648.
- [SHS⁺99] A. M. Shkel, R. Horowitz, A. A. Seshia, S. Park, and R. T. Roger T. R. T. Howe. Dynamics and control of micromachined gyroscopes. In *American Control Conference*, volume 3, pages 2119–2124 vol.3. IEEE, 1999. doi:10.1109/ACC.1999.786303.
- [SKL08] W.-T. T. Sung, T. Kang, and J. G. Lee. Controller Design of a MEMS Gyro-Accelerometer with a Single Proof Mass. *International Journal of Control, Automation and Systems*, 6(6):873–883, 2008.
- [SKP⁺20] F. Saggini, A. Kornienko, G. Papin, E. Markiewicz, Y. David, A. El Hajj, and G. Scorletti. H_∞ Design of an EM- $\Sigma\Delta$ Feedback for MEMS Gyroscopes. In *2020 DGON Inertial Sensors and Systems (ISS)*, pages 1–20. IEEE, sep 2020. doi:10.1109/ISS50053.2020.9244916.
- [SLSK04] W.-T. Sung, J. G. Lee, J. W. Song, and T. Kang. \mathcal{H}_∞ controller design of MEMS gyroscope and its performance test. In *IEEE Position Location and Navigation Symposium*, pages 63–69. IEEE, 2004. doi:10.1109/PLANS.2004.1308975.
- [Som17] J. Sommeria. Foucault and the rotation of the Earth. *Comptes Rendus Physique*, 18(9-10):520–525, 2017. doi:10.1016/j.crhy.2017.11.003.
- [SP01] S. Skogestad and I. Postlethwaite. *Multivariable Feedback Control - Analysis and Design*. John Wiley & Sons, second edition, 2001.

- [SPK⁺21] F. Saggin, C. Pernin, A. Korniienko, G. Scorletti, and C. Le Blanc. Digital Control of MEMS Gyroscopes: a Robust Approach. In *IEEE International Symposium on Inertial Sensors and Systems (INERTIAL)*, pages 1–4. IEEE, mar 2021.
- [SSK20] F. Saggin, G. Scorletti, and A. Korniienko. A novel phasor control design method: application to MEMS gyroscopes. In *2020 American Control Conference (ACC)*, pages 3236–3241. IEEE, jul 2020. doi:10.23919/ACC45564.2020.9147797.
- [SSL⁺08] W.-T. Sung, S. Sung, J.-Y. Lee, T. Kang, Y. J. Lee, and J. G. Lee. Development of a lateral velocity-controlled MEMS vibratory gyroscope and its performance test. *Journal of Micromechanics and Microengineering*, 18(5):055028, may 2008. doi:10.1088/0960-1317/18/5/055028.
- [ST04] R. Schreier and G. C. Temes. *Understanding Delta-Sigma Data Converters*. IEEE Press, Hoboken, NJ, USA, apr 2004.
- [TBR17] O. Troeng, B. Bernhardsson, and C. Rivetta. Complex-coefficient systems in control. In *American Control Conference*, number 4, pages 1721–1727. IEEE, 2017. doi:10.23919/ACC.2017.7963201.
- [TMF17] E. Tatar, T. Mukherjee, and G. K. Fedder. Stress Effects and Compensation of Bias Drift in a MEMS Vibratory-Rate Gyroscope. *Journal of Microelectromechanical Systems*, 26(3):569–579, jun 2017. doi:10.1109/JMEMS.2017.2675452.
- [Tro19] Tronic’s Microsystems S.A. GYPRO2300 Datasheet MCD001-E, 2019. URL: https://www.tronicsgroup.com/IMG/pdf/mcd001-e_datasheet_dsg2300.pdf.
- [TWY17] Q. Tang, X. Wang, and Q. Yang. Scale factor model analysis of MEMS gyroscopes. *Microsystem Technologies*, 23(5):1215–1219, may 2017. doi:10.1007/s00542-016-2825-3.
- [Vak96] D. Vakman. On the analytic signal, the Teager-Kaiser energy algorithm, and other methods for defining amplitude and frequency. *IEEE Transactions on Signal Processing*, 44(4):791–797, 1996. doi:10.1109/78.492532.
- [Ven94] V. Venkatasubramanian. Tools for dynamic analysis of the general large power system using time-varying phasors. *International Journal of Electrical Power & Energy Systems*, 16(6):365–376, 1994. doi:10.1016/0142-0615(94)90023-X.
- [Vid02] M. Vidyasagar. *Nonlinear systems analysis*, volume 42. Siam, 2002.
- [VV77] D. E. Vakman and L. A. Vainshtein. Amplitude, phase, frequency—fundamental concepts of oscillation theory. *Soviet Physics Uspekhi*, 20(12):1002–1016, 1977. doi:10.1070/PU1977v020n12ABEH005479.
- [Wai18] S. Waitman. A piecewise-affine approach to nonlinear performance. 2018. URL: <https://tel.archives-ouvertes.fr/tel-01917511>.
- [Wan19] P. Wang. *Active vibration control in a specific zone of smart structures*. Ph. D. thesis, Université de Lyon, 2019.
- [Wil71] J. C. Willems. *The Analysis of Feedback Systems*. Graham Foundation/Mit Press Series in Contemporary Architect. MIT Press, 1971.

- [WK11] R. Wilcock and M. Kraft. Genetic algorithm for the design of electro-mechanical sigma delta modulator MEMS sensors. *Sensors*, 11(10):9217–9232, 2011. doi:10.3390/s111009217.
- [WSNS⁺16] S. Wisher, P. Shao, A. Norouzpour-Shirazi, Y. Yang, E. Ng, I. Flader, Y. Chen, D. Heinz, T. Kenny, and F. Ayazi. A high-frequency epitaxially encapsulated single-drive quad-mass tri-axial resonant tuning fork gyroscope. In *International Conference on Micro Electro Mechanical Systems (MEMS)*, volume 5, pages 930–933. IEEE, jan 2016. doi:10.1109/MEMSYS.2016.7421784.
- [XCWL09] D. Xia, S. Chen, S. Wang, and H. Li. Microgyroscope Temperature Effects and Compensation-Control Methods. *Sensors*, 9(12):8349–8376, oct 2009. doi:10.3390/s91008349.
- [YAN98] N. Yazdi, F. Ayazi, and K. Najafi. Micromachined inertial sensors. *Proceedings of the IEEE*, 86(8):1640–1659, 1998. doi:10.1109/5.704269.
- [YF13] W. Yan and J. Fei. Adaptive Control of MEMS Gyroscope Based on Global Terminal Sliding Mode Controller. *Mathematical Problems in Engineering*, 2013. doi:10.1155/2013/797626.
- [Yol20] Yole Développement (institution). Status of the MEMS Industry 2020: Market and Technology Report (Sample), jun 2020. URL: <https://s3.i-micronews.com/uploads/2020/07/YDR20104-Status-of-the-MEMS-Industry-2020-Sample-Yole-Développement.pdf>.
- [You11] M. I. Younis. *MEMS Linear and Nonlinear Statics and Dynamics*, volume 20 of *Microsystems*. Springer US, Boston, MA, 2011. doi:10.1007/978-1-4419-6020-7.
- [Zam81] G. Zames. Feedback and optimal sensitivity: Model reference transformations, multiplicative seminorms, and approximate inverses. *IEEE Transactions on Automatic Control*, 26(2):301–320, apr 1981. doi:10.1109/TAC.1981.1102603.
- [ZDG96] K. Zhou, J. C. Doyle, and K. Glover. *Robust and Optimal Control*. Prentice Hall, Englewood Cliffs, NJ, 1996.
- [ZH03] D. N. Zmood and D. G. Holmes. Stationary frame current regulation of PWM inverters with zero steady-state error. *IEEE Transactions on Power Electronics*, 18(3):814–822, may 2003. doi:10.1109/TPEL.2003.810852.
- [ZO12] C. Zhang and R. Ordóñez. *Extremum-Seeking Control and Applications: A Numerical Optimization-Based Approach*. Advances in Industrial Control. Springer London, London, 2012. doi:10.1007/978-1-4471-2224-1.
- [Zur15] Zurich Instruments. Control of MEMS Coriolis Vibratory Gyroscopes. Technical Report October, Zurich Instruments, 2015. URL: https://www.zhinst.com/sites/default/files/zi_appnote_mems_gyroscope.pdf.

Appendix A

Appendix of Chapter 2

A.1 Frequency-Domain Analysis of the Synchronous Demodulations

Here, in complement to the description of the synchronous demodulation given in Section 2.1.4, we make an analysis of the synchronous demodulation in the frequency domain. We recall its block diagram in Figure A.1.

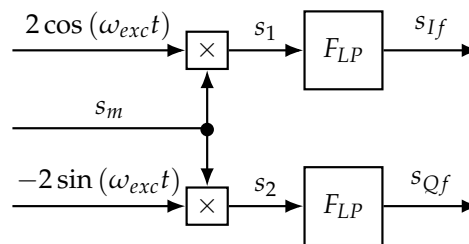


FIGURE A.1: Block diagram of the synchronous demodulator.

We consider the signal $s_m(t) \in \mathbb{R}$ of the form

$$s_m(t) = s_I(t) \cos(\omega_{exc} t) - s_Q(t) \sin(\omega_{exc} t) \quad (\text{A.1})$$

with $s_I(t) \in \mathbb{R}$ and $s_Q(t) \in \mathbb{R}$. With ω_{exc} constant, we can analyze the spectrum of the signals in each stage of the synchronous demodulator. Let the spectrum of s_I and s_Q be given by $\mathcal{F}[s_I]$ and $\mathcal{F}[s_Q]$. For the sake of illustration, we consider the spectra presented in Figure A.2. Moreover, s_I and s_Q are assumed to be bounded in frequency, that is, there exists a frequency ω_{max} such that

$$\forall |\omega| \geq \omega_{max}, \quad |\mathcal{F}[s_I](j\omega)| = 0 \quad \text{and} \quad |\mathcal{F}[s_Q](j\omega)| = 0.$$

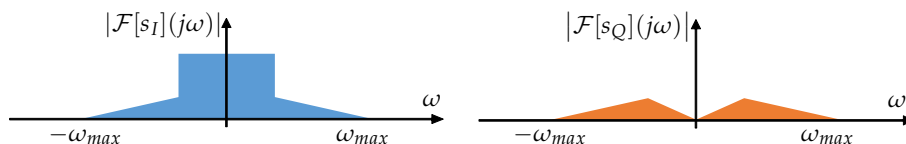
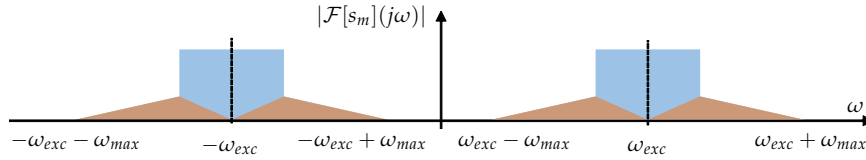


FIGURE A.2: Spectrum of the signals s_I and s_Q .

FIGURE A.3: Spectrum of the signals s_I and s_Q .

Based on (A.1), the spectrum of s_m is given by

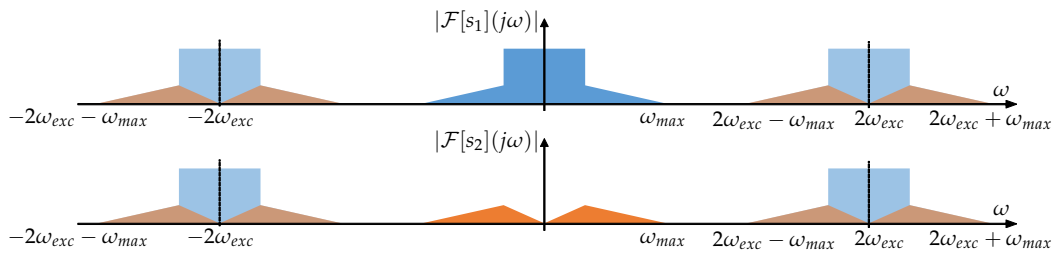
$$\begin{aligned}\mathcal{F}[s_m](j\omega) &= \mathcal{F}[s_I(\bullet) \cos(\omega_{exc}\bullet) - s_Q(\bullet) \sin(\omega_{exc}\bullet)](j\omega) \\ \mathcal{F}[s_m](j\omega) &= \mathcal{F}[s_I(\bullet) \cos(\omega_{exc}\bullet)](j\omega) - \mathcal{F}[s_Q(\bullet) \sin(\omega_{exc}\bullet)](j\omega) \\ \mathcal{F}[s_m](j\omega) &= \frac{1}{2} (\mathcal{F}[s_I](j\omega - j\omega_{exc}) + \mathcal{F}[s_I](j\omega + j\omega_{exc})) \\ &\quad + \frac{j}{2} (\mathcal{F}[s_Q](j\omega - j\omega_{exc}) - \mathcal{F}[s_Q](j\omega + j\omega_{exc})),\end{aligned}$$

as illustrated in Figure A.3.

The spectra of signals s_1 and s_2 are then given by

$$\begin{aligned}\mathcal{F}[s_1](j\omega) &= \mathcal{F}[s_I(\bullet) (1 + \cos(2\omega_{exc}\bullet)) - s_Q(\bullet) \sin(2\omega_{exc}\bullet)](j\omega) \\ \mathcal{F}[s_1](j\omega) &= \mathcal{F}[s_I](j\omega) + \mathcal{F}[s_I](j\omega + 2j\omega_{exc}) + \mathcal{F}[s_I](j\omega - 2j\omega_{exc}) \\ &\quad + j(\mathcal{F}[s_Q](j\omega + 2j\omega_{exc}) - \mathcal{F}[s_Q](j\omega - 2j\omega_{exc})) \\ \mathcal{F}[s_2](j\omega) &= \mathcal{F}[-s_I(\bullet) \sin(2\omega_{exc}\bullet) + s_Q(\bullet) (1 - \cos(2\omega_{exc}\bullet))](j\omega) \\ \mathcal{F}[s_2](j\omega) &= \mathcal{F}[s_Q](j\omega) - \mathcal{F}[s_2](j\omega + 2j\omega_{exc}) - \mathcal{F}[s_Q](j\omega - 2j\omega_{exc}) \\ &\quad - j(\mathcal{F}[s_I](j\omega + 2j\omega_{exc}) - \mathcal{F}[s_I](j\omega - 2j\omega_{exc}))\end{aligned}$$

and illustrated in Figure A.4. Thus, it is clear that, if $\omega_{max} < \omega_{exc}$, by filtering the high-frequency components out through ideal low-pass filters F_{LP} with cutoff frequency equal to ω_{exc} , $\mathcal{F}[s_{1f}] = \mathcal{F}[s_I]$ and $\mathcal{F}[s_{2f}] = \mathcal{F}[s_Q]$. If the condition $\omega_{max} < \omega_{exc}$ does not hold, then there is an overlap of the high and low-frequency terms, and $\mathcal{F}[s_{1f}] \neq \mathcal{F}[s_I]$ and $\mathcal{F}[s_{2f}] \neq \mathcal{F}[s_Q]$.

FIGURE A.4: Spectrum of the signals s_1 and s_2 .

A.2 On the Mechanical Model of the MEMS Gyroscope with Endogenous Forces

When the Coriolis and coupling forces are properly considered as endogenous signals, the mechanical part of the MEMS gyroscope (see (2.35)) is modeled as the linear time-varying

system (LTV) G^{mech, Ω_z} , which reads as

$$G^{mech, \Omega_z} : \begin{cases} \begin{bmatrix} \dot{q}(t) \\ \ddot{q}(t) \end{bmatrix} = \begin{bmatrix} 0 & I \\ -\mathbf{m}^{-1}\mathbf{k} & -\mathbf{m}^{-1}(\mathbf{d} - \tilde{C}_{Cor}(\Omega_z(t))) \end{bmatrix} \begin{bmatrix} q(t) \\ \dot{q}(t) \end{bmatrix} + \begin{bmatrix} 0 \\ I \end{bmatrix} F(t) \\ q(t) = [I \ 0] \begin{bmatrix} q(t) \\ \dot{q}(t) \end{bmatrix} \end{cases} \quad (\text{A.2})$$

with $q = \text{col}(x, y)$, $F = \text{col}(F_x, F_y)$, $\mathbf{m} = \text{diag}(m, m)$, $\mathbf{d} = \begin{bmatrix} d_{xx} & d_{xy} \\ d_{yx} & d_{yy} \end{bmatrix}$, $\mathbf{k} = \begin{bmatrix} k_{xx} & k_{xy} \\ k_{yx} & k_{yy} \end{bmatrix}$ and $\tilde{C}_{Cor}(\Omega_z(t)) = \Omega_z(t) \begin{bmatrix} 0 & 2m \\ -2m & 0 \end{bmatrix}$.

If we want to include the actuation and instrumentation gains, we have

$$G^{\Omega_z} : \begin{cases} \begin{bmatrix} \dot{q}(t) \\ \ddot{q}(t) \end{bmatrix} = \begin{bmatrix} 0 & I \\ -\mathbf{m}^{-1}\mathbf{k} & -\mathbf{m}^{-1}(\mathbf{d} - \tilde{C}_{Cor}(\Omega_z(t))) \end{bmatrix} \begin{bmatrix} q(t) \\ \dot{q}(t) \end{bmatrix} + \begin{bmatrix} 0 \\ k_{in} \end{bmatrix} u(t) \\ q_m(t) = [k_{out} \ 0] \begin{bmatrix} q(t) \\ \dot{q}(t) \end{bmatrix} \end{cases} \quad (\text{A.3})$$

with $q_m = \text{col}(x_m, y_m)$, $u = \text{col}(u_x, u_y)$, and the actuation and instrumentation gains, respectively $k_{in} = \text{diag}(k_{in,x}, k_{in,y})$ and $k_{out} = \text{diag}(k_{out,x}, k_{out,y})$.

Finally, G^{Ω_z} can be rewritten as the interconnection of the LTI system G

$$G : \begin{cases} \begin{bmatrix} \dot{q}(t) \\ \ddot{q}(t) \end{bmatrix} = \begin{bmatrix} 0 & I \\ -\mathbf{m}^{-1}\mathbf{k} & -\mathbf{m}^{-1}\mathbf{d} \end{bmatrix} \begin{bmatrix} q(t) \\ \dot{q}(t) \end{bmatrix} + \begin{bmatrix} 0 \\ k_{in} \end{bmatrix} (u(t) + u_{Cor}(t)) \\ q_m(t) = [k_{out} \ 0] \begin{bmatrix} q(t) \\ \dot{q}(t) \end{bmatrix} \end{cases} \quad (\text{A.4})$$

with $u_{Cor}(t) = C_{Cor}(\Omega_z(t)) q_m(t)$ and $C_{Cor}(\Omega_z(t)) = k_{in}^{-1} \tilde{C}_{Cor}(\Omega_z(t)) k_{out}^{-1}$, which reads as

$$C_{Cor}(\Omega_z(t)) = 2m\Omega_z(t) \begin{bmatrix} 0 & \frac{1}{k_{in,x}k_{out,y}} \\ \frac{-1}{k_{in,y}k_{out,x}} & 0 \end{bmatrix}. \quad (\text{A.5})$$

Appendix B

Appendix of Chapter 3

B.1 Noiseless Analysis

Here, we consider only the contributions of x_m^{ref} , $d_{Cor,x}$ and $d_{Cor,y}$ on the output signals of interest x_m , y_m and $\hat{u}_{Cor,y}$:

$$\begin{bmatrix} x_m(j\omega) \\ y_m(j\omega) \\ \hat{u}_{Cor,y}(j\omega) \end{bmatrix} = \begin{bmatrix} T_{x_m^{ref} \rightarrow x_m}(j\omega) & T_{d_{Cor,x} \rightarrow x_m}(j\omega) & T_{d_{Cor,y} \rightarrow x_m}(j\omega) \\ T_{x_m^{ref} \rightarrow y_m}(j\omega) & T_{d_{Cor,x} \rightarrow y_m}(j\omega) & T_{d_{Cor,y} \rightarrow y_m}(j\omega) \\ T_{x_m^{ref} \rightarrow \hat{u}_{Cor,y}}(j\omega) & T_{d_{Cor,x} \rightarrow \hat{u}_{Cor,y}}(j\omega) & T_{d_{Cor,y} \rightarrow \hat{u}_{Cor,y}}(j\omega) \end{bmatrix} \begin{bmatrix} x_m^{ref}(j\omega) \\ d_{Cor,x}(j\omega) \\ d_{Cor,y}(j\omega) \end{bmatrix}. \quad (\text{B.1})$$

B.1.1 Input Signals

The reference signal x_m^{ref} is given by (see (3.5))

$$x_m^{ref}(t) = A_{x,m}^{ref} \sin(\omega_{exc}t), \quad (\text{B.2})$$

or, in the frequency domain¹,

$$x_m^{ref}(j\omega) = jA_{x,m}^{ref} \frac{\delta(j\omega + j\omega_{exc}) - \delta(j\omega - j\omega_{exc})}{2} \quad (\text{B.3})$$

with δ being the Dirac delta function.

In its turn, the signal $d_{Cor,x}$, disturbing the drive mode, is given by (see (3.9))

$$d_{Cor,x}(t) = k_{ux} A_{y,m} \Omega_z(t) \cos(\omega_{exc}t), \quad (\text{B.4})$$

¹We recall that $2 \cos(\omega_{exc}t) = e^{j\omega_{exc}t} + e^{-j\omega_{exc}t}$ and the Fourier transform of $e^{j\omega_{exc}t}$ is given by

$$\mathcal{F} [e^{j\omega_{exc}\bullet}] (j\omega) = 2\pi\delta(j\omega - j\omega_{exc}).$$

where $A_{y,m} \in [0, \check{\xi}_y A_{x,m}^{ref}]$ and $k_{ux} = \frac{2m\omega_{exc}}{k_{out,y}k_{in,x}}$. In the frequency domain, it can be rewritten as²

$$d_{Cor,x}(j\omega) = k_{ux}A_{y,m} \cdot \Omega_z(\bullet) * \left(\frac{\delta(\bullet - j\omega_{exc}) + \delta(\bullet + j\omega_{exc})}{2} \right) (j\omega), \quad (\text{B.5})$$

where $*$ denotes the convolution product. Then, by developing the previous expression, we obtain

$$d_{Cor,x}(j\omega) = k_{ux}A_{y,m} \left(\frac{\Omega_z(j\omega - j\omega_{exc}) + \Omega_z(j\omega + j\omega_{exc})}{2} \right). \quad (\text{B.6})$$

Finally, the signal $d_{Cor,y}$, acting on the sense mode, is given by (see (3.10))

$$d_{Cor,y}(t) = \frac{k_{SF}A_{x,m}}{A_{x,m}^{ref}} \Omega_z(t) \cos(\omega_{exc}t), \quad (\text{B.7})$$

where $A_{x,m} \in [(1 - \check{\xi}_x) A_{x,m}^{ref}, (1 + \check{\xi}_x) A_{x,m}^{ref}]$ and $k_{SF} = \frac{-2mA_{x,m}^{ref}\omega_{exc}}{k_{out,y}k_{in,y}}$. In the frequency domain, (B.7) is written as

$$d_{Cor,y}(j\omega) = \frac{k_{SF}A_{x,m}}{A_{x,m}^{ref}} \cdot \Omega_z(\bullet) * \left(\frac{\delta(\bullet - j\omega_{exc}) + \delta(\bullet + j\omega_{exc})}{2} \right) (j\omega). \quad (\text{B.8})$$

Hence, we obtain

$$d_{Cor,y}(j\omega) = \frac{k_{SF}A_{x,m}}{A_{x,m}^{ref}} \left(\frac{\Omega_z(j\omega - j\omega_{exc}) + \Omega_z(j\omega + j\omega_{exc})}{2} \right). \quad (\text{B.9})$$

B.1.2 Output Signals

We can now determine the output signals of interest. From (B.1) and the expression of the input signals,

$$\begin{aligned} x_m(j\omega) &= A_{x,m}^{ref} \cdot T_{x_m^{ref} \rightarrow x_m}(j\omega) \left(\frac{\delta(j\omega - j\omega_{exc}) - \delta(j\omega + j\omega_{exc})}{j2} \right) \\ &\quad + k_{ux}A_{y,m} \cdot T_{d_{Cor,x} \rightarrow x_m}(j\omega) \left(\frac{\Omega_z(j\omega - j\omega_{exc}) + \Omega_z(j\omega + j\omega_{exc})}{2} \right) \\ &\quad + \frac{k_{SF}A_{x,m}}{A_{x,m}^{ref}} \cdot T_{d_{Cor,y} \rightarrow x_m}(j\omega) \left(\frac{\Omega_z(j\omega - j\omega_{exc}) + \Omega_z(j\omega + j\omega_{exc})}{2} \right) \end{aligned} \quad (\text{B.10})$$

or, equivalently,

$$\begin{aligned} x_m(j\omega) &= -A_{x,m}^{ref} \Im \left(T_{x_m^{ref} \rightarrow x_m}(j\omega_{exc}) \right) \\ &\quad + k_{ux}A_{y,m} \cdot T_{d_{Cor,x} \rightarrow x_m}(j\omega) \left(\frac{\Omega_z(j\omega - j\omega_{exc}) + \Omega_z(j\omega + j\omega_{exc})}{2} \right) \\ &\quad + \frac{k_{SF}A_{x,m}}{A_{x,m}^{ref}} \cdot T_{d_{Cor,y} \rightarrow x_m}(j\omega) \left(\frac{\Omega_z(j\omega - j\omega_{exc}) + \Omega_z(j\omega + j\omega_{exc})}{2} \right) \end{aligned} \quad (\text{B.11})$$

²Recalling that for two given signals g_1 and g_2 ,

$$\mathcal{F}[g_1 \cdot g_2](j\omega) = \frac{1}{2\pi} \mathcal{F}[g_1] * \mathcal{F}[g_2](j\omega).$$

The signal y_m is given, in the frequency domain, by

$$y_m(j\omega) = \left(T_{x_m^{ref} \rightarrow y_m}^{ref}(j\omega) \cdot x_m^{ref}(j\omega) + T_{d_{Cor,x} \rightarrow y_m}(j\omega) \cdot d_{Cor,x}(j\omega) + T_{d_{Cor,y} \rightarrow y_m}(j\omega) \cdot d_{Cor,y}(j\omega) \right). \quad (\text{B.12})$$

By replacing the input signal expressions into the above equation, we obtain

$$\begin{aligned} y_m(j\omega) = & jA_{x,m}^{ref} \cdot T_{x_m^{ref} \rightarrow y_m}^{ref}(j\omega) \left(\frac{\delta(j\omega + j\omega_{exc}) - \delta(j\omega - j\omega_{exc})}{2} \right) \\ & + k_{ux} A_{y,m} \cdot T_{d_{Cor,x} \rightarrow y_m}(j\omega) \left(\frac{\Omega_z(j\omega - j\omega_{exc}) + \Omega_z(j\omega + j\omega_{exc})}{2} \right) \\ & + \frac{k_{SF} A_{x,m}}{A_{x,m}^{ref}} \cdot T_{d_{Cor,y} \rightarrow y_m}(j\omega) \left(\frac{\Omega_z(j\omega - j\omega_{exc}) + \Omega_z(j\omega + j\omega_{exc})}{2} \right). \end{aligned} \quad (\text{B.13})$$

Similarly, the signal $\hat{u}_{Cor,y}$ is given by

$$\begin{aligned} \hat{u}_{Cor,y}(j\omega) = & jA_{x,m}^{ref} \cdot T_{x_m^{ref} \rightarrow \hat{u}_{Cor,y}}^{ref}(j\omega) \left(\frac{\delta(j\omega + j\omega_{exc}) - \delta(j\omega - j\omega_{exc})}{2} \right) \\ & + k_{ux} A_{y,m} \cdot T_{d_{Cor,x} \rightarrow \hat{u}_{Cor,y}}(j\omega) \left(\frac{\Omega_z(j\omega - j\omega_{exc}) + \Omega_z(j\omega + j\omega_{exc})}{2} \right) \\ & + \frac{k_{SF} A_{x,m}}{A_{x,m}^{ref}} \cdot T_{d_{Cor,y} \rightarrow \hat{u}_{Cor,y}}(j\omega) \left(\frac{\Omega_z(j\omega - j\omega_{exc}) + \Omega_z(j\omega + j\omega_{exc})}{2} \right). \end{aligned} \quad (\text{B.14})$$

B.1.3 Applying the Synchronous Demodulation

To obtain s_{If} , the synchronous demodulation is applied to $\hat{u}_{Cor,y}$, *i.e.*,

$$s_{If}(j\omega) = F_{LP}(j\omega) \cdot (\hat{u}_{Cor,y}(\bullet) * (\delta(\bullet - j\omega_{exc}) + \delta(\bullet + j\omega_{exc}))) (j\omega) \quad (\text{B.15})$$

$$s_{If}(j\omega) = F_{LP}(j\omega) \underbrace{(\hat{u}_{Cor,y}(j\omega - j\omega_{exc}) + \hat{u}_{Cor,y}(j\omega + j\omega_{exc}))}_{\mathcal{F}[s_1](j\omega)}. \quad (\text{B.16})$$

Now, we replace the expression of $\hat{u}_{Cor,y}$ (see (B.14)) into the above equation, obtaining

$$\begin{aligned} 2s_{If}(j\omega) = & F_{LP}(j\omega) \left(jA_{x,m}^{ref} \cdot T_{x_m^{ref} \rightarrow \hat{u}_{Cor,y}}^{ref}(j\omega - j\omega_{exc}) (\delta(j\omega) - \delta(j\omega - 2j\omega_{exc})) \right. \\ & + jA_{x,m}^{ref} \cdot T_{x_m^{ref} \rightarrow \hat{u}_{Cor,y}}^{ref}(j\omega + j\omega_{exc}) (\delta(j\omega + 2j\omega_{exc}) - \delta(j\omega)) \\ & + k_{ux} A_{y,m} \cdot T_{d_{Cor,x} \rightarrow \hat{u}_{Cor,y}}(j\omega - j\omega_{exc}) (\Omega_z(j\omega - 2j\omega_{exc}) + \Omega_z(j\omega)) \\ & + k_{ux} A_{x,m} \cdot T_{d_{Cor,x} \rightarrow \hat{u}_{Cor,y}}(j\omega + j\omega_{exc}) (\Omega_z(j\omega) + \Omega_z(j\omega + 2j\omega_{exc})) \\ & + \frac{k_{SF} A_{x,m}}{A_{x,m}^{ref}} \cdot T_{d_{Cor,y} \rightarrow \hat{u}_{Cor,y}}(j\omega - j\omega_{exc}) (\Omega_z(j\omega - 2j\omega_{exc}) + \Omega_z(j\omega)) \\ & \left. + \frac{k_{SF} A_{x,m}}{A_{x,m}^{ref}} \cdot T_{d_{Cor,y} \rightarrow \hat{u}_{Cor,y}}(j\omega + j\omega_{exc}) (\Omega_z(j\omega) + \Omega_z(j\omega + 2j\omega_{exc})) \right). \end{aligned} \quad (\text{B.17})$$

Since F_{LP} eliminates the high-frequency terms of s_1 (by Assumption 3.1, $\mathcal{F}[s_{If}](j\omega) = 0$ for $|\omega| \geq \omega_{exc}$) and, by Assumption 3.2, the bandwidth of Ω_z is smaller than ω_{exc} , we obtain

$$\begin{aligned} 2s_{If}(j\omega) &= jA_{x,m}^{ref} \left(T_{x_m^{ref} \rightarrow \hat{u}_{Cor,y}}(j\omega - j\omega_{exc}) - T_{x_m^{ref} \rightarrow \hat{u}_{Cor,y}}(j\omega + j\omega_{exc}) \right) \delta(j\omega) \\ &\quad + k_{ux} A_{y,m} \left(T_{d_{Cor,x} \rightarrow \hat{u}_{Cor,y}}(j\omega - j\omega_{exc}) + T_{d_{Cor,x} \rightarrow \hat{u}_{Cor,y}}(j\omega + j\omega_{exc}) \right) \Omega_z(j\omega) \\ &\quad + \frac{k_{SF} A_{x,m}}{A_{x,m}^{ref}} \left(T_{d_{Cor,y} \rightarrow \hat{u}_{Cor,y}}(j\omega - j\omega_{exc}) + T_{d_{Cor,y} \rightarrow \hat{u}_{Cor,y}}(j\omega + j\omega_{exc}) \right) \Omega_z(j\omega). \end{aligned} \quad (B.18)$$

Please note that the signal s_{If} can be slit into two terms:

$$s_{If}(j\omega) = s_{If}^L(j\omega) + s_{If}^0(j\omega), \quad (B.19)$$

where

$$\begin{aligned} s_{If}^L(j\omega) &= \left(\frac{k_{ux} A_{y,m}}{2} \left(T_{d_{Cor,x} \rightarrow \hat{u}_{Cor,y}}(j\omega - j\omega_{exc}) + T_{d_{Cor,x} \rightarrow \hat{u}_{Cor,y}}(j\omega + j\omega_{exc}) \right) \right. \\ &\quad \left. + \frac{k_{SF} A_{x,m}}{2A_{x,m}^{ref}} \left(T_{d_{Cor,y} \rightarrow \hat{u}_{Cor,y}}(j\omega - j\omega_{exc}) + T_{d_{Cor,y} \rightarrow \hat{u}_{Cor,y}}(j\omega + j\omega_{exc}) \right) \right) \Omega_z(j\omega) \end{aligned} \quad (B.20)$$

and

$$s_{If}^0(j\omega) = \frac{jA_{x,m}^{ref}}{2} \left(T_{x_m^{ref} \rightarrow \hat{u}_{Cor,y}}(j\omega - j\omega_{exc}) - T_{x_m^{ref} \rightarrow \hat{u}_{Cor,y}}(j\omega + j\omega_{exc}) \right) \delta(j\omega) \quad (B.21)$$

$$s_{If}^0(j\omega) = \frac{A_{x,m}^{ref}}{j2} \left(T_{x_m^{ref} \rightarrow \hat{u}_{Cor,y}}(j\omega_{exc}) - T_{x_m^{ref} \rightarrow \hat{u}_{Cor,y}}(-j\omega_{exc}) \right) \delta(j\omega) \quad (B.22)$$

$$s_{If}^0(j\omega) = A_{x,m}^{ref} \cdot \Im \left(T_{x_m^{ref} \rightarrow \hat{u}_{Cor,y}}(j\omega_{exc}) \right) \delta(j\omega). \quad (B.23)$$

Finally, we can rewrite (B.20) as

$$s_{If}^L(j\omega) = k_{SF} \cdot H_{gyro}(j\omega) \Omega_z(j\omega),$$

defining

$$\begin{aligned} H_{gyro}(j\omega) &= \frac{k_{ux} A_{y,m}}{2k_{SF}} \left(T_{d_{Cor,x} \rightarrow \hat{u}_{Cor,y}}(j\omega - j\omega_{exc}) + T_{d_{Cor,x} \rightarrow \hat{u}_{Cor,y}}(j\omega + j\omega_{exc}) \right) \\ &\quad + \frac{A_{x,m}}{2A_{x,m}^{ref}} \left(T_{d_{Cor,y} \rightarrow \hat{u}_{Cor,y}}(j\omega - j\omega_{exc}) + T_{d_{Cor,y} \rightarrow \hat{u}_{Cor,y}}(j\omega + j\omega_{exc}) \right) \end{aligned} \quad (B.24)$$

For the sake of completion, we can also compute the quadrature term s_{Qf} through the same procedure. To obtain s_{Qf} , the synchronous demodulation is applied to $\hat{u}_{Cor,y}$, i.e.,

$$s_{Qf}(j\omega) = jF_{LP}(j\omega) \cdot \left(\hat{u}_{Cor,y}(\bullet) * (\delta(\bullet - j\omega_{exc}) - \delta(\bullet + j\omega_{exc})) \right) (j\omega) \quad (B.25)$$

$$s_{Qf}(j\omega) = jF_{LP}(j\omega) \underbrace{\left(\hat{u}_{Cor,y}(j\omega - j\omega_{exc}) - \hat{u}_{Cor,y}(j\omega + j\omega_{exc}) \right)}_{\mathcal{F}[s_2](j\omega)}. \quad (B.26)$$

Then, we replace $\widehat{u}_{Cor,y}$ (see (B.14)) into the above equation, obtaining

$$\begin{aligned}
2s_{Qf}(j\omega) = & F_{LP}(j\omega) \left(-A_{x,m}^{ref} \cdot T_{x_m^{ref} \rightarrow \widehat{u}_{Cor,y}}(j\omega - j\omega_{exc}) (\delta(j\omega) - \delta(j\omega - 2j\omega_{exc})) \right. \\
& + A_{x,m}^{ref} \cdot T_{x_m^{ref} \rightarrow \widehat{u}_{Cor,y}}(j\omega + j\omega_{exc}) (\delta(j\omega + 2j\omega_{exc}) - \delta(j\omega)) \\
& + jk_{ux} A_{y,m} \cdot T_{d_{Cor,x} \rightarrow \widehat{u}_{Cor,y}}(j\omega - j\omega_{exc}) (\Omega_z(j\omega - 2j\omega_{exc}) + \Omega_z(j\omega)) \\
& - jk_{ux} A_{x,m} \cdot T_{d_{Cor,x} \rightarrow \widehat{u}_{Cor,y}}(j\omega + j\omega_{exc}) (\Omega_z(j\omega) + \Omega_z(j\omega + 2j\omega_{exc})) \\
& + j \frac{k_{SF} A_{x,m}}{A_{x,m}^{ref}} \cdot T_{d_{Cor,y} \rightarrow \widehat{u}_{Cor,y}}(j\omega - j\omega_{exc}) (\Omega_z(j\omega - 2j\omega_{exc}) + \Omega_z(j\omega)) \\
& \left. - j \frac{k_{SF} A_{x,m}}{A_{x,m}^{ref}} \cdot T_{d_{Cor,y} \rightarrow \widehat{u}_{Cor,y}}(j\omega + j\omega_{exc}) (\Omega_z(j\omega) + \Omega_z(j\omega + 2j\omega_{exc})) \right). \tag{B.27}
\end{aligned}$$

Since F_{LP} eliminates the high-frequency terms ($|\omega| \geq \omega_{exc}$) of s_2 , we obtain

$$\begin{aligned}
2s_{Qf}(j\omega) = & -A_{x,m}^{ref} \cdot \left(T_{x_m^{ref} \rightarrow \widehat{u}_{Cor,y}}(j\omega_{exc}) + T_{x_m^{ref} \rightarrow \widehat{u}_{Cor,y}}(-j\omega_{exc}) \right) \delta(j\omega) \\
& + jk_{ux} A_{y,m} \cdot \left(T_{d_{Cor,x} \rightarrow \widehat{u}_{Cor,y}}(j\omega - j\omega_{exc}) - T_{d_{Cor,x} \rightarrow \widehat{u}_{Cor,y}}(j\omega + j\omega_{exc}) \right) \Omega_z(j\omega) \\
& + j \frac{k_{SF} A_{x,m}}{A_{x,m}^{ref}} \cdot \left(T_{d_{Cor,y} \rightarrow \widehat{u}_{Cor,y}}(j\omega - j\omega_{exc}) - T_{d_{Cor,y} \rightarrow \widehat{u}_{Cor,y}}(j\omega + j\omega_{exc}) \right) \Omega_z(j\omega). \tag{B.28} \\
s_{Qf}(j\omega) = & -A_{x,m}^{ref} \cdot \Re \left(T_{x_m^{ref} \rightarrow \widehat{u}_{Cor,y}}(j\omega_{exc}) \right) \delta(j\omega) \\
& + j \frac{k_{ux} A_{y,m}}{2} \cdot \left(T_{d_{Cor,x} \rightarrow \widehat{u}_{Cor,y}}(j\omega - j\omega_{exc}) - T_{d_{Cor,x} \rightarrow \widehat{u}_{Cor,y}}(j\omega + j\omega_{exc}) \right) \Omega_z(j\omega) \\
& + j \frac{k_{SF} A_{x,m}}{2A_{x,m}^{ref}} \cdot \left(T_{d_{Cor,y} \rightarrow \widehat{u}_{Cor,y}}(j\omega - j\omega_{exc}) - T_{d_{Cor,y} \rightarrow \widehat{u}_{Cor,y}}(j\omega + j\omega_{exc}) \right) \Omega_z(j\omega). \tag{B.29}
\end{aligned}$$

For the particular case where $\Omega_z(t) \equiv \Omega_z^\infty$, s_{Qf} is a constant given by

$$\begin{aligned}
s_{Qf} = & -A_{x,m}^{ref} \cdot \Re \left(T_{x_m^{ref} \rightarrow \widehat{u}_{Cor,y}}(j\omega_{exc}) \right) \\
& + k_{ux} A_{y,m} \cdot \Im \left(T_{d_{Cor,x} \rightarrow \widehat{u}_{Cor,y}}(j\omega_{exc}) \right) \Omega_z^\infty \\
& + \frac{k_{SF} A_{x,m}}{A_{x,m}^{ref}} \cdot \Im \left(T_{d_{Cor,y} \rightarrow \widehat{u}_{Cor,y}}(j\omega_{exc}) \right) \Omega_z^\infty. \tag{B.30}
\end{aligned}$$

B.1.4 Compensating for the Scale Factor and Bias

We now apply the compensation function f_{comp} of (2.45) to (B.19), obtaining

$$\widehat{\Omega}_z(j\omega) = \Omega_z^L(j\omega) + \Omega_z^0(j\omega) \tag{B.31}$$

with $\Omega_z^L(j\omega) = k_{SF}/\widehat{k}_{SF} \cdot H_{gyro}(j\omega)\Omega_z(j\omega)$ and $\Omega_z^0(j\omega) = \varepsilon_{ZRO}\delta(j\omega)$. In this case, the error on the scale factor, ε_{SF} , is given by

$$\varepsilon_{SF} = \frac{k_{SF}}{\widehat{k}_{SF}} \cdot H_{gyro}(0) - 1 \tag{B.32}$$

and the residual bias error, ε_{ZRO} , is given by

$$\varepsilon_{ZRO} = \frac{A_{x,m}^{ref} \Im \left(T_{x_m^{ref} \rightarrow \widehat{u}_{Cor,y}}(j\omega_{exc}) \right) - \widehat{k}_{ZRO}}{\widehat{k}_{SF}}. \tag{B.33}$$

With the particular case of $\omega = 0$, we obtain the static gain of H_{gyro} (see (B.24)), which is given by

$$H_{gyro}(0) = \frac{k_{ux}A_{y,m}}{2k_{SF}} \left(T_{d_{Cor,x} \rightarrow \hat{u}_{Cor,y}}(-j\omega_{exc}) + T_{d_{Cor,x} \rightarrow \hat{u}_{Cor,y}}(j\omega_{exc}) \right) + \frac{A_{x,m}}{2A_{x,m}^{ref}} \left(T_{d_{Cor,y} \rightarrow \hat{u}_{Cor,y}}(-j\omega_{exc}) + T_{d_{Cor,y} \rightarrow \hat{u}_{Cor,y}}(j\omega_{exc}) \right) \quad (B.34)$$

$$H_{gyro}(0) = \frac{k_{ux}A_{y,m}}{k_{SF}} \Re \left(T_{d_{Cor,x} \rightarrow \hat{u}_{Cor,y}}(j\omega_{exc}) \right) + \frac{A_{x,m}}{A_{x,m}^{ref}} \Re \left(T_{d_{Cor,y} \rightarrow \hat{u}_{Cor,y}}(j\omega_{exc}) \right). \quad (B.35)$$

B.1.5 Analysis of the SFNL

The SFNL is defined as

$$\text{SFNL} \triangleq \max_{\Omega_z \in [-\Omega_z^{FS}, \Omega_z^{FS}]} \left(\frac{|\hat{\Omega}_z - \Omega_z|}{\Omega_z^{FS}} \right). \quad (B.36)$$

By replacing $\hat{\Omega}_z$ by $k_{SF}H_{gyro}(0)\Omega_z/\hat{k}_{SF}$ (see (B.31) with $\varepsilon_{ZRO} = 0$), we obtain

$$\text{SFNL} = \max_{\Omega_z \in [-\Omega_z^{FS}, \Omega_z^{FS}]} \left(\frac{|\Omega_z|}{\Omega_z^{FS}} \cdot \left| \frac{k_{SF}H_{gyro}(0) - \hat{k}_{SF}}{\hat{k}_{SF}} \right| \right). \quad (B.37)$$

Since the scale factor error ε_{SF} is defined as $\frac{k_{SF}H_{gyro}(0) - \hat{k}_{SF}}{\hat{k}_{SF}}$ (see (B.32)) and $|\Omega_z|/\Omega_z^{FS} \leq 1$, we can compute an upper bound on the SFNL, as follows:

$$\text{SFNL} \leq \max_{\Omega_z \in [-\Omega_z^{FS}, \Omega_z^{FS}]} (|\varepsilon_{SF}|). \quad (B.38)$$

To compute this upper bound, let us consider $\hat{k}_{SF} = k_{SF}$ and develop the expression of the scale factor relative error ε_{SF} (see (B.32) and (B.35)). Then, we obtain

$$\varepsilon_{SF} = \frac{k_{ux}A_{y,m}}{k_{SF}} \Re \left(T_{d_{Cor,x} \rightarrow \hat{u}_{Cor,y}}(j\omega_{exc}) \right) + \frac{A_{x,m}}{A_{x,m}^{ref}} \Re \left(T_{d_{Cor,y} \rightarrow \hat{u}_{Cor,y}}(j\omega_{exc}) \right) - 1. \quad (B.39)$$

We define $\varepsilon_{est} \triangleq d_{Cor,y} - \hat{u}_{Cor,y}$. Then, since $T_{d_{Cor,y} \rightarrow \varepsilon_{est}} = 1 - T_{d_{Cor,y} \rightarrow \hat{u}_{Cor,y}}$ and $T_{d_{Cor,x} \rightarrow \varepsilon_{est}} = -T_{d_{Cor,x} \rightarrow \hat{u}_{Cor,y}}$, we can rewrite ε_{SF} as

$$\varepsilon_{SF} = \frac{-k_{ux}A_{y,m}}{k_{SF}} \Re \left(T_{d_{Cor,x} \rightarrow \varepsilon_{est}}(j\omega_{exc}) \right) - \frac{A_{x,m}}{A_{x,m}^{ref}} \Re \left(T_{d_{Cor,y} \rightarrow \varepsilon_{est}}(j\omega_{exc}) \right) - 1 + \frac{A_{x,m}}{A_{x,m}^{ref}}. \quad (B.40)$$

Finally, if the objectives of reference tracking ($\check{\varepsilon}_x \ll 1 \implies A_{x,m} \approx A_{x,m}^{ref}$), disturbance rejection ($\check{\varepsilon}_y \ll 1 \implies A_{y,m} \ll 1$) and $|T_{d_{Cor,x} \rightarrow \varepsilon_{est}}(j\omega_{exc})| \ll 1$ are achieved, we can approximate the absolute value of ε_{SF} as

$$|\varepsilon_{SF}| \approx \left| \Re \left(T_{d_{Cor,y} \rightarrow \varepsilon_{est}}(j\omega_{exc}) \right) + 1 - \frac{A_{x,m}}{A_{x,m}^{ref}} \right| \quad (B.41)$$

and define the upper bound

$$|\varepsilon_{SF}| \leq \left| T_{d_{Cor,y} \rightarrow \varepsilon_{est}}(j\omega_{exc}) \right| + \check{\xi}_x. \quad (\text{B.42})$$

B.1.6 Analysis of the Bandwidth

The bandwidth is defined as the frequency ω_B such that

$$\forall |\omega| < \omega_B, \quad \left| 1 - \frac{H_{gyro}(j\omega)}{H_{gyro}(0)} \right| < 1 - \frac{\sqrt{2}}{2} \quad (\text{B.43})$$

with H_{gyro} given in (B.24). Then, we replace, in H_{gyro} , $T_{d_{Cor,x} \rightarrow \hat{u}_{Cor,y}}$ by $-T_{d_{Cor,x} \rightarrow \varepsilon_{est}}$ and $T_{d_{Cor,y} \rightarrow \hat{u}_{Cor,y}}$ by $1 - T_{d_{Cor,y} \rightarrow \varepsilon_{est}}$, obtaining

$$\begin{aligned} H_{gyro}(j\omega) &= \frac{-k_{ux}A_{y,m}}{2k_{SF}} (T_{d_{Cor,x} \rightarrow \varepsilon_{est}}(j\omega - j\omega_{exc}) + T_{d_{Cor,x} \rightarrow \varepsilon_{est}}(j\omega + j\omega_{exc})) \\ &\quad + \frac{A_{x,m}}{2A_{x,m}^{ref}} (2 - T_{d_{Cor,y} \rightarrow \varepsilon_{est}}(j\omega - j\omega_{exc}) - T_{d_{Cor,y} \rightarrow \varepsilon_{est}}(j\omega + j\omega_{exc})). \end{aligned} \quad (\text{B.44})$$

Now, if we have a good disturbance rejection (*i.e.*, $A_{y,m} \rightarrow 0$) and $|T_{d_{Cor,x} \rightarrow \varepsilon_{est}}(j\omega)| \ll 1$, we can approximate H_{gyro} as

$$H_{gyro}(j\omega) = \frac{A_{x,m}}{2A_{x,m}^{ref}} (2 - T_{d_{Cor,y} \rightarrow \varepsilon_{est}}(j\omega - j\omega_{exc}) - T_{d_{Cor,y} \rightarrow \varepsilon_{est}}(j\omega + j\omega_{exc})). \quad (\text{B.45})$$

Hence, the term on the left-hand side of (B.43) can be given by

$$\left| 1 - \frac{H_{gyro}(j\omega)}{H_{gyro}(0)} \right| = \left| 1 - \frac{2 - T_{d_{Cor,y} \rightarrow \varepsilon_{est}}(j\omega - j\omega_{exc}) - T_{d_{Cor,y} \rightarrow \varepsilon_{est}}(j\omega + j\omega_{exc})}{2 - 2\Re(T_{d_{Cor,y} \rightarrow \varepsilon_{est}}(j\omega_{exc}))} \right|. \quad (\text{B.46})$$

Since $\Re(T_{d_{Cor,y} \rightarrow \varepsilon_{est}}(j\omega_{exc})) \leq |T_{d_{Cor,y} \rightarrow \varepsilon_{est}}(j\omega_{exc})| < (1 - \lambda_{SFNL})k_{SFNL} \ll 1$, we can approximate

$$\left| 1 - \frac{H_{gyro}(j\omega)}{H_{gyro}(0)} \right| \approx \left| 1 - \frac{2 - T_{d_{Cor,y} \rightarrow \varepsilon_{est}}(j\omega - j\omega_{exc}) - T_{d_{Cor,y} \rightarrow \varepsilon_{est}}(j\omega + j\omega_{exc})}{2} \right| \quad (\text{B.47})$$

and define an upper bound,

$$\forall \omega \in \mathbb{R}, \quad \left| 1 - \frac{H_{gyro}(j\omega)}{H_{gyro}(0)} \right| \leq \left| \frac{T_{d_{Cor,y} \rightarrow \varepsilon_{est}}(j\omega - j\omega_{exc})}{2} \right| + \left| \frac{T_{d_{Cor,y} \rightarrow \varepsilon_{est}}(j\omega + j\omega_{exc})}{2} \right|.$$

Then, given $\omega_B^{\text{des}} \in \mathbb{R}_+$, if

$$\forall |\omega| < \omega_B^{\text{des}}, \quad \left| \frac{T_{d_{Cor,y} \rightarrow \varepsilon_{est}}(j\omega - j\omega_{exc})}{2} \right| + \left| \frac{T_{d_{Cor,y} \rightarrow \varepsilon_{est}}(j\omega + j\omega_{exc})}{2} \right| < 1 - \frac{\sqrt{2}}{2}, \quad (\text{B.48})$$

the condition (B.43) holds with $\omega_B \geq \omega_B^{\text{des}}$. Now, we consider the contributions of the two terms of the left-hand side to be equal, such that the

$$\forall |\omega| < \omega_B^{\text{des}}, \quad \left| T_{d_{Cor,y} \rightarrow \varepsilon_{est}}(j\omega - j\omega_{exc}) \right| < 1 - \frac{\sqrt{2}}{2} \quad \text{and} \quad \left| T_{d_{Cor,y} \rightarrow \varepsilon_{est}}(j\omega + j\omega_{exc}) \right| < 1 - \frac{\sqrt{2}}{2} \quad (\text{B.49})$$

implies (B.48) and also (B.43).

Finally, (B.49) can be rewritten as

$$\forall |\omega| \in [\omega_{exc} - \omega_B^{\text{des}}, \omega_{exc} + \omega_B^{\text{des}}], \quad \left| T_{d_{Cor,y} \rightarrow \varepsilon_{est}}(j\omega) \right| < \frac{2 - \sqrt{2}}{2} \approx 0.2929, \quad (\text{B.50})$$

defining a condition that implies a bandwidth ω_B larger than a given ω_B^{des} .

B.2 Analysis with Respect to Noise

Since e_x and e_y are assumed to be uncorrelated and with PSD equal to 1 (see Assumption 3.3, page 58), we can write the power spectral density of $\hat{u}_{Cor,y}$ as

$$\mathcal{S}_{\hat{u}_{Cor,y}}(\omega) = \left| T_{e_x \rightarrow \hat{u}_{Cor,y}}(j\omega) \right|^2 + \left| T_{e_y \rightarrow \hat{u}_{Cor,y}}(j\omega) \right|^2. \quad (\text{B.51})$$

If the controller is such that the specification (S4) (page 61) is verified, the $\hat{u}_{Cor,y}$ is a band-pass signal centered at ω_{exc} and of bandwidth smaller than $2\omega_{exc}$. Hence, after the synchronous demodulation, we obtain [Lat98, Sec. 11.5]

$$\mathcal{S}_{s_{If}}(\omega) = |F_{LP}(j\omega)|^2 \left(\mathcal{S}_{\hat{u}_{Cor,y}}(\omega + \omega_{exc}) + \mathcal{S}_{\hat{u}_{Cor,y}}(\omega - \omega_{exc}) \right), \quad (\text{B.52})$$

which, considering F_{LP} as an ideal low-pass filter with cutoff frequency $\omega_c = \omega_{exc}$, is equivalent to

$$\mathcal{S}_{s_{If}}(\omega) = \begin{cases} \mathcal{S}_{\hat{u}_{Cor,y}}(\omega + \omega_{exc}) + \mathcal{S}_{\hat{u}_{Cor,y}}(\omega - \omega_{exc}), & \forall |\omega| < \omega_{exc} \\ 0, & \text{otherwise.} \end{cases} \quad (\text{B.53})$$

We can now apply the compensation function f_{comp} (with $\hat{k}_{ZRO} = k_{ZRO}$), which gives

$$\hat{\Omega}_z(t) = s_{If}(t) / \hat{k}_{SF}. \quad (\text{B.54})$$

Finally, the PSD of $\hat{\Omega}_z$ is given by

$$\mathcal{S}_{\hat{\Omega}_z}(\omega) = \frac{\mathcal{S}_{s_{If}}(\omega)}{\left(\hat{k}_{SF} \right)^2} \quad (\text{B.55})$$

with $\mathcal{S}_{s_{If}}(\omega)$ given in (B.53).

Appendix C

Appendix of Chapter 4

C.1 Families of Weighting Functions

C.1.1 Amplification Weighting Function

This type of weighting function amplifies the signal around the frequency ω_0 and is defined as

$$W_{\text{amp}}(W_{\text{max}}, W_{\omega}, \omega_{\text{min}}, \omega_{\text{max}}, s) \triangleq \frac{s^2 + \alpha s + \omega_{\text{min}}\omega_{\text{max}}}{s^2 + \alpha/W_{\text{max}} \cdot s + \omega_{\text{min}}\omega_{\text{max}}} \quad (\text{C.1})$$

with

$$\alpha = (\omega_{\text{max}} - \omega_{\text{min}})W_{\text{max}} \sqrt{\frac{W_{\omega}^2 - 1}{W_{\text{max}}^2 - 1}},$$

where the parameters are represented in Figure C.1 et $\omega_0 = \sqrt{\omega_{\text{min}}\omega_{\text{max}}}$ [SF09]. Gains must be given in absolute value, not in decibel.

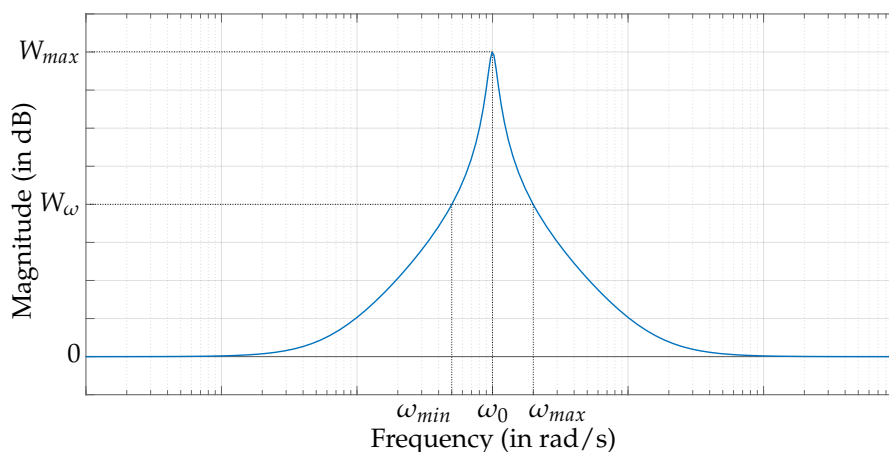


FIGURE C.1: Magnitude frequency response of $W_{\text{amp}}(W_{\text{max}}, W_{\omega}, \omega_{\text{min}}, \omega_{\text{max}}, s)$.

C.1.2 Attenuation Weighting Function

This type of weighting function attenuates the signal around the frequency ω_0 and is defined as

$$W_{\text{att}}(W_{\text{min}}, W_{\omega}, \omega_{\text{min}}, \omega_{\text{max}}, s) \triangleq \frac{s^2 + \beta W_{\text{min}}s + \omega_{\text{min}}\omega_{\text{max}}}{s^2 + \beta s + \omega_{\text{min}}\omega_{\text{max}}}, \quad (\text{C.2})$$

with

$$\beta = \frac{\omega_{max} - \omega_{min}}{W_\omega} \sqrt{\frac{1 - W_\omega^2}{1 - W_{min}^2}},$$

where the parameters are represented in Figure C.2 and $\omega_0 = \sqrt{\omega_{min}\omega_{max}}$ [SF09]. Gains must be given in absolute value, not in decibel.

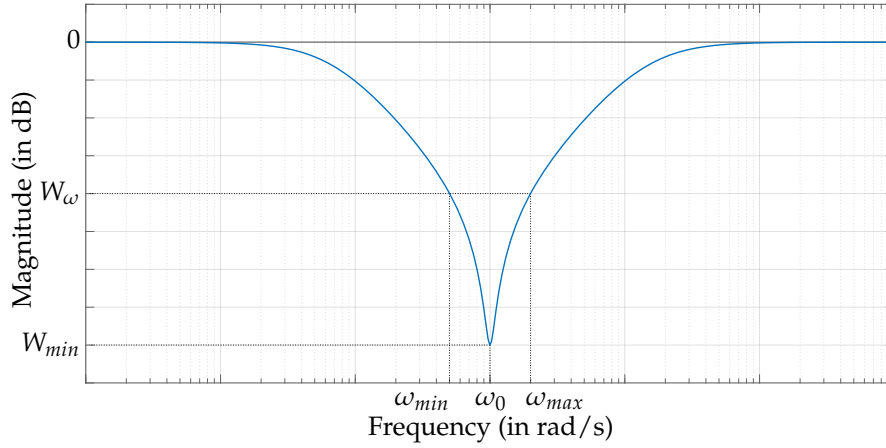


FIGURE C.2: Magnitude frequency response of $W_{att}(W_{min}, W_\omega, \omega_{min}, \omega_{max}, s)$.

C.2 Numerical Values of Example 4.2 – 1DoF Control of the Drive Mode

Normalized to-be-controlled plant (with $\Omega_z = 0$)

$$G_x(s) = \frac{2 \cdot 10^{-5}}{s^2 + 1 \cdot 10^{-5}s + 1}$$

Weighting functions

$$W_r(s) = \Delta M \cdot W_{amp} \left((\lambda_{SFNL} k_{SFNL} \Delta M)^{-1}, 0.25 (\lambda_{SFNL} k_{SFNL} \Delta M)^{-1}, \omega_{m\epsilon}, \omega_{m\epsilon}^{-1}, s \right)$$

$$W_d(s) = k_{x1}^{-1}$$

$$W_\epsilon(s) = 1$$

$$W_u(s) = 2500 \cdot W_{att} \left(4 \cdot 10^{-9}, 2.8 \cdot 10^{-4}, 0.5, 2, s \right)$$

with $\Delta M = 0.5$, $k_{SFNL} = 500 \cdot 10^{-6}$, $\lambda_{SFNL} = 0.5$, $\omega_{m\epsilon} = \frac{\omega_{exc} - 0.13}{\omega_{exc}}$ and $k_{x1} = 0.01$.

Controller

$$K_x(s) = \frac{0.49575(s - 0.998)(s + 1.867 \cdot 10^{-4})(s + 5357)(s^2 + 8.739 \cdot 10^{-6}s + 1)}{(s + 740.4)(s + 0.9991)(s^2 + 0.01698s + 1)(s^2 + 8.987 \cdot 10^{-7}s + 1)}$$

C.3 Numerical Values of Example 4.3 – 2DoF Control of the Drive Mode

Normalized to-be-controlled plant (with $\Omega_z = 0$)

$$G_x(s) = \frac{2 \cdot 10^{-5}}{s^2 + 1 \cdot 10^{-5}s + 1}$$

Weighting functions

$$W_r(s) = 0.5 \cdot W_{\text{amp}} \left(2 (\lambda_{\text{SFNL}} k_{\text{SFNL}})^{-1}, 0.5 (\lambda_{\text{SFNL}} k_{\text{SFNL}})^{-1}, \omega_{m\epsilon}, \omega_{m\epsilon}^{-1}, s \right)$$

$$W_d(s) = k_{x1}^{-1}$$

$$W_n(s) = 1 \cdot 10^4 \cdot W_{\text{att}} \left(1 \cdot 10^{-4}, 5 \cdot 10^{-2}, 0.5, 2, s \right)$$

$$W_e(s) = 1$$

$$W_u(s) = 1200 \cdot W_{\text{att}} \left(5 \cdot 10^{-8}, 2 \cdot 10^{-7}, 0.9, 0.9^{-1}, s \right)$$

with $k_{\text{SFNL}} = 500 \cdot 10^{-6}$, $\lambda_{\text{SFNL}} = 0.5$, $\omega_{m\epsilon} = \frac{\omega_{\text{exc}} - 0.13}{\omega_{\text{exc}}}$ and $k_{x1} = 0.01$.

Controller

$$K_{x1}(s) = \frac{0.010325(s+1.056 \cdot 10^6)(s-1.025)(s+9.474 \cdot 10^{-7})(s^2+0.006461s+1)(s^2+0.003543s+1)}{(s+12.45)(s+1.037)(s^2+0.105s+0.9308)(s^2+0.007197s+1)(s^2+0.105s+1.077)}$$

$$K_{x2}(s) = \frac{-1.0934 \cdot 10^{-6}(s+1.056 \cdot 10^6)(s+29.93)(s-1.024)(s+0.03341)(s+9.474 \cdot 10^{-7})(s^2+0.007197s+1)}{(s+12.45)(s+1.037)(s^2+0.105s+0.9308)(s^2+0.007197s+1)(s^2+0.105s+1.077)}$$

C.4 Numerical Values of Example 4.4 – 1DoF Control of the Sense Mode

Normalized to-be-controlled plant (with $\Omega_z = 0$)

$$G_y(s) = \frac{4.035 \cdot 10^{-3}}{s^2 + 1.004 \cdot 10^{-4}s + 1.009}$$

Weighting functions

$$W_d(s) = \Delta M \cdot W_{\text{amp}} \left((\lambda_{\text{SFNL}} k_{\text{SFNL}} \Delta M)^{-1}, (0.2929 \Delta M)^{-1}, \omega_{m\epsilon}, \omega_{m\epsilon}^{-1}, s \right)$$

$$W_n(s) = 180 \cdot W_{\text{att}} \left(5 \cdot 10^{-5}, 1 \cdot 10^{-4}, 0.92, 0.92^{-1}, s \right)$$

$$W_e(s) = 1$$

$$W_y(s) = 0.5$$

with $\Delta M = 0.5$, $k_{\text{SFNL}} = 500 \cdot 10^{-6}$, $\lambda_{\text{SFNL}} = 0.5$ and $\omega_{m\epsilon} = \frac{\omega_{\text{exc}} - \omega_B}{\omega_{\text{exc}}}$.

Controller

$$K_y(s) = \frac{6.284(s + 1670)(s - 0.9288)(s + 5.99 \cdot 10^{-4})(s^2 + 1.974 \cdot 10^{-3}s + 1.009)}{(s + 0.9007)(s + 1101)(s^2 + 2.963 \cdot 10^{-5}s + 1)(s^2 + 0.3668s + 1.04)}$$

C.5 Numerical Values of Example 4.5 – Multivariable Control (with

$$\hat{u}_{Cor,y} = -u_y)$$

Normalized to-be-controlled plant (with $\Omega_z = 0$)

$$G(s) = \begin{bmatrix} \frac{2 \cdot 10^{-5}}{s^2 + 1 \cdot 10^{-5}s + 1} & \frac{5.3302 \cdot 10^{-19}(s - 2.864 \cdot 10^9)}{(s^2 + 1 \cdot 10^{-5}s + 1)(s^2 + 1.004 \cdot 10^{-4}s + 1.009)} \\ \frac{8.2892 \cdot 10^{-20}(s - 5.581 \cdot 10^{10})}{(s^2 + 1 \cdot 10^{-5}s + 1)(s^2 + 1.004 \cdot 10^{-4}s + 1.009)} & \frac{4.035 \cdot 10^{-3}}{s^2 + 1.004 \cdot 10^{-4}s + 1.009} \end{bmatrix}$$

Weighting functions

$$W_{r1}(s) = 0.5 \cdot W_{amp} \left(2(\lambda_{SFNL} k_{SFNL})^{-1}, 0.5(\lambda_{SFNL} k_{SFNL})^{-1}, \omega_{mr1}, \omega_{mr1}^{-1}, s \right)$$

$$W_{d1}(s) = k_{x1}^{-1}$$

$$W_{d2}(s) = 0.5 \cdot W_{amp} \left(2((1 - \lambda_{SFNL})k_{SFNL})^{-1}, 2/0.2929, \omega_{md2}, \omega_{md2}^{-1}, s \right)$$

$$W_{n1}(s) = 1000 \cdot W_{att} \left(1 \cdot 10^{-4}, 5 \cdot 10^{-2}, 0.5, 2 \right)$$

$$W_{n2}(s) = 200 \cdot W_{att} \left(5 \cdot 10^{-5}, 1 \cdot 10^{-4}, 0.92, 0.92^{-1}, s \right)$$

$$W_{e1}(s) = 1$$

$$W_{e2}(s) = 0.015$$

$$W_{u1}(s) = 250 \cdot W_{att} \left(5 \cdot 10^{-7}, 5 \cdot 10^{-6}, 0.9, 0.9^{-1}, s \right)$$

$$W_{u2}(s) = 0.5 (W_{d2}(s))^{-1}$$

$$W_{est}(s) = 1$$

with $k_{SFNL} = 500 \cdot 10^{-6}$, $\lambda_{SFNL} = 0.5$, $\omega_{mr1} = \frac{\omega_{exc} - 0.13}{\omega_{exc}}$, $k_{x1} = 0.01$ and $\omega_{md2} = \frac{\omega_{exc} - \omega_B}{\omega_{exc}}$.

C.6 Numerical Values of Example 4.6 – Multivariable Control with Joint Estimation**Normalized to-be-controlled plant (with $\Omega_z = 0$)**

$$G(s) = \begin{bmatrix} \frac{2 \cdot 10^{-5}}{s^2 + 1 \cdot 10^{-5}s + 1} & \frac{5.3302 \cdot 10^{-19}(s - 2.864 \cdot 10^9)}{(s^2 + 1 \cdot 10^{-5}s + 1)(s^2 + 1.004 \cdot 10^{-4}s + 1.009)} \\ \frac{8.2892 \cdot 10^{-20}(s - 5.581 \cdot 10^{10})}{(s^2 + 1 \cdot 10^{-5}s + 1)(s^2 + 1.004 \cdot 10^{-4}s + 1.009)} & \frac{4.035 \cdot 10^{-3}}{s^2 + 1.004 \cdot 10^{-4}s + 1.009} \end{bmatrix}$$

Weighting functions

$$W_{r1}(s) = 0.5 \cdot W_{amp} \left(2(\lambda_{SFNL} k_{SFNL})^{-1}, 0.5(\lambda_{SFNL} k_{SFNL})^{-1}, \omega_{mr1}, \omega_{mr1}^{-1}, s \right)$$

$$W_{d1}(s) = k_{x1}^{-1}$$

$$W_{d2}(s) = 0.5 \cdot W_{\text{amp}} \left(2 / ((1 - \lambda_{\text{SFNL}}) k_{\text{SFNL}}), 2 / 0.2929, \omega_{md2}, \omega_{md2}^{-1}, s \right)$$

$$W_{n1}(s) = 0.5$$

$$W_{n2}(s) = 200 \cdot W_{\text{att}} \left(5 \cdot 10^{-5}, 1 \cdot 10^{-4}, 0.9, 0.9^{-1}, s \right)$$

$$W_{\varepsilon 1}(s) = 1$$

$$W_{\varepsilon 2}(s) = 0.5$$

$$W_{u1}(s) = 5 \cdot W_{\text{att}} \left(1 \cdot 10^{-4}, 5 \cdot 10^{-2}, 0.5, 0.5^{-1}, s \right)$$

$$W_{u2}(s) = 25 \cdot W_{\text{att}} \left(4 \cdot 10^{-8}, 2 \cdot 10^{-2}, 0.5, 0.5^{-1}, s \right)$$

$$W_{\text{est}}(s) = 1$$

with $k_{\text{SFNL}} = 500 \cdot 10^{-6}$, $\lambda_{\text{SFNL}} = 0.5$, $\omega_{mr1} = \frac{\omega_{\text{exc}} - 0.13}{\omega_{\text{exc}}}$, $k_{x1} = 0.01$ and $\omega_{md2} = \frac{\omega_{\text{exc}} - \omega_{\text{B}}}{\omega_{\text{exc}}}$.

C.7 Details of Section 4.4.1 – Quadratic Stability

Polytopic Model of the MEMS Gyroscope

The mechanical part of the MEMS gyroscopes can be modeled by $G^{\text{mech}, \Omega_z}$, see (A.2), recalled below

$$G^{\text{mech}, \Omega_z} : \begin{cases} \begin{bmatrix} \dot{q}(t) \\ \ddot{q}(t) \end{bmatrix} = \begin{bmatrix} 0 & I \\ -\mathbf{m}^{-1} \mathbf{k} & -\mathbf{m}^{-1} (\mathbf{d} - \tilde{\mathbf{C}}_{\text{Cor}}(\Omega_z(t))) \end{bmatrix} \begin{bmatrix} q(t) \\ \dot{q}(t) \end{bmatrix} + \begin{bmatrix} 0 \\ I \end{bmatrix} F(t) \\ q(t) = \begin{bmatrix} I & 0 \end{bmatrix} \begin{bmatrix} q(t) \\ \dot{q}(t) \end{bmatrix} \end{cases}, \quad (\text{C.3})$$

where $q = \text{col}(x, y)$, $u = \text{col}(u_x, u_y)$, $F = \text{col}(F_x, F_y)$, $\mathbf{m} = \text{diag}(m, m)$, $\mathbf{d} = \begin{bmatrix} d_{xx} & d_{xy} \\ d_{yx} & d_{yy} \end{bmatrix}$,

$\mathbf{k} = \begin{bmatrix} k_{xx} & k_{xy} \\ k_{yx} & k_{yy} \end{bmatrix}$ and $\tilde{\mathbf{C}}_{\text{Cor}}(\Omega_z(t)) = \Omega_z(t) \begin{bmatrix} 0 & 2m \\ -2m & 0 \end{bmatrix}$.

The actuation and instrumentation circuitry can be model through the constant gains $k_{in} = \text{diag}(k_{in,x}, k_{in,y})$ and $k_{out} = \text{diag}(k_{out,x}, k_{out,y})$, such that the whole gyroscope is modeled by $G^{\Omega_z} = k_{out} G^{\text{mech}, \Omega_z} k_{in}$, admitting the polytopic state-space representation below

$$G^{\Omega_z} : \begin{cases} \dot{x}_G(t) = A_G(\Omega_z(t)) x_G(t) + B_G u(t) \\ q_m(t) = C_G x_G(t) \end{cases}, \quad \Omega_z(t) \in [\Omega_{z,1}, \Omega_{z,2}], \quad (\text{C.4})$$

where $\Omega_{z,1} = -\Omega_z^{\text{FS}}$ and $\Omega_{z,2} = \Omega_z^{\text{FS}}$, $x_G = \text{col}(q, \dot{q})$, $u = \text{col}(u_x, u_y)$, $q_m = \text{col}(x_m, y_m)$,

$A_G(\Omega_z(t)) = \begin{bmatrix} 0 & I \\ -\mathbf{m}^{-1} \mathbf{k} & -\mathbf{m}^{-1} (\mathbf{d} - \tilde{\mathbf{C}}_{\text{Cor}}(\Omega_z(t))) \end{bmatrix}$, $B_G = \begin{bmatrix} 0 \\ k_{in} \end{bmatrix}$ and $C_G = [k_{out} \ 0]$.

$$B_K(\omega_{r,1}) = \begin{bmatrix} 17.71 & -11.58 \\ -25.13 & 11.58 \\ 0.07529 & -9.833 \cdot 10^{-6} \\ 48.42 & 0.2135 \\ -48.36 & -0.2141 \\ 0.2424 & -2.245 \cdot 10^{-5} \\ 16.47 & -1.228 \cdot 10^{-6} \\ 550.7 & -3.231 \cdot 10^{-5} \\ 407.5 & -3.5 \cdot 10^{-6} \\ -1.44 \cdot 10^4 & 0.0002209 \end{bmatrix}$$

$$C_K(\omega_{r,1}) = \begin{bmatrix} -5.852 \cdot 10^{-5} & -4.19 \cdot 10^{-5} & -10.28 & -0.006363 & -0.00452 & \dots \\ \dots & -4.365 & 0.01021 & 0.01449 & 0.00382 & 0.0005427 \end{bmatrix}$$

$$D_K(\omega_{r,1}) = [0 \ 0]$$

$$A_K(\omega_{r,2}) = \begin{bmatrix} -0.03095 & -0.969 & -0.0002696 & 0.0005702 & -0.000528 \\ 1.031 & -0.03106 & 0.0002546 & -0.000522 & 0.0005741 \\ -6.643 \cdot 10^{-6} & 8.029 \cdot 10^{-6} & -1.238 & -0.001521 & -0.0002638 \\ 0.1161 & -0.1161 & 5.031 \cdot 10^{-5} & -0.002144 & -0.998 \\ -0.1166 & 0.1166 & -0.001422 & 1.002 & -0.002157 \\ -9.316 \cdot 10^{-5} & 9.945 \cdot 10^{-5} & 0.4753 & 4.649 \cdot 10^{-5} & 0.0001141 \dots \\ -3.647 \cdot 10^{-5} & 3.646 \cdot 10^{-5} & 0.0002238 & 3.513 \cdot 10^{-7} & 3.525 \cdot 10^{-8} \\ -0.0009594 & 0.0009593 & -8.021 \cdot 10^{-5} & -9.163 \cdot 10^{-6} & -4.375 \cdot 10^{-6} \\ 0.01268 & -0.01268 & -0.03173 & -0.0002395 & 0.000238 \\ -0.5326 & 0.5327 & 0.1262 & 0.01052 & -0.009993 \\ \\ 0.001339 & -0.000288 & -0.009038 & -0.0007909 & 0.0009551 \\ -0.001402 & 0.0002247 & 0.007039 & 0.0008602 & 3.31 \cdot 10^{-5} \\ -6.489 & 0.07889 & 0.1242 & 7.803 & 100.7 \\ -0.005895 & -0.001187 & -0.03849 & 0.005812 & 0.06187 \\ -0.0008588 & 0.001261 & 0.03828 & 0.002435 & 0.04474 \\ \dots & -2.354 & 0.03897 & 0.05905 & 3.345 & 43.17 \\ -0.0001847 & -0.00048 & -1.012 & -0.01062 & -0.1366 \\ 0.0002712 & 0.986 & -0.4377 & -0.01651 & -0.1931 \\ 0.2058 & -0.01308 & -0.2395 & -0.6553 & -8.556 \\ 0.3981 & 0.3475 & 11.49 & 1.125 & -109.1 \end{bmatrix}$$

$$B_K(\omega_{r,2}) = \begin{bmatrix} 22.96 & -11.58 \\ -20.45 & 11.58 \\ -0.06965 & -9.833 \cdot 10^{-6} \\ 48.39 & 0.2135 \\ -47.96 & -0.2141 \\ 0.4613 & -2.245 \cdot 10^{-5} \\ 14.73 & -1.228 \cdot 10^{-6} \\ 551.2 & -3.231 \cdot 10^{-5} \\ 304.6 & -3.5 \cdot 10^{-6} \\ -1.463 \cdot 10^4 & 0.0002209 \end{bmatrix}$$

$$C_K(\omega_{r,2}) = \begin{bmatrix} -5.852 \cdot 10^{-5} & -4.19 \cdot 10^{-5} & -10.28 & -0.006363 & -0.00452 & \dots \\ \dots & -4.365 & 0.01021 & 0.01449 & 0.00382 & 0.0005427 \end{bmatrix}$$
$$D_K(\omega_{r,2}) = \begin{bmatrix} 0 & 0 \end{bmatrix}$$

Appendix E

Appendix of Chapter 6

E.1 Proof of Theorem 6.4

Proof. Please note that, by Definition 5.9 (page 130), for a given LPV system G^Θ (see (6.10), page 145) and $\gamma > 0$, $\|G^\Theta\|_{i_2}^q < \gamma$ if and only if, for all $\theta \in \Theta$, there exists a single symmetric matrix $X \succ 0$ such that (dropping the time dependence)

$$\begin{bmatrix} A(\theta)^\top X + XA(\theta) & XB(\theta) & C(\theta)^\top \\ B(\theta)^\top X & -\gamma I & D(\theta)^\top \\ C(\theta) & D(\theta) & -\gamma I \end{bmatrix} \prec 0. \quad (\text{E.1})$$

In its turn, being $G_{dp}^{\Theta, \Omega_{Ph}}$ the DPM of G^Θ for all $\omega_{Ph} \in \Omega_{Ph} [\omega_{Ph,1}, \omega_{Ph,2}]$, $\|G_{dp}^{\Theta, \Omega_{Ph}}\|_{i_2}^q < \gamma$ if and only if, for all $\theta \in \Theta$ and for all $\omega_{Ph} \in \Omega_{Ph} [\omega_{Ph,1}, \omega_{Ph,2}]$, there exists a single symmetric matrix $\underline{X} \succ 0$ such that

$$\begin{bmatrix} A_{dp}(\theta, \omega_{Ph})^\top \underline{X} + \underline{X}A_{dp}(\theta, \omega_{Ph}) & \underline{X}B_{dp}(\theta) & C_{dp}(\theta)^\top \\ B_{dp}(\theta)^\top \underline{X} & -\gamma I & D_{dp}(\theta)^\top \\ C_{dp}(\theta) & D_{dp}(\theta) & -\gamma I \end{bmatrix} \prec 0. \quad (\text{E.2})$$

We recall that

$$\left[\begin{array}{c|c} A_{dp}(\theta, \omega_{Ph}) & B_{dp}(\theta) \\ \hline C_{dp}(\theta) & D_{dp}(\theta) \end{array} \right] = \left[\begin{array}{cc|cc} A(\theta) & \omega_{Ph}I & B(\theta) & 0 \\ -\omega_{Ph}I & A(\theta) & 0 & B(\theta) \\ \hline C(\theta) & 0 & D(\theta) & 0 \\ 0 & C(\theta) & 0 & D(\theta) \end{array} \right]. \quad (\text{E.3})$$

($\exists X \Rightarrow \exists \underline{X}$) Let us assume that the LMI (E.1) admits a solution X for a given γ , implying that $\|G^\Theta\|_{i_2}^q < \gamma$. Then, we take this solution and build the matrix $\underline{X} = \text{diag}(X, X)$, which is solution of (E.2) since, after developing (E.2), the dependence on ω_{Ph} is canceled out, and we end up with (E.1) repeated twice in a block diagonal structure.

($\exists \tilde{X} \Rightarrow \exists X$) Now, let us assume that (E.2) admits a solution \tilde{X} for a given γ , implying that $\|G_{dp}^{\Theta, \Omega_{ph}}\|_{i2}^q < \gamma$. Then, by partitioning $\tilde{X} = \begin{bmatrix} X_1 & X_2 \\ X_2^\top & X_3 \end{bmatrix}$, the inequality (E.2) is rewritten as

$$\begin{bmatrix} \Pi_{X_1}(\theta, \omega_{ph}) & \Pi_{X_2}(\theta, \omega_{ph}) & X_1 B(\theta) & X_2 B(\theta) & C(\theta)^\top & 0 \\ \Pi_{X_2}(\theta, \omega_{ph})^\top & \Pi_{X_3}(\theta, \omega_{ph}) & X_2^\top B(\theta) & X_3 B(\theta) & 0 & C(\theta)^\top \\ \hline B(\theta)^\top X_1 & B(\theta)^\top X_2 & -\gamma I & 0 & D(\theta)^\top & 0 \\ B(\theta)^\top X_2^\top & B(\theta)^\top X_3 & 0 & -\gamma I & 0 & D(\theta)^\top \\ \hline C(\theta) & 0 & D(\theta) & 0 & -\gamma I & 0 \\ 0 & C(\theta) & 0 & D(\theta) & 0 & -\gamma I \end{bmatrix} \prec 0 \quad (\text{E.4})$$

with

$$\begin{aligned} \Pi_{X_1}(\theta, \omega_{ph}) &= A(\theta)^\top X_1 + \tilde{X}_1 A(\theta) - \omega_{ph}(X_2 + X_2^\top) \\ \Pi_{X_2}(\theta, \omega_{ph}) &= A(\theta)^\top X_2 + X_2 A(\theta) + \omega_{ph}(X_1 - X_3) \\ \Pi_{X_3}(\theta, \omega_{ph}) &= A(\theta)^\top X_3 + X_3 A(\theta) + \omega_{ph}(X_2 + X_2^\top) \end{aligned} .$$

By permuting the lines and columns of (E.4), we obtain

$$\begin{bmatrix} M_{X_1}(\theta, \omega_{ph}) & M_{X_2}(\theta, \omega_{ph}) \\ M_{X_2}(\theta, \omega_{ph})^\top & M_{X_3}(\theta, \omega_{ph}) \end{bmatrix} \prec 0 \quad (\text{E.5})$$

with

$$\begin{aligned} M_{X_1}(\theta, \omega_{ph}) &= \begin{bmatrix} \Pi_{X_1}(\theta, \omega_{ph}) & X_1 B(\theta) & C(\theta)^\top \\ B(\theta)^\top X_1 & -\gamma I & D(\theta)^\top \\ C(\theta) & D(\theta) & -\gamma I \end{bmatrix} \\ M_{X_2}(\theta, \omega_{ph}) &= \begin{bmatrix} \Pi_{X_2}(\theta, \omega_{ph}) & X_2 B(\theta) & 0 \\ B(\theta)^\top X_2 & 0 & 0 \\ 0 & 0 & 0 \end{bmatrix} \\ M_{X_3}(\theta, \omega_{ph}) &= \begin{bmatrix} \Pi_{X_3}(\theta, \omega_{ph}) & X_3 B(\theta) & C(\theta)^\top \\ B(\theta)^\top X_3 & -\gamma I & D(\theta)^\top \\ C(\theta) & D(\theta) & -\gamma I \end{bmatrix} . \end{aligned}$$

Since the matrix of (E.5) is negative definite, the sum of its main diagonal blocks is also negative definite, *i.e.*, $M_{X_1}(\theta, \omega_{ph}) + M_{X_3}(\theta, \omega_{ph}) \prec 0$. Note that when summing up M_{X_1} and M_{X_3} , ω_{ph} is canceled out. Therefore, by defining $\tilde{M}_X = \frac{1}{2}(M_{X_1} + M_{X_3})$ and $\tilde{X} = \frac{1}{2}(X_1 + X_3)$, we obtain

$$\tilde{M}_X = \begin{bmatrix} A(\theta)^\top \tilde{X} + \tilde{X} A(\theta) & \tilde{X} B(\theta) & C(\theta)^\top \\ B(\theta)^\top \tilde{X} & -\gamma I & D(\theta)^\top \\ C(\theta) & D(\theta) & -\gamma I \end{bmatrix} \prec 0.$$

This means that \tilde{X} is solution of the inequalities (E.1) of Theorem 6.4, concluding the proof. \square

E.2 Proof of Theorem 6.5

E.2.1 Proof or Property (i)

Proof. We prove that $(P^\Theta \star K^\Theta)_{dp}^{\Omega_{ph}} = \mathcal{P}_{dp}^{\Theta, \Omega_{ph}} \star K_{dp}^{\Theta, \Omega_{ph}}$ by writing the state-space representation of $(P^\Theta \star K^\Theta)_{dp}^{\Omega_{ph}}$ and $\mathcal{P}_{dp}^{\Theta, \Omega_{ph}} \star K_{dp}^{\Theta, \Omega_{ph}}$ from those of P^Θ and K^Θ , and by observing that

they are equal.

For all $\theta \in \Theta$, let P^Θ be given (see (5.50), page 131) by the matrices

$$\left[\begin{array}{c|cc} A_P(\theta) & B_P(\theta) & \\ \hline C_P(\theta) & D_P(\theta) & \end{array} \right] = \left[\begin{array}{c|cc} A_P(\theta) & B_w(\theta) & B_u \\ \hline C_z(\theta) & D_{zw}(\theta) & D_{zu} \\ C_y & D_{yw} & 0 \end{array} \right] \quad (\text{E.6})$$

and K^Θ (see (5.51), page 131) by

$$\left[\begin{array}{c|c} A_K(\theta) & B_K(\theta) \\ \hline C_K(\theta) & D_K(\theta) \end{array} \right]. \quad (\text{E.7})$$

Then, the closed-loop system $P^\Theta \star K^\Theta$ is given by the state-space matrices

$$\left[\begin{array}{c|cc} A_H(\theta) & B_H(\theta) & \\ \hline C_H(\theta) & D_H(\theta) & \end{array} \right] = \left[\begin{array}{cc|cc} A_P(\theta) + B_u D_K(\theta) C_y & B_u C_K(\theta) & B_w(\theta) + B_u D_K(\theta) D_{yw} & \\ B_K(\theta) C_y & A_K(\theta) & B_K(\theta) D_{yw} & \\ \hline C_z(\theta) + D_{zu} D_K(\theta) D_{yw} & D_{zu} C_K(\theta) & D_{zw}(\theta) + D_{zu} D_K(\theta) D_{yw} & \end{array} \right] \quad (\text{E.8})$$

and $(P^\Theta \star K^\Theta)_{dp}^{\Omega_{ph}}$ admits the following state-space matrices

$$\left[\begin{array}{c|cc} A_{H,dp}(\theta, \omega_{ph}) & B_{H,dp}(\theta) & \\ \hline C_{H,dp}(\theta) & D_{H,dp}(\theta) & \end{array} \right] = \left[\begin{array}{cc|cc} A_H(\theta) & \omega_{ph} I & B_H(\theta) & 0 \\ -\omega_{ph} I & A_H(\theta) & 0 & B_H(\theta) \\ \hline C_H(\theta) & 0 & D_H(\theta) & 0 \\ 0 & C_H(\theta) & 0 & D_H(\theta) \end{array} \right]. \quad (\text{E.9})$$

Let us now compute the state-space representation of $\mathcal{P}_{dp}^{\Theta, \Omega_{ph}} \star K_{dp}^{\Theta, \Omega_{ph}}$. From (E.6), $P_{dp}^{\Theta, \Omega_{ph}}$ is given by

$$\left[\begin{array}{c|cc} A_{P,dp}(\theta, \omega_{ph}) & B_{P,dp}(\theta) & \\ \hline C_{P,dp}(\theta) & D_{P,dp}(\theta) & \end{array} \right] = \left[\begin{array}{cc|cc} A_P(\theta) & \omega_{ph} I & B_P(\theta) & 0 \\ -\omega_{ph} I & A_P(\theta) & 0 & B_P(\theta) \\ \hline C_P(\theta) & 0 & D_P(\theta) & 0 \\ 0 & C_P(\theta) & 0 & D_P(\theta) \end{array} \right] \quad (\text{E.10})$$

and $\mathcal{P}_{dp}^{\Theta, \Omega_{ph}}$, defined as $\mathcal{P}_{dp}^{\Theta, \Omega_{ph}} \triangleq \mathcal{P}_{out} P_{dp}^{\Theta, \Omega_{ph}} \mathcal{P}_{in}$, admits the state-space matrices

$$\left[\begin{array}{c|ccc} A_{\mathcal{P},dp}(\theta, \omega_{ph}) & B_{w,dp}(\theta) & B_{u,dp} & \\ \hline C_{z,dp}(\theta) & D_{zw,dp}(\theta) & D_{zu,dp} & \\ C_{y,dp} & D_{yw,dp} & 0 & \end{array} \right] = \left[\begin{array}{cc|ccc} A_P(\theta) & \omega_{ph} I & B_w(\theta) & 0 & B_u & 0 \\ -\omega_{ph} I & A_P(\theta) & 0 & B_w(\theta) & 0 & B_u \\ \hline C_z(\theta) & 0 & D_{zw}(\theta) & 0 & D_{zu} & 0 \\ 0 & C_z(\theta) & 0 & D_{zw}(\theta) & 0 & D_{zu} \\ C_y & 0 & D_{yw} & 0 & 0 & 0 \\ 0 & C_y & 0 & D_{yw} & 0 & 0 \end{array} \right]. \quad (\text{E.11})$$

From (E.7), $K_{dp}^{\Theta, \Omega_{ph}}$ is given by the matrices

$$\left[\begin{array}{c|cc} A_{K,dp}(\theta, \omega_{ph}) & B_{K,dp}(\theta) & \\ \hline C_{K,dp}(\theta) & D_{K,dp}(\theta) & \end{array} \right] = \left[\begin{array}{cc|cc} A_K(\theta) & \omega_{ph} I & B_K(\theta) & 0 \\ -\omega_{ph} I & A_K(\theta) & 0 & B_K(\theta) \\ \hline C_K(\theta) & 0 & D_K(\theta) & 0 \\ 0 & C_K(\theta) & 0 & D_K(\theta) \end{array} \right] \quad (\text{E.12})$$

and $\mathcal{P}_{dp}^{\Theta, \Omega_{Ph}} \star K_{dp}^{\Theta, \Omega_{Ph}}$ is given by the matrices $\left[\begin{array}{c|c} A_{\tilde{H}, dp}(\theta, \omega_{Ph}) & B_{\tilde{H}, dp}(\theta) \\ \hline C_{\tilde{H}, dp}(\theta) & D_{\tilde{H}, dp}(\theta) \end{array} \right]$ with

$$\begin{aligned} A_{\tilde{H}, dp}(\theta, \omega_{Ph}) &= \begin{bmatrix} A_{\mathcal{P}, dp}(\theta, \omega_{Ph}) + B_{u, dp} D_{K, dp}(\theta) C_{y, dp} & B_{u, dp} C_{K, dp}(\theta) \\ B_{K, dp}(\theta) C_{y, dp} & A_{K, dp}(\theta, \omega_{Ph}) \end{bmatrix} \\ B_{\tilde{H}, dp}(\theta) &= \begin{bmatrix} B_{w, dp}(\theta) + B_{u, dp} D_{K, dp}(\theta) D_{yw, dp} \\ B_{K, dp}(\theta) D_{yw, dp} \end{bmatrix} \\ C_{\tilde{H}, dp}(\theta) &= [C_{z, dp}(\theta) + D_{zu, dp} D_{K, dp}(\theta) D_{yw, dp} \quad D_{zu, dp} C_{K, dp}(\theta)] \\ D_{\tilde{H}, dp}(\theta) &= [D_{zw, dp}(\theta) + D_{zu, dp} D_{K, dp}(\theta) D_{yw, dp}] \end{aligned} \quad (\text{E.13})$$

Finally, with a linear transformation, we have $A_{H, dp}(\theta, \omega_{Ph}) = \mathbf{T} A_{\tilde{H}, dp}(\theta, \omega_{Ph}) \mathbf{T}^{-1}$, $B_{H, dp}(\theta) = \mathbf{T} B_{\tilde{H}, dp}(\theta)$, $C_{H, dp}(\theta) = C_{\tilde{H}, dp}(\theta) \mathbf{T}^{-1}$ and $D_{H, dp}(\theta) = D_{\tilde{H}, dp}(\theta)$, where

$$\mathbf{T} = \mathbf{T}^{-1} = \begin{bmatrix} I_n & 0 & 0 & 0 \\ 0 & 0 & I_n & 0 \\ 0 & I_n & 0 & 0 \\ 0 & 0 & 0 & I_n \end{bmatrix},$$

completing the proof. \square

E.2.2 Proof or Property (ii)

Proof. This proof is simple and follows directly from Property (i), which states that

$$(P^{\Theta} \star K^{\Theta})_{dp}^{\Omega_{Ph}} = \mathcal{P}_{dp}^{\Theta, \Omega_{Ph}} \star K_{dp}^{\Theta, \Omega_{Ph}},$$

and from Theorem 6.4, which gives $\|P^{\Theta} \star K^{\Theta}\|_{i2}^q = \left\| (\mathcal{P}_{dp}^{\Theta, \Omega_{Ph}} \star K_{dp}^{\Theta, \Omega_{Ph}}) \right\|_{i2}^q$. \square

E.2.3 Proof or Property (iii)

Proof. Please note that, by Theorem 5.2 (page 131), the existence of a controller K^{Θ} such that $\|P^{\Theta} \star K^{\Theta}\|_{i2}^q < \gamma$ for all trajectories of $\theta(t)$ in the polytope Θ of N_{θ} vertices θ_i is equivalent to the existence of the matrices $R = R^{\top}$ and $S = S^{\top}$ such that, for all $i \in \{1, \dots, N_{\theta}\}$,

$$[\diamond]_{\perp}^{\top} \begin{bmatrix} S A_{P, i}^{\top} + A_{P, i} S & B_{w, i} & S C_{z, i}^{\top} \\ B_{w, i}^{\top} & -\gamma I & D_{zw, i}^{\top} \\ C_{z, i} S & D_{zw, i} & -\gamma I \end{bmatrix} [B_u^{\top} \quad 0 \quad D_{zu}^{\top}]_{\perp} \prec 0, \quad (\text{E.14})$$

$$[\diamond]_{\perp}^{\top} \begin{bmatrix} A_{P, i}^{\top} R + R A_{P, i} & R B_{w, i} & C_{z, i}^{\top} \\ B_{w, i}^{\top} R & -\gamma I & D_{zw, i}^{\top} \\ C_{z, i} & D_{zw, i} & -\gamma I \end{bmatrix} [C_y \quad D_{yw} \quad 0]_{\perp} \prec 0 \quad (\text{E.15})$$

$$\text{and} \quad \begin{bmatrix} R & I \\ I & S \end{bmatrix} \succ 0 \quad (\text{E.16})$$

with $\begin{bmatrix} A_{P, i} & B_{w, i} \\ C_{z, i} & D_{zw, i} \end{bmatrix} = \begin{bmatrix} A_P(\theta_i) & B_w(\theta_i) \\ C_z(\theta_i) & D_{zw}(\theta_i) \end{bmatrix}$.

In its turn, again by Theorem 5.2, the existence of \underline{K}^{Θ} such that $\left\| \mathcal{P}_{dp}^{\Theta, \Omega_{Ph}} \star \underline{K}_{dp}^{\Theta, \Omega_{Ph}} \right\|_{i2}^q < \gamma$ is equivalent to the existence of matrices $\underline{R} = \underline{R}^{\top}$ and $\underline{S} = \underline{S}^{\top}$ such that, for all $\omega_{Ph} \in$

$\Omega_{Ph}[\omega_{Ph,1}, \omega_{Ph,2}]$ and for all $i \in \{1, \dots, N_\theta\}$,

$$[\diamond]_{\perp}^{\top} \begin{bmatrix} \mathfrak{S}A_{P,dp,i}(\omega_{Ph})^{\top} + A_{P,dp,i}(\omega_{Ph})\mathfrak{S} & B_{w,dp,i} & \mathfrak{S}C_{z,dp,i}^{\top} \\ B_{w,dp,i}^{\top} & -\gamma I & D_{zw,dp,i}^{\top} \\ C_{z,dp,i}\mathfrak{S} & D_{zw,dp,i} & -\gamma I \end{bmatrix} \begin{bmatrix} B_{u,dp}^{\top} & 0 & D_{zu,dp}^{\top} \end{bmatrix}_{\perp} \prec 0, \quad (\text{E.17})$$

$$[\diamond]_{\perp}^{\top} \begin{bmatrix} A_{P,dp,i}(\omega_{Ph})^{\top} \mathfrak{R} + \mathfrak{R}A_{P,dp,i}(\omega_{Ph}) & \mathfrak{R}B_{w,dp,i} & C_{z,dp,i}^{\top} \\ B_{w,dp,i}^{\top} \mathfrak{R} & -\gamma I & D_{zw,dp,i}^{\top} \\ C_{z,dp,i} & D_{zw,dp,i} & -\gamma I \end{bmatrix} \begin{bmatrix} C_{y,dp} & D_{yw,dp} & 0 \end{bmatrix}_{\perp} \prec 0 \quad (\text{E.18})$$

$$\text{and } \begin{bmatrix} \mathfrak{R} & I \\ I & \mathfrak{S} \end{bmatrix} \succ 0. \quad (\text{E.19})$$

For completeness, we recall that

$$\left[\begin{array}{c|c|c} A_{P,dp,i}(\omega_{Ph}) & B_{w,dp,i} & B_{u,dp} \\ \hline C_{z,dp,i} & D_{zw,dp,i} & D_{zu,dp} \\ \hline C_{y,dp} & D_{yw,dp} & 0 \end{array} \right] = \left[\begin{array}{cc|cc|cc} A_{P,i} & \omega_{Ph}I & B_{w,i} & 0 & B_u & 0 \\ -\omega_{Ph,i}I & A_{P,i} & 0 & B_{w,i} & 0 & B_u \\ \hline C_{z,i} & 0 & D_{zw,i} & 0 & D_{zu} & 0 \\ 0 & C_{z,i} & 0 & D_{zw,i} & 0 & D_{zu} \\ \hline C_y & 0 & D_{yw} & 0 & 0 & 0 \\ 0 & C_y & 0 & D_{yw} & 0 & 0 \end{array} \right] \quad (\text{E.20})$$

and $A_{P,i} = A_P(\theta_i)$, $B_{w,i} = B_w(\theta_i)$, $C_{z,i} = C_z(\theta_i)$, $D_{zw,i} = D_{zw}(\theta_i)$.

($\exists K^{\ominus} \Rightarrow \exists \underline{K}^{\ominus, \Omega_{Ph}}$) Let us assume that there exists K^{\ominus} such that $\|P^{\ominus} \star K^{\ominus}\|_{i2}^q < \gamma$. Then, we take the solutions of (E.14), (E.15) and (E.16), and build the matrices $\underline{\mathfrak{S}} = \text{diag}(S, S)$ and $\underline{\mathfrak{R}} = \text{diag}(R, R)$. These matrices are solution of (E.17), (E.18) and (E.19) since, after developing (E.17) and (E.18), the dependence on ω_{Ph} (off-diagonal terms of $A_{P,dp,i}$) is canceled out, and we end up with the equations (E.14)–(E.16) repeated in a block diagonal structure.

($\exists \underline{K}^{\ominus, \Omega_{Ph}} \Rightarrow \exists K^{\ominus}$) Now, assume that there exists $\underline{K}^{\ominus, \Omega_{Ph}}$ such that $\|\mathcal{P}_{dp}^{\ominus, \Omega_{Ph}} \star \underline{K}^{\ominus, \Omega_{Ph}}\|_{i2}^q < \gamma$. By partitioning

$$\underline{\mathfrak{S}} = \begin{bmatrix} S_1 & S_2 \\ S_2^{\top} & S_3 \end{bmatrix},$$

the inequality (E.17) can be rewritten as

$$\mathcal{N}^{\top} \left[\begin{array}{cc|cc|cc} \Pi_{S1,i} & \Pi_{S2,i} & B_{w,i} & 0 & S_1 C_{z,i}^{\top} & S_2 C_{z,i}^{\top} \\ \Pi_{S2,i}^{\top} & \Pi_{S3,i} & 0 & B_{w,i} & S_2^{\top} C_{z,i}^{\top} & S_3 C_{z,i}^{\top} \\ \hline B_{w,i}^{\top} & 0 & -\gamma I & 0 & D_{zw,i}^{\top} & 0 \\ 0 & B_{w,i}^{\top} & 0 & -\gamma I & 0 & D_{zw,i}^{\top} \\ \hline C_{z,i} S_1 & C_{z,i} S_2 & D_{zw,i} & 0 & -\gamma I & 0 \\ C_{z,i} S_2^{\top} & C_{z,i} S_3 & 0 & D_{zw,i} & 0 & -\gamma I \end{array} \right] \mathcal{N} \prec 0 \quad (\text{E.21})$$

with

$$\begin{aligned} \Pi_{S1,i} &= A_{P,i} S_1 + S_1 A_{P,i}^{\top} + \omega_{Ph} (S_2 + S_2^{\top}) \\ \Pi_{S2,i} &= A_{P,i} S_2 + S_2 A_{P,i}^{\top} + \omega_{Ph} (-S_1 + S_3) \\ \Pi_{S3,i} &= A_{P,i} S_3 + S_3 A_{P,i}^{\top} - \omega_{Ph} (S_2 + S_2^{\top}) \\ \mathcal{N} &= \begin{bmatrix} B_u^{\top} & 0 & 0 & 0 & D_{zu}^{\top} & 0 \\ 0 & B_u^{\top} & 0 & 0 & 0 & D_{zu}^{\top} \end{bmatrix}_{\perp}. \end{aligned}$$

Then, by permuting the rows and columns of (E.21), it is rewritten as

$$\begin{bmatrix} \mathcal{N}_B^\top M_{S1,i} \mathcal{N}_B & \mathcal{N}_B^\top M_{S2,i} \mathcal{N}_B \\ \mathcal{N}_B^\top M_{S2,i} \mathcal{N}_B & \mathcal{N}_B^\top M_{S3,i} \mathcal{N}_B \end{bmatrix} \prec 0 \quad (\text{E.22})$$

with

$$\begin{aligned} \mathcal{N}_B &= [B_u^\top \quad 0 \quad D_{zu}^\top]_\perp \\ M_{S1,i} &= \begin{bmatrix} \Pi_{S1,i} & B_{w,i} & S_1 C_{z,i}^\top \\ B_{w,i}^\top & -\gamma I & D_{zw,i}^\top \\ C_{z,i} S_1 & D_{zw,i} & -\gamma I \end{bmatrix} \\ M_{S2,i} &= \begin{bmatrix} \Pi_{S2,i} & 0 & S_2 C_{z,i}^\top \\ 0 & 0 & 0 \\ C_{z,i} S_2 & 0 & 0 \end{bmatrix} \\ M_{S3,i} &= \begin{bmatrix} \Pi_{S3,i} & B_{w,i} & S_3 C_{z,i}^\top \\ B_{w,i}^\top & -\gamma I & D_{zw,i}^\top \\ C_{z,i} S_3 & D_{zw,i} & -\gamma I \end{bmatrix}. \end{aligned}$$

Since the matrix of (E.22) is negative definite, the sum of its main diagonal blocks is also negative definite, *i.e.*,

$$\mathcal{N}_B^\top (M_{S1,i} + M_{S3,i}) \mathcal{N}_B \prec 0.$$

Thus, we also have

$$\mathcal{N}_B^\top \tilde{M}_{S,i} \mathcal{N}_B \prec 0$$

with $\tilde{M}_{S,i} = \frac{1}{2} (M_{S1,i} + M_{S3,i})$. If we apply the same procedure to (E.18) and (E.19), we finally obtain

$$\mathcal{N}_B^\top \tilde{M}_{S,i} \mathcal{N}_B \prec 0$$

$$\mathcal{N}_C^\top \tilde{M}_{R,i} \mathcal{N}_C \prec 0$$

$$\begin{bmatrix} \tilde{R} & I \\ I & \tilde{S} \end{bmatrix} \succ 0$$

with

$$\begin{aligned} \mathcal{N}_C &= [C_y \quad D_{yw} \quad 0]_\perp \\ \tilde{R} &= \frac{1}{2} (R_1 + R_3) \\ \tilde{S} &= \frac{1}{2} (S_1 + S_3) \\ \tilde{M}_{R,i} &= \begin{bmatrix} A_{P,i}^\top \tilde{R} + \tilde{R} A_{P,i} & \tilde{R} B_{w,i} & C_{z,i}^\top \\ B_{w,i}^\top \tilde{R} & -\gamma I & D_{zw,i}^\top \\ C_{z,i} & D_{zw,i} & -\gamma I \end{bmatrix} \\ \tilde{M}_{S,i} &= \begin{bmatrix} \tilde{S} A_{P,i}^\top + A_{P,i} \tilde{S} & B_{w,i} & \tilde{S} C_{z,i}^\top \\ B_{w,i}^\top \tilde{S} & -\gamma I & D_{zw,i}^\top \\ C_{z,i} \tilde{S} & D_{zw,i} & -\gamma I \end{bmatrix} \end{aligned}$$

This means that \tilde{R} and \tilde{S} are solution of the inequalities (5.53)–(5.55) of Theorem 5.2 (page 131). Hence, this theorem ensures that there exists a controller K^\ominus for P^\ominus defined in (5.50), such that $\|P \star K\|_{i2}^q < \gamma$. \square

E.3 Details of Example 6.6 – Nonideal Phasor Controller

To-be-controlled plant

The original to-be-controlled plant G admits the state-space representation with the matrices

$$A = \begin{bmatrix} 0 & 1 \\ -\omega_{0,x}^2 & -\omega_{0,x}/Q_x \end{bmatrix}, \quad B = \begin{bmatrix} 0 \\ k_{0,x}\omega_{0,x} \end{bmatrix}, \quad C = [1 \ 0] \quad \text{and} \quad D = 0$$

with $\omega_{0,x} = 2\pi 11500 \text{ rad s}^{-1}$, $Q_x = 100\,000$ and $k_{0,x} = 2 \cdot 10^{-5}$.

Its dynamic phasor model G_{dp} , which is considered for the controller design, admits the state-space representation with the matrices

$$A_{dp}(\omega_{ph}(t)) = \begin{bmatrix} A & \omega_{ph}(t)I \\ -\omega_{ph}(t)I & A \end{bmatrix},$$

$B_{dp} = \text{diag}(B, B)$, $C_{dp} = \text{diag}(C, C)$, $D_{dp} = \text{diag}(D, D)$ and $\omega_{ph}(t) = \omega_{ph}^\infty = \omega_{0,x}$.

Weighting functions

$$W_r(s) = \frac{\frac{1}{M_r}s + \omega_r}{s + \omega_r A_r}$$

$$W_d(s) = 0.4$$

$$W_n(s) = 1$$

$$W_\varepsilon(s) = 1$$

$$W_u(s) = \frac{s + \omega_u A_u}{\frac{1}{M_u}s + \omega_u}$$

with $A_r = k_{\text{SFNL}} \lambda_{\text{SFNL}} / \sqrt{2}$, $\omega_r = 9.2 \text{ rad s}^{-1}$, $M_r = 2$, $A_u = 1.25 \cdot 10^{-4}$, $\omega_u = 290 \text{ rad s}^{-1}$, $M_u = 750$, $k_{\text{SFNL}} = 500 \cdot 10^{-6}$ and $\lambda_{\text{SFNL}} = 0.5$.

Appendix F

Appendix of Chapter 7

F.1 On the Unstable Zeros of a PCT Model

Let a DT system G^d be defined by the state-space matrices (A^d, B^d, C^d, D^d) and with sampling period T_s . Its PCT equivalent system, G^p , can be given by the transfer function (matrix)

$$G^p(s_p) = C^p (s_p I - A^p)^{-1} B^p + D^p. \quad (\text{F.1})$$

Since the matrices (A^p, B^p, C^p, D^p) read as

$$\begin{aligned} A^p &= \frac{2}{T_s} (A^d - I) (A^d + I)^{-1} \\ B^p &= \frac{4}{T_s} (A^d + I)^{-1} B^d \\ C^p &= C^d (A^d + I)^{-1} \\ D^p &= D^d - C^d (A^d + I)^{-1} B^d, \end{aligned} \quad (\text{F.2})$$

(F.1) can be rewritten as

$$G^p(s_p) = \left(\frac{2}{T_s} - s_p \right) C^d \left(s_p (A^d + I) - \frac{2}{T_s} (A^d - I) \right)^{-1} B^d + D^d. \quad (\text{F.3})$$

Thus, if we consider $D^d = 0$, G^p has unstable zeros at $s_p = \frac{2}{T_s}$ in each of its individual transfers.

It is important to highlight that, among other limitations, unstable zeros constrain the bandwidth of the closed-loop system (see, *e.g.*, [FL85, SP01]). This means that it is impossible to have stability and tight performance constraints (*e.g.*, reference tracking or disturbance rejection) in the pseudo-frequency range close to $\frac{2}{T_s}$, *i.e.*, for $\omega \approx \frac{2}{T_s}$.

Now, if we consider the relationship between the real frequency ω and ω , *i.e.*,

$$\omega = g(\omega) \triangleq \frac{2}{T_s} \tan \left(\frac{\omega T_s}{2} \right), \quad (\text{F.4})$$

we have $\omega = (1/4 + k) 2\pi/T_s$ with $k \in \mathbb{Z}$ when $\omega = \frac{2}{T_s}$. If we take the case $k = 0$, we are unable to enforce tight performance constraints around $\omega_s/4$, where ω_s corresponds to the sampling frequency in rad/s.

F.2 On the “Normalizability” of the MEMS Gyroscope Model

In Section 7.4, one the main assumptions is the “normalizability” of the gyroscope model, that is, the parameter-varying model of the gyroscope is such that, in a “normalized-time” space ($t_n = \omega_0 t$), the same system can be represented by a single LTI system. This is true for the 2nd-order resonator of Remark 7.1 (page 185). Here, we show that for a real MEMS gyroscope, we can also define a single LTI that (approximately) describes the real system under different temperatures. For this purpose, we realize different identification experiments (see [Col20]) with the same MEMS gyroscope, but at different temperatures. The Bode diagrams of the identified models are presented in Figure F.1. The models are in the PCT space, which is the same used for the controller design. In this figure, we can note that as the temperature increases, the resonance frequencies get lower. The modifications of the other parameters (*e.g.*, gain and quality factors) are much less perceptible.

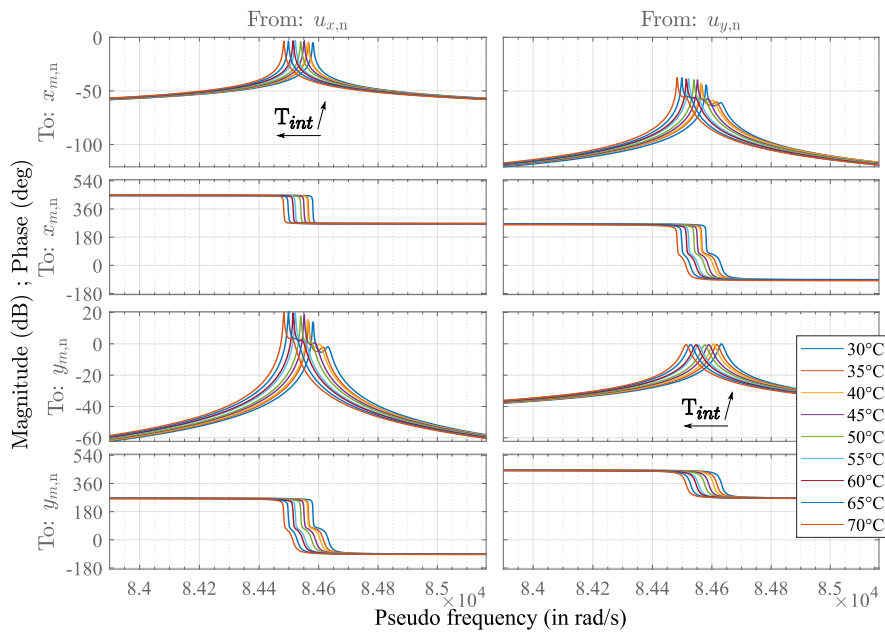


FIGURE F.1: Identified model of a MEMS gyroscope under different temperatures. Bode diagram in the pseudo frequency.

Now, if we normalize each model to its drive-mode resonance frequency $\omega_{0,x}$, we obtain the Bode diagrams presented in Figure F.2, where they are very close to each other. In this case, we could then consider that the model at 45 °C as a good approximation for the models at all temperatures in the normalized-frequency space, defining the fictitious model H_n^p . Some modeling errors are introduced (specially around the sense-mode resonance frequency – see transfer from $u_{y,n}$ to $y_{m,n}$), but this is the price to pay for the simple parametrization.

Therefore, with some approximations, the model of a real MEMS gyroscope is “normalizable”.

F.3 Details on the PCT Model of a 2nd-Order Resonator

Here, we intend to provide further details on $G^{\omega_{0,x}}$ when analyzing its PCT model, $G^{p,\omega_{0,x}}$. For this purpose, we first compute, with the sampling period T_s , the DT model $G^{d,\omega_{0,x}}$ of $G^{\omega_{0,x}}$ (we highlight that the former one takes the presence of the zero-order holder into account). Then, we apply the bilinear transform on $G^{d,\omega_{0,x}}$, obtaining the PCT model G^{p,ω_0} . The CT

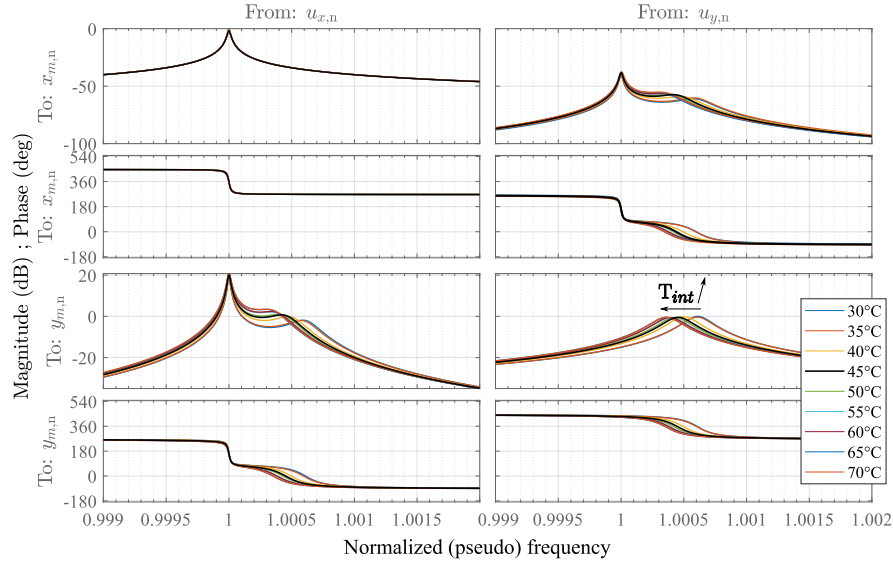


FIGURE F.2: Identified model of a MEMS gyroscope under different temperatures. Bode diagram in a normalized pseudo frequency.

model $G^{\omega_{0,x}}$ is given by

$$G^{\omega_{0,x}}(s) = \frac{x_m(s)}{u_x(s)} = \frac{k_{0,x}}{(s/\omega_{0,x})^2 + (s/\omega_{0,x})/Q_x + 1}. \quad (\text{F.5})$$

For $Q_x > 1/2$, the equivalent DT system $G^{d,\omega_{0,x}}$, with sampling period T_s , is given by (see [AW97, p. 55])

$$G^{d,\omega_{0,x}}(z) = k_{0,x} \frac{b_1 z + b_2}{z^2 + a_1 z + a_2}$$

with

$$\begin{aligned} a_1 &= -2e^{-\omega_{0,x}T_s/(2Q_x)} \cos(\omega_Q T_s) \\ a_2 &= e^{-\omega_{0,x}T_s/Q_x} \\ b_1 &= 1 - e^{-\omega_{0,x}T_s/(2Q_x)} (\zeta \sin(\omega_Q T_s) + \cos(\omega_Q T_s)) \\ b_2 &= e^{-\omega_{0,x}T_s/Q_x} + e^{-\omega_{0,x}T_s/(2Q_x)} (\zeta \sin(\omega_Q T_s) - \cos(\omega_Q T_s)) \\ \omega_Q &= \omega_{0,x} \frac{\sqrt{4Q_x^2 - 1}}{2Q_x} \\ \zeta &= (4Q_x^2 - 1)^{-1/2}. \end{aligned} \quad (\text{F.6})$$

Then, by applying the bilinear transform, *i.e.*, replacing z by $\frac{1+s_p T_s/2}{1-s_p T_s/2}$ (see (7.6), page 182), we obtain

$$G^{p,\omega_{0,x}}(s_p) = k_{0,x} \frac{(1 - s_p T_s/2)(1 + s_p z_1)}{(s_p/\tilde{\omega}_{0,x})^2 + (s_p/\tilde{\omega}_{0,x})/Q_x + 1} \quad (\text{F.7})$$

with

$$\begin{aligned} \tilde{\omega}_{0,x}^2 &= \frac{4}{T_s^2} \frac{1 + e^{-\omega_{0,x}T_s/Q_x} - 2e^{-\omega_{0,x}T_s/(2Q_x)} \cos(\omega_Q T_s)}{1 + e^{-\omega_{0,x}T_s/Q_x} + 2e^{-\omega_{0,x}T_s/(2Q_x)} \cos(\omega_Q T_s)} \\ \tilde{\omega}_{0,x} Q_x &= \frac{1}{T_s} \frac{1 + e^{-\omega_{0,x}T_s/Q_x} - 2e^{-\omega_{0,x}T_s/(2Q_x)} \cos(\omega_Q T_s)}{1 - e^{-\omega_{0,x}T_s/Q_x}} \\ z_1 &= \frac{T_s}{2} \frac{1 - e^{-\omega_{0,x}T_s/Q_x} - 2\zeta e^{-\omega_{0,x}T_s/(2Q_x)} \sin(\omega_Q T_s)}{1 + e^{-\omega_{0,x}T_s/Q_x} - 2e^{-\omega_{0,x}T_s/(2Q_x)} \cos(\omega_Q T_s)}. \end{aligned} \quad (\text{F.8})$$

For $Q_x \gg 1$, we can approximate $e^{-\omega_{0,x}T_s/(2Q_x)} \approx 1$, $1 + e^{-\omega_{0,x}T_s/Q_x} \approx 2$, $1 - e^{-\omega_{0,x}T_s/Q_x} \approx \omega_{0,x}T_s/Q_x$, $\omega_Q \approx \omega_{0,x}$ and $\zeta \approx 1/(2Q_x)$. Thus,

$$\begin{aligned}\tilde{\omega}_{0,x}^2 &\approx \frac{4}{T_s^2} \frac{1 - \cos(\omega_{0,x}T_s)}{1 + \cos(\omega_{0,x}T_s)} \implies \tilde{\omega}_{0,x} \approx \frac{2}{T_s} \tan\left(\frac{\omega_{0,x}T_s}{2}\right) = \omega_{0,x}, \\ \tilde{\omega}_{0,x} Q_x &\approx \frac{2Q_x}{T_s} \frac{1 - \cos(\omega_{0,x}T_s)}{\omega_{0,x}T_s} \implies Q_x \approx Q_x \operatorname{sinc}(\omega_{0,x}T_s), \\ z_1 &\approx \frac{T_s}{2} \frac{-\sin(\omega_{0,x}T_s)}{2Q_x(1 - \cos(\omega_{0,x}T_s))} \implies z_1 \approx \frac{1}{2Q_x\omega_{0,x}}.\end{aligned}\quad (\text{F.9})$$

In this case, (F.7) can then be rewritten as

$$G^{P,\omega_{0,x}}(s_p) = k_{0,x} \frac{(1 - (s_p/\omega_{0,x})\omega_{0,x}T_s/2)(1 + (s_p/\omega_{0,x})\omega_{0,x}/(2Q_x))}{(s_p/\omega_{0,x})^2 + (s_p/\omega_{0,x})/(Q_x \operatorname{sinc}(\omega_{0,x}T_s)) + 1}. \quad (\text{F.10})$$

F.4 Choice of the Fictitious Model of Example 7.1

Note that the structure of $G^{P,\omega_{0,x}}$ (see (F.10)) is slightly different from that of $G^{\omega_{0,x}}$ (see (F.5)). However, we can create a fictitious system $H^{P,\omega_{0,x}}$ that approximates $G^{P,\omega_{0,x}}$ for all $\omega_{0,x} \in [\omega_{0,x,1}, \omega_{0,x,2}]$ and that can be normalized. To this end, we evaluate the structural differences between G^{ω_0} and G^{P,ω_0} .

- (i) The resonance frequency $\omega_{0,x}$ is different from $\omega_{0,x}$ due to the distortion caused by the bilinear transform, see (7.10). So, instead of normalizing $G^{P,\omega_{0,x}}$ with respect to $\omega_{0,x}$, it is rather normalized with respect to $\tilde{\omega}_{0,x}$.
- (ii) The quality factor is reduced by a factor $\operatorname{sinc}(\omega_{0,x}T_s)$ due to the filtering effect of the ZOH. Then, from the performance point of view, we consider as worst case when the reduction is maximum, *i.e.*, for $\omega_{0,x} = \omega_{0,x,2}$, giving the smallest quality factor.
- (iii) The unstable zero that appears at $s_p = 2/T_s$ has the inconvenient properties to: (i) reduce the phase of the system; and (ii) impose limitations on the closed-loop bandwidth [FL85]. Then, we take as worst case the scenario where this zero is closer to the resonance frequency, *i.e.*, for $\omega_{0,x} = \omega_{0,x,2}$.
- (iv) The stable zero can be neglected since it is far from $\omega_{0,x}$.

Therefore, we can approximate $G^{P,\omega_{0,x}}$ (see (F.10)) by

$$H^{P,\omega_{0,x}}(s_p) = \frac{k_{0,x}(1 - (s_p/\omega_{0,x})/z_u)}{(s_p/\omega_{0,x})^2 + (s_p/\omega_{0,x})/(Q_x \operatorname{sinc}(\omega_{0,x,2}T_s)) + 1} \quad (\text{F.11})$$

with $z_u = \tan(\omega_{0,x,2}T_s/2)^{-1}$.

F.5 Details on the SISO Controllers

F.5.1 2DoF Drive-Mode SISO Controller

The choice of the weighting functions follows the procedure illustrated in Example 4.3 (page 88). They are presented with the obtained closed-loop transfer functions in Figure F.3 and Figure F.4. The only difference compared to the example is that, here, we enforce a

better disturbance rejection, obtaining $|T_{d_{Cor,x} \rightarrow \varepsilon_x}(j\omega_{exc})| < -100$ dB and $|T_{x_m^{ref} \rightarrow \varepsilon_x}(j\omega_{exc})| < -90$ dB.

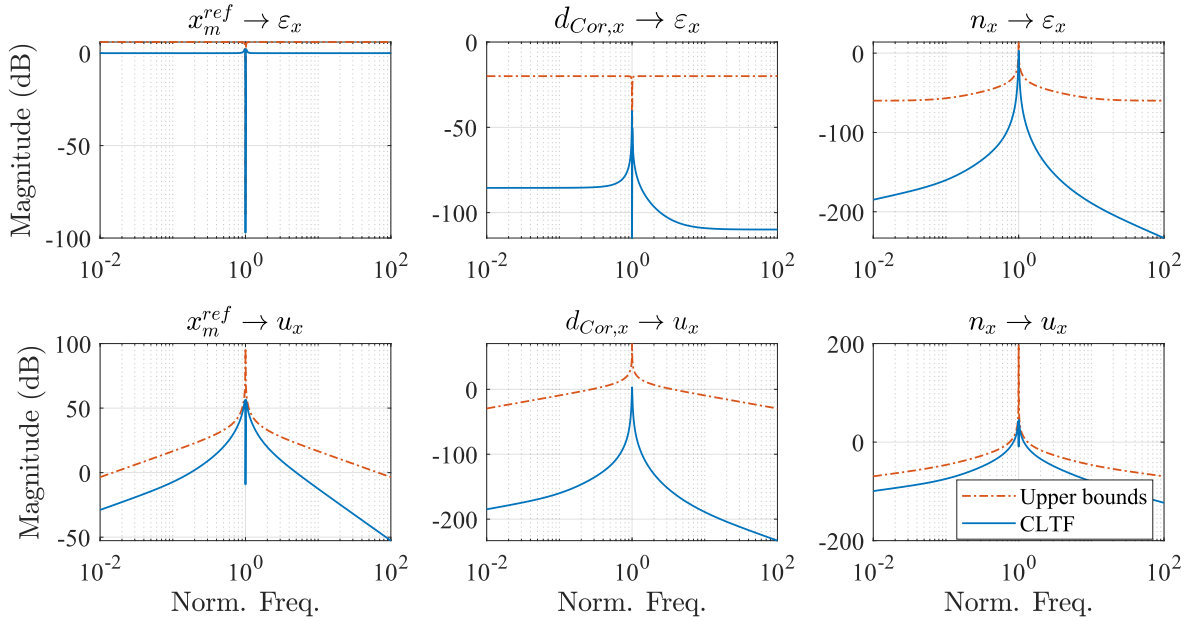


FIGURE F.3: Upper bounds and closed-loop transfer functions of the drive-mode control loop.

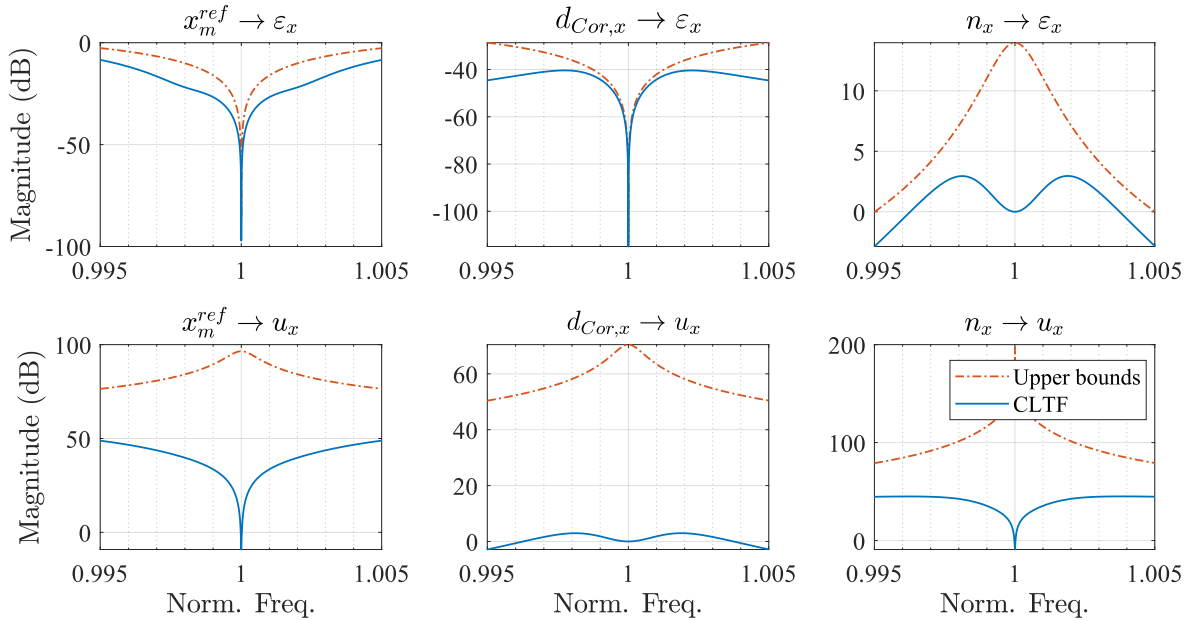


FIGURE F.4: Upper bounds and closed-loop transfer functions of the drive-mode control loop. Zoom around ω_{exc} .

The (normalized) controller, obtained with $\gamma = 0.9803$, is given by $K_{x,n}^P = [K_{x1,n}^P, K_{x2,n}^P]$ with

$$K_{x1,n}^P(s_n) = \frac{71.36 \cdot s_n(s_n + 0.6952)(s_n + 54.97)(s_n^2 + 3.108 \cdot 10^{-3}s_n + 0.9973)}{(s_n + 0.6949)(s_n^2 + 0.0303s_n + 0.9817)(s_n^2 + 0.02237s_n + 1)} \cdot \frac{(s_n^2 + 9.803 \cdot 10^{-3}s_n + 1)(s_n^2 + 3.108 \cdot 10^{-3}s_n + 1.003)}{(s_n^2 + 3.465 \cdot 10^{-7}s_n + 1)(s_n^2 + 0.03049s_n + 1.019)(s_n^2 + 12.94s_n + 83.59)}$$

$$K_{x2,n}^P(s_n) = \frac{-0.0261 \cdot s_n(s_n + 57.79)(s_n + 7.482)(s_n + 0.6952)}{(s_n + 0.6949)(s_n^2 + 0.0303s_n + 0.9817)(s_n^2 + 0.02237s_n + 1) \cdot (s_n + 0.1337)(s_n^2 + 0.02527s_n + 1)(s_n^2 + 2.221 \cdot 10^{-3}s_n + 1) \cdot (s_n^2 + 3.465 \cdot 10^{-7}s_n + 1)(s_n^2 + 0.03049s_n + 1.019)(s_n^2 + 12.94s_n + 83.59)}$$

and $s_n = s_p/\omega_{0,x}$. Its Bode diagram is presented in Figure F.5, which is similar to the one of Example 4.3. However, since we ask for a better disturbance rejection at $\omega = \omega_{exc}$, the present controller has an important resonance at this frequency.

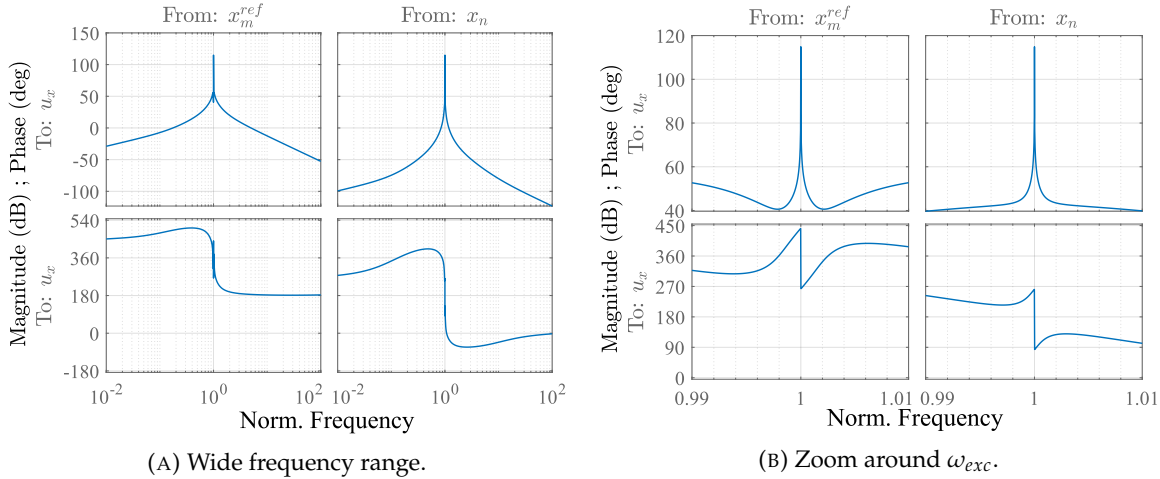


FIGURE F.5: Bode diagrams of the drive-mode controller.

F.5.2 1DoF Sense-Mode SISO Controller

The choice of the weighting functions follows the procedure of Example 4.4 (page 94). They are presented with the obtained closed-loop transfer functions in Figure F.6 and Figure F.7. The results are very similar to those of the example. The (normalized) controller, obtained with $\gamma = 1.0068$, is given by

$$K_{y,n}^P(s_n) = \frac{-8.433(s_n - 18.2)(s_n + 0.6229)(s_n + 9.745 \cdot 10^{-3})}{(s_n + 0.631)(s_n^2 + 0.3154s_n + 0.7102)(s_n^2 + 1.039 \cdot 10^{-5}s_n + 1) \cdot (s_n + 9.744 \cdot 10^{-4})(s_n^2 + 0.01012s_n + 1.019) \cdot (s_n^2 + 0.3365s_n + 1.416)(s_n^2 + 17.85s_n + 133.4)}$$

with $s_n = s_p/\omega_{0,x}$. Its Bode diagram is presented in Figure F.8, which is also very similar to the one of Example 4.4. Small differences are mainly due to the differences on the sense-mode models. Here, we highlight that the obtained relative error for the Coriolis force estimation is close to -80 dB, *i.e.*, $\left| T_{d_{Cor,y} \rightarrow \epsilon_{est}}(j\omega_{exc}) \right| \approx -80$ dB.

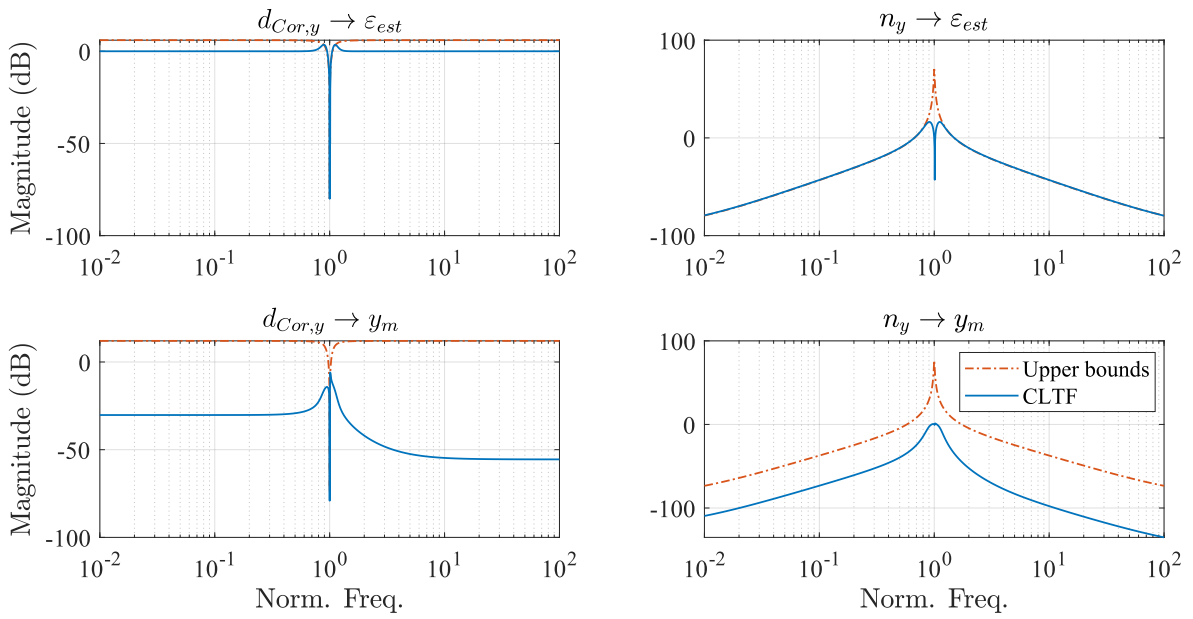


FIGURE F.6: Upper bounds and closed-loop transfer functions of the sense-mode control loop.

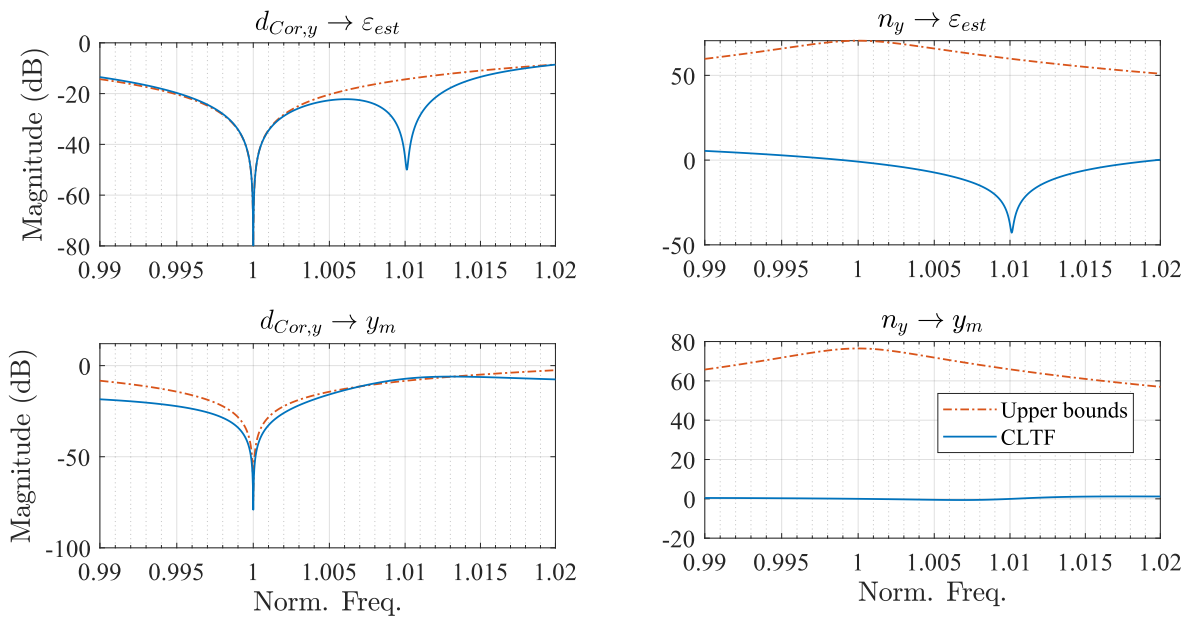


FIGURE F.7: Upper bounds and closed-loop transfer functions of the sense-mode control loop. Zoom around ω_{exc} .

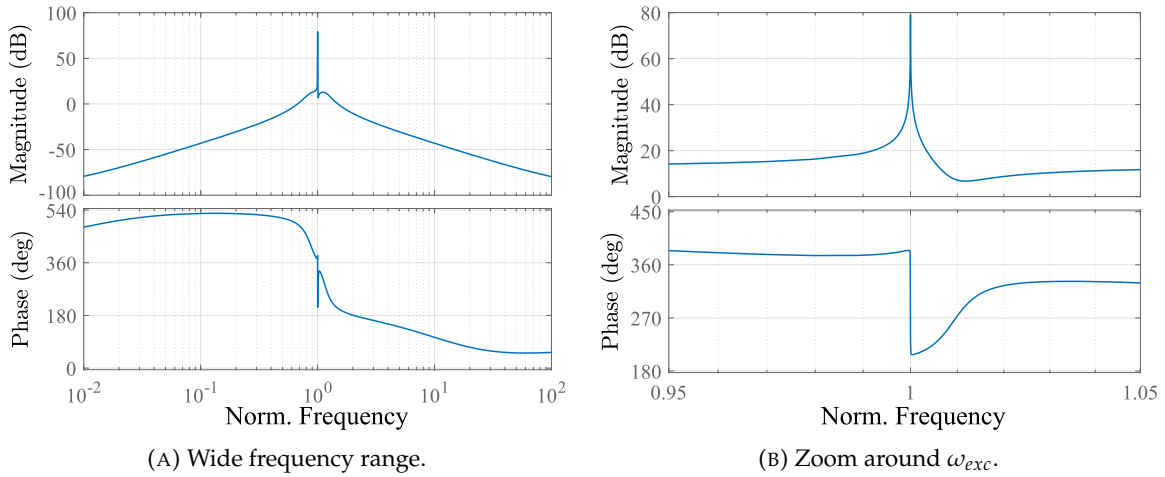


FIGURE F.8: Bode diagrams of the sense-mode controller.

F.6 Details on the MIMO Controller with Joint Estimation

The choice of the weighting functions also follows the procedure illustrated in Example 4.6 (page 104). They are presented with the obtained closed-loop transfer functions in Figure F.9 and Figure F.10. The only difference compared to the example is that, here, we enforce a better disturbance rejection, obtaining $|T_{d_{Cor,x} \rightarrow \varepsilon_x}(j\omega_{exc})| < -90$ dB and $|T_{x_m^{ref} \rightarrow \varepsilon_x}(j\omega_{exc})| < -72$ dB, as required. For the Coriolis force, we also obtain a relative error for the estimation that is close to -80 dB, *i.e.*, $|T_{d_{Cor,y} \rightarrow \varepsilon_{est}}(j\omega_{exc})| \approx -80$ dB.

The Bode diagram of the multivariable controller, obtained with $\gamma = 0.9878$, is presented in Figure F.11 and Figure F.12, which is similar to the one of Example 4.6. However, similar to the SISO case, since we ask for a better drive-mode disturbance rejection at $\omega = \omega_{exc}$, the present controller has an important resonance at this frequency on the first row, which computes u_x .

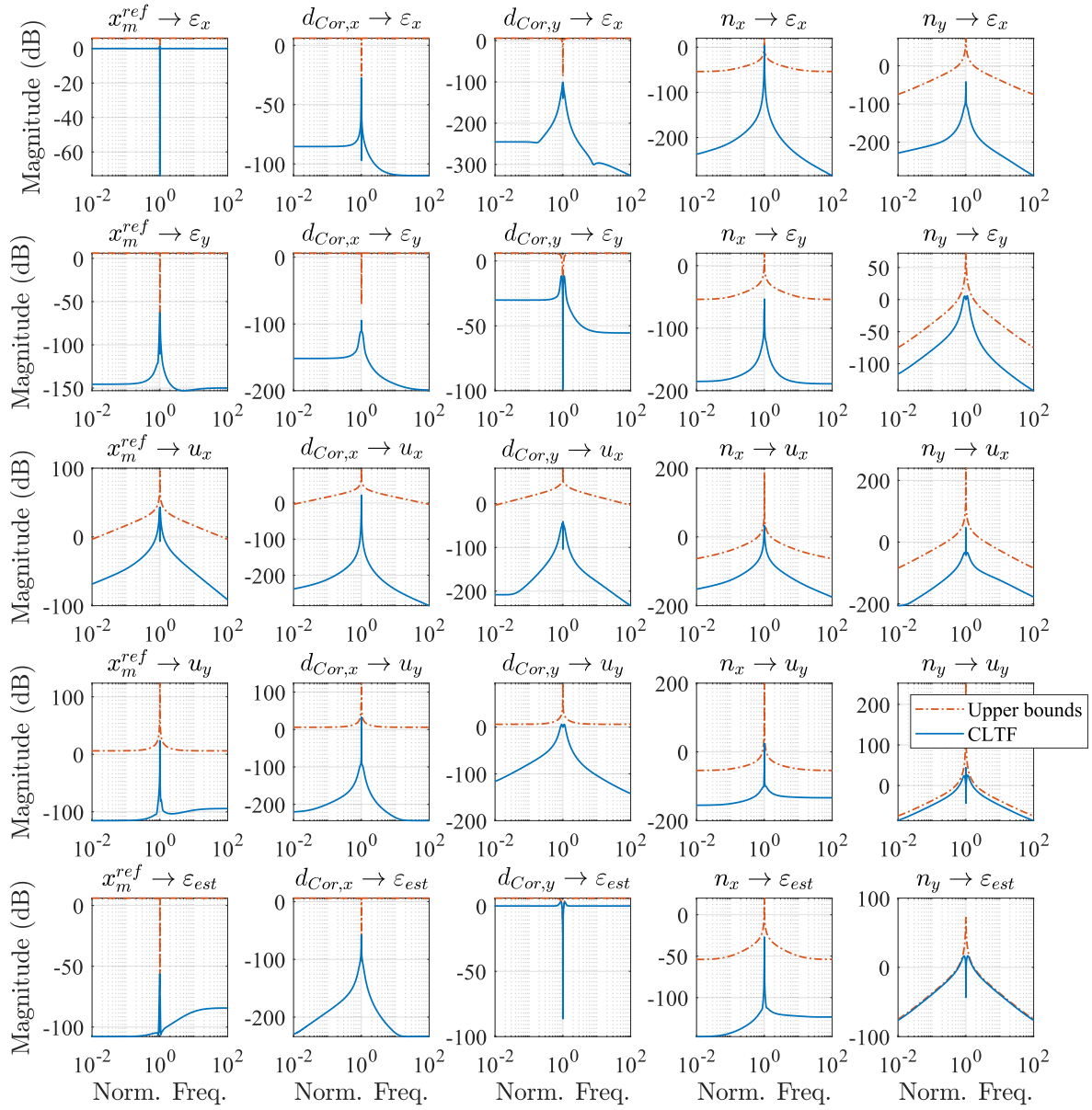


FIGURE F.9: Upper bounds and closed-loop transfer functions of the MIMO approach.

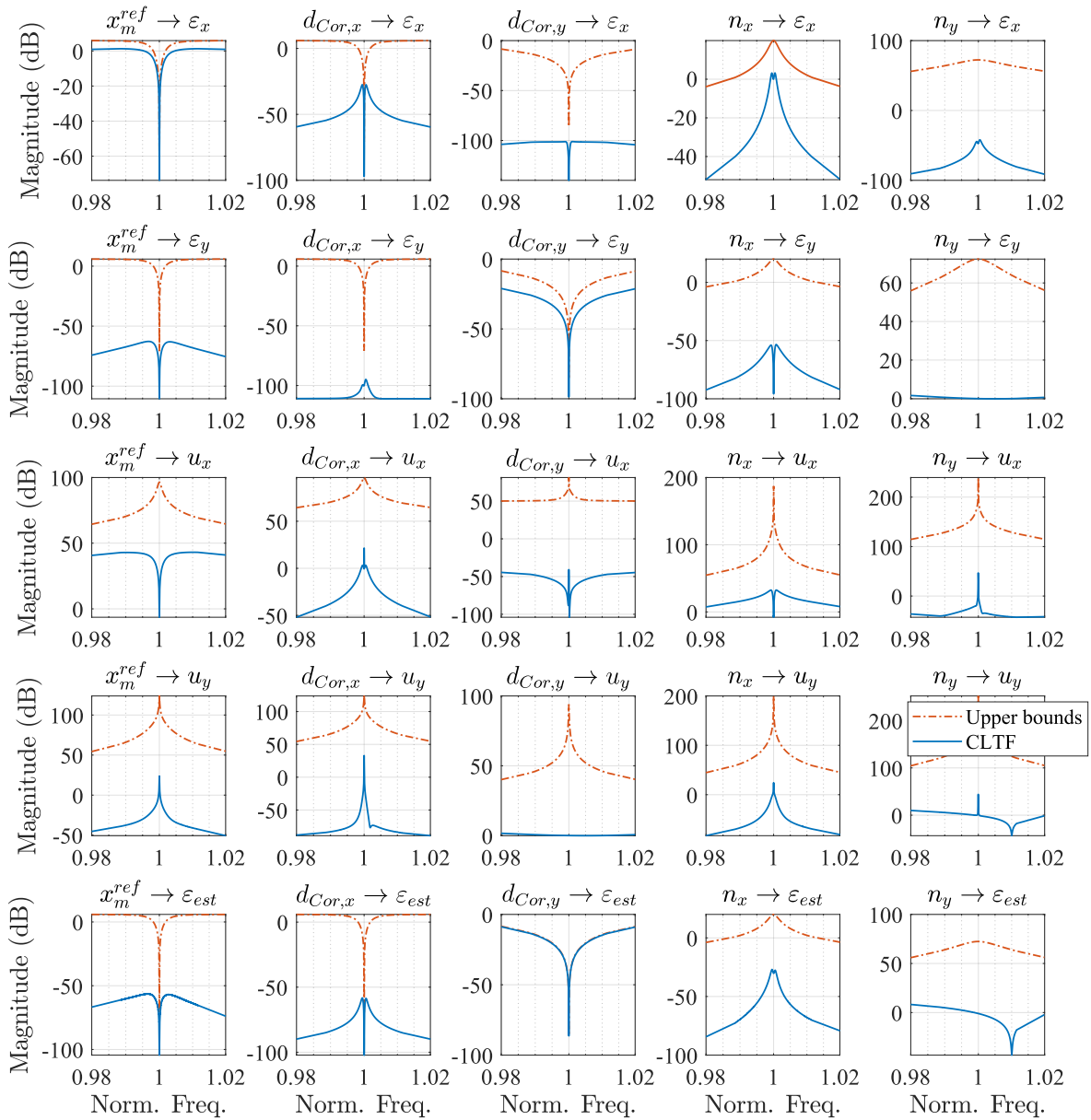


FIGURE F.10: Upper bounds and closed-loop transfer functions of the MIMO approach. Zoom around ω_{exc} .

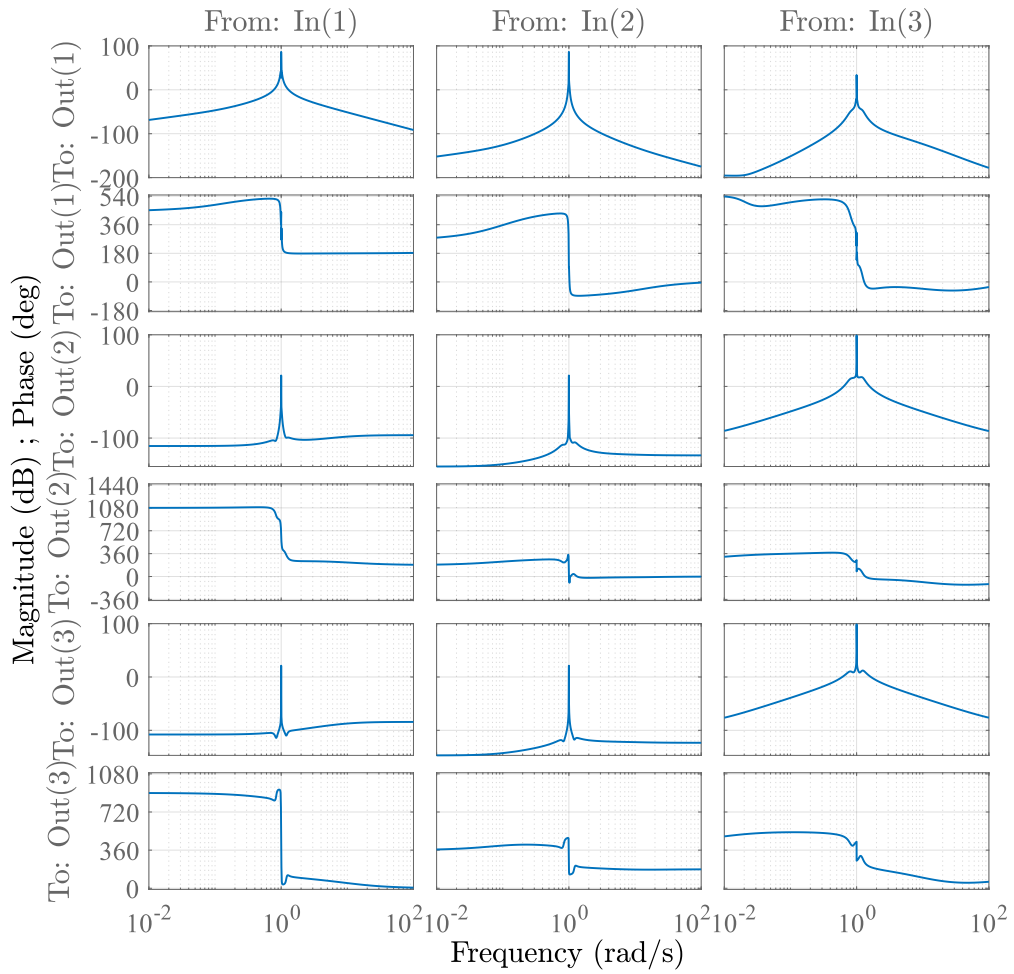


FIGURE F.11: Bode diagram of the MIMO controller.

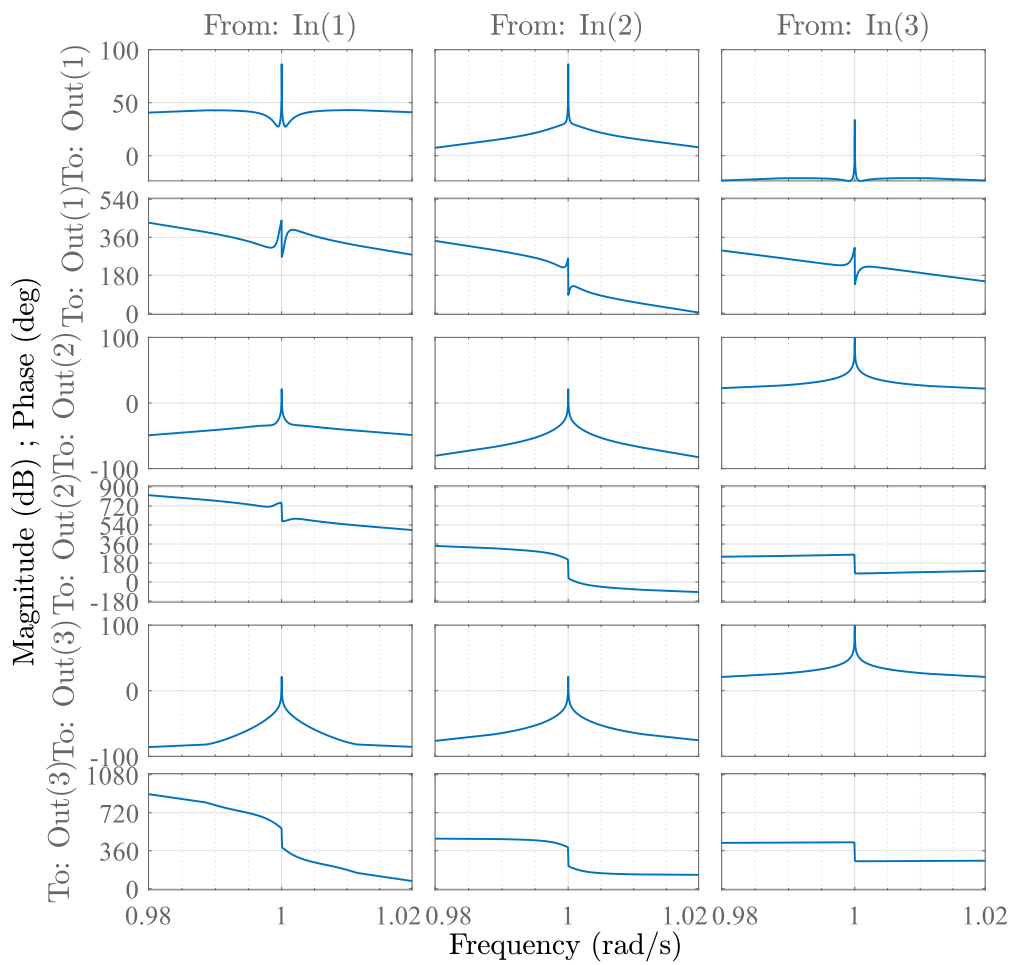


FIGURE F.12: Bode diagram of the MIMO controller. Zoom around ω_{exc} .